

Development of therapeutic glycopolymers for the treatment of peripheral neuropathies and viral infections

Inauguraldissertation

zur

Erlangung der Würde eines Doktors der Philosophie

vorgelegt der

Philosophisch-Naturwissenschaftlichen Fakultät

der Universität Basel

von

Butrint Aliu

Originaldokument gespeichert auf dem Dokumentenserver der Universität Basel edoc.unibas.ch

Basel, 2023

Genehmigt von der Philosophisch-Naturwissenschaftlichen Fakultät auf Antrag von:

Prof. Dr. Daniel Ricklin, Department Pharmazeutische Wissenschaften, Universität Basel

Prof. em. Dr. Beat Ernst, Department Pharmazeutische Wissenschaften, Universität Basel

Prof. Dr. Henriette Meyer zu Schwabedissen, Department Pharmazeutische Wissenschaften,
Universität Basel

Dr. John Gatfield, Idorsia Pharmaceuticals Ltd., Allschwil

Basel, 21.09.2021

Prof. Dr. Marcel Mayor

Dean of Faculty

Summary

Immune mediated neuropathies are a group of heterogeneous disorders affecting the peripheral nervous system. Characteristic for these diseases is the involvement of an immune response against autoantigens on axonal membranes or surrounding myelin. In a variety of peripheral neuropathies autoantibodies target glycan or peptide epitopes in the nodal and paranodal region. These polyneuropathies can have chronic or acute manifestations but generally respond to immunotherapies. Most treatment options however target the immune system unspecifically and can cause serious adverse effects. In some cases, patients do not respond to treatment or even show deterioration. In anti-MAG neuropathy and multifocal motor neuropathy the antigen-specific pathogenic autoantibodies have been well described and therapeutic intervention is aimed at reducing antibody levels or interfering with its effector functions.

A recently developed glycopolymer-based therapeutic approach for the treatment of anti-MAG neuropathy (PPSGG) specifically targets these disease-causing autoantibodies by presenting multiple carbohydrate mimetic copies of its antigen on a biodegradable poly-L-lysine (PLL) scaffold.

In this thesis we review the importance of a reduction of autoantibody levels for clinical improvement in anti-MAG neuropathy, discuss the mechanism of action of PPSGG, evaluate its safety profile, and develop new glycopolymers to treat related peripheral neuropathies and viral infections.

Despite clinical evidence for the pathogenicity of anti-MAG IgM autoantibodies, the significance of antibody titers as a predictive factor for response to therapy remains controversial. Current literature does not provide conclusive evidence on the association between reduced anti-MAG IgM titers and clinical improvement of neuropathic symptoms. We performed a retrospective study to test our hypothesis that changes in antibody titers are correlated with clinical response in anti-MAG neuropathy patients. We included 50 studies involving 410 anti-MAG neuropathy patients undergoing immunotherapy in our analysis and characterized relative change in anti-MAG IgM titers, paraprotein levels, and total IgM prior, during, or post-treatment. Patients were categorized according to their response to treatment into “responders”, “non-responders”, or “acute deteriorating” and the studies were qualified as “supportive” or “not supportive”. 40 studies supported the hypothesis that “responders” showed relative reduction of anti-MAG IgM titers and “non-responders” did not show significant change in antibody titers, confirming our hypothesis.

In an experimental study we further investigated the pharmacodynamic properties of PPSGG and tested its inhibitory potential on peripheral nerves. The polymer selectively prevented binding of anti-MAG IgM from patient sera to non-human primate sciatic nerves. In an immunological mouse model, PPSGG showed superiority in removing anti-MAG IgM antibodies compared to B-cell depletion with an anti-CD20 antibody (analogous to Rituximab). Safety evaluation with human and murine peripheral blood mononuclear cells (PBMC) showed no interaction. Furthermore, no increase in systemic inflammatory markers was observed in mice or in human PBMC *ex vivo* after treatment.

We investigated the binding characteristics of PPSGG and anti-MAG IgM as well as pharmacokinetic properties to understand the mode of action of the glycopolymer. First, physicochemical and morphological characteristics of the polymer were investigated. The linear rod-shaped PPSGG showed an approximate length of 100 nm, a hydrodynamic radius of around 60 nm, and a highly negative charge (-46 mV). Because of its high negative charge density, it was readily taken up by liver- and spleen-resident macrophages through scavenger receptors, explaining the previously observed short half-life in mice (approx. 17 min). No large aggregate formation *in vitro* and no immune complex deposition in murine liver, spleen, kidney, or brain was observed. Despite the extensive uptake in Kupffer cells in the liver, it did not exhibit hepatotoxic effects in a human hepatic tissue *ex vivo*. In the presence of anti-MAG IgM, PPSGG preferentially formed complexes in a 1:1 or 1:2 stoichiometry *in vitro*, supporting previously reported dose titration experiments with an immunological mouse model.

Analogous to the approach for the treatment of anti-MAG neuropathy, we developed a glycopolymer displaying GM1 carbohydrate mimetics on a PLL backbone to treat anti-GM1 mediated peripheral neuropathies. A series of ten mimetics was synthesized and conjugated to the PLL backbone for testing with MMN patient sera. The specificity and inhibitory potential of the glycopolymers was assessed by competitive ELSIA. After screening of 22 MMN patient samples we identified three interesting candidates for further evaluation in functional assays. One of most active glycopolymers was carrying the natural GM1 carbohydrate epitope and was excluded for further selection, because the aim of the project was to develop simplified glycomimetics that retain or increase binding affinity while simultaneously reducing synthetic complexity. One of the two remaining candidates showed high temperature sensitivity and could not inhibit anti-GM1 antibody binding to GM1 at physiological temperatures. The remaining glycopolymer, composed of the natural GM1 core epitope with only a replacement of the terminal glucose by a tyramine moiety, prevented anti-GM1 antibody binding to

terminal axonal networks *in vitro* and *ex vivo* using an animal model for acute motor axonal neuropathy.

Being confronted with the surge of the COVID-19 pandemic and the rapid progress in scientific discoveries and understanding of SARS-CoV-2, we applied our expertise in glycopolymer development to tackle SARS-CoV-2 infections. Increasing evidence was pointing at the involvement of DC-SIGN in the pathogenesis of COVID-19. Interaction of viral spike protein with DC-SIGN was reported to lead to internalization of the virus by immune cells, thus presenting an alternative entry receptor for SARS-CoV-2, independent of ACE2. Infection of immune cells is involved in exaggerated immune response in severe COVID-19. It was later reported that DC-SIGN levels were increased in severe COVID-19 patients showing elevated levels of proinflammatory macrophages, inflammatory cytokines and chemokines. Inhibition of the interaction between DC-SIGN and spike protein might serve as a strategy to prevent these severe disease courses. We demonstrated that mannose-functionalized PLL glycopolymers efficiently inhibit the attachment of spike protein to DC-SIGN presenting cells with picomolar affinity in a competitive setting. Pre-treatment of the cells lead to prolonged receptor internalization and protected the cells for up to 6 h from virus binding. Moreover, DC-SIGN acts as a receptor for multiple viruses and we could additionally demonstrate effective inhibition of HIV and Ebola viral glycoprotein binding to DC-SIGN presenting cells. This host-directed approach might not only be applicable for multiple unrelated viral infections but could be unaffected by the rapidly mutating variants of SARS-CoV-2.

In a follow-up study we reported the discovery of a new class of potent glycomimetic DC-SIGN ligands from a library of triazole-based mannose analogs. Structure-based optimization yielded a glycomimetic ligand with over 100-fold improved binding affinity compared to methyl α -D-mannopyranoside. Multivalent display of the ligand on PLL was able to inhibit SARS-CoV-2 spike glycoprotein binding to DC-SIGN expressing cells, as well as DC-SIGN mediated trans-infection of ACE2 expressing cells by SARS-CoV-2 spike protein expressing viruses in nanomolar concentrations.

| | |
|---|-----------|
| SUMMARY | 3 |
| INTRODUCTION | 7 |
| IMMUNE MEDIATED NEUROPATHIES | 7 |
| ANTI-MAG NEUROPATHY | 8 |
| <i>Introduction.....</i> | 8 |
| MAG | 9 |
| <i>Disease mechanism.....</i> | 9 |
| <i>Current treatment.....</i> | 10 |
| MULTIFOCAL MOTOR NEUROPATHY..... | 13 |
| <i>Introduction.....</i> | 13 |
| GM1..... | 13 |
| <i>Disease mechanism.....</i> | 14 |
| <i>Current treatment.....</i> | 15 |
| REFERENCES | 18 |
| RESULTS..... | 27 |
| CHAPTER 1 | 27 |
| <i>Retrospective study: Decrease in serum anti-MAG autoantibodies is associated with therapy response in anti-MAG neuropathy patients</i> | 27 |
| CHAPTER 2 | 96 |
| <i>Selective inhibition of anti-MAG IgM autoantibody binding to myelin by an antigen-specific glycopolymer</i> | 96 |
| CHAPTER 3 | 130 |
| <i>Glycopolymer binds pathogenic IgM autoantibodies and pulls them into the mononuclear phagocyte system for degradation</i> | 130 |
| CHAPTER 4 | 172 |
| <i>Development of an anti-GM1 antibody-specific therapy for the treatment of Guillain-Barré Syndrome and Multifocal Motor Neuropathy.....</i> | 172 |
| CHAPTER 5 | 230 |
| <i>Poly-L-lysine Glycoconjugates Inhibit DC-SIGN-mediated Attachment of Pandemic Viruses.....</i> | 230 |
| CHAPTER 6 | 265 |
| <i>Sweet Drugs for Bad Bugs: A Glycomimetic Strategy Against the DC-SIGN-mediated Dissemination of SARS-CoV-2.....</i> | 265 |

Introduction

Immune Mediated Neuropathies

Immune-mediated neuropathies represent a group of heterogeneous peripheral nerve disorders within the spectrum of neuromuscular disease. Characteristic is the involvement of various pathophysiological inflammatory components. They can be classified according to their diverse clinical signs and symptoms, disease time course, and biomarkers. Diagnosis of the disorders can be rather complex and despite recent progress in the development of preclinical models and the finding of novel therapeutic targets, the origins and underlying pathological molecular and cellular disease mechanisms remain unknown for most of these disorders.

Generally, these polyneuropathies can be described by immune responses targeting autoantigens in the peripheral nervous system (PNS). Depending on the anatomical and functional localization of the disruption they cause different clinical signs including sensory symptoms like numbness, pain, and paresthesia or motor symptoms like muscle weakness and wasting. More broadly, they are divided into acute disorders such as Guillain–Barré syndrome (GBS), including many of its subtypes, and chronic disorders, such as chronic inflammatory demyelinating polyradiculoneuropathy (CIDP), multifocal motor neuropathy (MMN), and anti-myelin associated glycoprotein (anti-MAG) neuropathy.¹⁻⁴ Therapeutic interventions include immunomodulatory and cytostatic treatment using plasma exchange, IVIg intravenous immunoglobulin (IVIg), corticosteroids, anti-B cell monoclonal antibodies, and supportive care.^{5,6}

Response to treatment with these therapies suggests the involvement of humoral and cellular immune components in the development of the disease and has been confirmed by the identification of immune cell infiltration, autoreactive antibody and complement deposition in nerve biopsy samples.⁷⁻¹⁰ Many of these autoantibodies recognize proteins and glycolipids located in the Schwann cells or axonal membranes at the node of Ranvier. In anti-MAG neuropathy patients carry autoantibodies against the carbohydrate epitope HNK-1, present on multiple myelin antigens such as the glycoprotein MAG and the glycolipid SGPG. In different GBS variants autoantibodies against multiple gangliosides such as GM1, GM1b, GD1a and GalNAc- GD1a have been described.¹¹ CIDP variants usually show the presence of antibodies that disrupt adhesion molecules (anti-neurofascin and anti-contactin autoantibodies) located at the paranode (Figure 1).¹² Recent progress in the identification of these biomarkers has paved

the way for more specific diagnostic criteria and the development and application of more specific treatment options. In the following chapters the focus will be on immune mediated neuropathies with involvement of autoreactive antibodies targeting carbohydrate epitopes.

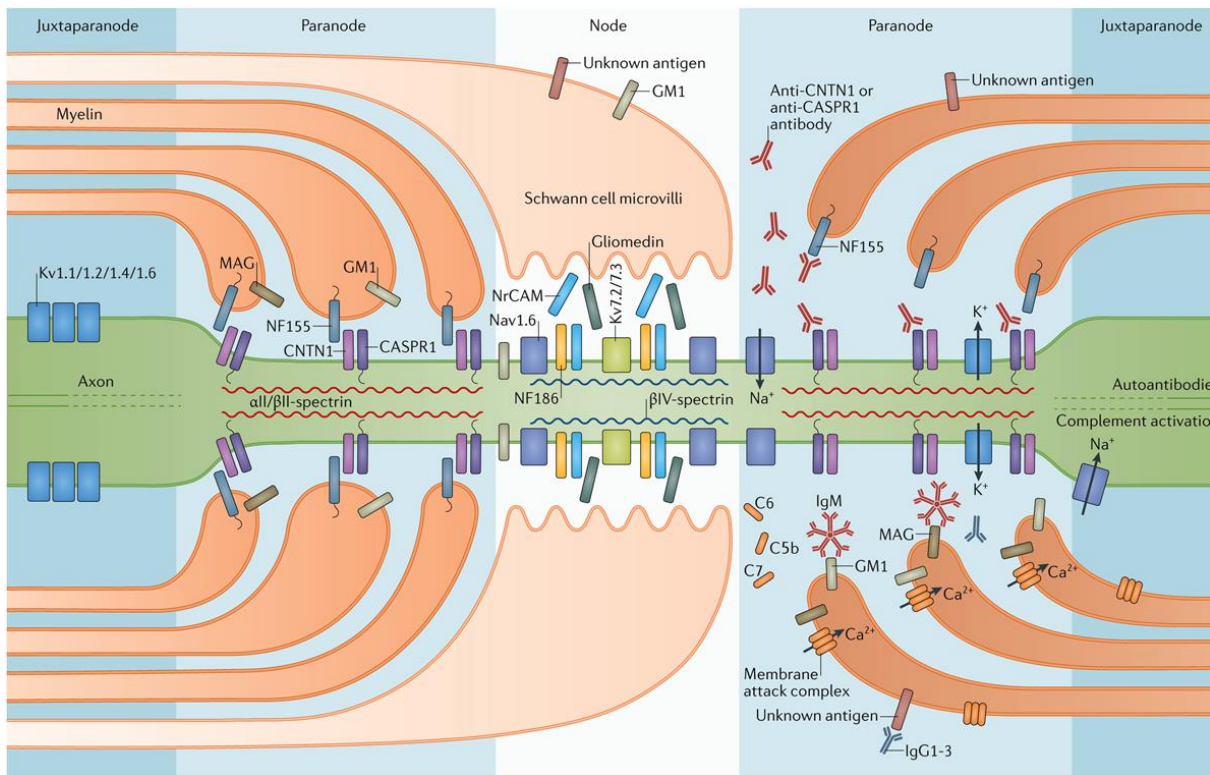


Figure 1. Node of Ranvier depicting multiple components that are targets of autoantibodies in autoimmune neuropathies. Disruption of the paranode is mediated by IgG autoantibodies in CIDP variants affecting NF155 and CNTN1 and IgM autoantibodies in that bind to MAG in anti-MAG neuropathy or GM1 in MMN. (Figure from¹²⁾)

Anti-MAG neuropathy

Introduction

Anti-MAG neuropathy is a rare form of acquired demyelinating polyneuropathy associated with IgM monoclonal gammopathy of unknown significance (MGUS)¹³ Monoclonal gammopathy, also called proteinemia, or plasma cell dyscrasia describes a hematological condition where excessive amounts of IgM immunoglobulins are produced by abnormal proliferation of B cells or plasma cells.¹⁴ In the case of anti-MAG, highly elevated IgM levels arise from expansion of somatically hypermutated B cell clones that acquire IgM secretory activity.¹⁵ The disease is characterized by a slowly progressing demyelinating neuropathy primarily affecting sensory nerves.¹⁶ Patients have high serum levels of pathogenic IgM autoantibodies that recognize the human natural killer 1 (HNK-1) carbohydrate epitope on

MAG.⁴ Anti-MAG is a rare disease and has a prevalence of about 1 in 100,000, affecting men 2.7 more frequently compared to women and usually has a disease onset after the age of 50, with increasing prevalence at higher age.^{13, 17-19} The symptoms of the chronic neuropathy are sensorimotor deficits that start in the fingers and toes; sensory ataxia, paresthesia, muscle weakness, neuropathic pain, and tremor. Over the course of the disease, the patients can become severely disabled and wheelchair-bound.^{20,21} There is evidence that a reduction of anti-MAG IgM serum titers leads to clinical improvement.²²⁻²⁴

MAG

MAG a member of the sialic acid-binding immunoglobulin-like lectins (siglecs), classified as Siglec-4, is located in the periaxonal membranes of oligodendroglial cells of the central nervous system and in Schwann cells of the PNS, where it is localized in the paranodal loops and Schmidt-Lanterman incisures.^{6, 25, 26} MAG is involved in the formation and maintenance of the myelin sheaths, interacting with the cytoskeletal components of the Schwann cells as adhesion mediator between the axon and the myelinating Schwann cells, and simultaneously acting as a ligand for axonal receptors and as a glial receptor for axonal signals.^{27,28} As a siglec, MAG preferentially binds N-acetylneuraminic acid (Neu5Ac), but is itself also heavily glycosylated. It displays eight glycosylation sites that carry N-linked oligosaccharides, with all of them carrying the HNK-1 epitope sulfated trisaccharide 3-O-sulfo- β -D-GlcA-(1 \rightarrow 3)- β -D-Gal-(1 \rightarrow 4)-D-GlcNAc that is recognized by the anti-MAG IgM autoantibodies.²⁹

Besides MAG, the HNK-1 epitope is additionally expressed on multiple myelin antigens such as the two glycolipids sulfoglucuronyl paragloboside (SGPG) and sulfoglucuronyl lactosaminyl paragloboside (SGLPG), as well as on the myelin glycoprotein zero (P0) and peripheral myelin protein-22 (PMP22).^{28, 30}

Disease mechanism

Sural nerve biopsies of affected patients show demyelination and widening of myelin lamellae, as well as deposits of anti-MAG IgM on myelin.^{31,32} IgM antibodies localized in areas of split myelin indicate a role of the antibodies in myelin disintegration, with a correlation between the level of penetration of the antibodies in the myelinated fibers and the extent of widening.³³ Studies have also reported the deposition of complement proteins co-localized with anti-MAG IgM.^{34, 35} These observations suggest a pathogenic mechanism of complement activation

through anti-MAG IgM autoantibodies that results in myelin damage. Further proof of the pathogenicity of anti-MAG antibodies for the development of anti-MAG neuropathy was provided, when passive transfer of patients' antibodies to healthy animals (cats³⁶, chicks³⁷) lead to peripheral nerve damage with similar disease characteristics to the human disease.³⁸ Additionally, active immunization with SGPG induced ataxic sensory neuropathy in a cat model that was similar to human anti-MAG neuropathy.³⁹

Current treatment

The treatment of anti-MAG neuropathy patients is directed towards either reduction of anti-MAG IgM levels, targeting of antibody producing B cells, or blocking of downstream effects caused by the antibodies, e.g. complement factors. Current treatment choices are governed by disease severity and burden for the patients as well as probability for clinical improvement and cost.⁴⁰ Clinical improvement can be assessed by different scoring systems such as the Inflammatory Cause and Treatment (INCAT) disability scale or Overall Neuropathy Disability Scale (ONLS). There is, however, no anti-MAG neuropathy specific standardized quantitative assessment for clinical outcome. This has led to issues in comparing different therapeutic interventions and their respective effects, although to date no randomized controlled study has been able to show high level evidence for long-term clinical improvement. Nevertheless, some of these treatments have shown to be beneficial to some patients and need to be assessed on an individual case by case basis.⁴¹ Following off-label therapeutic options have been investigated by clinicians throughout the years (a detailed overview over the clinical studies can be found in Chapter 1).

Chemotherapeutics

Some of the early treatment options after the discovery of anti-MAG neuropathy were chemotherapy and cytotoxic drugs, with some success in single cases, but with the majority of the patients not responding to therapy.⁴² Patients have been treated with fludarabine⁴³ and cladribine⁴⁴, both purine analogues, with cyclophosphamide in combination with PE⁴⁵ or more recently with Rituximab⁴⁶. If an underlying lymphoproliferative condition is diagnosed, patients have been treated with Rituximab in addition to bendamustine, bortezomib and thalidomide-based options.⁴⁷ Most of these harsh cytostatic therapies unfortunately lead to

severe adverse effects and generally act via unspecific immunosuppression, with some of them having fatal outcomes.⁴⁸

Plasma exchange

Plasma exchange (or plasmapheresis) is an extracorporeal therapy aimed at physically removing disease-causing anti-MAG IgM autoantibodies from the blood circulation. In this process the patients' plasma containing the anti-MAG IgM is replaced with clean substitute plasma. It has been shown to be successful in improving neurological symptoms in some patients, either accompanying chemotherapy or as a standalone treatment, with benefits lasting up to three years.^{45, 49} However, no studies could show systematic significant improvement under PE treatment.⁴¹

Intravenous immunoglobulin

Purified immunoglobulin from healthy donors is a popular therapeutic option to treat many different health conditions, and especially immune mediated diseases.⁵⁰ In the case of acute immune mediated neuropathies it has replaced PE in many centers for the treatment of acute immune neuropathies because of its convenience and availability.⁵¹ According to placebo-controlled studies, there might be a short-term benefit in anti-MAG patients,^{41, 52} however the reported significant effect might not be clinically relevant.⁵³

Corticosteroids

Immunosuppressive glucocorticoids like dexamethasone and prednisolone have been used either as monotherapy or in combination with PE or cytotoxic therapies. Even if some patients responded to dexamethasone treatment, it was not recommended as first line therapy because of the severe side effects.⁵⁴ Besides that, there is no clinical data showing statistically significant benefits for patients.⁴¹

Interferon alpha-2a

Results of trials with interferon alpha-2a are inconclusive. While a clinical study found interferon alpha-2a to be superior to treatment with IVIg⁵⁵, the same author later concluded in

a second placebo-controlled trial, that the effects were not statistically significant.⁵⁶ They point out the need for double-blind randomized clinical studies versus placebo in these disorders. Additionally, highlighting another problem of rare disorders, they criticize the dependence on studies with small cohorts, two factors that potentially influence these results.

Rituximab

The anti-CD20 monoclonal antibody rituximab is used most frequently to treat anti-MAG neuropathy patients and has been the most promising prospect backed by many case reports and clinical studies.^{6, 24, 41} The monoclonal antibody recognizes B cells expressing surface CD20 and causes antibody-dependent cellular toxicity and complement-mediated cytotoxicity. Placebo-controlled studies have shown reduction in circulating B cells with reduction in anti-MAG IgM serum titers, as well as resulting clinical improvements.⁵⁷ However, a more recent study did not show significant improvement in primary-outcome measures (absolute change in inflammatory neuropathy cause and treatment (INCAT) sensory score (ISS)), but reported significant improvement in secondary outcome measures (relative ISS, number of B cells, CD20⁺ B cell count, and anti-MAG antibody titers).⁵⁸ Most notably, the reduction of circulation B cells and anti-MAG IgM titers has been linked to clinical improvements,⁴⁸ while high levels of memory B cells have been associated with unfavorable clinical responses.¹⁵ Apart from unselectivity for anti-MAG IgM producing B cells, by targeting all CD20 expressing B cells, Rituximab has been linked to cases of acute clinical worsening, that might be caused by large release of anti-MAG IgM molecules after cellular lysis.⁵⁹⁻⁶² Nevertheless, currently most anti-MAG patients are treated with Rituximab. Given the challenging circumstances surrounding this rare disease, there is a need for clear standards on how to assess and treat patients with anti-MAG neuropathy. Many studies fail to show significance because of flawed study design; like low cohort size, short follow-up periods, and the use of inappropriate outcome measures.^{53, 63} This is especially of great importance, if we are going to assess new treatment modalities or successors of established therapies.

Multifocal Motor Neuropathy

Introduction

Multifocal motor neuropathy is a chronic inflammatory neuropathy, characterized by progressive multifocal, asymmetric muscle weakness. It typically originates in the distal upper extremities. With a prevalence of around 0.6 in 100,00 MMN is a rare disorder and has a median age of onset at around 40, affecting men 2.7 times more frequently compared to women.^{64, 65} The hallmark of the disease is the presence of conduction block in motor nerves without significant sensory alterations. Additionally, MMN patients carry IgM antibodies against ganglioside GM1, which is abundantly expressed on axolemma and myelin of peripheral nerves.^{3 66} Since MMN is prone for misdiagnosis, these features can help to distinguish MMN from amyotrophic lateral sclerosis (ALS) and other chronic immune mediated neuropathies, such as CIDP.⁶⁷ Despite recent progress in understanding the pathophysiology of MMN, the disease origin remains unresolved. Genetic predisposition to autoimmune disease or a preceding infection triggering the production of autoantibodies may be involved in the production of anti-GM1 antibodies and the development of MMN.⁶⁸⁻⁷¹ However, to date, no clear correlation could be found. A recent study suggests that anti-GM1 IgM antibodies are produced by a single B cell clone in most patients.⁷² Most frequent affected nerves are the ulnar, median, radial and tibial.^{65, 67} Patients frequently report wrist drop, reduced grip strength and foot drop as initial symptoms. Weakness mostly starts in forearm or hand muscles, in rare cases it can also affect the upper arm or distal leg. Weakness in the arms is the most prominent disease characteristic and can spread to the upper arm over time.⁶⁴ MMN patients are usually treated with IVIg and have been shown to respond to treatment, but long-term success is unlikely. Patients usually continue to develop slowly progressive axonal degeneration leading to muscle weakness and disability.^{73, 74} The presence of anti-GM1 antibodies however, was shown to be a positive predictor for response to immunotherapy and sustained treatment response.⁷⁵ Reduction of anti-GM1 IgM antibody levels has been shown to correlate to clinical improvement.^{3, 23}

GM1

GM1 is a ganglioside, composed of a ceramide base with an oligosaccharide epitope carrying a sialic acid with following structure; β -Gal-(1 \rightarrow 3)- β -GalNAc-(1 \rightarrow 4)-[α -Neu5Ac-(2 \rightarrow 3)-] β -Gal-(1 \rightarrow 4)- β -Glc-(1 \rightarrow 1)-Ceramide. Together with other gangliosides, cholesterol, and proteins, it assembles in lipid rafts on plasma membranes and is involved in membrane

signaling and trafficking throughout the body and acts as a receptor for neurotrophic factors affecting apoptosis and neuritogenesis.⁷⁶⁻⁷⁹ GM1 is ubiquitously expressed and can be found in the central and peripheral nervous system.⁶⁶ In motor, as well as sensory peripheral nerves, it localizes in the axolemma and myelin sheaths with highest abundance at the nodes of Ranvier and adjacent paranodes.⁸⁰ GM1 is involved in paranodal stabilization and ion channel clustering.¹⁰ It facilitates maintenance of tight junctions, ion channel clustering by providing an anchor for potassium channels in paranodal regions and sodium channels at the nodes, and cellular calcium homeostasis.^{10, 66, 81} The combination of these functions provides the basis for action potential propagation and conduction velocity maintenance.

Disease mechanism

Recent progress in understanding the disease mechanisms of MMN has been focused on understanding the mechanisms leading to conduction block and determining the role of anti-GM1 IgM autoantibodies. Unfortunately, pathological studies with motor nerves from patients are rare and have limited validity, often reporting contradictory results.⁶⁴ Characteristic for MMN is conduction block and was originally thought to arise from paranodal demyelination, but recent findings support the idea that antibody mediated functional disruption at the node of Ranvier and paranodal regions may be the cause.^{82, 83} However, despite reporting anti-GM1 IgM antibodies since the earliest descriptions of MMN, the pathogenicity of the autoantibodies has been questioned. A major factor for this uncertainty is the variability in reported prevalence of anti-GM1 IgM antibodies in MMN patients. The findings highly depend on diagnostic methodology and without established standard method, may have insufficient diagnostic value. Reports range from 30-60% and in the largest study to date Cats. *et al* reported a prevalence of 43%.^{67, 84-86} Nevertheless several studies have presented evidence for the pathogenicity of anti-GM1 IgM, suggesting that the antibodies act through multiple direct and indirect pathways. Antibodies from MMN patient sera were shown to activate complement after binding to GM1 *in vitro*. Deposition of complement correlated with antibody titers and was successfully inhibited by IVIg.⁸⁷ Using an induced-pluripotent stem cell model of MMN, a recent study showed complement dependent and complement independent calcium homeostasis disruption and axonal damage.⁸¹ Again the effect could be reduced by IVIg. Anti-GM1 antibodies also caused direct functional effects by increasing the potassium current at paranodes and by disruption of calcium-signaling pathways.⁸⁸ It is therefore probable that conduction block is a result of multiple processes at the nodes of Ranvier with anti-GM1 antibodies directly disrupting the cellular homeostasis and indirectly recruiting complement.⁸⁹ No animal models

for MMN are available, but data from related GBS models support the in vitro findings of MMN experiments. Binding of anti-GM1 antibodies to paranodal GM1 caused similar disruption of sodium and potassium channel clusters and activation of complement. The pathogenic effects were effectively inhibited by antibody or complement inhibition.^{10, 90-92}

Current treatment

MMN usually follows a slow progressive course and treatment of patients aims to reduce motor deficits and conduction block, slow down axonal degeneration, and support reinnervation and remyelination. Clinical course and treatment effects should be followed by applying standardized outcome measures. Patients might be prone to report improvement based on subjective symptoms, without being clinically significant. Unfortunately, there is no consensus on standardized outcome measures. Past studies have used different subjective or objective scoring systems, such as the Modified rankin scale, the Neuropathy Impairment Score-Motor subset, Medical Research Council (MRC) grading, the MRC sum score, grip strength, and self-evaluation scores. Responsiveness of these measures was however poor and the Peripheral Neuropathy Outcome Measures Standardization (PeriNomS) study group suggest using a combination of scores to assess the whole complexity of the disease.⁴⁰

The main therapeutic option remains IVIg. Most patients require continuous treatment for years and only few show sustained clinical improvement after initial treatment. The European Federation of Neurological Societies/ Peripheral Nerve Society has developed guidelines for appropriate treatment of MMN patients and summarizes that different IVIg regimes should be assessed if first line IVIg treatment is not successful. Immunosuppressive treatment should only be considered if patients do not respond to IVIg therapy, corticosteroids are not recommended.⁹³ Because of the early discoveries suggesting antibody involvement in the disease, many immunomodulatory therapies have been tested over time.

Intravenous immunoglobulin

IVIg is currently the gold standard in treatment of MMN. First data showing clinical improvement was reported shortly after discovery of the disease.⁹⁴ In the meantime there have been multiple randomized controlled trials (RTC) assessing the benefits of IVIg versus placebo, showing improvement of clinical symptoms.⁹⁵⁻⁹⁸ Four trials were part of a metaanalysis that involved 34 patients and demonstrated muscle strength improvement in 78% of patients receiving IVIg, compared to 4% in the placebo group.⁹⁹ 39% of the IVIg group showed improvement in disability, however not statistically significant. In two retrospective studies

IVIg was effective in 70% of 22 patients and in 94% of 88 patients showing improved motor strength.^{67, 74} In another RCT, 44 MMN patients were randomized in two groups and received IVIg or placebo for the first 12 weeks. After this period, they received the same treatment in reverse order for the next 12 weeks. With IVIg treatment the maximal grip strength increased slightly by 4% while it deteriorated by 31% in the placebo group. While on placebo worsening of disability was observed in 36% of patients, but stopped after switching to IVIg treatment. Disability worsened in 12% of patients first receiving IVIg, but also stopped when they switched to placebo treatment. 69% of patients had to be switched prematurely from placebo to IVIg therapy because of significant deterioration under placebo. While IVIg treatment clearly improved clinical symptoms in some patients, it also showed negative effects in a small patient population.¹⁰⁰ Although IVIg is effective in most patients, it does not prevent gradual decline and long-term clinical worsening. Multiple studies have shown that despite continued IVIg therapy, patients show disease progression and require higher doses over time.^{67, 73, 74, 101, 102} IVIg treatment may induce remyelination and reinnervation but has not been shown to prevent axon loss over time and the most important factor for developing muscle weakness was axon loss. To date, early diagnosis and treatment with the right dose of IVIg presents the best long-term prediction against axon loss and disability.^{103, 104} IVIg therapy could however be limited by adverse effects and in patients not responding to therapy.

Subcutaneous immunoglobulin

For patients on IVIg maintenance therapy subcutaneous immunoglobulin (SCIG) poses multiple advantages. Patients benefit from convenience, avoidance of hospitalization, milder adverse effects, and cost benefits. SCIG enables more stable serum level maintenance and avoids adverse events associated with high serum level of IVIg. Studies have shown comparable efficacy compared to IVIg, but recommend higher equivalent dosing to maintain stability.¹⁰⁵⁻¹⁰⁸

Cyclophosphamide

There is conflicting evidence on the use of cyclophosphamide for the treatment of MMN. There are early studies demonstrating clinical improvement with oral and intravenous cyclophosphamide.^{3, 109} However, other studies suggest that it is not beneficial.¹⁰² Because of insufficient evidence of efficacy and because of its toxicological profile, EFNS/PNS guidelines do not recommend its use.⁹³

Steroids and plasma exchange

Both corticosteroids and plasma exchange have not demonstrated any clinical benefit, in some cases even showing acute deterioration.^{102, 110} Due to lack of efficacy and unclear safety profile these therapeutic interventions are not recommended. The mechanism behind these unexpected effects is not understood and is particularly curious since these therapeutic interventions are routinely applied in other immune neuropathies. An explanation could be the dysregulation of the balance between regulatory and damaging immune components, resulting in clinical worsening.

Rituximab

A few small studies have described clinical improvement under Rituximab therapy in addition to IVIg, that resulted in increased intervals between IVIg dosing.²³ Other studies were unable to demonstrate clinical benefits and reported cases of clinical worsening.^{111, 112} Due to lack of evidence Rituximab is not recommended, but similar to cyclophosphamide, could be used as a therapy of last resort in patients that do not respond to other treatment.

Eculizumab

The involvement of the complement system in the pathogenesis of MMN has led to the hypothesis that complement inhibition could prevent anti-GM1 IgM mediated damage to motor neurons. Eculizumab is a humanized monoclonal antibody that specifically targets complement component C5 and inhibits the complement cascade that results in MAC formation and cellular lysis. It has shown beneficial effects in the complement mediated diseases paroxysmal nocturnal hemoglobinuria and refractory antibody positive myasthenia gravis.^{113, 114} An open-label study assessed eculizumab with 13 MMN patients over 14 weeks.¹¹⁵ The therapy was well tolerated and patients reported subjective improvements. Increased muscle strength measured by myometry, as well as a small but significant decrease in CB was reported. These initial findings demonstrate the potential of complement inhibition but have to be further evaluated in larger RCT. The effects of eculizumab demonstrate the potential of complement inhibition and pave the way for novel therapeutic interventions. Motor nerve injury in MMN could potentially be prevented by specific upstream targeting of complement activating anti-GM1 IgM.

References

1. Goodfellow, J. A.; Willison, H. J., Guillain-Barré syndrome: a century of progress. *Nat Rev Neurol* **2016**, *12* (12), 723-731.
2. Vallat, J. M.; Sommer, C.; Magy, L., Chronic inflammatory demyelinating polyradiculoneuropathy: diagnostic and therapeutic challenges for a treatable condition. *Lancet Neurol* **2010**, *9* (4), 402-12.
3. Pestronk, A.; Cornblath, D. R.; Ilyas, A. A.; Baba, H.; Quarles, R. H.; Griffin, J. W.; Alderson, K.; Adams, R. N., A treatable multifocal motor neuropathy with antibodies to GM1 ganglioside. *Ann Neurol* **1988**, *24* (1), 73-8.
4. Steck, A. J.; Stalder, A. K.; Renaud, S., Anti-myelin-associated glycoprotein neuropathy. *Curr Opin Neurol* **2006**, *19* (5), 458-63.
5. Latov, N., Diagnosis and treatment of chronic acquired demyelinating polyneuropathies. *Nat Rev Neurol* **2014**, *10* (8), 435-46.
6. Dalakas, M. C., Pathogenesis and Treatment of Anti-MAG Neuropathy. *Curr Treat Options Neurol* **2010**, *12* (2), 71-83.
7. Mathey, E. K.; Park, S. B.; Hughes, R. A.; Pollard, J. D.; Armati, P. J.; Barnett, M. H.; Taylor, B. V.; Dyck, P. J.; Kiernan, M. C.; Lin, C. S., Chronic inflammatory demyelinating polyradiculoneuropathy: from pathology to phenotype. *J Neurol Neurosurg Psychiatry* **2015**, *86* (9), 973-85.
8. Berger, M.; McCallus, D. E.; Lin, C. S., Rapid and reversible responses to IVIG in autoimmune neuromuscular diseases suggest mechanisms of action involving competition with functionally important autoantibodies. *J Peripher Nerv Syst* **2013**, *18* (4), 275-96.
9. Hafer-Macko, C. E.; Sheikh, K. A.; Li, C. Y.; Ho, T. W.; Cornblath, D. R.; McKhann, G. M.; Asbury, A. K.; Griffin, J. W., Immune attack on the Schwann cell surface in acute inflammatory demyelinating polyneuropathy. *Ann Neurol* **1996**, *39* (5), 625-35.
10. Susuki, K.; Rasband, M. N.; Tohyama, K.; Koibuchi, K.; Okamoto, S.; Funakoshi, K.; Hirata, K.; Baba, H.; Yuki, N., Anti-GM1 antibodies cause complement-mediated disruption of sodium channel clusters in peripheral motor nerve fibers. *J Neurosci* **2007**, *27* (15), 3956-67.
11. Steck, A.; Yuki, N.; Graus, F., Antibody testing in peripheral nerve disorders. *Handb Clin Neurol* **2013**, *115*, 189-212.
12. Querol, L.; Devaux, J.; Rojas-Garcia, R.; Illa, I., Autoantibodies in chronic inflammatory neuropathies: diagnostic and therapeutic implications. *Nat Rev Neurol* **2017**, *13* (9), 533-547.
13. Talamo, G.; Mir, M. A.; Pandey, M. K.; Sivik, J. K.; Raheja, D., IgM MGUS associated with anti-MAG neuropathy: a single institution experience. *Ann Hematol* **2015**, *94* (6), 1011-6.
14. Rison, R. A.; Beydoun, S. R., Paraproteinemic neuropathy: a practical review. *BMC Neurol* **2016**, *16*, 13.
15. Maurer, M. A.; Rakocevic, G.; Leung, C. S.; Quast, I.; Lukačičin, M.; Goebels, N.; Münz, C.; Wardemann, H.; Dalakas, M.; Lünemann, J. D., Rituximab induces sustained reduction of pathogenic B cells in patients with peripheral nervous system autoimmunity. *J Clin Invest* **2012**, *122* (4), 1393-402.

16. Latov, N.; Braun, P. E.; Gross, R. B.; Sherman, W. H.; Penn, A. S.; Chess, L., Plasma cell dyscrasia and peripheral neuropathy: identification of the myelin antigens that react with human paraproteins. *Proc Natl Acad Sci U S A* **1981**, 78 (11), 7139-42.
17. Mahdi-Rogers, M.; Hughes, R. A., Epidemiology of chronic inflammatory neuropathies in southeast England. *Eur J Neurol* **2014**, 21 (1), 28-33.
18. Heesters, B. A.; van der Poel, C. E.; Das, A.; Carroll, M. C., Antigen Presentation to B Cells. *Trends Immunol* **2016**, 37 (12), 844-854.
19. Kyle, R. A.; Therneau, T. M.; Rajkumar, S. V.; Larson, D. R.; Plevak, M. F.; Offord, J. R.; Dispenzieri, A.; Katzmann, J. A.; Melton, L. J., Prevalence of monoclonal gammopathy of undetermined significance. *N Engl J Med* **2006**, 354 (13), 1362-9.
20. Dalakas, M. C., Pathogenesis of immune-mediated neuropathies. *Biochim Biophys Acta* **2015**, 1852 (4), 658-66.
21. Magy, L.; Kaboré, R.; Mathis, S.; Lebeau, P.; Ghorab, K.; Caudie, C.; Vallat, J. M., Heterogeneity of Polyneuropathy Associated with Anti-MAG Antibodies. *J Immunol Res* **2015**, 2015, 450391.
22. Benedetti, L.; Briani, C.; Grandis, M.; Vigo, T.; Gobbi, M.; Ghiglione, E.; Carpo, M.; Cocito, D.; Caporale, C. M.; Sormani, M. P.; Mancardi, G. L.; Nobile-Orazio, E.; Schenone, A., Predictors of response to rituximab in patients with neuropathy and anti-myelin associated glycoprotein immunoglobulin M. *J Peripher Nerv Syst* **2007**, 12 (2), 102-7.
23. Pestronk, A.; Florence, J.; Miller, T.; Choksi, R.; Al-Lozi, M. T.; Levine, T. D., Treatment of IgM antibody associated polyneuropathies using rituximab. *J Neurol Neurosurg Psychiatry* **2003**, 74 (4), 485-9.
24. Renaud, S.; Fuhr, P.; Gregor, M.; Schweikert, K.; Lorenz, D.; Daniels, C.; Deuschl, G.; Gratwohl, A.; Steck, A. J., High-dose rituximab and anti-MAG-associated polyneuropathy. *Neurology* **2006**, 66 (5), 742-4.
25. Kelm, S.; Pelz, A.; Schauer, R.; Filbin, M. T.; Tang, S.; de Bellard, M. E.; Schnaar, R. L.; Mahoney, J. A.; Hartnell, A.; Bradfield, P., Sialoadhesin, myelin-associated glycoprotein and CD22 define a new family of sialic acid-dependent adhesion molecules of the immunoglobulin superfamily. *Curr Biol* **1994**, 4 (11), 965-72.
26. Erb, M.; Flueck, B.; Kern, F.; Erne, B.; Steck, A. J.; Schaeren-Wiemers, N., Unraveling the differential expression of the two isoforms of myelin-associated glycoprotein in a mouse expressing GFP-tagged S-MAG specifically regulated and targeted into the different myelin compartments. *Mol Cell Neurosci* **2006**, 31 (4), 613-27.
27. Tang, S.; Shen, Y. J.; DeBellard, M. E.; Mukhopadhyay, G.; Salzer, J. L.; Crocker, P. R.; Filbin, M. T., Myelin-associated glycoprotein interacts with neurons via a sialic acid binding site at ARG118 and a distinct neurite inhibition site. *J Cell Biol* **1997**, 138 (6), 1355-66.
28. Quarles, R. H., Myelin-associated glycoprotein (MAG): past, present and beyond. *J Neurochem* **2007**, 100 (6), 1431-48.

29. Spagnol, G.; Williams, M.; Srinivasan, J.; Golier, J.; Bauer, D.; Lebo, R. V.; Latov, N., Molecular cloning of human myelin-associated glycoprotein. *J Neurosci Res* **1989**, *24* (2), 137-42.
30. Voshol, H.; van Zuylen, C. W.; Orberger, G.; Vliegenthart, J. F.; Schachner, M., Structure of the HNK-1 carbohydrate epitope on bovine peripheral myelin glycoprotein P0. *J Biol Chem* **1996**, *271* (38), 22957-60.
31. Steck, A. J.; Murray, N.; Meier, C.; Page, N.; Perruisseau, G., Demyelinating neuropathy and monoclonal IgM antibody to myelin-associated glycoprotein. *Neurology* **1983**, *33* (1), 19-23.
32. Lombardi, R.; Erne, B.; Lauria, G.; Pareyson, D.; Borgna, M.; Morbin, M.; Arnold, A.; Czaplinski, A.; Fuhr, P.; Schaeren-Wiemers, N.; Steck, A. J., IgM deposits on skin nerves in anti-myelin-associated glycoprotein neuropathy. *Ann Neurol* **2005**, *57* (2), 180-7.
33. Ritz, M. F.; Erne, B.; Ferracin, F.; Vital, A.; Vital, C.; Steck, A. J., Anti-MAG IgM penetration into myelinated fibers correlates with the extent of myelin widening. *Muscle Nerve* **1999**, *22* (8), 1030-7.
34. Hays, A. P.; Lee, S. S.; Latov, N., Immune reactive C3d on the surface of myelin sheaths in neuropathy. *J Neuroimmunol* **1988**, *18* (3), 231-44.
35. Monaco, S.; Bonetti, B.; Ferrari, S.; Moretto, G.; Nardelli, E.; Tedesco, F.; Mollnes, T. E.; Nobile-Orazio, E.; Manfredini, E.; Bonazzi, L., Complement-mediated demyelination in patients with IgM monoclonal gammopathy and polyneuropathy. *N Engl J Med* **1990**, *322* (10), 649-52.
36. Willison, H. J.; Trapp, B. D.; Bacher, J. D.; Dalakas, M. C.; Griffin, J. W.; Quarles, R. H., Demyelination induced by intraneural injection of human antimyelin-associated glycoprotein antibodies. *Muscle Nerve* **1988**, *11* (11), 1169-76.
37. Tatum, A. H., Experimental paraprotein neuropathy, demyelination by passive transfer of human IgM anti-myelin-associated glycoprotein. *Ann Neurol* **1993**, *33* (5), 502-6.
38. Trojaborg, W.; Galassi, G.; Hays, A. P.; Lovelace, R. E.; Alkaitis, M.; Latov, N., Electrophysiologic study of experimental demyelination induced by serum of patients with IgM M proteins and neuropathy. *Neurology* **1989**, *39* (12), 1581-6.
39. Ilyas, A. A.; Gu, Y.; Dalakas, M. C.; Quarles, R. H.; Bhatt, S., Induction of experimental ataxic sensory neuronopathy in cats by immunization with purified SGPG. *J Neuroimmunol* **2008**, *193* (1-2), 87-93.
40. Pruppers, M. H. J.; Merkies, I. S. J.; Lunn, M. P. T.; Notermans, N. C.; Group, I. S., 230th ENMC International Workshop:: Improving future assessment and research in IgM anti-MAG peripheral neuropathy: A consensus collaborative effort, Naarden, The Netherlands, 24-26 February 2017. *Neuromuscul Disord* **2017**, *27* (11), 1065-1072.
41. Lunn, M. P.; Nobile-Orazio, E., Immunotherapy for IgM anti-myelin-associated glycoprotein paraprotein-associated peripheral neuropathies. *Cochrane Database Syst Rev* **2016**, *10*, CD002827.
42. Nobile-Orazio, E.; Baldini, L.; Barbieri, S.; Marmiroli, P.; Spagnol, G.; Francomano, E.; Scarlato, G., Treatment of patients with neuropathy and anti-MAG IgM M-proteins. *Ann Neurol* **1988**, *24* (1), 93-7.
43. Wilson, H. C.; Lunn, M. P.; Schey, S.; Hughes, R. A., Successful treatment of IgM paraproteinaemic neuropathy with fludarabine. *J Neurol Neurosurg Psychiatry* **1999**, *66* (5), 575-80.

44. Ghosh, A.; Littlewood, T.; Donaghy, M., Cladribine in the treatment of IgM paraproteinemic polyneuropathy. *Neurology* **2002**, *59* (8), 1290-1.
45. Blume, G.; Pestronk, A.; Goodnough, L. T., Anti-MAG antibody-associated polyneuropathies: improvement following immunotherapy with monthly plasma exchange and IV cyclophosphamide. *Neurology* **1995**, *45* (8), 1577-80.
46. Hospital, M. A.; Viala, K.; Dragomir, S.; Levy, V.; Cohen-Aubart, F.; Neil, J.; Musset, L.; Choquet, S.; Leger, J. M.; Leblond, V., Immunotherapy-based regimen in anti-MAG neuropathy: results in 45 patients. *Haematologica* **2013**, *98* (12), e155-7.
47. Treon, S. P., How I treat Waldenström macroglobulinemia. *Blood* **2015**, *126* (6), 721-32.
48. Nobile-Orazio, E.; Meucci, N.; Baldini, L.; Di Troia, A.; Scarlato, G., Long-term prognosis of neuropathy associated with anti-MAG IgM M-proteins and its relationship to immune therapies. *Brain* **2000**, *123* (Pt 4), 710-7.
49. Haas, D. C.; Tatum, A. H., Plasmapheresis alleviates neuropathy accompanying IgM anti-myelin-associated glycoprotein paraproteinemia. *Ann Neurol* **1988**, *23* (4), 394-6.
50. Orange, J. S.; Hossny, E. M.; Weiler, C. R.; Ballow, M.; Berger, M.; Bonilla, F. A.; Buckley, R.; Chinen, J.; El-Gamal, Y.; Mazer, B. D.; Nelson, R. P.; Patel, D. D.; Secord, E.; Sorensen, R. U.; Wasserman, R. L.; Cunningham-Rundles, C.; Primary Immunodeficiency Committee of the American Academy of Allergy, A. t. a. I., Use of intravenous immunoglobulin in human disease: a review of evidence by members of the Primary Immunodeficiency Committee of the American Academy of Allergy, Asthma and Immunology. *J Allergy Clin Immunol* **2006**, *117* (4 Suppl), S525-53.
51. van Doorn, P. A.; Kuitwaard, K.; Walgaard, C.; van Koningsveld, R.; Ruts, L.; Jacobs, B. C., IVIG treatment and prognosis in Guillain-Barré syndrome. *J Clin Immunol* **2010**, *30* Suppl 1, S74-8.
52. Comi, G.; Roveri, L.; Swan, A.; Willison, H.; Bojar, M.; Illa, I.; Karageorgiou, C.; Nobile-Orazio, E.; van den Bergh, P.; Swan, T.; Hughes, R.; Aubry, J.; Baumann, N.; Hadden, R.; Lunn, M.; Knapp, M.; Léger, J. M.; Bouche, P.; Mazanec, R.; Meucci, N.; van der Meché, F.; Toyka, K.; Group, I. N. C. a. T., A randomised controlled trial of intravenous immunoglobulin in IgM paraprotein associated demyelinating neuropathy. *J Neurol* **2002**, *249* (10), 1370-7.
53. Pruppers, M. H. J.; Merkies, I. S. J.; Notermans, N. C., Chapter 5 - Monoclonal gammopathy associated neuropathy: Focusing on IgM M-protein associated neuropathy. In *Dysimmune Neuropathies*, Rajabally, Y. A., Ed. Academic Press: 2020; pp 109-127.
54. Notermans, N. C.; Vermeulen, M.; Lokhorst, H. M.; Van Doorn, P. A.; Van den Berg, L. H.; Teunissen, L. L.; Wokke, J. H., Pulsed high-dose dexamethasone treatment of polyneuropathy associated with monoclonal gammopathy. *J Neurol* **1997**, *244* (7), 462-3.
55. Mariette, X.; Chastang, C.; Louboutin, J.-P.; Leger, J.-M.; Clavelou, P.; Brouet, J.-C., A randomised clinical trial comparing interferon- α and intravenous immunoglobulin in polyneuropathy associated with monoclonal IgM. *Journal of Neurology, Neurosurgery & Psychiatry* **1997**, *63* (1), 28.
56. Mariette, X.; Brouet, J.-C.; Chevret, S.; Leger, J.-M.; Clavelou, P.; Pouget, J.; Vallat, J.-M.; Vial, C., A randomised double blind trial versus placebo does not confirm the benefit of α -interferon in

- polyneuropathy associated with monoclonal IgM. *Journal of Neurology, Neurosurgery & Psychiatry* **2000**, *69* (2), 279.
57. Dalakas, M. C.; Rakocevic, G.; Salajegheh, M.; Dambrosia, J. M.; Hahn, A. F.; Raju, R.; McElroy, B., Placebo-controlled trial of rituximab in IgM anti-myelin-associated glycoprotein antibody demyelinating neuropathy. *Ann Neurol* **2009**, *65* (3), 286-93.
 58. Léger, J. M.; Viala, K.; Nicolas, G.; Créange, A.; Vallat, J. M.; Pouget, J.; Clavelou, P.; Vial, C.; Steck, A.; Musset, L.; Marin, B.; Switzerland), R. S. G. F. a., Placebo-controlled trial of rituximab in IgM anti-myelin-associated glycoprotein neuropathy. *Neurology* **2013**, *80* (24), 2217-25.
 59. Broglio, L.; Lauria, G., Worsening after rituximab treatment in anti-mag neuropathy. *Muscle Nerve* **2005**, *32* (3), 378-9.
 60. Stork, A. C.; Notermans, N. C.; Vrancken, A. F.; Cornblath, D. R.; van der Pol, W. L., Rapid worsening of IgM anti-MAG demyelinating polyneuropathy during rituximab treatment. *J Peripher Nerv Syst* **2013**, *18* (2), 189-91.
 61. Sala, E.; Robert-Varvat, F.; Paul, S.; Camdessanché, J. P.; Antoine, J. C., Acute neurological worsening after Rituximab treatment in patients with anti-MAG neuropathy. *J Neurol Sci* **2014**, *345* (1-2), 224-7.
 62. Weiss, M. D.; Becker, P., Paradoxical worsening of anti-myelin-associated glycoprotein polyneuropathy following rituximab. *Muscle Nerve* **2014**, *49* (3), 457-8.
 63. Pruppers, M. H.; Merkies, I. S.; Notermans, N. C., Recent advances in outcome measures in IgM-anti-MAG+ neuropathies. *Curr Opin Neurol* **2015**, *28* (5), 486-93.
 64. Vlam, L.; van der Pol, W. L.; Cats, E. A.; Straver, D. C.; Piepers, S.; Franssen, H.; van den Berg, L. H., Multifocal motor neuropathy: diagnosis, pathogenesis and treatment strategies. *Nat Rev Neurol* **2011**, *8* (1), 48-58.
 65. Slee, M.; Selvan, A.; Donaghy, M., Multifocal motor neuropathy: the diagnostic spectrum and response to treatment. *Neurology* **2007**, *69* (17), 1680-7.
 66. Willison, H. J.; Yuki, N., Peripheral neuropathies and anti-glycolipid antibodies. *Brain* **2002**, *125* (Pt 12), 2591-625.
 67. Cats, E. A.; van der Pol, W. L.; Piepers, S.; Franssen, H.; Jacobs, B. C.; van den Berg-Vos, R. M.; Kuks, J. B.; van Doorn, P. A.; van Engelen, B. G.; Verschuuren, J. J.; Wokke, J. H.; Veldink, J. H.; van den Berg, L. H., Correlates of outcome and response to IVIg in 88 patients with multifocal motor neuropathy. *Neurology* **2010**, *75* (9), 818-25.
 68. Cats, E. A.; Bertens, A. S.; Veldink, J. H.; van den Berg, L. H.; van der Pol, W. L., Associated autoimmune diseases in patients with multifocal motor neuropathy and their family members. *J Neurol* **2012**, *259* (6), 1137-41.
 69. Sutedja, N. A.; Otten, H. G.; Cats, E. A.; Piepers, S.; Veldink, J. H.; van der Pol, W. L.; van den Berg, L. H., Increased frequency of HLA-DRB1*15 in patients with multifocal motor neuropathy. *Neurology* **2010**, *74* (10), 828-32.

70. Taylor, B. V.; Phillips, B. A.; Speed, B. R.; Kaldor, J.; Carroll, W. M.; Mastaglia, F. L., Serological evidence for infection with *Campylobacter jejuni/coli* in patients with multifocal motor neuropathy. *J Clin Neurosci* **1998**, *5* (1), 33-5.
71. Terenghi, F.; Allaria, S.; Scarlato, G.; Nobile-Orazio, E., Multifocal motor neuropathy and *Campylobacter jejuni* reactivity. *Neurology* **2002**, *59* (2), 282-4.
72. Cats, E. A.; van der Pol, W. L.; Tio-Gillen, A. P.; Diekstra, F. P.; van den Berg, L. H.; Jacobs, B. C., Clonality of anti-GM1 IgM antibodies in multifocal motor neuropathy and the Guillain-Barré syndrome. *J Neurol Neurosurg Psychiatry* **2015**, *86* (5), 502-4.
73. Van den Berg-Vos, R. M.; Franssen, H.; Wokke, J. H.; Van den Berg, L. H., Multifocal motor neuropathy: long-term clinical and electrophysiological assessment of intravenous immunoglobulin maintenance treatment. *Brain* **2002**, *125* (Pt 8), 1875-86.
74. Léger, J. M.; Viala, K.; Cancalon, F.; Maisonnobe, T.; Gruwez, B.; Waegemans, T.; Bouche, P., Intravenous immunoglobulin as short- and long-term therapy of multifocal motor neuropathy: a retrospective study of response to IVIg and of its predictive criteria in 40 patients. *J Neurol Neurosurg Psychiatry* **2008**, *79* (1), 93-6.
75. Martinez-Thompson, J. M.; Snyder, M. R.; Ettore, M.; McKeon, A.; Pittock, S. J.; Roforth, M. M.; Mandrekar, J.; Mauermann, M. L.; Taylor, B. V.; Dyck, P. J. B.; Windebank, A. J.; Klein, C. J., Composite ganglioside autoantibodies and immune treatment response in MMN and MADSAM. *Muscle Nerve* **2018**, *57* (6), 1000-1005.
76. Lingwood, D.; Simons, K., Lipid rafts as a membrane-organizing principle. *Science* **2010**, *327* (5961), 46-50.
77. Hall, A.; Róg, T.; Karttunen, M.; Vattulainen, I., Role of glycolipids in lipid rafts: a view through atomistic molecular dynamics simulations with galactosylceramide. *J Phys Chem B* **2010**, *114* (23), 7797-807.
78. Yates, A. J.; Rampersaud, A., Sphingolipids as receptor modulators. An overview. *Ann N Y Acad Sci* **1998**, *845*, 57-71.
79. Da Silva, J. S.; Hasegawa, T.; Miyagi, T.; Dotti, C. G.; Abad-Rodriguez, J., Asymmetric membrane ganglioside sialidase activity specifies axonal fate. *Nat Neurosci* **2005**, *8* (5), 606-15.
80. Corbo, M.; Quattrini, A.; Lugaresi, A.; Santoro, M.; Latov, N.; Hays, A. P., Patterns of reactivity of human anti-GM1 antibodies with spinal cord and motor neurons. *Ann Neurol* **1992**, *32* (4), 487-93.
81. Harschnitz, O.; van den Berg, L. H.; Johansen, L. E.; Jansen, M. D.; Kling, S.; Vieira de Sá, R.; Vlam, L.; van Rheenen, W.; Karst, H.; Wierenga, C. J.; Pasterkamp, R. J.; van der Pol, W. L., Autoantibody pathogenicity in a multifocal motor neuropathy induced pluripotent stem cell-derived model. *Ann Neurol* **2016**, *80* (1), 71-88.
82. Franssen, H., The node of Ranvier in multifocal motor neuropathy. *J Clin Immunol* **2014**, *34 Suppl 1*, S105-11.
83. Uncini, A.; Kuwabara, S., Nodopathies of the peripheral nerve: an emerging concept. *J Neurol Neurosurg Psychiatry* **2015**, *86* (11), 1186-95.

84. van Schaik, I. N.; Bossuyt, P. M.; Brand, A.; Vermeulen, M., Diagnostic value of GM1 antibodies in motor neuron disorders and neuropathies: a meta-analysis. *Neurology* **1995**, *45* (8), 1570-7.
85. Taylor, B. V.; Gross, L.; Windebank, A. J., The sensitivity and specificity of anti-GM1 antibody testing. *Neurology* **1996**, *47* (4), 951-5.
86. Cats, E. A.; Jacobs, B. C.; Yuki, N.; Tio-Gillen, A. P.; Piepers, S.; Franssen, H.; van Asseldonk, J. T.; van den Berg, L. H.; van der Pol, W. L., Multifocal motor neuropathy: association of anti-GM1 IgM antibodies with clinical features. *Neurology* **2010**, *75* (22), 1961-7.
87. Yuki, N.; Watanabe, H.; Nakajima, T.; Späth, P. J., IVIG blocks complement deposition mediated by anti-GM1 antibodies in multifocal motor neuropathy. *J Neurol Neurosurg Psychiatry* **2011**, *82* (1), 87-91.
88. Takigawa, T.; Yasuda, H.; Kikkawa, R.; Shigeta, Y.; Saida, T.; Kitasato, H., Antibodies against GM1 ganglioside affect K⁺ and Na⁺ currents in isolated rat myelinated nerve fibers. *Ann Neurol* **1995**, *37* (4), 436-42.
89. Beadon, K.; Guimarães-Costa, R.; Léger, J. M., Multifocal motor neuropathy. *Curr Opin Neurol* **2018**, *31* (5), 559-564.
90. Susuki, K.; Baba, H.; Tohyama, K.; Kanai, K.; Kuwabara, S.; Hirata, K.; Furukawa, K.; Rasband, M. N.; Yuki, N., Gangliosides contribute to stability of paranodal junctions and ion channel clusters in myelinated nerve fibers. *Glia* **2007**, *55* (7), 746-57.
91. Jacobs, B. C.; O'Hanlon, G. M.; Bullens, R. W.; Veitch, J.; Plomp, J. J.; Willison, H. J., Immunoglobulins inhibit pathophysiological effects of anti-GQ1b-positive sera at motor nerve terminals through inhibition of antibody binding. *Brain* **2003**, *126* (Pt 10), 2220-34.
92. Halstead, S. K.; Zitman, F. M.; Humphreys, P. D.; Greenshields, K.; Verschuuren, J. J.; Jacobs, B. C.; Rother, R. P.; Plomp, J. J.; Willison, H. J., Eculizumab prevents anti-ganglioside antibody-mediated neuropathy in a murine model. *Brain* **2008**, *131* (Pt 5), 1197-208.
93. PNS, J. T. F. o. t. E. a. t., European Federation of Neurological Societies/Peripheral Nerve Society guideline on management of multifocal motor neuropathy. Report of a joint task force of the European Federation of Neurological Societies and the Peripheral Nerve Society--first revision. *J Peripher Nerv Syst* **2010**, *15* (4), 295-301.
94. Kaji, R.; Shibasaki, H.; Kimura, J., Multifocal demyelinating motor neuropathy: cranial nerve involvement and immunoglobulin therapy. *Neurology* **1992**, *42* (3 Pt 1), 506-9.
95. Federico, P.; Zochodne, D. W.; Hahn, A. F.; Brown, W. F.; Feasby, T. E., Multifocal motor neuropathy improved by IVIg: randomized, double-blind, placebo-controlled study. *Neurology* **2000**, *55* (9), 1256-62.
96. Léger, J. M.; Chassande, B.; Musset, L.; Meininger, V.; Bouche, P.; Baumann, N., Intravenous immunoglobulin therapy in multifocal motor neuropathy: a double-blind, placebo-controlled study. *Brain* **2001**, *124* (Pt 1), 145-53.
97. Van den Berg, L. H.; Kerkhoff, H.; Oey, P. L.; Franssen, H.; Mollee, I.; Vermeulen, M.; Jennekens, F. G.; Wokke, J. H., Treatment of multifocal motor neuropathy with high dose intravenous

- immunoglobulins: a double blind, placebo controlled study. *J Neurol Neurosurg Psychiatry* **1995**, *59* (3), 248-52.
98. Azulay, J. P.; Blin, O.; Pouget, J.; Boucraut, J.; Billé-Turc, F.; Carles, G.; Serratrice, G., Intravenous immunoglobulin treatment in patients with motor neuron syndromes associated with anti-GM1 antibodies: a double-blind, placebo-controlled study. *Neurology* **1994**, *44* (3 Pt 1), 429-32.
99. van Schaik, I. N.; van den Berg, L. H.; de Haan, R.; Vermeulen, M., Intravenous immunoglobulin for multifocal motor neuropathy. *Cochrane Database Syst Rev* **2005**, (2), CD004429.
100. Hahn, A. F.; Beydoun, S. R.; Lawson, V.; Oh, M.; Empson, V. G.; Leibl, H.; Ngo, L. Y.; Gelmont, D.; Koski, C. L.; Team, I. i. M. S., A controlled trial of intravenous immunoglobulin in multifocal motor neuropathy. *J Peripher Nerv Syst* **2013**, *18* (4), 321-30.
101. Bouche, P.; Moulounguet, A.; Younes-Chennoufi, A. B.; Adams, D.; Baumann, N.; Meininger, V.; Léger, J. M.; Said, G., Multifocal motor neuropathy with conduction block: a study of 24 patients. *J Neurol Neurosurg Psychiatry* **1995**, *59* (1), 38-44.
102. Azulay, J. P.; Rihet, P.; Pouget, J.; Cador, F.; Blin, O.; Boucraut, J.; Serratrice, G., Long term follow up of multifocal motor neuropathy with conduction block under treatment. *J Neurol Neurosurg Psychiatry* **1997**, *62* (4), 391-4.
103. Van Asseldonk, J. T.; Van den Berg, L. H.; Kalmijn, S.; Van den Berg-Vos, R. M.; Polman, C. H.; Wokke, J. H.; Franssen, H., Axon loss is an important determinant of weakness in multifocal motor neuropathy. *J Neurol Neurosurg Psychiatry* **2006**, *77* (6), 743-7.
104. Vucic, S.; Black, K. R.; Chong, P. S.; Cros, D., Multifocal motor neuropathy: decrease in conduction blocks and reinnervation with long-term IVIg. *Neurology* **2004**, *63* (7), 1264-9.
105. Harbo, T.; Andersen, H.; Hess, A.; Hansen, K.; Sindrup, S. H.; Jakobsen, J., Subcutaneous versus intravenous immunoglobulin in multifocal motor neuropathy: a randomized, single-blinded cross-over trial. *Eur J Neurol* **2009**, *16* (5), 631-8.
106. Racosta, J. M.; Sposato, L. A.; Kimpinski, K., Subcutaneous versus intravenous immunoglobulin for chronic autoimmune neuropathies: A meta-analysis. *Muscle Nerve* **2017**, *55* (6), 802-809.
107. Harbo, T.; Andersen, H.; Jakobsen, J., Long-term therapy with high doses of subcutaneous immunoglobulin in multifocal motor neuropathy. *Neurology* **2010**, *75* (15), 1377-80.
108. Katzberg, H. D.; Rasutis, V.; Bril, V., Subcutaneous immunoglobulin for treatment of multifocal motor neuropathy. *Muscle Nerve* **2016**, *54* (5), 856-863.
109. Meucci, N.; Cappellari, A.; Barbieri, S.; Scarlato, G.; Nobile-Orazio, E., Long term effect of intravenous immunoglobulins and oral cyclophosphamide in multifocal motor neuropathy. *J Neurol Neurosurg Psychiatry* **1997**, *63* (6), 765-9.
110. Claus, D.; Specht, S.; Zieschang, M., Plasmapheresis in multifocal motor neuropathy: a case report. *J Neurol Neurosurg Psychiatry* **2000**, *68* (4), 533-5.
111. Gorson, K. C.; Natarajan, N.; Ropper, A. H.; Weinstein, R., Rituximab treatment in patients with IVIg-dependent immune polyneuropathy: a prospective pilot trial. *Muscle Nerve* **2007**, *35* (1), 66-9.

112. Chaudhry, V.; Cornblath, D. R., An open-label trial of rituximab (Rituxan®) in multifocal motor neuropathy. *J Peripher Nerv Syst* **2010**, *15* (3), 196-201.
113. Howard, J. F.; Utsugisawa, K.; Benatar, M.; Murai, H.; Barohn, R. J.; Illa, I.; Jacob, S.; Vissing, J.; Burns, T. M.; Kissel, J. T.; Muppidi, S.; Nowak, R. J.; O'Brien, F.; Wang, J. J.; Mantegazza, R.; Group, R. S., Safety and efficacy of eculizumab in anti-acetylcholine receptor antibody-positive refractory generalised myasthenia gravis (REGAIN): a phase 3, randomised, double-blind, placebo-controlled, multicentre study. *Lancet Neurol* **2017**, *16* (12), 976-986.
114. Dhillon, S., Eculizumab: A Review in Generalized Myasthenia Gravis. *Drugs* **2018**, *78* (3), 367-376.
115. Fitzpatrick, A. M.; Mann, C. A.; Barry, S.; Brennan, K.; Overell, J. R.; Willison, H. J., An open label clinical trial of complement inhibition in multifocal motor neuropathy. *J Peripher Nerv Syst* **2011**, *16* (2), 84-91.

Results

Chapter 1

Retrospective study: Decrease in serum anti-MAG autoantibodies is associated with therapy response in anti-MAG neuropathy patients

Pascal Hänggi^{1,2}, Butrint Aliu², Kea Martin¹, Ruben Herrendorff^{1,2}, Andreas Steck³

¹Polyneuron Pharmaceuticals AG, 4057 Basel, Switzerland

²Institute of Molecular Pharmacy, Pharmacenter, University of Basel,
4056 Basel, Switzerland

³Clinic of Neurology, Department of Medicine, University
Hospital Basel, University of Basel, 4031 Basel, Switzerland

Corresponding author:

Pascal Hänggi, pascarhaenggi@gmail.com, <https://orcid.org/0000-0002-7941-2475>

Contributions of Butrint Aliu

- Manuscript preparation
- Data acquisition
- Data analysis and interpretation

Abstract

The objective of the retrospective analysis was to test the hypothesis that changes in serum anti-myelin-associated glycoprotein (MAG) autoantibodies are associated with clinical response to immunotherapy in anti-MAG neuropathy patients. **Methods:** As of January 29th 2020, we used anti-myelin-associated glycoprotein related search strings in the MEDLINE database to identify studies that provided information on anti-MAG IgM autoantibodies and clinical outcomes during immunotherapies. The relative change in anti-MAG IgM titers, paraprotein levels, or total IgM was determined prior, during, or post-treatment and patients were assigned to ‘responder’, ‘non-responder’ or ‘acute deteriorating’ category depending on their clinical response to treatment. The studies were qualified as ‘supportive’ or ‘not supportive’ depending on the percentage of patients exhibiting an association between relative change of anti-MAG antibody titers or levels and change in clinical outcomes. **Results:** Fifty studies with 410 anti-MAG neuropathy patients were included in the analysis. Forty studies with 303 patients supported the hypothesis that a ‘responder’ patient had a relative reduction of anti-MAG antibody titers or levels which is associated with clinical improvements and ‘non-responder’ patients exhibited no significant change in anti-MAG IgM antibodies. Six studies with 93 patients partly supported and four studies with 26 patients did not support the hypothesis. **Conclusion:** The retrospective analysis confirmed the hypothesis that a relative reduction in serum anti-MAG IgM antibodies is associated with a clinical response to immunotherapies; a sustained reduction of at least 50% compared to pre-treatment titers or levels could be a valuable indicator for therapeutic response.

Introduction

Anti-myelin-associated glycoprotein (MAG) neuropathy is a rare form of acquired demyelinating polyneuropathy associated with a monoclonal gammopathy of undetermined significance (MGUS) ⁴². The gammopathy leads to the production of monoclonal anti-MAG IgM antibodies that recognize the CD57/HNK-1 carbohydrate epitope, which is highly expressed on adhesion molecules such as MAG, myelin protein zero, or sulphated glucuronyl glycolipids in the peripheral nervous system (PNS) ⁴³⁻⁴⁶. There is considerable evidence that the deposition of anti-MAG IgM autoantibodies on myelin sheaths is responsible for widening of the myelin lamellae and demyelination. The slowly progressing neuropathy causes sensorimotor deficits, sensory ataxia, paresthesia, muscle weakness, neuropathic pain, and tremor ^{16, 20, 21, 47, 48}. Typically, the disease onset occurs after the age of 50 years and is 2.7 times more frequent in men than in women with a prevalence of about 1 in 100,000 ^{17, 48, 49}. Currently, there is no approved treatment for anti-MAG neuropathy. However, given the high unmet medical need, over the last three decades many different immunotherapies have been used for the management of anti-MAG neuropathy including IV immunoglobulins (IVIg), therapeutic plasma exchange, chemotherapeutic drugs, and various biologic drugs such as rituximab and obinutuzumab ^{47, 48, 50, 51}.

The significance of the anti-MAG antibody titers or levels as predictive of response to therapy is controversial. Although there is considerable evidence for the pathogenicity of anti-MAG IgM autoantibodies, the association of reduced serum levels of anti-MAG IgM autoantibodies and clinical improvement of neuropathic symptoms is less clear based on the available literature and reviews ^{41, 47}. Therefore, we performed a systematic literature search and a retrospective analysis to investigate a relationship of change in serum anti-MAG IgM titers or levels and clinical outcome during immunotherapies and to evaluate if the change in anti-MAG IgM antibodies is a predictive biomarker of response to immunotherapies in anti-MAG neuropathy patients.

Methods

Data sources and search strategy

A systematic literature search in Medline Epub has been performed for all published work up to January 29th, 2020 (as detailed in Figure 1) to investigate if changes in clinical signs of neuropathy are associated with changes in anti-MAG IgM titers or levels of patients with anti-MAG neuropathy during treatment with immunotherapies. The search strings “anti-MAG neuropathy OR anti-myelin-associated glycoprotein”, “monoclonal IgM AND polyneuropathy“ and “IgM paraproteinemia AND neuropathy” were used to identify studies, providing information on anti-MAG autoantibody titers or levels and clinical outcomes at different time points, *i.e.* in particular pre- and post-treatment.

This search yielded 1143 hits, of which 1091 were excluded after abstract screening for the following reasons: duplicates, not original publications (e.g. reviews), publications with non-clinical data (e.g. animal studies), or focus on a non-relevant disease (e.g. neuropathy without anti-MAG antibody). During full-text appraisal of the 52 remaining publications, eight publications were excluded as they did not provide information on anti-MAG IgM titers, paraprotein levels, total IgM levels and/or pre- and post-treatment clinical data (supplemental data, Table e-1) ⁵²⁻⁵⁹. In addition, six publications were hand-selected and added to the list of 44 publications, e.g. as they were presented as abstracts at conferences ^{23, 60-64}. Data were extracted from the 50 remaining publications and summarized (supplemental data, Table e-2) ^{22-24, 42, 50, 51, 60-104}. Of note, all publications that provided information on anti-MAG IgM, paraprotein, and total IgM levels as well as on clinical symptoms at different time points were included in this analysis, regardless of results and the class of evidence (given the limited number of randomized controlled trials).

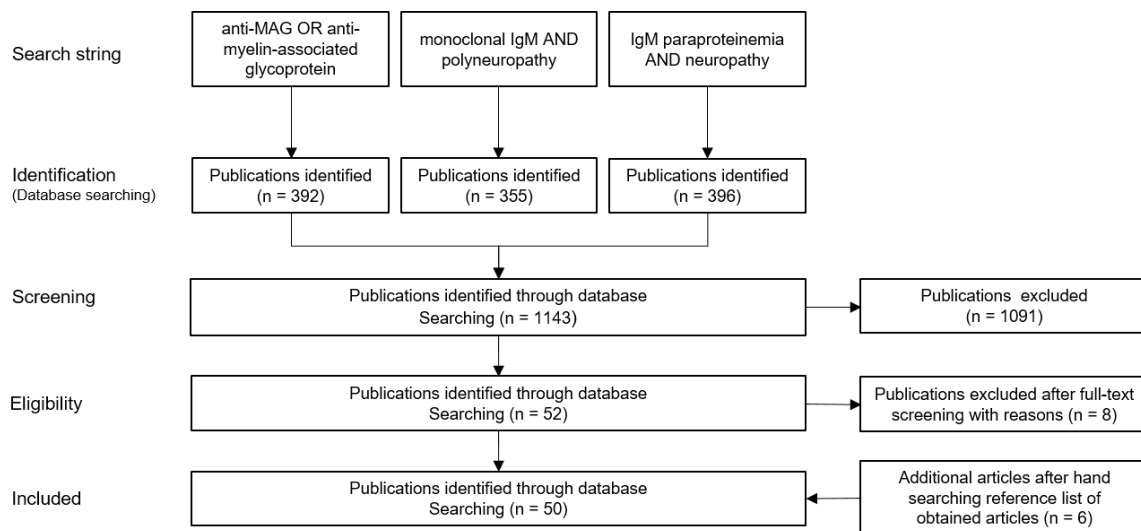


Figure 1. Overview of the systematic literature search in Medline Epub. All published work has been included until January 29th, 2020, independent of the type of intervention or class of evidence given the limited number of class I evidence studies. Data of 50 publications were included and analyzed.

Data extraction, analysis, and synthesis

Data from the fifty identified clinical publications were analyzed for the relative change in anti-MAG IgM autoantibody titers units, paraprotein levels (g/L), total IgM levels (g/L) from pre-treatment (baseline) to post-treatment and compared with changes in clinical outcomes (supplemental data, Table e-2). The methods used to assay the anti-MAG IgM antibodies are listed in the supplemental data Table e-3. In accordance with the recently suggested cut-off value of > 7'000 BTU instead of > 1'500 BTU in the Bühlmann test by Liberatore *et al.* 2020¹⁰⁵, in 48 of the analyzed studies, patients exhibited titers above this higher cut-off value. Only in two studies, patients were included with titers values below the 7'000 BTU cut-off value^{68, 76}.

Individual patients were assigned to 1 of 3 categories ('responder', 'non-responder' or 'acute deteriorating') depending on their clinical response to treatment in terms of primary and secondary outcome measures as defined by the authors of the original publications. Consistent with the original articles and to avoid a potential bias of the analysis, we separated the small subset of 'acute deteriorating' patients from the 'non-responder' patients, as they exhibited, mostly, a transient worsening of the clinical symptoms⁵³. However, the transient worsening was not necessarily a sign of long-term treatment failure.

Studies were assigned to one of two categories ('supportive', or 'not supportive') depending on whether the majority of patients exhibited an association between change in anti-MAG antibody titers or levels and change in clinical outcome or not (Table 1).

Table 1: Overview of the categories and the criteria for the assignment.

| Category | Criteria for the assignment |
|---|---|
| <p>Supportive - The majority of patients (>50%) fulfilled the criteria for the assignment.*</p> | <ul style="list-style-type: none"> • Responder: Relative reduction in anti-MAG IgM antibodies and clinical improvements were present in the majority of patients. • Non-Responder: No or only minimal change in anti-MAG IgM antibodies and stabilizations or slight worsening were present in the majority of patients. • Acute deteriorating: Acute worsening was associated with an increase in anti-MAG IgM titers. |
| <p>Not supportive - The minority of patients (<50%) fulfilled the criteria for the assignment.*</p> | <ul style="list-style-type: none"> • Responder: Patients exhibited an increase in anti-MAG IgM antibodies and clinical improvements. • Acute deteriorating: Patients exhibited acute worsening and a relative reduction in anti-MAG titers. • Responder and non-responder exhibited a similar relative reduction in anti-MAG IgM antibodies. |

*Cut-off value of 50% was applied when mean or median data of anti-MAG IgM titers or levels were reported.

Patient cohort and treatment interventions

All participants with anti-MAG IgM antibody-associated demyelinating peripheral neuropathy with MGUS were included, independent of age, pre-treatment and treatment status, severity and duration of the neuropathy.

The evaluated studies included the following interventions: 1) plasma exchange, plasmapheresis or selective apheresis (protein A column), 2) IVIg 3) rituximab or obinutuzumab, 4) interferon alpha-2a (IFN- α 2a), 5) purine analogs: fludarabine, or cladribine, 6) alkylating agents: cyclophosphamide, chlorambucil, bendamustine, 7) corticosteroids: dexamethasone, prednisone and other immunosuppressants such as cyclosporine and lenalidomide, 8) placebo or no treatment. The studies included either single treatment interventions, combination treatment protocols or comparisons versus placebo. Overall, most patients (n = 162) received either rituximab alone (39.5%) or in combination (9.5%) with plasma exchange, fludarabine, cyclophosphamide, dexamethasone or bendamustine. In a few studies, this regimen was shortened or prolonged based on clinical response observed in

patients. Almost a fifth (18.5%) of the participants received placebo (15.6%) or no treatment (2.9%). For our analysis, these patients are considered an important indicator for treatment-unrelated changes and fluctuation in anti-MAG titers. Symptom severity, clinical improvement, or acute deterioration were assessed with different methods, such as grip strength, the Inflammatory Neuropathy Cause and Treatment (INCAT) disability score, the Medical Research Council (MRC) sum score, the Neuropathy Disability Score (NDS), the Overall Neuropathy Limitations Scale (ONLS), or the Total Neuropathy Score (TNS), Neuropathy Impairment Scale (NIS), the modified Rankin Scale (mRS), the Rasch-built Overall Disability Scale (R-ODS), 10-metre walk time, and electrophysiological parameters. Change in subjective clinical scores and scales were assessed at various time points in the course of treatment course (supplemental data Table e-2). Patients with Waldenström Macroglobulinemia (WM), multiple myeloma (MM), lymphoma, or monoclonal gammopathy of non IgM type (e.g. IgG, IgA, IgD) were excluded. In many studies performed in WM or MM, different clinical assessments were used (primarily oncological outcome measures), making an evaluation of the neurological outcome measures difficult.

Data availability statement

All data and the statistical analysis are available in the manuscript, the supplemental data or are reported in the original articles cited in the manuscript.

Results

To obtain a more homogenous patient population, only anti-MAG neuropathy patients and MGUS associated with elevated anti-MAG IgM were included in the analysis. Other pathologies associated with monoclonal anti-MAG IgM including WM were excluded from the analysis, unless indicated (supplemental data, Table e-2).

The systematic literature analysis showed that out of the fifty studies (n = 410 participants), forty studies (n = 303 participants) support the hypothesis that (i) clinical improvements are associated with a relative reduction in anti-MAG IgM antibodies, (ii) non-responders exhibit no, or only minimal change in anti-MAG IgM antibodies and (iii) acute deteriorating was associated with an increase in anti-MAG titers.

Of note, out of the ten studies that were not supportive (n = 119 participants), only four studies did not support the hypothesis at all (n = 26 participants). However, in six of these studies (n = 93 participants) at least some anti-MAG IgM neuropathy patients (< 50%) showed a relationship between change in anti-MAG antibodies and clinical outcome (supplemental data, Table e-2).

In order to further test the hypothesis, the studies and the extracted data of each group (responder, non-responder, and acute deteriorating) were analyzed for the relative change in anti-MAG IgM titers, paraprotein levels, or total IgM levels (Figure 2). Of importance, all studies and participants were included in the analysis regardless of whether the study was categorized as supportive or not supportive. In most studies the anti-MAG IgM titers were assessed but only a minority of studies measured paraprotein (commonly referred to as M-protein or monoclonal protein), or total IgM levels. Based on the systematic literature search, a strong association was observed between clinical improvements in the responder group (n = 208 participants) and a significant reduction in anti-MAG titers, paraprotein, and/or total IgM levels ($p > 0.001$) compared to the non-responder group (n = 191 participants), or the acute deteriorating group (n = 11 participants). If the two follow-up studies are excluded, therefore reducing the bias of including the same patient twice^{24, 71}, the total number of participants is 394 anti-MAG patients, of which 197 patients (50.0%) are considered as responders and 185 (47.0%) as non-responders to the treatment.

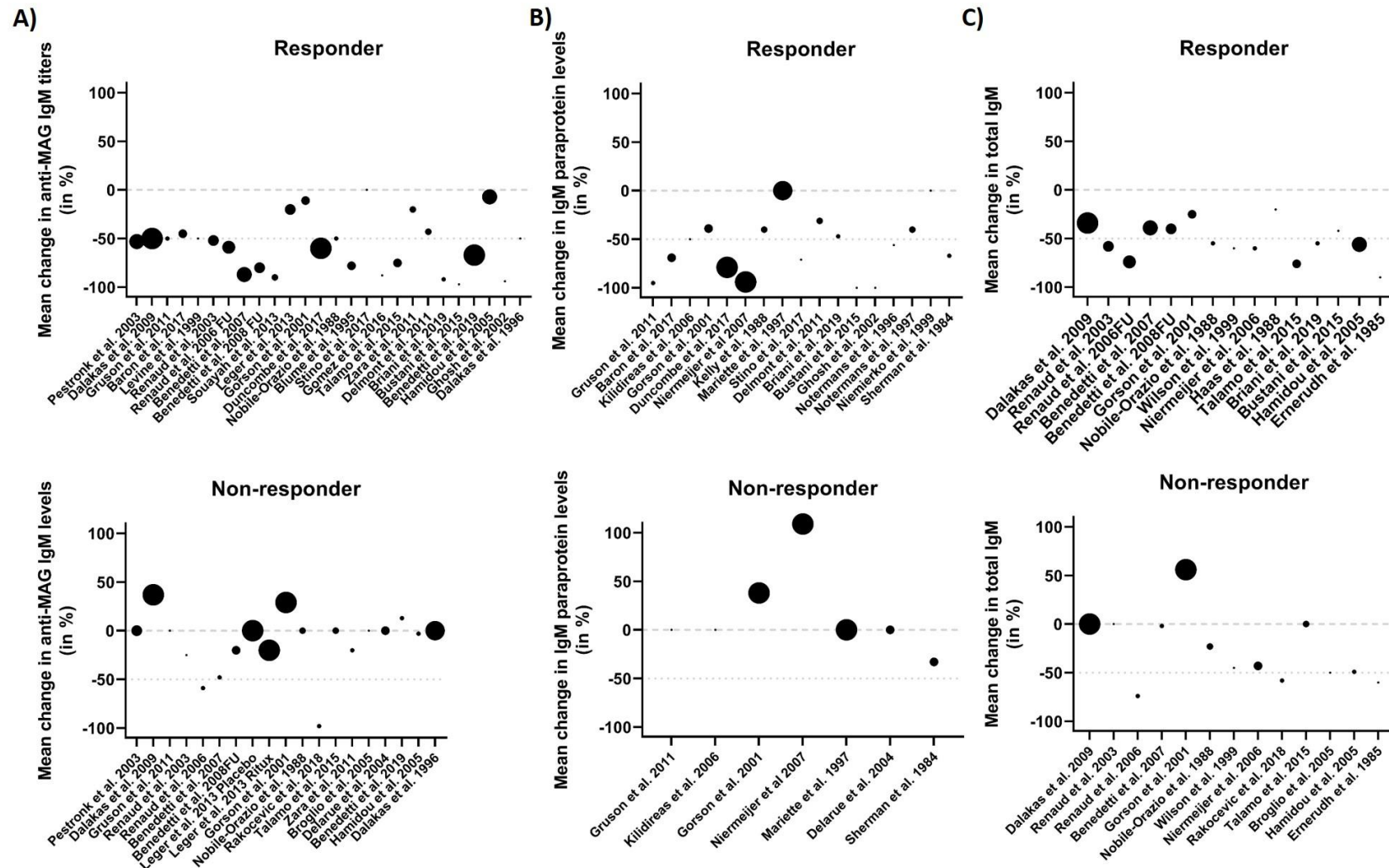


Figure 2. Relative change in serum anti-MAG IgM titers or levels and response to immunotherapies in anti-MAG neuropathy patients. Overview of the studies that assessed the relative change in anti-MAG IgM autoantibodies (pre- and post-treatment) and clinical response to immunotherapies. **A)** Relative change in anti-MAG IgM titers in the responder and the non-responder group. **B)** Relative change in paraprotein levels in the responder and the non-responder group. **C)** Relative change in total IgM levels in the responder and the non-responder group. Data are indicated as mean values and the circle size represents comparative size of the study (number of participants). FU: Follow-up study

Regardless of whether the anti-MAG IgM antibodies were assessed in titer units (e.g. Bühlmann Titer Units, or Western Blotting), paraprotein levels (g/L), or total IgM levels (g/L), a significant reduction was observed in the responder group compared to the non-responder or acute deteriorating group (Figure 3). In the responder group the mean anti-MAG IgM titers were reduced by 57.5% \pm 28.1% SD, the mean paraprotein levels by 57.5% \pm 31.3% SD, and the mean total IgM levels by 52.3% \pm 19.3% SD compared to pre-treatment levels. The non-responder group exhibited a reduction of 11.3% \pm 30.9% SD in anti-MAG IgM titers, an increase in paraprotein levels of 16.3% \pm 45.8% SD, and in total IgM levels of 26.8% \pm 36.0% SD compared with pre-treatment levels. The acute deteriorating group exhibited an increase in anti-MAG titers of 204.3% \pm 253.4% SD, an increase in paraprotein levels of 11.50% \pm 3.5 SD, and a reduction of -0.5% \pm 54.64% SD in total IgM levels. However, the small number of patients and the large standard deviation, makes it difficult to conclude that the transient acute worsening is associated with an increase in anti-MAG titers.

Remarkably, 77.7% of all responders exhibited a relative reduction of more than 50.0% in anti-MAG IgM titers compared with pre-treatment titers. In responders, 62.1% experienced more than a 50.0% reduction in IgM paraprotein and 49.2% experienced more than a 50% reduction in total IgM levels. Conversely, more than 90.0% of non-responders showed a reduction of less than 20.0% in anti-MAG IgM titers (94.1%) or IgM paraprotein (93.3%), and 70.9% of non-responders showed a reduction of less than 20.0% in total IgM levels compared with pre-treatment levels.

Besides the comparison of the relative change in serum anti-MAG IgM titers or levels and clinical outcome measures, we analyzed the responder and non-responder groups in terms of age at neuropathy onset, age when patients participated in the clinical studies, and the duration of the neuropathy until the patients participated in the clinical trial and received the specific treatment (Figure 4).

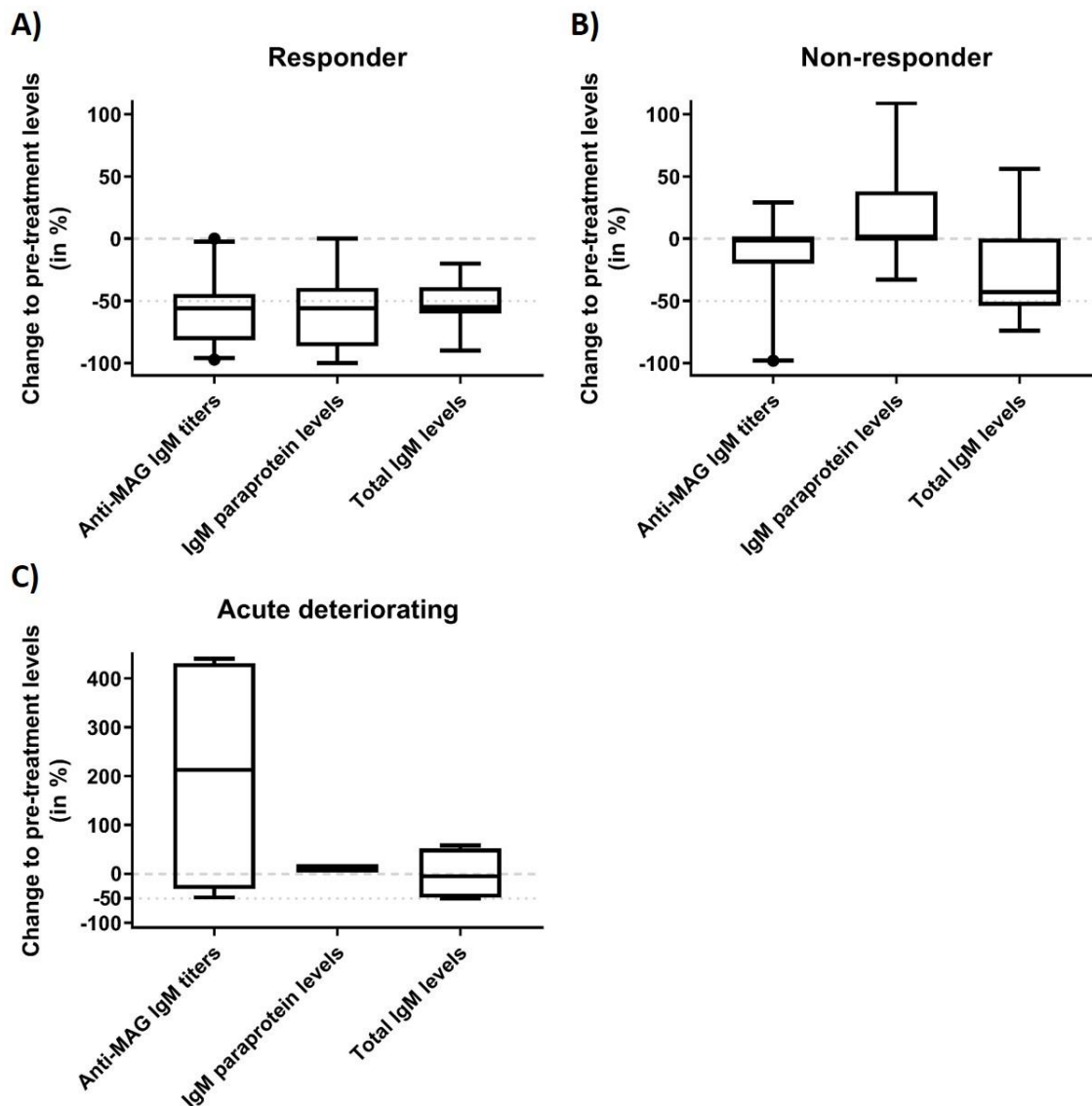


Figure 3. Comparison of the relative change in serum anti-MAG IgM titers or levels between responder, non-responder, and acute deteriorating groups. Comparison of clinical improvement and relative change in serum anti-MAG IgM titers, paraprotein levels, and total IgM levels in the **A)** responder group, **B)** non-responder group, **C)** and the acute deteriorating group. Data are shown as median and 95% confidence intervals.

The mean age at onset of the neuropathy in the non-responder group (60.1 years \pm 6.5 years SD) was significantly ($p \leq 0.05$) higher compared to the responder group (55.3 years \pm 8.5 years SD). Likewise, the mean age when the anti-MAG neuropathy patients were included in the clinical study was significantly higher in the non-responder group with 65.8 years (\pm 7.1 years SD) compared to 60.7 years (\pm 9.1 years SD) in the responder group ($p \leq 0.05$). Surprisingly, there was no significant difference in the duration of the neuropathy at the time point when the participants were included in the clinical study and receiving immunotherapies in the non-responder group (6.0 years \pm 3.4 years SD) compared to the responder group (5.4 years \pm 5.2 years SD, $p > 0.05$).

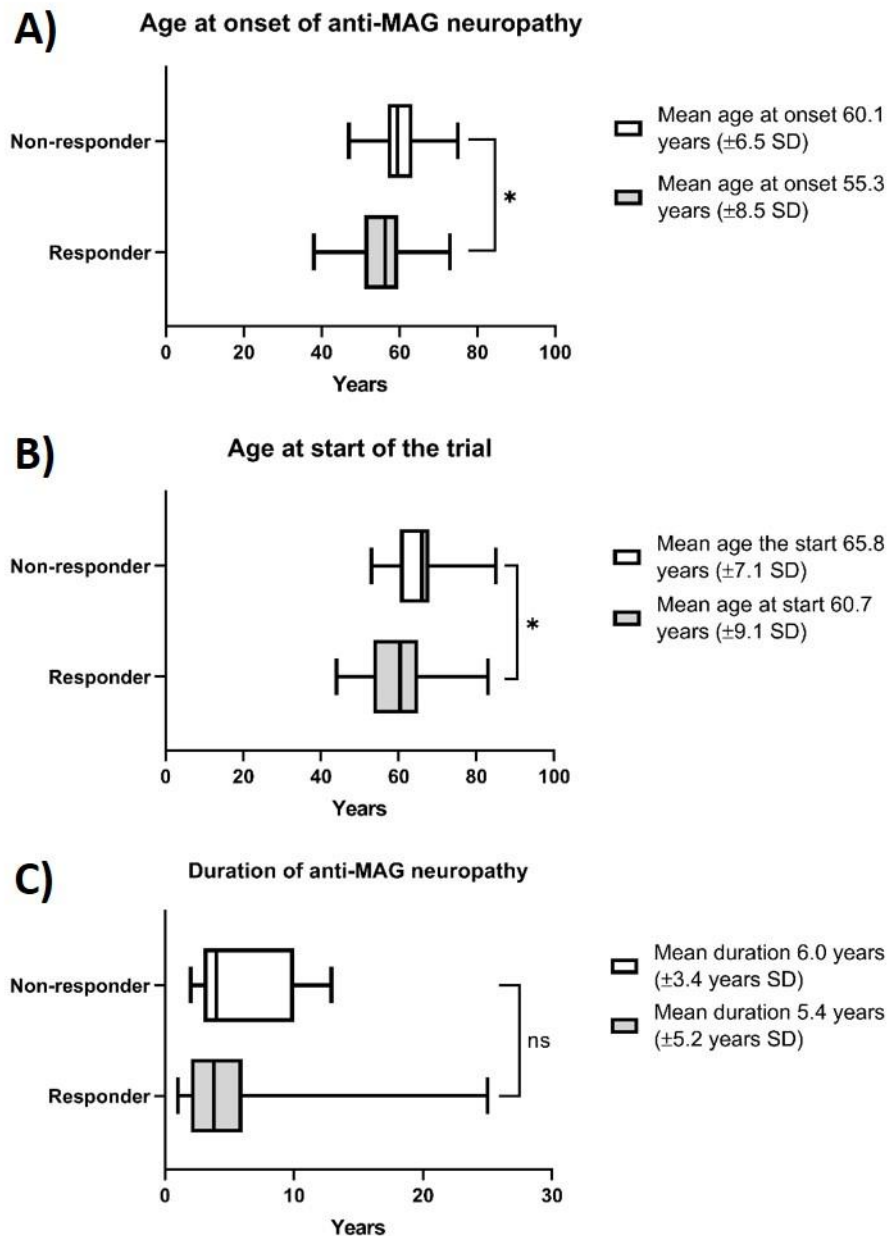


Figure 4. Analysis of the clinical study patient population. **A)** Mean age at onset of the neuropathy and **B)** The mean age at the start of the clinical study was significantly lower in the responder group ($n = 208$ participants) compared to the non-responder group ($n = 191$ participants). **C)** The difference in disease duration until the patients participated in the clinical study was not significant. Data are shown as median and 95% confidence intervals, an independent t-test and Tukey Kramer test were performed ($p < 0.05$).

Discussion

To date, an association between anti-MAG IgM titers or paraprotein levels and either the severity spectrum or the progression of anti-MAG neuropathy has not been convincingly shown^{53, 80}. However, this retrospective analysis of 50 clinical trials in anti-MAG neuropathy

demonstrates that a majority of analyzed studies are supportive of the hypothesis that (i) a relative reduction in anti-MAG IgM antibodies was associated with clinical improvement in the responder group, (ii) the non-responder group exhibited no or only minimal change in anti-MAG IgM titers and levels, and (iii) acute worsening was associated with an increase in anti-MAG titers.

The variety of the clinical outcome measures, including disability scores, strength and ataxia scores, or patient reported outcomes makes a direct comparison of the clinical outcomes among studies difficult, especially as many of the measures are nominal or ordinal and, therefore, are descriptive values. They are often misinterpreted as numerical values including the assumption of linearity which would be required for statistical calculations ¹⁰⁶. Hence, a correlation coefficient was not calculated for reduction of autoantibodies and clinical improvements. Nonetheless, a strong association between relative reduction in anti-MAG antibodies and clinical improvements is supported by this retrospective analysis. Independent of whether the assessment was done in anti-MAG IgM titer units, or paraprotein levels (g/L), most responders (77.7%) exhibited a mean reduction of more than 50% compared to their pre-treatment values. In addition, only 6% of non-responders exhibited a reduction of more than 20% in anti-MAG IgM titers or paraprotein during the clinical studies. These findings suggest that a relative reduction of more than 50% in anti-MAG IgM titer units or paraprotein levels during the course of treatment is a useful biomarker for sustained clinical improvement; whilst a relative reduction of less than 20% indicates an insufficient response to the immunotherapy, regardless of whether it is assessed in anti-MAG titer units or paraprotein levels.

In most of the studies not supporting the hypothesis, the authors commented on possible reasons for the contradictory observations. For example, in several studies, patients exhibited anti-MAG IgM titers above the upper cut-off value of the ELISA, making it difficult to detect a reduction of anti-MAG IgM titers ^{62, 63, 89, 107}. In contrast to anti-MAG IgM titers, monoclonal IgM paraprotein levels are assessed as absolute amounts (g/L) with no specific upper cut-off value and may be considered as more reliable indicators of the hematological response in patients with high anti-MAG IgM titers ¹⁰⁸. Nonetheless, measuring changes in paraprotein levels in patients with low baseline levels is challenging due to the lower limit of detection ^{99, 100, 109}. In addition, paraprotein measurements neither assess the reactivity nor affinity of the monoclonal component. Total IgM measurement is the least sensitive method as shown in different studies ^{92, 97}. In light of these findings, it might be beneficial for future clinical studies

to measure both anti-MAG IgM titers and paraprotein levels in order to cover the entire range of anti-MAG IgM autoantibodies during immunotherapy.

Two factors that may affect the response to treatment are the advanced stage of disease and the severity of axonal damage as discussed by Rakocevic and colleagues⁵¹. They suggest advanced axonal damage as a reason for the observation that even an almost complete depletion of CD20⁺ B cells and circulating anti-MAG antibodies did not lead to clinical improvements. Biomarkers of axonal damage, such as neurofilament light chain could prove to be a valuable indicator of poor response to treatment in anti-MAG neuropathy, as has been described in other peripheral neuropathies like Guillain-Barré syndrome or chronic inflammatory demyelinating polyneuropathy¹¹⁰⁻¹¹². Furthermore, cases of CD20⁺ B cell depletion by rituximab without a reduction of anti-MAG IgM autoantibodies or clinical improvement, suggests that anti-MAG IgM antibody producing cells were most likely late-stage CD20⁻ B cells or plasma cells⁹⁵.

Another factor that should be taken in account, is the time of the treatment relative to clinical assessment and, importantly, the follow-up phase after the course of treatment. Peripheral nerves have the potential for both remyelination and regeneration, which requires time¹¹³. As a consequence, efficient and sustained depletion of anti-MAG IgM autoantibodies from the circulation would not necessarily, immediately, remove the pathogenic antibodies from myelin, but could, at least, prevent the binding of new autoantibodies to myelin, leading to long-term stabilization or improvement of the disease. Current outcome measures are often limited in their ability to capture minimal but clinically important differences in disease status. Clinical assessment of anti-MAG neuropathy patients may, thus, need to be adjusted to better capture early clinically meaningful signs of improvements⁴⁰.

Other parameters of the patient population were analyzed. Interestingly, the duration of the neuropathy until participation in the clinical studies had no significant impact on the response to treatment. However, responders had a significant lower age at onset of the neuropathy and were significantly younger at the time point when they participated in the clinical study. Based on the limited data, no firm conclusion can be made and a sufficiently large natural history study may be more appropriate to clarify the impact of the onset and duration of neuropathy on treatment outcome.

Taken together, the majority of the studies support the hypothesis that there is a strong association between relative changes in anti-MAG IgM autoantibodies and clinical outcomes in anti-MAG neuropathy patients and, specifically, that a reduction in anti-MAG

autoantibodies is associated with improvement of symptoms. The retrospective analysis indicates that a sustained relative reduction of more than 50% compared to the pre-treatment anti-MAG IgM titers units or paraprotein levels is associated with clinical improvements. Thus, both of these parameters could be valuable biomarkers and predictors for long-term immunotherapy response anti-MAG neuropathy patients.

Author disclosures:

P.H., R.H., and A.J.S. are co-founders of a University of Basel spin-off, Polyneuron Pharmaceuticals AG, whose activity is related to the subject matter of this article. R.H. is also a member of the board of directors and P.H., K.M., and R.H., are employees of Polyneuron Pharmaceuticals AG.

References

1. Talamo, G., et al., IgM MGUS associated with anti-MAG neuropathy: a single institution experience. *Annals of Hematology*, 2015. **94**(6): p. 1011-1016.
2. Quarles, R.H., Myelin-associated glycoprotein (MAG): past, present and beyond. *Journal of Neurochemistry*, 2007. **100**(6): p. 1431-1448.
3. Voshol, H., et al., Structure of the HNK-1 carbohydrate epitope on bovine peripheral myelin glycoprotein P0. *Journal of Biological Chemistry*, 1996. **271**(38): p. 22957-22960.
4. Crocker, P.R., J.C. Paulson, and A. Varki, Siglecs and their roles in the immune system. *Nature Reviews Immunology*, 2007. **7**(4): p. 255-266.
5. Kelm, S., et al., Sialoadhesin, myelin-associated glycoprotein and CD22 define a new family of sialic acid-dependent adhesion molecules of the immunoglobulin superfamily. *Current Biology*, 1994. **4**(11): p. 965-972.
6. Latov, N., et al., Plasma cell dyscrasia and peripheral neuropathy: identification of the myelin antigens that react with human paraproteins. *Proc Natl Acad Sci U S A*, 1981. **78**(11): p. 7139-42.
7. Dalakas, M.C., Pathogenesis of immune-mediated neuropathies. *Biochim Biophys Acta*, 2015. **1852**(4): p. 658-66.
8. Dalakas, M.C., Advances in the diagnosis, immunopathogenesis and therapies of IgM-anti-MAG antibody-mediated neuropathies. *Ther Adv Neurol Disord*, 2018. **11**: p. 1756285617746640.
9. Magy, L., et al., Heterogeneity of Polyneuropathy Associated with Anti-MAG Antibodies. *J Immunol Res*, 2015. **2015**: p. 450391.
10. Vallat, J.M., et al., Therapeutic options and management of polyneuropathy associated with anti-MAG antibodies. *Expert Rev Neurother*, 2016. **16**(9): p. 1111-9.
11. Mygland, A. and P. Monstad, Chronic polyneuropathies in Vest-Agder, Norway. *Eur J Neurol*, 2001. **8**(2): p. 157-65.
12. Mahdi-Rogers, M. and R.A. Hughes, Epidemiology of chronic inflammatory neuropathies in southeast England. *Eur J Neurol*, 2014. **21**(1): p. 28-33.
13. Briani, C., et al., Obinutuzumab, a new anti-CD20 antibody, and chlorambucil are active and effective in anti-myelin-associated glycoprotein antibody polyneuropathy. *Eur J Neurol*, 2019. **26**(2): p. 371-375.

14. Rakocevic, G., U. Martinez-Outschoorn, and M.C. Dalakas, Obinutuzumab, a potent anti-B-cell agent, for rituximab-unresponsive IgM anti-MAG neuropathy. *Neurol Neuroimmunol Neuroinflamm*, 2018. **5**(4): p. e460.
15. Lunn, M.P. and E. Nobile-Orazio, Immunotherapy for IgM anti-myelin-associated glycoprotein paraprotein-associated peripheral neuropathies. *Cochrane Database Syst Rev*, 2016. **10**: p. CD002827.
16. Codron, P., et al., Therapeutic plasma exchange in chronic dysimmune peripheral neuropathies: A 10-year retrospective study. *J Clin Apher*, 2017. **32**(6): p. 413-422.
17. Svahn, J., et al., Anti-MAG antibodies in 202 patients: clinicopathological and therapeutic features. *J Neurol Neurosurg Psychiatry*, 2017.
18. Dyck, P.J., et al., Plasma exchange in polyneuropathy associated with monoclonal gammopathy of undetermined significance. *N Engl J Med*, 1991. **325**(21): p. 1482-6.
19. Oksenhendler, E., et al., Plasma exchange and chlorambucil in polyneuropathy associated with monoclonal IgM gammopathy. IgM-associated Polyneuropathy Study Group. *J Neurol Neurosurg Psychiatry*, 1995. **59**(3): p. 243-7.
20. Comi, G., et al., A randomised controlled trial of intravenous immunoglobulin in IgM paraprotein associated demyelinating neuropathy. *J Neurol*, 2002. **249**(10): p. 1370-7.
21. Noronha, V., T.M. Fynan, and T. Duffy, Flare in neuropathy following rituximab therapy for Waldenstrom's macroglobulinemia. *J Clin Oncol*, 2006. **24**(1): p. e3.
22. Rudnicki, S.A., et al., Nervous system dysfunction in Waldenström's macroglobulinemia: response to treatment. *Neurology*, 1998. **51**(4): p. 1210-3.
23. Ellie, E., et al., Neuropathy associated with "benign" anti-myelin-associated glycoprotein IgM gammopathy: clinical, immunological, neurophysiological pathological findings and response to treatment in 33 cases. *J Neurol*, 1996. **243**(1): p. 34-43.
24. Pestronk, A., et al., Treatment of IgM antibody associated polyneuropathies using rituximab. *J Neurol Neurosurg Psychiatry*, 2003. **74**(4): p. 485-9.
25. Levine, T.D. and A. Pestronk, IgM antibody-related polyneuropathies: B-cell depletion chemotherapy using Rituximab. *Neurology*, 1999. **52**(8): p. 1701-4.
26. Wilson, H.C., et al., Successful treatment of IgM paraproteinaemic neuropathy with fludarabine. *Journal of Neurology Neurosurgery and Psychiatry*, 1999. **66**(5): p. 575-580.
27. Doneddu, P.E., et al., Deterioration of tremor after treatment with rituximab in anti-MAG neuropathy. *J Neurol Sci*, 2017. **373**: p. 344-345.

28. Zara, G., R. Zambello, and M. Ermani, Neurophysiological and clinical responses to rituximab in patients with anti-MAG polyneuropathy. *Clin Neurophysiol*, 2011. **122**(12): p. 2518-22.
29. Sherman, W.H., et al., Plasma exchange treatment of peripheral neuropathy associated with plasma cell dyscrasia. *J Neurol Neurosurg Psychiatry*, 1984. **47**(8): p. 813-9.
30. Dalakas, M.C., et al., Placebo-controlled trial of rituximab in IgM anti-myelin-associated glycoprotein antibody demyelinating neuropathy. *Ann Neurol*, 2009. **65**(3): p. 286-93.
31. Gruson, B., et al., Long-term response to rituximab and fludarabine combination in IgM anti-myelin-associated glycoprotein neuropathy. *J Peripher Nerv Syst*, 2011. **16**(3): p. 180-5.
32. Weiss, M.D. and P. Becker, Paradoxical worsening of anti-myelin-associated glycoprotein polyneuropathy following rituximab. *Muscle & Nerve*, 2014. **49**(3): p. 457-458.
33. Sala, E., et al., Acute neurological worsening after Rituximab treatment in patients with anti-MAG neuropathy. *J Neurol Sci*, 2014. **345**(1-2): p. 224-7.
34. Baron, M., et al., Plasma exchanges for severe acute neurological deterioration in patients with IgM anti-myelin-associated glycoprotein (anti-MAG) neuropathy. *J Neurol*, 2017. **264**(6): p. 1132-1135.
35. Renaud, S., et al., Rituximab in the treatment of polyneuropathy associated with anti-MAG antibodies. *Muscle & Nerve*, 2003. **27**(5): p. 611-615.
36. Renaud, S., et al., High-dose rituximab and anti-MAG-associated polyneuropathy. *Neurology*, 2006. **66**(5): p. 742-4.
37. Benedetti, L., et al., Predictors of response to rituximab in patients with neuropathy and anti-myelin associated glycoprotein immunoglobulin M. *J Peripher Nerv Syst*, 2007. **12**(2): p. 102-7.
38. Benedetti, L., et al., Long-term effect of rituximab in anti-mag polyneuropathy. *Neurology*, 2008. **71**(21): p. 1742-4.
39. Kilidireas, C., et al., Rituximab therapy in monoclonal IgM-related neuropathies. *Leuk Lymphoma*, 2006. **47**(5): p. 859-64.
40. Souayah, N., R. Noopur, and P.S. Tick-Chong, Beneficial effects of Rituximab in patients with anti-MAG (myelin-associated glycoprotein) neuropathy: case reports. *Immunopharmacol Immunotoxicol*, 2013. **35**(5): p. 622-4.

41. Léger, J.M., et al., Placebo-controlled trial of rituximab in IgM anti-myelin-associated glycoprotein neuropathy. *Neurology*, 2013. **80**(24): p. 2217-25.
42. Iancu Ferfoglia, R., et al., Long-term efficacy of rituximab in IgM anti-myelin-associated glycoprotein neuropathy: RIMAG follow-up study. *J Peripher Nerv Syst*, 2016. **21**(1): p. 10-4.
43. Hospital, M.A., et al., Immunotherapy-based regimen in anti-MAG neuropathy: results in 45 patients. *Haematologica*, 2013. **98**(12): p. e155-7.
44. Gorson, K.C., et al., Treatment experience in patients with anti-myelin-associated glycoprotein neuropathy. *Muscle Nerve*, 2001. **24**(6): p. 778-86.
45. Duncombe, A.S., et al., R-CP Chemoimmunotherapy in Patients with IgM Paraproteinaemic Neuropathy Produces Improvements In Functional, Electrophysiological and Serological Outcomes. *Hematological Oncology*, 2017. **35**(S2): p. 217-218.
46. Nobile-Orazio, E., et al., Treatment of patients with neuropathy and anti-MAG IgM M-proteins. *Ann Neurol*, 1988. **24**(1): p. 93-7.
47. Campagnolo, M., et al., IgM MGUS and Waldenstrom-associated anti-MAG neuropathies display similar response to rituximab therapy. *J Neurol Neurosurg Psychiatry*, 2017. **88**(12): p. 1094-1097.
48. Niermeijer, J.M., et al., Intermittent cyclophosphamide with prednisone versus placebo for polyneuropathy with IgM monoclonal gammopathy. *Neurology*, 2007. **69**(1): p. 50-9.
49. Niermeijer, J.M., et al., Neurologic and hematologic response to fludarabine treatment in IgM MGUS polyneuropathy. *Neurology*, 2006. **67**(11): p. 2076-9.
50. Kelly, J.J., et al., Polyneuropathies associated with IgM monoclonal gammopathies. *Arch Neurol*, 1988. **45**(12): p. 1355-9.
51. Haas, D.C. and A.H. Tatum, Plasmapheresis alleviates neuropathy accompanying IgM anti-myelin-associated glycoprotein paraproteinemia. *Ann Neurol*, 1988. **23**(4): p. 394-6.
52. Blume, G., A. Pestronk, and L.T. Goodnough, Anti-MAG antibodies-associated polyneuropathies- improvement following immunotherapy with monthly plasma-exchange and IV-Cyclophosphamide. *Neurology*, 1995. **45**(8): p. 1577-1580.
53. Mariette, X., et al., A randomised clinical trial comparing interferon-alpha and intravenous immunoglobulin in polyneuropathy associated with monoclonal IgM. *Journal of Neurology Neurosurgery and Psychiatry*, 1997. **63**(1): p. 28-34.

54. Stino, A.M. and Y. Efebera, Lenalidomide-responsive anti-myelin-associated glycoprotein neuropathy. *Muscle Nerve*, 2017. **56**(4): p. E31-E32.
55. Gomez, A. and J.E. Hoffman, Anti Myelin-Associated-Glycoprotein Antibody Peripheral Neuropathy Response to Combination Chemoimmunotherapy With Bendamustine/Rituximab in a Patient With Biclonal IgM κ and IgM λ : Case Report and Review of the Literature. *Clin Lymphoma Myeloma Leuk*, 2016. **16**(7): p. e101-8.
56. Vo, M.L., P. Martin, and N. Latov, Correlation of Changes in Gait Parameters, With Phenotype, Outcome Measures, and Electrodiagnostic Abnormalities in a Patient With Anti-MAG Neuropathy After Exacerbation and Improvement. *J Clin Neuromuscul Dis*, 2015. **17**(1): p. 22-6.
57. Delmont, E., et al., Treatment with rituximab in patients with polyneuropathy with anti-MAG antibodies. *J Neurol*, 2011. **258**(9): p. 1717-9.
58. Stork, A.C.J., et al., Rapid worsening of IgM anti-MAG demyelinating polyneuropathy during rituximab treatment. *Journal of the Peripheral Nervous System*, 2013. **18**(2): p. 189-191.
59. Broglio, L. and G. Lauria, Worsening after rituximab treatment in anti-mag neuropathy. *Muscle Nerve*, 2005. **32**(3): p. 378-9.
60. Gironi, M., et al., Clinical and immunological worsening in a patient affected with Waldenstrom macroglobulinemia and anti-mag neuropathy after treatment with rituximab. *Haematologica*, 2006. **91**(6 Suppl): p. ECR17.
61. Al-Bustani, N. and M.D. Weiss, Marked and sustained improvement on nerve conduction study of anti-myelin-associated glycoprotein neuropathy following rituximab therapy. *Muscle Nerve*, 2016. **53**(3): p. 489-90.
62. Delarue, R., et al., Rituximab in Anti-Mag Associated Neuropathy : A Monocentric Experience. *Blood*, 2004. **104**(11): p. 4909-4909.
63. Benedetti, L., et al., Outcomes after single-cycle rituximab monotherapy in patients with anti-MAG polyneuropathy: A bi-center experience with an average follow-up of 11 years. *J Neuroimmunol*, 2019. **337**: p. 577081.
64. Hamidou, M.A., et al., Intravenous cyclophosphamide in refractory polyneuropathy associated with IgM monoclonal gammopathy: an uncontrolled open trial. *Am J Med*, 2005. **118**(4): p. 426-30.
65. Ghosh, A., T. Littlewood, and M. Donaghy, Cladribine in the treatment of IgM paraproteinemic polyneuropathy. *Neurology*, 2002. **59**(8): p. 1290-1.

66. Notermans, N.C., et al., Intermittent cyclophosphamide and prednisone treatment of polyneuropathy associated with monoclonal gammopathy of undetermined significance. *Neurology*, 1996. **47**(5): p. 1227-33.
67. Notermans, N.C., et al., Pulsed high-dose dexamethasone treatment of polyneuropathy associated with monoclonal gammopathy. *J Neurol*, 1997. **244**(7): p. 462-3.
68. Niemierko, E. and R. Weinstein, Response of patients with IgM and IgA-associated peripheral polyneuropathies to off-line immunoadsorption treatment using the ProSORBA protein A column. *J Clin Apher*, 1999. **14**(4): p. 159-62.
69. Ernerudh, J., et al., Peripheral neuropathy and monoclonal IgM with antibody activity against peripheral nerve myelin; effect of plasma exchange. *J Neuroimmunol*, 1986. **11**(3): p. 171-8.
70. Ernerudh, J.H., et al., Immunochemical and clinical effects of immunosuppressive treatment in monoclonal IgM neuropathy. *J Neurol Neurosurg Psychiatry*, 1992. **55**(10): p. 930-4.
71. Dalakas, M.C., et al., A controlled study of intravenous immunoglobulin in demyelinating neuropathy with IgM gammopathy. *Ann Neurol*, 1996. **40**(5): p. 792-5.
72. Liberatore, G., et al., Sensitivity and specificity of a commercial ELISA test for anti-MAG antibodies in patients with neuropathy. *J Neuroimmunol*, 2020. **345**: p. 577288.
73. Pruppers, M.H., I.S. Merkies, and N.C. Notermans, Recent advances in outcome measures in IgM-anti-MAG+ neuropathies. *Curr Opin Neurol*, 2015. **28**(5): p. 486-93.
74. Leger, J.-M., et al., Placebo-controlled trial of rituximab in IgM anti-myelin-associated glycoprotein neuropathy. *Neurology*, 2013. **80**(24): p. 2217-2225.
75. Latov, N., Diagnosis and treatment of chronic acquired demyelinating polyneuropathies. *Nature Reviews Neurology*, 2014. **10**(8): p. 435-446.
76. Weiss, M.D., C.A. Luciano, and R.H. Quarles, Nerve conduction abnormalities in aging mice deficient for myelin-associated glycoprotein. *Muscle & Nerve*, 2001. **24**(10): p. 1380-1387.
77. Altmann, P., et al., Increased serum neurofilament light chain concentration indicates poor outcome in Guillain-Barré syndrome. *J Neuroinflammation*, 2020. **17**(1): p. 86.
78. Gaetani, L., et al., Neurofilament light chain as a biomarker in neurological disorders. *J Neurol Neurosurg Psychiatry*, 2019. **90**(8): p. 870-881.
79. van Lieverloo, G.G.A., et al., Serum neurofilament light chain in chronic inflammatory demyelinating polyneuropathy. *J Peripher Nerv Syst*, 2019. **24**(2): p. 187-194.

80. Zhou, Y. and L. Notterpek, Promoting peripheral myelin repair. *Exp Neurol*, 2016. **283**(Pt B): p. 573-80.
81. Pruppers, M.H.J., et al., 230th ENMC International Workshop:: Improving future assessment and research in IgM anti-MAG peripheral neuropathy: A consensus collaborative effort, Naarden, The Netherlands, 24-26 February 2017. *Neuromuscul Disord*, 2017. **27**(11): p. 1065-1072.

Supporting Information

Table e-1. Overview of clinical data excluded from the 52 publications identified in the systematic literature search

| Study type, Reference | Treatment and Nr. of anti-MAG neuropathy patients (n) | Change in anti MAG IgM, IgM paraprotein, total IgM | Clinical outcome measures | Comment |
|--|---|--|---|--|
| Retrospective study, Codron <i>et al.</i> 2017 ⁵² | Plasma exchange (n=9) | No information available | <p>Responder (2/9) Improvements in Hughes score</p> <p>Non-responder (7/9) No improvements in Hughes score</p> | No anti-MAG IgM titres or paraprotein levels were measured. Short term reduction can be anticipated as patients underwent plasmapheresis cycles. |
| Retrospective and prospective study, Svahn <i>et al.</i> 2017 ⁵³ | Various treatment interventions (n=202) | No information available | No information regarding change of the anti-MAG IgM levels and the clinical outcome measurements. | Detection of anti-MAG IgM was performed before treatment in 186 patients but only in 16 patients after treatment. |
| Case study, Noronha <i>et al.</i> 2006 ⁵⁷ | Rituximab (n=1) | +30% paraprotein | <p>Acute deteriorating (1/1) Flair in neuropathy</p> | Waldenström's macroglobulinemia patient. |
| Case study, Rudnicki <i>et al.</i> 1998 ⁵⁸ | Autologous bone marrow (n=1) | -99% in anti-MAG IgM titers | <p>Responder (1/1) Fast electrophysiological response, slow symptomatic improvements</p> | Waldenström's macroglobulinemia patient with atypical parkinsonism. |
| Placebo controlled, double blind and open label crossover study, Dyck <i>et al.</i> 1991 ⁵⁴ | <p>Plasma exchange (n=11)</p> <p>Sham exchange (n=10)</p> | No information available | Clinical improvements observed in the patients. However, they did not reach significant improvements in the PE group compared to the sham exchange. | No anti-MAG IgM titres or paraprotein levels were measured. Short term reduction can be anticipated as patients underwent PE cycles. |

| Study type, Reference | Treatment and Nr. of anti-MAG neuropathy patients (n) | Change in anti MAG IgM, IgM paraprotein, total IgM | Clinical outcome measures | Comment |
|--|---|--|--|--|
| Open label study, Oksenhendler <i>et al.</i> 1995 ⁵⁵ | Chlorambucil (n=22) | Limited information available | Responder (8/22) <ul style="list-style-type: none"> • Improvements in self-reported outcome Non-Responder (14/22) <ul style="list-style-type: none"> • Worsening in self-reported outcome (n=8) • Stabilization (n=6) | PE seemed to confer no additional benefit in the treatment of polyneuropathy associated with monoclonal IgM. |
| | Chlorambucil and PE (n=22) | | Responder (7/22) <ul style="list-style-type: none"> • Improvements in self-reported outcome Non-Responder (15/22) <ul style="list-style-type: none"> • Worsening in self-reported outcome (n=7) • Stabilization (n=8) | |
| Randomized, crossover, placebo controlled trial, Comi <i>et al.</i> 2002 ⁵⁶ | IVIg, placebo (n=11) | No information available | IVIg phase <ul style="list-style-type: none"> • Responder (10/22) • Non-responder (12/22), stable n=11, deteriorated n=1 | Only modest benefit of IVIg in a minority of patients. |
| | Placebo, IVIg (n=11) | | Placebo phase <ul style="list-style-type: none"> • Responder (4/22) • Non-responder (18/22), stable n=14, deteriorated n=4 | |
| Open label study, Ellie <i>et al.</i> 1995 ⁵⁹ | Various, PE, prednisone, IVIg, cytotoxic drugs | Limited information available | Responder (22/37) <ul style="list-style-type: none"> • Only mild and transient improvements | Only modest benefit independent from the treatment. Four patients |

| Study type, Reference | Treatment and Nr. of anti-MAG neuropathy patients (n) | Change in anti MAG IgM, IgM paraprotein, total IgM | Clinical outcome measures | Comment |
|--------------------------|---|---|---|----------------------------------|
| | (n=33) | | Non-responder (11/37) <ul style="list-style-type: none"> • No treatment response or worsening | died during the follow-up phase. |

Table e-2. Overview of clinical data extracted from the 50 publications identified in the systematic literature search.

| Study type, Class of evidence, Reference | Treatment and Nr. of anti-MAG neuropathy patients (n) | Change in anti MAG IgM | Change in para- protein | Change in total IgM | Clinical outcomes measures | Time to response ^A | Supporting change in anti-MAG IgM and clinical symptoms correlation and comments |
|---|--|------------------------------|-------------------------------|------------------------|---|--|--|
| Retrospective study, Class VI, Pestronk <i>et al.</i> 2003 ^{23*} | Rituximab (n=7) | -57% | NR | NR | Responder (7/7) • Improvements in strength (+24%) | Response • 6 months (1 st FU) | Supportive • Patients with other polyneuropathies (e.g. anti-GM1 IgM) were included in the study as well. |
| | Placebo (n=5) | No change | NR | NR | Non-Responder (5/5) • No improvements (0%) in strength compare to pre- treatment after 24 months | No response • Stable for 24 months | |
| Double blind, placebo-controlled study, Class I Dalakas <i>et al.</i> 2009 ⁶⁵ | Rituximab (n=13) | -50% | NR | -34% | Responder (7/13) • Improvements in INCAT (4/13) • Walking improved (7/13) | Response • 2 months (start to improve) | Supportive • Improvements would have been significant if one patient with a disability score of 0 at baseline was excluded. |
| | Placebo (n=13) | +37% | NR | +5% | Non-Responder (13/13) • No change in INCAT • No improvement in walking | No response • Stable for 8 months | |
| Open label study, Class IV, Gruson <i>et al.</i> 2011 ⁶⁶ | Rituximab and fludarabine (n=2) | > -50% | -95% | NR | Responder (2/2) • Improvements in INCAT (-3.5) • Improvements in MCV (≥10%, range 10-50%) and decrease in DML (≥10%, range 10-25%) | Response • 6 months (end of treatment) | Supportive • One patient had baseline values of >70,000 BTU and the post treatment levels were 65,000 BTU. Therefore the actual reduction would be higher. |

| Study type, Class of evidence, Reference | Treatment and Nr. of anti-MAG neuropathy patients (n) | Change in anti MAG IgM | Change in para- protein | Change in total IgM | Clinical outcomes measures | Time to response ^A | Supporting change in anti-MAG IgM and clinical symptoms correlation and comments |
|--|--|------------------------------|-------------------------------|------------------------|--|---|---|
| Case study, Class IV Weiss <i>et al.</i> 2014 114 | Rituximab (n=1) | +404% | NR | +34% | Acute deteriorating (1/1) • Neurological deterioration (sensory ataxia and impaired ambulation) • Acute IgM flare | Worsening • 2 weeks | Supportive • Serological and neurological parameters returned to baseline after 6 weeks. |
| Case study, Class IV, Sala <i>et al.</i> 2014 ⁶⁸ | Rituximab (n=3) | +440% | NR | NR | Acute deteriorating (3/3) • Deterioration in INCAT (+3.5) • Increased distal latencies and reduced MCV and cMAP | Worsening • 2 weeks | Supportive • Deterioration was reversible within some weeks to several months. |
| Open label study, Class IV, Baron <i>et al.</i> 2017 ⁶⁹ | Plasma exchange (PE) (n=4) | -54% | -69% | NR | Responder (4/4) • Improvements in ONLS (-3) | Response • 1-2 months (1-6 PE) | Supportive • Plasma exchange was performed in anti-MAG patients after acute deterioration. • One patient showed immediate response to PE. |
| Open label study, Class IV, Levine <i>et al.</i> 1999 60* | Rituximab (n=1) | More than -50% | NR | NR | Responder (1/1) • Improvements in strength index (+20%) | Response • 3 months | Supportive • Only 1 anti-MAG neuropathy patient was included in the study. |
| Open label study, Class IV, Renaud <i>et al.</i> 2003 70 | Rituximab (n=6) | More than -52% | NR | -58% | Responder (5/6) • Improvements in NDS (more than -3 points) • Increase in ulnar MCV | Response • 6-12 months (NDS) | Supportive • One patient was deteriorating, but was excluded due to severe occlusive arterial disease. |

| Study type, Class of evidence, Reference | Treatment and Nr. of anti-MAG neuropathy patients (n) | Change in anti MAG IgM | Change in para- protein | Change in total IgM | Clinical outcomes measures | Time to response ^A | Supporting change in anti-MAG IgM and clinical symptoms correlation and comments |
|---|--|------------------------------|-------------------------------|------------------------|---|--|---|
| | | -25% | NR | No change | Non-responder (1/6) <ul style="list-style-type: none"> • Stabilization in NDS • Decrease in ulnar MCV | No response <ul style="list-style-type: none"> • 12 months | |
| Follow up, open label study, Class IV, Renaud <i>et al.</i> 2006 ²⁴ (responder of the previous study ⁷⁰) | Rituximab (n=8) | -59% (median) | NR | -74% (median) | Responder (6/8) <ul style="list-style-type: none"> • Improvements in NDS • Improvements motor nerve conduction velocity by ≥10% | Response <ul style="list-style-type: none"> • 12 months | Supportive <ul style="list-style-type: none"> • One patient that did not respond to the low dose but did respond to the high rituximab dose (reduction of the titers). Unclear if improvements occurred before the FU at 12-months. • Two patients with Waldenström or Non-Hodgkin Lymphoma are included in this cohort. |
| | | | | | Non-responder (2/8) <ul style="list-style-type: none"> • Stabilization in NDS, n=1 • Deterioration in NDS (+2), n=1 | No response <ul style="list-style-type: none"> • 12 months | |
| Open label study, Class IV, Benedetti <i>et al.</i> 2007 ²² | Rituximab (n=7) | -87% | NR | -39% | Responder (5/7) <ul style="list-style-type: none"> • Improvements in ISS • Clinical improvement did not always correlate with electrophysiological improvement (MCV, DML, cMAP). • Electrophysiological improvement was usually more evident in the ulnar nerve than in the peroneal nerve. | Response <ul style="list-style-type: none"> • 12 months | Supportive <ul style="list-style-type: none"> • Improvements in ISS (1.9 point), as well as improvements in MRC sum score and INCAT disability score, but not significant. Unclear if patients exhibited signs of improvements at earlier time points. • Deteriorating patient showed no change in anti-MAG levels. |

| Study type, Class of evidence, Reference | Treatment and Nr. of anti-MAG neuropathy patients (n) | Change in anti MAG IgM | Change in para- protein | Change in total IgM | Clinical outcomes measures | Time to response ^A | Supporting change in anti-MAG IgM and clinical symptoms correlation and comments |
|---|--|------------------------------|-------------------------------|------------------------|---|--|---|
| | | -48% | NR | -2% | Non-responder (2/7) <ul style="list-style-type: none"> • Stabilization in ISS, MRC, INCAT, n=1 • Deterioration in ISS, MRC, INCAT, n=1 | No response <ul style="list-style-type: none"> • 12 months | |
| Follow up open label study, Class IV, Benedetti <i>et al.</i> 2008 ⁷¹ (responder of the previous study ²²) | No treatment (n=9) | -80% | NR | -40% | Sustained responder (5/9) <ul style="list-style-type: none"> • Improvements in INCAT (-1.2) | Response <ul style="list-style-type: none"> • Persistent for 24 months in 80% • Persistent for 36 months in 60% | Supportive <ul style="list-style-type: none"> • Deterioration coincided with or followed an anti-MAG IgM titers increase. • Not clear if all MGUS patients were included in the follow-up study. |
| | | -20% | NR | | Transient responder (4/9) <ul style="list-style-type: none"> • Deterioration in INCAT (+0.759) | | |
| Open label study, Class IV, Kilidireas <i>et al.</i> 2006 ⁷² | Rituximab (n=2) | NR | -50% | NR | Responder (1/2) <ul style="list-style-type: none"> • Improvements in hand grip • Improvements in MRC • Improvements in 10 m walk test • Increase in MNCV, SNCV at 6 weeks • Increase in cMAP, SNAP at 6 weeks | Response <ul style="list-style-type: none"> • 6 weeks | Supportive <ul style="list-style-type: none"> • Transient worsening of MRC in a patient 3 weeks after initiation of rituximab coincided with an IgM flair. Only SGPG and not MAG reactivity was assessed. |

| Study type, Class of evidence, Reference | Treatment and Nr. of anti-MAG neuropathy patients (n) | Change in anti MAG IgM | Change in para- protein | Change in total IgM | Clinical outcomes measures | Time to response ^A | Supporting change in anti-MAG IgM and clinical symptoms correlation and comments |
|--|--|------------------------------|-------------------------------|--|---|---|---|
| | | NR | No reduction | NR | Non-responder (1/2) <ul style="list-style-type: none"> • Stabilization in MRC • Decrease in MNCV, SNCV at 12 months • Increase in cMAP, SNAP at 12 months | No response <ul style="list-style-type: none"> • 12 months | |
| Open label study, Class IV, Souayah <i>et al.</i> 2013 73 | Rituximab (n=3) | More than -90% | NR | NR | Responder (2/2) <ul style="list-style-type: none"> • Improvements in TNS (-10) • Only in one patient improvements in the nerve conduction studies were observed | Response <ul style="list-style-type: none"> • 2-6 months | Supportive <ul style="list-style-type: none"> • Post-analysis was only done for 2 of 3 patients |
| Double blind, placebo controlled study, Class I, Leger <i>et al.</i> 2013 ¹⁰⁷ | Rituximab (n=26) | -20% (median) | NR | NR | Primary outcome: Non-responder (20/20) <ul style="list-style-type: none"> • No significant difference in ISS compare to placebo) | Response <ul style="list-style-type: none"> • 12 months (1st FU) | Partly supportive <ul style="list-style-type: none"> • Withdrawal: n=6 rituximab, n=1 placebo. Typically, a reduction of anti-MAG IgM of at least around 50% is considered necessary for clinical improvements, which may explain the lack of clinical effect in this study⁴¹. |
| | | | | Secondary outcome: responder (5/20) <ul style="list-style-type: none"> • Improvements in INCAT disability score, n=4 (≥2) • Self-evaluated improvements (n=5) | | | |

| Study type, Class of evidence, Reference | Treatment and Nr. of anti-MAG neuropathy patients (n) | Change in anti MAG IgM | Change in para- protein | Change in total IgM | Clinical outcomes measures | Time to response ^A | Supporting change in anti-MAG IgM and clinical symptoms correlation and comments |
|---|--|--|-------------------------------|--|---|---|---|
| | Placebo (n=28) | 0% (median) | NR | NR | Non-responder (27/27) <ul style="list-style-type: none"> No significant change in ISS No change in INCAT disability score No change in SF-36 questionnaire | No Response <ul style="list-style-type: none"> 12 months | |
| Follow up study, Class I, Ferfaglia <i>et al.</i> 2016 ⁷⁵ (Patients of the previous study ¹⁰⁷) | Group 1 (2/7 rituximab and 5/7 no treatment) (n=7) | +6% | NR | NR | Comparison of Group 1 (7/7) and Group 2 (8/8) <ul style="list-style-type: none"> No significant difference in ISS No significant difference in INCAT disability score Worsening in the 10 meter walking test in Group 2 | Median FU 6 months | Not applicable <ul style="list-style-type: none"> Cross-over design makes it challenging to assess the responder to the treatment. Withdrawal: n=1 group 1, n=2 group 2. The authors commented that considering the small number of patients and the heterogeneity of treatments during the FU period, they could not perform any comparison between the groups. |
| <ul style="list-style-type: none"> Group 1: previously rituximab (n=8) Group 2: previously placebo (n=10) | Group 2 (6/8 rituximab and 2/8 no treatment) (n=8) | -39% | NR | NR | | | |
| Retrospective study, Class IV, Hospital <i>et al.</i> 2013 ⁷⁶ | Rituximab (n=26) | No change in anti- MAG IgM titres | NR | Reduction (in responder only) | Responder (21/26) <ul style="list-style-type: none"> Improvements in mRS Non-responder (5/26) <ul style="list-style-type: none"> Stabilization in mRS, n=4 Deterioration in mRS, n=1 | Response <ul style="list-style-type: none"> 9.5 months (median) | Supportive <ul style="list-style-type: none"> IgM level decreased only in responder Anti-MAG IgM levels above the upper cut-off of the ELISA, |

| Study type, Class of evidence, Reference | Treatment and Nr. of anti-MAG neuropathy patients (n) | Change in anti MAG IgM | Change in para- protein | Change in total IgM | Clinical outcomes measures | Time to response ^A | Supporting change in anti-MAG IgM and clinical symptoms correlation and comments |
|---|--|------------------------------|-------------------------------|------------------------|---|--|--|
| | Rituximab Combination (n=19) | | | | Responder (16/19) <ul style="list-style-type: none"> Improvements in mRS Non-responder (3/19) <ul style="list-style-type: none"> Stabilization in mRS, n=2 Deterioration in mRS, n=1 | Response <ul style="list-style-type: none"> 5 months (median) | <p>therefore no difference was observed in the responder group.</p> <ul style="list-style-type: none"> Electrophysiological evaluation in 23 responders confirmed clinical improvements. Significant improvements in mean median nerve distal latencies and cMAP of the peroneal nerve. |
| Open label study, Class IV, Gorson <i>et al.</i> 2001 77 | <p>Various treatment interventions (n=24)</p> <p>PE, IVIg, Prednisone, cyclophosphamide, PE and cyclophosphamide, INF-α2a chlorambucil, azathioprine</p> | -11% (median) | -39% (median) | -25% (median) | Sustained responder (4/24) <ul style="list-style-type: none"> Improvements in Rankin disability scale Improvements in sensory score Improvements in MRC (-1.4) Only median motor nerve distal latency was more prolonged and the sural sensory nerve action potential was more often absent in responder and transient responders. | Response <ul style="list-style-type: none"> 1-6 months 4.8 years mean FU 2.8 years median FU | Supportive <ul style="list-style-type: none"> Due to frequent relapses or lack of a response, patients were treated with an average of three different modalities. The authors concluded that with a larger cohort (powered study) the difference would have been significant. Results in Table 1-3 are not consistent with the main text of the manuscript. |

| Study type, Class of evidence, Reference | Treatment and Nr. of anti-MAG neuropathy patients (n) | Change in anti MAG IgM | Change in para- protein | Change in total IgM | Clinical outcomes measures | Time to response ^A | Supporting change in anti-MAG IgM and clinical symptoms correlation and comments |
|--|--|------------------------------|--|--|--|---|--|
| | | +29.3% (median) | +20% (median) +38% (mean) | +26% (median) +56% (mean) | Transient responder (8/24) <ul style="list-style-type: none"> • Transient improvements in Rankin disability scale, sensory score, MRC • Improvements in MRC | | |
| | | | | | Non-responders (12/24) <ul style="list-style-type: none"> • Deterioration in MRC (+0.5) | No response <ul style="list-style-type: none"> • 4.8 years mean FU • 2.8 years median FU | |
| Open label study, Class IV, Duncombe <i>et al.</i> 2017 ⁷⁸ | Rituximab and cyclophosphamide (n=13) | -60% | -79% | NR | Responder (13/13) <ul style="list-style-type: none"> • Significant clinical improvements in ONLS and NCS | Response <ul style="list-style-type: none"> • 12 months (2nd FU) | Supportive <ul style="list-style-type: none"> • Unclear if a higher relative reduction in each single patient was associated with a better clinical outcome. |

| Study type, Class of evidence, Reference | Treatment and Nr. of anti-MAG neuropathy patients (n) | Change in anti MAG IgM | Change in para- protein | Change in total IgM | Clinical outcomes measures | Time to response ^A | Supporting change in anti-MAG IgM and clinical symptoms correlation and comments |
|---|--|------------------------------|-------------------------------|------------------------|--|---|--|
| Open label study, Class IV, Nobile-Orazio <i>et al.</i> 1988 ⁷⁹ | Chlorambucil (n=5) | -50% | NR | -54.5% | Responder (2/5) <ul style="list-style-type: none"> • Improvements in disability and ataxia score • Improvements in MCV and SNAP | Response <ul style="list-style-type: none"> • 2 months | Supportive <ul style="list-style-type: none"> • Non-responders did not show an alteration in the anti-MAG levels. |
| | | No reduction | NR | -22.5% | Non-Responder (3/5) <ul style="list-style-type: none"> • No change in disability and ataxia score • Nerve conduction velocities were decreased in 2 non-responders | No response <ul style="list-style-type: none"> • 14 months | |
| Open label study, Class IV, Wilson <i>et al.</i> 1999 ^{61*} | Fludarabine (n=2) | NR | NR | -71.5% | Responder (1/2) <ul style="list-style-type: none"> • Improvements in mRS (-3) • Increase in median MCV and SAP | Response <ul style="list-style-type: none"> • 3 months | Partly supportive <ul style="list-style-type: none"> • No anti-MAG levels were measured. |
| | | NR | NR | -45% | Non-responder (1/2) <ul style="list-style-type: none"> • Stabilization in mRS • Increase in median MCV and SAP | No response <ul style="list-style-type: none"> • 6 months | |
| Retrospective study, Class VI, Campagnolo <i>et al.</i> 2017 ⁸⁰ | Rituximab (n=25) | -60% | NR | NR | Responder (15/25) <ul style="list-style-type: none"> • Improvements in INCAT • Improvements in ISS | No response <ul style="list-style-type: none"> • 12 months (1st FU) | Partly supportive <ul style="list-style-type: none"> • Unclear if the patients with reduced anti-MAG levels were the same patients that showed clinical improvements. |
| | | | | | Non-responder (10/25) <ul style="list-style-type: none"> • No improvements in INCAT • No improvements in ISS | No response <ul style="list-style-type: none"> • 12 months (1st FU) | |

| Study type, Class of evidence, Reference | Treatment and Nr. of anti-MAG neuropathy patients (n) | Change in anti MAG IgM | Change in para- protein | Change in total IgM | Clinical outcomes measures | Time to response ^A | Supporting change in anti-MAG IgM and clinical symptoms correlation and comments |
|---|--|------------------------------|-------------------------------|--------------------------|---|---|--|
| Prospective uncontrolled trial, Class VI, Niermeijer <i>et al.</i> 2006 ⁸² | Fludarabine (n=6) | NR | NR | -60% | Responder (2/6) <ul style="list-style-type: none"> • Improvements in raking scale • Median values of EMG variables did not change significantly after treatment • Tendency for improvements of the MCV (>10%) | Response <ul style="list-style-type: none"> • 12 months (1st FU) | Partly supportive <ul style="list-style-type: none"> • Patients exhibited a switch from monoclonal to polyclonal (n=4), and vice-versa (n=1). |
| | | NR | NR | -42.75% | Non-responder (4/6) <ul style="list-style-type: none"> • Stabilization in raking scale • Median values of EMG variables did not change significantly after treatment | No response <ul style="list-style-type: none"> • 12 months (1st FU) | |
| Double-blind randomized, placebo controlled study, Class I, Niermeijer <i>et al.</i> 2007 ⁸¹ | Cyclophosphamide and prednisone (n=16) | NR | -94% | NR (pre-treatment level) | Responder (5/15) <ul style="list-style-type: none"> • Improvements in Rivermead mobility index $\alpha(\geq 1)$, n=5 • More improvements in the secondary outcome measures, including Rankin scale, MRC, and sensory sum score | Response <ul style="list-style-type: none"> • 6 months (1st FU) | Supportive <ul style="list-style-type: none"> • Supportive as more than 50% of the patients (placebo& treatment) exhibited the expected result. • One patient in the treatment group stopped because of angina pectoris. |

| Study type, Class of evidence, Reference | Treatment and Nr. of anti-MAG neuropathy patients (n) | Change in anti MAG IgM | Change in para- protein | Change in total IgM | Clinical outcomes measures | Time to response ^A | Supporting change in anti-MAG IgM and clinical symptoms correlation and comments |
|--|--|------------------------------|---|---------------------------------|--|---|--|
| | Placebo (n=19) | NR | +106% | NR (pre- treatment level) | Non-responder (15/19) <ul style="list-style-type: none"> Improvements in Rivermead mobility index ≥ 1, n=4 More improvements in the secondary outcome measures compare to the treatment group | Response <ul style="list-style-type: none"> 6 months (1st FU) | <ul style="list-style-type: none"> Beneficial effects on most secondary outcome measures for impairment in addition to biologic effects on the M protein concentration and nerve conduction after 6 months and on the MRC sum score thereafter. |
| Open label study, Class IV, Kelly <i>et al.</i> 1988 ⁸³ | Various treatment interventions (n=5) | NR | -40% | NR | Responder (3/3) <ul style="list-style-type: none"> Improvements in NDS | Response <ul style="list-style-type: none"> 3 months | Supportive <ul style="list-style-type: none"> Two patients were excluded due to the development of severe comorbidities. |
| Open label study, Class IV, Haas <i>et al.</i> 1988 ⁸⁴ | Plasmapheresis (n=1) | NR | NR | -20% | Responder (1/1) <ul style="list-style-type: none"> Improvements in MRC Conduction velocity and distal latency did not change appreciably | Response <ul style="list-style-type: none"> 1 month | Supportive <ul style="list-style-type: none"> Case study of repeated plasmapheresis. |
| Open label study, Class IV, Blume <i>et al.</i> 1995 ⁸⁵ | Plasma exchange and IV cyclophosphamide (n=4) | -78% | NR | NR | Responder (4/4) <ul style="list-style-type: none"> Improvements in strength (+34%) | Response <ul style="list-style-type: none"> 3-9 months (depending on the FU time) | Supportive <ul style="list-style-type: none"> All patients showed improvements. |
| Prospective, randomised, open clinical trial, Class I, | IFN- α treatment (n=10) | NR | More than -50 % (in two responde r) | NR | Responder (8/10) <ul style="list-style-type: none"> Improvements in CNDS (-7.5) Non-responder (2/10) <ul style="list-style-type: none"> No change in CNDS | Response <ul style="list-style-type: none"> 6 months (1st FU) | Not supportive <ul style="list-style-type: none"> No significant decrease in IgM paraprotein was noted. The authors suggested that IFN-α |

| Study type, Class of evidence, Reference | Treatment and Nr. of anti-MAG neuropathy patients (n) | Change in anti MAG IgM | Change in para- protein | Change in total IgM | Clinical outcomes measures | Time to response ^A | Supporting change in anti-MAG IgM and clinical symptoms correlation and comments |
|---|--|------------------------------|-------------------------------|------------------------|--|--|--|
| Mariette <i>et al.</i> 1997 ⁸⁶ | IVIg treatment (n=10) | NR | No reduction | NR | <p>Responder (1/10)</p> <ul style="list-style-type: none"> • Improvements in CNDS (only transient) <p>Non-responder (9/10)</p> <ul style="list-style-type: none"> • Worsening in CNDS (+2.3) | <p>No response</p> <ul style="list-style-type: none"> • 6 months | <p>decreases the permeability of the blood nerve barriers and therefore, explained why 6 patients showed clinical improvements without lowering the total IgM.</p> <ul style="list-style-type: none"> • The mean value of ulnar motor-nerve conduction velocities and distal latencies were not different between the two groups. • Due to the large number of patients with no SNAP at baseline in the two groups, it was impossible to compare the evolution of sensory nerve conduction velocities. |
| Open label study, Class IV, Rakocevic <i>et al.</i> 2018 ⁵¹ | Obinutuzumab (n=2) | -98% | NR | -58% | <p>Non-Responders (2/2)</p> <ul style="list-style-type: none"> • No improvement or worsening in neuropathic symptoms | <p>No response</p> <ul style="list-style-type: none"> • 6 months | <p>Not supportive</p> <ul style="list-style-type: none"> • The authors suggested that due to the patients' advanced disease and severe axonal degeneration, no clinical response was detected. |

| Study type, Class of evidence, Reference | Treatment and Nr. of anti-MAG neuropathy patients (n) | Change in anti MAG IgM | Change in para- protein | Change in total IgM | Clinical outcomes measures | Time to response ^A | Supporting change in anti-MAG IgM and clinical symptoms correlation and comments |
|---|--|------------------------------|-------------------------------|------------------------|--|---|--|
| Case study, open label, Class IV, Stino <i>et al.</i> 2017 ⁸⁷ | Lenalidomide (n=1) | No reduction | -71% | NR | Responder (1/1) <ul style="list-style-type: none"> • Improvements in I-RODS (22%) • No improvements in INCAT • Mild to modest improvements in NCS (median and ulnar DML), MCV unchanged | Response <ul style="list-style-type: none"> • 7 months (1st FU) | Supportive <ul style="list-style-type: none"> • Anti-MAG IgM levels are above the upper detection limit. Therefore, a reduction cannot be detected by ELISA. |
| Case Study, Class IV, Doneddu <i>et al.</i> 2017 ^{62*} | Rituximab (n=2) | NR | +8.5% | NR | Acute deteriorating (2/2) <ul style="list-style-type: none"> • Worsening in MRC • Worsening of tremor • Evidence of severe demyelinating neuropathy with significantly prolonged distal latencies | Worsening <ul style="list-style-type: none"> • 2-4 weeks | Supportive <ul style="list-style-type: none"> • The pre-treatment anti-MAG titers were already above the threshold of the ELISA (70'000 BTU) or rituximab potentially increased the permeability of the blood-brain barrier, allowing enhance migrating of the anti-MAG IgM in the CNS. |
| Case study, Class IV, Gomez <i>et al.</i> 2016 ⁸⁸ | Bendamustine/ Rituximab (n=1) | -88% | NR | NR | Responder (1/1) <ul style="list-style-type: none"> • Improvements in strength and Romberg test | Response <ul style="list-style-type: none"> • 1 month | Supportive <ul style="list-style-type: none"> • One year after starting Bendamustine/Rituximab treatment, new worsening symptoms with evidence of progressive increase anti-MAG IgM. |

| Study type, Class of evidence, Reference | Treatment and Nr. of anti-MAG neuropathy patients (n) | Change in anti MAG IgM | Change in para- protein | Change in total IgM | Clinical outcomes measures | Time to response ^A | Supporting change in anti-MAG IgM and clinical symptoms correlation and comments |
|--|---|------------------------------------|-------------------------------|------------------------|---|---|---|
| Case study, Class IV, Vo <i>et al.</i> 2015 ⁸⁹ | Rituximab (n=1) | NR | NR | -44% | Acute deteriorating (1/1) <ul style="list-style-type: none"> • Worsening in MRC • Worsening in INCAT • Worsening in grip strength • Worsening of previously noted demyelinating abnormalities (DML, cMAP, CMV) | Worsening <ul style="list-style-type: none"> • 2 weeks | Not supportive <ul style="list-style-type: none"> • Anti-MAG IgM levels were not assessed post treatment but patient improved after IVIg treatment. |
| Open label study, Class IV, Talamo <i>et al.</i> 2015 ⁴² | Rituximab and plasma exchange, rituximab, fludarabine (n=4) | -75% | NR | -76% | Responder (4/4) <ul style="list-style-type: none"> • Symptomatic improvements | Response <ul style="list-style-type: none"> • 6 months | Supportive <ul style="list-style-type: none"> • Only in two treated patient the total IgM was assessed pre- and post-treatment. One responder did not exhibit increased IgM levels (pre-treatment). |
| | Untreated (n=3) | No change | NR | No change | Non-responder(3/3) <ul style="list-style-type: none"> • Stable symptoms | No response <ul style="list-style-type: none"> • 6 or 12 months | |
| Prospective, open label study, Class IV, Zara <i>et al.</i> 2011 ^{63*} | Rituximab (n=5) | -20% (-49% to +53% range) | NR | NR | Responder (3/5) <ul style="list-style-type: none"> • Improvements in INCAT disability scale • Improvements in ISS | Response <ul style="list-style-type: none"> • 12 months | Not supportive <ul style="list-style-type: none"> • The authors indicated that two patients had anti-MAG IgM levels above the upper cut-off of |

| Study type, Class of evidence, Reference | Treatment and Nr. of anti-MAG neuropathy patients (n) | Change in anti MAG IgM | Change in para- protein | Change in total IgM | Clinical outcomes measures | Time to response ^A | Supporting change in anti-MAG IgM and clinical symptoms correlation and comments |
|--|--|------------------------------|-------------------------------|------------------------|--|---|--|
| | | -20% | NR | NR | Non-responder (2/5) <ul style="list-style-type: none"> • No improvements in INCAT • No improvement in ISS | No response <ul style="list-style-type: none"> • 12 months | <p>the ELISA and therefore, a potential reduction could not be detected. Figure 1C is not consistent with the main text of the manuscript.</p> <ul style="list-style-type: none"> • There was no evident correlation between anti-MAG serum antibodies and the electrodiagnostic data (except for absent SAP). Nor was there a correlation with the clinical scales, the slowing of motor conduction, TLI or cMAP amplitude reductions. |
| Open label study, Class IV, Delmont <i>et al.</i> 2011 90 | Rituximab (n=3) | -43% | -31% | NR | Responder (3/3) <ul style="list-style-type: none"> • Improvements in ISS, n=3 • Improvement in OLNS, n=2 • Improvement in MRC, n=3 • No change in individual or overall electrophysiological data | Response <ul style="list-style-type: none"> • 9 months (ONLS) • 3 months (ISS) | Supportive <ul style="list-style-type: none"> • Not specified which patient did show no improvements. |

| Study type, Class of evidence, Reference | Treatment and Nr. of anti-MAG neuropathy patients (n) | Change in anti MAG IgM | Change in para- protein | Change in total IgM | Clinical outcomes measures | Time to response ^A | Supporting change in anti-MAG IgM and clinical symptoms correlation and comments |
|---|--|------------------------------|-------------------------------|------------------------|--|---|---|
| Case study, Class IV, Stork <i>et al.</i> 2013 ¹¹⁵ | Rituximab (n=3) | -48% | +14% | -9% | Acute deteriorating (3/3) • Rapid worsening in MRC • NCS worsened in two patients | Worsening • during 1 st /2 nd treatment cycle | Not supportive • The authors suggested that the worsening might be related to significant side effects of rituximab, as seen in other studies ^{68, 92, 93} . |
| Case study, Class IV, Broglio <i>et al.</i> 2005 ⁹² | Rituximab (n=1) | No reduction | NR | -50% | Non-responder (1/1) • Worsening in MRC • Wheelchair-bound because of ataxia | Worsening • 2 months | Supportive • Authors suggested that the pathogenic anti-MAG IgM is produced by CD20 ⁺ cells. |
| Case Study, Class IV, Gironi <i>et al.</i> 2006 ⁹³ | Rituximab (n=1) | +21% | NR | +58% | Acute deteriorating (1/1) • Severe worsening of all neurological signs (specifically tremor) | Worsening • 3 months | Supportive • Patient with Waldenström macroglobulinemia and neuropathy associated with anti-MAG IgM/k antibodies. |

| Study type, Class of evidence, Reference | Treatment and Nr. of anti-MAG neuropathy patients (n) | Change in anti MAG IgM | Change in para- protein | Change in total IgM | Clinical outcomes measures | Time to response ^A | Supporting change in anti-MAG IgM and clinical symptoms correlation and comments |
|---|--|------------------------------|-------------------------------|------------------------|---|---|--|
| Open label, Class IV, Briani <i>et al.</i> 2019 ⁵⁰ | Obinutuzumab and chlorambucil (n=2) | > -92% (n=1) | -45% (n=1) | -55% (n=1) | Responder (2/2) <ul style="list-style-type: none"> • Improvements in MRC and INCAT (-1) • Neurophysiology improved | Response <ul style="list-style-type: none"> • 3-6 months | Supportive <ul style="list-style-type: none"> • Patients had anti-MAG antibody neuropathy and concurrent chronic lymphocytic leukaemia. Both patients developed neutropenia and one a fatal pneumonia. • Patient had baseline values of >70,000 BTU, therefore the actual reduction would be higher • Only limited data are available from both patients |
| Case study, Class IV, Al-Bustani <i>et al.</i> 2016 ⁹⁴ | Rituximab (n=1) | -97% | -100% | -42% | Responder (1/1) <ul style="list-style-type: none"> • Improvements in NCS • Electrodiagnostic testing correlated with clinical improvement | Response <ul style="list-style-type: none"> • 1 month | Supportive <ul style="list-style-type: none"> • Clinical improvements were still persistent 7 years after first treatment. |
| Prospective pilot study, Class IV, Delarue <i>et al.</i> 2004 ⁹⁵ | Rituximab (n=4) | No reduction | No reduction | NR | Non-Responder (4/4) <ul style="list-style-type: none"> • No improvements of clinical neurological symptoms | No response <ul style="list-style-type: none"> • 24 months FU (median) | Supportive <ul style="list-style-type: none"> • One patient exhibited later improvements after high dose Melphalan followed by autologous stem cell transplantation. |

| Study type, Class of evidence, Reference | Treatment and Nr. of anti-MAG neuropathy patients (n) | Change in anti MAG IgM | Change in para- protein | Change in total IgM | Clinical outcomes measures | Time to response ^A | Supporting change in anti-MAG IgM and clinical symptoms correlation and comments |
|--|--|--|-------------------------------|------------------------|---|--|--|
| Prospective study, Class IV, Benedetti <i>et al.</i> 2019 ⁹⁶ | Rituximab (n=18) | -67% (after 31/46 rituximab cycles) | NR | NR | Responder (16/18) <ul style="list-style-type: none"> • Improvements in INCAT disability scale • Improvements in MRC sum score • Improvements in ISS | Response <ul style="list-style-type: none"> • Clinical improvements after the first rituximab cycles lasted two or more years | Supportive <ul style="list-style-type: none"> • No maintenance therapy was performed, unless patients exhibited relapses, then additional rituximab cycles were used. One responder showed a 10% increase in anti-MAG IgM titers. |
| | | +13% (+0% to +25% range) | NR | NR | Non-responder (2/18) <ul style="list-style-type: none"> • No change in INCAT disability scale • No change MRC sum score • No change in ISS | No response <ul style="list-style-type: none"> • Time of FU is unclear | |
| Uncontrolled open study, Class III, Hamidou <i>et al.</i> 2005 ⁹⁷ | Cyclo- phosphamide (n=9) | -7% | NR | -56% | Responder (7/9) <ul style="list-style-type: none"> • Improvements in Ranking scale • Improvements in muscle strength • No significant changes in the electrophysiological measures | Response <ul style="list-style-type: none"> • 6 months (1st FU) | Supportive <ul style="list-style-type: none"> • All patients showed improvements in muscle strength and a significant reduction in total IgM |

| Study type, Class of evidence, Reference | Treatment and Nr. of anti-MAG neuropathy patients (n) | Change in anti MAG IgM | Change in para- protein | Change in total IgM | Clinical outcomes measures | Time to response ^A | Supporting change in anti-MAG IgM and clinical symptoms correlation and comments |
|---|--|------------------------------|---|------------------------|---|--|---|
| | | -3% | NR | -49% | Non-responder (2/9) <ul style="list-style-type: none"> • Stabilisation in Raking scale • Improvements in muscle strength (n=2) • No significant changes in the electrophysiological measures | No response <ul style="list-style-type: none"> • Stable over 18 months | |
| Case study, Class IV, Ghosh <i>et al.</i> 2002 ⁹⁸ | Cladribine (n=1) | -94% | disappearance of the IgM paraprotein | NR | Responder (1/1) <ul style="list-style-type: none"> • From effectively useless hands to grip objects, open hold a cup of coffee. • Able to climb stairs again and stand from a chair unaided. Walking improved. | Response <ul style="list-style-type: none"> • 10 months | Supportive <ul style="list-style-type: none"> • Disappearance of paraprotein and sustainable anti-MAG IgM reduction coincided with clinical improvements. |
| Open label study, Class III, Notermans <i>et al.</i> 1996 ⁹⁹ | Cyclophosphamide, prednisone (n=5) | NR | -56% (n=1, too low to quantify in n=4) | NR | Responder (5/5) <ul style="list-style-type: none"> • Reduction of bone marrow infiltration • Ulnar nerve conduction variables (DML, MCV, CMAP) were significantly better than before treatment | Response <ul style="list-style-type: none"> • 6 months (1st FU) | Supportive <ul style="list-style-type: none"> • Paraprotein was too low to quantify in 4 patients • Unclear if the clinical improvements occurred in the anti-MAG IgM MGUS cohort. |

| Study type, Class of evidence, Reference | Treatment and Nr. of anti-MAG neuropathy patients (n) | Change in anti MAG IgM | Change in para- protein | Change in total IgM | Clinical outcomes measures | Time to response ^A | Supporting change in anti-MAG IgM and clinical symptoms correlation and comments |
|--|--|------------------------------|--|------------------------|---|---|---|
| Open label study, Class IV, Notermans <i>et al.</i> 1997 ¹⁰⁰ | Dexamethasone (n=5) | NR | -40% (n=3, pre- treatment IgM too low to quantify in n=2) | NR | Responder (5/5) <ul style="list-style-type: none"> Improvements in motor sum score Improvements in disability scale | Response <ul style="list-style-type: none"> 3-6 months | Supportive <ul style="list-style-type: none"> Very high frequency of serious invalidating side effects occurred due to the treatment. One patient showed clinical improvements and paraprotein reduction (-60%) only after cyclophosphamide therapy. |
| Case study, Class IV, Niemierko <i>et al.</i> 1999 ¹⁰¹ | Immunu- adsorbption (Protein A column) (n=1) | NR | No reduction | NR | Responder (1/1) <ul style="list-style-type: none"> Improvements in motor functional score (+2) Improvements in gait, balance, and strength | Response <ul style="list-style-type: none"> NR, potentially data were assessed at the quarterly treatment cycles. | Not supportive <ul style="list-style-type: none"> 2nd IgM MGUS patient was included, however the reactivity of the paraprotein was not reported. As Proisorbat columns mainly remove IgG (95%) and only 30% of IgM, the authors suggested that reduced complement and/or enhanced clearance of soluble immune complexes may occurred ^{116, 117}. |

| Study type, Class of evidence, Reference | Treatment and Nr. of anti-MAG neuropathy patients (n) | Change in anti MAG IgM | Change in para- protein | Change in total IgM | Clinical outcomes measures | Time to response ^A | Supporting change in anti-MAG IgM and clinical symptoms correlation and comments |
|---|--|---|-------------------------------|------------------------|--|---|---|
| Case study, Class IV, Ernerudh <i>et al.</i> 1986 ¹⁰² | Plasma exchange (n=3) | NR | NR | Approx. -90% (n=1) | Responder (2/3) <ul style="list-style-type: none"> • Improvements in muscle strength and vibration sense • Increase of motor conduction velocity • Painful paraesthesia disappeared • Only NCS improvements in the arm of one patient | Response: <ul style="list-style-type: none"> • 4-6 weeks | Supportive <ul style="list-style-type: none"> • Slight clinical deterioration occurred 3 and 10 months after treatment. • PE of the non-responder was stopped due to low IgG levels |
| | | NR | NR | Approx. -60% | Non-responder (1/3) <ul style="list-style-type: none"> • No clinical or neurophysiological change | Non-response <ul style="list-style-type: none"> • Non clinical improvements after 5 PE runs | |
| Open study, Class IV, Ernerudh <i>et al.</i> 1992 ¹⁰³ | Various treatment (n=5) Plasma exchange, chlorambucil, prednisolone, | Approx. -60% (reduction 2=n, and increase n=1) | NR | NR | Responder (3/5) <ul style="list-style-type: none"> • Improvements in motor function of hands • Improvements in muscle weakness score • Disability score | Response <ul style="list-style-type: none"> • 1-6 months | Supportive <ul style="list-style-type: none"> • In 3 patients there was clear correlation between clinical effect and IgM concentration. • In 2 patients, there was no clear correlation (1 patient improved |

| Study type, Class of evidence, Reference | Treatment and Nr. of anti-MAG neuropathy patients (n) | Change in anti MAG IgM | Change in para- protein | Change in total IgM | Clinical outcomes measures | Time to response ^A | Supporting change in anti-MAG IgM and clinical symptoms correlation and comments |
|---|--|--|-------------------------------|------------------------|---|---|---|
| | melphalan | NR, (no reduction n=1, reduction n=1) | NR | NR | Non-responder (2/5) • No change in disability status and sensory status, as well as muscle weakness score | Non-response • NR | despite unchanged or increased antibodies and 1 patient did not improve despite lowered antibody concentrations). |
| Randomized, placebo controlled study, Class II, Dalakas <i>et al.</i> 1996 104 | IVIg (n=11) | Transiently decrease (approx. -50%) | NR | NR | Responder (1/9) • Increase in strength based on MRC • The electrophysiological findings remained unchanged | Response • 2 months | Supportive • Anti-MAG IgM did not appreciably change and only two patients modestly improved. • Two patients were excluded as the anti-MAG reactivity couldn't be confirmed. |
| | | No change | NR | NR | Non-responder (8/9) • No change in MRC • No clinically functional improvements • The electrophysiological findings remained unchanged | Non-response • Stable for 6 months | |
| Open label study, Class IV, Sherman <i>et al.</i> 1984 64* | Plasma exchange (n=6) | -75% | -67% | NR | Responder (2/6) • Able to walk again with a walker • Able to extend wrist against gravity • No change in the electrophysiological studies despite improvement | Response • 1-2 weeks | Supportive • The authors concluded that PE should be performed frequently enough to maintain the antibody titre at less than 50% of pre- treatment values |

| Study type, Class of evidence, Reference | Treatment and Nr. of anti-MAG neuropathy patients (n) | Change in anti MAG IgM | Change in para- protein | Change in total IgM | Clinical outcomes measures | Time to response ^A | Supporting change in anti-MAG IgM and clinical symptoms correlation and comments |
|--|--|------------------------------|-------------------------------|------------------------|--|----------------------------------|--|
| | | -41% | -33.3% | NR | Non-responder (4/6) <ul style="list-style-type: none"> • No change, n=3 • Worsening of weakness, n=1 • No change in the electrophysiological studies | | |

Hand selected publications; ^AAfter initiation of treatment; BTU: Bühlmann Titer Units; cMAP: compound motor action potential amplitude; CNDS: clinical neuropathy disability score; DML distal motor latency; F: Female; FU: Follow-up; INCAT: Inflammatory Neuropathy Cause and Treatment disability score; ISS: INCAT Sensory Score; I-RODS: Inflammatory Rasch-built Overall Disability Scale; M: Male; MCV: motor nerve conduction; MNCV: motor nerve conduction velocity; MRC: Medical Research Council sum score; mRS: modified Rankin Score; NDS: Neuropathy Disability Score; NR: not reported; OLNS: Overall Neuropathy Limitations Scale; SNAP: sensory nerve action potential; SNCV: sensory nerve conduction velocity; TLI: terminal latency index; TNS: Total Neuropathy Score

Table e-3. Overview of the participants from the 50 publications identified in the systematic literature search

| Study type Reference | Treatment outcome <i>(Number of patients)</i> | Age <i>Mean (Range)</i> | Age at disease onset <i>Mean (Range)</i> | Sex | | Laboratory testing | Pre-treatment anti-MAG IgM level (titers, paraprotein, total IgM <i>Mean (Range)</i> | Pre-treatment Scale/Score |
|---|---|--------------------------------|---|-----|----|---|--|---|
| | | | | F | M | | | |
| Pestronk <i>et al.</i> 2003 ²³ | Responder (n=7) Treatment group | NR | NR | NR | NR | ELISA, immunofixation | Anti-MAG IgM titers In percentage of initial values, Total IgM In percentage of initial values, | <ul style="list-style-type: none"> • Instability of gait • Reduction of strength: 57% (4% SEM) |
| | Non-Responder (n=5) Control group | NR | NR | NR | NR | | Anti-MAG IgM titers In percentage of initial values Total IgM In percentage of initial values | <ul style="list-style-type: none"> • Instability of gait • Reduction of strength: 63% (6% SEM) |
| Dalakas <i>et al.</i> 2009 ⁶⁵ , Treatment group | Responder (n=7) | 66.8 (±7.9 SD) | 12.9 (±7.2 SD) (mean disease duration) | 2 | 11 | Serum protein electrophoresis with immunofixation electrophoresis | Anti-MAG IgM titers 38.8 units/ml (±57.5 SD) Total IgM 599 mg/dl (±526 SD) | <ul style="list-style-type: none"> • INCAT: leg score: 1.46 (±1.0 SD) • 10m walk 8.3 sec (±3.2 SD) • MRC scale score: 134.6 (±11.9 SD) • Sensory score: 7.5 (±3.6 SD) |
| | Non-Responder (n=5) | | | | | | | |

| Study type Reference | Treatment outcome (Number of patients) | Age Mean (Range) | Age at disease onset Mean (Range) | Sex | | Laboratory testing | Pre-treatment anti-MAG IgM level (titers, paraprotein, total IgM Mean (Range) | Pre-treatment Scale/Score |
|---|---|------------------------|---|-----|---|---|--|--|
| | | | | F | M | | | |
| Dalakas <i>et al.</i> 2009 ⁶⁵ , Placebo group | Non-Responder (n=13) | 67.6 (±8.4 SD) | 12.9 (±6.5 SD) (mean disease duration) | 7 | 6 | Serum protein electrophoresis with immunofixation electrophoresis | Anti-MAG IgM titers 31.7 units/ml (±51.4 SD) Total IgM 698.5 mg/dl (±446 SD) | <ul style="list-style-type: none"> • INCAT: leg score: 1.45 (±0.7 SD) • 10m walk 9.5 sec (±4.2 SD) • MRC scale score: 131.6 (±11.2 SD) • Sensory score: 7.9 (±3.1 SD) |
| Gruson <i>et al.</i> 2011 ⁶⁶ | Responder (n=2) | 65 (64-66) | 64 (63-65) | 0 | 2 | Electrophoresis, immunofixation, ELISA | Anti-MAG IgM titers 62'500 BTU (55'000 - >70'000) | <ul style="list-style-type: none"> • INCAT: 4 • Assessment of MCV, DML (ulnar, peroneal) |
| Weiss <i>et al.</i> 2014 ¹¹⁴ | Acute deteriorating (n=1) | 85 | 83 | 0 | 1 | Serum protein electrophoresis, ELISA | Anti-MAG IgM titers 12'800 BTU Paraprotein Too small to detect Total IgM 190 mg/dl | <ul style="list-style-type: none"> • Advancing numbness in feet and imbalance • Stocking sensory loss • Mild sway with Romberg testing • Prolonged DML in upper and lower extremities • Reductions of MCV in the lower extremities • No motor conduction block |
| Sala <i>et al.</i> 2014 ⁶⁸ | Acute deteriorating (n=3) | 66 (63-69) | 64.7 (62- 67) | 1 | 2 | ELISA, total IgM NR | Anti-MAG IgM titers 50'461 BTU (1'366-86'567) Total IgM | <ul style="list-style-type: none"> • INCAT: 2 (1-3) |

| Study type Reference | Treatment outcome <i>(Number of patients)</i> | Age <i>Mean (Range)</i> | Age at disease onset <i>Mean (Range)</i> | Sex | | Laboratory testing | Pre-treatment anti-MAG IgM level (titers, paraprotein, total IgM <i>Mean (Range)</i> | Pre-treatment Scale/Score |
|--|---|--------------------------------|---|-----|---|----------------------------------|--|--|
| | | | | F | M | | | |
| | | | | | | | 4.64 g/dl (3.3-5.61) | <ul style="list-style-type: none"> • Leg paraesthesia, progressive ataxia, unsteadiness • MCV, DML, and cMAP in the peroneal, ulnar, and median nerve were assessed. |
| Baron <i>et al.</i> 2017 ⁶⁹ | Responder (n=4) | 68.5 (61-78) | 63.5 (60-66) | 1 | 3 | ELISA, Paraprotein NR | Anti-MAG IgM titers 25'550 (18'600-38'943) Paraprotein 4.075 g/L (0-9.5) | <ul style="list-style-type: none"> • ONLS: 4.25 (2-6) • Ataxia, paraesthesia, tremor • Electromyogram was used to determine the characteristics of the neuropathy |
| Levine <i>et al.</i> 1999 ⁶⁰ | Responder (n=1) | NR | NR | 1 | 0 | ELISA, serum immunofixation, | Anti-MAG IgM titers Only relative reduction reported Total IgM Only relative reduction reported | <ul style="list-style-type: none"> • Sensory loss, weakness • Reduced strength index (-20%) |
| Renaud <i>et al.</i> 2003 ⁷⁰ | Responder (n=5) | 60 (48-77) | 56 (42-75) | 2 | 3 | ELISA, immune electrophoresis | Anti-MAG IgM titers Only relative reduction of baseline shown Total IgM 1.5-15 g/L | <ul style="list-style-type: none"> • Only change in NSS shown • NDS: 30-70 • TLI >0.25 |

| Study type Reference | Treatment outcome <i>(Number of patients)</i> | Age <i>Mean (Range)</i> | Age at disease onset <i>Mean (Range)</i> | Sex | | Laboratory testing | Pre-treatment anti-MAG IgM level (titers, paraprotein, total IgM <i>Mean (Range)</i> | Pre-treatment Scale/Score |
|-------------------------------------|---|----------------------------|---|-----|---|------------------------|---|---|
| | | | | F | M | | | |
| | | | | | | | | <ul style="list-style-type: none"> Assessment of the Ulnar MCV |
| | Non-Responder (n=1) | 73 | 66 | 0 | 1 | | Anti-MAG IgM titers Only relative reduction of baseline shown Total IgM Approx. 4 g/L | <ul style="list-style-type: none"> Only change in NSS shown NDS: approx. 36 Assessment of the Ulnar MCV |
| Benedetti et al. 2007 ²² | Responder (n=5) | 61.8 (53-69) | 59.4 (51-68) | 3 | 2 | Western blot | Anti-MAG IgM titers 1:31'680 (1'600-51'200) Total IgM 495 mg/dl (300-887) | <ul style="list-style-type: none"> ISS: 9.4 (9-11) MRC: 56 (46-59) INCAT: 3.6 (2-8) |
| | Non-Responder (n=2) | 61.5 (62-62) | 58.5 (57-60) | 0 | 2 | Western blot, ELISA | Anti-MAG IgM titers 1:435'000 (70'000-800'000) Total IgM 600 mg/dl | <ul style="list-style-type: none"> ISS:10 (8-12) MRC: 55 (54-56) INCAT: 3 (2-4) MCV, DML, cMAP was assessed in the peroneal and ulnar nerve |

| Study type Reference | Treatment outcome <i>(Number of patients)</i> | Age <i>Mean (Range)</i> | Age at disease onset <i>Mean (Range)</i> | Sex | | Laboratory testing | Pre-treatment anti-MAG IgM level (titers, paraprotein, total IgM <i>Mean (Range)</i> | Pre-treatment Scale/Score |
|--|---|--------------------------------|---|-----|----|---|--|---|
| | | | | F | M | | | |
| Kilidireas <i>et al.</i> 2006 ⁷² | Responder (n=1) | 75 | 73 | 0 | 1 | ELISA, paraprotein NR | Anti-MAG IgM titers Only SGPG reactivity was assessed, but classified as anti-MAG neuropathy Paraprotein 341 mg/L | <ul style="list-style-type: none"> • 9 peg hole test: 21.3 (R), 22.8 (L) • Hand grip: 56 (R), 56 (L) • MRC: 60 • 10m walk: 6.3 • Assessment of the MNCV, SNCV, cMAP, SNAP in the ulnar nerve |
| | Non-Responder (n=1) | 60 | 58 | 0 | 1 | | | |
| Souayah <i>et al.</i> 2013 ⁷³ | Responder (n=2) | 67.5 (62-73) | 57 (53-61) | 0 | 2 | Anti-MAG IgM titers NR | Anti-MAG IgM titers 32'000 (12'800-51'200) | <ul style="list-style-type: none"> • Total neuropathic score: 14/36 • Assessment of DML, cMAP |
| Leger <i>et al.</i> 2013 ¹⁰⁷ , Treatment group | Responder (n=5) | 64.6 (±8.6 SD) | 3.3 (1.4-4.8) median | 8 | 18 | ELISA, immunofixation and monoclonal protein according | Anti-MAG IgM titers ≥70'000 median (33'000-≥70'000) Paraprotein | <ul style="list-style-type: none"> • INCAT disability score: 3 (2-4) • Median ISS: 6.5 (5-9) • 10m walk: 7.7 (6.0-10.7) |
| | Non-responder (n=21) | | | | | | | |

| Study type Reference | Treatment outcome <i>(Number of patients)</i> | Age <i>Mean (Range)</i> | Age at disease onset <i>Mean (Range)</i> disease duration | Sex | | Laboratory testing | Pre-treatment anti-MAG IgM level (titers, paraprotein, total IgM <i>Mean (Range)</i> | Pre-treatment Scale/Score |
|---|---|--------------------------------|--|-----|----|--|--|---|
| | | | | F | M | | | |
| | | | | | | to standard procedures | 6.9 g/L (4.2 SD), n=10 Total IgM 3.1 g/L (2.0-7.7), n=21 | <ul style="list-style-type: none"> • MRC: 56.5 (45-60) |
| Leger <i>et al.</i> 2013 ¹⁰⁷ , Placebo group | Non-responder (n=28) | 67.2 (±8.6 SD) | 3.8 (2.2- 7.9) median disease duration | 8 | 20 | ELISA, immunofixation and monoclonal protein according to standard procedures | Anti-MAG IgM titers ≥70'000 median (14'000- ≥70'000) Paraprotein 5.7 g/L (±2.9 SD), n=7 Total IgM 3.8 g/L (3.0-6.8), n=25 | <ul style="list-style-type: none"> • INCAT disability score:3 (2-4) • Median ISS: 8 (6-10) • 10m walk: 9.0 (7.5-12.1) • MRC: 55 (51.5-60) |
| Hospital <i>et al.</i> 2013 ⁷⁶ Rituximab treatment | Responder (n=21) | 67 (47-86) | NR | 12 | 14 | ELISA, Paraprotein NR | Anti-MAG IgM titers 61'000 BTU (5'800- >70'000) Paraprotein 0.35 g/L (0-1.52) | <ul style="list-style-type: none"> • mRS: 2.9 (2-5) • Sensory deficit, pain, ataxia, motor deficit • Assessment of nerve distal latencies and cMAP |
| | Non-responder (n=5) | | | | | | | |
| Hospital <i>et al.</i> 2013 ⁷⁶ Rituximab combination treatment | Responder (n=16) | 68 (42-85) | NR | 7 | 12 | ELISA, Paraprotein NR | Anti-MAG IgM titers 60'000 BTU (1'000- >70'000) Paraprotein 0.38 g/L (0-1.8) | <ul style="list-style-type: none"> • mRS: 2 (1-4) • Sensory deficit, pain, ataxia, motor deficit • Assessment of nerve distal latencies and cMAP |
| | Non-responder (n=3) | | | | | | | |

| Study type Reference | Treatment outcome <i>(Number of patients)</i> | Age <i>Mean (Range)</i> | Age at disease onset <i>Mean (Range)</i> | Sex | | Laboratory testing | Pre-treatment anti-MAG IgM level (titers, paraprotein, total IgM <i>Mean (Range)</i> | Pre-treatment Scale/Score |
|---|---|--------------------------------|---|-----|----|---|--|---|
| | | | | F | M | | | |
| Gorson <i>et al.</i> 2001 ⁷⁷ | Sustained responder (n=4) | 64 (42-88) | 2.5 (0.5- 27) median disease duration | 9 | 15 | ELISA, serum immune- electrophoresis or immunofixation (e.g. high- resolution agarose gel technique or nephelometry) | Anti-MAG IgM titers 1:57'480 (6'400-1'600'000) Paraprotein 996 mg/dL (224-2'530) | <ul style="list-style-type: none"> • MRC: 36.3 (32-40) • Sensory score: 13.7 (8-22) • Ranking score: 2.7 (2-3) • Median, ulnar, peroneal, and tibial motor nerves and median, ulnar, and sural sensory nerves were sampled. |
| | Transient responder (n=8) | | | | | | Anti-MAG IgM titers 1:309'605 (12'800-400'000) Paraprotein 624 mg/dL (69-2'083) | |
| | Non-responder (n=12) | | | | | | <ul style="list-style-type: none"> • MRC: 37.2 (24-40) • Sensory score: 13.3 (6-24) • Ranking score: 2 (1-4) • Electrophysiological assessment see responder group | |
| Duncombe <i>et al.</i> 2017 ⁷⁸ | Responder (n=13) | NR | NR | NR | NR | NR | Anti-MAG IgM titers 38'925 (median) Paraprotein 4.7 g/L (median) | <ul style="list-style-type: none"> • ONLS: 3 (median) • MRC sum score: 76 (median, n=18) |
| Nobile-Orazio <i>et al.</i> 1988 ⁷⁹ | Responder (n=2) | 61 (60-62) | 59 | 0 | 2 | ELISA, total IgM NR | Anti-MAG IgM titer 7.85 (6.8-8.9, normalized value >3) Total IgM 0.95 g/L (0.8-1.1) | <ul style="list-style-type: none"> • Disability score: 2 (1-3) • Ataxia score: 1 (0-2) |

| Study type Reference | Treatment outcome <i>(Number of patients)</i> | Age <i>Mean (Range)</i> | Age at disease onset <i>Mean (Range)</i> | Sex | | Laboratory testing | Pre-treatment anti-MAG IgM level (titers, paraprotein, total IgM <i>Mean (Range)</i> | Pre-treatment Scale/Score |
|--|---|--------------------------------|---|-----|---|---|--|--|
| | | | | F | M | | | |
| | | | | | | | | <ul style="list-style-type: none"> • Assessment of MCV (median, peroneal) and SNAP (median, sural) |
| | Non-Responder (n=3) | 65 (54-72) | 62 (53-69) | 0 | 3 | ELISA | Anti-MAG IgM titers 13.3 (9.8-19.5, normalized value >3) Total IgM 1.53 g/L (1-2) | <ul style="list-style-type: none"> • Disability score: 2.7 (2-3) • Ataxia score: 3.7 (3-4) • Assessment of MCV (median, peroneal) and SNAP (median, sural) |
| Wilson <i>et al.</i> 1999 ⁶¹ | Responder (n=1) | 45 | 41 | 1 | 0 | Protein electrophoresis and quantified by densitometry | Paraprotein 7 g/l | <ul style="list-style-type: none"> • mRS: 4 • MRC sum score 56 • Sensory sum score: 4 • 10-meter walk 15s (with one stick) • Median MCV and SAP were assessed |
| | Non-Responder (n=1) | 53 | 47 | 0 | 1 | | Paraprotein 5 g/l | <ul style="list-style-type: none"> • mRS: 2 • MRC sum score: 63 • Sensory sum score: 12 • 10-meter walk 7.1 • Median MCV and SAP were assessed |
| Campagnolo <i>et al.</i> 2017 ⁸⁰ | Responder (n=15) | 60.7 (44-72) | 56.7 (40-68) | 7 | 8 | | Anti-MAG IgM titers | <ul style="list-style-type: none"> • INCAT: 2.7 (1-6) • ISS: 7.9 (1-18) |

| Study type Reference | Treatment outcome <i>(Number of patients)</i> | Age <i>Mean (Range)</i> | Age at disease onset <i>Mean (Range)</i> | Sex | | Laboratory testing | Pre-treatment anti-MAG IgM level (titers, paraprotein, total IgM <i>Mean (Range)</i> | Pre-treatment Scale/Score |
|---|---|--------------------------------|---|-----|----|---|---|---|
| | | | | F | M | | | |
| | | | | | | Western blot, ELISA, total IgM NR | 52'480 BTU (10'000- 100'000) Total IgM 3.2 g/L (1.6-7.9) | • MRC: 56.3 (40-60) |
| | Non-Responder (n=10) | 65.1 (49- 87) | 59.8 (47- 71) | 2 | 8 | | Anti-MAG IgM titers 141'525 BTU (7'500- 800'000) Total IgM 3.3 g/L (1.08-6) | • INCAT: 2.5 (1-5) • ISS: 10.25 (2-18) • MRC: 57.1 (52-60) |
| Niermeijer <i>et al.</i> 2006 ⁸² | Responder (n=2) | 57 (53-61) | 44 | 2 | 0 | NR | Paraprotein 4.5 g/L (<1-8) Total IgM 14.5 g/L (6.4-21.6) | • Raking scale: 3 • Assessment of MCV |
| | Non-Responder (n=4) | 67.5 (60- 74) | 57 (55-60) | 0 | 4 | NR | Paraprotein 7.5 g/L (<1-16) Total IgM 14.2 g/L (6.4-21.1) | • Ranking scale: 2.25 (2-3) • Assessment of MCV |
| Niermeijer <i>et al.</i> 2007 ⁸¹ Treatment group | (n=16, anti-MAG IgM positive n=7) | 64.3 (9.2 SD) | 60.7 (9.3 SD) | 3 | 13 | Electrophoresis, immunofixation | Paraprotein 0.5 g/L (0.5–0.5) (interquartile range) | • Rivermead mobility index: 13.5 (12–14) • Rankin scale: 2 (2-3) • MRC sum score: 133 (123–138) • Sensory sum score: 39 (30–42) |

| Study type Reference | Treatment outcome <i>(Number of patients)</i> | Age <i>Mean (Range)</i> | Age at disease onset <i>Mean (Range)</i> | Sex | | Laboratory testing | Pre-treatment anti-MAG IgM level (titers, paraprotein, total IgM <i>Mean (Range)</i> | Pre-treatment Scale/Score |
|---|---|--------------------------------|---|-----|---|--|---|--|
| | | | | F | M | | | |
| Niermeijer <i>et al.</i> 2007 ⁸¹ Placebo group | (n=19, anti-MAG IgM positive n=10) | 64.2 (8.5 SD) | 59 (9.8 SD) | 11 | 8 | Electrophoresis, immunofixation | Paraprotein 0.5 g/L (0.5–0.5) (interquartile range) | <ul style="list-style-type: none"> • Rivermead mobility index: 14 (12–14) • Rankin scale: 2 (2-3) • MRC sum score: 136 (131–140) • Sensory sum score: 40 (33-47) |
| Kelly <i>et al.</i> 1988 ⁸³ | Responder (n=3) | 59 (48-78) | 28 (48-78) Disease duration in months | 1 | 2 | Western blot | Paraprotein 6.8 g/L (4.5-8.4) | <ul style="list-style-type: none"> • MRC distal legs and hands 4-4.5/5 • Weakness legs and hands • Only baseline electrophysiological assessments were performed |
| Haas <i>et al.</i> 1988 ⁸⁴ | Responder (n=1) | 44 | 38 | 0 | 1 | Serum immunofixation, immune- electrophoresis | Paraprotein 971 mg/dl | <ul style="list-style-type: none"> • Totally atrophic foot muscles (MRC 4- to 4+) • Assessment of the conduction velocity and distal latency of the median nerve |

| Study type Reference | Treatment outcome <i>(Number of patients)</i> | Age <i>Mean (Range)</i> | Age at disease onset <i>Mean (Range)</i> | Sex | | Laboratory testing | Pre-treatment anti-MAG IgM level (titers, paraprotein, total IgM <i>Mean (Range)</i> | Pre-treatment Scale/Score |
|--|---|--------------------------------|---|-----|---|---|---|---|
| | | | | F | M | | | |
| Blume <i>et al.</i> 1995 ⁸⁵ | Responder (n=4) | 54 (49-60) | 52.8 (47-58) | 1 | 3 | ELISA, Western blot methods, serum immunofixation | Anti-MAG IgM titers 1:362'294 (5475-1'300'000) | <ul style="list-style-type: none"> • Strength in % of normal: 45% (10-85%) • Only baseline nerve conduction studies were performed (ulnar and sural never) |
| Mariette <i>et al.</i> 1997 ⁸⁶ IFN- α treatment | Responder (n=8) | 67 (60-67) | 3.1 (0.3-6.1) | 1 | 9 | Immune-blotting on delipidated human myelin | Paraprotein Only relative reduction is reported | <ul style="list-style-type: none"> • Global score: 24.4 (\pm11.3 SD) • Motor score: 2.9 (\pm5.5 SD) • Sensory score: 16.0 (\pm5.7 SD) • Reflex score: 5.5 (\pm3.9 SD) • Assessment of cMAP, MNCV, distal latency, SNAP |
| | Non-responder (n=2) | | Duration of the neuropathy | | | | | |
| | Responder (n=1) | 66 (52-85) | 4.0 (0.4-17.8) | 3 | 7 | Immune-blotting on delipidated | Paraprotein | <ul style="list-style-type: none"> • Global score: 28.7 (\pm11.5 SD) |

| Study type Reference | Treatment outcome <i>(Number of patients)</i> | Age <i>Mean (Range)</i> | Age at disease onset <i>Mean (Range)</i> | Sex | | Laboratory testing | Pre-treatment anti-MAG IgM level (titers, paraprotein, total IgM <i>Mean (Range)</i> | Pre-treatment Scale/Score |
|---|---|--------------------------------|---|-----|---|---|---|--|
| | | | | F | M | | | |
| Blume <i>et al.</i> 1995 ⁸⁵ | Responder (n=4) | 54 (49-60) | 52.8 (47-58) | 1 | 3 | ELISA, Western blot methods, serum immunofixation | Anti-MAG IgM titers 1:362'294 (5475-1'300'000) | <ul style="list-style-type: none"> • Strength in % of normal: 45% (10-85%) • Only baseline nerve conduction studies were performed (ulnar and sural never) |
| Mariette <i>et al.</i> 1997 ⁸⁶ IVIg treatment | Non-responder (n=9) | | Duration of the neuropathy | | | human myelin, total IgM NR | Only relative reduction is reported | <ul style="list-style-type: none"> • Motor score: 3.5 (±3.3 SD) • Sensory score: 17.2 (±7.2 SD) • Reflex score: 8.0 (±4.0 SD) • Assessment of cMAP, MNCV, distal latency, SNAP |
| Rakocevic <i>et al.</i> 2018 ⁵¹ | Non-responder (n=2) | 68 (65-71) | 59.5 (52-67) | 0 | 2 | Anti-MAG titers by EIA, paraprotein NR | Anti-MAG IgM titers >1:102'400 Paraprotein 472 mg/dl (420-524 mg/dl) | <ul style="list-style-type: none"> • Sensory ataxia, muscle weakness • Feet paraesthesia, foot drop |
| Stino <i>et al.</i> 2017 ⁸⁷ | Responder (n=1) | 76 | 73 | 1 | 0 | Anti-MAG titers NR, paraprotein NR | Anti-MAG IgM titers 102'400 BTU Paraprotein 250 mg/dl | <ul style="list-style-type: none"> • Distal leg and intrinsic hand weakness MRC grade 4/5. • INCAT: 1 (lower limb) • I-RODS: 32 |

| Study type Reference | Treatment outcome <i>(Number of patients)</i> | Age <i>Mean (Range)</i> | Age at disease onset <i>Mean (Range)</i> | Sex | | Laboratory testing | Pre-treatment anti-MAG IgM level (titers, paraprotein, total IgM <i>Mean (Range)</i> | Pre-treatment Scale/Score |
|---|---|--------------------------------|---|-----|---|---|---|--|
| | | | | F | M | | | |
| Blume <i>et al.</i> 1995 ⁸⁵ | Responder (n=4) | 54 (49-60) | 52.8 (47-58) | 1 | 3 | ELISA, Western blot methods, serum immunofixation | Anti-MAG IgM titers 1:362'294 (5475-1'300'000) | <ul style="list-style-type: none"> • Strength in % of normal: 45% (10-85%) • Only baseline nerve conduction studies were performed (ulnar and sural never) |
| | | | | | | | | <ul style="list-style-type: none"> • Assessment of the NCS (median and ulnar DML), MCV |
| Doneddu <i>et al.</i> 2017 ⁶² | Acute deteriorating (n=2) | 74 (72-76) | 60.5 (47-74) | 0 | 2 | ELISA, paraprotein NR | Anti-MAG IgM titers >70'000 BTU Paraprotein 4.05 g/L (2-6.1 g/L) | <ul style="list-style-type: none"> • MRC sum score: 53-61 • RODS: 17 (n=1) • NCS |
| Gomez <i>et al.</i> 2016 ⁸⁸ | Responder (n=1) | 74 | 49 | 0 | 1 | ELISA | Anti-MAG IgM titers 1:51'200 | <ul style="list-style-type: none"> • Progressive paresthesia in the bilateral anterior tibial • Only baseline electro-diagnostic studies were performed. |

| Study type Reference | Treatment outcome <i>(Number of patients)</i> | Age <i>Mean (Range)</i> | Age at disease onset <i>Mean (Range)</i> | Sex | | Laboratory testing | Pre-treatment anti- MAG IgM level (titers, paraprotein, total IgM <i>Mean (Range)</i> | Pre-treatment Scale/Score |
|--|---|--------------------------------|--|-----|---|--|--|---|
| | | | | F | M | | | |
| Vo <i>et al.</i> 2015 ⁸⁹ | Acute deteriorating (n=1) | 53 | 52 | 1 | 0 | Anti-MAG IgM titers NR, total IgM NR | Anti-MAG IgM titers >1:102'400 Total IgM 443 mg/dl | <ul style="list-style-type: none"> • INCAT: 0 • MRC sum score: 60 • Grip strength: 76 • Assessment of DML, cMAP, CMV |
| Talamo <i>et al.</i> 2015 ⁴² | Responder (n=4) | 60.5 (51-73) | 52 (29-66) | 1 | 3 | Western blot, ELISA, total IgM NR | Anti-MAG IgM titers >1:102'400 Total IgM 607 mg/dl | <ul style="list-style-type: none"> • Numbness in extremities, gait imbalance, tingling, weakness, pain • Electrodiagnostic studies were only performed for baseline assessment |
| | Non-Responder (n=3) | 63.7 (62-66) | 61.7 (62-66) | 0 | 3 | | Anti-MAG IgM titers >1:72'533 (12'800- >102'400) Total IgM 647 mg/dl | <ul style="list-style-type: none"> • Numbness in extremities, gait imbalance, tingling, weakness, pain • Electrodiagnostic studies were only performed for baseline assessment |
| Zara <i>et al.</i> 2011 ⁶³ | Responder (n=3) | 59 (43-72) | 53.7 (42-60) | 1 | 2 | ELISA | Anti-MAG IgM titers 29'800 BTU | <ul style="list-style-type: none"> • INCAT Arm: 3-2 • INCAT Leg: 0-4 • MRC: 50-60 • ISS pinprick: 4 • TLI was assessed (median, ulnar, peroneal nerve) |

| Study type Reference | Treatment outcome <i>(Number of patients)</i> | Age <i>Mean (Range)</i> | Age at disease onset <i>Mean (Range)</i> | Sex | | Laboratory testing | Pre-treatment anti- MAG IgM level (titers, paraprotein, total IgM <i>Mean (Range)</i> | Pre-treatment Scale/Score |
|--|---|--------------------------------|--|-----|---|-------------------------------|--|--|
| | | | | F | M | | | |
| | Non-Responder (n=2) | 55 (48-62) | 51 (46-56) | 1 | 1 | | Anti-MAG IgM titers >70'000 BTU | <ul style="list-style-type: none"> • INCAT Arm: 0-4 • INCAT Leg: 1 • MRC: 48-60 • ISS pinprick: 2-6 • TLI was assessed (median, ulnar, peroneal nerve) |
| Delmont <i>et al.</i> 2011 ⁹⁰ | Responder (n=3) | 62.3 (57-62) | 57 (54-62) | 2 | 1 | ELISA, paraprotein NR | Anti-MAG IgM titer Only relative reduction of 44-87% reported Paraprotein 9.7 g/L (NR) | <ul style="list-style-type: none"> • ONLS: 4.7 (3-6) • ISS: 8.3 (2-12) • MRC: 129.3 (123-136) • Assessment of electrophysiological status |
| Stork <i>et al.</i> 2013 ¹¹⁵ | Acute deteriorating (n=3) | NR | NR | 1 | 2 | ELISA, paraprotein NR | Anti-MAG IgM titers 1:155'322 (7180- 409'600) Paraprotein 3.4 g/L (0.3-9) | <ul style="list-style-type: none"> • MRC grade: 4 • Weakness of hands and feet • Extensive nerve conduction studies were performed including DML, MCV, SNAP, cMAP, TLI of the median, ulnar tibial and peroneal nerve |
| Broglio <i>et al.</i> 2005 ⁹² | Non-Responder (n=1) | 75 | 71 | 1 | 0 | Western blot, total IgM NR | Anti-MAG IgM titers 1:400'000 Total IgM 620 mg/dl | <ul style="list-style-type: none"> • MRC scale 4 • Modified RSS: 3 • Only baseline TLI was reported |

| Study type Reference | Treatment outcome <i>(Number of patients)</i> | Age <i>Mean (Range)</i> | Age at disease onset <i>Mean (Range)</i> | Sex | | Laboratory testing | Pre-treatment anti- MAG IgM level (titers, paraprotein, total IgM <i>Mean (Range)</i> | Pre-treatment Scale/Score |
|---|---|--------------------------------|--|-----|---|--|--|---|
| | | | | F | M | | | |
| Gironi <i>et al.</i> 2006 ⁹³ | Acute deteriorating (n=1) | 64 | 56 | 1 | 0 | ELISA, nephelometry | Anti-MAG IgM titers 144'000 BTU Paraprotein 4-5 g/L | <ul style="list-style-type: none"> • Sever tremor • Unsteadiness of gait |
| Briani <i>et al.</i> 2019 ⁵⁰ | Responder (n=2) | 83 (82-84) | 84 (n=1) | 1 | 1 | ELISA, paraprotein NR, total IgM NR | Anti-MAG IgM titers >70'000 BTU Paraprotein 15.8 g/L (n=1) Total IgM 14.8 g/L (n=1) | <ul style="list-style-type: none"> • INCAT leg disability score: 2.5 (1-4) • Extensive nerve conduction studies were performed including DML, MCV, SNAP, cMAP, TLI |
| Al-Bustani <i>et al.</i> 2015 ⁹⁴ | Responder (n=1) | 63 | 60 | 1 | 0 | ELISA, serum protein electrophoresis | Anti-MAG IgM titers 1:25'600 Paraprotein 0.2 g/dl Total IgM 145 mg/dl | <ul style="list-style-type: none"> • Distal demyelinating sensory and motor polyneuropathy • No Romberg sign • Extensive nerve conduction studies were performed including DML, MCV, SNAP, cMAP, TLI |
| Delarue <i>et al.</i> 2004 ⁹⁵ | Non-Responder (n=4) | 64 (57-87) | 60 (NR) | 1 | 3 | Anti-MAG IgM titers NR, paraprotein NR | Anti-MAG IgM titers No disappearance reported after treatment Paraprotein No reduction reported after treatment | <ul style="list-style-type: none"> • Peripheral sensory-motor polyneuropathy with clinical and electrophysiological symptoms |
| Benedetti <i>et al.</i> 2019 ⁹⁶ | Responder (n=16) | 65 (48-77) | 61 (46-73) | 8 | 8 | Western blot | Anti-MAG IgM titers 1:40'450 (1600- 100'000) | <ul style="list-style-type: none"> • INCAT 2 (0-5) • MRC score: 57 (40-60) |

| Study type Reference | Treatment outcome <i>(Number of patients)</i> | Age <i>Mean (Range)</i> | Age at disease onset <i>Mean (Range)</i> | Sex | | Laboratory testing | Pre-treatment anti- MAG IgM level (titers, paraprotein, total IgM <i>Mean (Range)</i> | Pre-treatment Scale/Score |
|--|---|--------------------------------|--|-----|----|---|---|---|
| | | | | F | M | | | |
| | | | | | | | | <ul style="list-style-type: none"> ISS score: 6 (0-14) |
| Benedetti <i>et al.</i> 2019 [63] | Non-Responder (n=2) | 67.5 (61-74) | 57.5 (45-70) | 1 | 1 | Western blot | Anti-MAG IgM titers 1:425'000 (51'200-800'000) | <ul style="list-style-type: none"> INCAT: 2 MRC score: 58.5 (57-60) ISS score: 6 Electrophysiology studies were performed only at the time of diagnosis |
| Hamidou <i>et al.</i> 2005 ⁹⁷ | Responder (n=7) | 63 (\pm 12 SD) | 3.5 (\pm 2.8 SD) mean disease duration | 2 | 7 | ELISA, total IgM NR | Anti-MAG IgM titers 101'547 BTU (60'220-224'000) Total IgM 5.3 g/L (2.8-8) | <ul style="list-style-type: none"> Ranking scale: 4 (3-5) Muscle strength 76 (70-80) MCV, DML |
| | Non-Responder (n=2) | | | | | | Anti-MAG IgM titers 27'420 BTU (22'240-23'600) Total IgM 5.5. g/L (5-6) | <ul style="list-style-type: none"> Ranking scale: 3 Muscle strength: 81 (78-84) MCV, DML |
| Ghosh <i>et al.</i> 2002 ⁹⁸ | Responder (n=1) | 53 | 51 | 0 | 1 | ELISA, protein electrophoresis | Anti-MAG IgM titers >70'000 BTU Total IgM levels 2.67g/L | <ul style="list-style-type: none"> Ascending tingling, numbness Tremor and neuropathic pain Unable to use hands |
| Notermans <i>et al.</i> 1996 ⁹⁹ | Responder (n=5) | 49.2 (46-60) | NR | NR | NR | Western blot, electro- and immune-electrophoresis | Paraprotein 9 g/L (n=1) >1 g/L (n=4) | <ul style="list-style-type: none"> NR separately for the anti-MAG IgM MGUS cohort MCV, DML, cMAP, TLI were assessed |

| Study type Reference | Treatment outcome <i>(Number of patients)</i> | Age <i>Mean (Range)</i> | Age at disease onset <i>Mean (Range)</i> | Sex | | Laboratory testing | Pre-treatment anti- MAG IgM level (titers, paraprotein, total IgM <i>Mean (Range)</i> | Pre-treatment Scale/Score |
|---|---|--------------------------------|---|-----|----|--|--|--|
| | | | | F | M | | | |
| Notermans <i>et al.</i> 1997 ¹⁰⁰ | Responder (n=5) | 60.6 (47-70) | 59 (± 8 SD) | NR | NR | Paraprotein NR | Paraprotein 3.4 g/L (>1-5 g/L) | <ul style="list-style-type: none"> • Motor sum score: 110.6 (105-116) • Disability scale: 2.6 (2-3) |
| Niemierko <i>et al.</i> 1999 ¹¹⁸ | Responder (n=1) | 53 | 51 | 0 | 1 | Anti-MAG IgM titers NR, paraprotein NR | Anti-MAG IgM titers 1:52'000 Paraprotein 800 mg/dl | <ul style="list-style-type: none"> • Motor functional score: -3 • Unable to work • Distal weakness, ataxic gait • Baseline EMG values were assessed |
| Ernerudh <i>et al.</i> 1986 ¹⁰² | Responder (n=2) | 52 (40-64) | Steady progression for at least 2-3 years | 0 | 2 | ELISA, agarose isoelectric focusing, immunofixation, autoradiography | Anti-MAG IgM titers Only myelin reactivity was demonstrated Total IgM 9.2 g/L (3.7-14.2) | <ul style="list-style-type: none"> • Painful paraesthesia • Motor velocity condition block in the legs • NCS were assessed in the arms and legs • Predominantly motor and sensory symptoms |
| | Non-responder (n=1) | 59 | Steady progression for at least 2-3 years. | 1 | 0 | ELISA, agarose isoelectric focusing, immunofixation, autoradiography | Anti-MAG IgM titers Only myelin reactivity was demonstrated Total IgM 8.0 g/L | <ul style="list-style-type: none"> • Predominantly sensory symptoms • No velocity condition block • NCS were assessed in the arms and legs |

| Study type Reference | Treatment outcome <i>(Number of patients)</i> | Age <i>Mean (Range)</i> | Age at disease onset <i>Mean (Range)</i> | Sex | | Laboratory testing | Pre-treatment anti- MAG IgM level (titers, paraprotein, total IgM <i>Mean (Range)</i> | Pre-treatment Scale/Score |
|--|---|--------------------------------|--|-----|---|--|---|--|
| | | | | F | M | | | |
| Ernerudh <i>et al.</i> 1992 ¹⁰³ | Responder (n=3) | 57.7 (44-69) | 52.7 (40-69) | 1 | 2 | ELISA, western blot, radial immune diffusion technique | Anti-MAG IgM titers Only relative change shown Total IgM 5.0 g/L (3.0-6.8) | <ul style="list-style-type: none"> Disability status: 3.5 (3-4) Ataxia score 3.7 (3-5) Nerve conduction velocity: 10-43 m/s (motor), 0-51 m/s (sensory), only baseline reported |
| | Non-responder (n=2) | 70 (65-75) | 66.5 (62-71) | 1 | 1 | | | |
| Dalakas <i>et al.</i> 1996 ¹⁰⁴ | Responder (n=1) | 64 | 52 | 1 | 0 | ELISA, thin-layer chromatographic | Anti-MAG IgM titers >1:10'000 | <ul style="list-style-type: none"> MRC: 120 Neuromuscular symptom scores: 37 Sensory score: 35 |
| | Non-responder (n=8) | 66.3 (56-77) | 55.6 (37-70) | 2 | 6 | ELISA, thin-layer chromatographic | Anti-MAG IgM titers >1:10'000 | <ul style="list-style-type: none"> MRC: 146 (134-153) Neuromuscular symptom scores: 50 (43-56) Sensory score: 32.3 (19-46) |
| Sherman <i>et al.</i> 1984 ⁶⁴ | Responder (n=2) | 51.5 (45-58) | 45.5 (35-56) | 1 | 1 | Immuno-electrophoresis | Paraprotein 470 mg/dL (390-550) | <ul style="list-style-type: none"> Unable to walk or sit Weakness against gravity |

| Study type Reference | Treatment outcome <i>(Number of patients)</i> | Age <i>Mean (Range)</i> | Age at disease onset <i>Mean (Range)</i> | Sex | | Laboratory testing | Pre-treatment anti- MAG IgM level (titers, paraprotein, total IgM <i>Mean (Range)</i> | Pre-treatment Scale/Score |
|-------------------------|---|--------------------------------|--|-----|---|-----------------------|--|--|
| | | | | F | M | | | |
| | | | | | | | | <ul style="list-style-type: none"> • MCV in the median, peroneal, sural nerve |
| | Non-responder (n=4) | 60 (53-67) | 56.8 (48-66) | 2 | 2 | | Paraprotein 1'025 mg/dL (600- 1'200) | <ul style="list-style-type: none"> • Decreased sensation • Decreased vibration • MCV in the median, peroneal, sural nerve |

Hand selected publications; ^AAfter initiation of treatment; BTU: Bühlmann Titer Units; cMAP: compound motor action potential amplitude; CNDS: clinical neuropathy disability score; DML distal motor latency; F: Female; FU: Follow-up; INCAT: Inflammatory Neuropathy Cause and Treatment disability score; ISS: INCAT Sensory Score; I-RODS: Inflammatory Rasch-built Overall Disability Scale; M: Male; MCV: motor nerve conduction; MNCV: motor nerve conduction velocity; MRC: Medical Research Council sum score; mRS: modified Rankin Score; NDS: Neuropathy Disability Score; NR: not reported; OLNS: Overall Neuropathy Limitations Scale; SNAP: sensory nerve action potential; SNCV: sensory nerve conduction velocity; TLI: terminal latency index; TNS: Total Neuropathy Score

Chapter 2

Selective inhibition of anti-MAG IgM autoantibody binding to myelin by an antigen-specific glycopolymer

Butrint Aliu^{1*}, Delphine Demeestere^{1*}, Emilie Seydoux², José Boucraut^{3,4}, Emilien Delmont⁵, Alexandre Brodovitch^{3,5}, Thomas Oberholzer², Shahram Attarian⁵, Marie Théaudin⁶, Pinelopi Tsouni⁶, Thierry Kuntzer⁶, Tobias Derfuss⁷, Steck J. Andreas⁷, Beat Ernst¹, Ruben Herrendorff^{1,2}, Pascal Hänggi^{1,2}

* These authors contributed equally to the project

¹Institute of Molecular Pharmacy, Pharmacenter, University of Basel, 4056 Basel, Switzerland

²Polyneuron Pharmaceuticals AG, 4057 Basel, Switzerland

³Immunology laboratory, AP-HM, Marseille, France

⁴Aix-Marseille University, INT, UMR CNRS 7289, Marseille, France

⁵Center for neuromuscular disorders and ALS La Timone hospital, AP-HM, Marseille, France

⁶CHUV, Département des neurosciences cliniques, Service de neurologie, 1001 Lausanne, Switzerland

⁷Clinic of Neurology, Department of Medicine, University Hospital Basel, University of Basel, 4031 Basel, Switzerland





Corresponding author:

Pascal Hänggi, pascarhaenggi@gmail.com, <https://orcid.org/0000-0002-7941-2475>

Contributions of Butrint Aliu

- Writing and revision of manuscript
- Isolation and culture of human and murine B cells
- Epstein-Barr transformation of B cells
- Binding and activation experiments with human and murine B cells
- Anti-MAG autoantibodies ELISA
- Data analysis and interpretation

Selective inhibition of anti-MAG IgM autoantibody binding to myelin by an antigen-specific glycopolymer

Butrint Aliu¹  | Delphine Demeestere¹  | Emilie Seydoux²  | José Boucraut^{3,4}  |
Emilien Delmont⁵  | Alexandre Brodovitch^{3,5} | Thomas Oberholzer² |
Shahram Attarian⁵  | Marie Théaudin⁶  | Pinelopi Tsouni⁶  | Thierry Kuntzer⁶  |
Tobias Derfuss⁷  | Andreas J. Steck⁷ | Beat Ernst¹  | Ruben Herrendorff^{1,2} |
Pascal Hänggi^{1,2} 

¹Institute of Molecular Pharmacy, Department of Pharmaceutical Sciences, University of Basel, Basel, Switzerland

²Polyneuron Pharmaceuticals AG, Basel, Switzerland

³Immunology laboratory, AP-HM, Marseille, France

⁴INT, UMR CNRS 7289, Aix-Marseille University, Marseille, France

⁵Center for Neuromuscular Disorders and ALS La Timone Hospital, AP-HM, Marseille, France

⁶Nerve-Muscle Unit, Service of Neurology, Department of Clinical Neurosciences, Lausanne University Hospital (CHUV) and University of Lausanne, Lausanne, Switzerland

⁷Clinic of Neurology, Department of Medicine, University Hospital Basel, University of Basel, Basel, Switzerland

Correspondence

Pascal Hänggi, Polyneuron Pharmaceuticals AG, Hochbergerstrasse 60C, 4057 Basel Switzerland.
Email: pascalhaengg@gmail.com

Funding information

Neuromuscular Research Association Basel; Gebert RUF Stiftung. Grant/Award Number: GRS-044/15; Kommission für Technologie und Innovation, Grant/Award Number: 17485.1 PFLS-LS

Read the Editorial Highlight for this article on page 465.

Abstract

Anti-myelin-associated glycoprotein (MAG) neuropathy is a disabling autoimmune peripheral neuropathy that is caused by circulating monoclonal IgM autoantibodies directed against the human natural killer-1 (HNK-1) epitope. This carbohydrate epitope is highly expressed on adhesion molecules such as MAG, a glycoprotein present in myelinated nerves. We previously showed the therapeutic potential of the glycopolymer poly(phenyl disodium 3-O-sulfo-β-D-glucopyranuronate)-(1→3)-β-D-galactopyranoside (PPSGG) in selectively neutralizing anti-MAG IgM antibodies in an immunological mouse model and ex vivo with sera from anti-MAG neuropathy patients. PPSGG is composed of a biodegradable backbone that multivalently presents a mimetic of the HNK-1 epitope. In this study, we further explored the pharmacodynamic properties of the glycopolymer and its ability to inhibit the binding of anti-MAG IgM to peripheral nerves. The polymer selectively bound anti-MAG IgM autoantibodies and prevented the binding of patients' anti-MAG IgM antibodies to myelin of non-human primate sciatic nerves. Upon PPSGG treatment, neither activation nor inhibition of human and murine peripheral blood mononuclear cells nor alteration of systemic inflammatory markers was observed in mice or ex vivo in human peripheral blood mononuclear cells. Intravenous injections of PPSGG to mice immunized against the HNK-1 epitope removed anti-MAG IgM antibodies within less than 1 hr, indicating a fast and efficient mechanism of action as compared to a B-cell depletion with anti-CD20. In conclusion, these observations corroborate the therapeutic potential of PPSGG for an antigen-specific treatment of anti-MAG neuropathy.

Abbreviations: BSA, bovine serum albumin; BTU, Bühlmann titer units; CANOMAD, chronic ataxic neuropathy ophthalmoplegia M-protein agglutination disialosyl antibodies syndrome; CIDP, chronic inflammatory demyelinating polyneuropathy; DC, dendritic cells; EBV, Epstein-Barr virus; ELISA, enzyme-linked immunosorbent assay; FBS, fetal bovine serum; HNK-1, human natural killer 1; LPS, lipopolysaccharide; MAG, myelin associated glycoprotein; MFI, mean fluorescence intensity; MGUS, monoclonal gammopathy of unknown significance; PBMC, peripheral blood mononuclear cells; PBS, phosphate-buffered saline; PPSGG, poly(phenyl disodium 3-O-sulfo-β-D-glucopyranuronate)-(1→3)-β-D-galactopyranoside; RPMI, Roswell Park Memorial Institute medium; SGPG/SGLPG, sulfoglucuronyl paragloboside/sulfoglucuronyl-lactosaminyl-paragloboside.

Butrint Aliu and Delphine Demeestere contributed equally to this work.

This is an open access article under the terms of the Creative Commons Attribution-NonCommercial License, which permits use, distribution and reproduction in any medium, provided the original work is properly cited and is not used for commercial purposes.

© 2020 The Authors. *Journal of Neurochemistry* published by John Wiley & Sons Ltd on behalf of International Society for Neurochemistry

KEYWORDS

antigen-specific treatment, anti-MAG IgM autoantibodies, demyelinating peripheral neuropathy, monoclonal gammopathy of neurological significance, myelin-associated glycoprotein

1 | INTRODUCTION

Anti-myelin-associated glycoprotein (MAG) neuropathy is a rare form of acquired demyelinating polyneuropathy associated with IgM monoclonal gammopathy of neurological significance commonly referred as monoclonal gammopathy of undetermined significance (Talamo, Mir, Mir, Pandey, Sivik, & Raheja, 2015). Typically, the disease onset occurs after the age of 50 years and is 2.7 times more frequent in men than in women (Vallat *et al.* 2016) with a prevalence of about 1 in 100,000 (Heesters, van der Poel, Poel, Das, & Carroll, 2016; Mahdi-Rogers & Hughes, 2014; Mygland & Monstad, 2001; Talamo *et al.*, 2015). This gammopathy of neurological significance leads to the production of monoclonal anti-MAG IgM antibodies that recognize the human natural killer-1 (HNK-1) epitope, which is highly expressed on adhesion molecules such as MAG in the peripheral nervous system (Quarles, 2007; Steck, Stalder, Stalder, & Renaud, 2006). MAG, a member of the sialic acid-binding Ig-like lectins (siglecs), is located in the periaxonal membranes of oligodendroglial cells of the central nervous system and in Schwann cells of the peripheral nervous system (PNS), where it is localized in the paranodal loops and Schmidt-Lanterman incisures (Dalakas, 2010; Erb *et al.*, 2006; Kelm *et al.*, 1994). MAG is a mediator for the formation and maintenance of the myelin sheaths (Tang *et al.*, 1997). Anti-MAG IgM autoantibodies recognize the HNK-1 epitope, the sulfated trisaccharide 3-O-sulfo- β -D-GlcA-(1 \rightarrow 3)- β -D-Gal-(1 \rightarrow 4)-D-GlcNAc, which is expressed mainly on the glycoprotein MAG but also on PMP22 and glycolipids such as sulfoglucuronyl-paragloboside, and sulfoglucuronyl-lactosaminyl-paragloboside (Quarles, 2007). Nerve biopsies from affected patients show demyelination and widening of myelin lamellae (Ritz *et al.*, 1999; Steck, Murray, Murray, Meier, Page, & Perruisseau, 1983). There is strong evidence that the deposition of anti-MAG IgM on myelin sheath and myelin lamellae is responsible for the demyelination, which clinically manifests itself as a peripheral neuropathy affecting primarily sensory nerves (Gabriel *et al.*, 1998; Latov *et al.*, 1981; Willison *et al.*, 1988). Patients suffer from sensory ataxia with impaired gait, paresthesia, distal muscle weakness, and tremor (Braun, Frail, Frail, & Latov, 1982; Dalakas, 2010; Steck *et al.*, 1983). Progression of the chronic neuropathy is linked to the presence of anti-MAG IgM antibodies and there is evidence that the reduction in anti-MAG IgM titers leads to clinical improvements (Benedetti *et al.*, 2007; Gabriel *et al.*, 1996; Nobile-Orazio *et al.*, 1988; Pestronk *et al.*, 2003; Renaud *et al.*, 2006; Steck *et al.*, 2006). However, the causes and the exact mechanisms behind the expansion of anti-MAG IgM producing B-cell clones are not fully understood.

Most off-label treatments aim to reduce pathogenic autoantibody titers by depleting autoantibody-producing B-cell clones,

interfere with antibody-effector mechanisms, or physically remove autoantibodies from the circulation. Most frequently, the anti-CD20 monoclonal antibody rituximab is used to treat anti-MAG neuropathy patients (Dalakas, 2010; Lunn & Nobile-Orazio, 2016; Steck *et al.*, 2006). However, all of these treatment options lack selectivity, efficiency, or can induce severe adverse effects in some patients. For example, acute worsening of the condition related to an IgM flair and concurrent rise in anti-MAG IgM plasma titers has been described after rituximab treatment (Broglio & Lauria, 2005; Sala, Robert-Varvat, Paul, Camdessanché, & Antoine, 2014).

In a previous study, we described the glycopolymer poly(phenyl disodium 3-O-sulfo- β -D-glucopyranuronate)-(1 \rightarrow 3)- β -D-galactopyranoside (PPSGG) designed to specifically target the pathogenic anti-MAG IgM autoantibodies as a potential drug candidate for the treatment of anti-MAG neuropathy (Herrendorff *et al.*, 2017). The glycopolymer is composed of a biodegradable poly-L-lysine backbone (\approx 80 kDa) presenting multiple copies of a mimetic of the sulfated HNK-1 trisaccharide to facilitate a multivalent interaction with anti-MAG IgM autoantibodies. We previously showed in a competitive ELISA that PPSGG prevented the binding of patients' anti-MAG IgM autoantibodies to MAG at low nanomolar concentrations. Furthermore, we demonstrated a highly efficient reduction in anti-MAG IgM antibody titers in an immunological mouse model for anti-MAG neuropathy. In this study, the pharmacodynamic properties and potential immunomodulatory effects of PPSGG were further investigated. PPSGG was found to selectively and efficiently inhibit the binding of patients' anti-MAG IgM to sciatic nerve myelin of non-human primates. Furthermore, the pharmacodynamic profile of the glycopolymer was characterized, including a dose titration study in mice to predict the estimated dose required in anti-MAG neuropathy patients. Finally, it was shown that PPSGG removes the anti-MAG IgM autoantibodies in a highly selective fashion without the activation of murine or human immune cells.

2 | METHODS**2.1 | Patients and control blood samples**

All experiments using human samples were performed in accordance with the Declaration of Helsinki (1964, Association H. E. C. o. E. o. t. W. M. 1964). Patients and control subjects signed the written informed consent for their participation in this study. The study was not pre-registered and the protocol was approved by the Ethical Committees EKNZ, and CER-VD (Commission cantonale d'éthique de la recherche sur l'être humain), Switzerland (Study Nr. 01551). Heparinized whole blood of patients with clinically confirmed anti-MAG neuropathy

and healthy control subjects were obtained from the Department of Neurology of the University Hospital Basel (Basel, Switzerland), the Lausanne University Hospital (Lausanne, Switzerland), and Centre Hospitalier de la Timone, AP-HM (Assistance Public-Hôpitaux de Marseille), (Marseille, France). The blood samples of the anti-MAG patients were taken during regular visit at the center and the control samples were taken in the morning.

2.2 | Experimental animals

The wild type BALB/cJrj (Ref. C-BJ-56-M/F; Janvier Labs) mice (5–10 weeks old male and female ($n = 61$)) used in this study were

bred at the University Hospital Basel and kept under specific pathogen-free conditions in a controlled environment (12-hr light-dark cycle at 20°C) with food and water ad libitum. Unless stated, experiments were performed in the morning without blinding of the experimenter. Mice were allocated arbitrarily into the different groups and the dosing was increased from low to high. No anesthetic or medication was required to reduce treatment related effects and no animal was excluded or died during the studies. Mice were sacrificed by CO₂ suffocation and decapitation after the last blood sampling (Figure 1). The power calculation was based on the previous study (Herrendorff et al., 2017) where the null hypothesis was disproved and showed a concentration-dependent relationship of the PPSGG and the anti-MAG IgM binding (>80% relative reduction in

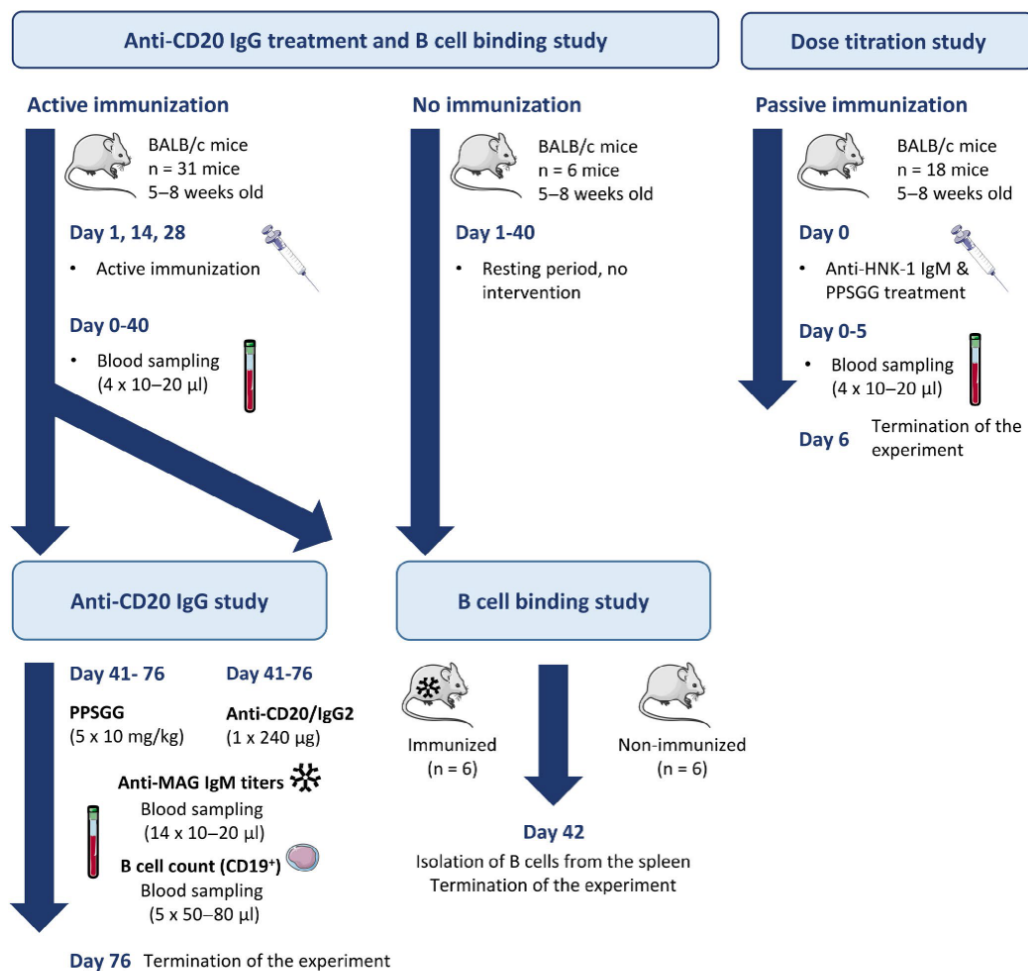


FIGURE 1 Flow chart of the animal experiments. Overview of the timelines of the animal experiments ($n = 61$). Images adapted from SMART Servier Medical ART

the anti-MAG IgM titers in the dose range of 2–10 mg/kg in mice). Therefore, we assume an alternative hypothesis ($\mu_A - \mu_B \neq 0$) for the primary endpoint that states that the anti-MAG IgM antibodies can be neutralized and removed by PPSGG in vivo compared to vehicle (phosphate-buffered saline, PBS) treatment (one-tailed) to have a power of >80% and a type I error of 5%, we would need six subjects per group to prove the effect is significant (2 independent means, one-sided, $\mu_A = 100$, $\mu_B = 20$, $\kappa = n_A/n_B = 1$, $\sigma = 20$). The study was not pre-registered and all animal experiments were performed in accordance with authorization No. 2778 of the Animal Research Authorities of the Canton of Basel-Stadt, Switzerland.

2.3 | Isolation and culture of human PBMC, B cells, and DC

Peripheral blood mononuclear cells (PBMC) were isolated from heparinized blood samples by gradient centrifugation according to the protocol provided by GE-Healthcare (Ficoll-Paque PLUS). B cells (CD19⁺) and monocytes (CD14⁺, CD16⁺) were isolated from PBMC by negative selection using the EasySep[™] EasySep[™] Magnet (18103), the EasySep[™] Human B Cell Isolation Kit (17954), and the EasySep[™] Human Monocyte Isolation Kit (19359) all provided by StemCell[™] Technologies.

B cells were maintained for up to 2 days in Roswell Park Memorial Institute medium (RPMI) 1640 medium (R8758, Roswell Park Memorial Institute medium; Sigma-Aldrich), supplemented with 10% fetal bovine serum (FBS, 10270–106), 1% antibiotic-antimycotic solution (AA, 15240062), and 1% L-glutamine solution (L-Gln, 11500626) all provided by Gibco, Thermo Fisher Scientific.

Monocytes were seeded and differentiated to dendritic cells (DC) in complete RPMI 1640 medium containing 10% FBS, 1% AA, 1% L-Gln and supplemented with 800 IU/ml recombinant GM-CSF (Granulocyte macrophage colony-stimulating factor) and 500 IU/ml recombinant IL-4 (R&D Systems) for 6 days at 37°C and 5% CO₂.

2.4 | Ex vivo Epstein–Barr transformation of B cells

To prolong the viability of primary human B cells ($n = 4$ anti-MAG neuropathy patients) ex vivo, the cells were transformed with Epstein–Barr virus (EBV) (Hollyoake, Stühler, Stühler, Farrell, Gordon, & Sinclair, 1995). Marmoset B95.8 Epstein–Barr virus-producing cells (RRID:CVCL_1953; Vircell) were maintained in complete RPMI 1640 medium containing 10% FBS, 1% AA, and 1% L-Gln. The supernatant containing the EBV was collected after 20 days by centrifuging cells (1400g, 15 min) and filtering the supernatant with a 0.45 μm and a 0.2 μm Filtropur S filter (83.1826; Sarstedt). Freshly isolated human PBMC (1×10^6 cells) were resuspended in 3 ml EBV supernatant and incubated for 24 hr before adding 7 ml complete RPMI 1640 medium supplemented with 20 ng/ml cyclosporin A (30024; Sigma-Aldrich). The cell growth was monitored and the medium changed every 2–3 days to achieve an efficient immortalization. After 14 days

of culture, cells were maintained in complete RPMI 1640 medium without cyclosporin A, at a density of approximately 5×10^5 to 1×10^6 cells/mL.

2.5 | Indirect immunofluorescence assay

Prior to the indirect immunofluorescence assay, the anti-MAG IgM titers were determined by ELISA (see below) in Bühlmann titer units (BTU). Anti-MAG neuropathy patients' sera ($n = 5$) and control neuropathy patient sera ($n = 1$ chronic ataxic neuropathy ophthalmoplegia M-protein agglutination disialosyl antibodies syndrome (CANOMAD) patient and $n = 1$ chronic inflammatory demyelinating polyneuropathy (CIDP) patient with IgM monoclonal gammopathy of unknown significance but no MAG or ganglioside activity) were used. Both control sera were previously tested for their positive reaction on sciatic nerves and negative for anti-MAG and anti-ganglioside antibodies. The CANOMAD patient sera was tested positive for anti-disialosyl antibodies, however, the exact target of the antibodies in case of the CIDP patient is unknown.

Undiluted sera were incubated for 30 min with different concentrations of PPSGG (62.5, 125 and 250 $\mu\text{g}/\text{ml}$ in PBS). The samples were then diluted 1:20 in PBS and incubated for 30 min with samples of sciatic nerve cynomolgus monkeys (Macaca fascicularis). The non-human primate sciatic nerve samples were part of the ImmuGlo[™] anti-MAG IFA kit (REF 1172, LOT 1905438B) and obtained from IMMCO Diagnostics. Data were analyzed and quantified by ImageJ software from ten fields of observation for each experimental condition.

2.6 | Anti-MAG autoantibodies ELISA

Sera from control subjects, commercially available ($n = 1$, H4522; Sigma-Aldrich) and non-commercial human serum ($n = 6$), and anti-MAG neuropathy patients ($n = 8$) were used to determine the reactivity of PPSGG to other immunoglobulins by ELISA. Maxisorp MP 96 wells plates (442404; Nunc, Sigma-Aldrich) were coated overnight at 4°C with 50 μl PPSGG (0.1 $\mu\text{g}/\text{ml}$ in PBS), then washed four times with 300 μl ELISA buffer (0.1% Tween 20 in PBS) and blocked with 100 μl of 5% bovine serum albumin (BSA, A9647; Sigma-Aldrich) in ELISA buffer for 2 hr at 20–25°C. The sera samples were diluted 1:1,000 (2.5% BSA in ELISA buffer) and added to the plates after another washing step. After incubating for 2 hr at 20–25°C, the plates were washed four times with 300 μl ELISA buffer and 100 μl of HRP-labeled anti-human IgM (1:2'000 in 1% BSA in ELISA buffer, RRID:AB_258318; Sigma-Aldrich), 100 μl HRP (horseradish peroxidase)-labeled anti-human IgG (1:10'000 in 1% BSA in ELISA buffer, RRID:AB_258388; Sigma-Aldrich), or the anti-human IgM antibody conjugated to HRP (B-MAG-ELM; Bühlmann Laboratories) were added and incubated for 2 hr at 20–25°C, respectively. To develop the assay, 50 μl of undiluted 3,3',5,5'-tetramethylbenzidine (B-TMB; Bühlmann Laboratories) was added and incubated at 20–25°C on a plate rotator (600 RPM) for 30 min. The stop solution

(50 μ l of 0.25 M H₂SO₄) was added and the optical density at 450 nm (OD₄₅₀) was determined within <5 min with the Spectra Max 190 (Molecular Devices).

2.7 | PPSGG dose titration study in mice

To estimate the dose of PPSGG required to bind and exhaustively eliminate anti-MAG IgM autoantibodies in anti-MAG neuropathy patients, a dose titration study was performed in mice. Therefore, naïve BALB/c mice were intravenously injected with 60 μ g ($n = 10$ mice) or 120 μ g ($n = 8$ mice) of purified, sodium azide- and BSA-free anti-HNK-1 IgM (ab187274, Abcam), followed by 1–20 μ g intravenous doses of PPSGG, 10–20 min after IgM administration. Blood samples were taken 5–10 min after PPSGG administration and the serum was collected and analyzed for unbound anti-HNK-1 IgM. Additional serum samples were taken and analyzed at a later time point (24 hr after administration) to confirm the removal of the injected anti-HNK-1 IgM antibodies by PPSGG. The detection of the free anti-HNK-1 IgM in mouse sera was performed as described elsewhere (Herrendorff et al., 2017).

2.8 | CD20⁺ cell depletion in mice

BALB/c mice were immunized with purified bovine sulfoglucuronyl paralogloboside/sulfoglucuronyl-lactosaminyl-paralogloboside mixed with keyhole limpet hemocyanin (KLH, H8283; Sigma-Aldrich) and TiterMax Gold (T2684; Sigma-Aldrich) (Herrendorff et al., 2017). After mouse anti-MAG IgM titers plateaued, single intravenous injections ($n = 6$ mice) of 240 μ g of anti-mouse CD20 IgG (RRID:AB_2629619; Biolegend) or 240 μ g of Ultra-LEAF Purified Rat IgG2b (RRID:AB_11149687; Biolegend) were performed ($n = 3$ mice). Blood samples were taken prior and at various time points after the treatment and collected in ethylenediaminetetraacetic acid (EDTA)-coated tubes from the vena saphena. To lyse the erythrocytes, 1 ml of ammonium-chloride-potassium lysing buffer (A10492-01; Gibco, Thermo Fisher Scientific) was added at 20–25°C, and after 5 min cells were washed with PBS and centrifuged (170 g, 5 min) before repeating the lysis step once more. Whole blood (40 μ l) was stained with 1 μ l of anti-mouse CD19-PECy7 (RRID:AB_657664; eBioscience) for 45 min at 4°C (protected from light). The samples were then diluted with PBS to a final volume of 200 μ l and stained with 1 μ l of DAPI (4',6-diamidino-2-phenylindol, D3571; Invitrogen) prior to the analysis of the cells by flow cytometry with the LSR Fortessa (Becton Dickinson). At least 10'000 events were recorded and data were further gated and analyzed with FlowJo v 10.2 (FlowJo LLC).

2.9 | Binding of PPSGG to murine and human B cells

The binding of PPSGG to B cells and their potential activation was studied by flow cytometry and fluorescence microscopy. Fluorescently labeled PPSGG (PPSGG, 5% loading with

sulforhodamine 101) was used to assess binding to the cells and Fluo-4 AM was used to determine the intracellular calcium (Ca²⁺) levels as a marker for B cell activation through the B cell receptor (Baba & Kurosaki, 2016). Isolated human PBMC, human B cells, murine splenocytes, and murine B cells were stained with anti-CD19 PE-Cy7 (mouse anti-human IgG1, RRID:AB_2535491; rat anti-mouse IgG2a, RRID:AB_657664) and anti-F4/80 eFluor 450 (rat anti-mouse IgG2a, RRID:AB_1548747), Fluo-4 AM (F14201; Thermo Fisher Scientific), propidium iodide (PI, P4170; Sigma Aldrich), and Hoechst 33258 solution (94403; Sigma Aldrich). The cells were loaded with 3 μ M Fluo-4 AM (cell-permeable, fluorescent Ca²⁺ indicator) for 30 min in the dark at 37°C and 5% CO₂ before the antibodies and PPSGG-S were added and incubated for another 30 min. The cells were washed once with extracellular solution (135 mM NaCl, 5 mM KCl, 5 mM HEPES, 10 mM D-glucose, 2 mM CaCl₂, pH 7.35) and kept in the dark for the immediate recording.

Isolated murine spleen cells and B cells ($n = 6$ naïve mice and $n = 6$ immunized mice) or PBMC and human B cells ($n = 4$ anti-MAG neuropathy patients and $n = 3$ healthy control donors) were incubated at approximately 1×10^6 cells/mL with 10 μ M or 1 μ M PPSGG-S. The fluorescently labeled antibodies were added at a concentration of 1 μ g/mL. For assessing B-cell activation, a control measurement was recorded to set the gate for the baseline signal and after addition of 100 μ M unlabeled PPSGG the sample was measured every 2 min on a LSR Fortessa (BD Biosciences). Murine cells treated with 3 μ M ionomycin acting as a Ca²⁺ ionophore and EBV transformed human B cells showing increased intracellular Ca²⁺ levels were used as positive controls. At least 10'000 events were recorded and data were analyzed with FlowJo.

The same setup was used to measure binding and activation with a fluorescence microscopy (Applied Precision Widefield DV Core microscope; GE Life Sciences). B cells were plated in Ibidi 8 well μ -Slides (80826; Ibidi GmbH) and loaded with 3 μ M Fluo-4 AM and incubated with PPSGG-S at 10 μ M or 1 μ M. The cells were washed once with extracellular solution and the plate was placed in a humidified atmosphere (37°C and 5% CO₂) on the microscope using 475 nm and 575 nm solid-state illumination and a 60 \times /1.42 oil-immersion objective (Plan Apo N). Five randomly taken spots per sample were identified and recorded. According to the flow cytometry experiments, Fluo-4 AM loaded samples were recorded before and after addition of 100 μ M PPSGG every 5 min for 20 min. The images were processed with softWoRx (GE Life Sciences) and analyzed with FIJI software. The PPSGG-S binding and the relative changes in intracellular Ca²⁺ concentration was assessed by measuring fluorescence intensity of each individual cell after background subtraction.

2.10 | Dendritic cell activation and intracellular cytokine analysis by flow cytometry

Non-adherent monocyte-derived DC ($n = 5$ healthy control donors) were reseeded at day 6 to a 96-well plate (1×10^5 cells per well) in complete RPMI 1640 media and incubated for 1 hr or 18 hr

FIGURE 2 Selective blocking of the binding of anti-myelin-associated glycoprotein (MAG) IgM from patients sera to sciatic nerve myelin of non-human primates. (a) After incubation of undiluted serum (with or without poly(phenyl disodium 3-O-sulfo- β -D-glucopyranuronate)-(1 \rightarrow 3)- β -D-galactopyranoside, PPSGG), the samples were diluted 1 in 20 in phosphate-buffered saline and the myelin-reactivity tested by indirect immunofluorescence. (b) Five anti-MAG neuropathy patients' and two control neuropathy patients' (chronic ataxic neuropathy ophthalmoplegia M-protein agglutination disialosyl antibodies syndrome and chronic inflammatory demyelinating polyneuropathy with IgM monoclonal gammopathy of unknown significance but no MAG or ganglioside activity) sera were tested in the indirect immunofluorescence assay. A concentration of 125 μ g/ml PPSGG completely blocked the binding of anti-MAG IgM to primate sciatic nerve myelin. However, (c) PPSGG had no inhibitory activity on the myelin reactivity of the control neuropathy patients

with lipopolysaccharide (LPS) (100 ng/ml), PPSGG (30 μ g/ml), or both LPS and PPSGG. Afterward, the DC were stained for 20 min at 20–25°C with CD14 FITC (RRID:AB_2571928), HLA-DR PerCP (RRID:AB_893574), CD40 BV605 (RRID:AB_2564243), CD83 APC (RRID:AB_314519), CD11b Alexa Fluor 700 (RRID:AB_493705), CD1c APC-Cy7 (RRID:AB_10643413), together with Fc receptor block (anti-CD16/32 Ab, RRID:AB_312801) in PBS supplemented with 1% BSA. The mean fluorescence intensity (MFI) $16'481 \pm 398$ cells per sample was assessed by flow cytometry (LSR Fortessa; BD Biosciences).

2.11 | Human interleukin-1 β ELISA

Supernatant from PBMC ($n = 5$ healthy control donors) stimulated for 6 hr with lipopolysaccharide (LPS, 100 ng/ml) or PPSGG (30 μ g/ml) in complete RPMI 1640 media (10% FBS, 1% AA, and 1% L-glut) was collected and stored at -20°C until use. Total production of IL-1 β was assessed using the eBioscience™ Human IL-1 beta ELISA Ready-SET-Go!™ (Invitrogen™ 88726122) according to the protocol provided by the manufacturer (Thermo Fisher).

2.12 | Intracellular cytokine analysis by flow cytometry

For the intracellular cytokine analysis, freshly isolated PBMC ($n = 5$ healthy control donors) were reseeded in complete RPMI 1640 media and stimulated for 2 hr with LPS (100 ng/ml) or PPSGG (30 μ g/ml) at 37°C and subsequently incubated with a mix of brefeldin A and monensin (both diluted 2'000 \times) for an additional 4 hr or 18 hr at 37°C . Cells were stained with HLA-DR PerCP (RRID:AB_893574), CD8 BV510 (RRID:AB_2561378), CD14 Alexa Fluor 700 (RRID:AB_2566715), CD4-PE (RRID:AB_1937246), CD11c PE-Alexa Fluor 594 (RRID:AB_2564082), and CD19 PE-Cy7 (RRID:AB_2564202) together with Fc receptor block (anti-CD16/32 Ab, RRID:AB_312801). PBMC were then fixed with 4% paraformaldehyde in PBS and permeabilized with PBS solution containing 0.5% BSA, 0.5% Tween 20, followed by intracellular staining with IL-6 FITC (RRID:AB_315151), IL-12/L-23 p40 Pacific Blue (RRID:AB_2124517), TNF α BV605 (RRID:AB_11203719), and IL-10 APC (RRID:AB_315456). Data were collected on a Fortessa flow cytometer (BD Biosciences) and analyzed using FlowJo.

2.13 | Statistical analysis

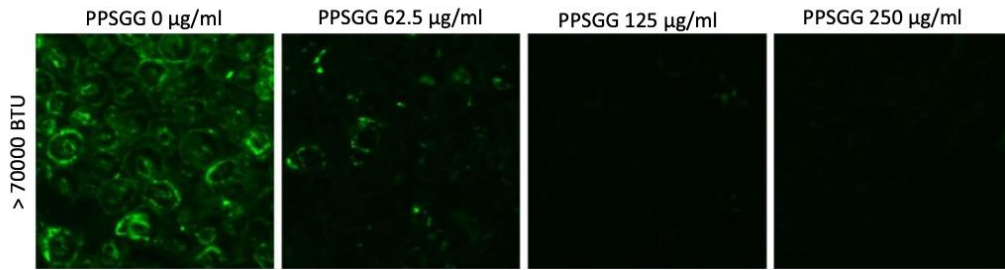
Unless stated, results are given as mean \pm SD of three experiments and analyzed by Prism GraphPad Software (Version 7.04). No test for outliers was conducted and no data point was excluded in the study. The normal distribution was assessed by D'Agostino and Pearson normality test. G*Power software (Version 3.1.9.4) was used to determine sample size within the animal approval (No. 2778). No additional sample calculation was performed for the experiments in this publication. Comparisons between two conditions were performed using either Student's *t* test or one-way ANOVA with Dunnett's multiple comparison posttest with a 0.05 confidence level accepted for statistical significance (* $p \leq .05$, ** $p \leq .01$, *** $p \leq .001$).

3 | RESULTS

3.1 | Inhibition of patients' anti-MAG IgM binding to myelin of non-human primates and highly selective binding of anti-MAG IgM by PPSGG

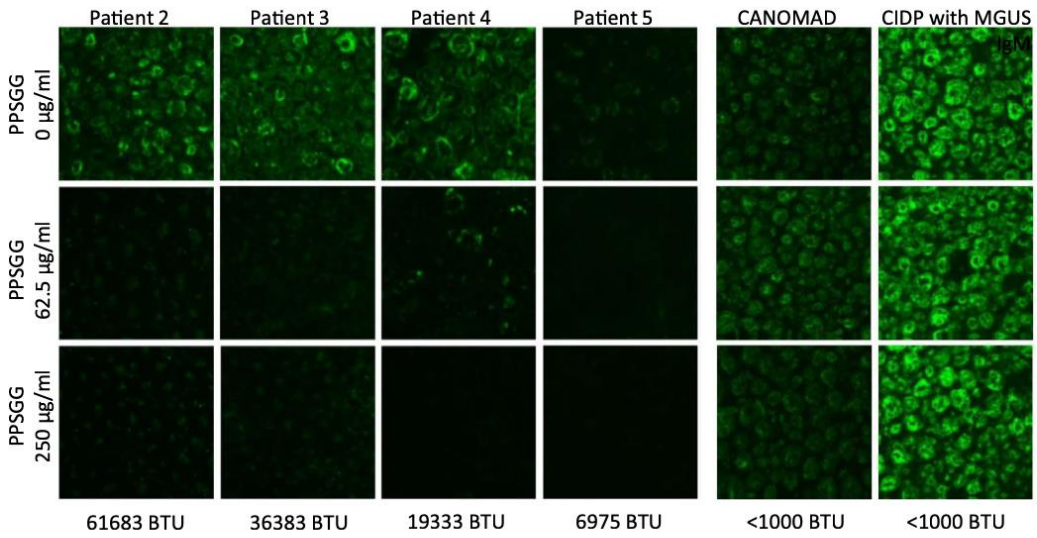
To assess the potential of PPSGG to inhibit patients' anti-MAG IgM binding to myelin of peripheral nerves, sciatic nerve preparation of cynomolgus monkeys were incubated with patients' sera and the myelin reactivity was determined by indirect immunofluorescence measurements (Figure 2). The five analyzed sera of anti-MAG neuropathy patients exhibited a wide range of anti-MAG IgM titers (6'975, 19'333, 36'383, 61'684, 249'600 BTU). As controls, the sera samples of a chronic ataxic neuropathy (CANOMAD) patient and a CIDP patient, with IgM monoclonal gammopathy and positive reaction on sciatic nerve but no MAG or ganglioside activity were used. They exhibited anti-MAG IgM titers below the threshold of 1'000 BTU in the ELISA. The normalized fluorescence intensity of all the anti-MAG neuropathy patients' samples decreased by 80% ($\pm 5\%$ SD), when the sera were incubated with 250 μ g/ml PPSGG. The incubation of the anti-MAG neuropathy patients' samples with 62.5 μ g/ml PPSGG already showed a decrease of 78% ($\pm 7\%$ SD) in the normalized fluorescence intensity. The serum of patient 4 exhibiting low anti-MAG titer (19'333 BTU) showed residual myelin binding compared to patient 2 (61'638 BTU) or 3 (36'383 BTU) with higher anti-MAG IgM titers at a PPSGG concentration of 62.5 μ g/ml. The anti-MAG neuropathy patient 1 with the highest titer showed almost a complete decrease in the normalized fluorescence intensity when the serum was incubated with 125 μ g/ml PPSGG. The control neuropathy patients showed no significant reduction of the normalized

(a) **Anti-MAG neuropathy patients (Patient A)**

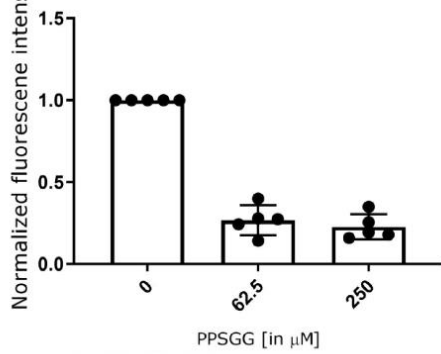


Anti-MAG neuropathy patients

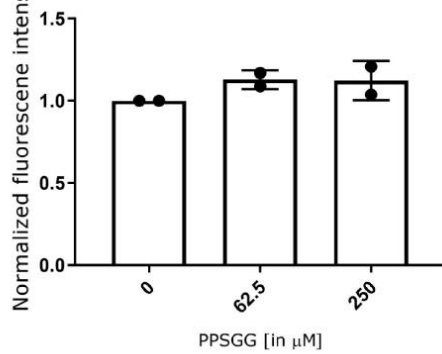
Control neuropathy patients



(b) **Anti-MAG neuropathy patients**



(c) **Control neuropathy patients**



fluorescence intensity when the undiluted sera were incubated with 250 $\mu\text{g/ml}$ PPSGG.

To confirm the selective blocking of anti-MAG IgM autoantibodies by PPSGG, the binding of control subject sera (commercial and non-commercial), and anti-MAG neuropathy patients' sera to PPSGG was tested. PPSGG showed only reactivity to IgM present in the serum samples of anti-MAG neuropathy patients. No reactivity of PPSGG to IgM of healthy control samples was detected. Moreover in neither control subject sera nor anti-MAG neuropathy patients' sera significant binding of IgG was detected (Figure 3). No significant difference in PPSGG reactivity between the commercial and non-commercial human serum was observed.

3.2 | Fast and efficient removal of circulating anti-HNK-1 IgM by PPSGG in BALB/c mice, while CD20⁺ cell depletion showed no significant effect on the anti-MAG IgM titers in the immunological mouse model for anti-MAG neuropathy

To estimate the PPSGG dose required to reduce anti-MAG IgM autoantibody titers in anti-MAG neuropathy patients, we performed a dose-finding study in mice (Figure 4). Therefore, naïve BALB/c mice were injected with different concentrations of murine anti-HNK-1 IgM (60, 120 $\mu\text{g/kg}$) followed by intravenous PPSGG injection (1–20 μg). Anti-MAG IgM titer analysis in mouse plasma samples taken 5–10 min after PPSGG administration showed that the administration of a 10 μg PPSGG dose was sufficient to bind 93.28% ($\pm 0.1\%$ SD) of the 60 μg anti-HNK1 IgM in vivo, as indicated by the measured baseline anti-MAG IgM titers. A dose range of 3–5 μg was still sufficient to reduce the anti-HNK1 IgM level by $\geq 88.56\%$ ($\pm 1.64\%$ SD). The lowest dose of 1 μg PPSGG still reduced the 60 μg anti-HNK1 IgM level by 23.08% ($\pm 0.64\%$ SD) compared to the pre-treatment level. At the dose of 120 μg anti-MAG IgM, 10 μg PPSGG

reduced the anti-MAG IgM titers by 97.85% ($\pm 0.50\%$ SD), 4 μg PPSGG reduced the titers by 88.74% ($\pm 8.68\%$ SD), and 2 μg PPSGG reduced the titers by 42.71% ($\pm 3.03\%$ SD) compared to the pre-treatment titers. To check whether anti-MAG IgM antibodies were permanently removed, mice were sampled at a later time points (24 and 96 hr after PPSGG administration) and showed persistent reduction of the titers.

To further verify the mechanism of anti-MAG IgM removal in vivo, we compared PPSGG treatment to treatment with a CD20⁺ B cell depleting monoclonal antibody (Figure 5). Therefore, wild type BALB/c mice were immunized against the HNK-1 bearing glycolipids sulfoglucuronyl paragloboside/sulfoglucuronyl-lactosaminyl-paragloboside. Once the mice exhibited a constant production of anti-MAG IgM antibodies, they were treated either with a single intravenous injection of mouse anti-CD20 IgG, rat IgG2b κ isotype control antibody, or with weekly injections of PPSGG (10 mg/kg). The number of B cells and anti-MAG IgM titers were followed up by flow cytometry and ELISA in the blood and serum, respectively. Flow cytometry of PBMC revealed the significant depletion of circulating B cells in the anti-CD20 antibody treated group, while no significant changes in the number of circulating B cell were observed in the IgG2 κ isotype control antibody group or PPSGG treated group. However, neither B-cell depletion nor IgG2 κ isotype control antibody changed the anti-MAG IgM antibody titers significantly during the follow-up period of 5 weeks. Only the mice treated once per week with 10 mg/kg PPSGG exhibited a significant reduction of the anti-MAG IgM titers.

3.3 | No murine or human leukocyte activation after incubation with PPSGG

As PPSGG presents multiple copies of the HNK-1 mimetic, it can be seen as multivalent soluble antigen which could be recognized by B cells and potentially trigger a humoral response (Heesters *et al.*,

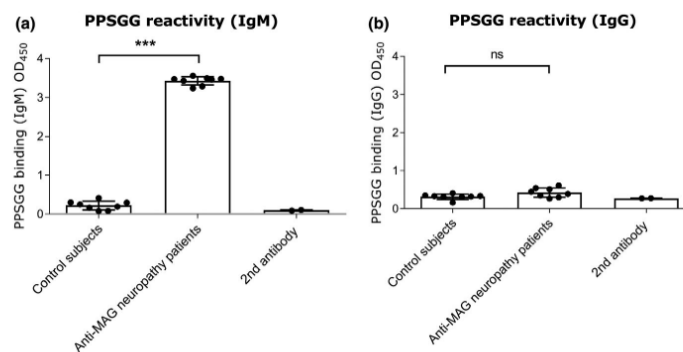


FIGURE 3 Reactivity of immunoglobulins (IgG and IgM) from healthy subjects and anti-myelin-associated glycoprotein (MAG) neuropathy patients to poly(phenyl disodium 3-O-sulfo- β -D-glucopyranuronate)-(1 \rightarrow 3)- β -D-galactopyranoside (PPSGG). A PPSGG-binding ELISA was performed with healthy controls (healthy control serum samples $n = 7$), commercially available normal human serum ($n = 1$), and anti-MAG neuropathy patient samples ($n = 8$). Only IgM (a) and no IgG (b) binding in sera samples of anti-MAG neuropathy patient exhibited PPSGG activity in the ELISA. Data are indicated by mean and standard deviation (one-way ANOVA, * $p \leq .05$, ** $p \leq .01$, *** $p \leq .001$)

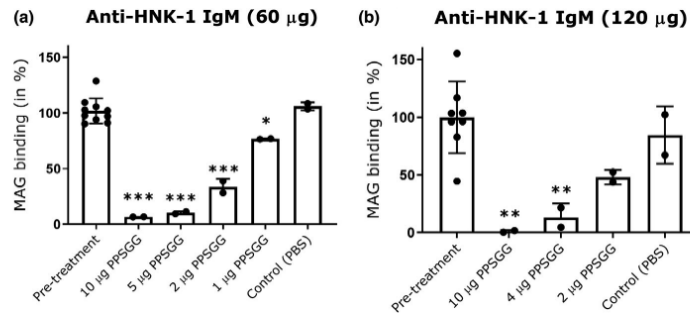


FIGURE 4 Poly(phenyl disodium 3-O-sulfo- β -D-glucopyranuronate)-(1 \rightarrow 3)- β -D-galactopyranoside (PPSGG) dose titration study in mice. The intravenous injection of 60 μ g ($n = 10$ mice) (a) or 120 μ g anti-human natural killer-1 (HNK-1) IgM ($n = 8$ mice) (b) was followed by the injection of different doses of PPSGG (<10 min). Blood samples were taken 5 to 15 min after PPSGG administration and the amount of PPSGG required to bind most of the administered mouse anti-HNK-1 IgM in circulation was determined by ELISA. The intravenous injection of 10 μ g was sufficient to deplete $\geq 92\%$ of the total IgM. Data are indicated by mean and standard deviation (one-way ANOVA with Dunnett's multiple comparisons test, * $p \leq .05$, ** $p \leq .01$, *** $p \leq .001$)

2016). Therefore, we assessed if there is specific binding of PPSGG to B cells of immunized and non-immunized mice, or to B cells of anti-MAG neuropathy patients and of healthy controls (Figure 6). Independent of the technique, neither the flow cytometry data nor the fluorescent microscopy data showed a significant difference between control (non-immunized) and anti-MAG IgM and IgG producing (immunized) B cells isolated from the murine spleen. Nonetheless, the percentage of B cells with surface PPSGG staining was highly dependent on the concentration of PPSGG. It was increased when murine B cells were incubated with 10 μ M PPSGG compared to 1 μ M PPSGG. A sulforhodamine 101 labeled thioglycerol capped poly-L-lysine backbone was used as control and showed no binding to isolated B cells at 1 or 10 μ M. The effect of PPSGG on intracellular Ca^{2+} signaling as a marker for B cell activation was assessed by flow cytometry and fluorescence microscopy (Donjerković & Scott, 2000). B cells of immunized and non-immunized mice did not exhibit an increase in the relative intracellular Ca^{2+} levels monitored over the time course of 8 min by flow cytometry and 20 min by fluorescence microscopy, even after incubation with 100 μ M PPSGG. B cells of anti-MAG neuropathy patients did not show enhanced binding of PPSGG compared to B cells of control subjects, when they were incubated for 30 min with 1 or 10 μ M PPSGG.

To confirm the presence of anti-MAG IgM producing B cells in the obtained peripheral blood samples from anti-MAG neuropathy patients, PBMC of four patients (Nr. 23, 27, 49, and 67) were transformed with EBV to increase viability of B cells ex vivo. Before the transformation, the anti-MAG IgM levels of patients 23, 27, and 49 were higher compared to patient 67. Fourteen days after transformation, the cell supernatants were analyzed by ELISA for their anti-MAG IgM titers. The cells of patient 49 had the highest anti-MAG IgM titer and maintained the ability to secrete anti-MAG IgM in vitro (Figure 7). Besides B cells activation, we assessed whether PPSGG can induce DC activation by measuring the expression of co-stimulatory molecules (Figure 8). Human monocyte-derived DC (CD11c⁺,

CD14⁺, and CD11b⁺) were incubated for 18 hr with 30 μ g/ml PPSGG, 100 ng/ml LPS, or with both PPSGG (30 μ g/ml) and LPS (100 ng/ml) and HLA-DR, CD40, and CD83 expression was determined for each condition. LPS was used as a positive control for DC activation and the co-incubation of PPSGG as well as to assess potential synergistic effects. We observed that MFI for CD40 and CD83 increased upon LPS exposure, but were unaffected by PPSGG treatment. A trend toward an increased MFI for HLA-DR was observed in the LPS-treated groups, but PPSGG had no significant influence on the expression of HLA-DR. To assess whether potential pro-anti-inflammatory reactions were induced by PPSGG, freshly isolated PBMC from healthy human donors were treated with 30 μ g/ml PPSGG, 100 ng/ml LPS, or a combination of both for 6 or 20 hr, respectively (Figure 9). Subsequently, TNF- α , IL-6, IL-10 and IL-12 production by CD14⁺ monocytes and HLA-DR⁺ CD11c⁺ DC was assessed by flow cytometry or ELISA. No significant induction of TNF- α , IL-6, IL-12, and IL-1 β was observed, when the CD14⁺ monocytes or CD11c⁺ DC were incubated with PPSGG. A significant increase in the production of TNF- α , IL-6, IL-12, and IL-1 β was only observed upon treatment with LPS, whereas no impact was observed when co-incubating PPSGG with LPS. In addition, to assess potential inflammatory or allergic-like reactions induced by the administration of PPSGG in BALB/c mice, a cytokine and chemokine array including IFN γ , IL-2, IL-6, and TNF α was performed. Neither a single nor multiple administrations (daily for five consecutive days) of 10 mg/kg PPSGG, led to a significant alteration of the studied cytokines and chemokines compared to the pre-treatment titers (Figures S1–S5 in supplementary information).

4 | DISCUSSION

Anti-MAG neuropathy is a disabling demyelinating peripheral neuropathy with an autoimmune etiology caused by monoclonal IgM

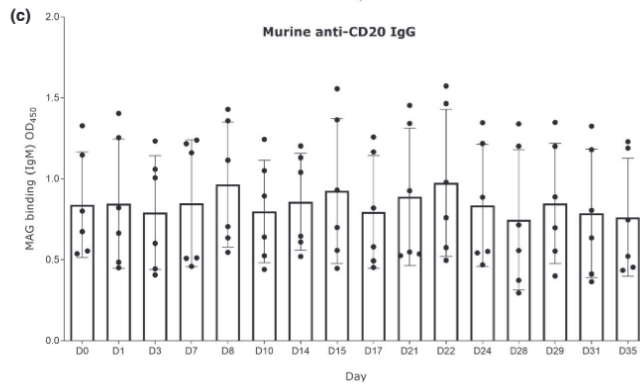
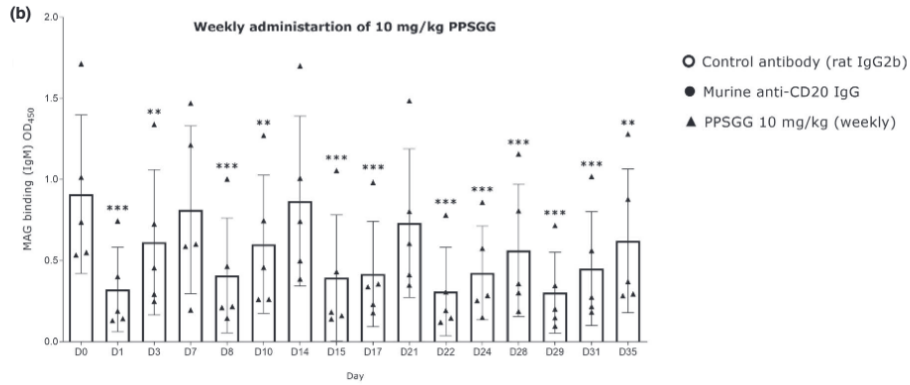
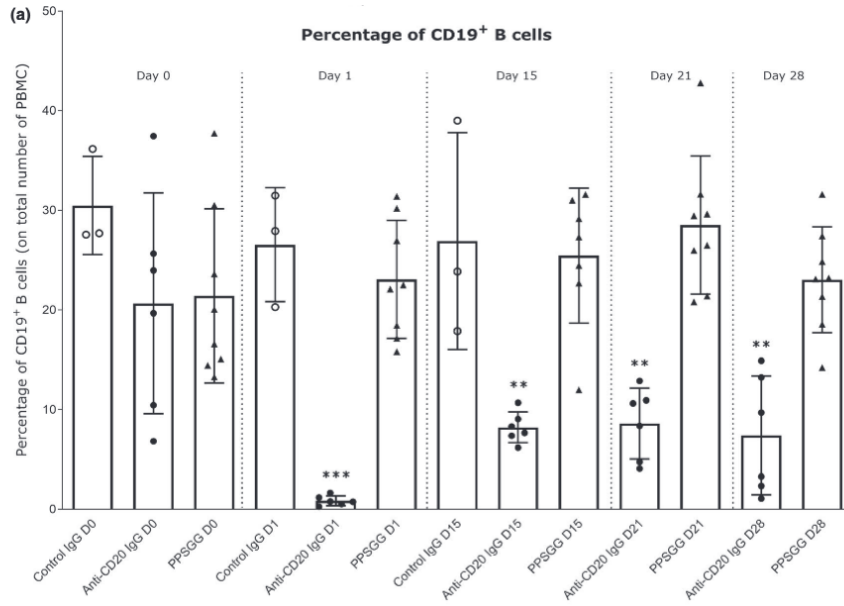


FIGURE 5 Effects of anti-CD20 antibody treatment, control antibody treatment, and poly(phenyl disodium 3-O-sulfo- β -D-glucopyranuronate)-(1 \rightarrow 3)- β -D-galactopyranoside (PPSGG) treatment on anti-myelin-associated glycoprotein (MAG) IgM antibodies in the immunological BALB/c mouse model for anti-MAG neuropathy. (a) Single injection of 240 μ g of anti-CD20 antibody ($n = 6$) depleted almost all circulating CD19⁺ B cells, whereas weekly PPSGG treatment (10 mg/kg, $n = 8$) or single treatment with a control rat IgG2b antibody ($n = 3$) did not affect the levels of circulating CD19⁺ B cells. Weekly PPSGG treatment (10 mg/kg, D1, D8, D15, D22, D28) lowered the anti-MAG IgM antibody titers significantly, compared to pre-treatment levels at D0 and depicted by the decreased binding of the anti-human natural killer-1 IgM to MAG ($n = 5$) (b). A single injection of 240 μ g of anti-CD20 antibody (c) and of 240 μ g ($n = 6$) of a control antibody (Figures S1–S5 in supplementary information) did not affect the anti-MAG IgM antibody titers in mice. Data are indicated by mean and standard deviation (one-way ANOVA, * $p \leq .05$, ** $p \leq .01$, *** $p \leq .001$).

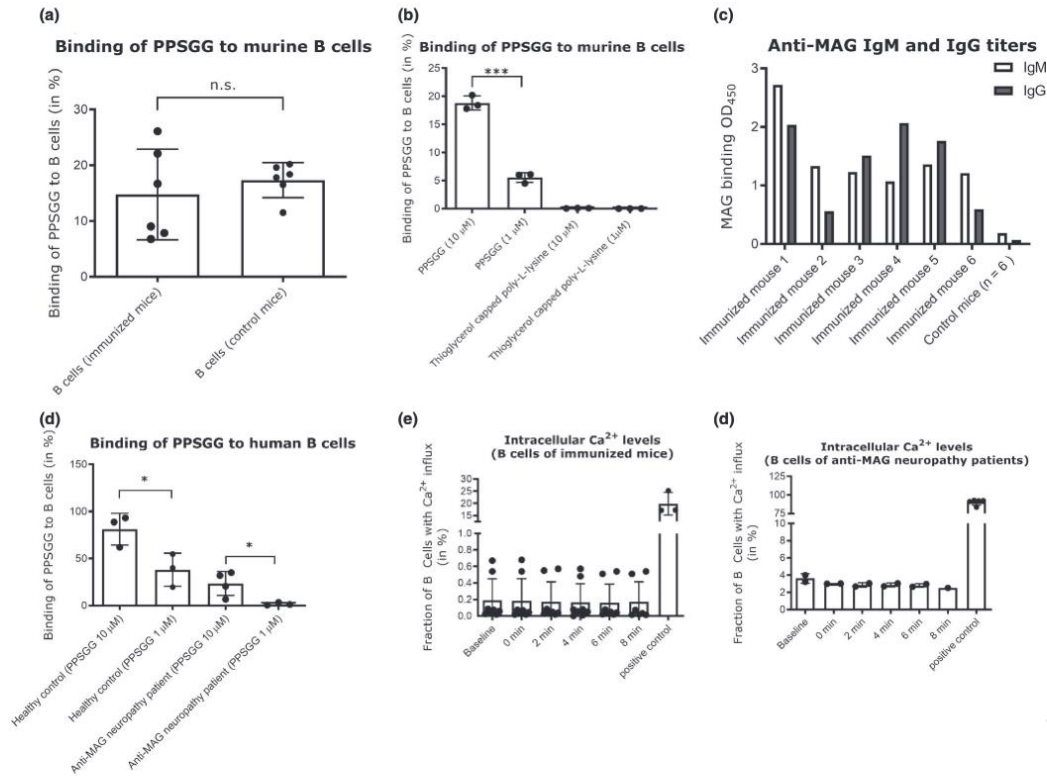


FIGURE 6 Concentration-dependent binding of poly(phenyl disodium 3-O-sulfo- β -D-glucopyranuronate)-(1 \rightarrow 3)- β -D-galactopyranoside (PPSGG) to murine and human B cells without increasing intracellular Ca^{2+} levels. Binding of fluorescently labeled PPSGG to B cells of immunized mice ($n = 6$), control mice ($n = 6$), anti-myelin-associated glycoprotein (MAG) neuropathy patients ($n = 4$), and healthy human controls ($n = 3$) were assessed by flow cytometry and fluorescent microscopy. B cells were either incubated with 10 μ M and 1 μ M PPSGG-S or as control with 10 μ M and 1 μ M fully thioglycerol capped poly-L-lysine backbone labeled with sulforhodamine 101 (a, b). B cells were binding PPSGG in a dose-dependent manner and showed no binding to thioglycerol capped poly-L-lysine backbone. There was no difference in binding of PPSGG in immunized versus control mice. To confirm that mice were immunized successfully, anti-MAG IgM and IgG titers were analysed in sera samples by ELISA (c). Anti-MAG neuropathy patient B cells and B cells from healthy controls were incubated with PPSGG for 30 min. Anti-MAG neuropathy patient B cells showed lower binding of PPSGG compared to the healthy controls (d). To determine changes in intracellular Ca^{2+} concentration induced by PPSGG binding, murine and human B cells were treated with 100 μ M PPSGG after loading with 3 μ M Fluo-4 AM. The changes in intracellular Ca^{2+} levels were monitored for the duration of 8 min, in 2 min intervals after a baseline measurement and the subsequent addition of 100 μ M PPSGG. Neither B cells from immunized mice (e) nor from anti-MAG neuropathy patients (f) exhibited increased intracellular Ca^{2+} concentration after PPSGG incubation. Data are shown as mean values \pm SD (unpaired, two-tailed t test, * $p \leq .05$, ** $p \leq .01$, *** $p \leq .001$)

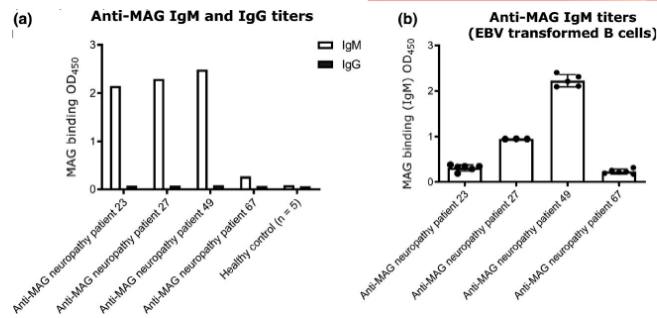


FIGURE 7 Anti-myelin-associated glycoprotein (MAG) IgM titers before and after transformation of B cells with Epstein-Barr virus (EBV). Antibody titers in the sera of anti-MAG patients and in the supernatants of EBV transformed B cells were determined by ELISA. Patients 23, 27, and 49 show high titers of anti-MAG IgM antibodies. Patient 49 exhibited the highest titers in the supernatant after the EBV transformation of the B cells, indicating that isolated B cells maintained their ability to secrete anti-MAG IgM after the transformation with EBV. Results are shown as mean \pm SD

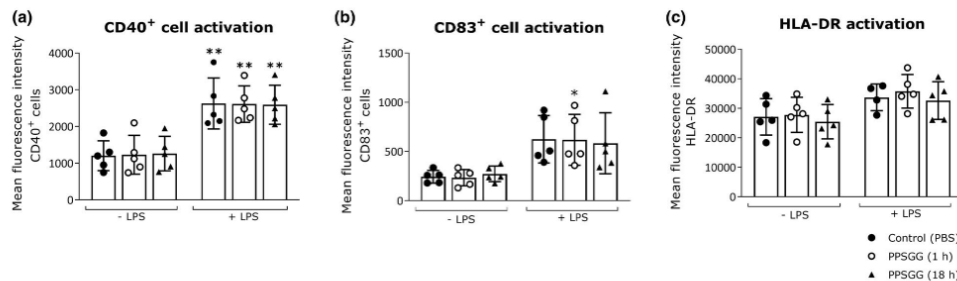


FIGURE 8 No indication of dendritic cells (DC) activation upon treatment with poly(phenyl disodium 3-O-sulfo- β -D-glucopyranuronate)-(1 \rightarrow 3)- β -D-galactopyranoside (PPSGG) ex vivo. Human monocyte-derived DC ($n = 5$ donors) were incubated overnight (18 hr) with lipopolysaccharide (LPS) (100 ng/ml), PPSGG (30 μ g/ml), or the combination of both for 1 hr or 18 hr. DC (CD1c⁺, CD14⁺, CD11b⁺) were gated and the mean fluorescence intensity (MFI) for CD40 (a), CD83 (b), and HLA-DR (c) was assessed by flow cytometry. An increase in MFI was observed for CD40 and CD83 in LPS-treated groups, but no increase of activation markers was related to PPSGG treatment. Results are shown as mean \pm SD (one-way ANOVA with Sidak posttest, * $p \leq .05$, ** $p \leq .01$, *** $p \leq .001$)

autoantibodies recognizing the HNK-1 epitope present on MAG as well as on other glycoproteins of the peripheral nervous system. Previously we have shown the efficient removal of anti-MAG autoantibodies by PPSGG in a mouse model for anti-MAG neuropathy (Herrendorff et al., 2017), reflecting the immunological aspects of gammopathy with continuous production of polyclonal IgM and IgG anti-MAG antibodies. The study suggested a therapeutic potential for PPSGG as a fast-acting antigen-specific agent which selectively targets and eliminates the disease-causing anti-MAG IgM autoantibodies. Such a therapeutic could be highly beneficial compared to unselective immunomodulatory or immunosuppressive agents currently used to treat anti-MAG neuropathy (Dalakas, 2018; Nobile-Orazio, Bianco, Bianco, & Nozza, 2017). In addition to the results of the immunological mouse model, we assessed the therapeutic potential of PPSGG in a monkey neurological target model. Furthermore, the selectivity of anti-MAG IgM binding and potential modulatory effects of PPSGG on the immune system were studied.

Finally, a dose titration study in mice was conducted in preparation for first-in-patient clinical trials.

In ex vivo binding studies of patients' anti-MAG IgM autoantibodies to myelin in cynomolgus monkey sciatic nerve preparations, we could demonstrate that myelin reactivity was completely blocked when undiluted sera of anti-MAG neuropathy patients were treated with PPSGG at low concentrations (250 μ g/ml PPSGG), independent of anti-MAG IgM autoantibody titers ($>70'000-6'975$ BTU). The applied concentration corresponds to a dose of approximately 10 mg/kg based on the total serum volume of humans. Although, the serum sample of patient 4 had only a low anti-MAG IgM autoantibody titer of 19'333 BTU, the sample still exhibited residual myelin binding at the lowest PPSGG concentration (62.5 μ g/ml PPSGG) in contrast to the samples of patient A, B, and C with higher titers ($>70'000-36'383$ BTU). Importantly, this dose of 62.5 μ g/ml, corresponding to a dose of approximately 2 mg/kg humans, reduced myelin binding to almost the same degree as the higher dose (corresponding to 10 mg/kg).

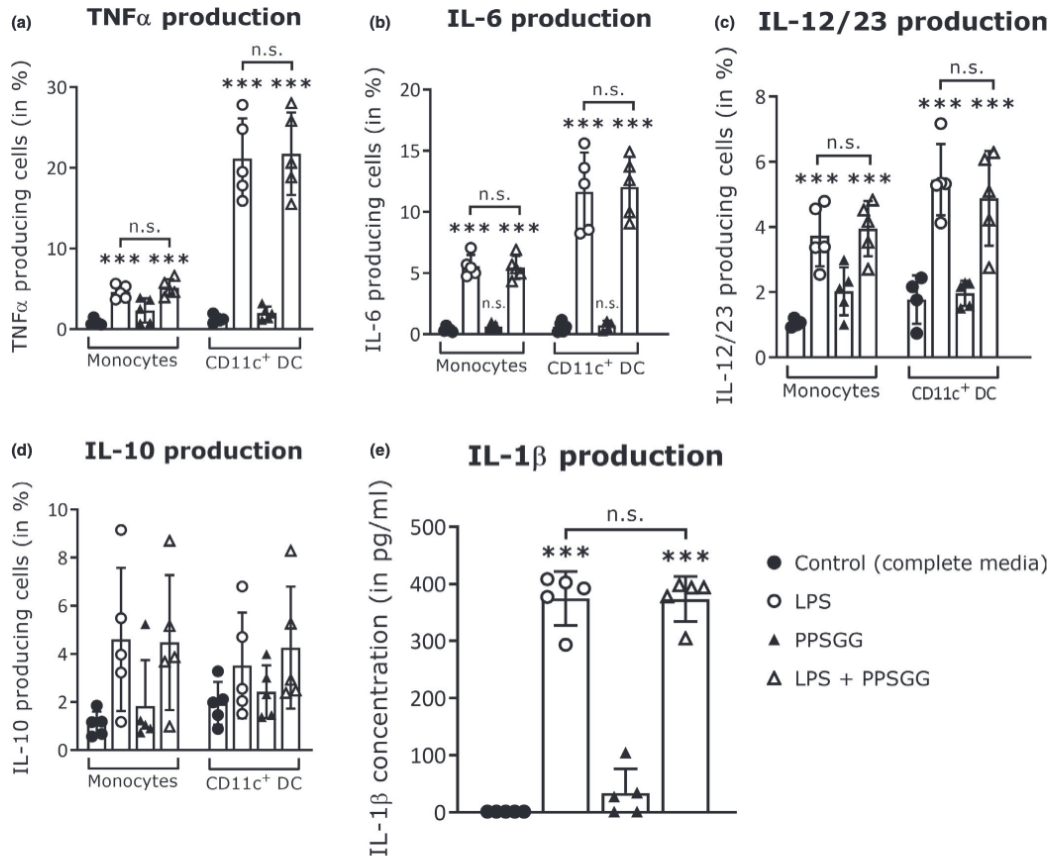


FIGURE 9 No significant cytokine production in peripheral blood mononuclear cells (PBMC) upon to poly(phenyl disodium 3-O-sulfo- β -D-glucopyranuronate)-(1 \rightarrow 3)- β -D-galactopyranoside (PPSGG) treatment ex vivo. Freshly isolated human PBMC ($n = 5$ donors) were treated with lipopolysaccharide (LPS) (100 ng/ml), PPSGG (30 μ g/ml), or the combination of both for 6 hr or in case of IL-10 production for 20 hr. The production of TNF α (a), IL-6 (b), IL-10 (c), and IL-12 (d) by CD14⁺ monocytes and HLA-DR⁺ CD11c⁺ Dendritic cells (DC) was subsequently assessed by flow cytometry. Release of IL-1 β in the supernatant of incubated cells was assessed by ELISA (e). No significant increase in the production of any measured cytokine was observed related to PPSGG treatment. Results are shown as mean \pm SD (one-way ANOVA with Sidak posttest, * $p \leq .05$, ** $p \leq .01$, *** $p \leq .001$)

These results are in line with the finding that anti-MAG IgM autoantibodies of different patients can have different affinities to the HNK-1 epitope and potentially explain why high anti-MAG IgM titers do not necessarily correlate with disease severity (Delmont et al., 2019; Ogino, Tatum, Tatum, & Latov, 1994). Selective inhibition of IgM binding to myelin was confirmed by the use of sera from two control neuropathy patients in the indirect fluorescent assay. Both, the CANOMAD and CIDP patients' sera exhibited IgM binding to myelin but no HNK-1 reactivity (<1'000 BTU). Neither of the control neuropathy patients' sera was inhibited by incubation with PPSGG. To further confirm selective binding of anti-MAG IgM, we showed that PPSGG does not bind to other immunoglobulins of the IgM or IgG subclass present in normal human sera.

To corroborate that the dose range of 2–10 mg/kg would be sufficient to deplete circulating anti-MAG autoantibodies in anti-MAG neuropathy patients, a dose-finding study in mice, using passive immunization with a mouse anti-HNK-1 IgM was performed. The intravenous injection of 5 μ g PPSGG turned out to be sufficient to bind 89.43% (± 1.33 SD) of the 60 μ g anti-MAG IgM and 10 μ g PPSGG was sufficient to bind 93.28% (± 0.50 SD) of the 120 μ g anti-HNK-1 IgM. Based on these findings, a dose of approximately 80 mg PPSGG would be sufficient to bind and remove 1 g of anti-MAG IgM, whereas 40 mg of PPSGG would be sufficient to bind and remove most of 1 g anti-MAG IgM autoantibodies in humans. Since the anti-HNK-1/MAG IgM antibody levels were reduced for up to 2 weeks post-administration of 60 μ g anti-HNK-1 IgM and 10 μ g

PPSGG (Figures S1–S5 in supplementary information) and remained undetectable, and given the short half-life of PPSGG, we conclude that it is a removal rather than a neutralization of the antibodies. The pentameric IgM has a molecular weight of 900–1000 kDa and is therefore approximately five times heavier than PPSGG with a calculated average weight of 194 kDa. Based on the results of our *in vivo* experiment, the binding stoichiometry of PPSGG:anti-HNK-1 IgM is around 1:1 to 1:2. In general, the paraprotein (monoclonal anti-MAG IgM) levels in anti-MAG patients are in the range of 1–10 g/L, whereas in healthy subjects the total IgM levels are between 0.5 and 3 g/L (Cook & Macdonald, 2007; Lunn & Nobile-Orazio, 2016). Based on a range of 1–10 g/L of monoclonal anti-MAG IgM (3–30 g total paraprotein), 240 mg to 2,400 mg of PPSGG are expected to be sufficient to completely remove the circulating anti-MAG IgM antibodies and at doses of 120–1200 mg most of the paraprotein load should be removed. Finally, based on an estimated population average of 4 g/L paraprotein, a dose of 1,000 mg PPSGG is expected to lead to a complete response for the majority of anti-MAG neuropathy patients.

To further evaluate the therapeutic potential of the glycopolymer PPSGG, its efficacy was compared with the B-cell depleting treatment by an anti-CD20 IgG antibody in actively immunized mice. Anti-CD20 B-cell depletion did not affect the anti-MAG IgM titers in mice, whereas PPSGG effectively reduced the antibody titers. The former was surprising given the half-life of a murine IgM (2–4 days), as it was expected that the significant reduction of B cells would reduce IgM titers during the following 5 weeks (Vieira & Rajewsky, 1988). Weekly treatment of immunized mice with PPSGG did not affect the number of circulating B cells (CD19⁺). This is consistent with the observation that PPSGG did not induce or lead to the release of the examined murine and human cytokines and chemokines *in vivo* and *ex vivo*, and did not activate B cells in immunized mice or anti-MAG neuropathy patients *ex vivo*. Given these findings, we conclude that the cells responsible for the production of anti-MAG IgM in the immunized mouse model are not circulating B cells but rather mature plasma cells or late stage B cells (CD20⁺) residing in the bone marrow or a small population of anti-CD20 treatment resistant B cells in the spleen (Ahuja, Anderson, Anderson, Khalil, & Shlomchik, 2008; DiLillo et al., 2008; Häusler et al., 2018; Hofmann, Clauder, Clauder, & Manz, 2018).

In contrast to the immunological murine model, B cells clones that produce anti-MAG IgM were successfully isolated from peripheral blood samples of anti-MAG neuropathy patients and transformed with EBV. They maintained the ability to secrete anti-MAG IgM antibodies *ex vivo*, showing that at least for some patients, anti-MAG IgM-producing B cells (CD20⁺) can be found in the periphery. Based on the observed limited efficacy of anti-CD20 IgG antibody treatment, it is likely that the disease has heterogeneous characteristics in terms of the anti-MAG IgM producing cells (Hammarlund et al., 2017; Leger et al., 2013; Nutt, Hodgkin, Hodgkin, Tarlinton, & Corcoran, 2015).

Since the immunized mice produce anti-MAG antibodies of both the IgM and IgG subtype, we assumed that the mice would have

memory B cells (CD20⁺) residing in peripheral lymphoid organs and in the circulation (Herrendorff et al., 2017). Nevertheless, we were unable to observe a specific binding of the fluorescently labeled glycopolymer to B cells isolated from the spleen of immunized mice, where the binding of PPSGG could potentially trigger an immune modulation. In B cells challenged with an antigen specific for the recognition by its B-cell receptors, a local clustering of these receptors has been observed and the activation of these B cells can be monitored by the changes in intracellular Ca²⁺ levels (Scharenberg, Humphries, Humphries, & Rawlings, 2007; Vig & Kinet, 2009).

Since neither in murine nor in human B cells significant changes of the intracellular Ca²⁺ were observed, the sustained antibody reduction seen in our previous studies is unlikely driven by B cells directly. Furthermore, as there was no induction of peripheral inflammatory cytokines and chemokines neither *in vivo* after single and multiple PPSGG administrations in naive mice, nor *ex vivo* in various subpopulation of isolated human and murine leukocytes, we assume that the treatment of anti-MAG neuropathy patients with PPSGG should not give rise to side effects by inducing acute inflammatory markers. However, some caution should be kept as some of these experiments were performed in the absence of its target (anti-MAG autoantibodies) and because of the limitations of the *in vivo* and *ex vivo* models.

5 | CONCLUSION

In contrast to treatments depleting anti-CD20⁺ cells like rituximab or obinutuzumab, PPSGG binds and removes anti-MAG IgM autoantibodies highly selectively within minutes. Our findings support a mechanism of action of PPSGG leading to a fast and selective *in vivo* depletion of pathogenic anti-MAG IgM autoantibodies, independent of the response of anti-MAG neuropathy patient to CD20⁺ B cells depleting treatments. This supports the use of PPSGG as a standalone therapy or in combination with immunosuppressive therapeutic agents, possibly at reduced doses, so that patients would benefit from both fast removal and long-term suppression of anti-MAG IgM autoantibody production.

ACKNOWLEDGMENTS

This work was funded by the Swiss Commission for Technology and Innovation, the Neuromuscular Research Association Basel, and the Gebert RUF Stiftung.

All experiments were conducted in compliance with the ARRIVE guidelines.

CONFLICT OF INTEREST

R.H., P.H., A.J.S., and B.E. are co-founders of a University of Basel spin-off, Polyneuron Pharmaceuticals AG, whose activity is related to the subject matter of this article. A.J.S. and B.E. are members of the advisory board, and R.H. is a member of the board of directors. R.H., A.J.S., and B.E. are named as co-inventors on relevant patent applications.

AUTHOR CONTRIBUTIONS

B.A., D.D., E.S., A.B., and T.O. performed experiments. E.D., T.D. M.T., P.T., and T.K. provided sera and information from patients. B.A., D.D., E.S., A.B., J.B., and P.H. analysed and interpreted data. B.A., D.D., E.S., J.B., and P.H. drafted the manuscript. B.A., A.J.S., B.E., R.H., and P.H. edited and revised the manuscript. All authors approved final version of the manuscript. R.H. and P.H. contributed to conception and design of research.

ORCID

Butrint Aliu  <https://orcid.org/0000-0002-4503-9289>
 Delphine Demeestere  <https://orcid.org/0000-0002-6948-0140>
 Emilie Seydoux  <https://orcid.org/0000-0003-1021-4056>
 José Boucraut  <https://orcid.org/0000-0002-3471-7769>
 Emilien Delmont  <https://orcid.org/0000-0002-5591-2774>
 Shahram Attarian  <https://orcid.org/0000-0002-7211-4694>
 Marie Théaudin  <https://orcid.org/0000-0002-3026-3595>
 Pinelopi Tsouni  <https://orcid.org/0000-0003-2210-6925>
 Thierry Kuntzer  <https://orcid.org/0000-0002-7788-1673>
 Tobias Derfuss  <https://orcid.org/0000-0001-8431-8769>
 Beat Ernst  <https://orcid.org/0000-0001-5787-2297>
 Pascal Hänggi  <https://orcid.org/0000-0002-7941-2475>

REFERENCES

- Ahuja, A., Anderson, S. M., Khalil, A., & Shlomchik, M. J. (2008). Maintenance of the plasma cell pool is independent of memory B cells. *Proceedings of the National Academy of Sciences of the United States of America*, 105(12), 4802–4807. <https://doi.org/10.1073/pnas.0800555105>
- Association H. E. C. o. E. o. t. W. M. (1964). Human experimentation: Code of Ethics of the World Medical Association (Declaration of Helsinki). *Canadian Medical Association Journal*, 91(11), 619.
- Baba, Y., & Kurosaki, T. (2016). Role of calcium signaling in B cell activation and biology. *Current Topics in Microbiology and Immunology*, 393, 143–174.
- Benedetti, L., Briani, C., Grandis, M., Vigo, T., Gobbi, M., Ghiglione, E., ... Schenone, A. (2007). Predictors of response to rituximab in patients with neuropathy and anti-myelin associated glycoprotein immunoglobulin M. *J Peripher Nerv Syst*, 12(2), 102–107. <https://doi.org/10.1111/j.1529-8027.2007.00129.x>
- Braun, P. E., Frail, D. E., & Latov, N. (1982). Myelin-associated glycoprotein is the antigen for a monoclonal IgM in polyneuropathy. *Journal of Neurochemistry*, 39(5), 1261–1265. <https://doi.org/10.1111/j.1471-4159.1982.tb12563.x>
- Broglio, L., & Lauria, G. (2005). Worsening after rituximab treatment in anti-mag neuropathy. *Muscle and Nerve*, 32(3), 378–379. <https://doi.org/10.1002/mus.20386>
- Cook, L., & Macdonald, D. H. (2007). Management of paraproteinaemia. *Postgraduate Medical Journal*, 83(978), 217–223. <https://doi.org/10.1136/pgmj.2006.054627>
- Dalakas, M. C. (2010). Pathogenesis and treatment of anti-MAG neuropathy. *Current Treatment Options in Neurology*, 12(2), 71–83. <https://doi.org/10.1007/s11940-010-0065-x>
- Dalakas, M. C. (2018). Advances in the diagnosis, immunopathogenesis and therapies of IgM-anti-MAG antibody-mediated neuropathies. *Therapeutic Advances in Neurological Disorders*, 11, 1756285617746640.
- Delmont, E., Attarian, S., Antoine, J. C., Paul, S., Camdessanché, J. P., Grapperon, A. M., ... Boucraut, J. (2019). Relevance of anti-HNK1 antibodies in the management of anti-MAG neuropathies. *Journal of Neurology*, 266(8), 1973–1979.
- DiLillo, D. J., Hamaguchi, Y., Ueda, Y., Yang, K., Uchida, J., Haas, K. M., ... Tedder, T. F. (2008). Maintenance of long-lived plasma cells and serological memory despite mature and memory B cell depletion during CD20 immunotherapy in mice. *The Journal of Immunology*, 180(1), 361–371.
- Donjerković, D., & Scott, D. W. (2000). Activation-induced cell death in B lymphocytes. *Cell Research*, 10(3), 179–192.
- Erb, M., Flueck, B., Kern, F., Erne, B., Steck, A. J., & Schaeren-Wiemers, N. (2006). Unraveling the differential expression of the two isoforms of myelin-associated glycoprotein in a mouse expressing GFP-tagged 5-MAG specifically regulated and targeted into the different myelin compartments. *Molecular and Cellular Neurosciences*, 31(4), 613–627.
- Gabriel, J. M., Erne, B., Bernasconi, L., Tosi, C., Probst, A., Landmann, L., & Steck, A. J. (1998). Confocal microscopic localization of anti-myelin-associated glycoprotein autoantibodies in a patient with peripheral neuropathy initially lacking a detectable IgM gammopathy. *Acta Neuropathologica*, 95(5), 540–546.
- Gabriel, J. M., Erne, B., Miescher, G. C., Miller, S. L., Vital, A., Vital, C., & Steck, A. J. (1996). Selective loss of myelin-associated glycoprotein from myelin correlates with anti-MAG antibody titre in demyelinating paraproteinaemic polyneuropathy. *Brain*, 119, 775–787.
- Hammarlund, E., Thomas, A., Amanna, I. J., Holden, L. A., Slayden, O. D., Park, B., ... Slifka, M. K. (2017). Plasma cell survival in the absence of B cell memory. *Nature Communications*, 8(1), 1781.
- Häusler, D., Häusser-Kinzel, S., Feldmann, L., Torke, S., Lepennetier, G., Bernard, C. C. A., ... Weber, M. S. (2018). Functional characterization of reappearing B cells after anti-CD20 treatment of CNS autoimmune disease. *Proceedings of the National Academy of Sciences of the United States of America*, 115(39), 9773–9778.
- Heesters, B. A., van der Poel, C. E., Das, A., & Carroll, M. C. (2016). Antigen presentation to B cells. *Trends in Immunology*, 37(12), 844–854.
- Herrendorff, R., Hänggi, P., Pfister, H., Yang, F., Demeestere, D., Hunziker, F., ... Ernst, B. (2017). Selective in vivo removal of pathogenic anti-MAG autoantibodies, an antigen-specific treatment option for anti-MAG neuropathy. *Proceedings of the National Academy of Sciences of the United States of America*, 114(18), E3689–E3698.
- Hofmann, K., Clauder, A. K., & Manz, R. A. (2018). Targeting B cells and plasma cells in autoimmune diseases. *Frontiers in Immunology*, 9, 835.
- Hollyoake, M., Stühler, A., Farrell, P., Gordon, J., & Sinclair, A. (1995). The normal cell cycle activation program is exploited during the infection of quiescent B lymphocytes by Epstein-Barr virus. *Cancer Research*, 55(21), 4784–4787.
- Kelm, S., Pelz, A., Schauer, R., Filbin, M. T., Tang, S., de Bellard, M. E., ... Bradfield, P. (1994). Sialoadhesin, myelin-associated glycoprotein and CD22 define a new family of sialic acid dependent adhesion molecules of the immunoglobulin superfamily. *Current Biology*, 4(11), 965–972.
- Latov, N., Braun, P. E., Gross, R. B., Sherman, W. H., Penn, A. S., & Chess, L. (1981). Plasma cell dyscrasia and peripheral neuropathy: Identification of the myelin antigens that react with human paraproteins. *Proceedings of the National Academy of Sciences of the United States of America*, 78(11), 7139–7142.
- Leger, J.-M., Viala, K., Nicolas, G., Creange, A., Vallat, J.-M., Pouget, J., ... Grp, R. S. (2013). Placebo-controlled trial of rituximab in IgM anti-myelin-associated glycoprotein neuropathy. *Neurology*, 80(24), 2217–2225.
- Lunn, M. P., & Nobile-Orazio, E. (2016). Immunotherapy for IgM anti-myelin-associated glycoprotein paraprotein-associated peripheral neuropathies. *Cochrane Database Systematic Review*, (10), CD002827.
- Mahdi-Rogers, M., & Hughes, R. A. (2014). Epidemiology of chronic inflammatory neuropathies in southeast England. *European Journal of Neurology*, 21(1), 28–33.

- Mygland, A., & Monstad, P. (2001). Chronic polyneuropathies in Vest-Agder, Norway. *European Journal of Neurology*, 8(2), 157–165.
- Nobile-Orazio, E., Baldini, L., Barbieri, S., Mamioli, P., Spagnol, G., Francomano, E., & Scarlato, G. (1988). Treatment of patients with neuropathy and anti-MAG IgM M-proteins. *Annals of Neurology*, 24(1), 93–97.
- Nobile-Orazio, E., Bianco, M., & Nozza, A. (2017). Advances in the treatment of paraproteinemic neuropathy. *Current Treatment Options in Neurology*, 19(12), 43.
- Nutt, S. L., Hodgkin, P. D., Tarlinton, D. M., & Corcoran, L. M. (2015). The generation of antibody-secreting plasma cells. *Nature Reviews Immunology*, 15(3), 160–171. <https://doi.org/10.1038/nri3795>
- Ogino, M., Tatum, A. H., & Latov, N. (1994). Affinity studies of human anti-MAG antibodies in neuropathy. *Journal of Neuroimmunology*, 52(1), 41–46. [https://doi.org/10.1016/0165-5728\(94\)90160-0](https://doi.org/10.1016/0165-5728(94)90160-0)
- Pestronk, A., Florence, J., Miller, T., Choksi, R., Al-Lozi, M. T., & Levine, T. D. (2003). Treatment of IgM antibody associated polyneuropathies using rituximab. *Journal of Neurology, Neurosurgery and Psychiatry*, 74(4), 485–489. <https://doi.org/10.1136/jnnp.74.4.485>
- Quarles, R. H. (2007). Myelin-associated glycoprotein (MAG): Past, present and beyond. *Journal of Neurochemistry*, 100(6), 1431–1448. <https://doi.org/10.1111/j.1471-4159.2006.04319.x>
- Renaud, S., Fuhr, P., Gregor, M., Schweikert, K., Lorenz, D., Daniels, C., ... Steck, A. J. (2006). High-dose rituximab and anti-MAG-associated polyneuropathy. *Neurology*, 66(5), 742–744. <https://doi.org/10.1212/01.wnl.0000201193.00382.b3>
- Ritz, M. F., Erne, B., Ferracin, F., Vital, A., Vital, C., & Steck, A. J. (1999). Anti-MAG IgM penetration into myelinated fibers correlates with the extent of myelin widening. *Muscle and Nerve*, 22(8), 1030–1037. [https://doi.org/10.1002/\(SICI\)1097-4598\(199908\)22:8<1030::AID-MUS4>3.0.CO;2-H](https://doi.org/10.1002/(SICI)1097-4598(199908)22:8<1030::AID-MUS4>3.0.CO;2-H)
- Sala, E., Robert-Varvat, F., Paul, S., Camdessanché, J. P., & Antoine, J. C. (2014). Acute neurological worsening after Rituximab treatment in patients with anti-MAG neuropathy. *Journal of the Neurological Sciences*, 345(1–2), 224–227.
- Scharenberg, A. M., Humphries, L. A., & Rawlings, D. J. (2007). Calcium signalling and cell-fate choice in B cells. *Nature Reviews Immunology*, 7(10), 778–789. <https://doi.org/10.1038/nri2172>
- Steck, A. J., Murray, N., Meier, C., Page, N., & Perruisseau, G. (1983). Demyelinating neuropathy and monoclonal IgM antibody to myelin-associated glycoprotein. *Neurology*, 33(1), 19–23.
- Steck, A. J., Stalder, A. K., & Renaud, S. (2006). Anti-myelin-associated glycoprotein neuropathy. *Current Opinion in Neurology*, 19(5), 458–463. <https://doi.org/10.1097/01.wco.0000245368.36576.0d>
- Talamo, G., Mir, M. A., Pandey, M. K., Sivik, J. K., & Raheja, D. (2015). IgM MGUS associated with anti-MAG neuropathy: A single institution experience. *Annals of Hematology*, 94(6), 1011–1016. <https://doi.org/10.1007/s00277-014-2294-7>
- Tang, S., Shen, Y. J., DeBellard, M. E., Mukhopadhyay, G., Salzer, J. L., Crocker, P. R., & Filbin, M. T. (1997). Myelin-associated glycoprotein interacts with neurons via a sialic acid binding site at ARG118 and a distinct neurite inhibition site. *Journal of Cell Biology*, 138(6), 1355–1366. <https://doi.org/10.1083/jcb.138.6.1355>
- Vallat, J.-M., Magy, L., Ciron, J., Corcia, P., Le Masson, G., & Mathis, S. (2016). Therapeutic options and management of polyneuropathy associated with anti-MAG antibodies. *Expert Review of Neurotherapeutics*, 16(9), 1111–1119.
- Vieira, P., & Rajewsky, K. (1988). The half-lives of serum immunoglobulins in adult mice. *European Journal of Immunology*, 18(2), 313–316. <https://doi.org/10.1002/eji.1830180221>
- Vig, M., & Kinet, J. P. (2009). Calcium signaling in immune cells. *Nature Immunology*, 10(1), 21–27. <https://doi.org/10.1038/nif.220>
- Willison, H. J., Trapp, B. D., Bacher, J. D., Dalakas, M. C., Griffin, J. W., & Quarles, R. H. (1988). Demyelination induced by intraneural injection of human antimyelin-associated glycoprotein antibodies. *Muscle and Nerve*, 11(11), 1169–1176. <https://doi.org/10.1002/mus.880111111>

SUPPORTING INFORMATION

Additional supporting information may be found online in the Supporting Information section.

How to cite this article: Aliu B, Demeestere D, Seydoux E, et al. Selective inhibition of anti-MAG IgM autoantibody binding to myelin by an antigen-specific glycopolymer. *J Neurochem*. 2020;154:486–501. <https://doi.org/10.1111/jnc.15021>

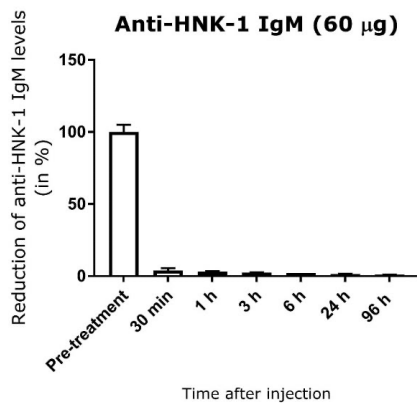
Selective inhibition of anti-MAG IgM autoantibody binding to myelin by an antigen specific glycopolymer

Butrint Aliu^{1*}, Delphine Demeestere^{1*}, Emilie Seydoux², Jose Boucraut^{3,4}, Emilien Delmont⁵, Alexandre Brodovitch^{3,5}, Thomas Oberholzer², Shahram Attarian⁵, Marie Théaudin⁶, Pinelopi Tsouni⁶, Thierry Kuntzer⁶, Tobias Derfuss⁷, Andreas J. Steck^{2,7}, Beat Ernst¹, Ruben Herrendorff^{1,2}, Pascal Hänggi^{1,2}

*equal contribution

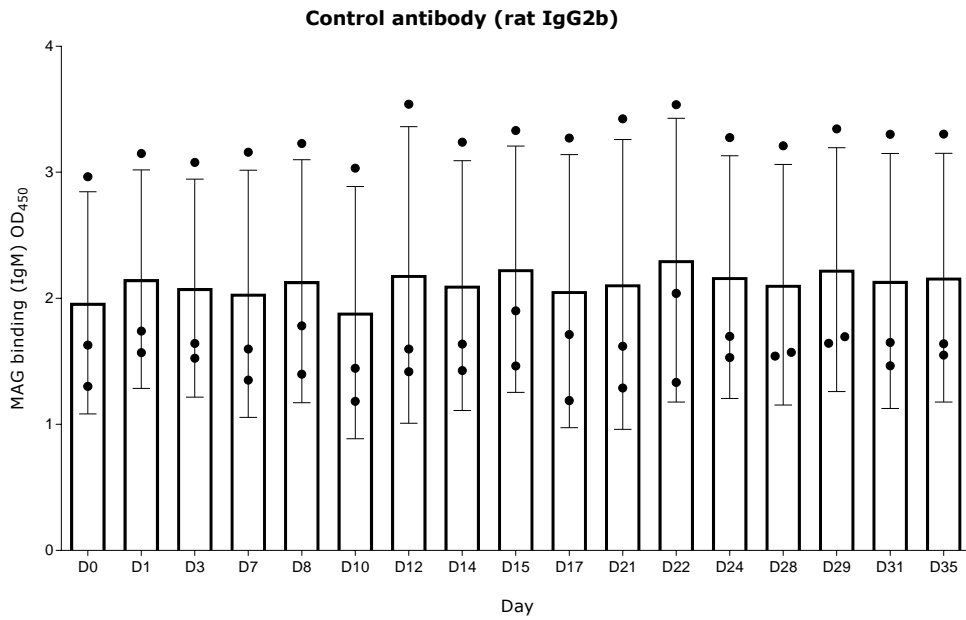
¹Molecular Pharmacy, Pharmacenter, University of Basel, 4056 Basel, Switzerland; ²Polyneuron Pharmaceuticals AG, 4057 Basel, Switzerland; ³Immunology laboratory, AP-HM, Marseille, France; ⁴Aix-Marseille University, INT, UMR CNRS 7289, Marseille, France; ⁵Center for neuromuscular disorders and ALS La Timone hospital, AP-HM, Marseille, France; ⁶Nerve-muscle unit, Service of Neurology, Department of Clinical Neurosciences, Lausanne University Hospital (CHUV) and University of Lausanne, 1011 Lausanne, Switzerland; ⁷Clinic of Neurology, Department of Medicine, University Hospital Basel, University of Basel, 4031 Basel, Switzerland.

Supplementary information

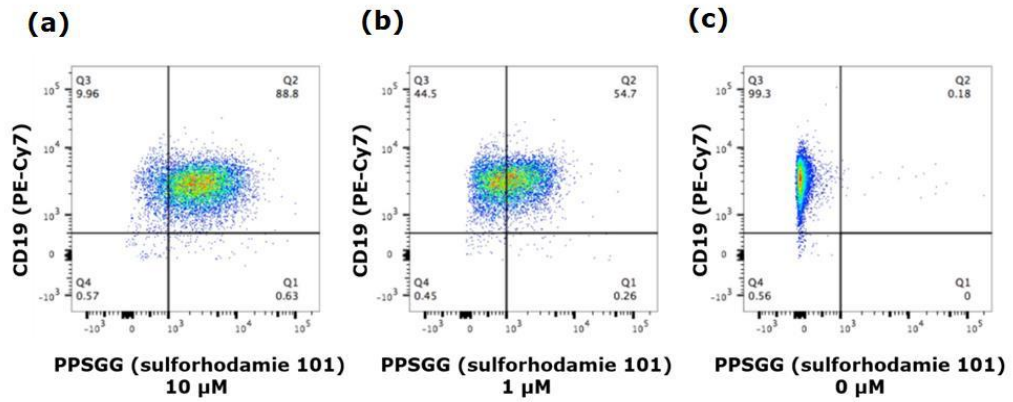


Supplementary Figure 1. Binding and removal of circulating anti-HNK-1 IgM by PPSGG in mice. Mice were intravenously injected with 60 µg (n = 3 mice) anti-HNK1 IgM (pre-treatment) was followed by the intravenous injection of 10 µg PPSGG (after 10 minutes). Blood samples were taken at

different time points (30 min to 96 h) after PPSGG administration and the titers of free anti-HNK-1 IgM were determined by ELISA.

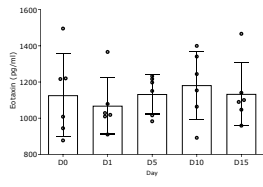


Supplementary Figure 2. Effects of antibody on anti-MAG IgM antibodies in the immunological BALB/c mouse model for anti-MAG neuropathy. Single intravenous injection of 240 μ g of a control antibody did not affect the anti-MAG IgM antibody titers in mice. Anti-MAG IgM titers were analysed by ELISA and data are indicated by mean and standard deviation in which the line represents the mean \pm SD.

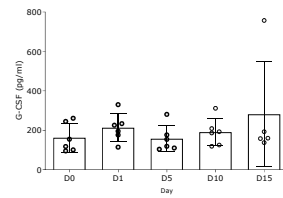


Supplementary Figure 3. Concentration-dependent binding of PPSGG to human B cells. Binding of fluorescently labelled PPSGG to B cells of anti-MAG neuropathy patients was assessed by flow cytometry and fluorescent microscopy. B cells were either incubated with 10 μ M PPSGG (A), 1 μ M PPSGG (B), or PBS (C).

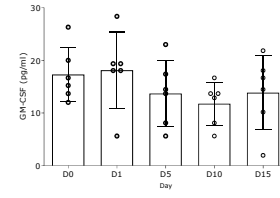
(a) Eotaxin



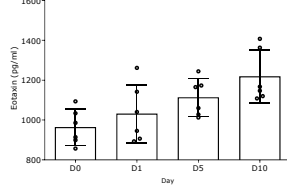
(b) G-CSF



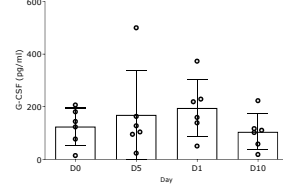
(c) GM-CSF



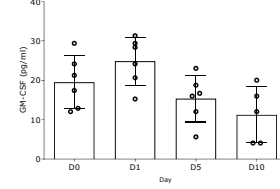
Single PPSGG administration



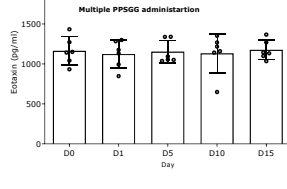
Single PPSGG administration



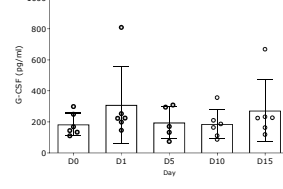
Single PPSGG administration



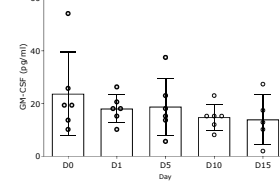
Multiple PPSGG administration



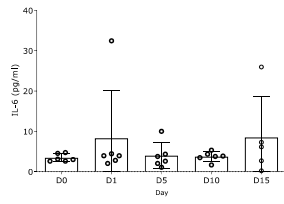
Multiple PPSGG administration



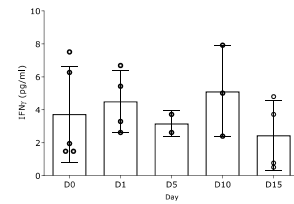
Multiple PPSGG administration



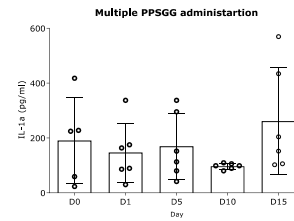
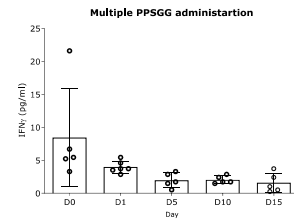
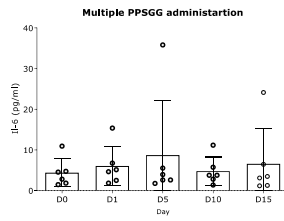
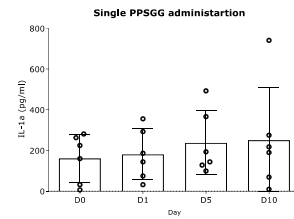
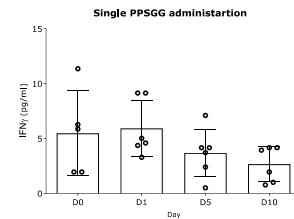
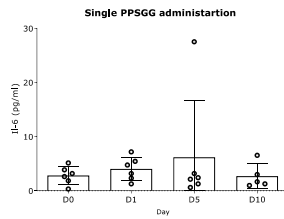
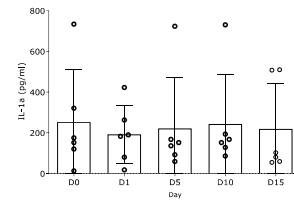
(d) IFN γ
Control PBS

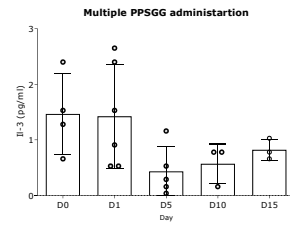
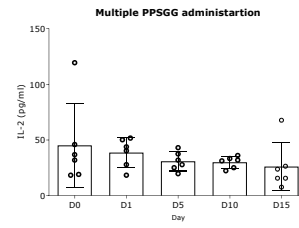
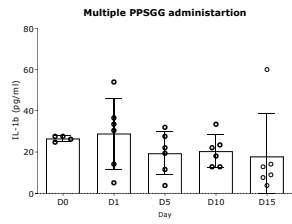
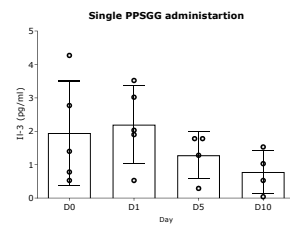
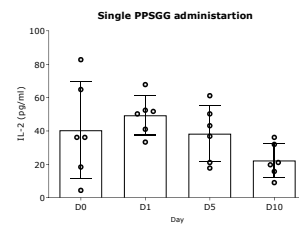
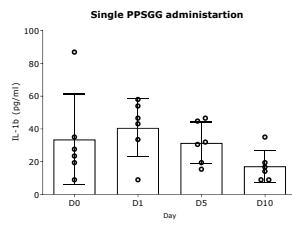
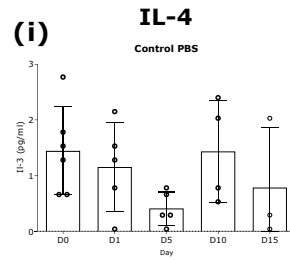
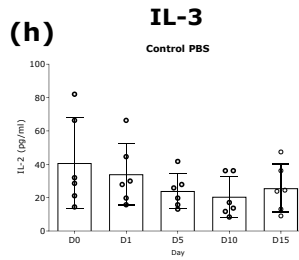
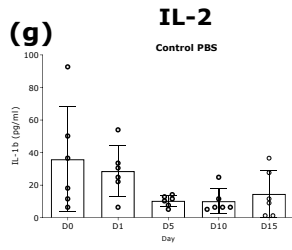


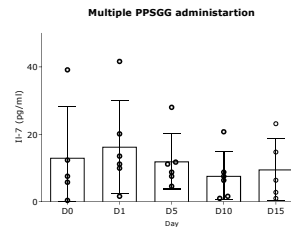
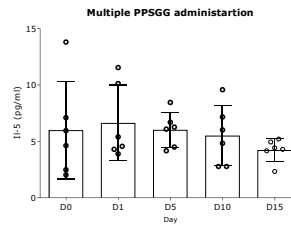
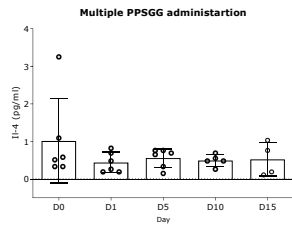
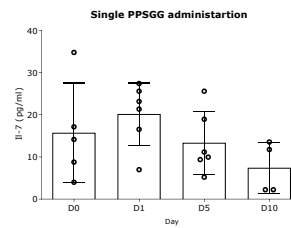
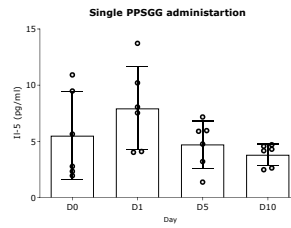
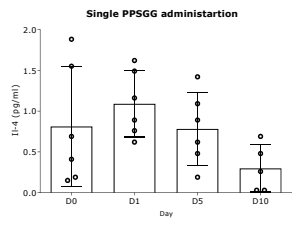
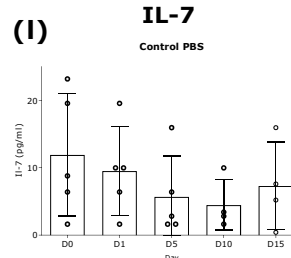
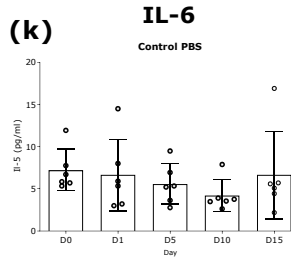
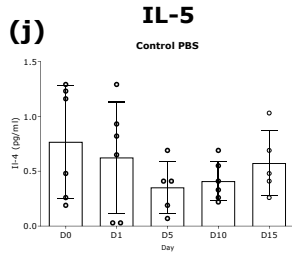
(e) IL-1 α
Control PBS



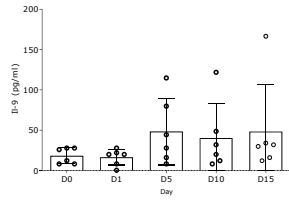
(f) IL-1 β
Control PBS



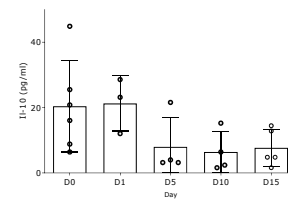




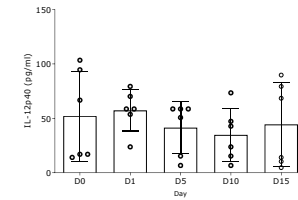
(m) IL-9
Control PBS



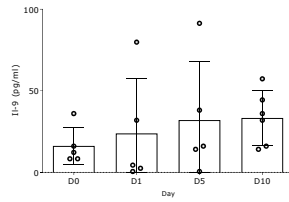
(n) IL-10
Control PBS



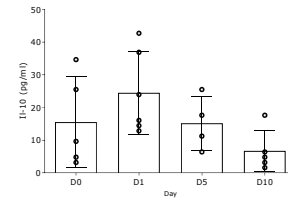
(o) IL-12 (p40)
Control PBS



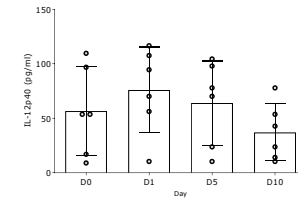
Single PPSGG administration



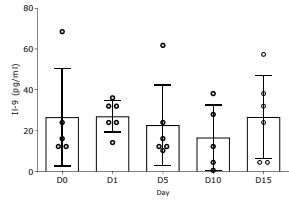
Single PPSGG administration



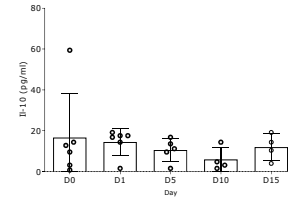
Single PPSGG administration



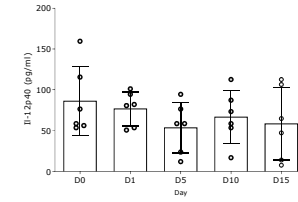
Multiple PPSGG administration



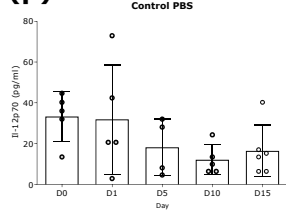
Multiple PPSGG administration



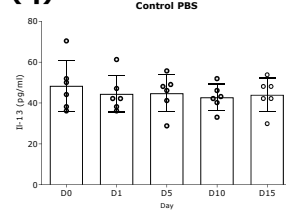
Multiple PPSGG administration



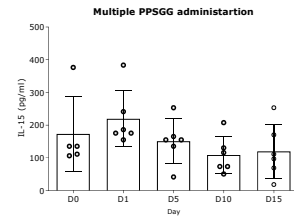
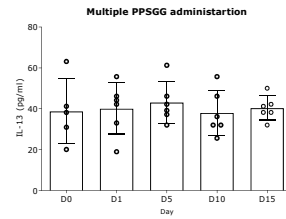
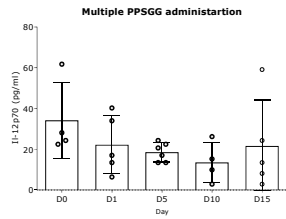
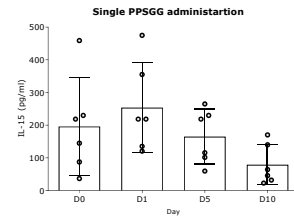
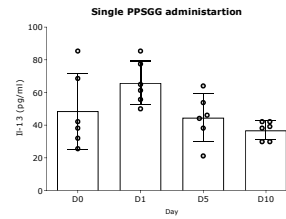
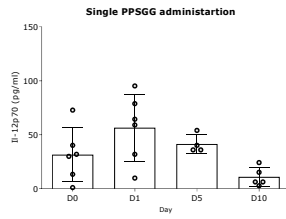
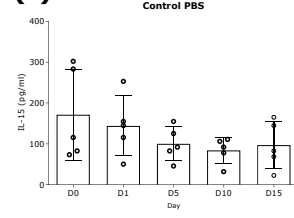
(p) IL-12 (p70)

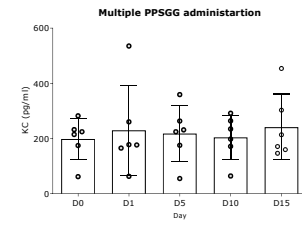
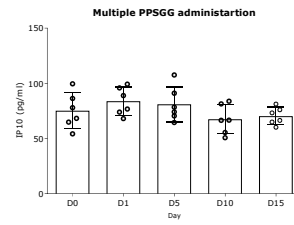
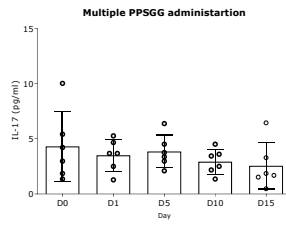
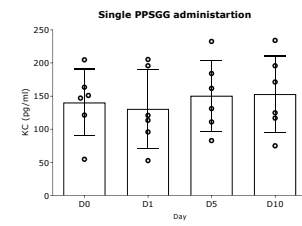
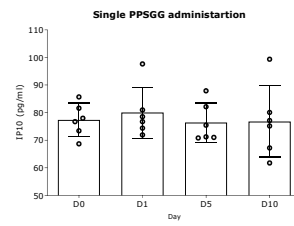
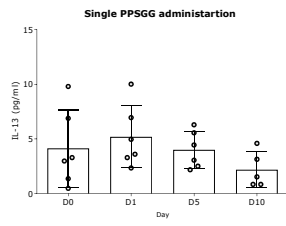
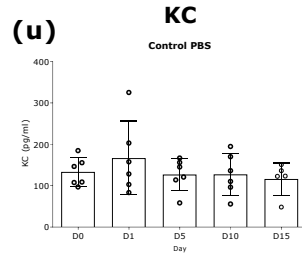
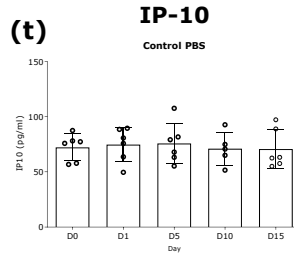
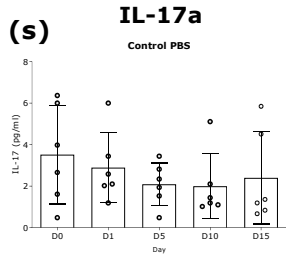


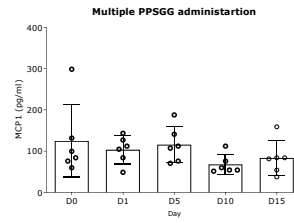
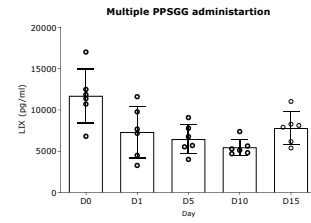
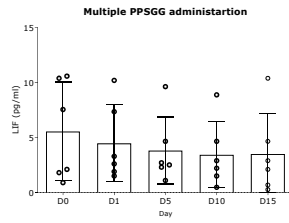
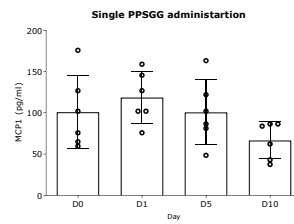
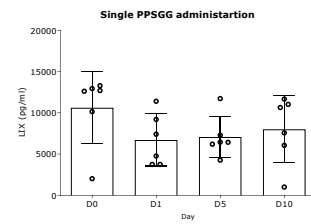
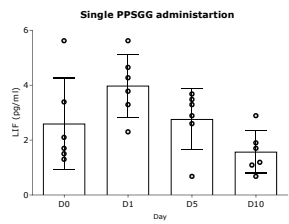
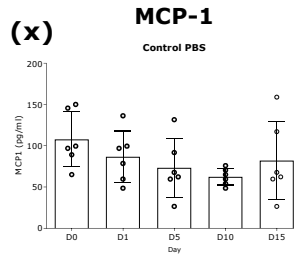
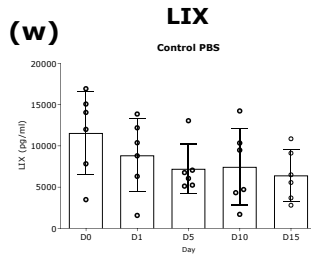
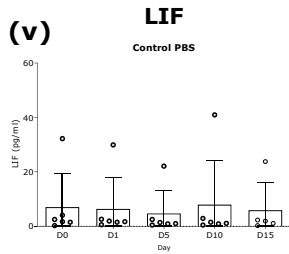
(q) IL-13

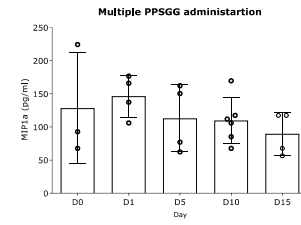
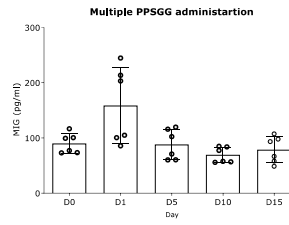
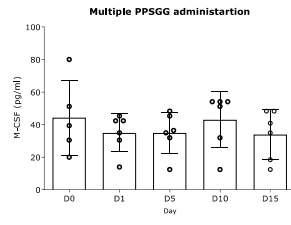
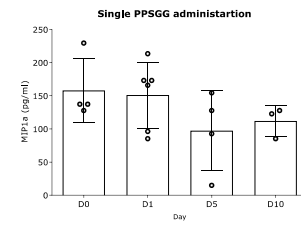
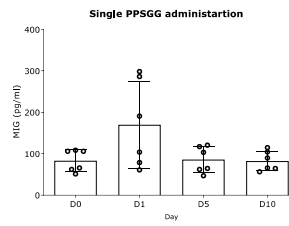
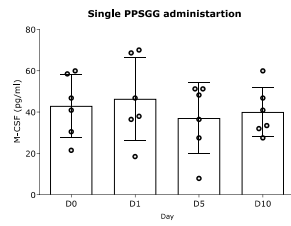
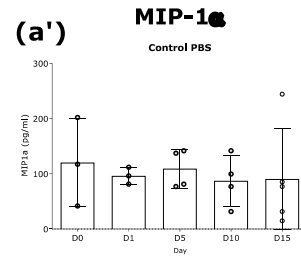
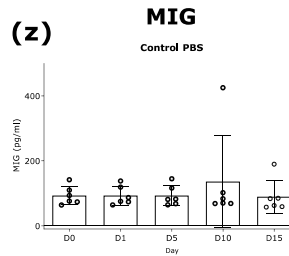
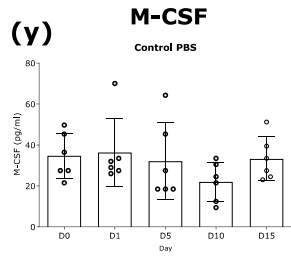


(r) IL-15

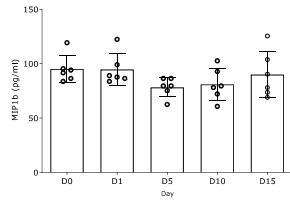




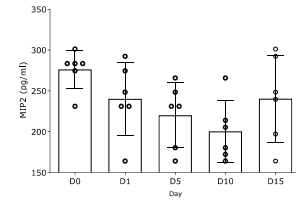




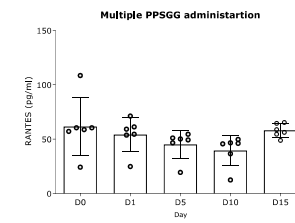
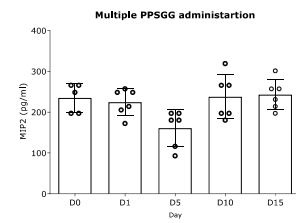
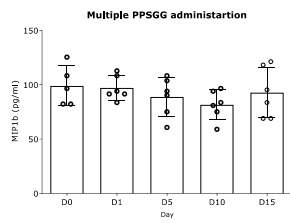
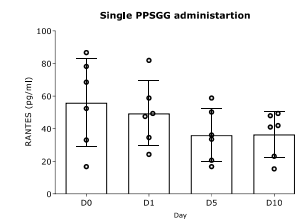
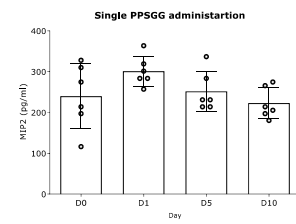
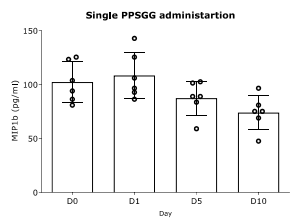
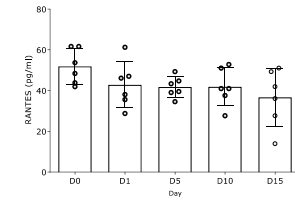
(b') **MIP-1 β**

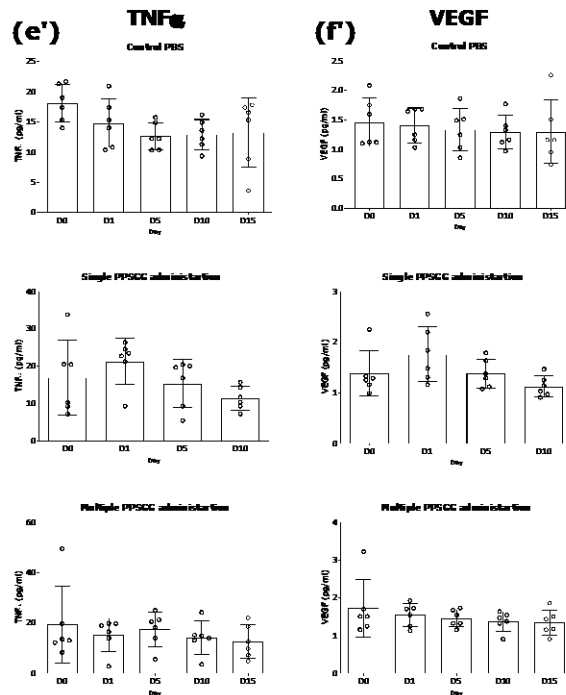


(c') **MIP-2**



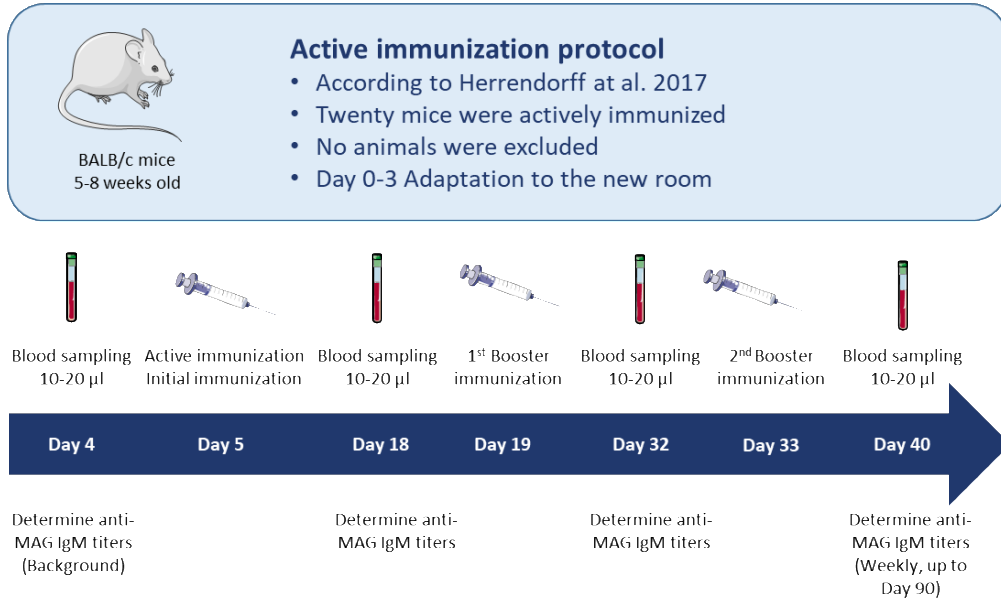
(d') **RANTES**



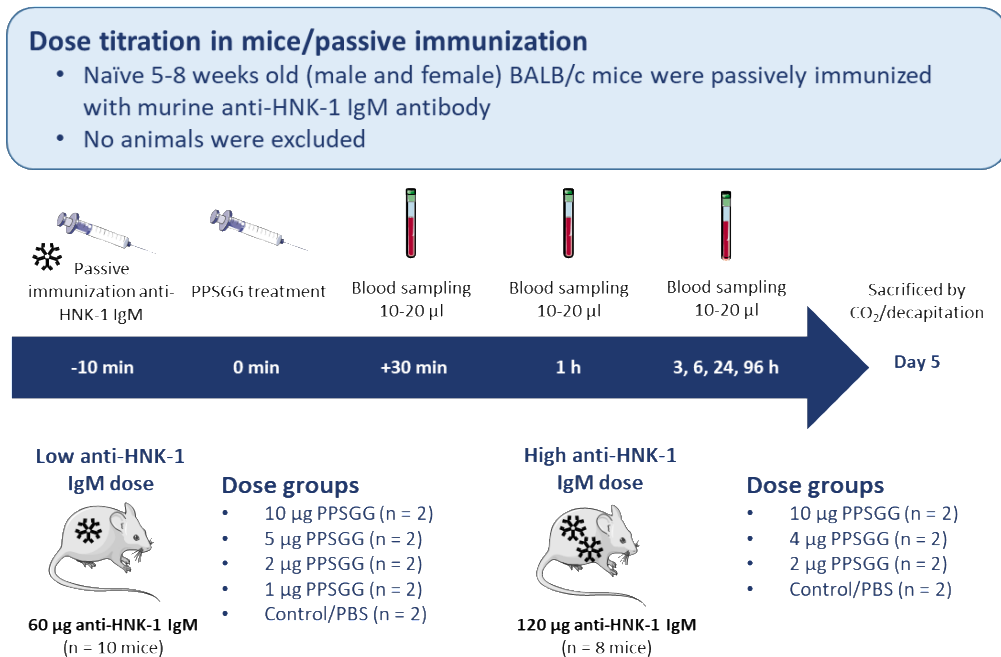


Supplementary Figure 4. Mouse cytokine and chemokine array after single and multiple PPSGG treatment. Thirty different cytokines and chemokines Eotaxin (A), G-CSF (B), GM-CSF (C), $\text{IFN}\gamma$ (D), $\text{IL-1}\alpha$ (E), $\text{IL-1}\beta$ (F), IL-2 (G), IL-3 (H), IL-4 (I), IL-5 (J), IL-6 (K), IL-7 (L), IL-9 (M), IL-10 (N), IL-12 (p40) (O), IL-12 (p70) (P), IL-13 (Q), IL-15 (R), IL-17a (S), IP-10 (T), KC (U), LIF (V), LIX (W), MCP-1 (X), M-CSF (Y), MIG (Z), MIP-1 α (A'), MIP-1 β (B'), MIP-2 (C'), RANTES (D'), $\text{TNF}\alpha$ (E'), VEGF (F')) were assessed after single and multiple administration of PPSGG. Mice were injected intravenously with a single dose of PPSGG (10 mg/kg), for five constitutive days with 10 mg/kg PPSGG, or five constitutive days with a corresponding volume of PBS (100 μl). Blood samples were taken via the vena saphena prior to initial injection (day 0), 24 h, 5 days, 10 days, or 15 days after the first injection in EDTA coated tubes. After centrifugation at 1000g for 1 min at 4°C, the plasma was collected, diluted 1 in 2 with PBS, and immediately stored at -80°C until analysis.

(a)



(b)



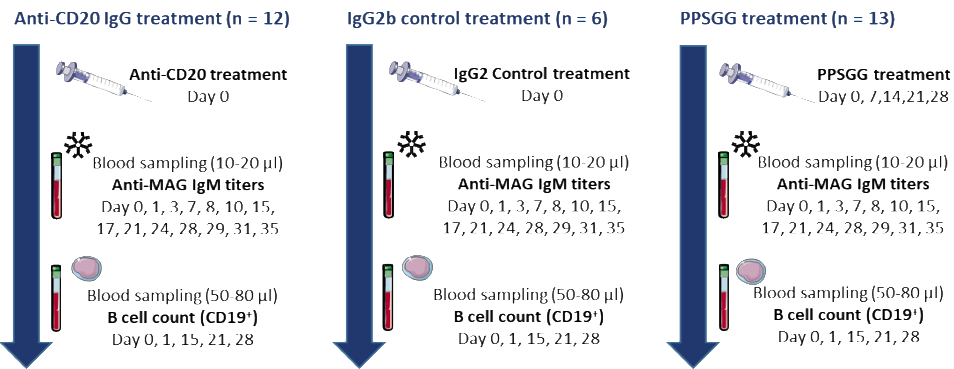
(c)

CD20⁺ cell depletion in mice

- Actively immunized BALB/c mice (n = 31 mice)
- 10 to 14 weeks old (male and female)



Anti-MAG/HNK-1 IgM



Mice were sacrificed by CO₂ suffocation and decapitation after the last blood sampling at day 35

(d)

Binding of PPSGG to murine B cells

- 10 to 14 weeks old (male and female)
- Immunized and non-immunized (naïve) BALB/c mice
- No animals were excluded

Non-immunized mice



Naïve BALB/c mice
(n = 6 mice)

Immunized mice



Anti-MAG/HNK-1 IgM
(n = 6 mice)



Mice were sacrificed to isolate the spleen



Murine spleen



Isolation and analysis of B cells from spleen



Murine B cells

Supplementary Figure 5. Flowcharts of the mouse experiment timelines. The flow charts depict the active immunization protocol of Balb/c mice (**a**), the passive immunization and dose titration study design (**b**), the CD20⁺ depletion experiment (**c**), and the PPSGG binding study (**d**). Images adapted from SMART Servier Medical ART (Retrieved from <https://smart.servier.com/>, January 2020).

Chapter 3

Glycopolymer binds pathogenic IgM autoantibodies and pulls them into the mononuclear phagocyte system for degradation

Butrint Aliu¹, Delphine Demeestere¹, Lijuan Pang^{1,2}, Timothy Sharpe³, Wolf Heusermann⁴,
Ruben Herrendorff^{1,2}, Beat Ernst¹, Pascal Hänggi^{1,2}

¹Institute of Molecular Pharmacy, Pharmacenter, University of Basel, 4056 Basel, Switzerland

²Polyneuron Pharmaceuticals AG, 4057 Basel, Switzerland

³Biophysics Facility, Biozentrum, University of Basel, 4056 Basel, Switzerland

⁴Imaging Core Facility, Biozentrum, University of Basel, 4056 Basel, Switzerland

Corresponding authors:

Pascal Hänggi, pascarhaenggi@gmail.com, <https://orcid.org/0000-0002-7941-2475>

Beat Ernst, +41 61 207 15 51, beat.ernst@unibas.ch, <https://orcid.org/0000-0001-5787-2297>

Contributions of Butrint Aliu

- Experimental conceptualization and design
- Writing and revision of manuscript
- DLS and Zeta potential measurements
- Cellular uptake and toxicity experiments
- Serial two-photon and confocal microscopy of murine tissue and human cells,
- Coordination and interpretation of SEC-MALS, AUC and TEM experiments
- Anti-MAG and anti-poly-L-lysine ELISA
- Data analysis and interpretation

Abstract

Anti-myelin associated glycoprotein (MAG) neuropathy patients exhibit high levels of monoclonal IgM autoantibodies against the carbohydrate epitope HNK-1 (human natural killer-1). This glycoepitope is presented in high abundance on the neural cell adhesion molecule MAG as well as on other glycoconjugates of the peripheral nervous system. Binding of the autoantibodies results in demyelination of the peripheral nerves causing severe sensorimotor deficits in anti-MAG neuropathy patients, including paresthesias, tremors, and sensory ataxia. We have previously reported the effective neutralization and removal of anti-HNK-1 IgM autoantibodies in an immunological mouse model with the glycopolymer PPSGG (poly(phenyl disodium 3-O-sulfo- β -D-glucopyranuronate)-(1 \rightarrow 3)- β -D-galactopyranoside). Here, we further explore the physicochemical characteristics and its mode of action. The linear glycopolymer PPSGG is highly negatively charged, with an approximate length of 100 nm, and is readily taken up by liver- and spleen-resident macrophages through scavenger receptors. No aggregate formation or immune complex deposition in these or other organs is observed and despite fast and extensive uptake of PPSGG into Kupffer cells of the liver, it does not exhibit hepatotoxic effects in human hepatic tissue *ex vivo*. In the presence of the anti-HNK-1 IgM antibodies, it preferentially forms complexes in a 1:1 or 1:2 binding stoichiometry (PPSGG/anti-HNK-1 IgM), without leading to aggregate formation though crosslinking of the multivalent binding partners *in vitro*. The complexes are actively taken up by murine macrophages *in vivo* and by human macrophages *in vitro*. PPSGG is designed to selectively and quickly remove disease-causing anti-HNK-1 IgM antibodies from circulation. Here, we demonstrate the unique mode of action of PPSGG and its therapeutic potential as the first antigen-specific treatment for anti-MAG neuropathy.

Introduction

Anti-MAG neuropathy is a slowly progressive polyneuropathy associated with IgM monoclonal gammopathy of neurological significance.¹¹⁹ The peripheral neuropathy is caused by pathogenic IgM autoantibodies that bind the human natural killer-1 (HNK-1) epitope, a carbohydrate epitope present on Schwann cells of the peripheral nerve fibers.⁴ The binding of anti-MAG autoantibodies induces slowly progressive and predominately distal demyelination of peripheral nerves leading to progressive disability through sensory ataxia with impaired gait, neuropathic pain, weakness, and tremor.⁶ There is a high unmet medical need for more specific options for the therapy of this chronic disease, since the currently used off-label treatments often lack efficacy and unspecifically modulate the immune system. Since the progression of this chronic neuropathy is closely related to the presence of anti-MAG IgM autoantibodies and since the relative reduction of autoantibody levels correlates well with a clinical improvement, a specific and efficient removal of the autoantibodies from circulation could be highly beneficial.¹²⁰ In previous studies, we demonstrated the efficient removal of anti-MAG IgM antibodies in an immunological mouse model with PPSGG,¹²¹ a glycopolymer consisting of a biodegradable poly-L-lysine backbone of approximately 400 lysine units, of which approximately 35% are linked to a mimetic of the HNK-1 glycoepitope. The remaining 65% of the lysine side chains are coupled with thioglycerol substituents to increase the solubility of PPSGG. This glycopolymer of a calculated average molecular mass of 194 kDa binds to the anti-MAG IgM in a highly selective and multivalent manner.¹¹⁹

The monovalent mimetic of the HNK-1 glycoepitope shows only high micromolar affinity to anti-MAG IgM autoantibodies of patients. However, when the glycoepitope is presented polyvalently the affinity increases up to 230'000-fold,¹²¹ firstly because of the high local density of the epitope leading to fast rebinding after dissociation and secondly because of simultaneous binding to multiple binding sites of the pentameric IgM.¹²² Targeting lectins with multivalent glycopolymers has gained increasing therapeutic interest, such as in the field of biological toxins, e.g. cholera toxin, shiga toxin, and ricin.¹²³ Furthermore, a similar approach was applied to remove host xenoantibodies against the $\alpha(1-3)$ -galactose epitope in xenotransplantation.¹²⁴

Comparable polyvalent epitope presentations by nanoparticles are also applied therapeutically. They are used for tissue-specific targeting, gene delivery, immunomodulatory purposes, as tracers for medical imaging, and carriers of drug loads.¹²⁵ However, toxicological profiles and quick

metabolic degradation are common challenges of nanoparticles.¹²⁶ Another problem related to nanoparticles is their short plasma half-life caused by phagocytosis, an obstacle that can be addressed by chemical modifications, most often by pegylation.¹²⁷ A comparable short plasma half-life was also observed for PPSGG. In this case it would however not be a disadvantage, because after binding to anti-HNK-1 IgM the quick removal from circulation could suppress antibody binding to the endogenous epitope on the myelin sheath.

In this communication, we investigated the mode of action of PPSGG by characterizing its shape and surface properties, its binding stoichiometry with the anti-HNK-1 IgM antibodies, as well as the size of the PPSGG/IgM complex. Furthermore, we studied tissue distribution of PPSGG and the PPSGG/IgM complexes as well as the elimination pathway including the specific cellular uptake mechanism.

Results and Discussion

The linear glycopolymer PPSGG preferably binds one or two anti-HNK-1 IgM antibodies in vitro

For a better understanding of the mode of action as well as related potential risks, we studied the morphological characteristics, tissues distribution, and route of elimination of PPSGG alone and of the PPSGG/anti-HNK-1 IgM complex.

For the assessment of the colloidal stability and aggregate formation of PPSGG (Figure 1), dynamic light scattering (DLS) measurements of anti-HNK-1 IgM and the PPSGG/IgM complex were performed. For PPSGG a single peak with a hydrodynamic diameter of 64.02 nm (± 3.34 nm SD) and a polydispersity index (PdI) of 0.357 (± 0.007 SD) (Figure 2A-1) was obtained. The hydrodynamic diameter of anti-HNK-1 IgM amounts to 46.18 nm (± 11.12 nm SD) with a PdI of 0.279 (± 0.032 nm SD) (Figure 2A-2) and is consistent with the elution behavior observed with size exclusion chromatography (SEC) during the multi angle light scattering (MALS) experiments (Supporting Information Figure S1). The peak broadness, however, results in a high PdI and is based on the polydispersity of diffusion coefficients in the sample, requiring contributions from a broader range of size classes, making exact mass estimates inaccurate. When PPSGG was co-incubated with anti-HNK-1 IgM and the PPSGG/anti-HNK-1 IgM complex was formed, a hydrodynamic diameter of 52.33 nm (± 11.01 nm SD) with a PdI of 0.271 (± 0.038 SD) was measured (Figure 2A-3 to 6). With increasing concentration of IgM, the peak size was not further affected. The multivalency of both glycopolymer and pentameric anti-HNK-1 IgM could potentially lead to crosslinked complexes and the formation of large aggregates, none of which were observed according to DLS data. For more accurate size and shape determination, transmission electron microscopy (TEM) was applied. PPSGG, anti-HNK-1 IgM, and mixtures thereof were incubated at room temperature for 30 minutes and stained with 2% uranyl acetate for analysis. PPSGG showed a rod-like linear polymer structure with an approximate length of 100 nm (Figure 3A), whereas the pentameric anti-HNK-1 IgM exhibited a diameter of approximately 50 nm (Figure 3B). When PPSGG was co-incubated with anti-HNK-1 IgM, spherical structures were formed with a diameter similar to the IgM alone (Figure 3C), confirming the results of the DLS and SEC-MALS experiments.

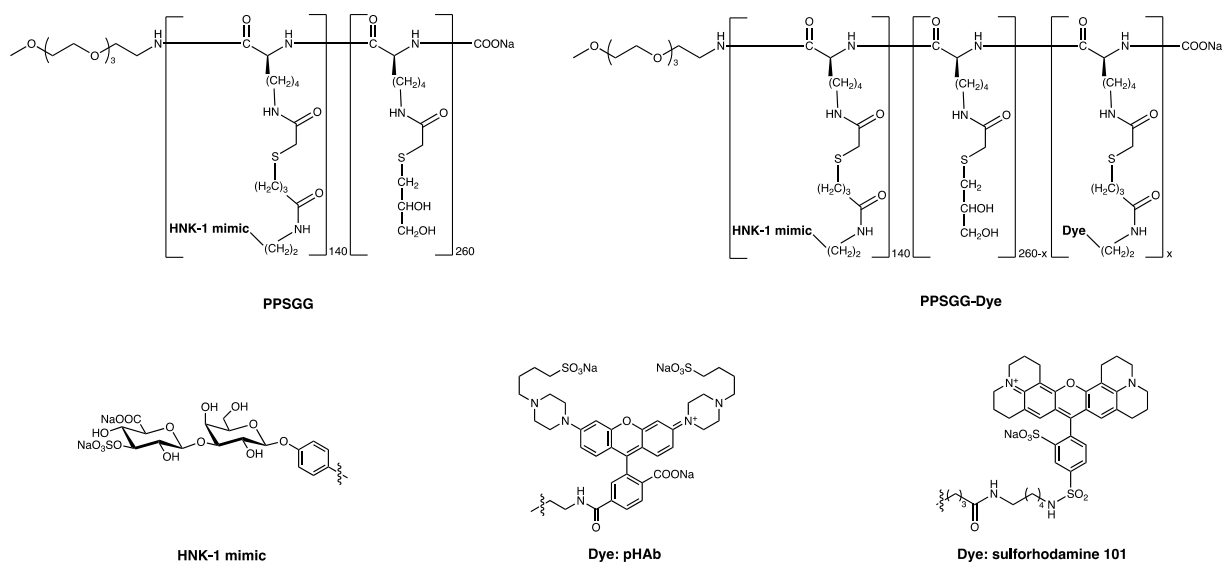


Figure 1. PPSGG: PLL bearing the HNK-1 mimic (PLL400, loaded with 35% HNK-1 mimic, 194 kDa); PPSGG-Dye: PPSGG labeled with the pH-sensitive dye pHAb (PPSGG-pHAb) or fluorescent dye sulforhodamine 101 (PPSGG-sulforhodamine). For protocols of the syntheses see Supporting Information.

A method for the assessment of the binding stoichiometry of complexes is based on the determination of the sedimentation coefficient by analytical ultracentrifugation (AUC), allowing the calculation of the molecular mass. PPSGG and the fluorescein isothiocyanate (FITC)-labeled anti-HNK-1 IgM were pre-incubated and the sedimentation velocity was monitored by fluorescence detection. The data was analyzed using a sedimentation coefficient distribution ($c(s)$) analysis. Based on the frictional ratio (f/f_0) and the sedimentation coefficient, the masses were calculated by two approaches. Firstly, a fixed frictional ratio for IgM of 1.82 was used¹²⁸, indicating that IgMs have a fairly extended structure compared to a perfect sphere with the frictional coefficient of 1.¹²⁹ Secondly, to account for the presence of differently sized species, a bimodal f/f_0 fitted distribution was applied. Both approximations led to similar results showing two distinct peaks for the sedimentation coefficient at 22 S and 33 S, corresponding to a molecular weight of 1.3 MDa (1:1-binding stoichiometry) and 2.3 MDa (1:2-binding stoichiometry), respectively. Furthermore, the peak intensities were dependent on the ratio of the two binding partners, meaning that higher amount of antibody lead to an increase of 1:2 binding (Figure 2B). In summary, we could confirm the 1:1- and 1:2-binding stoichiometry of the PPSGG/anti-HNK-1 IgM complex as suggested by a previous *in vivo* dose titration study in mice.¹¹⁹

An additional parameter of interest in polymer formulations is the colloidal stability described by the zeta potential, a measure of the charge density on the particle surface, which for homopolymers correlates with the propensity for flocculation. Thus, the zeta potential of 1 mg/ml PPSGG in 10 mM NaCl over a pH range from 4 to 10 amounted to an average of -46 mV (± 3.7 mV SD) over the whole pH range indicating a low probability for aggregate formation (Figure 2C). The surface charge of the PPSGG is a result of the negative charges of the carboxylate and sulfate group present on the HNK-1 epitope mimetic (Figure 1). The negative surface charge is unaffected over the whole pH range because at pH 4 the carboxylate ($pK_a = \leq 4$) is only partially protonated and the sulphate ($pK_a = \leq 2$) fully deprotonated. The negative zeta potential explains the observed short half-life of PPSGG *in vivo* (approx. 17 min in mice)¹²¹ due to the high level of negative charge enabling internalization through scavenger receptors (discussed in more detail later), and reduces some toxicity concerns related to positively charged nanoparticles, such as sequestration in the lungs.^{130 37} Compared to a reference glycopolymer (undisclosed) with similar carbohydrate mimetic density but only one negative charge per glycoepitope, the contribution of the negatively charged groups on the zeta potential becomes evident (Figure 2C).

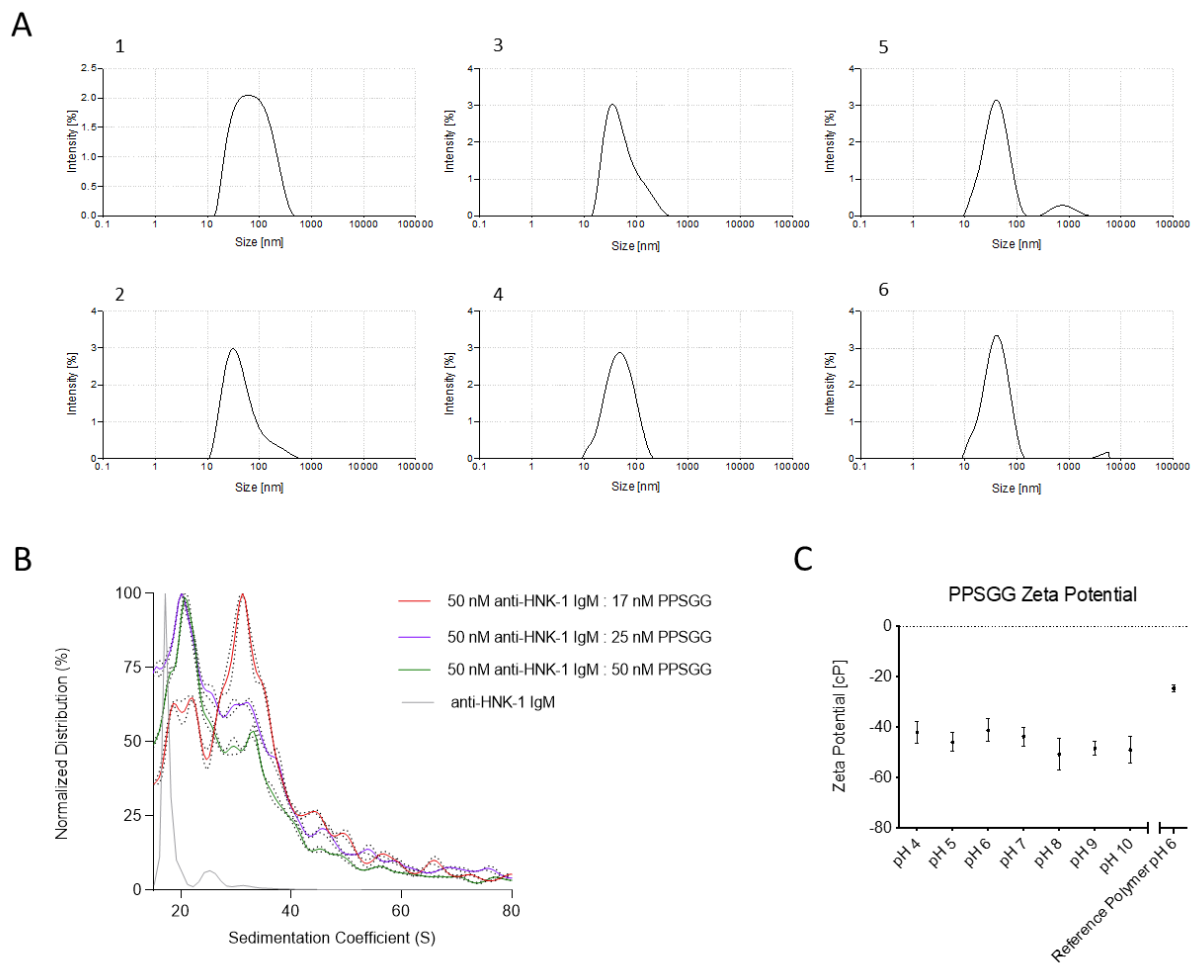


Figure 2. Hydrodynamic diameter, surface charge of PPSGG and stoichiometry of PPSGG/anti-HNK-1 IgM complex. **A)** DLS plots of PPSGG (A1), anti-HNK-1 IgM (A2), and a titration of increasing concentrations of anti-HNK-1 IgM [0.13 mg/ml (A3), 0.2 mg/ml (A4), 0.3 mg/ml (A5), and 0.33 mg/ml (A6)] with decreasing concentrations of PPSGG [0.267 mg/ml (A3), 0.2 mg/ml (A4), 0.1 mg/ml (A5), and 0.067 mg/ml (A6)] showing broad but monodisperse peaks remaining stable at around 50 nm. PPSGG and anti-HNK-1 IgM share similar hydrodynamic diameters which remain stable with increasing concentrations of anti-HNK-1 IgM. No formation of larger aggregates was observed. **B)** PPSGG was incubated with anti-HNK-1 IgM at RT for 30 min before measuring the fluorescence at a rotor speed of 30'000 rpm on a Beckman Coulter XL-1 AUC. The mass was calculated based on the frictional ratio of human IgM (f/f_0 , 1.82). Results show two peaks at 22 S and 33 S, which correspond to a molecular weight of 1.3 MDa and 2.3 MDa. Given the 950 kDa mass of IgM and approx. 200 kDa mass of PPSGG, the data indicates a 1:1 and 2:1 binding stoichiometry that is shifted towards 2:1 complexes in presence of larger amounts of IgM. **C)** PPSGG (1 mg/mL) was diluted in 10 mM NaCl and the zeta potential measured at 25°C using an applied voltage of 150 V. The average (five measurements) zeta potential values for PPSGG measured at different pH values (pH 4 to 10). The zeta potential averaged -46 mV (± 3.7 mV SD) over the whole pH range. A comparison with a reference polymer (undisclosed) with only half the negative charges per epitope reduces the zeta potential by approx. 50%.

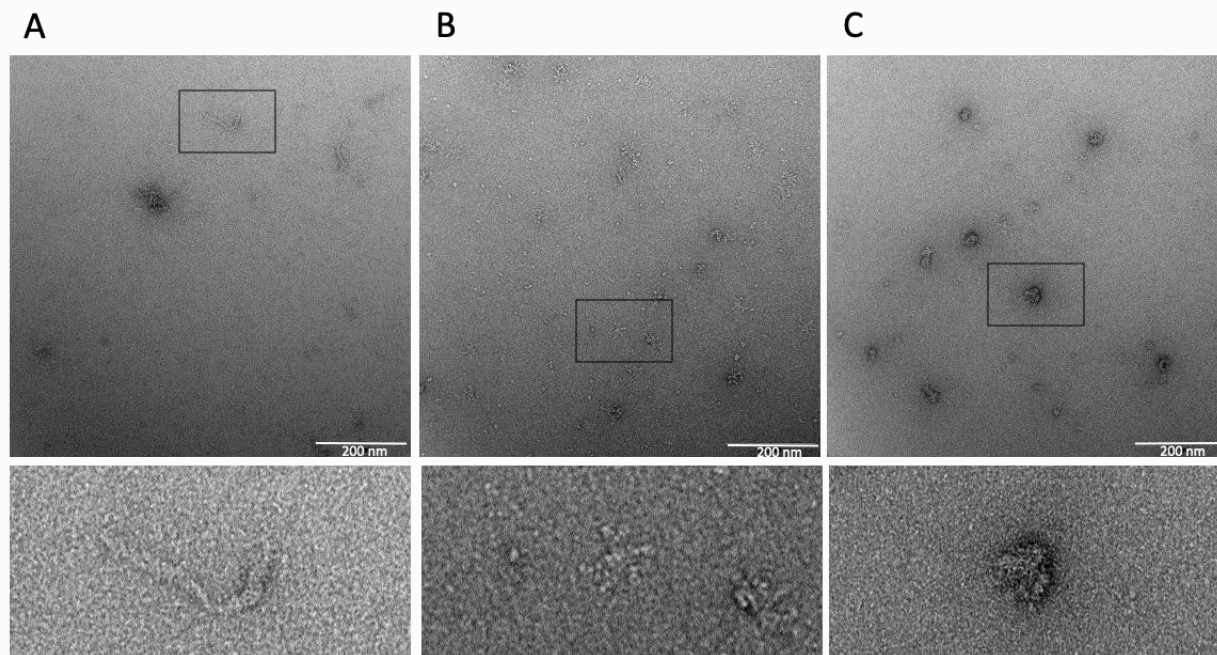


Figure 3. Transmission Electron Microscopy (TEM) images of PPSGG and the anti-HNK-1 IgM antibody with the lower panels displaying the squared areas of the images. The size and shape of PPSGG (A), anti-HNK-1 IgM (B), and the PPSGG/anti-HNK-1 IgM complex (C) were characterized by TEM. PPSGG and anti-HNK-1 IgM samples were incubated on a Copper grid 400 mesh coated with Parlodion and carbon, blotted and washed with water, and stained with 2% uranylacetate. Images were taken with a Tecnai G2 Spirit instrument (120kV TEM Microscope with EMSIS Morada camera). PPSGG has a size of approximately 100 nm, IgM is pentameric with a diameter of 40-50 nm, and the formed complexes are of similar size as the antibody. No crosslinking or aggregate formation was observed.

Uptake of PPSGG by liver and spleen resident macrophages

Similar to observations reported for nanoparticles,¹³¹ we expected that distribution and clearance of glycopolymers is also mediated by their chemical composition, size, shape, and surface charge. In a previous study, we demonstrated the plasma half-life of PPSGG in naïve BALB/c mice to be approximately 17 minutes.¹²¹ Therefore, we investigated the tissue distribution of PPSGG, its metabolic fate, and the possibility of the formation of aggregates and tissue accumulation *in vivo*. To monitor the tissue distribution, naïve mice were intravenously injected with the glycopolymer (10 mg/kg) labeled with the fluorescent dye sulforhodamine 101 (PPSGG-sulforhodamine, Figure 1). The animals were perfused, their organs harvested, and large sections of the organs embedded in activated agarose. The solidified agarose blocks were then processed with a microtome and images were recorded with a two-photon system; in red to detect the PPSGG-sulforhodamine and in green to show the naturally occurring autofluorescence of the organs,

enabling a label-free visualization of the organ structure. Analysis of the serial two-photon tomography showed extensive uptake of PPSGG-sulforhodamine by the liver and the spleen (Figure 4A). While liver uptake is distributed more broadly, the uptake by the spleen is localized in the marginal zone that surrounds the B and T cell rich follicular zone. Furthermore, the uptake of PPSGG-sulforhodamine into the brain of the experimental animals was studied. Sulforhodamine 101 has been widely used to fluorescently stain mouse brain astrocytes *in vivo*.¹³² No staining of the brain could be observed, and extracellular degradation of PPSGG-sulforhodamine, leading to a loss of the fluorescent dye, can be excluded. Thus, the crossing of the blood-brain barrier by PPSGG is unlikely (Supporting Information. Figure S2). The tissue distribution further supports the short half-life of PPSGG (approx. 17 min in mice)¹³³, emphasizing the quick uptake in the cells of the MPS already visible at 10 min post administration (Figure 4A). The uptake, however, does not lead to an excessive accumulation, since the fluorescence signal diminishes quickly and completely disappears after 6 h with sustained removal over 72 h post injection (Supporting Information Figure S3).

The liver and the splenic marginal zone are rich in macrophages that are involved in the clearance of endogenous debris as well as pathogens and therapeutics.¹³⁴ We therefore raised the hypothesis that the uptake of PPSGG is mediated by the mononuclear phagocyte system (MPS). To test this hypothesis, we analyzed liver sections by staining liver resident macrophages with anti-F4/80 antibodies, a marker for Kupffer cells.¹³⁵ When confocal microscopy images of PPSGG-sulforhodamine (red) and anti-F4/80 antibodies (in green) were recorded, colocalization of PPSGG-sulforhodamine and macrophages was depicted in yellow, confirming the specific uptake of PPSGG by cells of the MPS (Figure 4B). This distribution in the liver is very similar to the pattern described by Rothkopf *et al.*, showing uptake of liposomal nanoparticles not only in Kupffer cells but additionally in sinusoidal endothelial cells of the liver. A contribution of these cells to the uptake of PPSGG is likely, considering their scavenger receptor mediated uptake of anionic nanoparticles reported by Campbell *et al.*¹³⁶

To further elucidate the mode of action, naïve mice were intravenously injected with Pacific Blue™ labeled anti-HNK-IgM followed by an injection of PPSGG-sulforhodamine. The liver sections showed uptake of both PPSGG-sulforhodamine (red) and anti-HNK-1 IgM (blue) by cells of the MPS, leading to purple colocalization (Figure 4C). Given the excess of labeled PPSGG - sulforhodamine to anti-HNK-1 IgM, an increase of PPSGG-sulforhodamine uptake in

the liver was detected. However, the uptake of the PPSGG-sulforhodamine/anti-HNK-1 IgM complex appeared 60 minutes post injection compared to the rapid clearance of PPSGG-sulforhodamine within the first 10 min. This is illustrated by the lack of uptake after 10 min (injected with both PPSGG-sulforhodamine and anti-HNK-1 IgM, Supporting Information Figure S4) and the delayed signal one hour after administration in liver and spleen sections of mice (1h PPSGG + IgM, Figure 3A) compared to the much more pronounced fluorescent signal in the marginal zone of spleen and liver of animals treated with PPSGG-sulforhodamine only (Figure 4A). These results point out the importance of the negative charges of PPSGG and their accessibility for receptor recognition. In the PPSGG/anti-HNK-IgM complexes the surface charges are for steric reasons less accessible leading to delayed uptake into the MPS. Nevertheless, as shown in previous work, the *in vivo* elimination of anti-HNK-1 IgM after complex formation with PPSGG was highly selective and efficient. The reduction of anti-HNK-1 IgM levels upon treatment was sustained, even in the context of the continuous production of anti-HNK-1 IgM in the immunological mouse model.¹²¹

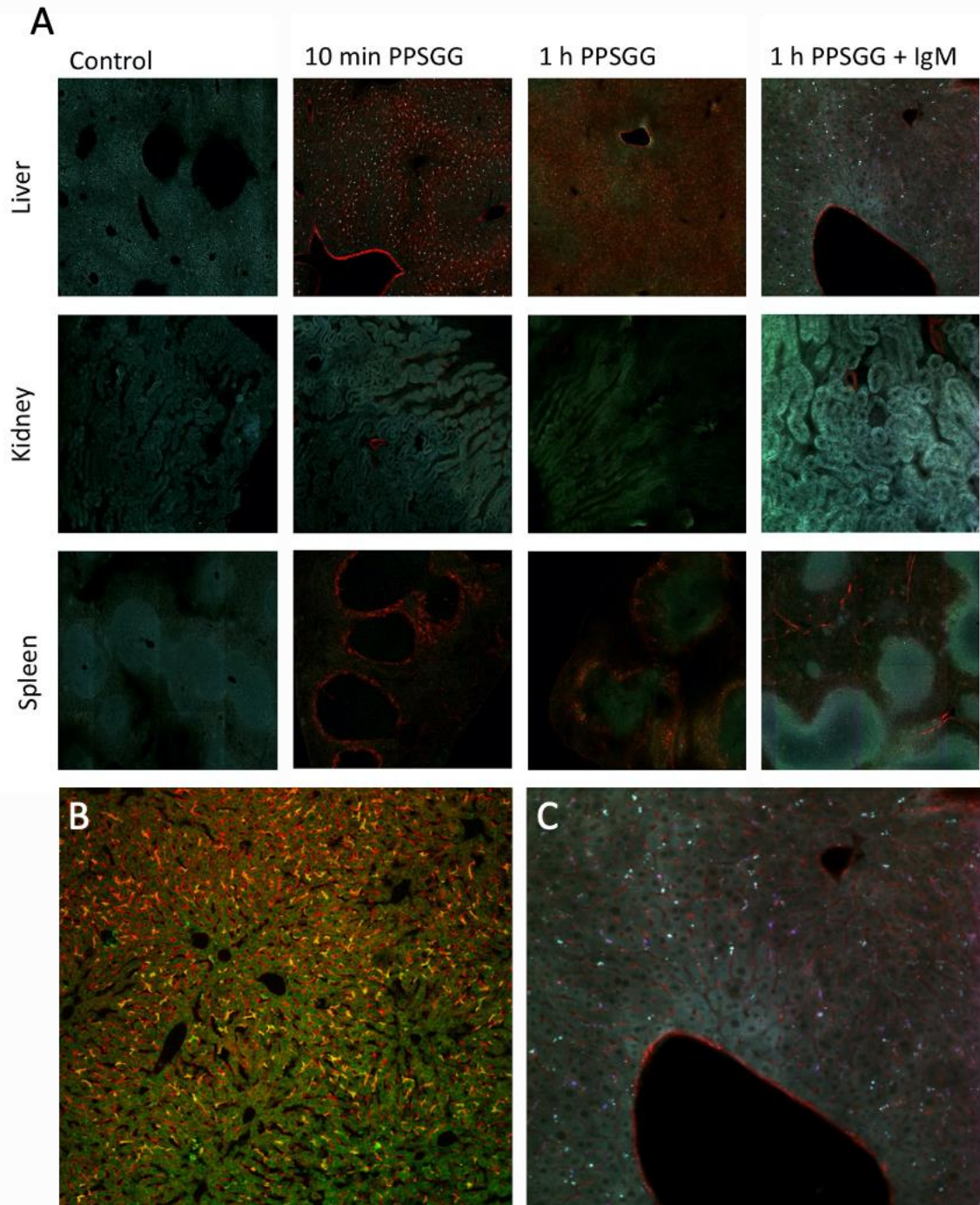


Figure 4. Tissue distribution of PPSGG-sulphorhodamine and anti-HNK-1 IgM in mice after intravenous injection. **A)** The tissue distribution of fluorescence labeled and IV injected 300 μg PPSGG-sulforhodamine (red) in BALB/c mice after 10 min and 60 min, in comparison to control samples. The perfused organs were harvested and embedded in agarose for imaging with a TissueVision by serial two-photon tomography. PPSGG-sulforhodamine did not form aggregates in the kidney and was quickly and extensively taken up by the liver and cells of the marginal zone of the spleen. **B)** The lower left panel shows a confocal microscopy image of the liver uptake of PPSGG-sulforhodamine

(red) after 15 min, with tissue resident macrophages (F4/80) stained in green and colocalization depicted in yellow. C) The image on the lower right shows the uptake of 60 μ g anti-MAG IgM (blue) when co-injected with 300 μ g PPSGG-sulforhodamine (red) after 60 min. The anti-HNK-1 IgM colocalized (purple) with PPSGG-sulforhodamine indicating a targeted degradation through the MPS.

Macrophage uptake of PPSGG mediated through scavenger receptors

After clarification of the binding stoichiometry and the metabolic pathway in mice, the uptake mechanism was studied in human macrophages. For this purpose, THP-1 monocytes were differentiated with phorbol 12-myristate 13-acetate (PMA, 100 nM), for 72 h into CD14⁺ mature macrophages.¹³⁷ These cells were then incubated with 0.1 mM PPSGG labeled with the pH-sensitive dye pHAb (PPSGG-pHAb, Figure 1) or with 0.1 mM non-glycosylated poly-L-lysine-pHAb and the fluorescence signal was recorded by fluorescence spectroscopy and point scanning confocal microscopy. Since the fluorescence intensity of the pHAb dye is drastically increased in an acidic environment,¹³⁸ the internalization of PPSGG-pHAb by macrophages via endosomes and lysosomes leading to the degradation of poly-L-lysine and the carbohydrate components, could be detected.¹³⁹ The active uptake mechanism was confirmed by incubating the cells at 4 °C,¹⁴⁰ where no signal could be detected in contrast to incubation at 37 °C (Supporting Information, Figure S5). Because PPSGG-pHAb was internalized to a much higher degree than even a ten-fold higher concentration of poly-L-lysine-pHAb, the major contribution of the HNK-1 mimetics to endocytosis (Figure 5A1) was confirmed.

As described by Campbell et al.¹⁴¹ and Rothkopf et al.¹⁴² polyanionic nanoparticles are readily taken up through scavenger receptors by cells of the MPS and liver sinusoidal endothelial cells. To investigate the contribution of this endocytic pathway to the uptake of PPSGG-pHAb, we treated the THP-1 derived macrophages with dextran sulfate (Figure 5A2), a negatively charged polysaccharide internalized by scavenger receptors.¹⁴³ Incubation with increasing concentrations of dextran sulfate inhibited the uptake of PPSGG-pHAb in a concentration-dependent manner, but had no effect on the uptake of poly-L-lysine-pHAb. This suggests that the uptake is considerably mediated by the two negative charges present on each carbohydrate moiety of the glycopolymer (see highly negative zeta potential, Figure 2C) and to a lesser extent by non-concentration-dependent mechanisms such as fluid-phase micropinocytosis.¹⁴⁴ The main members of the scavenger class A family, SR-A1 and SR-A6, formerly known as MARCO, are primarily

expressed on tissue macrophages such as Kupffer cells.¹⁴⁵ To further narrow in on the receptors responsible for the endocytosis of PPSGG, we incubated the cells with AcLDL (human acetylated low density lipoprotein, Figure 5A3), a specific ligand for SR-A1, but not for SR-A6.¹⁴⁶ The resulting inhibition of PPSGG uptake was similar to the result obtained by the treatment with the unspecific inhibitor dextran sulphate, indicating that SR-A1 is the main scavenger for the endocytosis of PPSGG.

When cells were treated with pre-incubated anti-HNK-1 IgM-FITC and PPSGG-pHAb, the uptake in acidic compartments of the macrophages could be demonstrated (Figure 5B3) for the individual components (red: PPSGG-pHAb, and green: anti-HNK-1 IgM-FITC), as well as the complexes (yellow: PPSGG-pHAb/anti-HNK-1 IgM-FITC). We conclude that the uptake of the complexes is mainly driven by the negatively charged PPSGG, since we have observed, that as a consequence of the formation of the spherical structures depicted in the TEM images (Figure 3C), the antibody is shielded by the glycopolymer, thus withdrawing the Fc part from recognition (Supporting Information, Figure S6).

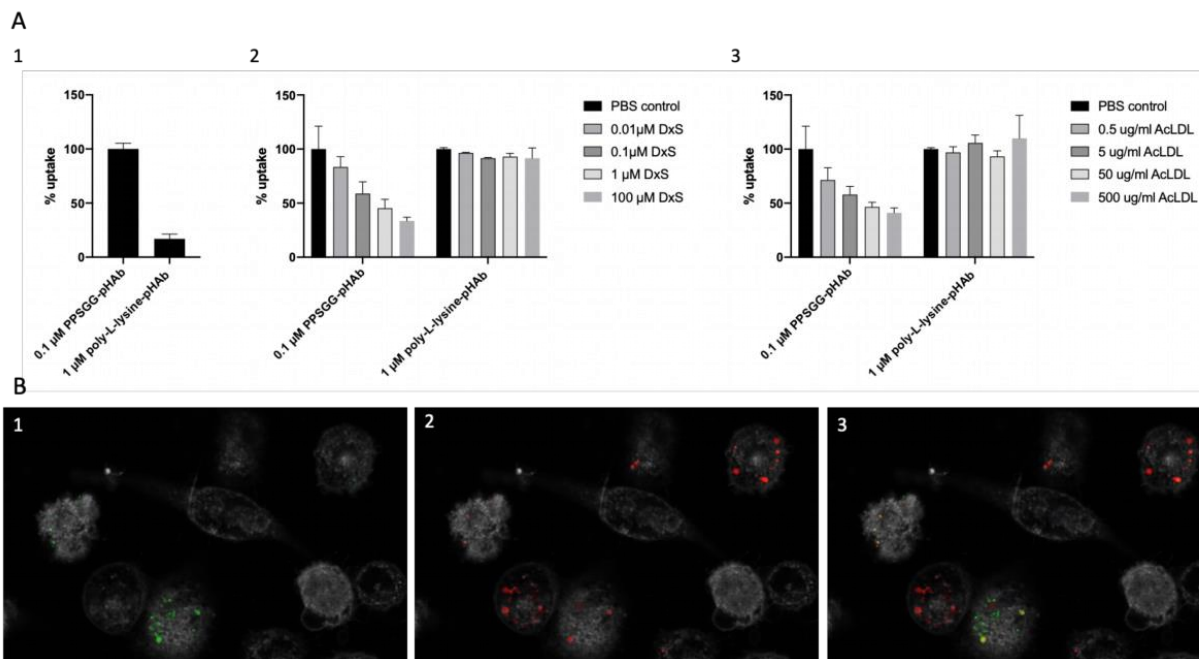


Figure 5. Scavenger receptor mediated uptake of PPSGG, anti-MAG IgM and complexes thereof into human macrophages. **A)** By measuring the pH-dependent fluorescence, the uptake efficiency of PPSGG-pHAb and poly-L-lysine-pHAb by THP-1 derived macrophages is compared. It emphasizes the dependence on the presence of negatively charged HNK-1 mimetics for an efficient uptake of the polymers. While only a fraction of the neutral

poly-L-lysine-pHAb is taken up, even at 10-fold higher concentration of 1 μM . Co-incubation with the scavenger receptor ligands dextran sulfate (A2) and AcLDL (A3) shows the concentration dependent inhibition of PPSGG-pHAb uptake, while having no effect on the uptake of the neutral poly-L-lysine-pHAb. **B)** Pre-incubation of anti-HNK-1-IgM-FITC (green, B1) with PPSGG-pHAb (red, B2) and subsequent incubation with THP-1 derived macrophages leads to an uptake of the two individual components, as well as the complexes (yellow, B3) in acidic compartments of the cells.

Uptake and elimination of PPSGG by the MPS does not induce hepatotoxicity (ex vivo)

To investigate if the extensive uptake by the liver could possibly lead to drug-induced liver injury, we tested the hepatotoxic potential of PPSGG on primary human-derived liver microtissue.¹⁴⁷ The cell clusters comprised of hepatocytes and Kupffer cells were incubated with PPSGG concentrations exceeding the anticipated human dose range by a factor of approx. 10.¹¹⁹ After an incubation period of 48 h, the viability of the liver cell was assessed by measuring free ATP with the CellTiter Glo Kit specifically designed to assess microtissue viability. Whereas the cell viability was not affected by high concentrations of PPSGG (38 mM, Figure 6B), chlorpromazine, used as a positive control, showed cytotoxicity ($\text{EC}_{50} = 14.3 \text{ mM}$, Figure 6C). The uptake of PPSGG in liver microtissue was confirmed by fluorescence microscopy (PPSGG-sulforhodamine, Figure 6A).

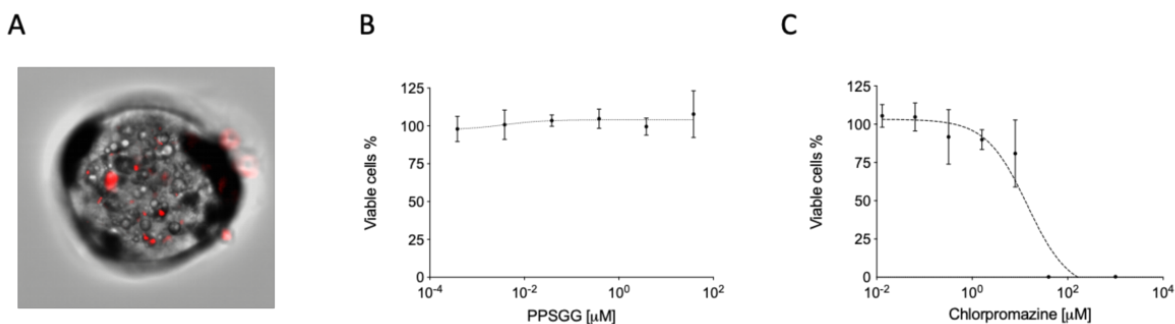


Figure 6. Hepatotoxicity evaluation of PPSGG in a primary human liver microtissue model. **A)** The uptake of PPSGG-sulforhodamine by primary human-derived liver microtissue. **B)** PPSGG showed no cytotoxic activity over a 48 h incubation period, **C)** while chlorpromazine was cytotoxic with an EC_{50} of 14.3 μM .

Conclusion

With our studies we gained insight into the mode of action of the glycopolymer PPSGG (Figure 7) and the suitability of its PK/PD profile for the therapeutic use in peripheral neuropathy caused by anti-MAG autoantibodies. We could show that PPSGG distributes to liver and spleen and that its elimination happens via the MPS through uptake by scavenger receptors on cells of the MPS. This uptake leads to quick endocytosis and subsequent degradation of PPSGG via acidic endosomes and lysosomes in liver and spleen.¹⁴⁸ These data explain the previously observed short half-life of PPSGG and the fast and efficient removal of anti-HNK-1 IgM antibodies in mice.¹²¹ The fast uptake of large amounts of PPSGG did not cause cytotoxicity in primary human liver microtissue and PPSGG showed favorable colloidal properties, i.e. no formation of aggregates in solution or *in vivo*, further mitigating toxicity concerns. In presence of anti-HNK-1 IgM antibody, PPSGG forms spherical complexes with the preferred binding stoichiometries of 1:1 or 1:2 (PPSGG/anti-HNK-1 IgM), confirming the suspected binding stoichiometry based on a dose titration study in mice.¹¹⁹ The PPSGG/anti-HNK-1 IgM complex is of comparable hydrodynamic size as PPSGG and the anti-HNK-1 IgM antibody alone. Moreover, in spite of the multivalent nature of both the glycopolymer and the anti-HNK-1 IgM, no aggregates are formed through crosslinking. The active uptake of PPSGG/anti-HNK-1 IgM complexes was shown in mice first, and then confirmed with a human macrophage cell line *in vitro*. In conclusion, we could show a unique mode of action for PPSGG which is characterized by a selective and efficient elimination of an anti-carbohydrate autoantibody (anti-HNK-1 IgM) via the MPS. PPSGG thus makes use of a natural degradation system of the immune system for the selective removal of a disease-causing autoantibody.

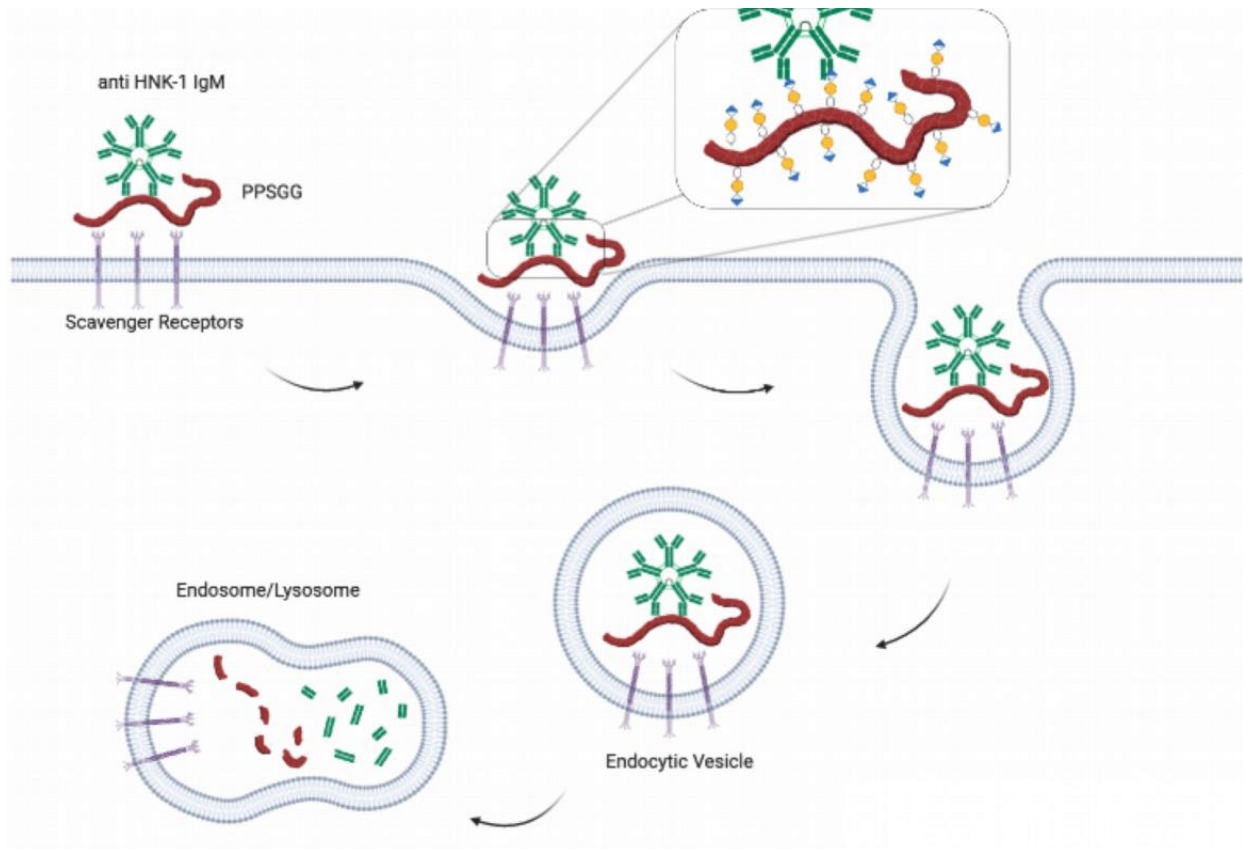


Figure 7. Mode of action of PPSGG: The polyanionic surface of PPSGG is recognized by scavenger receptors (SR - A1) on the surface of cells of the mononuclear phagocyte system (MPS). The binding of the PPSGG/anti- HNK- 1 IgM complexes leads to a receptor mediated endocytosis, forming endocytic vesicles that are further trafficked via the progressively increasing acidic environment of the endosome/lysosome pathway, resulting in the metabolism of the complexes.¹⁴⁹

Materials and Methods

Dynamic light scattering (DLS) and zeta potential

DLS (Figure 2A) and zeta potential (Figure 2C) of PPSGG (Supporting Information) was measured using a Zetasizer Nano ZS (Malvern Instruments, United Kingdom). DLS measurements of 0.2 mg/ml PPSGG and 0.2 mg/ml purified anti-HNK-1 IgM (3H5, DSHB, USA) in PBS were recorded in five runs for 50 s each at 25°C with a dispersant refractive index (RI) of 1.33 (water) and a sample RI of 1.45 (protein) in a quartz cuvette. A titration series of anti-HNK-1 IgM (C6680, Sigma-Aldrich, Switzerland) to PPSGG was recorded accordingly with 0.13 mg/ml (A3), 0.2 mg/ml (A4), 0.3 mg/ml (A5), and 0.33 mg/ml (A6) anti-HNK-1 IgM and 0.267 mg/ml (A3), 0.2 mg/ml (A4), 0.1 mg/ml (A5), and 0.067 mg/ml (A6) PPSGG (Figure 2A). The hydrodynamic diameter was plotted, and polydispersity index (PdI) calculated using Malvern Zetasizer Software. Zeta potential measurements were performed with 1 mg/ml PPSGG in 10 mM NaCl at 25°C by electrophoretic light scattering in disposable folded capillary cells (DTS1070, Malvern Instruments, United Kingdom) at different pH in the range from pH 4 to pH 10. The voltage (150 V), viscosity (0.8894 cP), and dielectric constant (78.6) was kept constant over five measurements per sample. Data were converted using the Smoluchowski model (Malvern Zetasizer Software).¹⁵⁰

Transmission electron microscopy (TEM)

The particle size and morphology of PPSGG, anti-HNK-1 IgM (C6680, Sigma-Aldrich, Switzerland), and their complexes were analyzed with TEM (Figure 3). Aliquots of 5 ml (0.025 mg/ml PPSGG, 0.04 mg/ml anti-HNK-1 IgM) were adsorbed onto a glow-discharged carbon film-coated copper grid 400 mesh (G400-Cu, EMS, USA), washed with four droplets of pure water and subsequently stained with 2% uranylacetate (22400, EMS, USA). Images were recorded using Tecnai G2 Spirit Electron Microscope (FEI, Netherlands) operating at 120 kV on an Morada CCD camera (EMSIS, Germany). The individual samples were blotted and stained immediately and the mixture of PPSGG and anti-HNK-1 IgM were incubated at room temperature for 30 minutes.

Analytical ultracentrifugation (AUC) with fluorescence detection

Sedimentation velocity experiments (Figure 2B) were performed for samples comprising PPSGG and anti-HNK-1 IgM FITC (TB01, Invitrogen, Thermo Fisher Scientific, Switzerland) in PBS containing 0.05% Tween20 (93773, Sigma-Aldrich, Switzerland) to suppress adsorption of

proteins to cell components. The buffer density (1.0052 g/ml) and viscosity (0.01022 Poise) were measured at 20°C using an DMA 4500M density meter (Anton Paar, Austria) and AMVn viscometer (Anton Paar, Austria). The 80 µL samples were housed in Spin Analytical AU-FDS 3 mm double sector charcoal-epon centrepieces, with sapphire windows. Centrifugation was performed at 30'000 rpm and 20°C using a Beckman XL-I AUC with a Beckman An-60 Ti rotor. The rotor was incubated for three hours prior to acceleration to ensure homogeneous temperature. Sedimentation was monitored using an AU-FDS detector (Aviv Biomedical, USA) with continuous scanning for ten hours. Sedimentation velocity data were fitted to a diffusion-deconvoluted sedimentation coefficient distribution, $c(s)$, using the software Sedfit.¹⁵¹ A sedimentation coefficient range of 1-100s was used with a resolution of 200 points. To obtain mass estimates for species of the size of IgM in the presence of a background of smaller fluorescent species, two approaches were used. In the first approach, the value of the frictional ratio (f/f_0) was fixed to a value of 1.82, calculated from literature values for IgM (sedimentation coefficient 18.5, MW 950 kDa).¹²⁸ In the second approach, a bimodal frictional ratio distribution was used allowing separate free-fitted values of f/f_0 for species sedimenting with a coefficient above or below 10s. As expected, the $c(s)$ distribution was very similar for these two approaches.

Experimental animals

The wild type BALB/cJRj (Ref. C-BJ-56-M/F, Janvier Labs, France) mice (5-10 weeks old male and female) were bred at the University Hospital Basel and kept under specific pathogen-free conditions in a controlled environment (12-hour light–dark cycle at 20°C) with food and water ad libitum. All animal experiments were approved by the local ethical committee in accordance with permit No. 2778 of the Animal Research Authorities of the Canton of Basel-Stadt, Switzerland.

Perfusion of mice

BALB/c mice were IV injected with 300 µg PPSGG-sulforhodamine (4% loading) only or with 60 µg Pacific Blue™-labeled anti-HNK-1 IgM (3H5, DSHB, USA) followed by 300 µg PPSGG-sulforhodamine after 1 h. In case of PPSGG-sulforhodamine only, organs were isolated 10 min, 1 h, 6 h, 24 h, 48 h, 72 h post-injection, while for the combination of anti-HNK-1 IgM and PPSGG-sulforhodamine, organs were isolated 10 min, 1 h, and 6 h after PPSGG-sulforhodamine injection. Mice were sedated with a ketamine/xylazine (5 mg/kg of 2% Rompun, Bayer HealthCare, Germany and 100 mg/kg of 10% Ketazol, Graeub, Switzerland) and transcardially perfused with PBS, followed by 4% PFA (paraformaldehyde, P6148, Sigma-Aldrich,

Switzerland). Organs were isolated and post-fixed overnight at 4 °C in 4% PFA. The next day, organs were cut in half and transferred into 50 mM of phosphate buffer (pH 7.4) for two-photon tomography or into 30% sucrose (84100, Sigma-Aldrich, Switzerland) for confocal microscopy imaging.

Confocal microscopy and F4/80 staining

Organs were embedded in cryomolds with OCT matrix (81-0771-00, Biosystems, Switzerland) and frozen on dry ice. Then 5 µm cryosections were cut. The macrophages were visualized by performing an immunofluorescent staining against the macrophage marker F4/80 (Figure 4B). For this, sections were thawed, and antigen retrieval was performed by heating the tissue sections for 10 min at 90°C in citrate buffer (10 mM, pH 6, 5949-29-1, Sigma-Aldrich, Switzerland). After cooling to room temperature, sections were incubated with blocking buffer containing 3% normal goat serum (10000C, Invitrogen, Thermo Fisher Scientific, Switzerland) and 0.5% Triton X (9002-93-1, Sigma-Aldrich, Switzerland) for 1 h at room temperature. Next, tissues were incubated with primary rat anti-mouse F4/80 antibody (1/1000 in blocking buffer, MCA497RT, Bio-Rad, Switzerland) overnight at 4 °C. For detection, the tissues were incubated with AF488 goat anti-rat IgG (1/1000 in blocking buffer, 112-545-003, Jackson laboratories, USA) for 2 h at room temperature and sections were mounted with Fluoromount-G mounting medium (BML-AP402, Invitrogen, Thermo Fisher Scientific, Switzerland) containing DAPI (nuclear staining).

Serial-two-photon tomography

Tissue distribution (Figure 4A) was assessed by whole organ imaging with a serial two-photon tomography system with included microtome (Tissue Cyte, TissueVision, Cambridge, USA). Liver, kidney, spleen, and brain were transferred into a 50 mM phosphate buffer 1 h before embedding in 4,5% activated agarose (A6013; NaIO₄, S1878; Sigma-Aldrich, Switzerland). The agarose block was stored in borohydride/borate solution (pH 9, 19 mg/ml Na₂B₄O₇·10H₂O 221732; 3 mg/ml H₃BO₃, B6768; 0.2 mg/ml NaBH₄, 452882; Sigma-Aldrich, Switzerland) at 4 °C overnight. The block was mounted in a 10 mM phosphate buffer bath and 30 µm sections were cut and recorded at two different depths of the section (15 µm). Two laser pulses at 800 nm (Mai Tai eHP) coupled to a 20x magnification lens (Zeiss Plan Apo, NA 1.0) were used as illumination source. The signal was recorded in the blue, green, and red channel, each split with a SP 500, a LP 500, and a LP 560 dichroic mirror. Approximately 300 sections were cut, and the tiles were automatically stitched (StichIt, MATLAB, The MathWorks, USA).

Cell culture

THP-1 cells (ATCC, TIB-202) were maintained in RPMI 1640 medium (Roswell Park Memorial Institute medium, R8758, Sigma-Aldrich, Switzerland) supplemented with 10% FBS (fetal bovine serum, 10270-106, Gibco, Thermo Fisher Scientific, Switzerland), 1% antibiotic-antimycotic solution (15240062, Gibco, Thermo Fisher Scientific, Switzerland) 10 mM HEPES buffer (5-31F00-H, BioConcept, Switzerland), 1% sodium pyruvate (S8636, Sigma-Aldrich, Switzerland), and 0.05 mM mercaptoethanol (11528926, Gibco, Thermo Fisher Scientific, Switzerland). To induce differentiation of THP1 monocytes into macrophages, PMA (16561-29-8, Sigma-Aldrich, Switzerland) at a final concentration of 100 nM was added to seeded THP-1 cells 72 hours prior to the uptake experiment. The cells were incubated with 1 mM poly-L-lysine-pHAb (1% loading) and 0.02 mg/ml anti-HNK-1 IgM FITC (TB01, Invitrogen, Thermo Fisher Scientific, Switzerland) in cell culture medium for 1 h and washed with PBS (20012068, Gibco, Thermo Fisher Scientific, Switzerland). Before imaging the cells were treated with 5 µg/ml CellMask Deep Red Plasma membrane stain (C10046, Invitrogen, Thermo Fisher Scientific, Switzerland). Images were recorded (Figure 5B) with the Leica SP8 confocal point scanning microscope using a HC PL Apo CS 20x (NA 0.75) and a HC PL Apo CS 40x (NA 1.1) objective (Leica Microsystems, Germany). Differentiated cells were also incubated with 0.1 mM PPSGG-pHAb and 1 mM poly-L-lysine-pHAb, pre-mixed with increasing concentrations of dextran sulfate (42867, Sigma-Aldrich, Switzerland) or AcLDL (L35354, Invitrogen, Thermo Fisher Scientific, Switzerland) and incubated for 9 h, for best signal to noise ratio. The cells were washed twice with 100 µl PBS before measuring fluorescence with the Tecan Spark (Tecan, Germany) microplate plate reader at Ex535/Em595 nm.

InSphero Liver Microtissue Toxicity

3D InSight™ Human Liver Microtissues (hLiMT280, IpHH_11, IPHN_10, InSphero AG, Switzerland) were maintained at 37 °C in a humidified 5% CO₂ cell-culture incubator in BSA-free 3D InSight™ Human Liver Maintenance Medium TOX (CS-07-001-02, m307/17, InSphero AG, Switzerland). Chlorpromazine hydrochloride (C8138, Sigma-Aldrich, Switzerland) and PPSGG were dissolved and diluted in Human Liver Maintenance Medium (hLiMT/M) – TOX. Triplicates of Human Liver Microtissues were incubated for 48 h with 1 mM (1/5 dilution series) chlorpromazine hydrochloride and 38 mM concentration (1/10 dilution series) PPSGG. Human Liver Microtissues were transferred to a white, clear-bottom 96-well Cell Culture Microplate

(655088, Greiner Bio One, Switzerland). The viability of Human Liver Microtissues was determined (Figure 6) at the end of the experiment with the CellTiter-Glo® 3D Cell Viability Assay (G9681, Promega, Switzerland). In brief, Human Liver Microtissues were incubated with equilibrated Celltiter Glo reagent (G9681, Promega, Switzerland) for 30 min and the plate shaken vigorously (5 min at 1350 rpm) for cell lysis, then the luminescence was measured with the Synergy HT (integration 1s, bottom measurement, gain 135, Biotek Instruments, Switzerland).

Author Information

Conflict of interest statement. R.H., P.H., and B.E. are co-founders of the University of Basel spin-off, Polyneuron Pharmaceuticals AG, whose activity is related to the subject matter of this article. B.E. is a member of the advisory board, and R.H. is a member of the board of directors. R.H. and B.E. are named as co-inventors on relevant patent applications.

Acknowledgements

This work was supported by the Swiss Commission for Technology and Innovation. We would like to thank Carola Alampi and Mohamed Chami from the C-CINA BioEM Lab for supporting us with the TEM images and Susanne Schenk for providing the THP-1 cell line.

References

1. Aliu, B.; Demeestere, D.; Seydoux, E.; Boucraut, J.; Delmont, E.; Brodovitch, A.; Oberholzer, T.; Attarian, S.; Théaudin, M.; Tsouni, P.; Kuntzer, T.; Derfuss, T.; Steck, A. J.; Ernst, B.; Herrendorff, R.; Hänggi, P., Selective inhibition of anti-MAG IgM autoantibody binding to myelin by an antigen specific glycopolymer. *J Neurochem* **2020**.
2. Steck, A. J.; Stalder, A. K.; Renaud, S., Anti-myelin-associated glycoprotein neuropathy. *Curr Opin Neurol* **2006**, *19* (5), 458-63.
3. Dalakas, M. C., Pathogenesis and Treatment of Anti-MAG Neuropathy. *Curr Treat Options Neurol* **2010**, *12* (2), 71-83.
4. Lunn, M. P.; Nobile-Orazio, E., Immunotherapy for IgM anti-myelin-associated glycoprotein paraprotein-associated peripheral neuropathies. *Cochrane Database Syst Rev* **2016**, *10*, CD002827.
5. Baron, M.; Lozeron, P.; Harel, S.; Bengoufa, D.; Vignon, M.; Asli, B.; Malphettes, M.; Parquet, N.; Brignier, A.; Ferman, J. P.; Kubis, N.; Arnulf, B., Plasma exchanges for severe acute neurological deterioration in patients with IgM anti-myelin-associated glycoprotein (anti-MAG) neuropathy. *J Neurol* **2017**, *264* (6), 1132-1135.
6. Benedetti, L.; Briani, C.; Grandis, M.; Vigo, T.; Gobbi, M.; Ghiglione, E.; Carpo, M.; Cocito, D.; Caporale, C. M.; Sormani, M. P.; Mancardi, G. L.; Nobile-Orazio, E.; Schenone, A., Predictors of response to rituximab in patients with neuropathy and anti-myelin associated glycoprotein immunoglobulin M. *J Peripher Nerv Syst* **2007**, *12* (2), 102-7.
7. Renaud, S.; Fuhr, P.; Gregor, M.; Schweikert, K.; Lorenz, D.; Daniels, C.; Deuschl, G.; Gratwohl, A.; Steck, A. J., High-dose rituximab and anti-MAG-associated polyneuropathy. *Neurology* **2006**, *66* (5), 742-4.
8. Nobile-Orazio, E.; Baldini, L.; Barbieri, S.; Marmioli, P.; Spagnol, G.; Francomano, E.; Scarlato, G., Treatment of patients with neuropathy and anti-MAG IgM M-proteins. *Ann Neurol* **1988**, *24* (1), 93-7.
9. Gabriel, J. M.; Erne, B.; Bernasconi, L.; Tosi, C.; Probst, A.; Landmann, L.; Steck, A. J., Confocal microscopic localization of anti-myelin-associated glycoprotein autoantibodies in a patient with peripheral neuropathy initially lacking a detectable IgM gammopathy. *Acta Neuropathol* **1998**, *95* (5), 540-6.
10. Pestronk, A.; Florence, J.; Miller, T.; Choksi, R.; Al-Lozi, M. T.; Levine, T. D., Treatment of IgM antibody associated polyneuropathies using rituximab. *J Neurol Neurosurg Psychiatry* **2003**, *74* (4), 485-9.
11. Herrendorff, R.; Hänggi, P.; Pfister, H.; Yang, F.; Demeestere, D.; Hunziker, F.; Frey, S.; Schaeren-Wiemers, N.; Steck, A. J.; Ernst, B., Selective in vivo removal of pathogenic anti-MAG autoantibodies, an antigen-specific treatment option for anti-MAG neuropathy. *Proc Natl Acad Sci U S A* **2017**, *114* (18), E3689-E3698.
12. Dam, T. K.; Gerken, T. A.; Brewer, C. F., Thermodynamics of multivalent carbohydrate-lectin cross-linking interactions: importance of entropy in the bind and jump mechanism. *Biochemistry* **2009**, *48* (18), 3822-7.

13. Kiessling, L. L.; Gestwicki, J. E.; Strong, L. E., Synthetic multivalent ligands in the exploration of cell-surface interactions. *Curr Opin Chem Biol* **2000**, *4* (6), 696-703.
14. Miura, Y.; Hoshino, Y.; Seto, H., Glycopolymer Nanobiotechnology. *Chem Rev* **2016**, *116* (4), 1673-92.
15. Polizzotti, B. D.; Kiick, K. L., Effects of polymer structure on the inhibition of cholera toxin by linear polypeptide-based glycopolymers. *Biomacromolecules* **2006**, *7* (2), 483-90.
16. Das, S.; Angsantikul, P.; Le, C.; Bao, D.; Miyamoto, Y.; Gao, W.; Zhang, L.; Eckmann, L., Neutralization of cholera toxin with nanoparticle decoys for treatment of cholera. *PLoS Negl Trop Dis* **2018**, *12* (2), e0006266.
17. Richards, S. J.; Jones, M. W.; Hunaban, M.; Haddleton, D. M.; Gibson, M. I., Probing bacterial-toxin inhibition with synthetic glycopolymers prepared by tandem post-polymerization modification: role of linker length and carbohydrate density. *Angew Chem Int Ed Engl* **2012**, *51* (31), 7812-6.
18. Haksar, D.; de Poel, E.; van Ufford, L. Q.; Bhatia, S.; Haag, R.; Beekman, J.; Pieters, R. J., Strong Inhibition of Cholera Toxin B Subunit by Affordable, Polymer-Based Multivalent Inhibitors. *Bioconjug Chem* **2019**, *30* (3), 785-792.
19. Watanabe, M.; Igai, K.; Matsuoka, K.; Miyagawa, A.; Watanabe, T.; Yanoshita, R.; Samejima, Y.; Terunuma, D.; Natori, Y.; Nishikawa, K., Structural analysis of the interaction between Shiga toxin B subunits and linear polymers bearing clustered globotriose residues. *Infect Immun* **2006**, *74* (3), 1984-8.
20. Nagatsuka, T.; Uzawa, H.; Sato, K.; Ohsawa, I.; Seto, Y.; Nishida, Y., Glycotechnology for decontamination of biological agents: a model study using ricin and biotin-tagged synthetic glycopolymers. *ACS Appl Mater Interfaces* **2012**, *4* (2), 832-7.
21. Katopodis, A. G.; Warner, R. G.; Duthaler, R. O.; Streiff, M. B.; Bruelisauer, A.; Kretz, O.; Dorobek, B.; Persohn, E.; Andres, H.; Schweitzer, A.; Thoma, G.; Kinzy, W.; Quesniaux, V. F.; Cozzi, E.; Davies, H. F.; Mañez, R.; White, D., Removal of anti-Gal α 1,3Gal xenoantibodies with an injectable polymer. *J Clin Invest* **2002**, *110* (12), 1869-77.
22. Li, J.; Yu, F.; Chen, Y.; Oupický, D., Polymeric drugs: Advances in the development of pharmacologically active polymers. *J Control Release* **2015**, *219*, 369-382.
23. Ekladius, I.; Colson, Y. L.; Grinstaff, M. W., Polymer-drug conjugate therapeutics: advances, insights and prospects. *Nat Rev Drug Discov* **2019**, *18* (4), 273-294.
24. Bartneck, M.; Schlöber, C. T.; Barz, M.; Zentel, R.; Trautwein, C.; Lammers, T.; Tacke, F., Immunomodulatory Therapy of Inflammatory Liver Disease Using Selectin-Binding Glycopolymers. *ACS Nano* **2017**, *11* (10), 9689-9700.
25. Aied, A.; Greiser, U.; Pandit, A.; Wang, W., Polymer gene delivery: overcoming the obstacles. *Drug Discov Today* **2013**, *18* (21-22), 1090-8.
26. Kulkarni, S. A.; Feng, S. S., Effects of particle size and surface modification on cellular uptake and biodistribution of polymeric nanoparticles for drug delivery. *Pharm Res* **2013**, *30* (10), 2512-22.

27. He, C.; Hu, Y.; Yin, L.; Tang, C.; Yin, C., Effects of particle size and surface charge on cellular uptake and biodistribution of polymeric nanoparticles. *Biomaterials* **2010**, *31* (13), 3657-66.
28. Zhou, D.; Li, C.; Hu, Y.; Zhou, H.; Chen, J.; Zhang, Z.; Guo, T., Glycopolymers modification on physicochemical and biological properties of poly(L-lysine) for gene delivery. *Int J Biol Macromol* **2012**, *50* (4), 965-73.
29. Rojko, J. L.; Evans, M. G.; Price, S. A.; Han, B.; Waine, G.; DeWitte, M.; Haynes, J.; Freimark, B.; Martin, P.; Raymond, J. T.; Evering, W.; Rebelatto, M. C.; Schenck, E.; Horvath, C., Formation, clearance, deposition, pathogenicity, and identification of biopharmaceutical-related immune complexes: review and case studies. *Toxicol Pathol* **2014**, *42* (4), 725-64.
30. Sukhanova, A.; Bozrova, S.; Sokolov, P.; Berestovoy, M.; Karaulov, A.; Nabiev, I., Dependence of Nanoparticle Toxicity on Their Physical and Chemical Properties. *Nanoscale Res Lett* **2018**, *13* (1), 44.
31. Alexis, F.; Pridgen, E.; Molnar, L. K.; Farokhzad, O. C., Factors affecting the clearance and biodistribution of polymeric nanoparticles. *Mol Pharm* **2008**, *5* (4), 505-15.
32. Liu, M.; Li, H.; Luo, G.; Liu, Q.; Wang, Y., Pharmacokinetics and biodistribution of surface modification polymeric nanoparticles. *Arch Pharm Res* **2008**, *31* (4), 547-54.
33. Owens, D. E.; Peppas, N. A., Opsonization, biodistribution, and pharmacokinetics of polymeric nanoparticles. *Int J Pharm* **2006**, *307* (1), 93-102.
34. Stevenson, L.; Huda, P.; Jeppesen, A.; Laursen, E.; Rowe, J. A.; Craig, A.; Streicher, W.; Barfod, L.; Hviid, L., Investigating the function of Fc-specific binding of IgM to Plasmodium falciparum erythrocyte membrane protein 1 mediating erythrocyte rosetting. *Cell Microbiol* **2015**, *17* (6), 819-31.
35. Schilling, K.; Krause, F., Analysis of antibody aggregate content at extremely high concentrations using sedimentation velocity with a novel interference optics. *PLoS One* **2015**, *10* (3), e0120820.
36. Ishiwata, H.; Suzuki, N.; Ando, S.; Kikuchi, H.; Kitagawa, T., Characteristics and biodistribution of cationic liposomes and their DNA complexes. *J Control Release* **2000**, *69* (1), 139-48.
37. Rothkopf, C.; Fahr, A.; Fricker, G.; Scherphof, G. L.; Kamps, J. A., Uptake of phosphatidylserine-containing liposomes by liver sinusoidal endothelial cells in the serum-free perfused rat liver. *Biochim Biophys Acta* **2005**, *1668* (1), 10-6.
38. Yue, Z. G.; Wei, W.; Lv, P. P.; Yue, H.; Wang, L. Y.; Su, Z. G.; Ma, G. H., Surface charge affects cellular uptake and intracellular trafficking of chitosan-based nanoparticles. *Biomacromolecules* **2011**, *12* (7), 2440-6.
39. Rasmussen, R.; Nedergaard, M.; Petersen, N. C., Sulforhodamine 101, a widely used astrocyte marker, can induce cortical seizure-like activity at concentrations commonly used. *Sci Rep* **2016**, *6*, 30433.
40. Mebius, R. E.; Kraal, G., Structure and function of the spleen. *Nat Rev Immunol* **2005**, *5* (8), 606-16.
41. Cataldi, M.; Vigliotti, C.; Mosca, T.; Cammarota, M.; Capone, D., Emerging Role of the Spleen in the Pharmacokinetics of Monoclonal Antibodies, Nanoparticles and Exosomes. *Int J Mol Sci* **2017**, *18* (6).

42. Austyn, J. M.; Gordon, S., F4/80, a monoclonal antibody directed specifically against the mouse macrophage. *Eur J Immunol* **1981**, *11* (10), 805-15.
43. Baratta, J. L.; Ngo, A.; Lopez, B.; Kasabwalla, N.; Longmuir, K. J.; Robertson, R. T., Cellular organization of normal mouse liver: a histological, quantitative immunocytochemical, and fine structural analysis. *Histochem Cell Biol* **2009**, *131* (6), 713-26.
44. Campbell, F.; Bos, F. L.; Sieber, S.; Arias-Alpizar, G.; Koch, B. E.; Huwyler, J.; Kros, A.; Busmann, J., Directing Nanoparticle Biodistribution through Evasion and Exploitation of Stab2-Dependent Nanoparticle Uptake. *ACS Nano* **2018**, *12* (3), 2138-2150.
45. Kettiger, H.; Sen Karaman, D.; Schiesser, L.; Rosenholm, J. M.; Huwyler, J., Comparative safety evaluation of silica-based particles. *Toxicol In Vitro* **2015**, *30* (1 Pt B), 355-63.
46. Takashiba, S.; Van Dyke, T. E.; Amar, S.; Murayama, Y.; Soskolne, A. W.; Shapira, L., Differentiation of monocytes to macrophages primes cells for lipopolysaccharide stimulation via accumulation of cytoplasmic nuclear factor kappaB. *Infect Immun* **1999**, *67* (11), 5573-8.
47. Nath, N.; Godat, B.; Zimprich, C.; Dwight, S. J.; Corona, C.; McDougall, M.; Urh, M., Homogeneous plate based antibody internalization assay using pH sensor fluorescent dye. *J Immunol Methods* **2016**, *431*, 11-21.
48. Flannagan, R. S.; Jaumouillé, V.; Grinstein, S., The cell biology of phagocytosis. *Annu Rev Pathol* **2012**, *7*, 61-98.
49. dos Santos, T.; Varela, J.; Lynch, I.; Salvati, A.; Dawson, K. A., Effects of transport inhibitors on the cellular uptake of carboxylated polystyrene nanoparticles in different cell lines. *PLoS One* **2011**, *6* (9), e24438.
50. Thelen, T.; Hao, Y.; Medeiros, A. I.; Curtis, J. L.; Serezani, C. H.; Kobzik, L.; Harris, L. H.; Aronoff, D. M., The class A scavenger receptor, macrophage receptor with collagenous structure, is the major phagocytic receptor for *Clostridium sordellii* expressed by human decidual macrophages. *J Immunol* **2010**, *185* (7), 4328-35.
51. Harris, E. N.; Weigel, P. H., The ligand-binding profile of HARE: hyaluronan and chondroitin sulfates A, C, and D bind to overlapping sites distinct from the sites for heparin, acetylated low-density lipoprotein, dermatan sulfate, and CS-E. *Glycobiology* **2008**, *18* (8), 638-48.
52. Marsche, G.; Zimmermann, R.; Horiuchi, S.; Tandon, N. N.; Sattler, W.; Malle, E., Class B scavenger receptors CD36 and SR-BI are receptors for hypochlorite-modified low density lipoprotein. *J Biol Chem* **2003**, *278* (48), 47562-70.
53. Seastone, D. J.; Harris, E.; Temesvari, L. A.; Bear, J. E.; Saxe, C. L.; Cardelli, J., The WASp-like protein scar regulates macropinocytosis, phagocytosis and endosomal membrane flow in *Dictyostelium*. *J Cell Sci* **2001**, *114* (Pt 14), 2673-83.
54. PrabhuDas, M. R.; Baldwin, C. L.; Bollyky, P. L.; Bowdish, D. M. E.; Drickamer, K.; Febbraio, M.; Herz, J.; Kobzik, L.; Krieger, M.; Loike, J.; McVicker, B.; Means, T. K.; Moestrup, S. K.; Post, S. R.; Sawamura,

- T.; Silverstein, S.; Speth, R. C.; Telfer, J. C.; Thiele, G. M.; Wang, X. Y.; Wright, S. D.; El Khoury, J., A Consensus Definitive Classification of Scavenger Receptors and Their Roles in Health and Disease. *J Immunol* **2017**, *198* (10), 3775-3789.
55. Elshourbagy, N. A.; Li, X.; Terrett, J.; Vanhorn, S.; Gross, M. S.; Adamou, J. E.; Anderson, K. M.; Webb, C. L.; Lysko, P. G., Molecular characterization of a human scavenger receptor, human MARCO. *Eur J Biochem* **2000**, *267* (3), 919-26.
 56. Plüddemann, A.; Mukhopadhyay, S.; Sankala, M.; Savino, S.; Pizza, M.; Rappuoli, R.; Tryggvason, K.; Gordon, S., SR-A, MARCO and TLRs differentially recognise selected surface proteins from *Neisseria meningitidis*: an example of fine specificity in microbial ligand recognition by innate immune receptors. *J Innate Immun* **2009**, *1* (2), 153-63.
 57. Godoy, P.; Hewitt, N. J.; Albrecht, U.; Andersen, M. E.; Ansari, N.; Bhattacharya, S.; Bode, J. G.; Bolleyn, J.; Borner, C.; Böttger, J.; Braeuning, A.; Budinsky, R. A.; Burkhardt, B.; Cameron, N. R.; Camussi, G.; Cho, C. S.; Choi, Y. J.; Craig Rowlands, J.; Dahmen, U.; Damm, G.; Dirsch, O.; Donato, M. T.; Dong, J.; Dooley, S.; Drasdo, D.; Eakins, R.; Ferreira, K. S.; Fonsato, V.; Fraczek, J.; Gebhardt, R.; Gibson, A.; Glanemann, M.; Goldring, C. E.; Gómez-Lechón, M. J.; Groothuis, G. M.; Gustavsson, L.; Guyot, C.; Hallifax, D.; Hammad, S.; Hayward, A.; Häussinger, D.; Hellerbrand, C.; Hewitt, P.; Hoehme, S.; Holzhütter, H. G.; Houston, J. B.; Hrach, J.; Ito, K.; Jaeschke, H.; Keitel, V.; Kelm, J. M.; Kevin Park, B.; Kordes, C.; Kullak-Ublick, G. A.; LeCluyse, E. L.; Lu, P.; Luebke-Wheeler, J.; Lutz, A.; Maltman, D. J.; Matz-Soja, M.; McMullen, P.; Merfort, I.; Messner, S.; Meyer, C.; Mwinyi, J.; Naisbitt, D. J.; Nussler, A. K.; Olinga, P.; Pampaloni, F.; Pi, J.; Pluta, L.; Przyborski, S. A.; Ramachandran, A.; Rogiers, V.; Rowe, C.; Schelcher, C.; Schmich, K.; Schwarz, M.; Singh, B.; Stelzer, E. H.; Stieger, B.; Stöber, R.; Sugiyama, Y.; Tetta, C.; Thasler, W. E.; Vanhaecke, T.; Vinken, M.; Weiss, T. S.; Widera, A.; Woods, C. G.; Xu, J. J.; Yarborough, K. M.; Hengstler, J. G., Recent advances in 2D and 3D in vitro systems using primary hepatocytes, alternative hepatocyte sources and non-parenchymal liver cells and their use in investigating mechanisms of hepatotoxicity, cell signaling and ADME. *Arch Toxicol* **2013**, *87* (8), 1315-530.
 58. Hoppe, C. A.; Lee, Y. C., Accumulation of a nondegradable mannose ligand within rabbit alveolar macrophages. Receptor reutilization is independent of ligand degradation. *Biochemistry* **1984**, *23* (8), 1723-30.
 59. Lokhande, A. S.; Jahagirdar, P.; Dandekar, P.; Devarajan, P. V., Scavenger Receptor and Targeting Strategies. In *Targeted Intracellular Drug Delivery by Receptor Mediated Endocytosis*, Devarajan, P. V.; Dandekar, P.; D'Souza, A. A., Eds. Springer International Publishing: Cham, 2019; pp 297-321.
 60. Clogston, J. D.; Patri, A. K., Zeta potential measurement. *Methods Mol Biol* **2011**, *697*, 63-70.
 61. Schuck, P., Size-distribution analysis of macromolecules by sedimentation velocity ultracentrifugation and lamm equation modeling. *Biophys J* **2000**, *78* (3), 1606-19.

Supporting Information

Glycopolymer binds pathogenic IgM autoantibodies and pulls them into the mononuclear phagocyte system for degradation

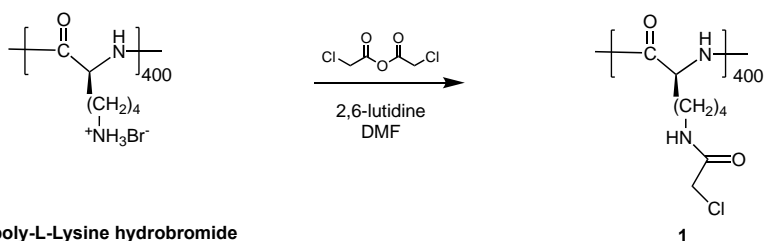
Butrint Aliu¹, Delphine Demeestere¹, Lijuan Pang^{1,2}, Timothy Sharpe³, Wolf Heusermann⁴, Ruben Herrendorff^{1,2}, Beat Ernst¹, Pascal Hänggi^{1,2*}

¹Institute of Molecular Pharmacy, Department of Pharmaceutical Sciences, University of Basel, 4056 Basel, Switzerland; ²Polyneuron Pharmaceuticals AG, 4057 Basel, Switzerland; ³Biophysics Facility, Biozentrum, University of Basel, 4056 Basel, Switzerland ⁴Imaging Core Facility, Biozentrum, University of Basel, 4056 Basel, Switzerland

Synthetic procedure of PPSGG labeled with sulforhodamine and pHAb

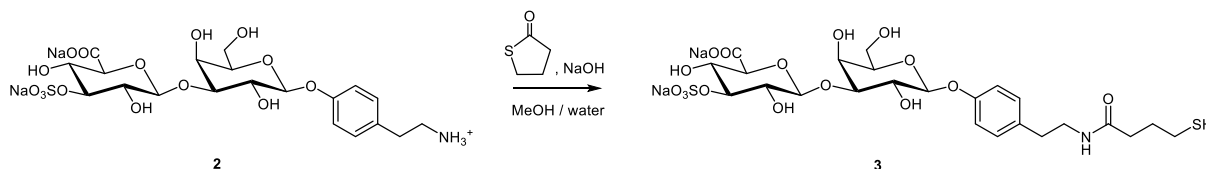
General methods. NMR spectra were recorded on a Bruker Avance DMX-500 (500 MHz) spectrometer. Chemical shifts are described in ppm using residual HDO as reference. Reactions were monitored by TLC using glass plates coated with silica gel 60 F254 (Merck) and visualized by using UV light and/or by heating to 140°C for 5 min after dipping in a molybdate solution (a 0.02 M solution of ammonium cerium(IV) sulfate dihydrate and ammonium molybdate tetrahydrate in aqueous 10% H₂SO₄). Commercially available reagents were purchased from Sigma-Aldrich, except the pHAb amine reactive dye, which was purchased from Promega Corporation. Column chromatography was performed on a CombiFlash Companion (Teledyne-ISCO, Inc.) using RediSep reverse phase C-18 flash columns.

Synthesis of chloroacetylated poly-L-lysine (1)



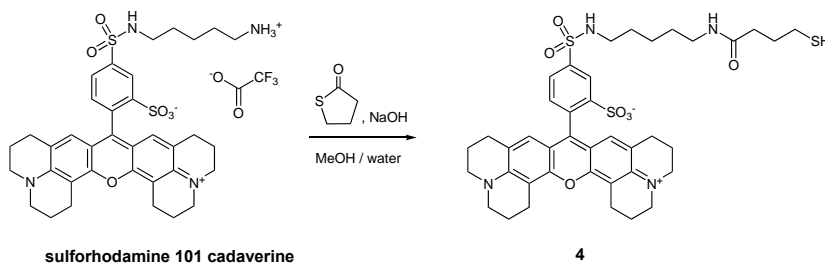
Poly-L-lysine hydrobromide (100 mg, 0.48 mmol of lysine units) was suspended in a mixture of DMF (2 mL) and 2,6-lutidine (0.5 mL). The mixture was cooled in ice-water bath, before chloroacetic anhydride (244 mg, dissolved in 0.5 mL of DMF) was added via syringe over 10 min. Poly-L-lysine was gradually dissolved during the addition of the chloroacetic anhydride solution, and the reaction mixture became clear before completely addition. The reaction mixture was then stirred at 4 °C for 16 hours. The product was precipitated by dropwise addition of the reaction mixture to 40 mL of a vigorously stirred 1:1 mixture of ethanol and diethyl ether. A cloudy precipitate was formed immediately. The mixture was centrifuged at 1000 rpm, 4-10 °C for 2 min. The solvent was decanted, and the residue was re-suspended in ethanol/ether (1:1, 30 mL). The centrifugation and re-suspension was repeated three times. The product was collected and dried under vacuum overnight. Yield: 92 mg (96%) as white solid. ¹HNMR data were identical to the previous report.¹

Synthesis of sulfhydryl-equipped disaccharide (3)



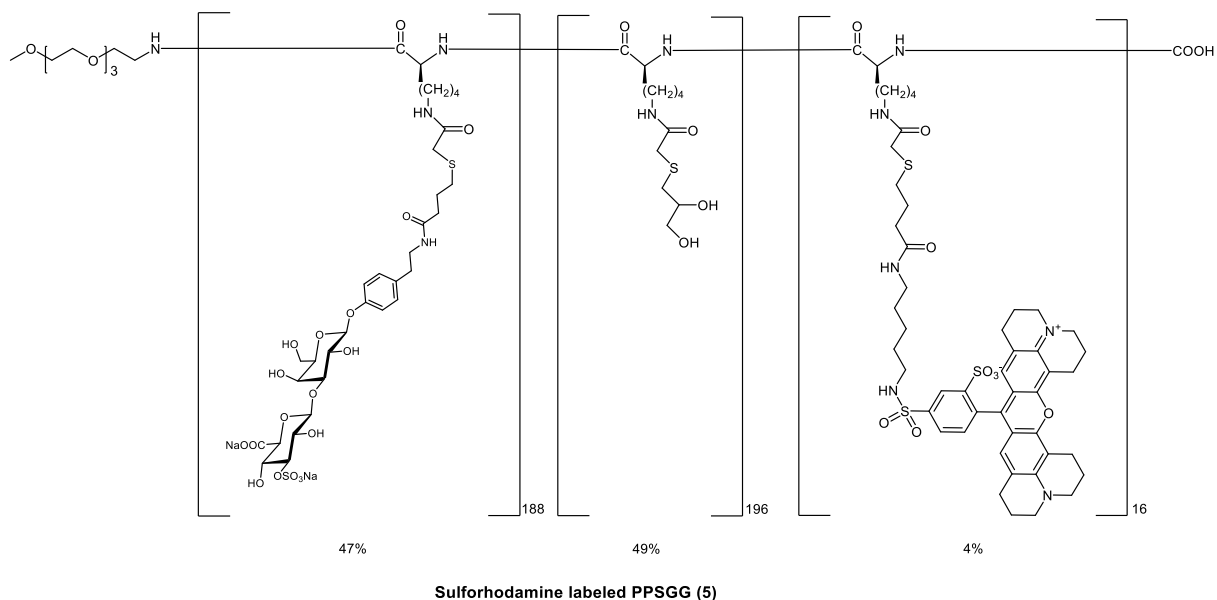
To a solution of disaccharide **2** (50 mg, 83.5 μmol)¹ in water (116 μL) at room temperature, were added 1M NaOH (72 μL), 4-butyrothiolactone (72 μL , 835 μmol) and methanol (300 μL). The reaction mixture was stirred at room temperature overnight. After removal of methanol under vacuum, the aqueous phase was washed with ethyl acetate (400 μL , 3 times). The aqueous phase was then lyophilized and used directly in next step. Yield: 55 mg (94%) as white solid. ¹HNMR data were identical to the previous report.¹

Synthesis of sulfhydryl-equipped sulforhodamine (4)



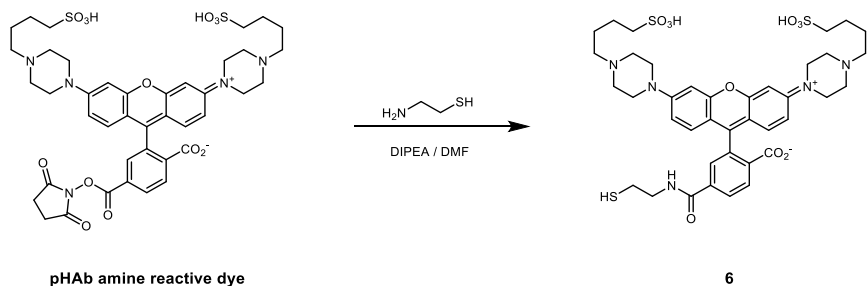
To a solution of sulforhodamine 101 cadaverine (5 mg, 6.22 μmole) in water (100 μL) were added 1M NaOH (18.6 μL), 4-butyrothiolactone (5.4 μL , 62.2 μmol) and methanol (100 μL). The reaction mixture was stirred at room temperature overnight. The mixture was loaded onto a reverse phase C-18 column, and the column eluted with 5% to 100% acetonitrile/water. The product fraction was collected, dried by lyophilization and yielded 1.2 mg (25%) of **4** as violet solid.

Synthesis of sulforhodamine labeled PPSGG (5)



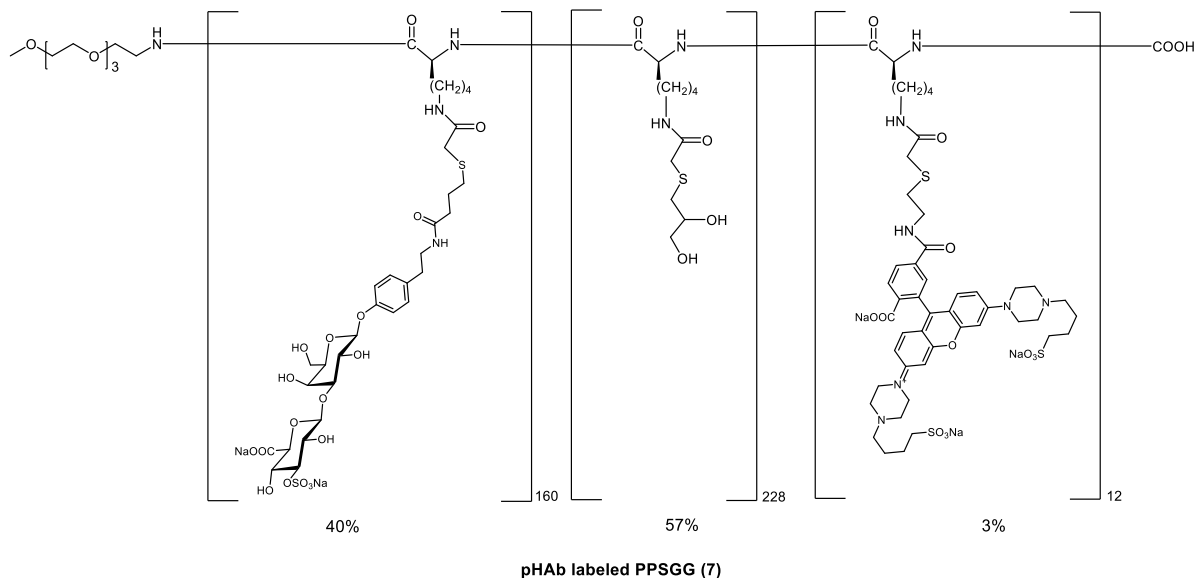
To a stirring solution of acetylated poly-L-lysine-400 (**1**) (8 mg, 39.1 μmol of lysine units) in DMF (389 μL), a solution of disaccharide (**3**) (10 mg, 17.6 μmol) in 30 μL of water and a solution of sulforhodamine (**4**) (0.26 mg, 0.7 μmol) in 50 μL of DMF were added. 1,8-diazabicyclo[5.4.0]undec-7-ene (5.8 μL , 39.1 μmol) was added to the above mixture. The reaction mixture was then stirred at room temperature under argon atmosphere for 1 hour. Thioglycerol (3.4 μL , μmol) and trimethylamine (5.5 μL , 39.1 μmol) were added and the mixture was stirred for additional 16 hours. The reaction mixture was added dropwise to a stirred solution of diethyl ether/ethanol (1:1; 3ml), leading to the precipitation of the polymer. The polymer was collected by centrifugation, washed with ethanol (3 mL), and then dissolved with 10 mL of water. 1M aqueous NaOH (0.1 mL) was added to the polymer solution to adjust the pH to basic. The solution was purified by ultracentrifugation (3 times from 10 mL to 0.5 mL; washed with water; molecular cutoff 50kDa). The product was lyophilized within four hours (Caution: over-dry can lead to insolubility in water) yielding 14.5 mg (63.7%) of the violet solid **5**. Loading: 47 % disaccharide determined by $^1\text{H-NMR}$ (integration of CH_2 sugar peak at 2.42 -2.56 ppm *versus* thioglycerol peak at 2.56-2.65 ppm).

Synthesis of sulfhydryl-equipped pHAb dye (6)



To a mixture of pHAb amine reactive dye (500 μg , 0.57 μmol) and *N,N*-diisopropylethylamine (10 μL , 57 μmol) in DMF (200 μL), an aqueous solution of 2-aminoethanethiol (2 μL , 0.1 mg/ μL) was added. The reaction mixture was stirred at room temperature until completion was detected by TLC (dichloromethane/methanol 1:1). The crude reaction mixture was used directly in the next step for the synthesis of the labeled polymers **7** and **8**.

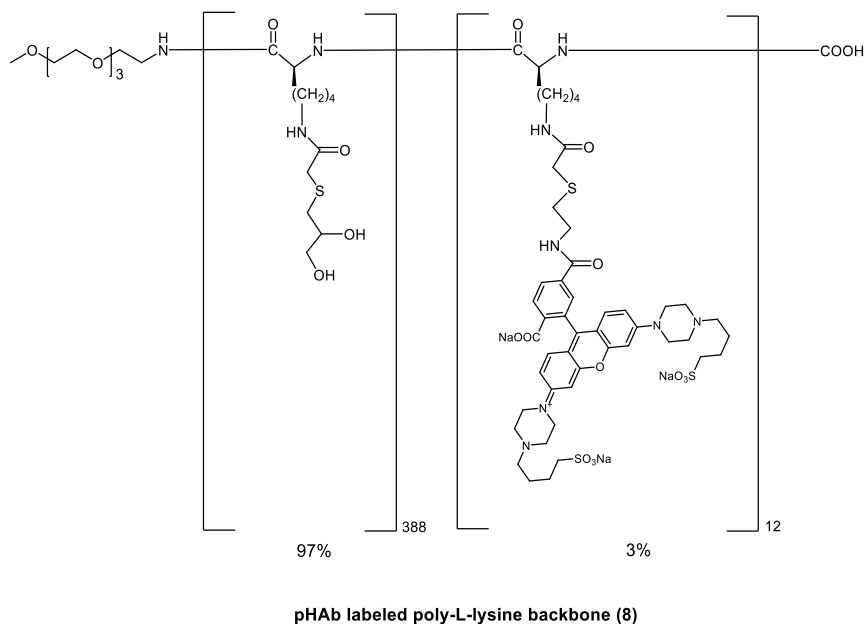
Synthesis of pHAb dye-labeled PPSGG (7)



To a stirred solution of acetylated poly-L-lysine (**1**) (3.8 mg, 18.9 μmol of lysine units) in DMF (300 μL), a solution of sulfhydryl-equipped pHAb dye (500 μg) containing *N,N*-diisopropylethylamine (10 μL , 57 μmol) and DMF (200 μL) was added. 1,8-diazabicyclo[5.4.0]undec-7-ene (2.8 μL , 18.9 μmol) was then added to the above mixture. The reaction mixture was stirred at room temperature under argon atmosphere for 10 minutes, before

a solution of disaccharide (**4**) (5.6 mg, 8 μmol) in 30 μL of water was added. The reaction mixture was stirred at room temperature under argon atmosphere for 45 minutes. Then thioglycerol (4.8 μL , 55.6 μmol) and trimethylamine (7.7 μL , 55.6 μmol) were added and the reaction mixture was stirred for additional 16 hours, before it was dropped into a stirred solution of diethyl ether/ethanol (1:1, 4ml), leading to polymer precipitate. The precipitate was collected by centrifugation, washed with ethanol (3 mL), and then dissolved with 10 mL of water. 1M aqueous NaOH (0.1 mL) was added to the polymer to adjust the pH to basic. The solution was purified by ultracentrifugation (3 times from 10 mL to 0.5 mL; washed with water; molecular cutoff 50kDa). The product was lyophilized within 6 hours (Caution: over-dry can lead to insolubility in water) Yield: 6 mg (60%) of a purple solid. Loading: 40 % disaccharide by $^1\text{H-NMR}$ integration (CH_2 sugar peak at 2.42 - 2.56 ppm *versus* thioglycerol peak at 2.56-2.65 ppm).

Synthesis of pHAb dye-labeled poly-L-lysine (**8**).

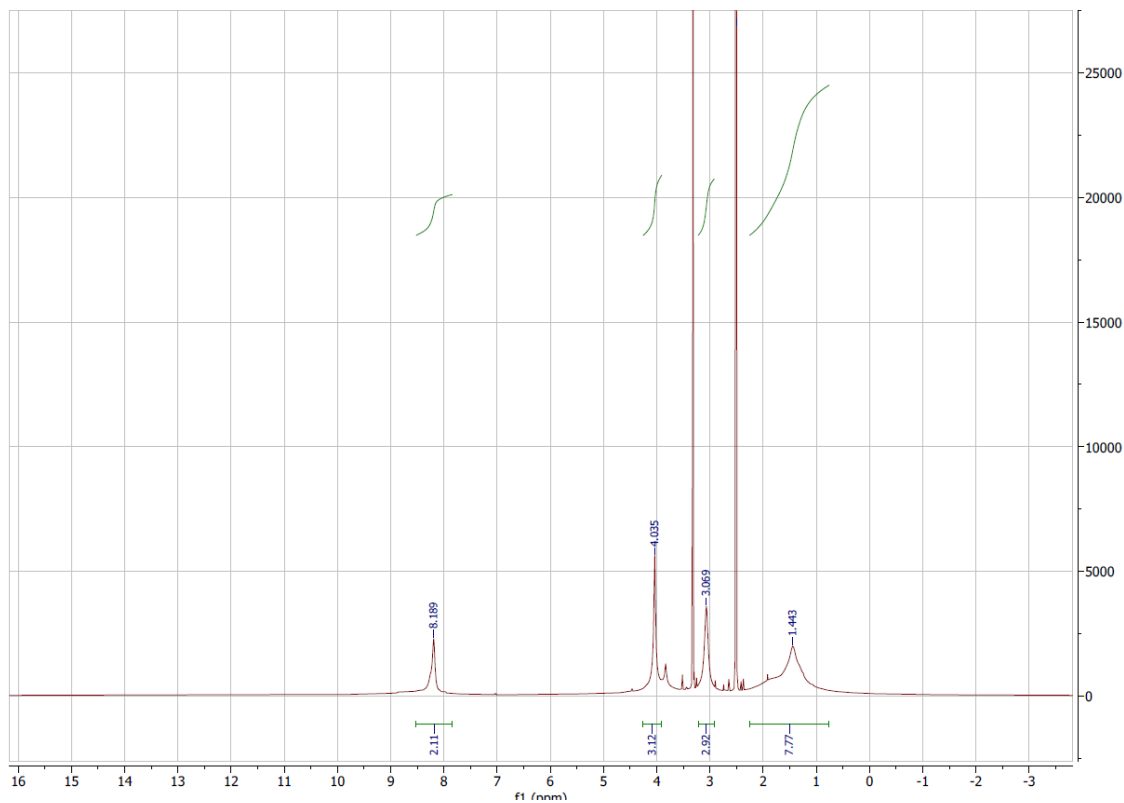


To a stirred solution of acetylated poly-L-lysine (**1**) (3.8 mg, 18.9 μmol) in DMF (262 μL), a solution of sulfhydryl-equipped pHAb dye (500 μg) containing *N,N*-diisopropylethylamine (10 μL , 57 μmol) and DMF (200 μL) was added. 1,8-diazabicyclo[5.4.0]undec-7-ene (2.8 μL , 18.9 μmol) was then added to the above mixture. The reaction mixture was stirred at room temperature under argon atmosphere for 10 minutes, followed the addition of 30 μL of water. The reaction mixture was stirred at room temperature under argon atmosphere for 45 minutes. Then thioglycerol (4.8 μL , 55.6 μmol) and trimethylamine (7.7 μL , 55.6 μmol) were added and the mixture was

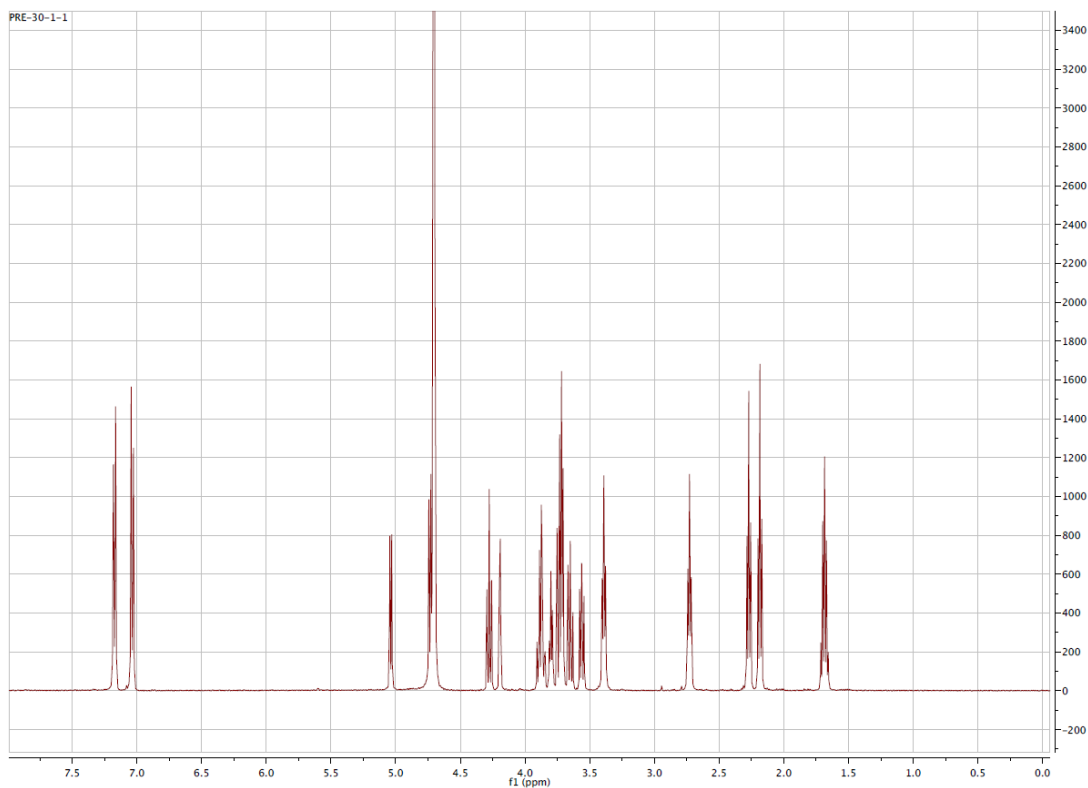
stirred for additional 16 hours. The reaction mixture was dropped into a stirred solution of diethyl ether/ethanol (1:1, 4ml), yielding to the precipitated polymer. The polymer was collected by centrifugation, washed with ethanol (3 mL), and then dissolved with 10 mL of water. 1M aqueous NaOH (0.1 mL) was added to the polymer solution to adjust the pH to basic. The solution was purified by ultracentrifugation (3 times from 10 mL to 0.5 mL; washed with water; molecular cutoff 50kDa). The product was lyophilized within 6 hours (Caution: over-dry can lead to insolubility in water). Yield: 3 mg (70 %) as a purple solid.

¹H-NMR Spectra

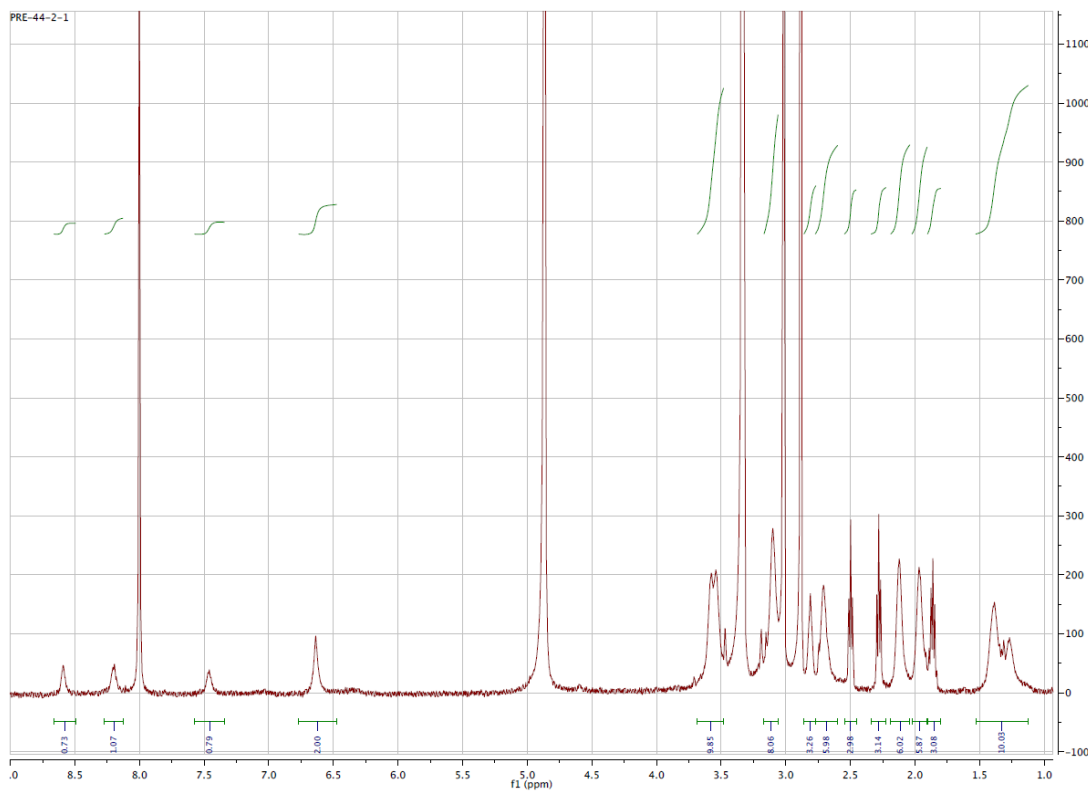
Compound 1 (500MHz, *d*₆-DMSO)



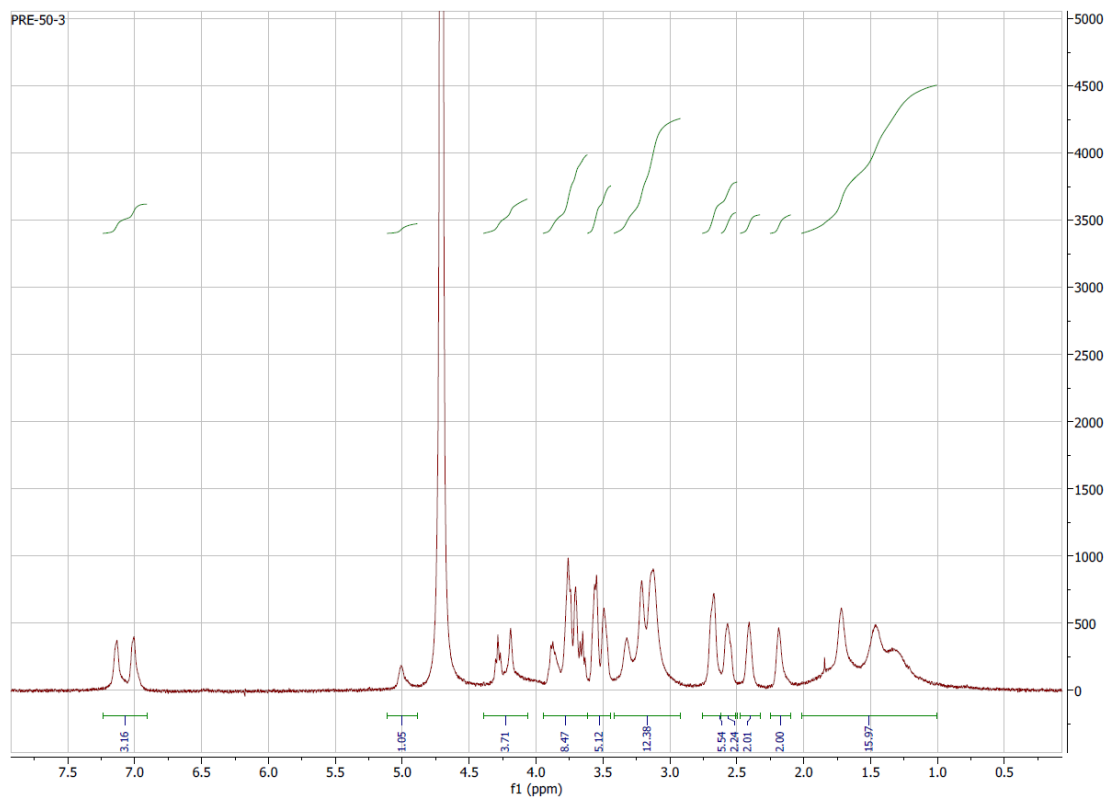
Compound 3 (500 MHz, D₂O)



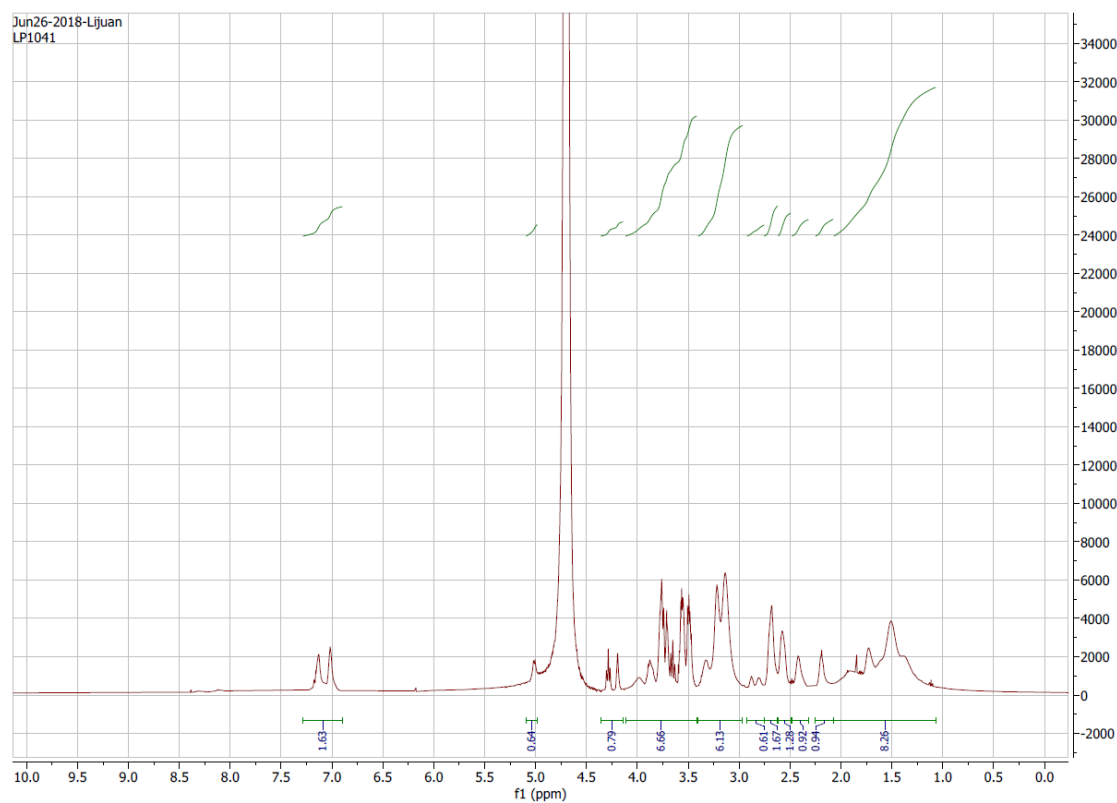
Compound 4 (500 MHz, D₂O)



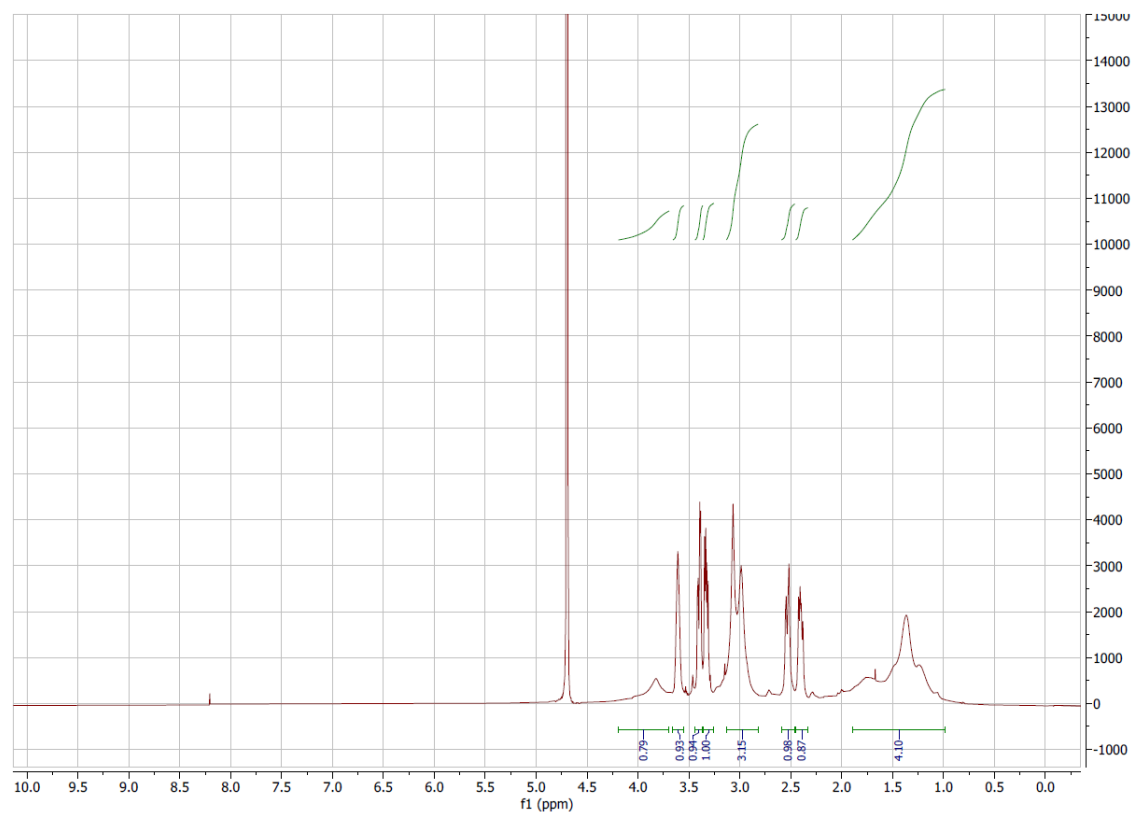
Compound 5 (500 MHz, D₂O)



Compound 7 (500 MHz, D₂O)



Compound 8 (500 MHz, D₂O)



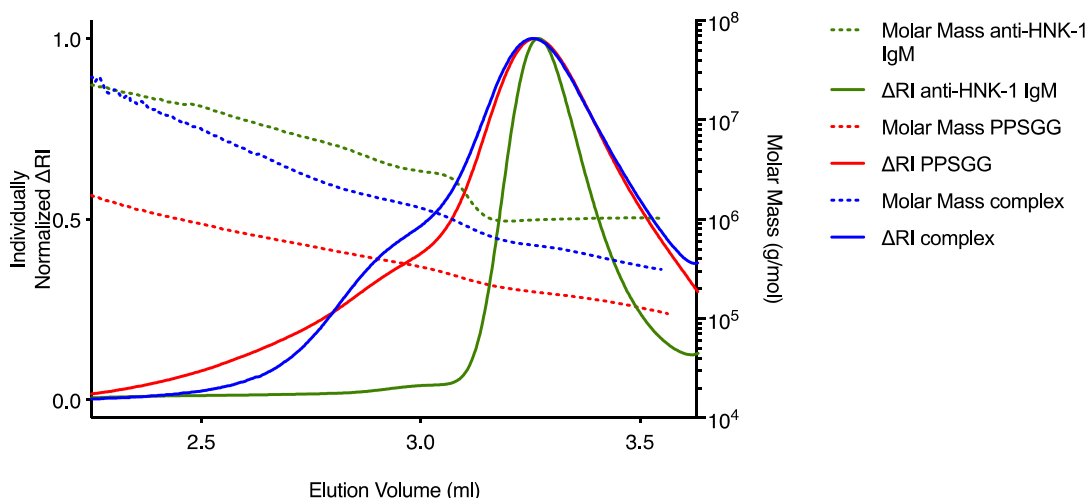


Figure S1. Size Exclusion Chromatography (SEC) - Multi Angle Light Scattering (MALS)

SEC-MALS measurements were performed on an Agilent 1260 HPLC coupled to an Agilent multi-wavelength absorbance detector, a Wyatt Heleos II 8+ MALS detector, and a Wyatt Optilab rEX differential refractive index detector (dRI), using a 1000 Å silica column (WTC1000N5, Silica SEC column, 4.6x300 mm, 5 micron beads, 1000 angstrom pore size, Wyatt Technology, United Kingdom). The column was equilibrated overnight in PBS to stabilize the baseline signals of the detectors. The alignment, band broadening and detector normalization was performed using thyroglobulin G (T9145, Sigma-Aldrich, Switzerland). Individual samples of PPSGG (1 mg/ml), anti-HNK-1 IgM (1 mg/ml, C6680, Sigma-Aldrich, Switzerland), and pre-incubated complexes of PPSGG and anti-HNK-1 IgM were separated. Anti-HNK-1 IgM shows a narrow peak at 3.3 ml (green graph) with a stable molecular weight of approx. 1 MDa. PPSGG shows a higher polydispersity and a broader size distribution with a shoulder at 3 mL (red graph). The polydispersity of PPSGG limits adequate peak discrimination for accurate stoichiometry estimation in the sample containing the complexes (blue graph).

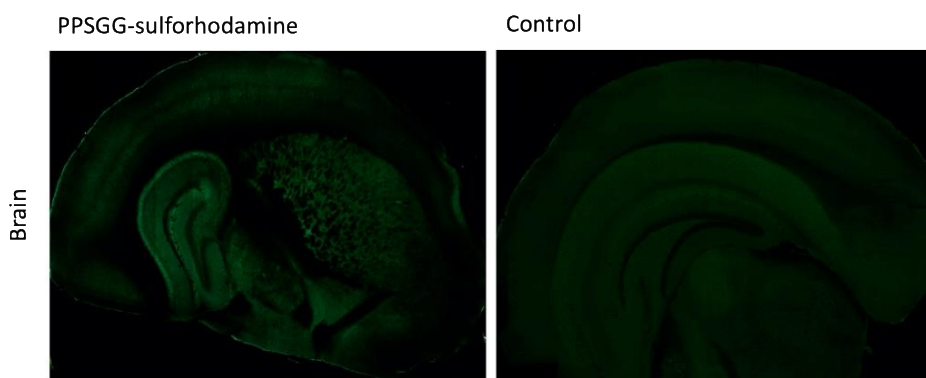


Figure S2. PPSGG-sulforhodamine (5) does not cross the blood-brain-barrier

The tissue distribution of fluorescence labeled and IV injected 300 µg PPSGG-sulforhodamine (5, red) 1 h. Perfused organs were harvested and embedded in agarose for imaging with a TissueVision by serial two-photon tomography. No staining of the brain by fluorescent PPSGG is observed and thus the crossing of the blood brain barrier is unlikely.

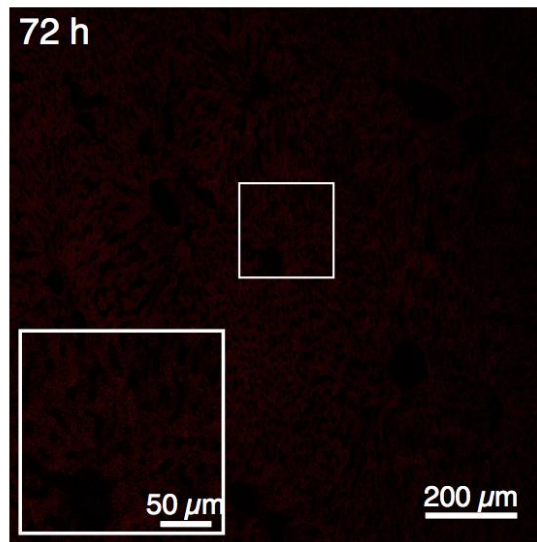
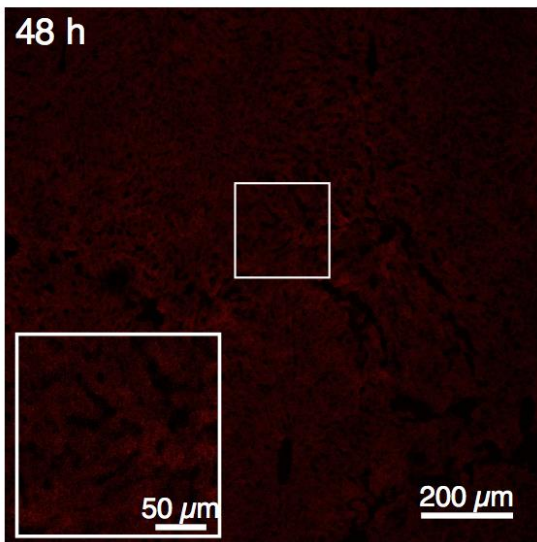
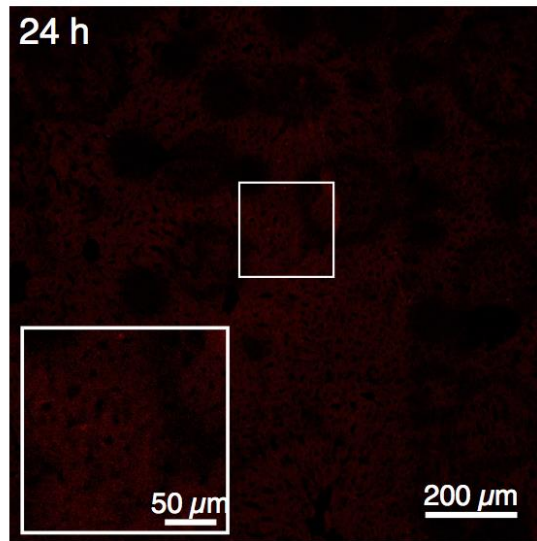
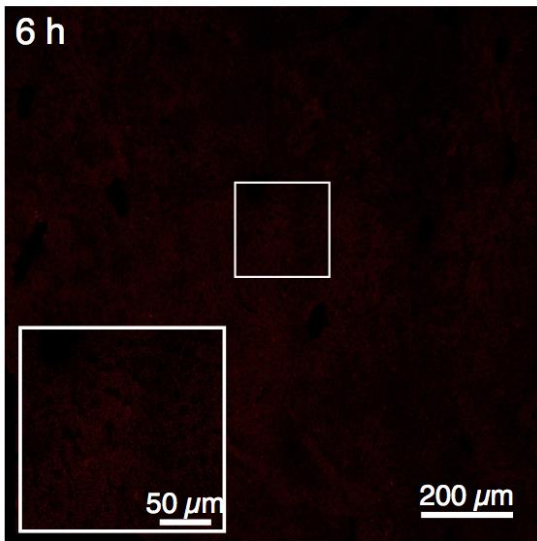
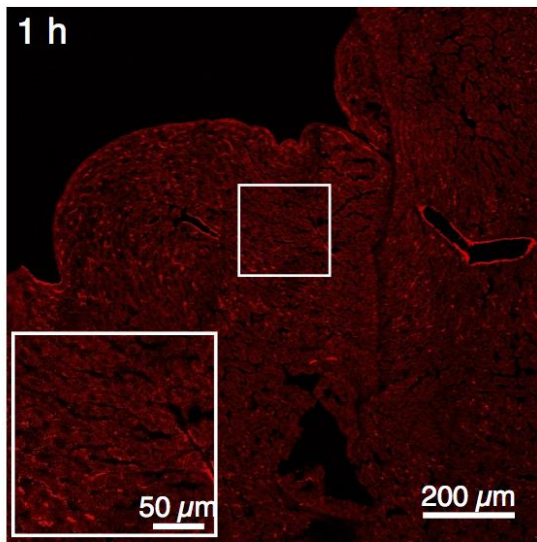
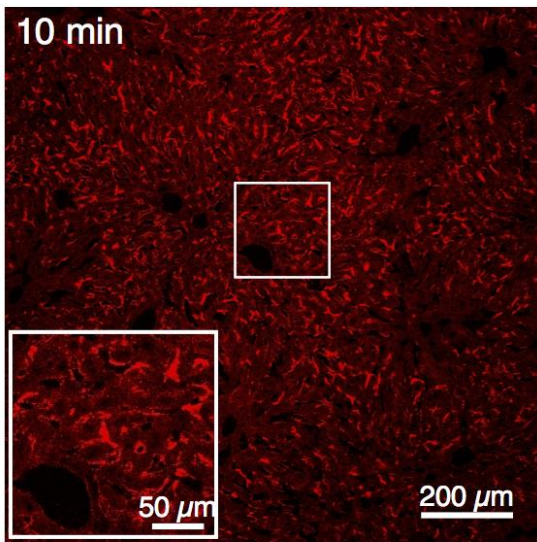


Figure S3. Time profile of PPSGG-sulforhodamine (5) elimination in the liver

Confocal images of liver sections from mice treated with 300 μg PPSGG-sulforhodamine (5, red) were recorded with the Leica SP8 point scanning confocal microscope. The images show a quick uptake of PPSGG-sulforhodamine (5) in the liver of the animals and a rapid and sustained decrease in signal after 1 h. No fluorescent signal was detected 6 h post IV injection of the mice. The later time points (24 h, 48 h, 72 h) confirm the sustained elimination of PPSGG-sulforhodamine (5).

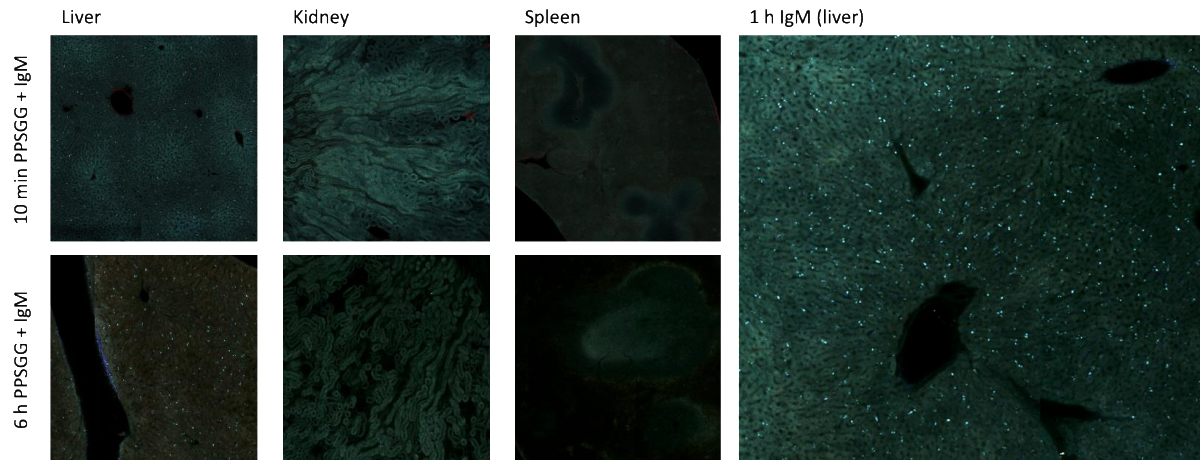


Figure S4. Tissue distribution of anti-HNK-1 IgM and PPSGG-sulforhodamine (5)

The tissue distribution of fluorescence labeled and IV injected 300 μg PPSGG-sulforhodamine (5, red) and 60 μg anti-MAG IgM (blue) in BALB/c mice after 10 min and 6 h. The right panel shows the injection of 60 μg anti-MAG IgM (blue) after 1 h. The perfused organs were harvested at the specific timepoints and embedded in agarose for imaging with a TissueVision by serial two-photon tomography.

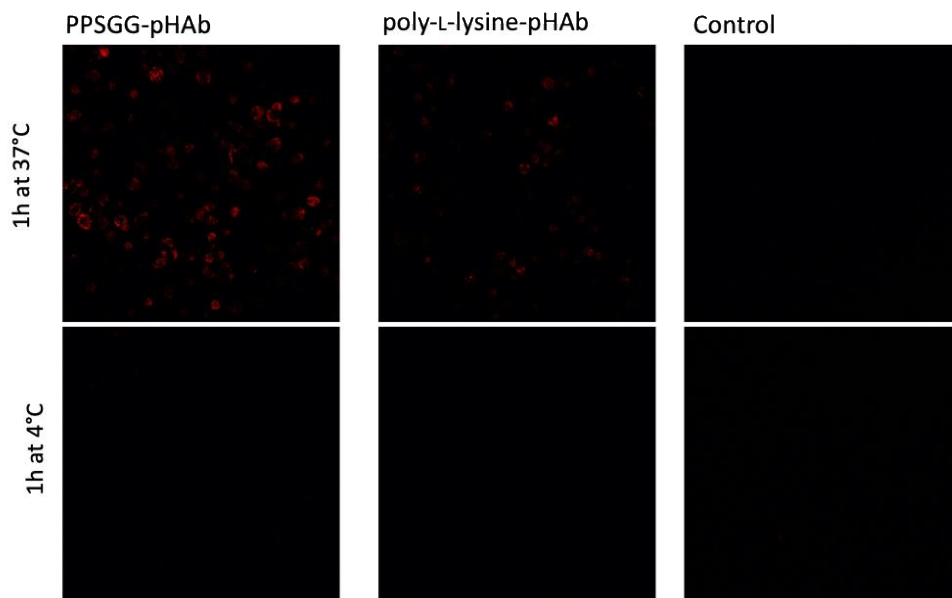


Figure S5. Active uptake of PPSGG-pHAb (7) is temperature dependent

Uptake of pHAb labelled PPSGG (7, 1 μ M) and pHAb labelled poly-L-lysine backbone (8, 1 μ M) in human macrophages (THP-1) is temperature dependent. No uptake takes place at 4°C, compared to an extensive uptake at 37°C, indicating an active uptake mechanism. The uptake of the carbohydrate bearing PPSGG-pHAb (7) is much more pronounced compared to the thioglycerol capped poly-L-lysine (poly-L-lysine-pHAb), highlighting the importance of the negatively charged carbohydrate epitopes for efficient uptake in the macrophages.

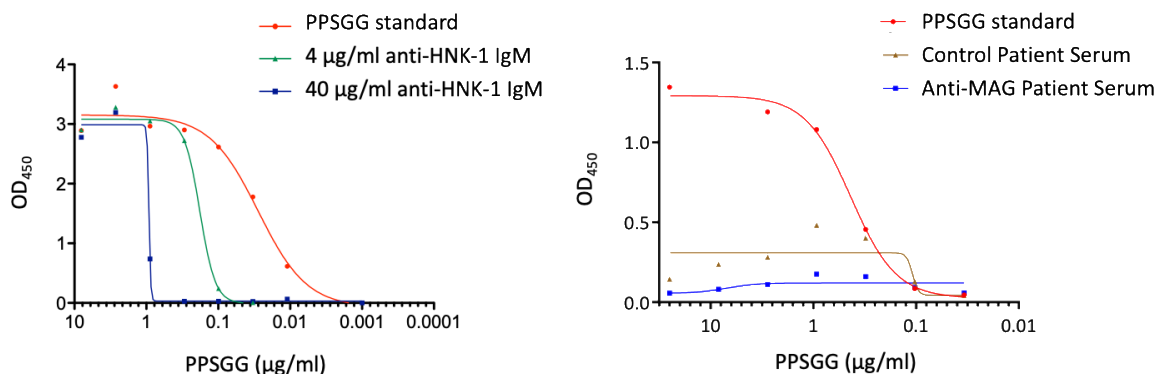


Figure S6. Recognition of the anti-HNK-1 IgM is reduced when co-incubated with PPSGG

PPSGG and anti-HNK-1 IgM form complexes in vitro and in vivo. PPSGG control samples and PPSGG co-incubated with anti-HNK-1 IgM antibody or anti-MAG patient sera were quantified by ELISA. The left panel shows the detection of PPSGG by Fab fragment (anti-poly-L-lysine) capturing and detection. When co-incubated with purified anti-HNK-1 antibody, the complexes were no longer detectable. The right panel shows the quantification of the complexes by capturing with an anti-human IgM antibody and with the detection by the anti-poly-L-lysine Fab fragments. The formation of the PPSGG / anti - HNK - 1 IgM complexes masked the IgM molecules from recognition.

1. Herrendorff, R.; Hänggi, P.; Pfister, H.; Yang, F.; Demeestere, D.; Hunziker, F.; Frey, S.; Schaeren-Wiemers, N.; Steck, A. J.; Ernst, B., Selective in vivo removal of pathogenic anti-MAG autoantibodies, an antigen-specific treatment option for anti-MAG neuropathy. *Proc Natl Acad Sci U S A* **2017**, *114* (18), E3689-E3698.

Chapter 4

Development of an anti-GM1 antibody-specific therapy for the treatment of Guillain-Barré Syndrome and Multifocal Motor Neuropathy

Butrint Aliu^{1*}, Lijuan Pang^{1, 2*}, Hannah Bialic^{3*}, Rhona McGonigal³, Emilie Seydoux², Delphine Demesteere², José Boucroust^{4,5}, Andreas Steck⁶, Hugh J. Willison³, Ruben Herrendorff^{1,2}, Pascal Hänggi^{1,2}, Beat Ernst¹

* These authors contributed equally to the project

¹Institute of Molecular Pharmacy, Pharmacenter, University of Basel, 4056 Basel, Switzerland

²Polyneuron Pharmaceuticals AG, 4057 Basel, Switzerland

³Institute of Infection, Immunity & Inflammation, University of Glasgow, Glasgow, UK

⁴Immunology laboratory, AP-HM, Marseille, France

⁵Aix-Marseille University, INT, UMR CNRS 7289, Marseille, France

⁶Clinic of Neurology, Department of Medicine, University Hospital Basel, University of Basel, 4031 Basel, Switzerland

Corresponding author:

Beat Ernst, +41 61 207 15 51, beat.ernst@unibas.ch

Contributions of Butrint Aliu

- Writing and revision of manuscript
- Anti-GM1 autoantibody screening and competitive ELISA
- Cholera Toxin Subunit B ELISA experiments
- Data analysis and interpretation

Abstract

Multifocal motor neuropathy (MMN) is a chronic peripheral neuropathy predominately affecting motor neurons and is caused by anti-GM1 IgM antibodies that target the ganglioside GM1. Deposition of these pathogenic autoantibodies on GM1 is associated with complement dependent nodal disruption and axonal damage in paranodal regions and neuromuscular junctions. It leads to conduction block, a hallmark of the disease. Besides chronic MMN, acute forms of peripheral neuropathy like Guillain-Barré-Syndrome (GBS) and its subforms, share GM1 as a target. While the pathogenic origins of MMN remain unclear, GBS has been shown to follow microbial infections as a result of molecular mimicry. Antibodies targeted at carbohydrate structures on bacteria and viruses, cross-react with endogenous epitopes, causing severe symptoms requiring urgent care. Acute therapies aim to reduce the effect caused by pathogenic autoantibodies by applying plasmapheresis or intravenous immunoglobulins. Chronic forms of anti-GM1 neuropathies are additionally treated with immunosuppressive medication. These therapeutic interventions, however, lack selectivity and in some instances even efficacy and can cause adverse effects. As demonstrated in a related peripheral neuropathy we hypothesize, that by selective removal of antigen specific anti-GM1 antibodies, these neuropathies can be treated more efficiently. This antibody removal can be achieved by multivalently presenting carbohydrate mimetics of the GM1 pentasaccharide on a biodegradable poly-L-lysine scaffold. Here we report the development and selection of a lead compound that successfully inhibits binding of anti-GM1 antibodies from patients' sera to GM1 and effectively prevents binding of anti-GM1 antibodies on terminal axonal networks *in vitro* and *ex vivo*.

Introduction

Various immune-mediated neuropathies are associated with increased levels of anti-glycan antibodies targeting specific carbohydrate structures expressed in the node of Ranvier or the neuromuscular junction.¹ Depending on the antigen, the immune-mediated neuropathy may arise from paranodal demyelination in the case of Schwann cell surface glycans, or axonal degradation in the case of antigens expressed on the axolemma. Anti-ganglioside antibodies, particularly anti-GM1 antibodies, have been detected in a series of related peripheral demyelinating neuropathies, including variants of Guillain-Barré-Syndrome (GBS)² such as acute motor axonal neuropathy (AMAN)³, acute motor-sensory axonal neuropathy (AMSAN)⁴, acute inflammatory demyelinating

polyneuropathy (AIDP)⁵, the pharyngeal-cervical-brachial variant of GBS⁶, as well as in chronic multifocal motor neuropathy (MMN)⁷.

Despite sharing the same antigen GM1, the clinical phenotypes of these conditions differ with regard to different effector sites and depend on the targeting of the myelin sheath, axons, or motor vs. sensory nerves by the autoantibodies.⁸ Another clinical differentiator is the acute vs. chronic manifestation that is best displayed in the timeline of GBS, showing a quick onset usually preceded by an infection, versus the progressive, steadily worsening muscle weakness in MMN.^{9,10} Since MMN is a rare disease with a prevalence of approximately 1 in 100,000 people and simultaneously shares clinical features with other motor neuron diseases, it is likely under-recognized and often misdiagnosed.⁷ Patients (males are 2.7 times more likely to develop the disease) suffer from slowly progressive, asymmetrical muscle weakness in the extremities without sensory impairment in most cases.¹¹ The disease onset usually occurs before the age of 50 and can lead to disability if left untreated or the patients do not respond to the treatment.¹² Besides the clinical phenotypes, the main pathophysiological features of MMN are the presence of anti-GM1 IgM antibodies and the development of a conduction block (CB).^{1,7} The ganglioside GM1, composed of a ceramide tail and a pentasacchride head group containing one sialic acid (N-acetylneuraminic acid, Neu5Ac), is the target of these auto-antibodies. GM1 is ubiquitously expressed but more abundant in peripheral motor nerves compared to sensory nerves, where it is localized in the axolemma and myelin and is clustered in cholesterol rich lipid membrane rafts. The highest abundance was detected in the node of Ranvier and adjacent paranodal regions as well as neuromuscular junctions.^{1,13}

Binding of anti-GM1 IgM antibodies is associated with complement-dependent as well as complement-independent pathways that can result in disruption of sodium channel clusters, interference with local calcium homeostasis, disruption of the nodes, and axonal damage, ultimately leading to nerve conduction block.¹⁴ While the origin of the disease in MMN is unknown, autoantibody production in GBS usually follows an infection with *Campylobacter jejuni* or other microbes and is a result of molecular mimicry, where GM1-like lipooligosaccharides provoke an immune response and lead to production of antibodies that cross-react with endogenous GM1.¹⁵ GBS has a general incidence rate of approximately 1-2 in 100,000 but can occur more frequent in certain clusters. Most notably, the relative rates of the different subtypes of GBS show great geographical variability. While GBS patients in Europe and the US are most likely to suffer from acute inflammatory demyelinating polyneuropathy (AIDP), the

demyelinating subtype of GBS, patients in Asia and Central/South America are more likely to show symptoms of AMAN, characterized by direct attack of the axolemma instead of demyelination.¹⁶ These differences can be largely attributed to genetic variation and exposure to different types of infectious stimuli. The occurrence of multiple closely related gangliosides that share important epitopes further increases the complexity of GBS variants. Besides different clinical features the subtypes can also be distinguished by antibody reactivity towards different ganglioside epitopes.^{17,18} This variability can lead to challenges in the development of appropriate diagnostic assays for disease characterization, because of the propensity of patients' autoantibodies to cross-react with multiple related gangliosides. Nevertheless, the pathogenicity of anti-GM1 IgG antibodies in AIDP, AMAN, and AMSAN and anti-GM1 IgM antibodies in MMN is well established and clinical features have been reproduced in animal models by active immunization with GM1 or passive transfer of anti-GM1 antibodies.^{19,20} Finally, although not all MMN patients show anti-GM1 IgM antibody titers (potentially due to detection limitations)²¹, the presence of the autoantibodies has been associated with increased disease severity and their reduction has been shown to correlate with clinical improvement.^{7,22,23} Acute treatment usually involves plasmapheresis and IVIg for GBS²⁴, while chronic MMN patients may additionally receive immune suppressive medication.²⁵ These therapeutics are however rather unspecific and besides being ineffective in some patient populations, they can also cause serious side effects. A more specific therapeutic intervention targeting the pathogenic auto-antibodies might therefore be safer and more efficient.

In this study we report the development of antigen-specific glycopolymers comprised of a biodegradable poly-L-lysine backbone multivalently displaying glycomimetics of the GM1 pentasaccharide. The display of multiple copies of the glycomimetic ligands on the polymer scaffold enables specific and high-affinity interactions with anti-GM1 IgG and IgM autoantibodies with a vastly increased macroscopic apparent binding affinity compared to the individual monovalent interactions. Here we demonstrate that our glycopolymers effectively inhibit binding of anti-GM1 antibodies to GM1 *in vitro* and successfully prevent antibody binding to GM1 at the nerve terminal axonal networks *in vitro* and *ex vivo* in an animal model of AMAN.

Results and Discussion

Synthesis of GM1 mimetics and glycopolymers comprising the GM1 mimetic epitopes

A large obstacle for the development of an effective therapeutic glycopolymer for the treatment of these autoantibody mediated diseases is finding highly specific and selective epitopes that recognize a wide variety of the patients' antibodies. Based on the intrinsic variability of the polyclonal anti-GM1 autoantibodies in different patients, a shared minimal GM1 epitope has to be defined that effectively binds anti-GM1 antibodies in a large part of the patient population. Bernardi and co-workers have previously reported a series of GM1 glycomimetics as cholera toxin ligands, however optimization on GM1 structure for anti-GM1 autoantibody binding has not been reported to date.²⁶⁻²⁸ Therefore, we generated a library of GM1 glycomimetics modified with the goal to simplify the pentasaccharide structure in order to reduce synthetic complexity while simultaneously increasing affinity and selectivity towards anti-GM1 antibodies.

During this optimization process we defined parts of the epitope to be more critical for recognition and parts that can be substituted by simple non-carbohydrate moieties or bioisosteres (Figure 1). Based on previous work²⁹, we hypothesized that binding affinity should not be affected when the glucose moiety (Part-I) at the reducing end is replaced by a tyramine aglycone (\rightarrow **2**). This was confirmed in the bio-assays showing similar binding of **1** and **2** and no loss in affinity towards anti-GM1 antibodies (Supporting Information, Figure S4, **59** vs. **63** and **62** vs. **64**). Additionally, introduction of an aromatic functional group to the glycomimetic and ultimately multiple copies thereof on the poly-L-lysine scaffold, could facilitate the development of analytical methods for compound characterization. A major opportunity for modification was the bioisosteric replacement of Neu5Ac (Part-II) with 3-cyclohexylpropionic acid, 3- phenylpropanoic acid, and propanoic acid (\rightarrow **3-9**). Furthermore, when the terminal Gal-GalNAc moiety (Part-III) was replaced with lactose (\rightarrow **10**), it turned out that the Gal-GalNAc branch is critical for anti-GM1 antibody binding and therefore should not be altered. This lack of reactivity towards anti-GM1 antibodies becomes evident from the inhibitory potential of the glycopolymers containing Gal-GalNAc (\rightarrow **56**, **57** & **59**) and the glycopolymer **65** containing lactose (Figure 3A).

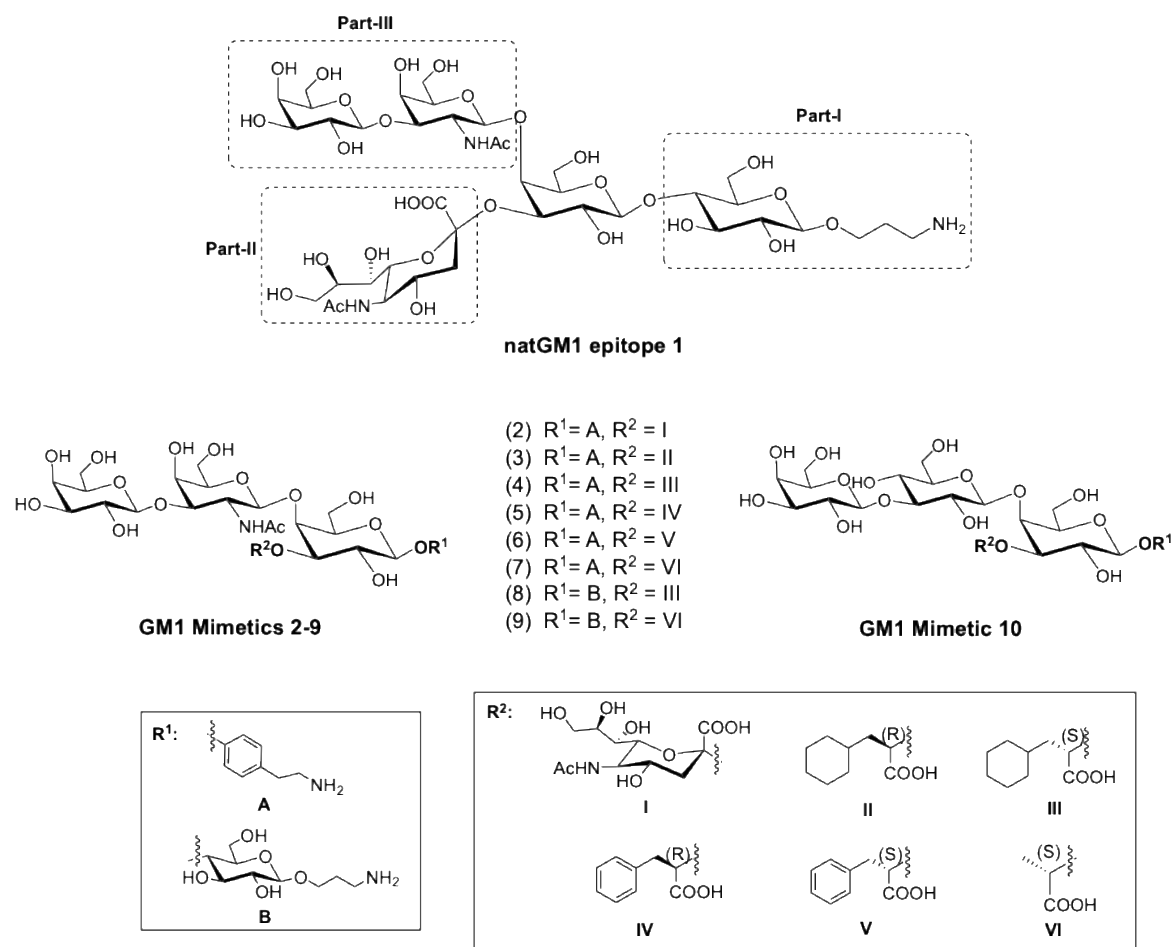
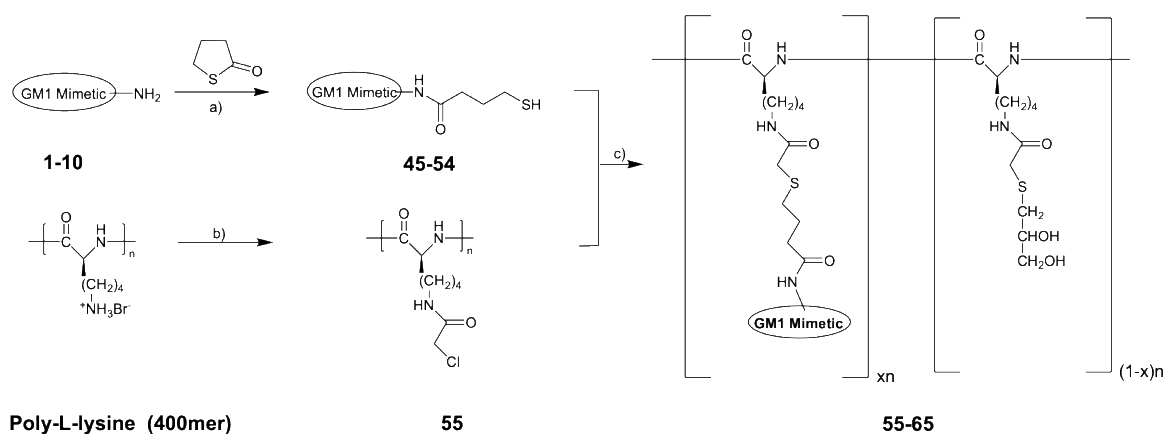


Figure 1. Representative structures of the natural GM1 epitope (1) and a series of GM1 glycomimetics with modifications on the GM1 core structure, such as replacement of the terminal glucose (Part-I) with a tyramine moiety (2-7), replacement of the Neu5Ac (Part-II) with 3-cyclohexylpropanoic acid, 3-phenylpropanoic acid, and propanoic acid (3-9), or replacement of the Gal-GalNAc branch (Part-III) with a lactose moiety (10).



| Glycoconjugate | 56 | 57 | 58 | 59 | 60 | 61 | 62 | 63 | 64 | 65 |
|---------------------|-----------|-----------|-----------|-----------|-----------|-----------|-----------|-----------|-----------|-----------|
| GM1 epitope | 1 | 2 | 3 | 4 | 5 | 6 | 7 | 8 | 9 | 10 |
| Epitope loading (%) | 26 | 30 | 24 | 25 | 25 | 26 | 26 | 35 | 30 | 28 |

Figure 2. Synthesis of the GM1 mimetic poly-L-lysine conjugates **56-65**. Monomeric GM1 analogues **1-10** were firstly functionalized with a mercapto-butanamide linker to yield compounds **45-54**. The commercial linear poly-L-lysines was activated through chloroacetylation (\rightarrow **55**). Sub-stoichiometric amounts of the GM1 analogues were coupled to the lysine units through nucleophilic substitution of the chloride by sulfhydryl, and the remaining chloroacetamides were capped with thioglycerol in order to improve solubility (\rightarrow **56-65**). Reagents and conditions: a) GM1 mimetic **1-10**, γ -thiobutyrolactone, TEA, MeOH, RT, yield: quant.; b) 2,6-lutidine, chloroacetic anhydride, DMF, 4°C, yield: 96%; c) i. DIPEA, DBU, water, DMF, RT; ii. 1-thioglycerol, TEA, water, DMF, RT, yield: 60-90% (20-40% GM1-epitope loading).

The general synthetic procedure for the preparation of GM1 glycopolymers is depicted in Figure 2. The monomeric GM1 analogues **1-10** were firstly reacted with thiobutyrolactone in the presence of triethylamine to introduce a mercapto-butanamide linker (\rightarrow **45-54**). The commercial linear poly-L-lysine (400mer) was chloroacetylated, giving the activated poly-L-lysine **55**. Sub-stoichiometric amounts of the GM1 analogues **45-54** were coupled to the lysine side chains by nucleophilic substitution of the chloride by sulfhydryl. In order to improve the aqueous solubility of the glycosylated-poly-L-lysine polymers, the remaining chloroacetamides were capped with thioglycerol. By nanofiltration low-MW impurities were removed and the target glycopolymers **56-65** were obtained in pure form. An optimal epitope loading of 25 to 30% was identified by testing a wide loading range with natural GM1 epitope **1** (Figure 2).

***In vitro* inhibitory activity of GM1 glycoconjugates on MMN patient serum anti-GM1 IgM binding to GM1**

In order to classify the MMN patients and assess the inhibitory efficacy of the glycomimetic glycoconjugates, we developed a set of *in vitro* assays based on GM1 coated ELISA.

First, the specificity of antibody binding to GM1 was evaluated by blocking GM1 epitopes on ELISA plates with cholera toxin subunit B and subsequently incubating blocked plates with the MMN patient's serum. While some patient sera showed good correlation of decreased IgM binding to GM1 with increasing cholera toxin subunit B concentrations, a series of patient sera were not affected by blocking with cholera toxin subunit B and for a few patient sera even increased binding with increasing cholera toxin subunit B concentrations was observed (Supporting Information, Figure S2). The aim of these initial experiments was to pre-screen the patient sera with cholera toxin subunit B before further assessing the inhibitory potential of the glycoconjugates. However, the hypothesis, that specific GM1 binding should lead to similar response in the inhibitory assays, could not be confirmed. In some cases, patient sera that were not affected by cholera toxin subunit B blocking, were readily inhibited by the glycopolymers and in some instances, sera that showed reduced binding to GM1 plates when blocked with cholera toxin subunit B, could not be inhibited by any glycoconjugate (Supporting Information, Figure S2 and Figure S5). Increased binding to blocked plates was found to be caused by the cholera toxin subunit B, rather than potential gangliosides impurities on the plate caused by insufficient GM1 purification. Coating with cholera toxin subunit B and measuring MMN patients sera IgM binding showed similar binding patterns (Supporting Information, Figure S3). A literature study revealed that heat-labile enterotoxin subunit B originating from *Escherichia coli* shares over 80% sequence identity with its homologous cholera toxin subunit B.³⁰ We therefore tested the reactivity of our patient population towards heat-labile enterotoxin in the same setting, revealing strong IgM binding in the same patient sera that had reacted with cholera toxin subunit B (Supporting Information, Figure S3). These findings additionally complicate this assay format, since patients that have suffered from a recent *E. coli* infection might show inverse results to the expected reduced binding to GM1. Nevertheless, despite inconclusive findings, the inability to effectively suppress antibody binding to GM1 by cholera toxin subunit B, suggests that some MMN patients might carry IgM antibodies that recognize different orientations of GM1 or might cross-react with closely related ganglioside structures. This is emphasized by recent reports that GM1 recognition by antibodies can vary

depending on the surrounding milieu and that a lipid-rich environment might influence GM1 orientation and enhance binding specificity and sensitivity.²¹ Based on the possibility of multiple different binding modes, especially between different patients, we tested our series of glycomimetic glycoconjugates **56-65** to find a suitable candidate with high affinity for a wide range of patient antibodies.

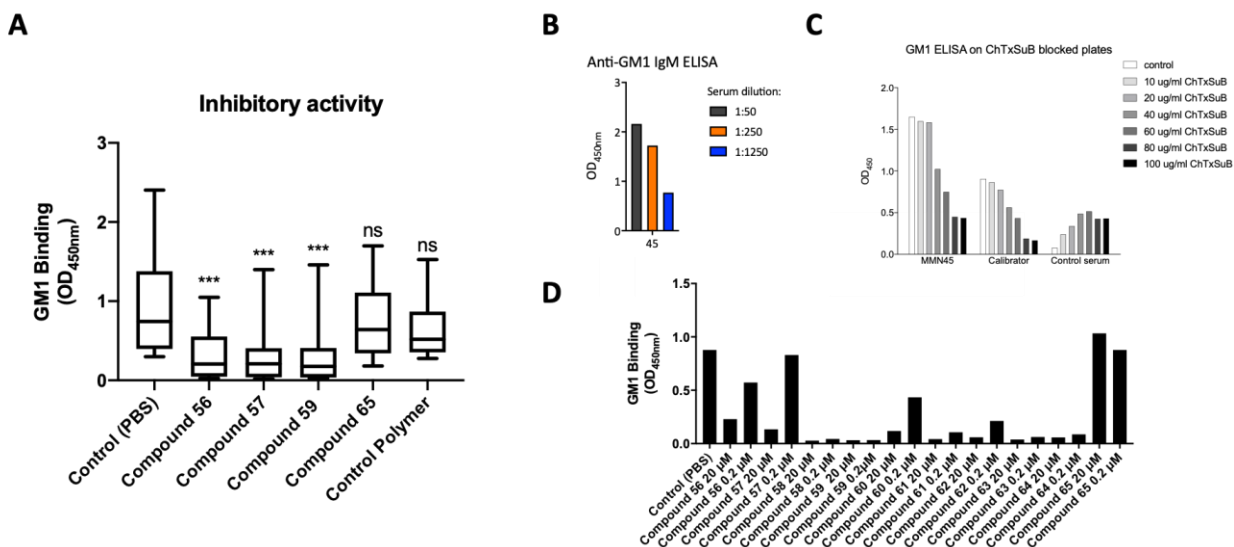


Figure 3. *In vitro* inhibitory activity of GM1 glycoconjugates on GM1 binding to anti-GM1 IgM in patient sera. **A)** Summary of 22 MMN patient sera incubated with different glycopolymers at 20 nM, showing strong inhibition of **56**, **57**, and **59**, compared to control polymer and inactivity with **65** (one-way ANOVA, *** $p \leq 0.001$) **B/C/D)** Exemplified testing procedure with patient serum samples to determine sensitivity, specificity, and inhibitory effects of the glycopolymers. **B)** Serum of MMN Patient#45 was titrated to achieve appropriate OD₄₅₀ values to be used in the binding assays. **C)** GM1-coated plates (Bühlmann) were first blocked with cholera toxin subunit B, then binding of MMN patient IgM was measured to assess binding specificity to GM1. The result shows that IgM antibodies of MMN Patient#45 specifically bind to the GM1 epitope on the ELISA plates and the binding is reduced with increasing cholera toxin subunit B concentrations. **D)** Glycoconjugates **56-65** were incubated with MMN Patient#45 serum at fixed concentration to determine their inhibitory potency in a competitive binding assay. The GM1 glycoconjugates showed inhibition of anti-GM1 IgM binding to GM1 with either comparable or superior affinity compared to the natural GM1 epitope glycoconjugate **56**. **65** shows no inhibition emphasizing the importance of the Gal-GalNAc branch.

Figure 3A summarizes the inhibitory data of a selection of the most promising glycoconjugates with appropriate controls (all compounds in Supporting Information, Figure S4). The control polymer carrying an unrelated carbohydrate mimetic²⁹ did not inhibit binding, thus confirming the

specificity of the glycoconjugates for anti-GM1 antibodies. Modification of the Gal-GalNAc branch (→ **65**), led to a loss of the interaction across all patient samples and confirmed its role for antibody recognition, and thus should not be altered. Most interesting were replacements of the glucose with a tyramine moiety (→ **57**) and replacement of Neu5Ac with a cyclohexyl moiety (→ **59**). These modifications led to improved binding compared to natural GM1 **56** in most responding patients. **57** and **59** were therefore selected for further *in vitro* and *ex vivo* evaluation.

An exemplary experimental series with MMN patient #45 depicts the assessment performed for all patients and shows initial anti-GM1 IgM level titration to define a suitable working dilution (Figure 3B) and subsequent specificity (Figure 3C) and inhibition (Figure 3D). Direct binding and inhibition ELISA were performed using a commercial GM1 ELISA kit (Bühlmann). In the competitive inhibition assay, patient's serum was firstly pre-incubated with the GM1 mimetic glycoconjugates at different concentrations as indicated and then added to the ELISA plate to assess binding to GM1. In the wells, the GM1 mimetic glycoconjugates compete with GM1 coated to the plate for binding to MMN patients' autoantibodies. Among the glycoconjugates, **57** and **59** showed a higher inhibitory potential and were further tested. Natural GM1 glycoconjugate **56** and control polymer were used as positive and negative controls. Testing of 22 MMN patient sera enabled the detection of individual differences among patients regarding anti-GM1 IgM titers and its binding affinity and specificity towards GM1 as well as to the glycoconjugates. Although the inhibitory potential of the glycoconjugate varies among patient sera, we were able to identify three interesting glycoconjugates **56**, **57** and **59**, exhibiting broad patient coverage (SI, Figure 5).

***Ex vivo* AMAN model for validation of inhibitory efficacy of the selected glycoconjugates**

The *ex vivo* animal model relies on a monoclonal IgG3 antibody (DG2) raised against GM1 and was used for proof of concept in IgG mediated acute neuropathy targeting GM1 and as a surrogate marker for MMN. Initial experiments were able to reproduce the findings generated with MMN patients anti-GM1 IgM and found strong inhibitory potential of **57**. The dose-titration of **57** showed effective and complete inhibition of anti-GM1 antibody binding to GM1, while binding was not affected by the control polymer (Figure 4A). While both **57** and **59** were interesting mimetic glycoconjugates, binding studies at different temperatures revealed superiority of **57**. Binding of anti-GM1 IgG was inhibited across a wide temperature range by **57** (Figure 4B), whereas **59** was only able to inhibit binding at 4°C and lost its inhibitory potential at physiologically important

37°C (Supporting Information, Figure S1). Going forward, only **57** was used to assess functional binding inhibition. Binding of anti-GM1 antibody and inhibition by **57** to distal axons was performed using murine diaphragm incubated with anti-GM1 antibody in presence of **57** and controls. *In situ*, **57** effectively inhibited binding over a broad concentration range (Figure 4C), demonstrating the protective potential for axonal membranes. Figure 4D depicts the accumulation of anti-GM1 antibody in the absence of **57**, a partial decrease in anti-GM1 antibody signal at 0.1 µg/ml **57** and complete depletion in the presence of more than 0.5 µg/ml **57**.

The potential to displace pre-bound anti-GM1 antibodies with GM1 glycoconjugates was investigated by ELISA and with an *ex vivo* neuromuscular model. **57** was able to compete with GM1 when incubated simultaneously *in vitro*, but not when anti-GM1 antibody was pre-incubated on the plate. It was however very effective in preventing binding of anti-GM1 antibody to GM1 when pre-administered on the plate (Figure 5A). *Ex vivo*, however, using living *Triangularis sterni* muscle, **57** was able to displace bound anti-GM1 antibodies on the neuromuscular junction (Figure 5B). Control polymers neither interfered with the binding nor were able to displace bound anti-GM1 antibody, demonstrating the selectivity of the GM1 glycomimetic glycoconjugate. **57** was able to prevent binding and displace pre-bound anti-GM1 antibody over a wide dose range at the nerve terminal axonal network *in vitro* and *ex vivo*. Significant reduction of anti-GM1 antibody was observed at concentrations as low as 0.1 µg/ml *in vitro* and 35 µg/ml *ex vivo*.

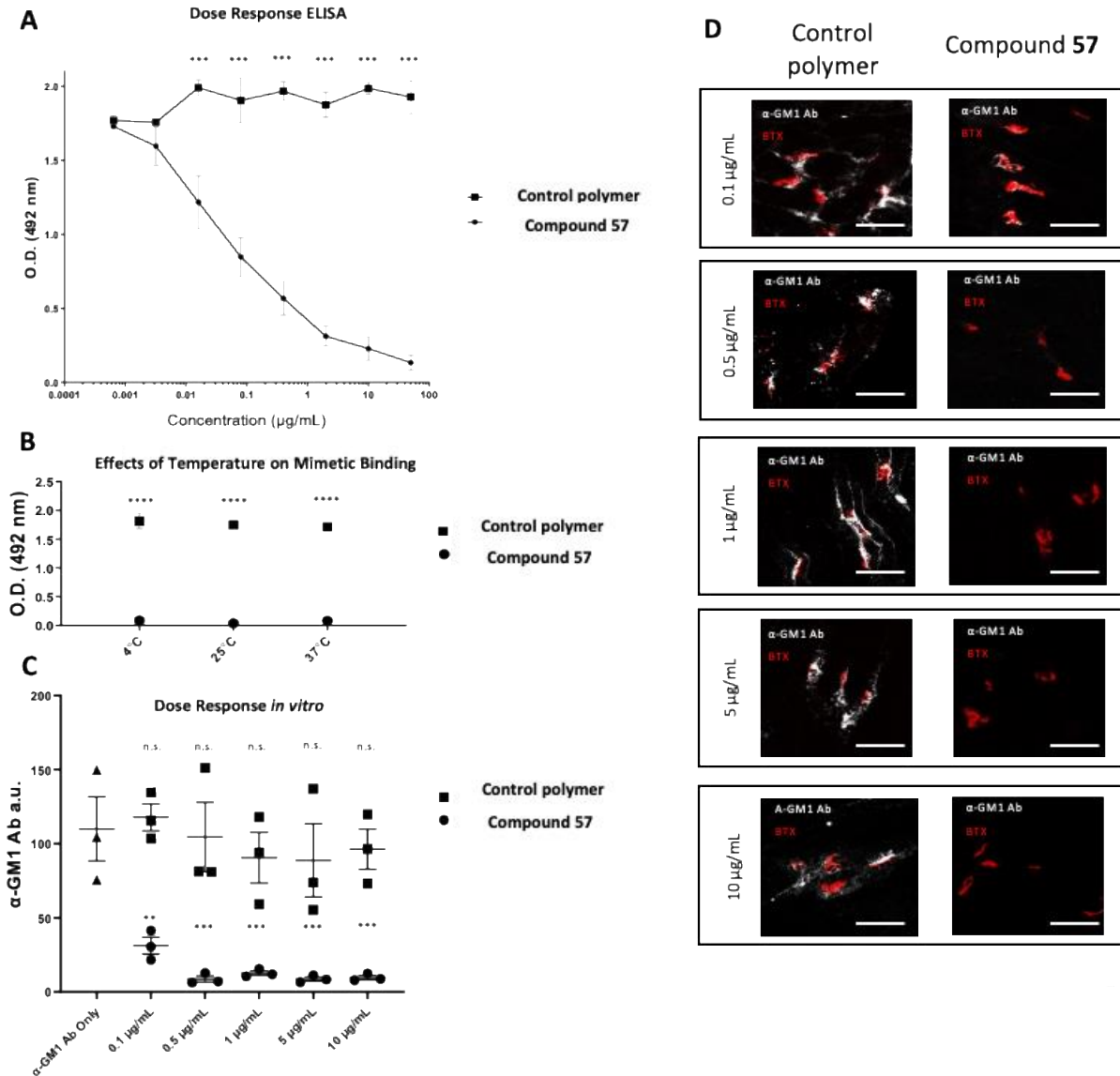


Figure 4. Glycopolymer **57** binds and sequesters anti-GM1 antibody in a dose dependent manner across a temperature range of 4° to 37° C; **A**) An ELISA dose response curve demonstrates that **57** effectively inhibits anti-GM1 antibody binding at all concentrations compared to a control polymer. Measurements were taken in duplicate per plate and analyzed over three separate plates for an n=3 (**p ≤ 0.001). Statistics were determined with a two-way ANOVA. **B**) The ELISA temperature assay demonstrates efficacy of anti-GM1 antibody inhibition by **57** at a range of temperature range of 4° to 37° C . Measurements were taken in duplicate per plate and analyzed over three separate plates for an n=3 (***p ≤ 0.0001). Statistics were determined with a two-way ANOVA. **C/D**) An *in vitro* dose response demonstrates **57** effectively inhibits anti-GM1 antibody binding at all concentrations compared to control polymer. An n of 3 was used for each condition and imaged in duplicate (**p ≤ 0.01; ***p ≤ 0.001; n.s. = not significant). Statistics determined with a one-way ANOVA against anti-GM1 antibody control. BTX = binds post-synaptic nicotinic acetylcholine receptor; scale bar = 50 µm.

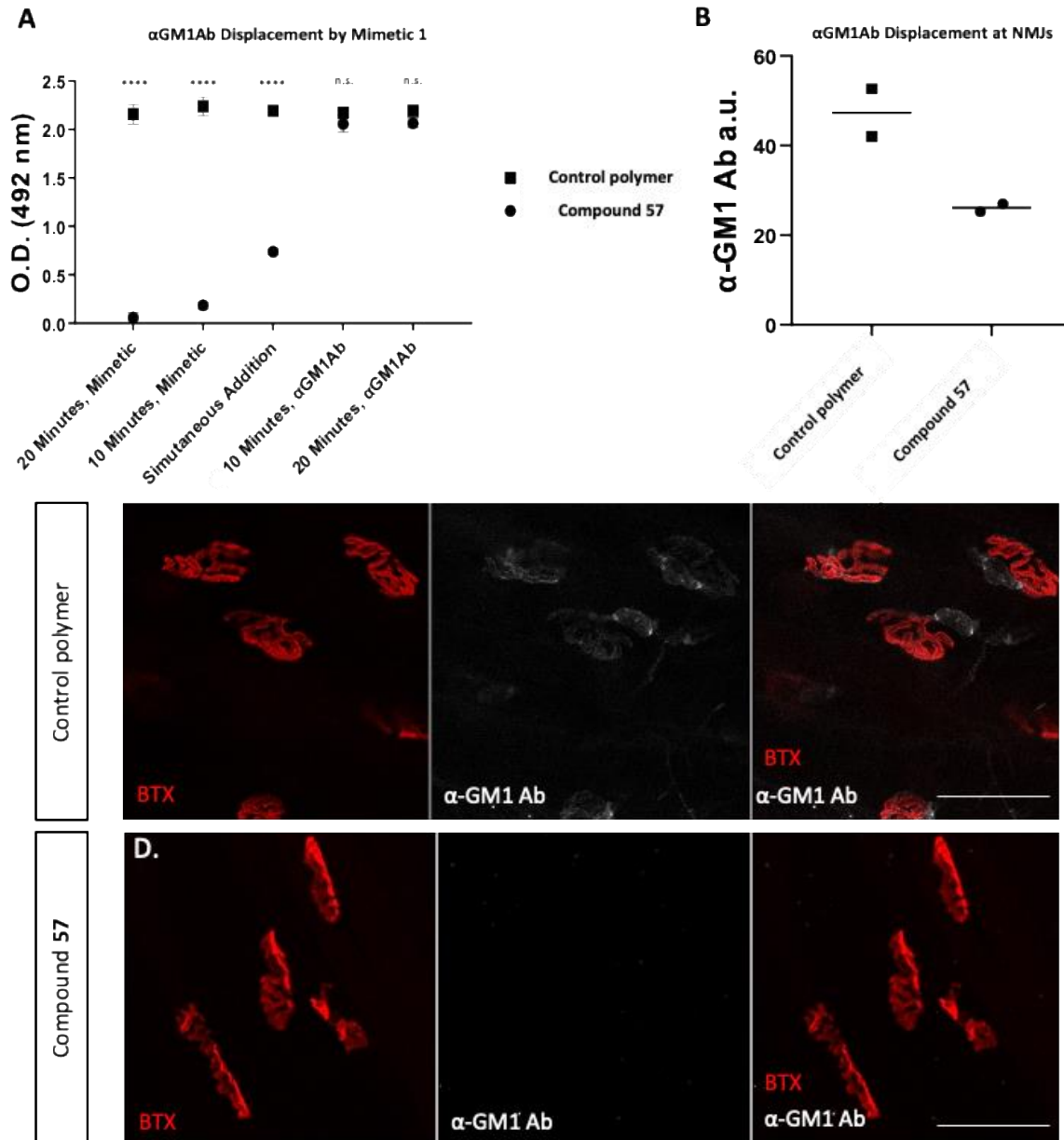


Figure 5. anti-GM1 antibody displacement dynamics by **57**. **A)** An ELISA displacement assay demonstrates that **57** effectively competes with anti-GM1 antibody binding of GM1 ganglioside compared to control polymer. Measurements were taken in duplicate per plate and analyzed over three separate plates for an $n=3$ (**** $p \leq 0.0001$; n.s. = not significant). Statistics determined with a two-way ANOVA. **B/C/D)** An *ex vivo* displacement assay demonstrates that **57** displaces bound anti-GM1 antibody at the neuromuscular junction. Two groups of two mice were completed and stained independently for an $n=2$. A final group of 2 mice is forthcoming to complete the experimental set. BTX = binds post-synaptic nicotinic acetylcholine receptor; scale bar = 50 μ m.

Conclusion

In this study we explored the potential of GM1 mimetic glycopolymers as potential therapeutic options for anti-GM1 antibody mediated neuropathies. Ten GM1 analogues were designed and synthesized aiming to simplify the complex structure and chemical synthesis of GM1. The goal was that the compounds maintained or increased binding affinity and specificity towards anti-GM1 antibodies. The development of these compounds revealed critical epitope features that are necessary to effectively bind anti-GM1 antibodies in a diverse patient population. While modification at terminal glucose did not alter binding characteristics, the exposed Gal-GalNAc branch was critical for antibody recognition and could not be modified. Replacement of sialic acid initially seemed to maintain binding affinities and showed superior affinity compared to natural GM1 in some patients. However, its drawback was temperature sensitivity, i.e. the loss of affinity at crucial physiological temperatures. We also learned that some MMN patients carry antibodies that cannot be fully inhibited by GM1 specific blocking or competitive inhibition. We could, however, demonstrate that GM1 mimetic glycoconjugates, in MMN patients that showed GM1 specific binding, were able to inhibit binding of both pathogenic anti-GM1 IgM and IgG antibodies to GM1 *in vitro*. Our most promising candidate was effective in inhibiting antibody binding to GM1 over a physiologically relevant temperature range and was effective in reducing anti-GM1 antibody binding in functional assays at nerve terminal axonal networks *in vitro* and *ex vivo*. The successful application of the AMAN injury models and the screening of multiple MMN patient sera demonstrate the potential of GM1 mimetic glycoconjugates as selective precision treatment options for anti-GM1 antibody mediated neuropathies.

Materials and Methods

Patient Sera

Sera from MMN or healthy individuals were investigated. They were tested for anti-GM1 IgM antibodies by ELISA. Serum anti-GM1 antibody titers were determined by an ELISA assay from Bühlmann Laboratories (Schönenbuch, Switzerland). MMN sera were obtained from the immunology laboratory of the University Hospital Marseille (Marseille, France). Sera from healthy individuals (without neuropathy) negative for anti-GM1 reactivity served as controls and were obtained from the blood bank in Basel (Blutspendezentrum SRK beider Basel, Basel, Switzerland). All participants signed an informed consent.

Competitive ELISA

For the competitive ELISA, the synthesized carbohydrate polymers **56-65** were tested in the GM1 ELISA (Bühlmann Laboratories, Schönenbuch, Switzerland) for their inhibitory activity (inhibition of patients' serum anti-GM1 IgM antibodies to the GM1 ganglioside). The 96-well microtiter plates coated with purified GM1 ganglioside were washed twice with Washing Buffer (300 µl/well) before adding 50 µl carbohydrate polymers dissolved in PBS and 50 µl/well diluted patient sera (1:25 dilution in PBS). The final volume was 100 µl of the mixture per well, which was incubated for two hours at 4-8°C. The plates were washed four times with washing buffer (300 µl/well) before either the anti-human IgM antibody-horseradish peroxidase conjugate or the anti-human IgG antibody-horseradish peroxidase conjugate were added (100 µl/well). The plate was incubated for two hours at 4-8°C. After washing the wells (4 x 300 µl/well), the substrate 3,3',5,5'-tetramethylbenzidine (TMB) was added (100 µl/well) and the plate incubated for further 30 minutes at 600 rpm and room temperature, protected from light. Finally, a stop solution (0.25 M sulfuric acid) was added (100 µl/well) and the degree of colorimetric reaction was determined by absorption measurement at 450 nm with a microplate reader (Synergy H1, Microplate reader, BioTek).

Mice

GalNAcT^{-/-} Tg(neuronal) transgenic mice were used for *ex vivo* and *in vitro* experiments. The GalNAcT enzyme, under the control of the Thy1.2 promoter, is restricted to mature neurons. Thy1.2-GalNAcT transgenic mice backcrossed seven generations on a C57BL/6 background were interbred with GalNAcT^{-/-} mice³¹ to create 2 lines of GalNAcT^{-/-}-Tg(neuronal) mice. Restoration of GalNAcT enzyme activity was determined via a glycosyltransferase activity assay as described previously.^{32,33} The genotype of these transgenic mice was identified by PCR before use. Mice were 4-6 weeks old, both male and female, had unlimited access to food and water and were housed with a light/dark cycle of 12 h/12 h under a constant temperature of 22°C. Mice were sacrificed by CO₂ inhalation. Experiments complied with UK Home Office Guidelines.

Antibodies and Reagents

The IgG3 anti-GM1 ganglioside mAb (DG2) was derived from GalNAcT^{-/-} mice which were inoculated with the GM1 ganglioside mimicking *Campylobacter jejuni* HS19 lipooligosaccharide.

^{34,35} DG2 concentration was measured using a quantitative ELISA (Bethyl Laboratories, Texas, USA). α -bungarotoxin (BTx) is a post-synaptic nicotinic acetylcholine receptor and α -bungarotoxin/AlexaFluor 555 conjugate (Molecular Probes, UK) was used to delineate neuromuscular junctions (NMJs).

ELISA – Temperature dependent binding

To determine the binding dynamics of **57** against a control polymer (PPSGG³⁶), ganglioside ELISAs were performed. Immulon-2HB 96 well plates (Thermo Fisher Scientific, USA) were coated with 100 μ l at 2 μ g/ml of GM1 (Sigma, UK), diluted in methanol (methanol only for control wells). Plates were blocked with 2% bovine serum albumin in PBS solution for 1 hour at 4°C after which the solution was discarded and a concentration range of **57** applied (0.64 ng/mL, 3.2 ng/mL, 16 ng/mL, 0.08 μ g/mL, 0.5 μ g/mL, 2 μ g/mL, 10 μ g/mL, 50 μ g/mL), (diluted in 0.1% BSA solution) overnight at 4°C. All mimetic formulations were measured in duplicate and assessed across three separate ELISA plates to constitute an n of 3. Anti-GM1 monoclonal antibody only was used as a positive control and applied at 5 μ g/ml in 0.1% BSA. Plates were washed 3 times with PBS and then goat anti-mouse IgG-HRP (1:3000, Sigma Aldrich) in 0.1% BSA was added to all wells and incubated for 1 hour at 4°C. After another three 3 PBS washes, the *o*-phenylenediamine dihydrochloride (OPD) substrate solution (30 ml dH₂O, 16 ml 0.2 M Na₂HPO₄, 14 ml 0.1 M C₆HgO₇, 1 OPD tablet and 20 μ l 30% H₂O₂ added immediately prior to use) was added for 15 minutes at room temperature in the dark followed by 50 μ l of stop solution (4 M H₂SO₄). Plates were read immediately at 492 nm on a Tecan Sunrise™ automated microplate reader (Tecan Group Ltd, Männedorf, Switzerland) using Magellan™ software. The average O.D. from matched control wells was subtracted from corresponding antibody wells to correct for background.

***In vitro* Preparations**

GalNAcT^{-/-} Tg(neuronal) mice were sacrificed and diaphragms removed, snap frozen, and stored at -70°C. Tissue was sectioned on the cryostat (Bright Instruments, UK) at 10 μ m and collected on APES coated slides. Sections were stored at -20°C. Immunostaining was conducted to analyse the dose dependent efficacy of **57** on *in vitro* preparations of diaphragm sections. Slides were incubated with a concentration range (0.1 μ g/mL, 0.5 μ g/mL, 1 μ g/mL, 5 μ g/mL, 10 μ g/mL) of

57 or control polymer and 20 µg/mL anti-GM1 antibody for 4 hours at 4°C. Slides were dip washed 3 times in PBS followed by an incubation with goat anti-mouse anti-IgG3 antibody (1:300, Invitrogen, USA), α-bungarotoxin/AlexaFluor 555 conjugate (1:750) and 3% Normal Goat Serum (NGS) for 2 hours at room temperature. After secondary antibody incubation tissue was dip washed 3 times with PBS and mounted in CitiFluor mounting medium. Sections were stored at -20°C until imaging. Each slide had three diaphragm sections from three different *GalNAcT-/-Tg(neuronal)* mice to give each experimental condition an n of 3. The experiment was blinded to the experimenter and all slides were imaged in duplicate.

***Ex vivo* Preparations**

Triangularis sterni (TS) muscle was maintained alive post-dissection in Ringer's physiological solution (116 mM NaCl, 4.5 mM KCl, 1 mM MgCl₂, 2 mM CaCl₂, 1 mM NaH₂PO₄, 23 mM NaHCO₃, 11 mM glucose, pH 7.2-7.4) pre-gassed with 95% O₂/5% CO₂ at room temperature. TS muscle preparations were incubated first with 100 µg/mL anti-GM1 antibody in Ringer's to allow anti-GM1 antibody binding for 1 hour and then washed in Ringer's, after which preparations were incubated with either 25 µg/mL of control polymer or 25 µg/mL of **57** for 1 hour. Preparations were rinsed 3 times with Ringer's prior to fixation with 4% paraformaldehyde (PFA) for 20 minutes at 4°C. After fixation, the tissue was rinsed in PBS, 0.1 M glycine, and again in PBS. To analyze the ability of **57** to displace bound anti-ganglioside antibody *ex vivo*, TS preparations were incubated with goat anti-mouse anti-IgG3 antibody (1:500), α-bungarotoxin/AlexaFluor 555 conjugate (1:500) and 3% normal goat serum (NGS) as a blocking agent for 3 hours in the dark at room temperature. After secondary antibody incubation tissue was washed 3 times with PBS and mounted in CitiFluor mounting medium on APES coated slides. Sections were stored at -20°C until imaging. Control polymer and **57** were matched per mouse and the experiment was blinded to the experimenter. The *ex vivo* displacement experiment was done in two groups of two mice to provide a biological duplicate for each n. A third group, to bring the total n to 3, is forthcoming.

Image Acquisition and Analysis

For quantification of anti-GM1 antibody deposition at NMJs, images were captured on a Zeiss LSM880 confocal microscope. For diaphragm sections, 15 images (~50 NMJs) were captured per

section with a total of 45 images per slide. For triangularis sterni muscle preparations 15 images were captured per tissue (~50 NMJs). The mean intensity of staining overlying the NMJ (delineated by BTx stain) was measured in each case. Images were analysed using the v1.51 Fiji (v1.51) distribution of ImageJ software (NIH). ANOVA analysis was used to compare statistical differences between groups.

References

- 1 Willison, H. J. & Yuki, N. Peripheral neuropathies and anti-glycolipid antibodies. *Brain* **125**, 2591-2625, doi:10.1093/brain/awf272 (2002).
- 2 Ogawara, K. *et al.* Axonal Guillain-Barre syndrome: relation to anti-ganglioside antibodies and *Campylobacter jejuni* infection in Japan. *Ann Neurol* **48**, 624-631 (2000).
- 3 Hadden, R. D. *et al.* Electrophysiological classification of Guillain-Barre syndrome: clinical associations and outcome. Plasma Exchange/Sandoglobulin Guillain-Barre Syndrome Trial Group. *Ann Neurol* **44**, 780-788, doi:10.1002/ana.410440512 (1998).
- 4 Yuki, N., Kuwabara, S., Koga, M. & Hirata, K. Acute motor axonal neuropathy and acute motor-sensory axonal neuropathy share a common immunological profile. *J Neurol Sci* **168**, 121-126, doi:10.1016/s0022-510x(99)00180-x (1999).
- 5 Kuwabara, S. *et al.* IgG Anti-GM1 antibody is associated with reversible conduction failure and axonal degeneration in guillain-barré syndrome. *Annals of Neurology* **44**, 202-208, doi:https://doi.org/10.1002/ana.410440210 (1998).
- 6 Nagashima, T., Koga, M., Odaka, M., Hirata, K. & Yuki, N. Continuous spectrum of pharyngeal-cervical-brachial variant of Guillain-Barre syndrome. *Arch Neurol* **64**, 1519-1523, doi:10.1001/archneur.64.10.1519 (2007).
- 7 Pestronk, A. *et al.* A treatable multifocal motor neuropathy with antibodies to GM1 ganglioside. *Ann Neurol* **24**, 73-78, doi:10.1002/ana.410240113 (1988).
- 8 Wakerley, B. R. & Yuki, N. Mimics and chameleons in Guillain-Barre and Miller Fisher syndromes. *Pract Neurol* **15**, 90-99, doi:10.1136/practneurol-2014-000937 (2015).
- 9 van den Berg, B. *et al.* Guillain-Barre syndrome: pathogenesis, diagnosis, treatment and prognosis. *Nat Rev Neurol* **10**, 469-482, doi:10.1038/nrneurol.2014.121 (2014).
- 10 Slee, M., Selvan, A. & Donaghy, M. Multifocal motor neuropathy: the diagnostic spectrum and response to treatment. *Neurology* **69**, 1680-1687, doi:10.1212/01.wnl.0000277697.55288.d0 (2007).
- 11 Vlam, L. *et al.* Multifocal motor neuropathy: diagnosis, pathogenesis and treatment strategies. *Nat Rev Neurol* **8**, 48-58, doi:10.1038/nrneurol.2011.175 (2011).
- 12 Nobile-Orazio, E., Cappellari, A. & Priori, A. Multifocal motor neuropathy: current concepts and controversies. *Muscle Nerve* **31**, 663-680, doi:10.1002/mus.20296 (2005).

- 13 Corbo, M. *et al.* Patterns of reactivity of human anti-GM1 antibodies with spinal cord and motor neurons. *Ann Neurol* **32**, 487-493, doi:10.1002/ana.410320402 (1992).
- 14 Beadon, K., Guimarães-Costa, R. & Léger, J. M. Multifocal motor neuropathy. *Curr Opin Neurol* **31**, 559-564, doi:10.1097/WCO.0000000000000605 (2018).
- 15 Yuki, N. & Hartung, H. P. Guillain-Barre syndrome. *N Engl J Med* **366**, 2294-2304, doi:10.1056/NEJMra1114525 (2012).
- 16 Doets, A. Y. *et al.* Regional variation of Guillain-Barre syndrome. *Brain* **141**, 2866-2877, doi:10.1093/brain/awy232 (2018).
- 17 Willison, H. J. & Veitch, J. Immunoglobulin subclass distribution and binding characteristics of anti-GQ1b antibodies in Miller fisher syndrome. *Journal of Neuroimmunology* **50**, 159-165, doi:https://doi.org/10.1016/0165-5728(94)90042-6 (1994).
- 18 Yuki, N. Guillain-Barre syndrome and anti-ganglioside antibodies: a clinician-scientist's journey. *Proc Jpn Acad Ser B Phys Biol Sci* **88**, 299-326, doi:10.2183/pjab.88.299 (2012).
- 19 Yuki, N. *et al.* Animal model of axonal Guillain-Barre syndrome induced by sensitization with GM1 ganglioside. *Ann Neurol* **49**, 712-720 (2001).
- 20 Greenshields, K. N. *et al.* The neuropathic potential of anti-GM1 autoantibodies is regulated by the local glycolipid environment in mice. *J Clin Invest* **119**, 595-610, doi:10.1172/JCI37338 (2009).
- 21 Galban-Horcajo, F. *et al.* The Diagnostic Utility of Determining Anti-GM1: GalC Complex Antibodies in Multifocal Motor Neuropathy: A Validation Study. *J Neuromuscul Dis* **2**, 157-165, doi:10.3233/JND-150080 (2015).
- 22 Cats, E. A. *et al.* Correlates of outcome and response to IVIg in 88 patients with multifocal motor neuropathy. *Neurology* **75**, 818-825, doi:10.1212/WNL.0b013e3181f0738e (2010).
- 23 Pestronk, A. *et al.* Treatment of IgM antibody associated polyneuropathies using rituximab. *J Neurol Neurosurg Psychiatry* **74**, 485-489, doi:10.1136/jnnp.74.4.485 (2003).
- 24 Willison, H. J., Jacobs, B. C. & van Doorn, P. A. Guillain-Barre syndrome. *Lancet* **388**, 717-727, doi:10.1016/S0140-6736(16)00339-1 (2016).
- 25 PNS, J. T. F. o. t. E. a. t. European Federation of Neurological Societies/Peripheral Nerve Society guideline on management of multifocal motor neuropathy. Report of a joint task force of the European Federation of Neurological Societies and the Peripheral Nerve

- Society--first revision. *J Peripher Nerv Syst* **15**, 295-301, doi:10.1111/j.1529-8027.2010.00290.x (2010).
- 26 Bernardi, A., Checchia, A., Brocca, P., Sonnino, S. & Zuccotto, F. Sugar Mimics: An Artificial Receptor for Cholera Toxin. *Journal of the American Chemical Society* **121**, 2032-2036, doi:10.1021/ja983567c (1999).
- 27 Arosio, D., Baretta, S., Cattaldo, S., Potenza, D. & Bernardi, A. Ganglioside GM1 mimics: lipophilic substituents improve affinity for cholera toxin. *Bioorg Med Chem Lett* **13**, 3831-3834, doi:10.1016/j.bmcl.2003.07.007 (2003).
- 28 Cheshev, P. *et al.* Synthesis and affinity evaluation of a small library of bidentate cholera toxin ligands: towards nonhydrolyzable ganglioside mimics. *Chemistry* **16**, 1951-1967, doi:10.1002/chem.200902469 (2010).
- 29 Herrendorff, R. *et al.* Selective in vivo removal of pathogenic anti-MAG autoantibodies, an antigen-specific treatment option for anti-MAG neuropathy. *Proc Natl Acad Sci U S A* **114**, E3689-E3698, doi:10.1073/pnas.1619386114 (2017).
- 30 Rodighiero, C. *et al.* Structural basis for the differential toxicity of cholera toxin and Escherichia coli heat-labile enterotoxin. Construction of hybrid toxins identifies the A2-domain as the determinant of differential toxicity. *J Biol Chem* **274**, 3962-3969, doi:10.1074/jbc.274.7.3962 (1999).
- 31 Takamiya, K. *et al.* Mice with disrupted GM2/GD2 synthase gene lack complex gangliosides but exhibit only subtle defects in their nervous system. *Proc Natl Acad Sci U S A* **93**, 10662-10667, doi:10.1073/pnas.93.20.10662 (1996).
- 32 Ruan, S. & Lloyd, K. O. Glycosylation pathways in the biosynthesis of gangliosides in melanoma and neuroblastoma cells: relative glycosyltransferase levels determine ganglioside patterns. *Cancer Res* **52**, 5725-5731 (1992).
- 33 Ruan, S., Raj, B. K., Furukawa, K. & Lloyd, K. O. Analysis of melanoma cells stably transfected with beta 1,4GalNAc transferase (GM2/GD2 synthase) cDNA: relative glycosyltransferase levels play a dominant role in determining ganglioside expression. *Arch Biochem Biophys* **323**, 11-18, doi:10.1006/abbi.1995.0003 (1995).
- 34 Townson, K. *et al.* Solid phase immunoabsorption for therapeutic and analytical studies on neuropathy-associated anti-GM1 antibodies. *Glycobiology* **17**, 294-303, doi:10.1093/glycob/cw1074 (2007).

- 35 Bowes, T. *et al.* Tolerance to self gangliosides is the major factor restricting the antibody response to lipopolysaccharide core oligosaccharides in *Campylobacter jejuni* strains associated with Guillain-Barre syndrome. *Infect Immun* **70**, 5008-5018, doi:10.1128/IAI.70.9.5008-5018.2002 (2002).
- 36 Aliu, B. *et al.* Selective inhibition of anti-MAG IgM autoantibody binding to myelin by an antigen specific glycopolymer. *J Neurochem*, doi:10.1111/jnc.15021 (2020).

Materials and Methods

Patient Sera

Sera from MMN or healthy individuals were investigated. They were tested for anti-GM1 IgM antibodies by ELISA. Serum anti-GM1 antibody titers were determined by an ELISA assay from Bühlmann Laboratories (Schönenbuch, Switzerland). MMN sera were obtained from the immunology laboratory of the University Hospital Marseille (Marseille, France). Sera from healthy individuals (without neuropathy) negative for anti-GM1 reactivity served as controls and were obtained from the blood bank in Basel (Blutspendezentrum SRK beider Basel, Basel, Switzerland). All participants signed an informed consent.

Competitive ELISA

For the competitive ELISA, the synthesized carbohydrate polymers **56-65** were tested in the GM1 ELISA (Bühlmann Laboratories, Schönenbuch, Switzerland) for their inhibitory activity (inhibition of patients' serum anti-GM1 IgM antibodies to the GM1 ganglioside). The 96-well microtiter plates coated with purified GM1 ganglioside were washed twice with Washing Buffer (300 µl/well) before adding 50 µl carbohydrate polymers dissolved in PBS and 50 µl/well diluted patient sera (1:25 dilution in PBS). The final volume was 100 µl of the mixture per well, which was incubated for two hours at 4-8°C. The plates were washed four times with washing buffer (300 µl/well) before either the anti-human IgM antibody-horseradish peroxidase conjugate or the anti-human IgG antibody-horseradish peroxidase conjugate were added (100 µl/well). The plate was incubated for two hours at 4-8°C. After washing the wells (4 x 300 µl/well), the substrate 3,3',5,5'-tetramethylbenzidine (TMB) was added (100 µl/well) and the plate incubated for further 30 minutes at 600 rpm and room temperature, protected from light. Finally, a stop solution (0.25 M sulfuric acid) was added (100 µl/well) and the degree of colorimetric reaction was determined by absorption measurement at 450 nm with a microplate reader (Synergy H1, Microplate reader, BioTek).

Mice

GalNAcT^{-/-} Tg(neuronal) transgenic mice were used for *ex vivo* and *in vitro* experiments. The GalNAcT enzyme, under the control of the Thy1.2 promoter, is restricted to mature neurons. Thy1.2–GalNAcT transgenic mice backcrossed seven generations on a C57BL/6 background were

interbred with GalNAcT^{-/-} mice (Takamiya, 1996) to create 2 lines of GalNAcT^{-/-}-Tg(neuronal) mice. Restoration of GalNAcT enzyme activity was determined via a glycosyltransferase activity assay as described previously (Ruan, 1992; Ruan, 1995). The genotype of these transgenic mice was identified by PCR before use. Mice were 4-6 weeks old, both male and female, had unlimited access to food and water and were housed with a light/dark cycle of 12 h/12 h under a constant temperature of 22°C. Mice were sacrificed by CO₂ inhalation. Experiments complied with UK Home Office Guidelines.

Antibodies and Reagents

The IgG3 anti-GM1 ganglioside mAb (DG2) was derived from GalNAcT^{-/-} mice which were inoculated with the GM1 ganglioside mimicking *Campylobacter jejuni* HS19 lipooligosaccharide (Townson, 2007; Bowes, 2002). DG2 concentration was measured using a quantitative ELISA (Bethyl Laboratories, Texas, USA). α -bungarotoxin (BTx) is a post-synaptic nicotinic acetylcholine receptor and α -bungarotoxin/AlexaFluor 555 conjugate (Molecular Probes, UK) was used to delineate neuromuscular junctions (NMJs).

ELISA – Temperature dependent binding

To determine the binding dynamics of **57** against a control polymer (PPSGG³), ganglioside ELISAs were performed. Immulon-2HB 96 well plates (Thermo Fisher Scientific, USA) were coated with 100 μ l at 2 μ g/ml of GM1 (Sigma, UK), diluted in methanol (methanol only for control wells). Plates were blocked with 2% bovine serum albumin in PBS solution for 1 hour at 4°C after which the solution was discarded and a concentration range of **57** applied (0.64 ng/mL, 3.2 ng/mL, 16 ng/mL, 0.08 μ g/mL, 0.5 μ g/mL, 2 μ g/mL, 10 μ g/mL, 50 μ g/mL), (diluted in 0.1% BSA solution) overnight at 4°C. All mimetic formulations were measured in duplicate and assessed across three separate ELISA plates to constitute an n of 3. Anti-GM1 monoclonal antibody only was used as a positive control and applied at 5 μ g/ml in 0.1% BSA. Plates were washed 3 times with PBS and then goat anti-mouse IgG-HRP (1:3000, Sigma Aldrich) in 0.1% BSA was added to all wells and incubated for 1 hour at 4°C. After another three 3 PBS washes, the *o*-phenylenediamine dihydrochloride (OPD) substrate solution (30 ml dH₂O, 16 ml 0.2 M Na₂HPO₄, 14 ml 0.1 M C₆H₉O₇, 1 OPD tablet and 20 μ l 30% H₂O₂ added immediately prior to use) was added for 15 minutes at room temperature in the dark followed by 50 μ l of stop solution (4 M

H₂SO₄). Plates were read immediately at 492 nm on a Tecan Sunrise™ automated microplate reader (Tecan Group Ltd, Männedorf, Switzerland) using Magellan™ software. The average O.D. from matched control wells was subtracted from corresponding antibody wells to correct for background.

***In vitro* Preparations**

GalNAcT^{-/-} Tg(neuronal) mice were sacrificed and diaphragms removed, snap frozen, and stored at -70°C. Tissue was sectioned on the cryostat (Bright Instruments, UK) at 10 µm and collected on APES coated slides. Sections were stored at -20°C. Immunostaining was conducted to analyse the dose dependent efficacy of **57** on *in vitro* preparations of diaphragm sections. Slides were incubated with a concentration range (0.1 µg/mL, 0.5 µg/mL, 1 µg/mL, 5 µg/mL, 10 µg/mL) of **57** or control polymer and 20 µg/mL anti-GM1 antibody for 4 hours at 4°C. Slides were dip washed 3 times in PBS followed by an incubation with goat anti-mouse anti-IgG3 antibody (1:300, Invitrogen, USA), α-bungarotoxin/AlexaFluor 555 conjugate (1:750) and 3% Normal Goat Serum (NGS) for 2 hours at room temperature. After secondary antibody incubation tissue was dip washed 3 times with PBS and mounted in CitiFluor mounting medium. Sections were stored at -20°C until imaging. Each slide had three diaphragm sections from three different *GalNAcT^{-/-} Tg(neuronal)* mice to give each experimental condition an n of 3. The experiment was blinded to the experimenter and all slides were imaged in duplicate.

***Ex vivo* Preparations**

Triangularis sterni (TS) muscle was maintained alive post-dissection in Ringer's physiological solution (116 mM NaCl, 4.5 mM KCl, 1 mM MgCl₂, 2 mM CaCl₂, 1 mM NaH₂PO₄, 23 mM NaHCO₃, 11 mM glucose, pH 7.2-7.4) pre-gassed with 95% O₂/5% CO₂ at room temperature. TS muscle preparations were incubated first with 100 µg/mL anti-GM1 antibody in Ringer's to allow anti-GM1 antibody binding for 1 hour and then washed in Ringer's, after which preparations were incubated with either 25 µg/mL of control polymer or 25 µg/mL of **57** for 1 hour. Preparations were rinsed 3 times with Ringer's prior to fixation with 4% paraformaldehyde (PFA) for 20 minutes at 4°C. After fixation, the tissue was rinsed in PBS, 0.1 M glycine, and again in PBS. To analyze the ability of **57** to displace bound anti-ganglioside antibody *ex vivo*, TS preparations were incubated with goat anti-mouse anti-IgG3 antibody (1:500), α-

bungarotoxin/AlexaFluor 555 conjugate (1:500) and 3% normal goat serum (NGS) as a blocking agent for 3 hours in the dark at room temperature. After secondary antibody incubation tissue was washed 3 times with PBS and mounted in CitiFluor mounting medium on APES coated slides. Sections were stored at -20°C until imaging. Control polymer and **57** were matched per mouse and the experiment was blinded to the experimenter. The *ex vivo* displacement experiment was done in two groups of two mice to provide a biological duplicate for each n. A third group, to bring the total n to 3, is forthcoming.

Image Acquisition and Analysis

For quantification of anti-GM1 antibody deposition at NMJs, images were captured on a Zeiss LSM880 confocal microscope. For diaphragm sections, 15 images (~50 NMJs) were captured per section with a total of 45 images per slide. For triangularis sterni muscle preparations 15 images were captured per tissue (~50 NMJs). The mean intensity of staining overlying the NMJ (delineated by BTx stain) was measured in each case. Images were analysed using the v1.51 Fiji (v1.51) distribution of ImageJ software (NIH). ANOVA analysis was used to compare statistical differences between groups.

Supplementary Information

Table of Content

| | |
|--|----|
| 1. Syntheses of epitopes and glycopolymers | 1 |
| 2. Biological assays | 22 |
| 3. MD simulation for structural comparison of selected glycomimetics to natural GM1 epitope | 30 |

1. Syntheses of epitopes and glycopolymers

General Methods. NMR spectra were recorded on a Bruker Avance DMX-500 (500.1 MHz) spectrometer. Assignment of ^1H and ^{13}C NMR spectra was achieved using 2D methods (COSY, HSQC, HMBC). Chemical shifts are expressed in ppm using residual CHCl_3 , CHD_2OD or H_2O as references. Electron spray ionization mass spectra (ESI-MS) were obtained on a Waters micromass ZQ. The LC/HRMS analysis were carried out using a Agilent 1100 LC equipped with a photodiode array detector and a Micromass QTOF I equipped with a 4 GHz digital-time converter. Reactions were monitored by TLC using glass plates coated with silica gel 60 F₂₅₄ (Merck) and visualized by using UV light and/or by charring with a molybdate solution (a 0.02 M solution of ammonium cerium sulfate dihydrate and ammonium molybdate tetrahydrate in aqueous 10% H_2SO_4). MPLC separations were carried out on a CombiFlash Companion or Rf from Teledyne Isco equipped with RediSep normal-phase or RP-18 reversed-phase flash columns. LC-MS separations were done on a Waters system equipped with sample manager 2767, pump 2525, PDA 2525 and micromass ZQ. Size-exclusion chromatography was performed on Bio-Gel[®] P-2 Gel (45-90 mm) from Bio-Rad (Reinach, Switzerland). All compounds used for biological assays are at least of 98% purity based on HPLC analytical results. Commercially available reagents were purchased from Sigma-Aldrich (Buchs, Switzerland), Acros (Geel, Belgium), Abcr (Germany), suppliers other than normal ones such as Glycosyn (New Zealand) and TCG (India) and et al. Solvents were purchased from Sigma-Aldrich (Buchs, Switzerland) or Acros Organics (Geel, Belgium) and were dried prior to use where indicated. Dichloromethane (DCM) was dried by filtration over Al_2O_3 (Fluka, type 5016 A basic). Molecular sieves 4Å were activated in vacuo at 500 °C for 1 h immediately before use. Building blocks **11** [Ref: Z. Wang et al., *J. Org. Chem.* **2007**, 72: 4209-6420], **12** [Ref: B. Sun et al., *Sci. China. Chem.* **2012**, 55: 31-35], **15** [Ref: A. Bércecs et al., *Can. J. Chem.* 2004, 82: 1157-1171], **16** [S. Ramadan et al., *Org. Lett.* 2017, 19: 4838-4841], **26a** [Ref: B. Sun et al., *Sci. China. Chem.* **2012**, 55: 31-35], **26b** [Patent: WO2018/167230, **2018**, A1], **27** [Ref: X.T. Zhang et al., *Carbohydrate Research* **2014**, 388: 1-7], **31** [Patent: B. Ernst et al., WO2017/46172, **2017**, A1], **35** [Patent: B. Ernst et al., WO2017/46172, **2017**, A1], and **36** [Patent: B. Ernst et al., WO2017/46172, **2017**, A1] were prepared according to similar procedures in listed literatures.

Description of Schemes

Starting from known glycosyl donors (**11** and **15**) and glycosyl acceptors (**12** and **16**), two fully protected Gal-GalN disaccharides (**13** and **17**) were synthesized. By using AgOTf/pTolSCl promoter system, donor **11** was pre-activated which resulted in high reactivity and selectivity therefore high yield for **13**. The conventional TfOH/NIS condition was used for the preparation of **17**. After removal of benzylidene protection, the diol intermediates were acetylated to yield the Gal-GalN disaccharide building blocks (**14** and **18**) (Scheme S1).

Scheme S2 outlines the representative synthesis of the propionic acid analogues and the triflate building blocks (**23** and **25**), which involves the conversion of amino- to hydroxyl-group under Sandmeyer Reaction condition ($\text{NaNO}_2/\text{H}_2\text{SO}_4$), benzylation of the carboxylic acid, and triflation.

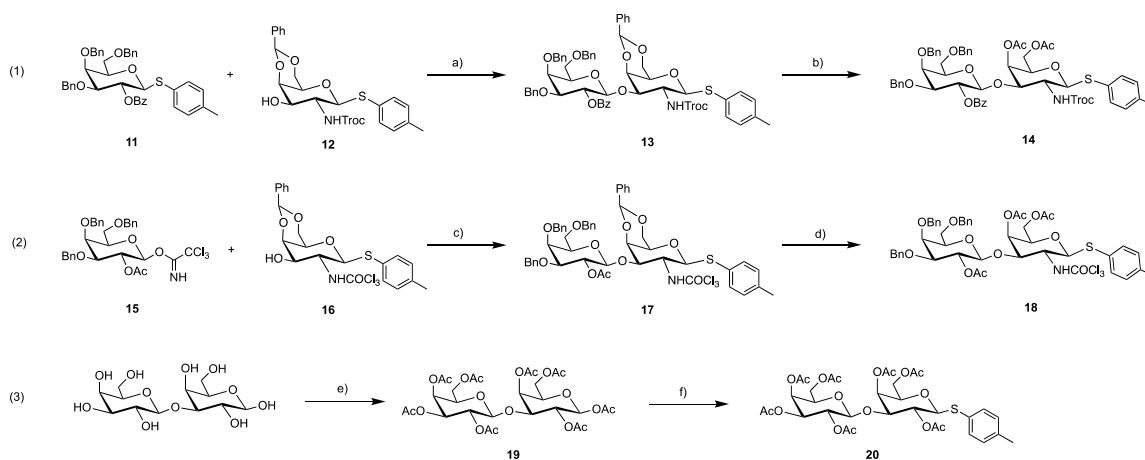
Compound **2** shares most of the structural features as natural GM1 epitope (**1**), except a tyramine moiety instead of amino-propyl glucoside (Part-I). Thus **1** and **2** were synthesized according to similar synthetic routes (Scheme S3). Sialic acid was firstly attached to the 3-position of the galactosides (**26a-b**) via NIS/TfOH sialylation conditions. Peracetylated sialyl donor (**27**) is known to have lower reactivity than common pyranosyl donors, due to the electron-withdrawing carbonyl group presenting at the anomeric carbon, therefore primarily reacts with the more reactive 3-OH on the galactosyl acceptor (**26a-b**). Under AgOTf/pTolSCl-promoting pre-activation conditions, glycosylation between Gal-GalN donor (**14**) and sialosyl acceptors (**28a-b**) proceeded in 4-5 hours and gave fully-protected nat-GM1 and GM1 mimetic (**29a-b**) in good yields. Acetyl- and benzoyl-protection of hydroxyls and NTroc were removed at once under basic condition at elevated temperature, and the acetamide was introduced to the 2-NH₂ of GalN fragment with Ac₂O/MeOH/triethylamine. Both hydrogenation conditions, such as in-situ hydrogen generation with ammonium formate/palladium black (\rightarrow natGM1 **1**), and palladium hydroxide/charcoal catalyzed hydrogenation (\rightarrow GM1 mimetic **2**), successfully removed the benzyl and Cbz protecting groups to yield the targeting oligosaccharides (**1-2**).

The synthesis of Neu5Ac (Part II)-replaced GM1 mimetics (**3-9**) was depicted in Scheme S4-S6. Basically, the sialic acid moiety was replaced by a series of propionic acid analogs, which were introduced to the galactose acceptor (**26a-b**) via tin-mediated alkylation reaction by using -OTf as leaving group. Then Gal-GalN fragment (**14** or **18**) was coupled to the 4-position of galactoside or lactoside acceptors (**32a-c**, **37a-b**, **40a-b**) to give the fully-protected oligosaccharides (**33a-c**, **38a-b** and **41a-b**). After saponification, N-acetylation, hydrogenolysis, GM1 mimetics with replacement at Part-II (**3-9**) were obtained in good to excellent yields.

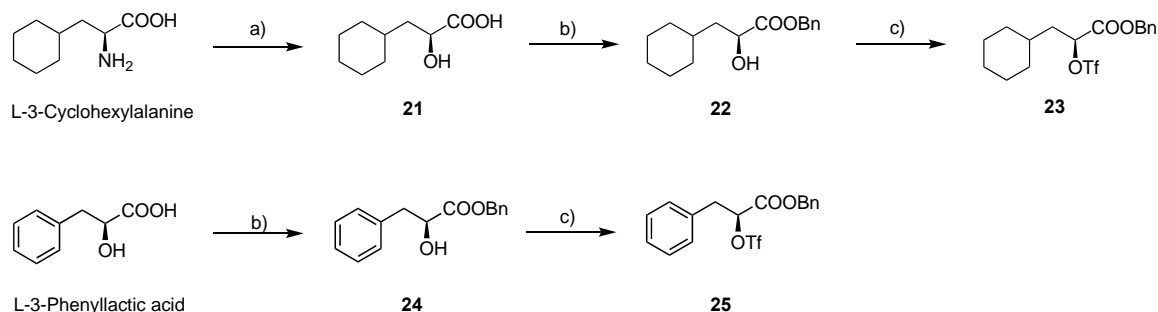
Compound **10** was synthesized according to similar procedure for natGM1 (**1**) and mimetic **2**. In Scheme S7, through pre-activation glycosylation between lactose donor (**20**) and sialosyl acceptor (**28a**), fully-protected precursor of mimetic (**10**) was obtained with high stereo selectivity and good yield. Subsequent saponification and hydrogenation gave the target mimetic with Part I-lactose replacement.

To synthesize the GM1 glyco-polymers, the monomeric GM1 analogues (**1-10**) were firstly reacted with thiobutylolactone and triethylamine to attach a mercapto-butanamide linker (\rightarrow **45-54**). The commercial polylysines (hydrobromide salts) were chloroacetylated, giving the activated polylysines – structurally represented as **55**. Sub-stoichiometric amounts of the GM1 analogues were coupled to the lysine units through nucleophilic substitution of the chloride by sulfhydryl. In order to improve the aqueous solubility of the glycosylated-polylysine polymers, the remaining chloroacetamides were capped with thioglycerol. Nanofiltration with appropriate MW cut-off

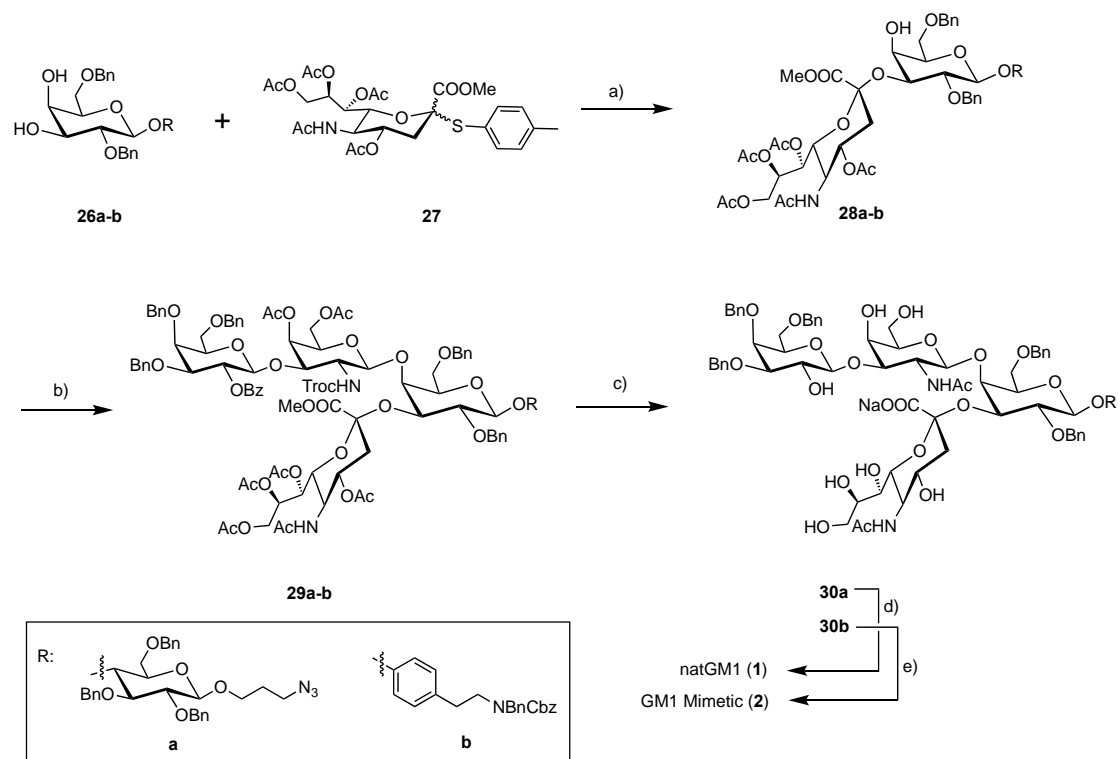
removed small-size impurities and the target glyco-polymers (**55-65**) were obtained as white solids after lyophilization.



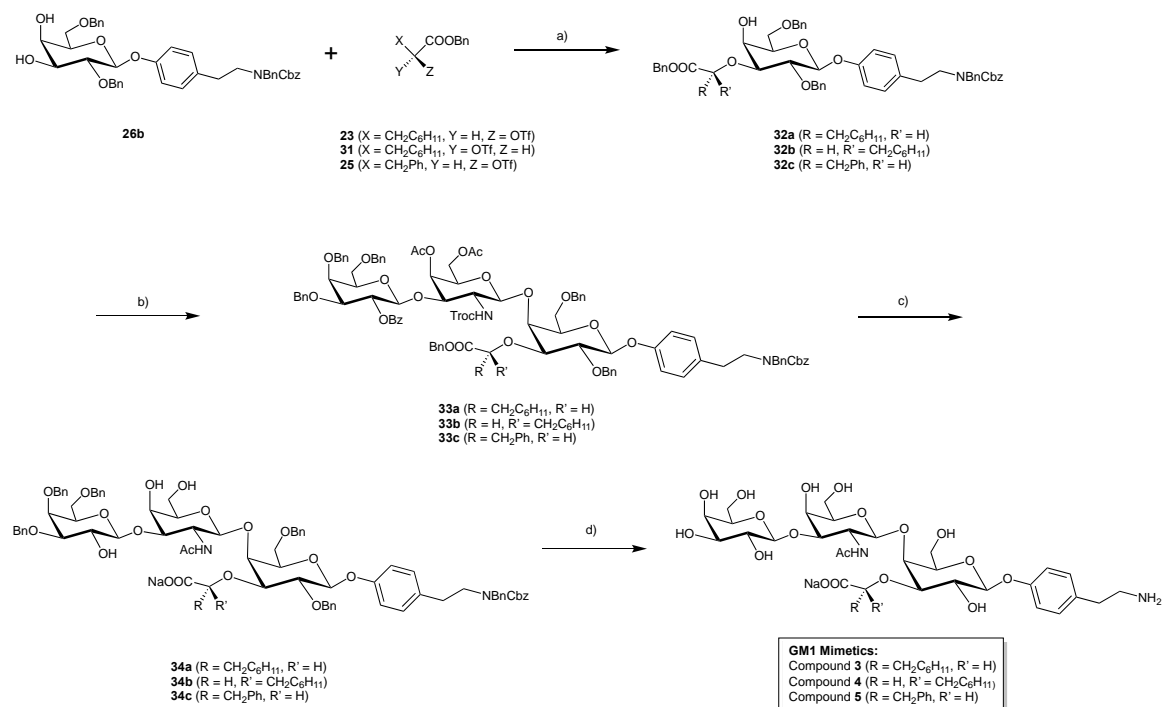
Scheme S1. Synthesis of Gal-GalN disaccharide donors (**14** and **18**) via route (1) and (2), and lactose disaccharide donor (**21**) via route (3). Reagents and conditions: a) AgOTf, pTolSfCl, TTBP, 4Å MS, CH₃CN/DCM (1:10), -70 to -10°C, yield: 72%; b) i. TsOH, CH₃CN/MeOH (1:1), RT; ii. Ac₂O, pyridine, 0°C to RT, yield: 96%; c) TMSOTf, 4Å MS, DCM/petrol ether (2:1), -10 °C, yield: 40%; d) i. TsOH, water, MeOH, RT; ii. Ac₂O, 4-DMAP, pyridine, 0°C to RT, yield: 81%; e) Ac₂O, pyridine, 0°C to RT, yield: quant.; f) TolSH, BF₃·Et₂O, 4Å MS, DCM, 0°C to RT, yield: 12%.



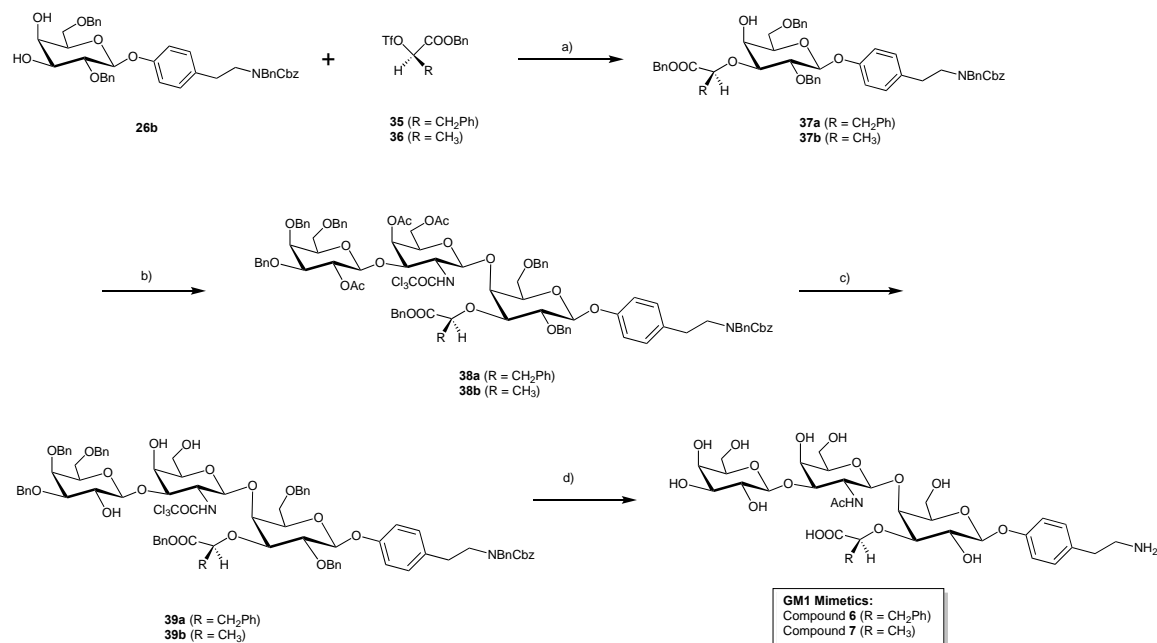
Scheme S2. Synthesis of propionic acid analogs and triflate building blocks (**23** and **25**). Reagents and conditions: a) i. NaNO₂, H₂SO₄, water, 0°C to RT, yield: 55%; b) i. Cs₂CO₃, MeOH/H₂O (5:1), RT; ii. BnBr, DMF, RT, yield over two steps: 44% for **22**, 78% for **24**; c) Tf₂O, 2,6-lutidine, DCM, -15°C, yield: 78% for **23**, 90% for **25**.



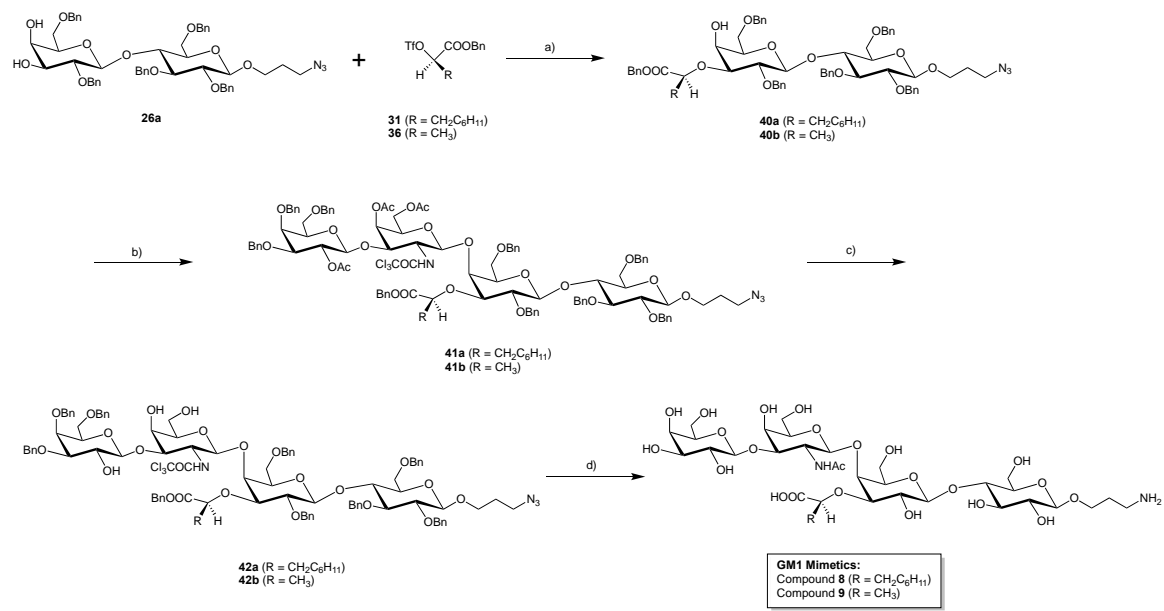
Scheme S3. Synthesis of natural GM1a epitope (**1**) and GM1 mimetic (**2**). Reagents and conditions: a) NIS, TfOH, 4Å MS, CH₃CN, -40°C to RT, yield: 47% for **28a**, 58% for **28b**; b) **14**, AgOTf, pTolSCl, 4Å MS, CH₃CN/DCM (1:10), -70 to 0°C, yield: 41% for **29a**, 71% for **29b**; c) i. 1N NaOH(aq.), THF, 50°C; ii. Ac₂O, TEA, MeOH, RT, yield: quant. for **30a**, 79% for **30b**; d) HCOONH₄, Pd black, MeOH, water, RT, yield: 85%; e) H₂ (gas), Pd(OH)₂/C, 1,4-dioxane, water, RT, yield: 83%.



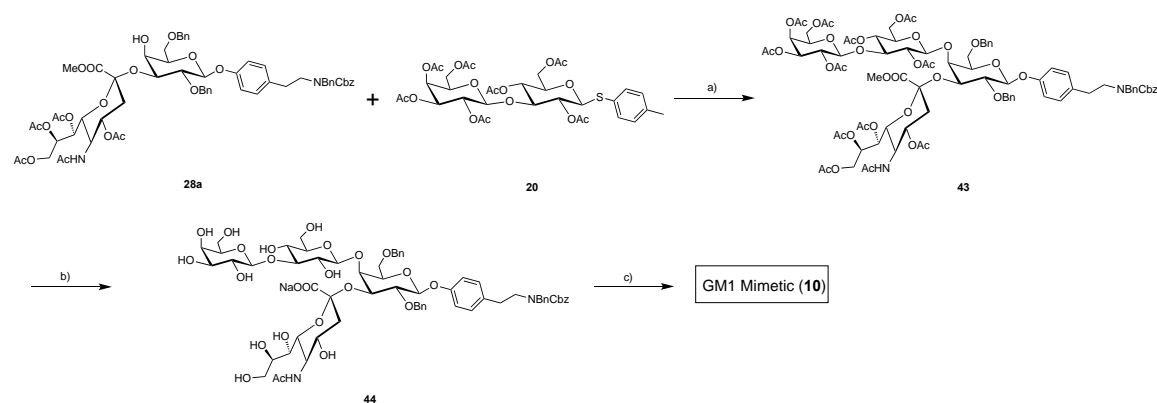
Scheme S4. Synthesis of GM1 mimetic (**3-5**). Reagents and conditions: a) i. Bu_2SO , toluene, reflux; ii. triflate (**23**, **31**, **25**), CsF , DME, RT, yield: 65% for **32a**, 72% for **32b**, 54% for **32c**; b) donor **14**, AgOTf , pTolSCl , 4\AA MS, $\text{CH}_3\text{CN}/\text{DCM}$ (1:10), -70 to 0°C , yield: 83% for **33a**, 95% for **33b**, 65% for **33c**; c) i. 1N NaOH(aq.) , THF, 50°C ; ii. Ac_2O , TEA, MeOH, RT, yield over two steps: 94% for **34a**, 96% for **34b**, 79% for **34c**; d) e) H_2 (gas), $\text{Pd(OH)}_2/\text{C}$, 1,4-dioxane or tBuOH, water, RT, yield: 81% for **3**, 95% for **4**, 80% for **5**.



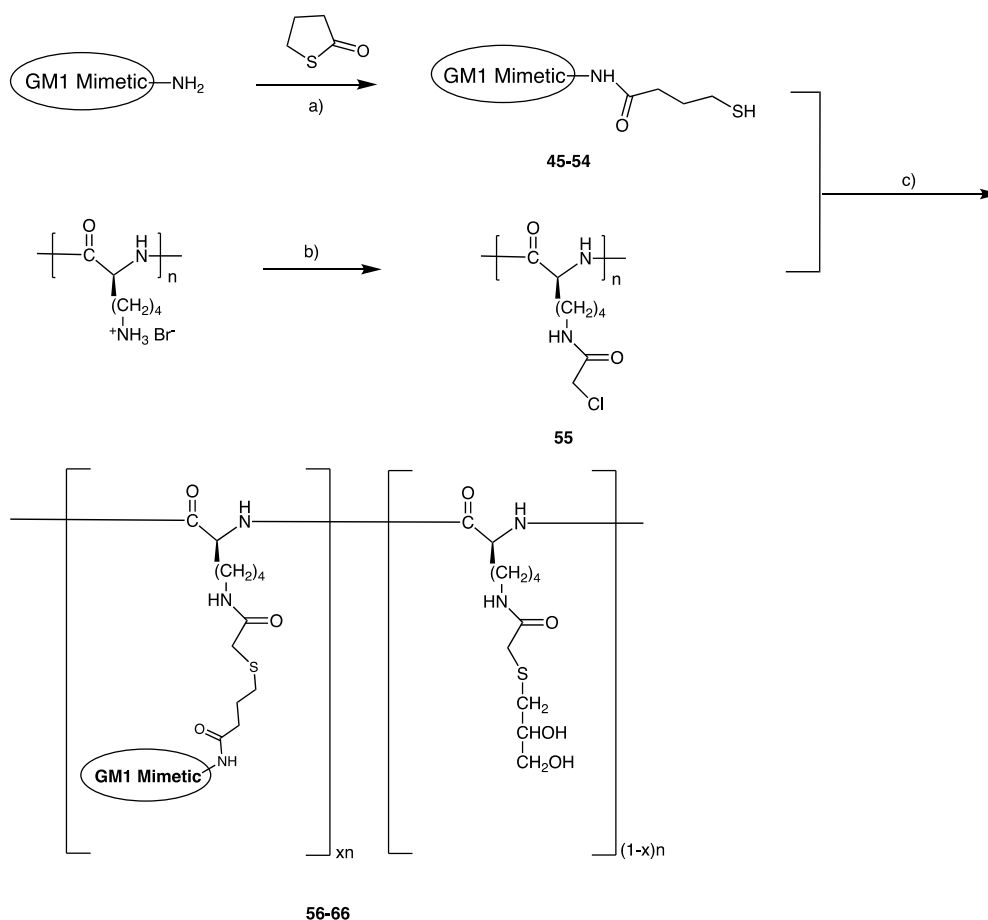
Scheme S5. Synthesis of GM1 mimetic (**6-7**). Reagents and conditions: a) i. Bu_2SO , toluene, reflux; ii. triflate (**35**, **36**), CsF , DME, RT, yield: 55% for **37a**, 84% for **37b**; b) donor **18**, TfoH, NIS, DCM, -20 to -5°C , yield: 26% for **38a**, 26% for **38b**; c) NaOMe , MeOH, RT, yield: quant. for both **39a-b**; d) H_2 (gas), $\text{Pd(OH)}_2/\text{C}$, tBuOH, DCM, AcOH, water, RT, yield: 24% for **6**, 19% for **7**.



Scheme S6. Synthesis of GM1 mimetic (**8-9**). Reagents and conditions: a) i. Bu₂SO, toluene, reflux; ii. triflate (**31**, **36**), CsF, DME, RT, yield: 55% for **40a**, 93% for **40b**; b) donor **18**, TfOH, NIS, DCM, -20 to -5°C, yield: 45% for **41a**, 18% for **41b**; c) NaOMe, MeOH, RT, yield: quant. for both **42a-b**; d) H₂ (gas), Pd(OH)₂/C, tBuOH, AcOH, water, RT, yield: 40% for **8**, 57% for **9**.



Scheme S7. Synthesis of GM1 mimetic (**10**). Reagents and conditions: a) AgOTf, pTolSCL, 4Å MS, CH₃CN/DCM (1:10), -70 to 0°C, yield: 48%; b) 1N NaOH(aq.), THF, 50°C, yield: 85%, c) H₂ (gas), Pd(OH)₂/C, 1,4-dioxane, water, RT, yield: 64%.



Scheme S8. Synthesis of GM1 mimetic-polymer conjugates (**56-65**). Reagents and conditions: a) GM1 mimetic (**1-10**), γ -thiobutyrolactone, TEA, MeOH, RT, yield: quant.; b) 2,6-lutidine, chloroacetic anhydride, DMF, 4°C, yield: 96%; c) i. DIPEA, DBU, water, DMF, RT; ii. 1-thioglycerol, TEA, water, DMF, RT, yield: 60-90% (20-40% GM1-epitope loading).

Synthetic procedures and structural characterization

Compound 13: Glycosyl donor **11** (847 mg, 1.28 mmol) was dissolved in anhydrous DCM (15 mL) and then mixed with freshly activated 4Å molecular sieves at room temperature for 30 min. The above mixture was then cooled down to -70 °C. AgOTf (988 mg, 3.8 mmol) in anhydrous CH_3CN (1 mL) was added to the reaction mixture drop wise, after the mixture was stirred for 5 min, p-TolSCl (203 mg, 1.28 mmol) was added. The orange color of pTolSCl disappeared immediately upon dropping into the vigorously stirred reaction mixture. A mixture of glycosyl acceptor **12** (702 mg, 1.28 mmol) and TTBP (318 mg, 1.28 mmol) in DCM/ CH_3CN (4:1, 5 mL) was then added to the reaction mixture along the side of the reaction flask to ensure no temperature fluctuation. The reaction mixture was then gradually warmed up to -10 °C within 4 hours. The reaction was diluted with DCM (50 mL), and then filtered through Celite. The filtrate was washed twice with sat. NaHCO_3 (50 mL). The organic phase was collected and concentrated. The residue was purified on silica gel MPLC with 30-40% EtOAc/petrol ether to yield the product **13** as colorless oil (1 g, yield: 72%). TLC condition: Petrol ether / EtOAc (2:1), $R_f = 0.4$. $^1\text{H NMR}$ (500

MHz, CDCl₃): δ = 7.98 (d, J = 7.3 Hz, 2H, Ar-H), 7.57 (t, J = 7.4 Hz, 1H, Ar-H), 7.47 – 7.38 (m, 4H, Ar-H), 7.37 – 7.25 (m, 14H, Ar-H), 7.14 (dd, J = 29.5, 4.4 Hz, 6H, Ar-H), 6.91 (d, J = 7.9 Hz, 2H, Ar-H), 5.60 (dd, J = 9.8, 8.2 Hz, 1H), 5.33 (s, 1H), 5.20 (d, J = 7.1 Hz, 1H), 5.15 (d, J = 10.0 Hz, 1H), 4.96 (d, J = 11.7 Hz, 1H), 4.73 (d, J = 8.0 Hz, 1H), 4.66 (d, J = 12.1 Hz, 1H), 4.59 (dd, J = 12.0, 4.9 Hz, 2H), 4.50 – 4.39 (m, 3H), 4.36 (dd, J = 10.6, 2.8 Hz, 1H), 4.30 – 4.22 (m, 2H), 4.18 (d, J = 12.1 Hz, 1H), 3.94 (d, J = 2.5 Hz, 1H), 3.85 (d, J = 11.7 Hz, 1H), 3.68 – 3.49 (m, 4H), 3.39 (d, J = 24.8 Hz, 2H), 2.26 (s, 3H) ppm; ¹³C NMR (125 MHz, CDCl₃): δ = 165.14, 153.73, 138.35, 137.96, 137.71, 137.42, 133.66, 133.11, 130.07, 129.88, 129.63, 128.69, 128.59, 128.50, 128.43, 128.38, 128.35, 128.03, 127.99, 127.93, 127.81, 127.77, 127.71, 126.47, 101.00, 100.64, 95.78, 84.30, 80.10, 75.57, 74.78, 74.53, 73.91, 73.83, 73.65, 72.41, 71.88, 71.55, 69.99, 69.26, 68.70, 51.41, 21.21 ppm; ESI-MS: m/z : calcd for C₅₇H₅₆Cl₃NNaO₁₂S [M + Na]⁺: 1106.25, found: 1106.29.

Compound 14: To a solution of compound **13** (790 mg, 0.73 mmol) in CH₃CN/MeOH (1:1, 20 mL), TsOH monohydrate (277 mg, 1.46 mmol) was added at RT. The reaction mixture was stirred at RT and monitored by TLC. After 16 hours, the reaction was complete, and then neutralized with triethylamine (0.25 mL, 1.8 mmol) and concentrated under vacuum. The crude residue was dissolved in pyridine (4 mL), followed by addition of acetic anhydride at 0°C drop wise. The reaction mixture was then warmed up and stirred at room temperature overnight. The reaction was concentrated and the residue was purified on silica gel MPLC with 30-40% EtOAc/petrol ether to give the product as white solid (750 mg, yield: 96%). TLC condition: Petrol ether / EtOAc (2:1), R_f = 0.3. ¹H NMR (500 MHz, CDCl₃): δ = 8.05 – 7.99 (m, 2H), 7.64 – 7.56 (m, 1H), 7.47 (t, J = 7.8 Hz, 2H), 7.37 – 7.26 (m, 12H), 7.18 (dq, J = 6.9, 2.5 Hz, 1H), 7.14 – 7.08 (m, 4H), 7.03 (d, J = 8.0 Hz, 2H), 5.53 (dd, J = 10.0, 7.9 Hz, 1H), 5.36 (d, J = 3.3 Hz, 1H), 5.09 (d, J = 7.3 Hz, 1H), 5.05 (d, J = 10.3 Hz, 1H), 4.94 (d, J = 11.6 Hz, 1H), 4.62 – 4.55 (m, 3H), 4.54 – 4.37 (m, 4H), 4.31 (dd, J = 10.3, 3.2 Hz, 1H), 4.12 (dd, J = 11.7, 4.4 Hz, 1H), 4.07 – 3.95 (m, 2H), 3.90 (d, J = 12.1 Hz, 1H), 3.75 (dd, J = 7.7, 4.5 Hz, 1H), 3.69 – 3.49 (m, 4H), 3.33 (d, J = 7.4 Hz, 1H), 2.30 (s, 3H), 2.01 (s, 3H), 1.99 (s, 3H) ppm; ¹³C NMR (125 MHz, CDCl₃): δ = 170.49, 170.01, 165.02, 153.45, 138.52, 138.06, 137.86, 137.42, 133.08, 132.80, 130.12, 129.87, 129.55, 128.87, 128.49, 128.31, 128.22, 127.95, 127.93, 127.87, 127.73, 127.70, 127.52, 101.35, 95.58, 85.48, 79.50, 75.26, 74.42, 73.63, 73.61, 72.18, 71.79, 71.54, 69.10, 68.09, 63.05, 52.99, 21.11, 20.75, 20.69 ppm; ESI-MS: m/z : calcd for C₅₄H₅₆Cl₃NNaO₁₄S [M + Na]⁺: 1102.24, found: 1102.22.

Compound 17: Compound **15** (500 mg, 0.79 mmol), **16** (285 mg, 0.55 mmol) and freshly activated 4Å molecular sieves were mixed in DCM/petrol ether (10 mL, 2:1). The mixture was cooled to -10°C, and then added TMSOTf (17 mg, 0.08 mmol) drop wise. The reaction mixture was stirred at -10°C for 10 min then quenched with triethylamine. The reaction mixture was filtered and concentrated, and the residue was purified on silica gel MPLC with 30-40% EtOAc/petrol ether to give the product as white solid (710 mg, yield: 40%). TLC condition: Petrol ether / EtOAc (3:2), R_f = 0.59. ¹H NMR (500 MHz, CDCl₃): δ = 7.57 – 7.49 (m, 2H), 7.48 – 7.40 (m, 2H), 7.39 - 7.18 (m, 17H), 7.01 (d, J = 7.6 Hz, 2H), 6.84 (d, J = 7.1 Hz, 2H), 5.48 (s, 1H), 5.36 – 5.23 (m, 2H), 4.90 (d, J = 10 Hz, 1H), 4.63 (d, J = 12.2 Hz, 1H), 4.60 – 4.48 (m, 3H), 4.48 – 4.37 (m, 3H), 4.37 – 4.27 (m, 2H), 3.97 – 3.85 (m, 2H), 3.77 – 3.66 (m, 1H), 3.62 – 3.50 (m, 3H), 3.43 (q, J = 1.5 Hz, 1H), 3.36 (dd, J = 10.0, 2.8 Hz, 1H), 2.31 (s, 3H), 1.90 (s, 3H) ppm; ESI-MS: m/z : calcd for C₅₀H₅₂Cl₃NNaO₁₁S [M + Na]⁺: 1002.22 found: 1002.25.

Compound 18: Compound **17** (710 mg, 0.72 mmol) was dissolved in MeOH (20 mL) and *p*-toluenesulfonic acid monohydrate (204 mg, 1.07 mmol) with water (250 μ L) was added at RT. The solution was stirred overnight and then quenched with triethylamine (0.5 mL). The reaction mixture was vacuum dried and the residue was treated with pyridine (10 mL). To the above mixture, Ac₂O (1.09 g, 10.7 mmol) and 4-DMAP (8.7 mg, 0.07 mmol) was added at 0°C. The reaction mixture was stirred at RT overnight, concentrated and the residue was purified on silica gel MPLC with acetone/toluene to give the product as white solid (570 mg, yield: 81%). TLC condition: Petrol ether / EtOAc (3:2), R_f = 0.4. ¹H NMR (500 MHz, CDCl₃): δ = 7.46 – 7.38 (m, 2H), 7.35–7.24 (m, 14H), 7.10 (d, *J* = 7.9 Hz, 2H), 6.93 (d, *J* = 7.6 Hz, 1H), 5.39 (d, *J* = 3.3 Hz, 1H), 5.23 (dd, *J* = 10.1, 7.9 Hz, 1H), 5.07 (d, *J* = 10.3 Hz, 1H), 4.89 (d, *J* = 11.6 Hz, 1H), 4.62 (d, *J* = 12.3 Hz, 1H), 4.56 – 4.40 (m, 5H), 4.37 (dd, *J* = 10.4, 3.3 Hz, 1H), 4.11 (dd, *J* = 11.7, 4.9 Hz, 1H), 4.05 (dd, *J* = 11.7, 7.6 Hz, 1H), 3.89 (d, *J* = 2.7 Hz, 1H), 3.81 – 3.71 (m, 2H), 3.60 – 3.50 (m, 2H), 3.50 (t, *J* = 6.4 Hz, 1H), 3.38 (dd, *J* = 10.1, 2.8 Hz, 1H), 2.34 (s, 3H), 2.04 (s, 3H), 2.03 (s, 3H), 1.98 (s, 3H) ppm; ¹³C NMR (125 MHz, CDCl₃): δ = 170.51, 169.90, 169.70, 161.52, 138.53, 138.41, 137.78, 137.64, 133.24, 129.72, 128.49, 128.47, 128.44, 128.21, 127.98, 127.90, 127.83, 127.54, 127.51, 100.52, 85.25, 79.96, 75.35, 74.33, 73.96, 73.85, 73.56, 72.20, 71.77, 70.91, 69.07, 68.32, 62.74, 53.58, 21.21, 21.18, 20.77, 20.67 ppm; ESI-MS: *m/z*: calcd for C₄₇H₅₂Cl₃NNaO₁₃S [M + Na]⁺: 998.21, found: 998.41.

Compound 19: To a mixture of D-lactose (10g, 0.029 mol) in pyridine (50 mL) at 0°C, acetic anhydride (33 mL) was added drop wise. The reaction mixture was stirred at RT overnight. The next day, the reaction was cooled to 0°C and MeOH (30 mL) was slowly added. After stirring at 0°C for 30 min, the reaction mixture was concentrated under vacuum. The residue was dissolved in DCM (100 mL) and washed with 1N HCl aq (100 mL) and sat. NaHCO₃ (100 mL \times 2). The organic phase was collected and dried over Na₂SO₄. The product solution was filtered and concentrated to give the product as white solid (20 grams, quant.), which was used directly in next step. ESI-MS: *m/z*: calcd for C₂₈H₃₈NaO₁₉ [M + Na]⁺: 701.19, found: 701.18.

Compound 20: To a mixture of compound **19** (2 g, 2.95 mmol), TolSH (0.44 g, 3.54 μ mol) and freshly activated 4Å molecular sieves in dry DCM (10 mL), BF₃·Et₂O (1 g, 7.08 mmol) was added drop wise at 0 °C. The reaction mixture was stirred at RT overnight. The reaction mixture was filtered and concentrated, and the residue was purified on silica gel MPLC with 80% EtOAc/petrol ether to give the product as white solid (260 mg, yield: 12%). ¹H NMR (500 MHz, CDCl₃): δ = 7.38 – 7.35 (m, 2H), 7.11 (d, *J* = 7.9 Hz, 2H), 5.36 – 5.32 (m, 1H), 5.20 (t, *J* = 9.2 Hz, 1H), 5.09 (dd, *J* = 10.4, 7.9 Hz, 1H), 4.95 (dd, *J* = 10.4, 3.5 Hz, 1H), 4.90 – 4.82 (m, 1H), 4.60 (d, *J* = 10.1 Hz, 1H), 4.53 (dd, *J* = 11.9, 2.0 Hz, 1H), 4.48 (d, *J* = 7.9 Hz, 1H), 4.10 – 4.04 (m, 2H), 3.90 – 3.84 (m, 1H), 3.74 (t, *J* = 9.5 Hz, 1H), 3.66 – 3.59 (m, 1H), 2.34 (s, 3H), 2.14 (s, 3H), 2.11 (s, 3H), 2.09 (s, 3H), 2.04 (d, 6H), 2.03 (s, 3H), 1.96 (s, 3H) ppm; ¹³C NMR (125 MHz, CDCl₃): δ = 170.28, 170.23, 170.11, 170.01, 169.69, 169.52, 169.01, 138.61, 133.73, 129.61, 127.72, 100.97, 85.60, 76.64, 76.09, 73.89, 70.95, 70.66, 70.25, 69.09, 66.61, 62.10, 60.79, 21.15, 20.81, 20.77, 20.76, 20.60, 20.58, 20.47 ppm; ESI-MS: *m/z*: calcd for C₃₃H₄₂NaO₁₇S [M + Na]⁺: 765.20, found: 765.21.

Compound 21: To a stirring mixture of L-3-cyclohexylalanine (1 g, 5.8 mmol) and 1M H₂SO₄ (10 mL) at 0 °C, NaNO₂ aqueous solution (6 mL, 0.4 g/mL) was added drop wise over 30 min. After stirring at 0 °C for 1 hour, the reaction mixture was warmed up to RT and stirred overnight.

The reaction mixture was diluted with DCM (80 mL) and extracted with brine (50 mL × 3). The organic layer was collected, dried over Na₂SO₄, filtered and concentrated to give the product as colorless oil, which was used directly in the next step. ESI-MS: *m/z*: calcd for C₉H₁₆NaO₃ [M + Na]⁺: 195.10, found: 195.17.

General procedure for synthesis of compound **22** and **24**: (S)-3-cyclohexyl-2-hydroxypropanoic acid (**21**) or L-3-phenyllactic acid (300-500 mg, 1 equiv.) was dissolved in MeOH (5 mL) and then mixed with 1.5N Cs₂CO₃ aqueous solution (1 equiv.). After stirring at RT for 1 hour, the reaction mixture was dried under vacuum. The residue was mixed with DMF (5 mL) and BnBr (1.1 equiv.) was added drop wise. After stirring at RT overnight, the reaction mixture was extracted with EtOAc (30 mL) and water (30 mL). The organic phase was collected, dried over Na₂SO₄, and concentrated. The residue was purified on silica gel MPLC with 20% EtOAc/petrol ether to give the product as colorless oil.

Compound 22: 240 mg (44%). ¹H NMR (500 MHz, CDCl₃): δ = 7.44 – 7.31 (m, 5H, Ph), 5.20 (s, 2H, CH₂Ph), 4.37 – 4.23 (m, 1H, OH), 2.67 (d, *J* = 5.5 Hz, 1H, -CHOH), 1.88 – 1.47 (m, 8H), 1.34 – 1.08 (m, 3H), 1.02 – 0.82 (m, 2H) ppm; ESI-MS: *m/z*: calcd for C₁₆H₂₂NaO₃ [M + Na]⁺: 285.15, found: 285.49.

Compound 24: 363 mg (78%). ¹H NMR (500 MHz, CDCl₃): δ = 7.44 – 7.27 (m, 5H), 7.26 – 7.16 (m, 3H), 7.13 (dd, *J* = 7.5, 1.5 Hz, 2H), 5.15 (d, *J* = 3.3 Hz, 2H), 4.46 (q, *J* = 5.0 Hz, 1H), 3.10 (dd, *J* = 13.9, 4.7 Hz, 1H), 2.96 (dd, *J* = 13.9, 6.6 Hz, 1H), 2.84 (d, *J* = 5.1 Hz, 1H) ppm; ESI-MS: *m/z*: calcd for C₁₆H₁₆NaO₃ [M + Na]⁺: 279.10, found: 279.17.

General procedure for synthesis of compound 23 and 25: A solution of **22** or **24** (300-400 mg, 1 equiv.) and 2,6-lutidine (2 equiv.) in DCM (6 mL) was cooled to -15°C and triflic acid anhydride (1.5 equiv. in 4 mL of DCM) was added drop wise. After stirring for 40 min, cooling bath was removed; reaction mixture was stirred at RT. After 0.5 hour, the reaction mixture was quenched with ice-cold sat. Na₂CO₃ (aq.) (20 mL) and brine (20 mL). The organic layer was dried over Na₂SO₄, filtered and concentrated. The residue was filtered through silica gel cartridge with a elution of 5% EtOAc/petrol ether to give the product as colorless oil (**23** and **25**). Due to the instability of triflate products, the product was collected, vacuum dried and then used immediately in next step.

General procedure for the synthesis of 28a-b: A mixture of glycosyl acceptor **26a** or **26b** (1 – 3 g, 1 equiv.), glycosyl donor **27** (1 – 3 g, 1.2 equiv.), NIS (0.6 – 2.7 g, 2.4 equiv.) and freshly activated 4Å molecular sieves in anhydrous CH₃CN (20 – 40 mL) was stirred at RT for 30 min. The mixture was then cooled to -30°C, and TfOH (25-80 μL, 0.2 equiv.) was added drop wise. The reaction was stirred at -30 °C for 4 hours, and then slowly warmed up to RT overnight. The reaction was quenched with triethylamine (100 μL), and then filtered and concentrated. The residue was dissolved in EtOAc (50 – 100 mL) and washed with sat. Na₂S₂O₃(aq) (50 – 100 mL). The organic phase was collected, concentrated, and the residue was purified on silica gel MPLC with 5 – 10% iPrOH/(petrol ether/DCM 2:1) to give the product (**28a-b**) as white or light yellow solid.

Compound 28a: 1.92 g (47%) as light yellow solid. ^1H NMR (500 MHz, CDCl_3): $\delta = 7.37\text{--}7.33$ (m, 2H), 7.30 $\text{--}7.13$ (m, 23 H), 6.50 (d, $J = 10$ Hz, 1 H, NH), 5.38 $\text{--}5.33$ (m, 1 H), 5.26 $\text{--}5.21$ (m, 1 H), 5.05 $\text{--}4.97$ (m, 1 H), 4.94 (d, $J = 10.0$ Hz, 1 H), 4.77 (d, $J = 10.0$ Hz, 1 H), 4.74 $\text{--}4.61$ (m, 4 H), 4.53 (d, $J = 10.0$ Hz, 1 H), 4.50 $\text{--}4.36$ (m, 3 H), 4.33 $\text{--}4.27$ (m, 2 H), 4.27 $\text{--}4.21$ (dd, $J = 15.0$, 5.0 Hz, 1H), 4.18 $\text{--}4.13$ (dd, $J = 15.0$, 5.0Hz,1 H), 4.01 $\text{--}4.37$ (dd, $J = 10.0$, 5.0 Hz, 1 H), 3.96 $\text{--}3.85$ (m, 3 H), 3.79 (d, $J = 5.0$ Hz, 1 H), 3.73 (s, 3 H), 3.70 $\text{--}3.67$ (m, 2 H), 3.66 $\text{--}3.60$ (dd, $J = 11.5$, 9.0 Hz, 1 H), 3.60 $\text{--}3.42$ (m, 6 H), 3.36 $\text{--}3.28$ (m, 4 H), 2.54 $\text{--}2.49$ (dd, $J = 10.0$ Hz, 5.0 Hz, 1 H), 2.11 (s, 3 H, 2.05 (s, 3 H), 1.97 (t, $J = 10.0$ Hz, 1 H), 1.96 (s, 3 H), 1.91 (s, 3 H), 1.85 (s, 3 H), 1.84 $\text{--}1.77$ (m, 2 H) ppm; ^{13}C NMR (125 MHz, CDCl_3): $\delta = 172.9$, 171.1, 171.0, 170.0, 166.7, 153.9, 139.2, 138.7, 138.4, 138.3, 138.2, 128.6, 128.58, 128.3, 128.2, 128.1, 128.0, 127.93, 127.91, 127.88, 127.8, 127.7, 127.6, 103.8, 102.6, 99.3, 83.0, 81.9, 78.1, 77.7, 76.2, 75.6, 75.5, 75.3, 75.2, 74.5, 73.7, 73.5, 72.6, 69.3, 66.7, 63.5, 59.6, 53.1, 48.5, 29.5, 25.0, 24.4, 21.4, 21.0 ppm; ESI-MS: m/z : calcd for $\text{C}_{70}\text{H}_{84}\text{N}_4\text{NaO}_{23}$ $[\text{M} + \text{Na}]^+$: 1371.54, found: 1371.58.

Compound 28b: 0.96 g (58%) as white solid. ^1H NMR (500 MHz, CDCl_3): $\delta = 7.45\text{--}7.22$ (m, 18H), 7.14 (s, 1H), 7.04 (d, $J = 7.6$ Hz, 1H), 7.00 $\text{--}6.89$ (m, 4H), 5.42 (ddd, $J = 8.4$, 5.9, 2.7 Hz, 1H), 5.31 (dd, $J = 8.1$, 2.1 Hz, 1H), 5.18 (s, 2H), 5.16 (d, $J = 9.7$ Hz, 1H), 5.01 (s, 1H), 4.93 $\text{--}4.79$ (m, 3H), 4.58 $\text{--}4.55$ (m, 2H), 4.46 $\text{--}4.34$ (m, 2H), 4.36 $\text{--}4.25$ (m, 2H), 4.09 $\text{--}3.92$ (m, 4H), 3.86 $\text{--}3.74$ (m, 8H), 3.49 $\text{--}3.32$ (m, 2H), 2.82 $\text{--}2.66$ (m, 2H), 2.57 (dd, $J = 13.0$, 4.6 Hz, 1H), 2.10 (s, 2H), 2.04 (brs, 4H), 2.00 (s, 3H), 1.99 (s, 3H), 1.95 (s, 2H) ppm; ESI-MS: m/z : calcd for $[\text{M} + \text{Na}]^+$: 1199.46, found: 1199.53.

General procedure of the preactivation-based glycosylation reactions for the synthesis of 29a-b, 33a-c, 43: Glycosyl donor **14** (70 $\text{--}200$ mg, 1 equiv.) with glycosyl acceptor **28a/b**, **32a/b/c** (1.5 equiv.), or glycosyl donor **20** (100 mg, 0.13 mmol) with glycosyl acceptor **28b** (70 mg, 0.06 mmol), were dissolved in anhydrous DCM (20 mL) and mixed with freshly activated 4Å molecular sieves at room temperature for 30 min. The above mixture was then cooled down to -70 °C. AgOTf (3 equiv.) in anhydrous CH_3CN (2 mL) was added to the reaction mixture, after stirring for 5 min, followed by addition of p-TolSCL (1 equiv.) drop wise. The reaction mixture was gradually warmed up to 0 °C within 5 hours, then diluted with DCM (80 mL) and filtered through Celite. The filtrate was concentrated and the residue was purified on silica gel MPLC with 0-6% iPrOH / (PE/DCM (2:1)) to yield the product (**29a-b**, **33a-c**, **43**).

Compound 29a: 176 mg (41%) as colorless oil. ^1H NMR (500 MHz, CDCl_3): $\delta = 7.95$ (s, 2 H), 7.54 $\text{--}6.99$ (m, 45 H), 5.52 $\text{--}5.46$ (t, 1 H), 5.44 (d, $J = 7.0$ Hz, 1H), 5.39 (d, $J = 3.0$ Hz, 1H), 5.25 $\text{--}5.20$ (m, 2 H), 5.16 (d, $J = 10$ Hz, 2 H), 5.05 $\text{--}5.00$ (m, 1 H), 4.94 (d, $J = 10$ Hz, 2 H), 4.76 $\text{--}4.76$ (m, 3 H), 4.75 $\text{--}4.65$ (m, 3 H), 4.63 $\text{--}4.52$ (m, 4 H), 4.51 $\text{--}4.37$ (m, 5 H), 4.36 $\text{--}4.30$ (m, 2 H), 4.26 $\text{--}4.08$ (m, 2 H), 4.05 $\text{--}3.76$ (m, 11 H), 3.72 $\text{--}3.55$ (m, 8 H), 3.54 $\text{--}3.47$ (t, 2H), 3.45 $\text{--}3.39$ (m, 2H), 3.38 $\text{--}3.36$ (m, 5 H), 2.11 $\text{--}1.97$ (m, 8 H), 1.96 (s, 6H), 1.89 (s, 3 H), 1.88 (s, 3 H), 1.87 $\text{--}1.70$ (m, 5 H); ^{13}C NMR (125 MHz, CDCl_3): $\delta = 170.9$, 170.5, 170.47, 170.2, 168.7, 165.3, 162.2, 139.11, 139.1, 139.0, 138.9, 138.8, 138.5, 138.0, 133.2, 130.5, 130.1, 129.3, 128.6, 128.57, 128.5, 128.49, 128.4, 128.36, 128.2, 128.15, 127.8, 127.77, 127.7, 127.6, 127.5, 126.6, 126.5, 103.7, 102.7, 100.9, 100.6, 100.5, 83.1, 82.5, 81.9, 80.3, 76.8, 76.0, 75.6, 75.5, 75.45, 75.4, 74.0, 73.4, 73.3, 73.1, 73.0, 72.9, 72.3, 71.8, 70.2, 69.4, 69.1, 68.5, 67.7, 67.6, 67.2, 66.7, 66.4, 62.4, 53.1, 51.8, 48.6, 29.9, 25.5, 21.7, 21.0, 20.9, 20.8 ppm; ESI-MS: m/z : calcd for $\text{C}_{117}\text{H}_{132}\text{Cl}_3\text{N}_5\text{NaO}_{37}$ $[\text{M} + \text{Na}]^+$: 2326.76, found: 2327.00.

Compound 29b: 225 mg (71%) as colorless oil. ^1H NMR (500 MHz, CDCl_3): δ = 8.06 (d, J = 7.7 Hz, 2H), 8.01 (s, 1H), 7.60 (t, J = 7.4 Hz, 1H), 7.50 – 7.43 (m, 3H), 7.39 – 7.27 (m, 22H), 7.25 – 7.20 (m, 4H), 7.17 – 7.09 (m, 6H), 7.05 – 6.87 (m, 4H), 5.50 (dd, J = 10.1, 7.8 Hz, 1H), 5.40 – 5.30 (m, 4H), 5.30 – 5.24 (m, 1H), 5.18 (s, 3H), 5.01 – 4.84 (m, 5H), 4.71 – 4.54 (m, 5H), 4.52 – 4.33 (m, 9H), 4.25 – 4.15 (m, 2H), 4.07 – 3.83 (m, 7H), 3.77 – 3.56 (m, 9H), 3.53 – 3.33 (m, 4H), 2.94 (s, 3H), 2.87 (s, 3H), 2.82 – 2.62 (m, 3H), 2.51 (dd, J = 13.2, 4.7 Hz, 1H), 2.03 (brs, 4H), 1.95 (d, J = 5.8 Hz, 6H), 1.91 (s, 6H) ppm; ^{13}C NMR (125 MHz, CDCl_3): δ = 170.78, 170.42, 170.31, 170.15, 169.76, 168.40, 164.97, 162.57, 153.72, 138.83, 138.56, 138.35, 137.86, 137.76, 137.51, 136.76, 132.97, 130.33, 129.93, 129.64, 128.56, 128.52, 128.49, 128.40, 128.34, 128.30, 128.23, 128.18, 128.10, 128.01, 127.89, 127.85, 127.72, 127.55, 127.50, 127.40, 127.36, 127.28, 117.06, 101.14, 99.70, 98.40, 95.99, 79.50, 74.98, 74.41, 73.71, 73.51, 73.46, 72.40, 72.26, 71.72, 70.53, 69.73, 69.00, 68.20, 64.39, 62.50, 62.07, 52.88, 50.97, 49.34, 36.48, 31.44, 29.69, 25.35, 23.87, 23.17, 21.15, 20.79, 20.63, 20.60 ppm; ESI-MS: m/z : calcd for $\text{C}_{110}\text{H}_{120}\text{Cl}_3\text{N}_3\text{NaO}_{34}$ $[\text{M} + \text{Na}]^+$: 2154.67, found: 2154.38.

Compound 33a: 132 mg (83%) as colorless oil. ^1H NMR (500 MHz, CDCl_3): δ = 8.08 (d, J = 7.8 Hz, 2H), 7.60 – 7.52 (m, 1H), 7.46 (t, J = 7.7 Hz, 2H), 7.40 – 7.11 (m, 40H), 6.99 (d, J = 7.9 Hz, 1H), 6.87 (s, 3H), 5.84 (d, J = 8.0 Hz, 1H), 5.55 (t, J = 9.0 Hz, 1H), 5.36 (d, J = 3.6 Hz, 1H), 5.17 (s, 2H), 5.06 (d, J = 8.4 Hz, 1H), 5.00 – 4.90 (m, 3H), 4.84 – 4.56 (m, 7H), 4.53 – 4.21 (m, 10H), 4.18 – 4.03 (m, 1H), 4.03 – 3.89 (m, 2H), 3.83 (t, J = 8.5 Hz, 1H), 3.77 – 3.48 (m, 10H), 3.46 – 3.31 (m, 2H), 2.81 – 2.61 (m, 2H), 2.13 – 2.03 (m, 4H), 1.95 (s, 3H), 1.69 – 1.48 (m, 7H), 1.17 – 0.98 (m, 4H), 0.94 – 0.70 (m, 3H) ppm; ^{13}C NMR (125 MHz, CDCl_3): δ = 170.48, 170.20, 165.13, 155.87, 138.71, 138.51, 138.27, 137.98, 137.81, 137.65, 136.81, 135.40, 132.93, 130.55, 130.01, 129.72, 128.60, 128.56, 128.50, 128.43, 128.40, 128.36, 128.26, 128.25, 128.01, 127.96, 127.92, 127.89, 127.85, 127.73, 127.66, 127.58, 127.46, 117.13, 101.37, 100.08, 100.00, 96.21, 79.65, 79.25, 77.98, 74.56, 74.40, 74.12, 73.70, 73.61, 73.25, 72.59, 71.85, 71.78, 71.53, 69.58, 69.37, 68.42, 67.34, 67.20, 66.43, 62.75, 54.97, 50.99, 48.29, 40.42, 34.05, 33.52, 33.19, 26.22, 26.15, 20.74, 20.71 ppm; ESI-MS: m/z : calcd for $\text{C}_{106}\text{H}_{113}\text{Cl}_3\text{N}_2\text{NaO}_{24}$ $[\text{M} + \text{Na}]^+$: 1925.66, found: 1925.76.

Compound 33b: 180 mg (95%) as colorless oil. ^1H NMR (400 MHz, CDCl_3): δ = 8.06 (d, J = 7.7 Hz, 1H), 7.62 – 7.55 (m, 1H), 7.50 – 7.44 (m, 2H), 7.40 – 7.09 (m, 40H), 7.02 – 6.83 (m, 4H), 5.54 (t, J = 8.9 Hz, 1H), 5.34 (d, J = 3.5 Hz, 1H), 5.27 (d, J = 7.3 Hz, 1H), 5.16 (d, J = 15.7 Hz, 4H), 5.07 (d, J = 12.1 Hz, 2H), 4.97 (d, J = 11.8 Hz, 2H), 4.76 (s, 1H), 4.68 – 4.56 (m, 5H), 4.51 – 4.30 (m, 10H), 4.21 (d, J = 12.0 Hz, 2H), 3.97 (dd, J = 3.0, 1.0 Hz, 1H), 3.92 (dd, J = 11.4, 6.7 Hz, 1H), 3.82 – 3.29 (m, 11H), 2.82 – 2.62 (m, 2H), 2.07 (s, 3H), 2.04 (s, 3H), 2.01 (s, 3H), 1.58 (d, J = 13.8 Hz, 8H), 1.05 (d, J = 8.4 Hz, 3H), 0.85 – 0.67 (m, 2H) ppm; ^{13}C NMR (101 MHz, CDCl_3): δ = 173.56, 170.64, 170.26, 165.11, 155.91, 138.78, 138.48, 138.04, 137.88, 137.68, 136.88, 135.42, 133.01, 130.04, 129.77, 128.82, 128.78, 128.67, 128.62, 128.59, 128.50, 128.42, 128.31, 128.10, 128.05, 128.02, 127.95, 127.79, 127.73, 127.67, 127.52, 117.13, 102.05, 81.78, 79.65, 75.14, 74.41, 74.13, 73.67, 72.51, 71.83, 71.75, 71.30, 69.48, 68.46, 67.39, 66.79, 62.58, 55.11, 51.05, 48.36, 41.29, 34.22, 33.65, 33.60, 33.09, 26.35, 26.03, 20.90, 20.83 ppm; ESI-MS: m/z : calcd for $\text{C}_{106}\text{H}_{113}\text{Cl}_3\text{N}_2\text{NaO}_{24}$ $[\text{M} + \text{Na}]^+$: 1925.66, found: 1925.68.

Compound 33c: 80 mg (65%) as colorless oil. ^1H NMR (500 MHz, CDCl_3): δ = 8.07 (d, J = 7.2 Hz, 2H), 7.56 (t, J = 7.4 Hz, 1H), 7.46 (t, J = 7.6 Hz, 2H), 7.39 – 7.03 (m, 45H), 6.97 (s, 1H), 6.85

(s, 3H), 5.82 (d, $J = 7.8$ Hz, 1H), 5.53 (t, $J = 8.8$ Hz, 1H), 5.29 (s, 1H), 5.17 (s, 2H), 5.02 – 4.89 (m, 3H), 4.78 – 4.54 (m, 9H), 4.53 – 4.30 (m, 7H), 4.07 (dd, $J = 11.0, 5.2$ Hz, 1H), 4.04 – 3.87 (m, 2H), 3.81 (s, 1H), 3.75 – 3.49 (m, 7H), 3.48 – 3.28 (m, 5H), 3.04 (dd, $J = 14.1, 5.0$ Hz, 1H), 2.95 (d, $J = 7.4$ Hz, 1H), 2.82 – 2.59 (m, 2H), 2.03 (d, $J = 5.4$ Hz, 4H), 2.00 (s, 3H) ppm; ^{13}C NMR (125 MHz, CDCl_3): $\delta = 170.53, 170.19, 155.80, 138.63, 137.92, 137.77, 136.78, 135.16, 132.89, 129.98, 129.66, 129.44, 128.58, 128.51, 128.35, 128.30, 128.24, 128.07, 127.94, 127.87, 127.71, 127.54, 127.49, 117.08, 102.01, 101.15, 99.97, 96.29, 79.68, 74.40, 73.74, 73.62, 71.84, 62.63, 50.97, 49.23, 48.27, 39.21, 39.07, 20.79, 20.69, 0.03$ ppm; ESI-MS: m/z : calcd for $\text{C}_{106}\text{H}_{107}\text{Cl}_3\text{N}_2\text{NaO}_{24}$ $[\text{M} + \text{Na}]^+$: 1919.62, found: 1919.63.

Compound 43: 50 mg (48%) as colorless oil. ^1H NMR (500 MHz, CDCl_3): $\delta = 7.42 - 7.22$ (m, 19H), 7.14 (d, $J = 7.0$ Hz, 1H), 7.06 – 6.91 (m, 4H), 5.36 (d, $J = 3.1$ Hz, 1H), 5.30 (dd, $J = 9.4, 1.7$ Hz, 1H), 5.27 – 5.18 (m, 4H), 5.16 – 5.11 (m, 2H), 5.00 – 4.95 (m, 2H), 4.93 – 4.88 (m, 2H), 4.70 (d, $J = 8.2$ Hz, 1H), 4.57 (dd, $J = 11.3, 3.6$ Hz, 2H), 4.54 – 4.48 (m, 1H), 4.45 – 4.34 (m, 2H), 4.17 – 3.95 (m, 6H), 3.91 (s, 3H), 3.90 – 3.67 (m, 10H), 3.60 (t, $J = 8.7$ Hz, 1H), 3.48 – 3.33 (m, 2H), 2.85 – 2.68 (m, 2H), 2.50 (dd, $J = 13.3, 4.6$ Hz, 1H), 2.16 (s, 3H), 2.14 (s, 3H), 2.07 (s, 3H), 2.06 (s, 3H), 2.05 (d, $J = 1.5$ Hz, 6H), 2.03 (s, 3H), 2.01 (s, 3H), 2.00 (s, 3H), 1.98 (s, 3H), 1.95 (s, 3H), 1.88 (s, 3H) ppm; ESI-MS: m/z : calcd for $\text{C}_{89}\text{H}_{106}\text{N}_2\text{NaO}_{37}$ $[\text{M} + \text{Na}]^+$: 1817.64, found: 1817.85.

General procedure for the synthesis of 30a-b, 34a-c: Compound **29a/b** (200 mg, 1 equiv.) was dissolved in a mixture of 1N NaOH (aq.)/THF (5:1, 12 mL) and stirred at RT. The reaction progress was monitored by TLC (DCM/MeOH 12:1). After the starting material was fully consumed, THF was removed by evaporation, and the residue was extracted with DCM (50 mL) and water (30 mL). The organic layer was concentrated to dryness to give the deacetylation intermediate. The intermediate was then dissolved in a mixture of methanol (6 mL), triethylamine (20 equiv.) and acetic anhydride (20 equiv.). The reaction mixture was stirred at RT for 4 hours, and then concentrated. The residue was purified by passing through a silica cartridge with elution of 10-20% MeOH/DCM. The product (**30a-b, 34a-c**) was collected, concentrated and used directly in next hydrogenation step.

Compound 1: Compound **30a** (20 mg, 0.011 mmol) was dissolved in MeOH/water (1:1, 0.8 mL) to form a white slurry mixture after sonication for a few seconds. Pd black (10 mg) and ammonium formate (10 mg) was added to above mixture and then heated at 50 °C. The reaction was monitored by LC-MS, and after 2.5 hours complete conversion from **30a** to compound **1** was observed. The reaction mixture was filtered, then concentrated and lyophilized from water to give the product as white solid (10 mg, yield: 85%). ^1H NMR (500 MHz, D_2O): $\delta = 4.71$ (d, 1H, $J = 8.5$ Hz), 4.50 □ 4.43 (m, 3 H), 4.12 □ 4.05 (m, 3 H), 4.01 - 3.89 (m, 3 H), 3.85 (d, 1H, $J = 3.5$ Hz), 3.81 (dd, 1H, $J = 13.0, 4.0$ Hz), 3.79 □ 3.65 (m, 14 H), 3.65 □ 3.50 (m, 7 H), 3.46 □ 3.41 (m, 2 H), 3.32 □ 3.23 (m, 2 H), 3.07 (t, 2 H, $J = 6.6$ Hz), 2.60 (dd, 1 H, $J = 12.5, 4.0$ Hz), 1.97 (s, 3 H), 1.94 (s, 3 H), 1.94 (t, 1 H, $J = 12$ Hz), 1.90 □ 1.84 (m, 2 H).; ^{13}C NMR (125 MHz, D_2O): $\delta = 181.6, 175.1, 174.9, 174.2, 104.8, 102.7, 102.6, 102.2, 101.8, 80.5, 78.7, 77.2, 75.0, 74.9, 74.5, 74.2, 73.2, 72.8, 72.6, 72.4, 70.8, 68.8, 68.7, 68.1, 68.0, 63.0, 61.2, 61.1, 60.8, 60.2, 51.7, 51.3, 37.7, 27.1, 23.4, 22.7, 22.2$ ppm; HRMS: m/z : calcd for $\text{C}_{40}\text{H}_{69}\text{N}_3\text{NaO}_{29}$ $[\text{M} + \text{Na}]^+$: 1078.3914, found: 1078.3914.

General procedure of the Pd(OH)₂/C catalyzed hydrogenation reactions for the synthesis of GM1 mimetics (**2-10**): Compound **29b**, **34a/b/c** was dissolved in a mixture of 1,4-dioxane/water (1:1 for **29b**, 2:1 for **34a** and **34c**) or in a mixture of tBuOH/water (7:3 for **34b**). Pd(OH)₂/C (20-100% weight of the glycan) was added and the reaction mixture was stirred under H₂ atmosphere (balloon) at RT. The progress of reaction was monitored by TLC and LC-MS. After 16-24 hours, the reaction mixture was filtered through Celite and the filtrate was concentrated under vacuum. The residue was dissolved with DI water, filtered through 0.22 μm PTFE filter, and lyophilized from water to give the product (**2-10**).

Compound 2: 53 mg (83%) as white solid. ¹H NMR (500 MHz, D₂O): δ = 7.23 (d, *J* = 8.6 Hz, 2H), 7.06 (d, *J* = 8.6 Hz, 2H), 5.07 (d, *J* = 7.9 Hz, 1H), 4.49 (d, *J* = 7.8 Hz, 1H), 4.19 (dd, *J* = 9.8, 2.9 Hz, 1H), 4.11 (dd, *J* = 10.9, 2.7 Hz, 2H), 4.00 (dd, *J* = 10.7, 8.7 Hz, 1H), 3.89 – 3.60 (m, 15H), 3.60 – 3.51 (m, 4H), 3.46 (ddd, *J* = 9.8, 4.7, 2.8 Hz, 2H), 3.19 (t, *J* = 7.1 Hz, 2H), 2.90 (t, *J* = 7.2 Hz, 2H), 2.68 – 2.58 (m, 1H), 1.98 (s, 3H), 1.97 (s, 3H), 1.88 (t, *J* = 11.9 Hz, 1H) ppm; ¹³C NMR (125 MHz, D₂O): δ = 175.04, 174.80, 174.08, 155.54, 130.20, 117.21, 104.72, 102.56, 101.58, 100.26, 80.21, 76.72, 74.88, 74.37, 74.11, 73.06, 72.49, 72.28, 70.67, 69.43, 68.65, 68.58, 68.04, 67.88, 62.84, 61.08, 60.93, 60.16, 51.58, 51.21, 40.63, 37.01, 31.97, 22.59, 22.04 ppm; HRMS: *m/z*: calcd for C₃₉H₆₁N₃NaO₂₄ [M + Na]⁺: 978.3537, found: 978.3540.

Compound 3: 42 mg (81%) as white solid. ¹H NMR (500 MHz, D₂O): δ = 7.22 (t, *J* = 8.4 Hz, 2H), 7.06 (d, *J* = 8.7 Hz, 2H), 4.99 (d, *J* = 7.8 Hz, 1H), 4.75 (d, *J* = 8.5 Hz, 1H), 4.42 (d, *J* = 7.7 Hz, 1H), 4.28 (d, *J* = 2.4 Hz, 1H), 4.14 (d, *J* = 3.1 Hz, 1H), 4.12 – 4.06 (m, 1H), 3.99 (dd, *J* = 10.9, 8.5 Hz, 1H), 3.85 (d, *J* = 3.3 Hz, 1H), 3.83 – 3.64 (m, 9H), 3.64 – 3.55 (m, 3H), 3.52 (dd, *J* = 10.0, 2.5 Hz, 1H), 3.47 (dd, *J* = 9.9, 7.7 Hz, 1H), 3.38 – 3.29 (m, 2H), 2.97 (t, *J* = 7.7 Hz, 2H), 2.04 (s, 3H), 1.84 – 1.49 (m, 7H), 1.43 – 1.30 (m, 1H), 1.23 – 1.07 (m, 3H), 0.95 (dt, *J* = 11.7, 5.7 Hz, 2H) ppm; ¹³C NMR (125 MHz, D₂O): δ = 181.43, 174.95, 155.69, 130.80, 130.39, 130.18, 130.14, 130.08, 117.13, 104.74, 101.45, 100.81, 81.35, 80.05, 79.83, 75.09, 74.89, 74.77, 72.79, 72.46, 70.64, 69.81, 68.60, 68.06, 61.00, 60.89, 60.48, 58.54, 51.60, 50.12, 42.76, 40.88, 40.61, 34.11, 33.35, 32.79, 32.67, 31.90, 29.37, 25.99, 22.46 ppm; HRMS: *m/z*: calcd for C₃₇H₅₉N₂O₁₈ [M + H]⁺: 819.3757, found: 819.3757.

Compound 4: 20 mg (95%) as white solid. ¹H NMR (500 MHz, D₂O): δ = 7.29 – 7.15 (m, 2H), 7.10 – 6.96 (m, 2H), 4.95 (d, *J* = 7.8 Hz, 1H), 4.74 (d, *J* = 8.6 Hz, 1H), 4.45 (d, *J* = 7.8 Hz, 1H), 4.20 (d, *J* = 2.7 Hz, 1H), 4.08 (d, *J* = 3.2 Hz, 1H), 4.03 – 3.93 (m, 2H), 3.87 – 3.79 (m, 2H), 3.79 – 3.52 (m, 11H), 3.50 – 3.41 (m, 2H), 3.17 (t, *J* = 7.2 Hz, 2H), 2.88 (t, *J* = 7.2 Hz, 2H), 2.05 (s, 3H), 1.80 – 1.39 (m, 7H), 1.27 – 1.02 (m, 3H), 0.97 – 0.82 (m, 2H) ppm; ¹³C NMR (125 MHz, D₂O): δ = 81.18, 174.91, 155.75, 131.16, 130.18, 117.20, 104.73, 102.08, 100.78, 80.70, 80.39, 80.29, 74.91, 74.56, 74.41, 74.39, 72.49, 70.67, 70.24, 68.59, 68.04, 60.95, 60.36, 51.40, 40.61, 40.33, 33.24, 33.11, 33.03, 31.92, 26.11, 25.88, 22.65 ppm; HRMS: *m/z*: calcd for C₃₇H₅₈N₂NaO₁₈ [M + Na]⁺: 841.3577, found: 841.3572

Compound 5: 23 mg (80%) as white solid. ¹H NMR (500 MHz, D₂O): δ = 7.49 – 7.42 (m, 4H), 7.36 (ddd, *J* = 8.4, 5.7, 2.7 Hz, 1H), 7.21 (d, *J* = 8.7 Hz, 2H), 7.08 – 6.99 (m, 2H), 4.97 (d, *J* = 7.7 Hz, 1H), 4.54 (dd, *J* = 9.7, 3.1 Hz, 1H), 4.34 (d, *J* = 7.8 Hz, 1H), 3.98 (d, *J* = 3.1 Hz, 1H), 3.89 (dd, *J* = 6.1, 2.7 Hz, 2H), 3.83 – 3.57 (m, 11H), 3.53 (dd, *J* = 10.0, 2.5 Hz, 1H), 4.34 (d, *J* = 7.8 Hz, 1H), 3.27 – 3.10 (m, 5H), 3.01 – 2.85 (m, 3H), 2.16 (s, 1H), 2.03 (s, 3H) ppm; ¹³C NMR (125

MHz, D₂O): δ = 180.31, 174.84, 155.59, 138.97, 131.08, 130.16, 129.37, 129.16, 127.35, 117.06, 104.60, 101.34, 100.80, 100.00, 81.35, 79.31, 75.24, 74.49, 74.29, 73.52, 72.40, 70.60, 69.76, 68.62, 67.83, 61.08, 60.81, 60.18, 51.07, 40.61, 39.18, 31.89, 22.61 ppm; HRMS: m/z : calcd for C₃₇H₅₃N₂O₁₈ [M + H]⁺: 813.3288, found: 813.3289.

Compound 6: 18 mg (24%) as white solid. ¹H NMR (500 MHz, D₂O): δ = 7.44 – 7.25 (m, 4H), 7.25 – 7.16 (m, 3H), 7.09 – 6.97 (m, 2H), 5.04 – 4.89 (m, 1H), 4.59 (d, J = 8.6 Hz, 1H), 4.41 (dd, J = 7.8, 1.6 Hz, 1H), 4.28 (t, J = 5.9 Hz, 1H), 4.20 (d, J = 1.8 Hz, 1H), 4.06 (d, J = 3.4 Hz, 1H), 4.01 – 3.91 (m, 1H), 3.83 (d, J = 3.6 Hz, 1H), 3.78 – 3.50 (m, 11H), 3.50 – 3.38 (m, 1H), 3.16 (t, J = 7.2 Hz, 2H), 3.07 (t, J = 5.1 Hz, 2H), 2.87 (t, J = 7.2 Hz, 2H), 1.98 (s, 3H), 1.91 (s, 2H) ppm; ¹³C NMR (125 MHz, D₂O): δ = 178.68, 177.38, 174.89, 170.28, 155.68, 137.48, 131.17, 130.17, 129.74, 129.63, 128.53, 128.49, 126.76, 126.73, 117.19, 117.16, 104.69, 104.64, 101.97, 100.68, 80.25, 80.22, 80.08, 74.91, 74.61, 74.56, 74.36, 74.06, 72.46, 70.65, 70.12, 68.58, 68.02, 60.96, 60.36, 51.88, 51.33, 42.80, 40.60, 38.18, 31.91, 22.58, 20.94 ppm; HRMS: m/z : calcd for C₃₇H₅₃N₂O₁₈ [M + H]⁺: 813.3288, found: 813.3288.

Compound 7: 15 mg (19%) as white solid. ¹H NMR (500 MHz, D₂O): δ = 7.30 – 7.17 (m, 2H), 7.12 – 7.02 (m, 2H), 5.01 (d, J = 7.5 Hz, 1H), 4.60 (dd, J = 8.6, 2.1 Hz, 1H), 4.45 (d, J = 7.8 Hz, 1H), 4.27 (d, J = 2.6 Hz, 1H), 4.16 – 4.09 (m, 1H), 4.01 (ddd, J = 10.5, 8.6, 2.1 Hz, 1H), 3.85 (d, J = 3.5 Hz, 1H), 3.81 – 3.54 (m, 13H), 3.46 (dd, J = 9.9, 7.8 Hz, 1H), 3.19 (t, J = 7.2 Hz, 2H), 2.89 (t, J = 7.2 Hz, 2H), 2.05 (s, 3H), 1.97 (s, 3H) ppm; ¹³C NMR (125 MHz, D₂O): δ = 174.90, 155.57, 131.20, 130.18, 117.18, 104.75, 102.11, 100.46, 80.47, 78.66, 75.87, 74.89, 74.69, 74.67, 74.42, 73.48, 72.48, 70.67, 69.91, 68.59, 68.06, 60.95, 60.43, 51.32, 40.60, 31.91, 22.55, 17.80 ppm; HRMS: m/z : calcd for C₃₁H₄₈N₂NaO₁₈ [M + Na]⁺: 759.2794, found: 759.2795.

Compound 8: 36 mg (40%) as white solid. ¹H NMR (500 MHz, D₂O): δ = 4.66 (d, J = 8.6 Hz, 1H), 4.38 (d, J = 7.9 Hz, 2H), 4.33 – 4.27 (m, 1H), 4.08 (d, J = 2.0 Hz, 1H), 4.02 (d, J = 3.2 Hz, 1H), 3.95 – 3.82 (m, 4H), 3.80 – 3.75 (m, 1H), 3.74 (dd, J = 10.8, 3.2 Hz, 1H), 3.72 – 3.44 (m, 16H), 3.39 (dd, J = 9.9, 7.8 Hz, 1H), 3.29 (d, J = 6.0 Hz, 2H), 3.18 (dd, J = 9.3, 8.0 Hz, 1H), 3.02 (t, J = 7.0 Hz, 2H), 1.95 (s, 3H), 1.94 – 1.81 (m, 2H), 1.66 – 1.32 (m, 8H), 1.13 – 0.98 (m, 3H), 0.81 (d, J = 11.7 Hz, 2H) ppm; ¹³C NMR (125 MHz, D₂O): δ = 181.32, 181.18, 174.80, 104.68, 102.94, 101.98, 80.73, 80.41, 80.28, 78.57, 74.84, 74.75, 74.71, 74.47, 74.27, 72.55, 72.39, 70.72, 70.58, 68.50, 67.96, 67.78, 60.87, 60.72, 59.91, 51.30, 40.26, 37.50, 33.17, 33.04, 32.98, 26.60, 26.04, 25.82, 25.76, 22.58 ppm; HRMS: m/z : calcd for C₃₈H₆₆N₂NaO₂₃ [M + Na]⁺: 941.3949, found: 941.3947

Compound 9: 27 mg (57%) as white solid. ¹H NMR (500 MHz, D₂O): δ = 4.57 (d, J = 8.6 Hz, 1H), 4.43 (dd, J = 7.9, 2.5 Hz, 2H), 4.39 (d, J = 7.8 Hz, 1H), 4.20 (d, J = 2.7 Hz, 1H), 4.12 – 4.05 (m, 2H), 4.02 – 3.88 (m, 3H), 3.84 (d, J = 3.5 Hz, 1H), 3.79 – 3.51 (m, 16H), 3.51 – 3.40 (m, 2H), 3.36 (dd, J = 9.8, 7.8 Hz, 1H), 3.25 (dd, J = 9.2, 8.0 Hz, 1H), 3.09 (t, J = 6.9 Hz, 2H), 2.00 (s, 3H), 1.98 – 1.89 (m, 2H), 1.34 (d, J = 6.7 Hz, 3H) ppm; ¹³C NMR (125 MHz, D₂O): δ = 180.30, 177.09, 174.84, 104.73, 102.73, 102.10, 102.05, 80.49, 78.99, 78.45, 75.86, 74.89, 74.76, 74.65, 74.31, 74.00, 72.64, 72.48, 70.66, 70.52, 68.58, 68.03, 67.85, 60.95, 60.82, 60.02, 51.29, 37.59, 26.64, 22.55 ppm; HRMS: m/z : calcd for C₃₂H₅₉N₂NaO₂₃ [M + Na]⁺: 859.3166, found: 859.3165.

Compound 10: 7 mg (64%) as white solid. $^1\text{H NMR}$ (500 MHz, D_2O): $\delta = 7.27 - 7.21$ (m, 2H), 7.07 (dd, $J = 9.1, 2.6$ Hz, 2H), 5.11 (d, $J = 7.9$ Hz, 1H), 4.83 (d, $J = 8.0$ Hz, 1H), 4.37 (d, $J = 7.8$ Hz, 1H), 4.25 (dd, $J = 9.9, 3.0$ Hz, 1H), 4.17 (d, $J = 3.0$ Hz, 1H), 3.94 – 3.47 (m, 22H), 3.33 – 3.26 (m, 1H), 3.19 (t, $J = 7.2$ Hz, 2H), 2.90 (t, $J = 7.2$ Hz, 2H), 2.69 (dd, $J = 12.6, 4.7$ Hz, 1H), 1.97 (s, 3H), 1.81 (d, $J = 12.3$ Hz, 1H) ppm; HRMS: m/z : calcd for $\text{C}_{37}\text{H}_{58}\text{N}_2\text{NaO}_{24}$ [$\text{M} + \text{Na}$] $^+$: 937.3272, found: 937.3278.

General procedure for the synthesis of cyclohexyl-, phenyllactic acid and lactic acid derivatives 32a-c, 37a-b, and 40a-b: A mixture of compound **26b** (for synthesis of **32a-c** and **37a-b**) or compound **26a** (for synthesis of **40a-b**) (1 equiv, 0.2N in anhydrous toluene) and Bu_2SnO (1.1 equiv.) was heated to reflux under argon atmosphere while stirring. After 2 hours, the clear solution was cooled to RT, and the triflate (1.5 equiv.), anhydrous CsF (2 equiv.), anhydrous DME (equivalent volume to toluene) were added. The suspension was then stirred for 2 hours at RT under argon. The reaction mixture was diluted with EtOAc and washed with water. The organic phase was collected, dried over Na_2SO_4 , and concentrated. The residue was purified on silica gel MPLC with 10-30% EtOAc/petrol ether to give the product (**32a-c**, **37a-b**, and **40a-b**).

Compound 32a: 416 mg (65%) as colorless oil. $^1\text{H NMR}$ (500 MHz, CDCl_3): $\delta = 7.39 - 7.17$ (m, 35H), 7.12 (d, $J = 6.1$ Hz, 1H), 7.03 (d, $J = 7.4$ Hz, 1H), 6.94 (dd, $J = 16.2, 7.5$ Hz, 5H), 5.03 (d, $J = 12.2$ Hz, 1H), 4.95 (d, $J = 11.2$ Hz, 1H), 4.91 – 4.80 (m, 3H), 4.54 (s, 2H), 4.40 (d, $J = 11.1$ Hz, 1H), 4.33 (dd, $J = 7.9, 5.6$ Hz, 2H), 4.06 (d, $J = 3.5$ Hz, 1H), 3.96 – 3.88 (m, 1H), 3.82 (dd, $J = 10.0, 5.5$ Hz, 1H), 3.75 (dd, $J = 9.9, 6.2$ Hz, 1H), 3.65 (t, $J = 5.7$ Hz, 1H), 3.59 (dd, $J = 9.2, 3.3$ Hz, 1H), 3.48 – 3.29 (m, 3H), 2.84 – 2.63 (m, 5H), 1.77 – 1.57 (m, 13H), 1.38 (dq, $J = 9.9, 3.3$ Hz, 2H), 1.13 (tt, $J = 14.3, 7.6$ Hz, 5H), 0.96 – 0.82 (m, 4H) ppm; $^{13}\text{C NMR}$ (125 MHz, CDCl_3): $\delta = 172.22, 156.12, 138.78, 138.12, 137.90, 136.89, 135.66, 129.81, 128.68, 128.60, 128.55, 128.51, 128.42, 128.25, 128.04, 127.96, 127.82, 127.51, 127.39, 117.28, 102.09, 81.03, 77.94, 76.32, 74.76, 73.80, 73.64, 69.31, 67.41, 66.90, 66.61, 51.06, 40.82, 33.94, 33.71, 33.00, 26.48, 26.22, 26.18$ ppm; ESI-MS: m/z : calcd for $\text{C}_{59}\text{H}_{65}\text{NNaO}_{10}$ [$\text{M} + \text{Na}$] $^+$: 970.45, found: 970.42.

Compound 32b: 3.5 g (72%) as colorless oil. $^1\text{H NMR}$ (500 MHz, CDCl_3): $\delta = 7.41 - 7.20$ (m, 24H), 7.13 (d, $J = 7.2$ Hz, 1H), 7.02 (d, $J = 8.1$ Hz, 1H), 6.99 – 6.87 (m, 3H), 5.25 – 5.16 (m, 3H), 5.12 (d, $J = 12.0$ Hz, 1H), 5.01 (d, $J = 11.0$ Hz, 1H), 4.92 – 4.85 (m, 1H), 4.76 (d, $J = 11.0$ Hz, 1H), 4.58 (d, $J = 11.8$ Hz, 1H), 4.53 (d, $J = 11.9$ Hz, 1H), 4.46 – 4.31 (m, 2H), 4.18 (dd, $J = 8.6, 4.4$ Hz, 1H), 3.94 (dd, $J = 9.3, 7.8$ Hz, 1H), 3.86 – 3.81 (m, 1H), 3.76 (dd, $J = 5.9, 1.8$ Hz, 2H), 3.65 (d, $J = 6.0$ Hz, 1H), 3.49 (s, 1H), 3.39 (qd, $J = 15.2, 4.2$ Hz, 3H), 2.84 – 2.63 (m, 2H), 1.76 – 1.63 (m, 2H), 1.64 – 1.45 (m, 6H), 1.11 – 0.94 (m, 3H), 0.83 (dq, $J = 15.2, 12.1, 3.2$ Hz, 2H) ppm; $^{13}\text{C NMR}$ (125 MHz, CDCl_3): $\delta = 174.88, 129.66, 128.70, 128.66, 128.60, 128.58, 128.39, 128.28, 127.83, 127.75, 127.68, 127.57, 117.13, 101.95, 83.37, 77.63, 75.26, 73.73, 73.64, 69.44, 67.20, 66.86, 41.33, 33.75, 33.24, 32.65, 26.31, 25.91$ ppm; ESI-MS: m/z : calcd for $\text{C}_{59}\text{H}_{65}\text{NNaO}_{10}$ [$\text{M} + \text{Na}$] $^+$: 970.45, found: 970.42.

Compound 32c: 360 mg (54%) as colorless oil. $^1\text{H NMR}$ (500 MHz, CDCl_3): $\delta = 7.43 - 7.17$ (m, 28H), 7.12 (d, $J = 7.1$ Hz, 1H), 7.01 (d, $J = 8.0$ Hz, 1H), 6.95 – 6.85 (m, 4H), 5.17 (s, 2H), 5.04 (d, $J = 12.2$ Hz, 1H), 4.97 – 4.86 (m, 2H), 4.81 (d, $J = 11.2$ Hz, 2H), 4.53 – 4.31 (m, 6H), 3.86 – 3.77 (m, 1H), 3.69 – 3.53 (m, 4H), 3.49 (d, $J = 6.2$ Hz, 1H), 3.42 (dd, $J = 9.3, 3.2$ Hz, 2H), 3.39 – 3.31

(m, 1H), 3.10 (dd, $J = 13.8, 4.1$ Hz, 1H), 3.02 – 2.93 (m, 1H), 2.82 – 2.63 (m, 2H) ppm; ^{13}C NMR (125 MHz, CDCl_3): $\delta = 170.93, 155.96, 138.62, 138.06, 136.91, 135.35, 129.65, 129.33, 128.77, 128.57, 128.55, 128.51, 128.47, 128.41, 128.37, 128.16, 128.12, 127.86, 127.70, 127.66, 127.47, 127.22, 117.18, 101.84, 81.47, 79.15, 74.72, 73.64, 73.32, 68.99, 66.82, 39.49$ ppm; ESI-MS: m/z : calcd for $\text{C}_{59}\text{H}_{59}\text{NNaO}_{10} [\text{M} + \text{Na}]^+$: 964.40, found: 964.51.

Compound 37a: 293 mg (55%) as colorless oil. ^1H NMR (500 MHz, CDCl_3): $\delta = 7.40 - 7.10$ (m, 30H), 7.05 – 6.86 (m, 4H), 5.18 (s, 2H), 5.12 (d, $J = 12.1$ Hz, 1H), 5.05 (d, $J = 12.1$ Hz, 1H), 4.89 – 4.79 (m, 2H), 4.60 – 4.49 (m, 3H), 4.47 – 4.30 (m, 3H), 3.94 (t, $J = 2.4$ Hz, 1H), 3.86 (dd, $J = 9.3, 7.8$ Hz, 1H), 3.74 (d, $J = 5.7$ Hz, 2H), 3.62 (d, $J = 5.9$ Hz, 1H), 3.48 – 3.31 (m, 3H), 3.08 – 3.02 (m, 3H), 2.83 – 2.64 (m, 2H) ppm; ^{13}C NMR (125 MHz, CDCl_3): $\delta = 172.89, 155.91, 138.35, 136.39, 135.00, 129.68, 129.56, 128.66, 128.63, 128.57, 128.51, 128.38, 128.32, 128.01, 127.94, 127.86, 127.73, 127.67, 127.63, 126.85, 117.07, 101.90, 81.87, 80.43, 78.69, 74.83, 73.72, 73.71, 69.39, 67.60, 67.16, 50.99, 39.60$ ppm; ESI-MS: m/z : calcd for $\text{C}_{59}\text{H}_{59}\text{NNaO}_{10} [\text{M} + \text{Na}]^+$: 964.40, found: 964.51.

Compound 37b: 414 mg (84%) as colorless oil. ^1H NMR (500 MHz, CDCl_3): $\delta = 7.40 - 7.26$ (m, 19H), 7.14 (s, 1H), 7.07 – 6.90 (m, 4H), 5.24 – 5.17 (m, 3H), 5.11 (d, $J = 12.0$ Hz, 1H), 4.96 (d, $J = 10.9$ Hz, 1H), 4.86 (t, $J = 7.0$ Hz, 1H), 4.76 (d, $J = 10.8$ Hz, 1H), 4.61 – 4.51 (m, 2H), 4.47 – 4.33 (m, 2H), 4.28 (q, $J = 6.9$ Hz, 1H), 3.97 – 3.89 (m, 2H), 3.82 – 3.71 (m, 2H), 3.64 (d, $J = 6.0$ Hz, 1H), 3.49 – 3.33 (m, 3H), 2.85 – 2.64 (m, 2H), 1.46 (d, $J = 6.9$ Hz, 3H) ppm; ^{13}C NMR (125 MHz, CDCl_3): $\delta = 174.20, 156.00, 138.29, 138.13, 128.69, 128.61, 128.57, 128.42, 128.39, 128.18, 127.85, 127.79, 127.74, 127.67, 117.16, 101.90, 82.89, 78.53, 76.76, 76.04, 75.48, 69.45, 67.15$ ppm; ESI-MS: m/z : calcd for $\text{C}_{53}\text{H}_{55}\text{NNaO}_{10} [\text{M} + \text{Na}]^+$: 888.37, found: 888.42.

Compound 40a: 282 mg (56%) as colorless oil. ^1H NMR (500 MHz, CDCl_3): $\delta = 7.45 - 7.38$ (m, 2H), 7.37 – 7.21 (m, 28H), 5.21 (d, $J = 12.1$ Hz, 1H), 5.13 (d, $J = 12.1$ Hz, 1H), 5.01 (d, $J = 10.6$ Hz, 1H), 4.85 – 4.68 (m, 5H), 4.55 (d, $J = 12.1$ Hz, 1H), 4.48 (d, $J = 12.0$ Hz, 1H), 4.42 – 4.33 (m, 3H), 4.31 (d, $J = 7.8$ Hz, 1H), 4.16 – 4.08 (m, 2H), 3.99 – 3.91 (m, 2H), 3.79 (dt, $J = 3.3, 1.6$ Hz, 1H), 3.74 (dd, $J = 10.9, 4.2$ Hz, 1H), 3.69 (dd, $J = 9.8, 6.9$ Hz, 1H), 3.65 – 3.47 (m, 5H), 3.41 – 3.31 (m, 5H), 3.26 (ddd, $J = 9.8, 4.2, 1.9$ Hz, 1H), 3.16 (dd, $J = 9.3, 3.2$ Hz, 1H), 1.86 (dtd, $J = 12.3, 6.9, 5.6$ Hz, 2H), 1.66 (ddd, $J = 13.7, 8.3, 5.3$ Hz, 2H), 1.56 – 1.36 (m, 5H), 1.07 – 0.89 (m, 3H), 0.85 – 0.73 (m, 2H) ppm; ^{13}C NMR (125 MHz, CDCl_3): $\delta = 174.86, 139.03, 138.78, 138.64, 138.52, 138.30, 135.16, 128.69, 128.63, 128.60, 128.45, 128.33, 128.19, 128.07, 127.92, 127.74, 127.66, 127.59, 127.55, 127.50, 127.30, 127.28, 127.17, 103.52, 102.37, 83.82, 82.90, 81.77, 79.13, 77.61, 76.16, 75.47, 75.04, 73.48, 72.99, 68.69, 68.13, 67.17, 66.47, 66.45, 48.35, 41.39, 33.69, 33.23, 32.75, 29.27, 26.29, 25.86, 25.77$ ppm; ESI-MS: m/z : calcd for $\text{C}_{66}\text{H}_{77}\text{N}_3\text{NaO}_{13} [\text{M} + \text{Na}]^+$: 1142.53, found: 1142.68.

Compound 40b: 440 mg (93%) as colorless oil. ^1H NMR (500 MHz, CDCl_3): $\delta = 7.44 - 7.39$ (m, 2H), 7.35 – 7.19 (m, 30H), 5.22 (d, $J = 12.1$ Hz, 1H), 5.13 (d, $J = 12.1$ Hz, 1H), 5.01 (d, $J = 10.7$ Hz, 1H), 4.82 (d, $J = 11.0$ Hz, 1H), 4.78 – 4.66 (m, 4H), 4.55 (d, $J = 12.1$ Hz, 1H), 4.47 (d, $J = 12.1$ Hz, 1H), 4.43 – 4.32 (m, 4H), 4.20 (q, $J = 6.9$ Hz, 1H), 4.01 – 3.92 (m, 2H), 3.91 – 3.87 (m, 1H), 3.77 (dd, $J = 10.9, 4.3$ Hz, 1H), 3.73 – 3.65 (m, 2H), 3.65 – 3.54 (m, 3H), 3.50 (dd, $J = 9.8, 5.6$ Hz, 1H), 3.42 – 3.31 (m, 5H), 3.19 (dt, $J = 6.0, 3.3$ Hz, 2H), 1.87 (dtd, $J = 12.2, 7.0, 5.6$ Hz, 2H), 1.42 (d, $J = 7.0$ Hz, 3H) ppm; ^{13}C NMR (125 MHz, CDCl_3): $\delta = 174.25, 139.03, 138.62,$

138.56, 138.44, 138.28, 135.20, 128.70, 128.61, 128.44, 128.36, 128.33, 128.29, 128.25, 128.06, 127.91, 127.81, 127.70, 127.66, 127.61, 127.59, 127.51, 127.49, 127.26, 103.54, 102.42, 83.41, 82.88, 81.78, 79.38, 76.44, 75.81, 75.17, 75.04, 73.54, 73.19, 73.04, 68.72, 68.19, 67.16, 66.84, 66.47, 48.35, 29.28, 19.15 ppm; ESI-MS: m/z : calcd for $C_{60}H_{67}N_3NaO_{13}$ $[M + Na]^+$: 1060.46, found: 1060.55.

General procedure of the NIS/TfOH promoted glycosylation for the synthesis of 38a-b and 41a-b: A mixture of glycosyl donor **18** (0.9 equiv.), glycosyl acceptor **37a/b** or **40a/b** (100-300 mg, 1 equiv.), NIS (1.6 equiv.) and freshly activated 3Å molecular sieves in anhydrous DCM (2-5 mL) was stirred at RT for 30 mins. The mixture was then cooled to -20°C, and TfOH (0.1 equiv.) was added. While stirring the reaction mixture was slowly warmed up to -5°C within 2 hours. The reaction mixture was diluted with DCM and washed with sat. $Na_2S_2O_3$ (aq.), sat. $NaHCO_3$ (aq.). The organic phase was collected, concentrated, and the residue was purified on silica gel MPLC with 20-40% EtOAc/petrol ether to give the product (**38a-b** and **41a-b**).

Compound 38a: 150 mg (29%) as colorless oil. 1H NMR (500 MHz, $CDCl_3$): δ = 7.37 – 7.21 (m, 32H), 7.19 – 7.11 (m, 10H), 7.02 – 6.88 (m, 7H), 5.31 – 5.20 (m, 2H), 5.18 (s, 2H), 5.00 (dd, J = 11.8, 9.5 Hz, 2H), 4.96 – 4.89 (m, 2H), 4.80 (q, J = 8.3 Hz, 2H), 4.69 – 4.31 (m, 12H), 4.19 (d, J = 3.2 Hz, 1H), 4.10 (dt, J = 11.2, 5.4 Hz, 2H), 3.89 (ddd, J = 17.9, 8.2, 5.2 Hz, 4H), 3.72 – 3.61 (m, 4H), 3.56 (q, J = 6.3 Hz, 2H), 3.47 – 3.31 (m, 5H), 3.14 (dd, J = 13.9, 4.5 Hz, 1H), 2.99 (dd, J = 14.0, 7.5 Hz, 1H), 2.85 – 2.62 (m, 2H), 2.09 (s, 3H), 2.06 (s, 2H), 2.03 (s, 3H) ppm; ^{13}C NMR (125 MHz, $CDCl_3$): δ = 172.35, 170.48, 170.07, 169.81, 161.15, 155.82, 138.54, 138.44, 138.34, 137.83, 137.80, 136.04, 135.00, 129.69, 129.48, 129.05, 128.55, 128.52, 128.50, 128.43, 128.43, 128.39, 128.38, 128.32, 128.02, 127.88, 127.82, 127.81, 126.88, 125.31, 117.12, 102.21, 100.82, 99.21, 81.69, 81.31, 79.66, 79.42, 75.15, 74.38, 74.27, 74.00, 73.67, 73.53, 72.75, 72.56, 71.82, 71.07, 70.71, 69.98, 69.11, 68.53, 66.74, 62.11, 55.25, 39.17, 21.22, 20.81, 20.69 ppm; ESI-MS: m/z : calcd for $C_{100}H_{103}Cl_3N_2NaO_{23}$ $[M + Na]^+$: 1827.59, found: 1827.70.

Compound 38b: 200 mg (26%) as colorless oil. 1H NMR (500 MHz, $CDCl_3$): δ = 7.41 – 7.21 (m, 38H), 7.20 – 7.10 (m, 2H), 7.04 – 6.87 (m, 4H), 5.29 (t, J = 2.1 Hz, 1H), 5.24 (dd, J = 10.1, 7.9 Hz, 1H), 5.18 (s, 2H), 5.11 – 5.02 (m, 2H), 5.01 – 4.90 (m, 2H), 4.78 (d, J = 8.0 Hz, 1H), 4.66 – 4.24 (m, 12H), 4.17 (d, J = 3.2 Hz, 1H), 4.11 (dd, J = 11.4, 5.8 Hz, 1H), 3.90 (dt, J = 9.7, 6.4 Hz, 3H), 3.82 (dd, J = 9.5, 7.7 Hz, 1H), 3.74 – 3.49 (m, 6H), 3.37 (td, J = 10.4, 3.2 Hz, 4H), 2.84 – 2.63 (m, 2H), 2.09 (s, 3H), 2.06 (s, 3H), 2.02 (s, 3H), 1.40 (d, J = 6.9 Hz, 3H) ppm; ^{13}C NMR (125 MHz, $CDCl_3$): δ = 176.61, 173.70, 170.49, 170.06, 169.74, 161.18, 155.86, 138.56, 138.31, 137.84, 137.80, 135.31, 129.04, 128.71, 128.68, 128.57, 128.44, 128.39, 128.35, 128.19, 128.05, 127.88, 127.85, 127.83, 127.82, 127.80, 127.78, 127.75, 127.65, 127.61, 127.56, 127.45, 117.13, 102.16, 100.77, 99.67, 81.63, 79.60, 79.37, 77.28, 77.02, 76.77, 75.33, 74.40, 74.25, 73.89, 73.71, 73.68, 73.52, 72.61, 72.47, 71.77, 71.11, 70.77, 70.07, 68.41, 66.81, 62.20, 55.41, 21.21, 20.79, 20.68, 19.08 ppm; ESI-MS: m/z : calcd for $C_{94}H_{99}Cl_3N_2NaO_{23}$ $[M + Na]^+$: 1751.56, found: 1751.64.

Compound 41a: 200 mg (45%) as colorless oil. 1H NMR (500 MHz, $CDCl_3$): δ = 7.50 – 7.43 (m, 2H), 7.36 – 7.13 (m, 43H), 5.31 (dd, J = 3.4, 1.1 Hz, 1H), 5.23 (dd, J = 10.2, 7.9 Hz, 1H), 5.11 (d, J = 12.0 Hz, 1H), 5.03 (d, J = 11.9 Hz, 1H), 5.00 – 4.89 (m, 3H), 4.85 – 4.75 (m, 3H), 4.68 (d, J = 10.0 Hz, 1H), 4.63 (d, J = 11.6 Hz, 1H), 4.62 – 4.53 (m, 3H), 4.51 (d, J = 7.9 Hz, 1H), 4.43 (d, J = 12.3 Hz, 1H), 4.41 – 4.36 (m, 3H), 4.35 – 4.27 (m, 3H), 4.21 (d, J = 12.0 Hz, 1H), 4.19 – 4.10

(m, 3H), 4.09 – 4.00 (m, 2H), 4.00 – 3.87 (m, 4H), 3.64 (t, $J = 5.7$ Hz, 3H), 3.60 – 3.46 (m, 7H), 3.46 – 3.42 (m, 1H), 3.40 – 3.29 (m, 6H), 3.28 – 3.20 (m, 2H), 3.11 (dd, $J = 9.6, 3.2$ Hz, 1H), 2.21 (s, 3H), 2.01 (s, 3H), 1.91 (s, 3H), 1.85 (dtd, $J = 12.1, 6.9, 5.4$ Hz, 2H), 1.59 – 1.40 (m, 8H), 1.03 – 0.91 (m, 2H), 0.92 – 0.60 (m, 3H) ppm; ^{13}C NMR (125 MHz, CDCl_3): $\delta = 173.86, 169.97, 160.92, 138.96, 138.75, 138.54, 138.19, 137.80, 135.26, 129.04, 128.91, 128.79, 128.75, 128.44, 128.37, 128.33, 128.32, 128.26, 128.23, 128.21, 128.19, 128.10, 127.87, 127.85, 127.81, 127.75, 127.58, 127.53, 127.47, 127.36, 127.28, 126.72, 125.30, 103.54, 102.32, 100.68, 99.97, 82.00, 81.90, 79.92, 79.51, 79.31, 75.75, 75.09, 74.73, 74.42, 73.86, 73.52, 73.45, 73.26, 72.94, 72.75, 71.75, 71.04, 70.73, 69.28, 69.28, 68.48, 66.79, 66.42, 62.06, 55.01, 48.32, 33.33, 32.79, 29.25, 26.20, 21.46, 21.06, 20.77$ ppm; ESI-MS: m/z : calcd for $\text{C}_{107}\text{H}_{121}\text{Cl}_3\text{N}_4\text{NaO}_{26} [\text{M} + \text{Na}]^+$: 2005.72, found: 2005.93.

Compound 41b: 137 mg (18%) as colorless oil. ^1H NMR (500 MHz, CDCl_3): $\delta = 7.49 - 7.46$ (m, 2H), 7.41 (d, $J = 8.2$ Hz, 1H), 7.37 – 7.16 (m, 43H), 5.30 (d, $J = 3.2$ Hz, 1H), 5.24 (dd, $J = 10.1, 7.9$ Hz, 1H), 5.09 (d, $J = 12.0$ Hz, 1H), 5.00 (d, $J = 12.1$ Hz, 1H), 4.97 (d, $J = 10.1$ Hz, 1H), 4.93 (d, $J = 11.8$ Hz, 1H), 4.86 (d, $J = 8.2$ Hz, 1H), 4.84 – 4.74 (m, 3H), 4.70 (d, $J = 10.0$ Hz, 1H), 4.67 – 4.51 (m, 6H), 4.47 – 4.27 (m, 9H), 4.24 – 4.05 (m, 5H), 4.01 (d, $J = 3.3$ Hz, 1H), 3.92 (ddt, $J = 15.6, 11.2, 7.9$ Hz, 4H), 3.72 – 3.45 (m, 10H), 3.43 – 3.29 (m, 7H), 3.27 (t, $J = 5.7$ Hz, 1H), 3.14 (dd, $J = 9.5, 3.3$ Hz, 1H), 2.21 (s, 3H), 2.01 (s, 3H), 1.93 (s, 3H), 1.90 – 1.81 (m, 3H), 1.35 (d, $J = 6.9$ Hz, 3H) ppm; ^{13}C NMR (125 MHz, CDCl_3): $\delta = 173.65, 170.51, 169.98, 169.93, 161.04, 138.93, 138.69, 138.64, 138.50, 138.19, 137.78, 137.76, 135.26, 128.41, 128.40, 128.36, 128.33, 128.29, 128.28, 128.25, 128.23, 128.19, 128.18, 127.86, 127.82, 127.53, 127.47, 103.55, 102.26, 100.60, 100.39, 82.78, 81.77, 81.54, 80.03, 79.54, 77.28, 77.03, 76.77, 75.93, 75.84, 75.74, 75.14, 75.10, 74.46, 73.97, 73.67, 73.52, 73.45, 73.42, 73.27, 72.67, 72.59, 71.77, 71.01, 70.49, 69.25, 69.16, 68.49, 68.09, 66.94, 66.45, 61.99, 54.89, 48.33, 29.27, 21.08, 20.74, 20.72, 18.97$ pm; ESI-MS: m/z : calcd for $\text{C}_{101}\text{H}_{111}\text{Cl}_3\text{N}_4\text{NaO}_{26} [\text{M} + \text{Na}]^+$: 1923.64, found: 1923.73.

General procedure of trans-esterification/de-acetylation for the synthesis of 39a-b and 42a-b: To a mixture of **38a/b** or **41a/b** (100-200 mg, 1 equiv.) and anhydrous MeOH (2-4 mL), 25% w/w NaOMe/MeOH (0.1 equiv.) was added at RT. The reaction mixture was stirred at RT and the progress of reaction was monitored by TLC. After reaction completion, the mixture was neutralized with IR-120 (H^+) resin to pH 7 and then filtered. The filtrate was concentrated under vacuum and the residue was used directly in next hydrogenation step.

Compound 44: Compound 43 (48 mg, 0.042 mmol) was added to a mixture of THF (6 mL) and 1N NaOH (0.8 mL, 0.843 mmol). The reaction mixture was stirred at RT overnight and then concentrated under vacuum. The residue was filtered through a C18 cartridge and washed with MeOH/water. The fractions were collected and concentrated. The resulted residue was used directly in the hydrogenation reaction. ESI-MS: m/z : calcd for $\text{C}_{66}\text{H}_{83}\text{N}_2\text{O}_{26} [\text{M} + \text{H}]^+$: 1319.52, found: 1319.44.

General procedure for the synthesis of mercaptobutanamide-functionalized GM1 mimetics (45-54): To a solution of GM1 mimetic (**1-10**) (4-20 mg, 1 equiv.) in dry methanol (2-10 mL), triethylamine (10 equiv.) and γ -thiobutyrolactone (10 equiv.) were added. The reaction mixture was stirred under argon atmosphere at RT overnight. The reaction mixture was concentrated under vacuum. The residue was dissolved with DI water and extracted with EtOAc for three times. The

aqueous phase was then lyophilized to give the product (**45-54**) as white solid, which was used directly in next step.

Chloroacetylated poly-L-lysine 55: Poly-L-lysine hydrobromide (100 mg, 0.48 mmol of lysine units) was suspended in a mixture of DMF (2 mL) and 2,6-lutidine (0.5 mL). The mixture was cooled in ice-water bath, and then chloroacetic anhydride (244 mg in 0.5 mL of DMF) was added over 10 min. Poly-L-lysine was gradually dissolved during the addition of the chloroacetic anhydride solution. The reaction mixture was then stirred at 4 °C for 16 hours. The product was precipitated by drop-wise addition of the reaction mixture to vigorously stirring solvent mixture (ethanol/diethyl ether 1:1, 40 mL). The mixture was centrifuged at 1000 rpm, 4-10 °C, for 2 min. The solvent was decanted, and the residue was re-suspended in ethanol/ether (1:1, 30 mL). The centrifugation and re-suspension was repeated three times. The product precipitates were collected and dried under vacuum overnight to give the product as white solid (92 mg, 96%). ¹H-NMR data were identical to the previous report. [Ref: G. Thoma et al., J. Am. Chem. Soc. 1999, 121: 5919-5929]

To a stirring solution of acetylated poly-L-lysine (**55**) (8 mg, 39.1 μmol of lysine units, 1 equiv.) in DMF (389 μL), a solution of GM1 mimetic (**45-54**) (50% mole ratio to the lysine units) in 30 μL of water was added. *N,N*-Diisopropylethylamine (78.2 μmol) and 1,8-diazabicyclo[5.4.0]undec-7-ene (39.1 μmol) were added to the above mixture. The reaction mixture was then stirred at RT under argon atmosphere for 45 min. 1-Thioglycerol (117.3 μmol) and trimethylamine (117.3 μmol) were added and the mixture was stirred for additional 16 hours. The reaction mixture was dropped into a stirring solution of diethyl ether/ethanol (1:1; 3ml), leading to the precipitation of the polymer. The precipitates were collected by centrifugation, washed with ethanol (3 mL), and then dissolved with 10 mL of water. The crude product solution was adjusted to pH 9-10 by addition of 1M NaOH. Further purification was achieved by means of ultrafiltration. Ultracentrifugation was performed using Sartorius Stedim Vivaspin tubes (volume 15 mL, MWCO 50KDa). The ultracentrifugation was repeated four times (from 10 mL to 1 mL), on each occasion the volume was filled up with DI water. Lyophilization gave the GM1 mimetic-polymer conjugate (**56-65**) as white solid. According to ¹H-NMR, the product contained approximately 20-40% monomer carbohydrate units linked to the polymer.

Representative epitope loadings

Polymer **56**: natGM1 epitope **1**-polymer conjugate, monomer loading: 26%.

Polymer **57**: GM1 mimetic **2**-polymer conjugate, monomer loading: 30%.

Polymer **58**: GM1 mimetic **3**-polymer conjugate, monomer loading: 24%.

Polymer **59**: GM1 mimetic **4**-polymer conjugate, monomer loading: 25%.

Polymer **60**: GM1 mimetic **5**-polymer conjugate, monomer loading: 25%.

Polymer **61**: GM1 mimetic **6**-polymer conjugate, monomer loading: 26%.

Polymer **62**: GM1 mimetic **7**-polymer conjugate, monomer loading: 26%.

Polymer **63**: GM1 mimetic **8**-polymer conjugate, monomer loading: 35%.

Polymer **64**: GM1 mimetic **9**-polymer conjugate, monomer loading: 30%.

Polymer **65**: GM1 mimetic **10**-polymer conjugate, monomer loading: 28%.

2. Biological Assays

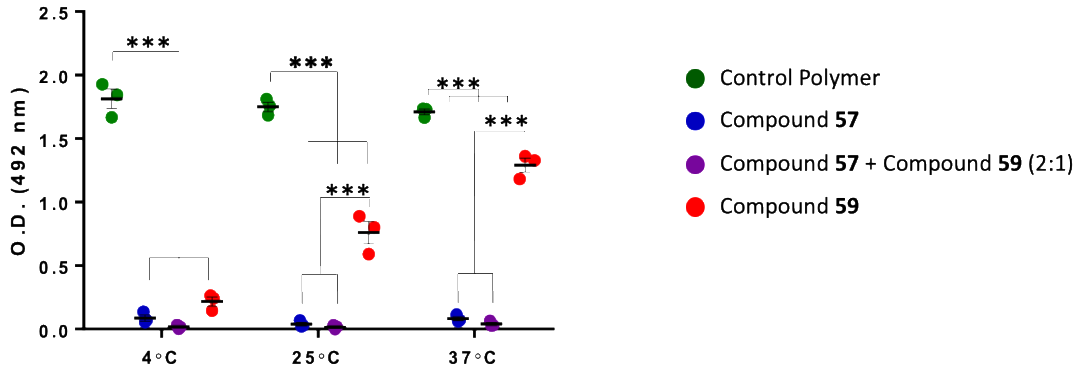


Figure S1: The ELISA temperature assay shows α -GM1 Ab inhibition by compound **57** and compound **59** or a mixture of both at different temperatures. Compound **57** successfully inhibits binding at all temperatures, whereas compound **59** is only efficient at 4°C and loses effectivity at increasing temperatures with no activity at most relevant physiological temperature of 37°C. Measurements were taken in duplicate per plate and analyzed over three separate plates for an n=3 (***) $p \leq 0.001$). Statistics determined with a two-way ANOVA. Assay setup according to inhibition ELISA.

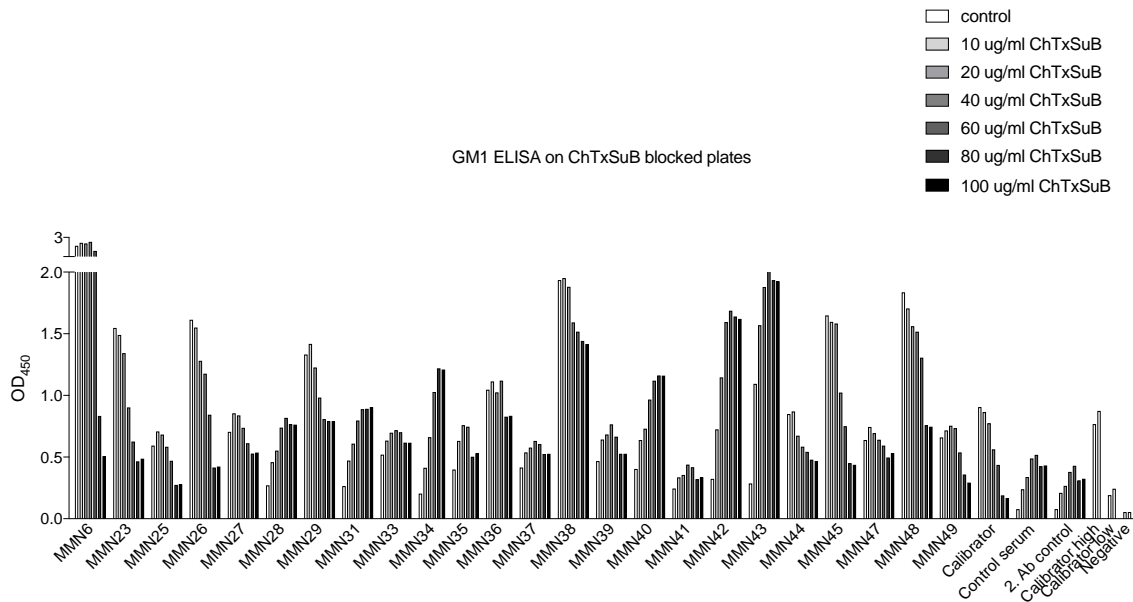


Figure S2: To assess the binding specificity of the MMN patient's IgM antibodies to GM1, the GM1 ELISA plates (Bühlmann, EK-GM1-GM, Lot 0756) were incubated with Cholera Toxin Subunit B (Sigma, C3741, Lot 067M4102V) for 2h at 4°C with gentle shaking (300 rpm). After incubation of the GM1, the Bühlmann anti-GM1 ELISA kit was used as previously described to measure IgM antibody binding of MMN patient sera to GM1 on the plates.

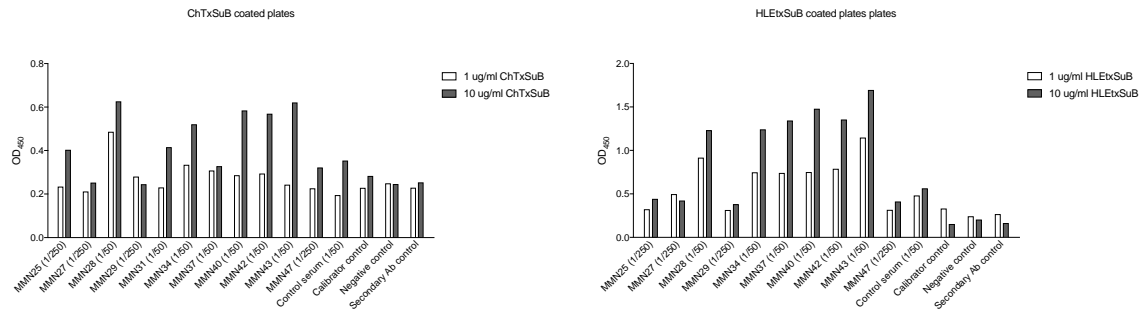


Figure S3: Cholera Toxin Subunit B was coated on a Maxisorp plate (Nunc F96, Lot: B272018) to measure direct binding. A serial dilution in ELISA coating buffer (Bühlmann, EK-GM1-GM, Lot 0756) was coated over night at 4°C. The plate was washed 3x with wash buffer and blocked with BSA (1% in PBS) for 1h at RT before incubating the patient samples and secondary antibodies according to the previously described protocol. To check for direct binding to heat labile enterotoxin subunit B, the same procedure was applied.

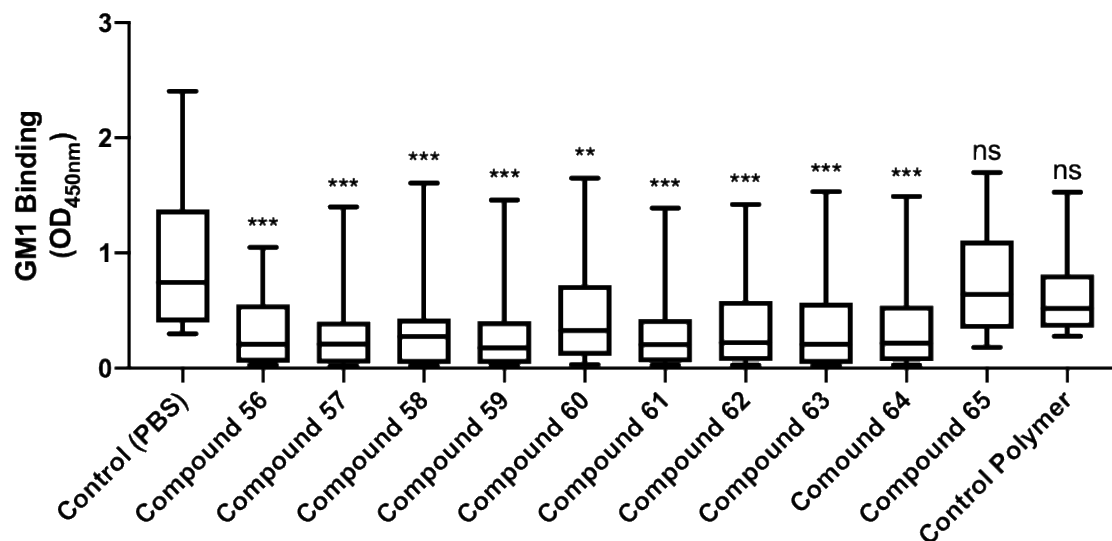
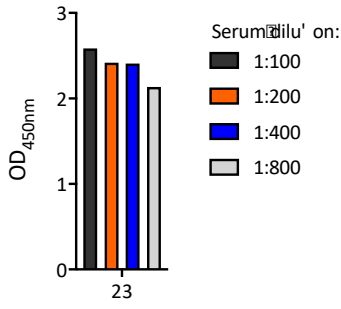
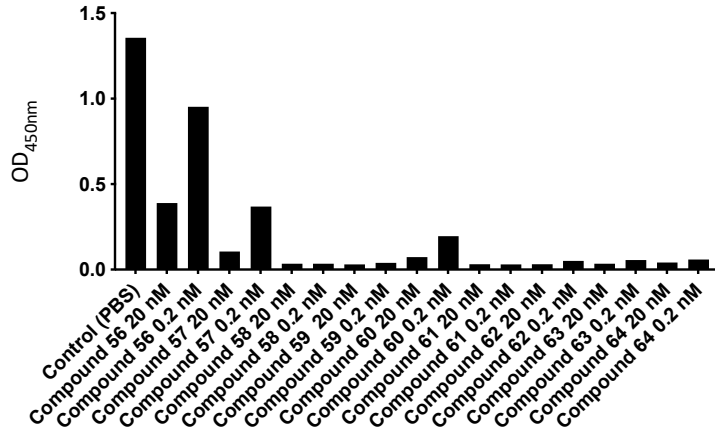


Figure S4: In vitro inhibitory activity of GM1 glycoconjugates on GM1 binding to anti-GM1 IgM in patient serum. Summary of 22 MMN patient sera incubated with the different compounds at 20 nM (one-way ANOVA, ** $p \leq 0.01$, *** $p \leq 0.001$)

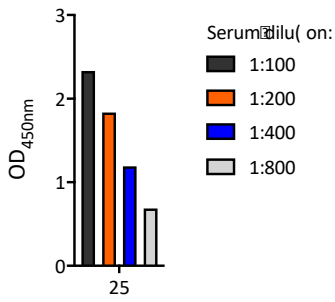
An(-GM1) IgM ELISA



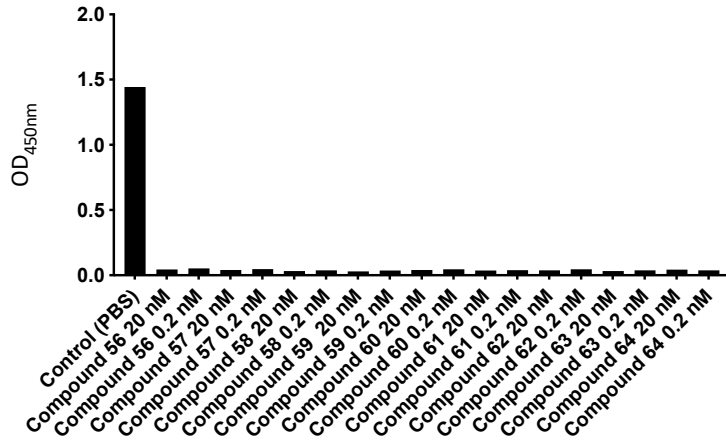
MMN23 (1:1600)



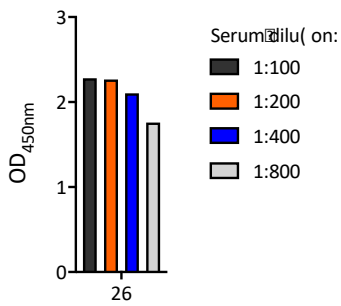
An(-GM1) IgM ELISA



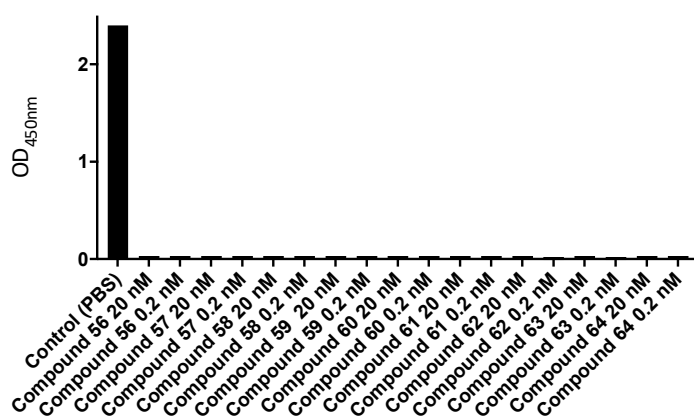
MMN25 (1:200)



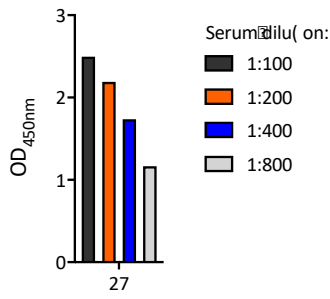
An(-GM1) IgM ELISA



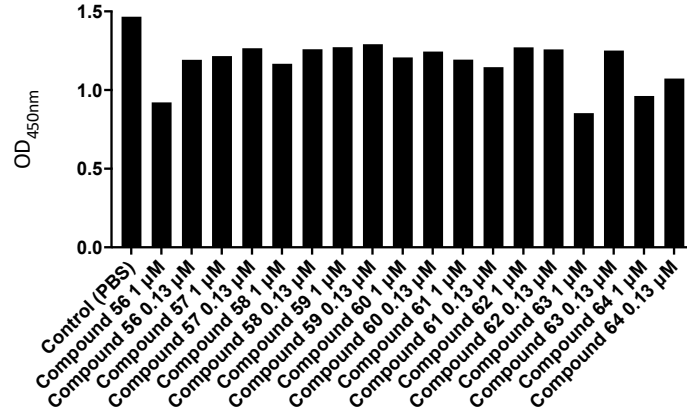
MMN26 (1:1600)



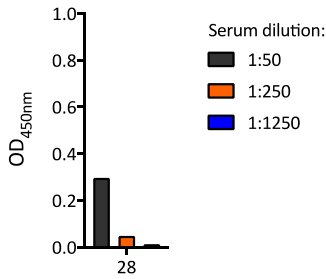
An(-GM1) IgM ELISA



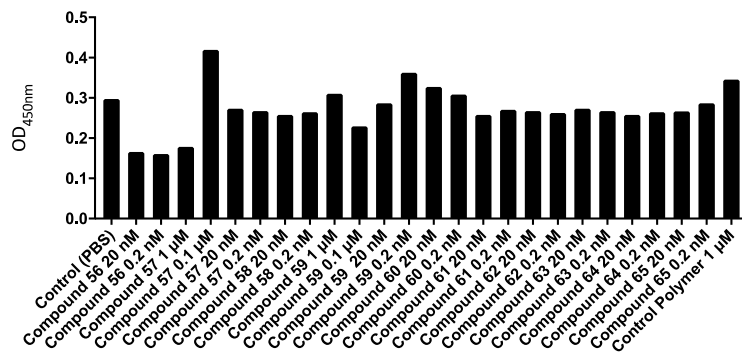
MMN27 (1:300)



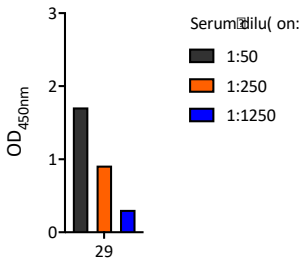
Anti-GM1 IgM ELISA



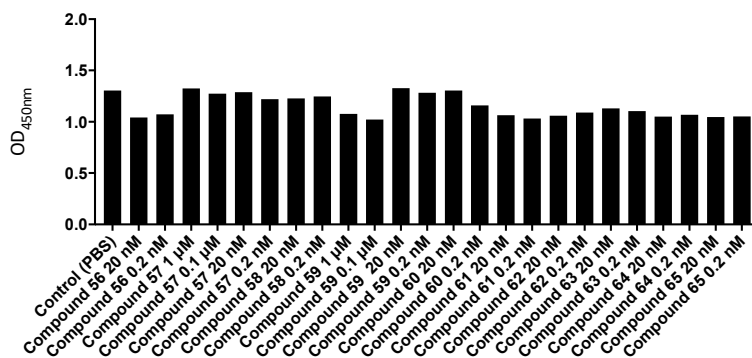
MMN28 (1:50)



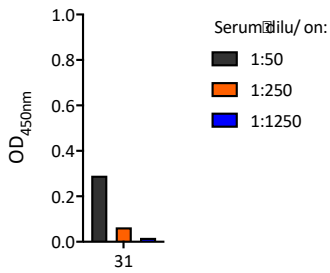
An(-GM1) IgM ELISA



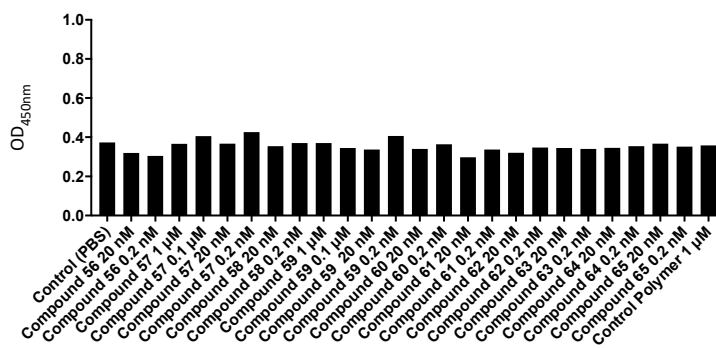
MMN29 (1:250)



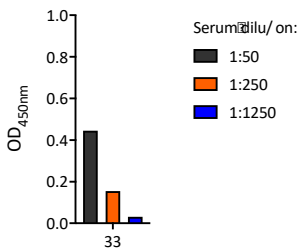
An/-GM1 β GM α ELISA



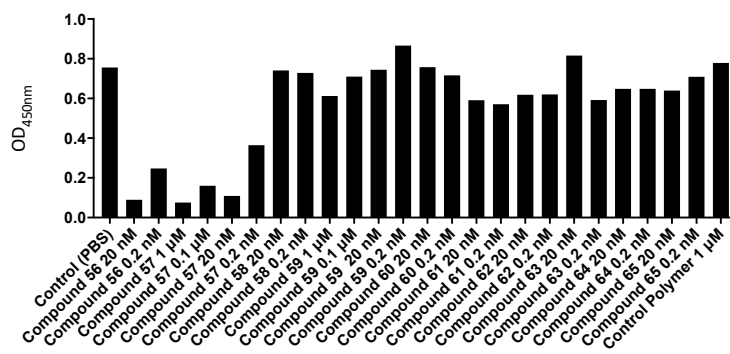
MMN31 (1:50)



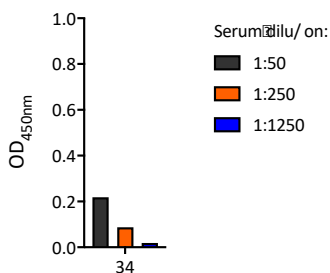
An/-GM1 β GM α ELISA



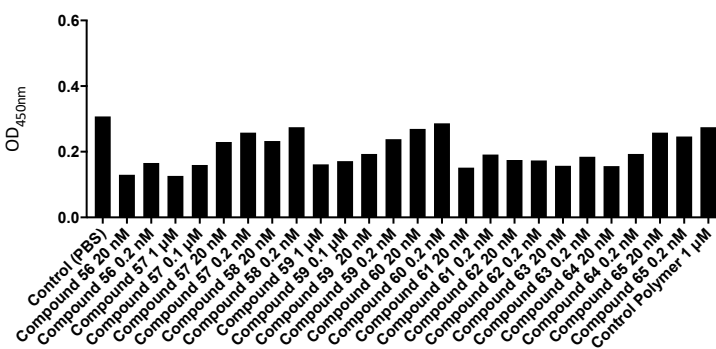
MMN33 (1:50)



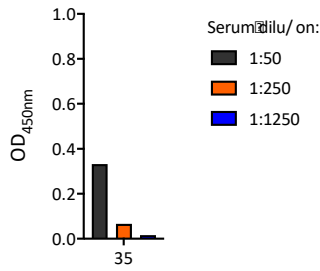
An/-GM1 β GM α ELISA



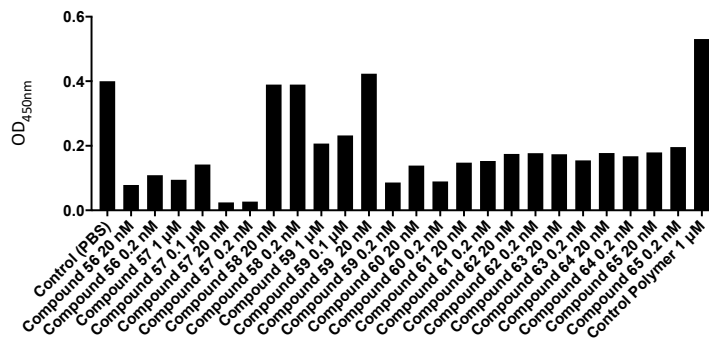
MMN34 (1:50)



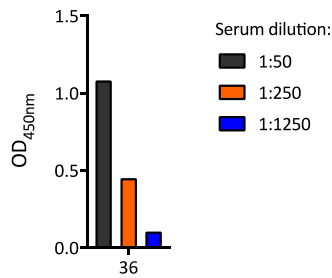
An/-GM1 IgM ELISA



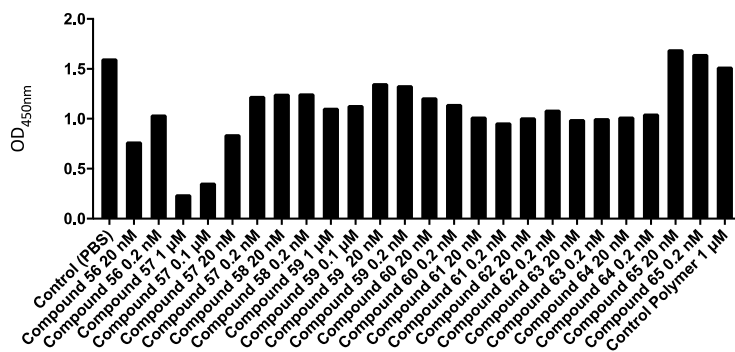
MMN35 (1:50)



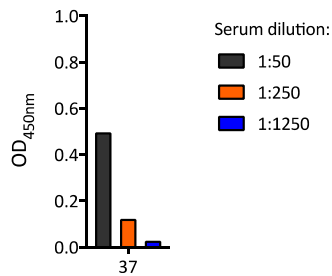
Anti-GM1 IgM ELISA



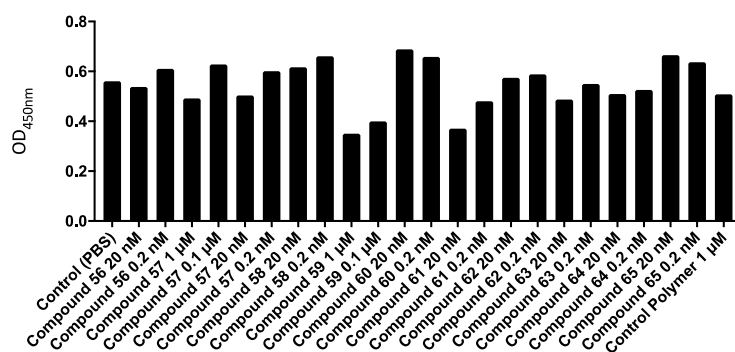
MMN36 (1:50)



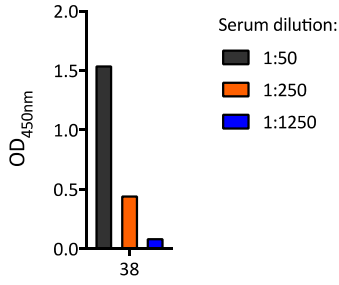
Anti-GM1 IgM ELISA



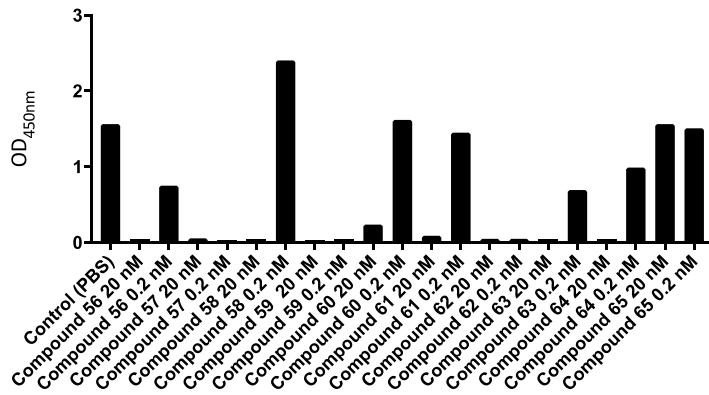
MMN37 (1:50)



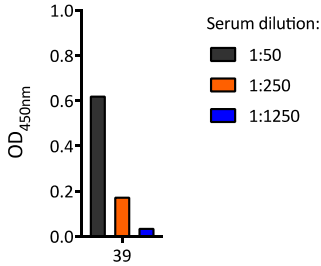
Anti-GM1 IgM ELISA



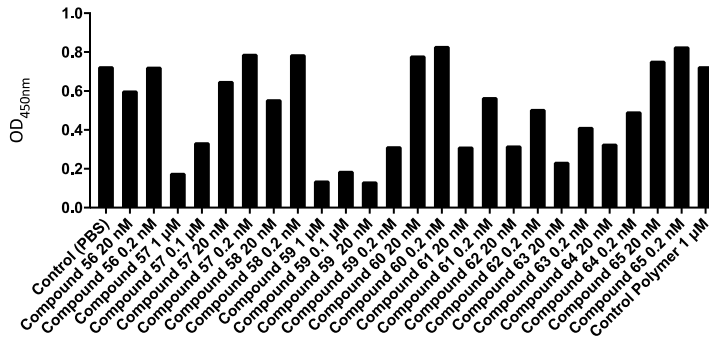
MMN38 (1:100)



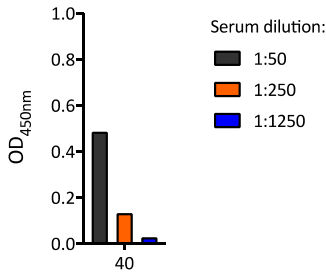
Anti-GM1 IgM ELISA



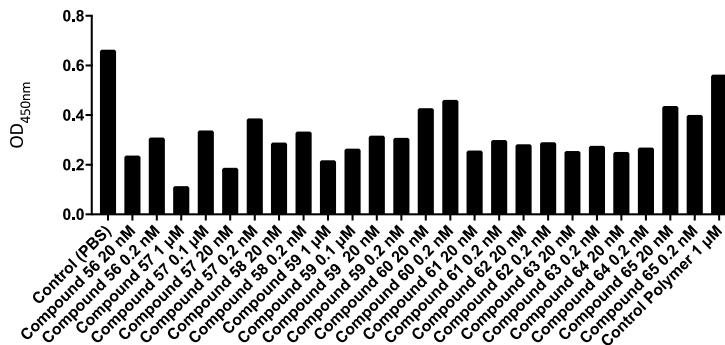
MMN39 (1:50)



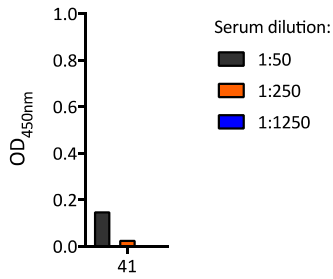
Anti-GM1 IgM ELISA



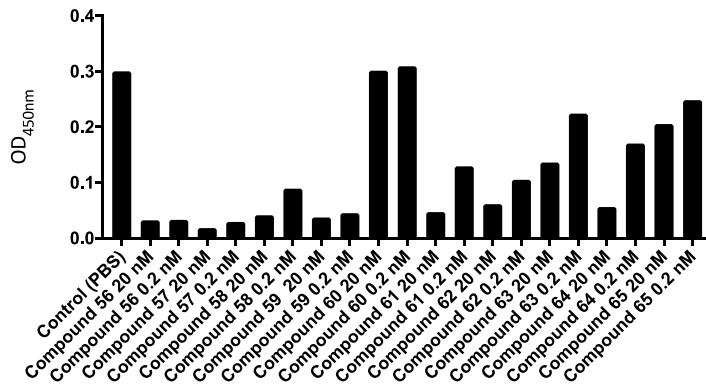
MMN40 (1:50)



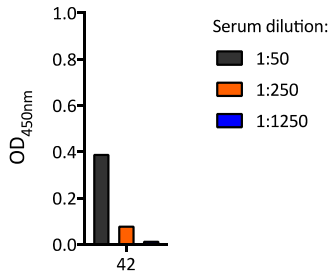
Anti-GM1 IgM ELISA



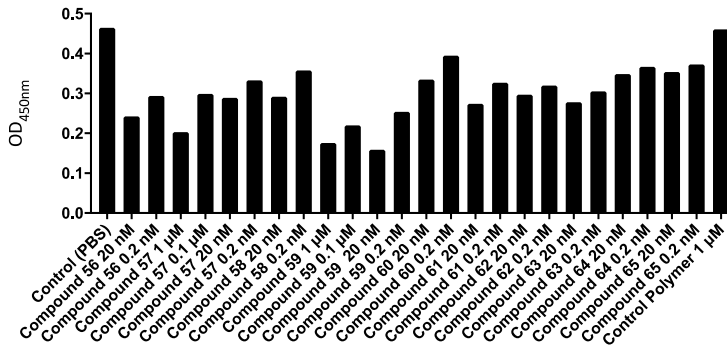
MMN41 (1:50)



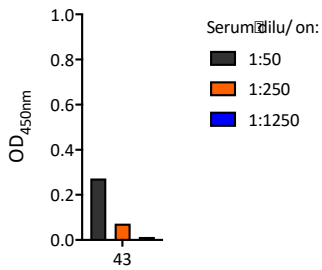
Anti-GM1 IgM ELISA



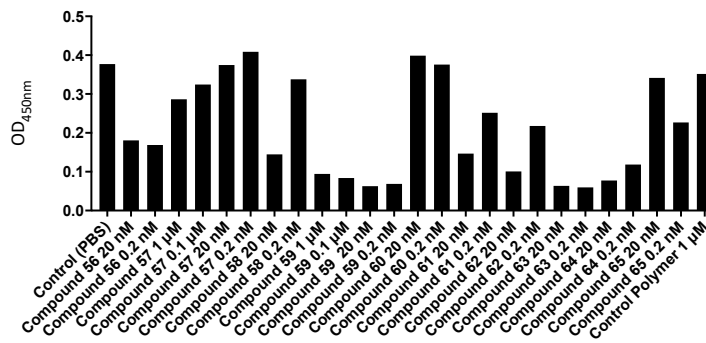
MMN42 (1:50)



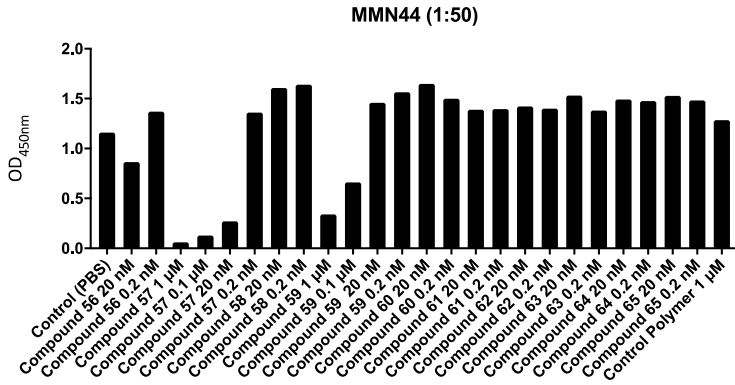
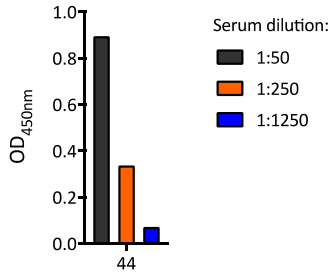
Anti-GM1 IgM ELISA



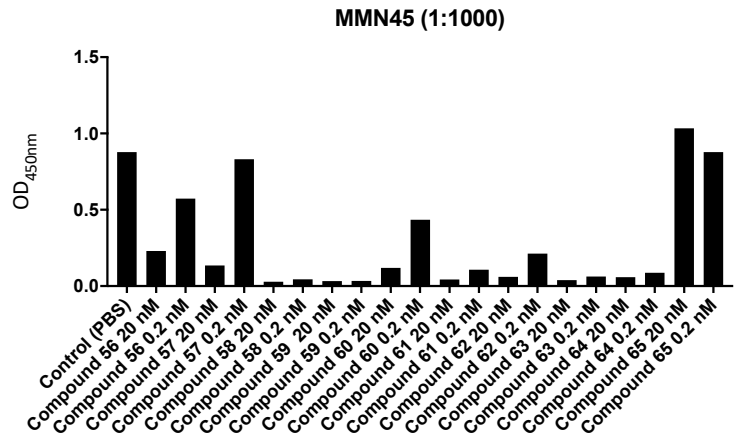
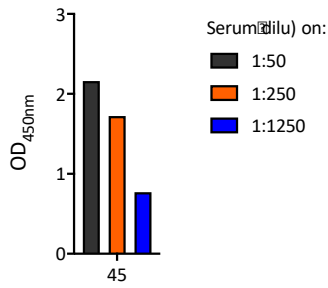
MMN43 (1:50)



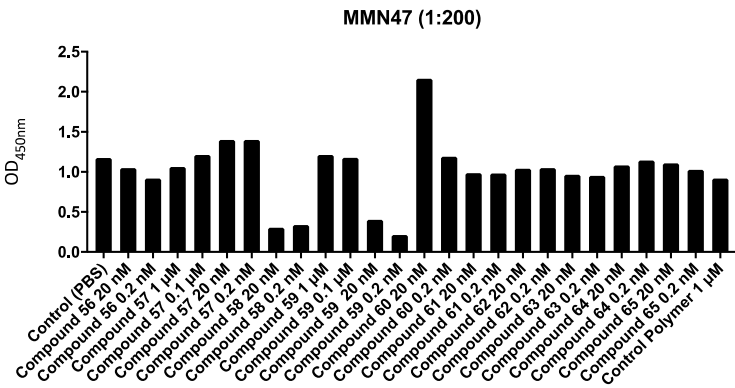
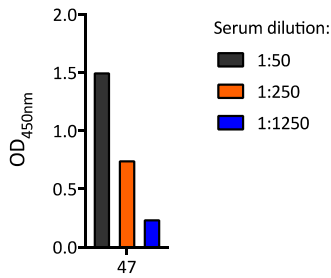
Anti-GM1 IgM ELISA



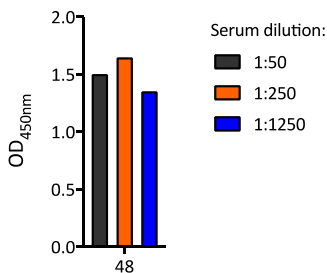
An) -GM1 IgM ELISA



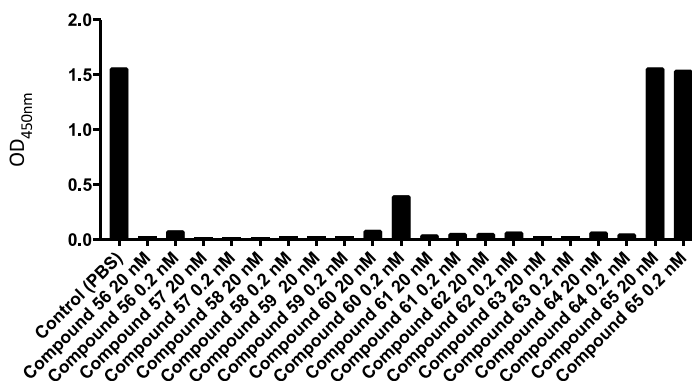
Anti-GM1 IgM ELISA



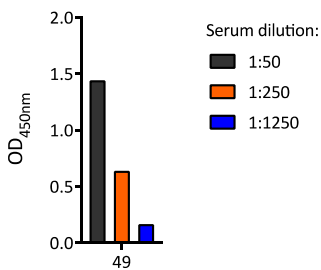
Anti-GM1 IgM ELISA



MMN48 (1:1500)



Anti-GM1 IgM ELISA



MMN49 (1:100)

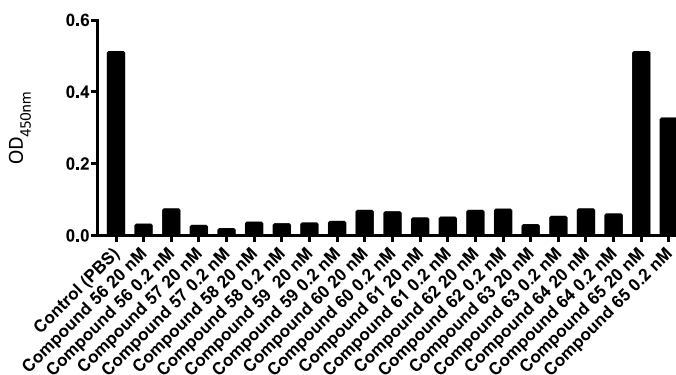


Figure S5: Summary of in vitro anti-GM1 IgM titer screening of MMN patient sera and inhibitory activity measurements of GM1 glycoconjugates on GM1 binding.

3. MD simulation for structural comparison of selected glycomimetics to natural GM1 epitope

In order to select the GM1 structure for MD simulation, **3CHB**, i.e., Cholera toxin B-pentamer complexed with GM1 pentasaccharide (natGM1), was selected from the PDB. In order to find the optimum condition for the clustering analysis of the mimetics, first GM1 structure was run under different clustering methods. At 1.5Å the clustering analysis resulted in minimum number of structures. Hence, clustering condition at 1.5Å was selected to run all other GM1 mimetics. On superimposing all the structures of natGM1 obtained from the clustering data, interaction between the ring oxygen of the central Gal and 3-OH of glucose was seen. Also, the ring oxygen of NeuNAc and O2-hydroxyl of Gal forms a hydrogen bond. On superimposing the obtained conformation of mimetic (**2**) with natGM1 both showed almost similar backbone arrangement, with similar N-acetyl group orientation for the GalNAc moiety. In the case of mimetic (**4**) the cyclohexyl ring and carboxylic group moved away from the OH of galactose, and the arrangement of the N-acetyl of GalNAc was also found to be different. The orientation of H in natGM1 is away from the glycosidic oxygen whereas; the H-orientation is towards the glycosidic oxygen in mimetic (**4**) which stabilizes via H bonding. Also, H-bonding is seen between the 2-OH of the terminal galactose and the carbonyl group of N-acetyl. As shown in the superimposed structures, mimetic (**2**) showed the closed structural similarity which could explain the inhibitory potency as similar to natGM1. It is also interesting to observe how the cyclohexyl moiety in mimetic (**4**) altering the H-bonding networks, which could potentially impact the binding affinity and selectivity to anti-GM1 antibodies.

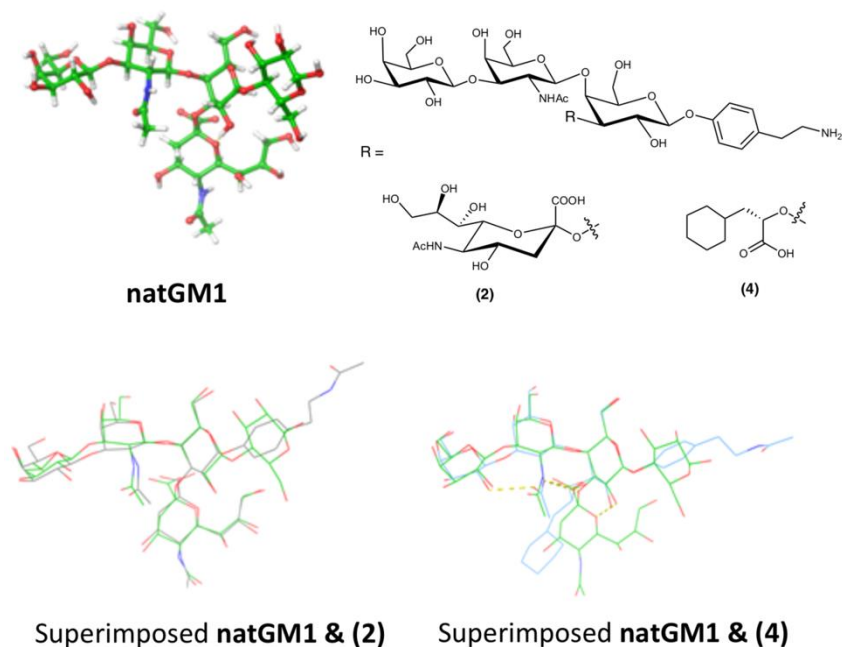


Figure S6: Structural comparison by superimposing natural GM1 pentasaccharide with monomeric glycomimetics (**2** and **4**). Natural GM1 pentasaccharide was selected from x-ray structure in complex with cholera toxin-B pentamer (PDB: 3CHB) and optimized by MD simulation. Clustering condition was optimized to minimize the number of

clustering structures. Superimposing natural GM1 epitope with the selected monomeric mimetics show more structural insights to the different binding affinity.

Method

Depending on the system (all originating from crystal structures), molecular dynamics simulations were carried out with Desmond (using the OPLS 2003 force-field as implemented in the Schrödinger 2016 suite). The systems were solvated using an orthorhombic, TIP3P water box with periodic boundary conditions at a minimum distance of 10 Å from the solute Na⁺ and Cl⁻ ions were added to neutralize the charges and account for physiological salt concentration (0.15 M). The systems were then equilibrated using the default Desmond relaxation routine followed by a gradual temperature increase from 100 to 300 K over a period of 25 picoseconds (ps). Long-range electrostatic interactions (cut at 8.0 Å) were handled using the particle mesh Ewald summation. The SHAKE algorithm was applied to all hydrogen atoms. Production runs were carried out using the Martyna-Tobias-Klein isothermal-isobaric ensemble (NPT), maintaining a constant temperature of 300 K. Unless stated otherwise, these runs covered the span of either 2 or 30 nanoseconds (ns; referred to as “short” and “long” respectively). Energetic and structural data were recorded in 4.8 ps intervals for a simulation time step of 2.0 femtoseconds (fs).

Chapter 5

Poly-L-lysine Glycoconjugates Inhibit DC-SIGN-mediated Attachment of Pandemic Viruses

Jonathan Cramer^{1,3*}, Butrint Aliu^{1*}, Xiaohua Jiang¹, Timothy Sharpe², Lijuan Pang¹, Adrian Hadorn¹, Said Rabbani¹, Beat Ernst¹

* These authors contributed equally to the project

¹Institute of Molecular Pharmacy, Pharmacenter, University of Basel,
4056 Basel, Switzerland

²Biophysics Facility, Biozentrum, University of Basel, 4056 Basel, Switzerland

³Institute for Pharmaceutical and Medicinal Chemistry, Heinrich-Heine-University of Düsseldorf,
40225 Düsseldorf, Germany

Corresponding authors:

Jonathan Cramer, jonathan.cramer@hhu.de
Beat Ernst, +41 61 207 15 51, beat.ernst@unibas.ch

Contributions of Butrint Aliu

- Support in manuscript preparation and revision
- DLS measurements
- Cellular inhibition experiments
- Cellular uptake experiments
- Data analysis and interpretation

Special
Collection

Poly-l-lysine Glycoconjugates Inhibit DC-SIGN-mediated Attachment of Pandemic Viruses

Jonathan Cramer^{*, [a, c]} Butrint Aliu^{*, [a]} Xiaohua Jiang,^[a] Timothy Sharpe,^[b] Lijuan Pang,^[a] Adrian Hadorn,^[a] Said Rabbani,^[a] and Beat Ernst^{*, [a]}

The C-type lectin receptor DC-SIGN mediates interactions with envelope glycoproteins of many viruses such as SARS-CoV-2, ebola, and HIV and contributes to virus internalization and dissemination. In the context of the recent SARS-CoV-2 pandemic, involvement of DC-SIGN has been linked to severe cases of COVID-19. Inhibition of the interaction between DC-SIGN and viral glycoproteins has the potential to generate broad spectrum antiviral agents. Here, we demonstrate that mannose-functionalized poly-l-lysine glycoconjugates effi-

ciently inhibit the attachment of viral glycoproteins to DC-SIGN-presenting cells with picomolar affinity. Treatment of these cells leads to prolonged receptor internalization and inhibition of virus binding for up to 6 h. Furthermore, the polymers are fully bio-compatible and readily cleared by target cells. The thermodynamic analysis of the multivalent interactions reveals enhanced enthalpy-driven affinities and promising perspectives for the future development of multivalent therapeutics.

Introduction

Envelope glycoproteins of a variety of viruses are densely covered with host-derived carbohydrates. These glycan structures shield viruses from antibody-mediated immune responses and enable their attachment to the host's lectins.^[1,2] One of these lectins is the C-type lectin receptor (CLR) DC-SIGN (dendritic cell-specific intercellular adhesion molecule 3 grabbing non-integrin), a surface receptor expressed by innate immune cells. It has been demonstrated that DC-SIGN acts as an entry receptor for pathogens and plays a detrimental role in the pathology of many viral infections by promoting virus dissemination and immune evasion.^[1–4] High-mannose glycan epitopes on envelope glycoproteins of epidemic and pandemic viruses such as HIV,^[5] ebola,^[6,7] influenza A,^[8] hepatitis C,^[9] SARS,^[10] zika,^[11] dengue,^[12] and others,^[1] have been shown to

exploit DC-SIGN mediated attachment and internalization, either for *cis*-infection of myeloid cells or for *trans*-infection of other cell types.^[4,10,13,14]

In the context of the ongoing SARS-CoV-2 pandemic, increasing evidence points to a possible involvement of DC-SIGN in the attachment of viruses to innate immune cells.^[15] The SARS-CoV-2 spike protein is heavily glycosylated with high mannose and complex N-glycans, which potentially could serve for the attachment to host lectins.^[16] In fact, several groups have demonstrated that these glycans are indeed recognized with picomolar affinity by various CLRs such as DC-SIGN and the closely related DC-SIGNR.^[17–20] The interaction of the viral spike glycoprotein leads to internalization in DC-SIGN-presenting cells, strongly implicating DC-SIGN as an ACE2-independent entry receptor for SARS-CoV-2. Infection of innate immune cells by this mechanism could contribute to the exaggerated immune response in severe COVID-19. This is consistent with the fact that DC-SIGN expression levels were increased in severe COVID-19 patients with elevated amounts of proinflammatory monocyte-derived macrophages, inflammatory cytokines and chemokines.^[17] Another recent study confirmed DC-SIGN-mediated internalization of SARS-CoV-2 pseudovirions into monocyte-derived dendritic cells, albeit without *cis*-infection of the cells.^[21] However, dendritic cells pre-treated with SARS-CoV-2 pseudovirions efficiently infected ACE2⁺ Vero cells in a *trans*-infection assay, thereby indicating a deciding role of DC-SIGN for virus dissemination from the lung to other tissues. Importantly, *trans*-infection could be inhibited with a known DC-SIGN ligand.^[21] Differences in SARS-CoV-2 virulence due to mutation in the viral spike glycoprotein, such as the prominent D614G mutation, have been attributed to potential variations in glycosylation, resulting in differences in the interaction with DC-SIGN and DC-SIGNR.^[15] Furthermore, a recent study concluded that genetic variants in the *ABO* gene locus correlate with DC-SIGN expression levels and that increased DC-SIGN expression represents a genetic risk factor for severe COVID-19,

[a] Dr. J. Cramer,* B. Aliu,* Dr. X. Jiang, Dr. L. Pang, A. Hadorn, Dr. S. Rabbani, Prof. B. Ernst
Department of Pharmaceutical Sciences
University of Basel
Klingelbergstrasse 50
4056 Basel (Switzerland)
E-mail: jonathan.cramer@hu.de
beat.ernst@unibas.ch

[b] Dr. T. Sharpe
Biophysics Facility
BioCenter of the University of Basel
Klingelbergstrasse 70
4056 Basel (Switzerland)

[c] Dr. J. Cramer*
Institute for Pharmaceutical and Medicinal Chemistry
Heinrich-Heine-University of Düsseldorf
Universitätsstraße 1
40225 Düsseldorf (Germany)

[*] These authors contributed equally to this work.

Supporting information for this article is available on the WWW under <https://doi.org/10.1002/cmdc.202100348>

This article belongs to the Early-Career Special Collection, "EuroMedChem Talents".

indicating a central role of the innate immune system in this disease.^[22]

With this background, inhibition of DC-SIGN-mediated attachment of viral particles to innate immune cells represents a promising strategy for the development of antiviral drugs.^[23–25] In the past, this strategy has been investigated for the treatment of HIV,^[26] ebola,^[27] zika,^[28] and dengue infections.^[28] In view of the recent emergence of the SARS-CoV-2 pandemic, DC-SIGN-targeted antivirals could represent a promising host-directed treatment option for COVID-19. Importantly, metabolic pathways responsible for glycosylation of viral proteins, as well as the targeted glycan receptors are evolutionarily conserved in the host genome. It can therefore be assumed, that the pharmacological interference in this mechanism with antiviral therapeutics is insensitive to viral resistance mutations and additionally provides the possibility for an early containment of infections from newly emerging virus strains with pandemic potential.^[29]

Multivalent presentations of viral glycans employing mannose or fucose epitopes have been explored as potential inhibitors of DC-SIGN-mediated virus attachment. Multivalent carbohydrate-lectin interactions often proceed via statistical rebinding, or a bind-and-jump mechanism.^[30,31] Accordingly, carbohydrate epitopes on a multivalent scaffold migrate along a surface presenting the carbohydrate recognition domain (CRD) of the lectin, while undergoing numerous association and dissociation events. Even though the individual monovalent interactions of the epitopes are weak, the macroscopic apparent binding affinity, i.e. the probability of the lectin being bound to any carbohydrate ligand on the surface, is much higher. This mechanism leads to an increase in apparent binding affinity of protein-carbohydrate interactions of up to a factor of 10^6 .^[32,33] In this context, functionalized polymeric supports,^[34] peptides,^[35] dendrimers,^[36] nanoparticles,^[37] fullerenes,^[28] carbon nanotubes,^[27] and thiacalixarenes^[38] have been studied. However, a severe drawback of some of these non-biodegradable multivalent scaffolds is their potential accumulation and associated toxicity, especially when prolonged pulmonary applications are considered.^[39–41]

Here, we report the synthesis and biological evaluation of mannosylated poly-L-lysine glycoconjugates (Man-PLL) **1a–d** as multivalent ligands for DC-SIGN. By relying on poly-L-lysine as a

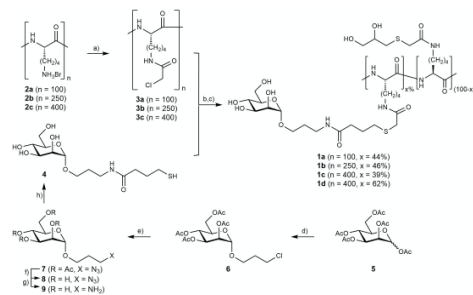
polymeric scaffold we resort to a broadly available system that is easily modified, non-immunogenic, biodegradable, and extensively studied for biological applications.^[42–45] We demonstrate that glycopolymers **1a–d** efficiently block the interaction of DC-SIGN-expressing (DC-SIGN⁺) cells with viral glycoproteins from HIV, ebola, and SARS-CoV-2. In addition, we show that the glycopolymers are readily cleared by the target cells and, thus, show great potential for compatibility with prolonged pulmonary application in a therapeutic setting. In addition, binding affinity, thermodynamics, and stoichiometry of the multivalent interactions between glycopolymers **1a–d** and recombinant DC-SIGN are characterized by isothermal titration calorimetry (ITC).

Results and Discussion

Man-PLL **1a–d** were synthesized from commercially available poly-L-lysine hydrobromide (**2**) by chloroacetylation (\rightarrow **3**) followed by chloride substitution with various amounts of the thiol functionalized mannoside (**4**) (Scheme 1). This procedure was based on a previously published protocol employing γ -thiobutylolactone as a bifunctional linker.^[46] The unreacted chloroacetamides were then reacted with an excess of thioglycerol. This operationally simple synthetic sequence yielded the water-soluble glycopolymers **1a–d** with varying carbohydrate loadings. It is important to note that commercially available poly-L-lysine polymers are polydisperse systems with a degree of polymerization distributed around a statistical mean. This affects all calculations of concentration, loading, and affinity, which represent estimates based on the assumption of an ideal, monodisperse polymer.



Jonathan Cramer graduated in Pharmacy and Medicinal Chemistry from Philipps-Universität Marburg (Germany). He obtained his PhD from the same institution under the guidance of Gerhard Klebe, studying the role of water networks in protein-ligand interactions. He then joined the group of Beat Ernst at the University of Basel (Switzerland), where he worked on the development of glycomimetic drugs for the treatment of bacterial and viral infections. He recently joined the Heinrich-Heine-University of Düsseldorf as an assistant professor, where his group is focused on the medicinal chemistry and chemical biology of carbohydrate-derived drugs.



Scheme 1. Synthesis of the mannosylated poly-L-lysine glycoconjugates **1a–d**: (a) 2,6-lutidine, chloroacetic anhydride, 4 °C, 16 h (**3a** (92%), **3b** (62%), **3c** (96%)); (b) 1,8-diazabicyclo(5.4.0)undec-7-ene/DMF, building block **4**, without purification (c) thioglycerol, Et₃N, shaken overnight: **1a** (45%, loading 44%); **1b** (64%, loading 46%); **1c** (68%, loading 39%); **1d** (51%, loading 62%). (d) 3-chloro-1-propanol, BF₃·Et₂O/CH₂Cl₂, rt, overnight, (65%); (e) Na₂S/DMF, 60 °C, 2 h, (95%); (f) MeONa/MeOH, rt, overnight, (83%); (g) Pd(OH)₂/C in MeOH, H₂, (84%); (h) γ -thiobutylolactone, MeOH/Et₃N, rt, overnight, (68%).

| Compound | Degree of polymerization; lysine residues n | Absolute number of mannose residues by NMR | Carbohydrate loading x | Average molecular weight [kDa] |
|------------------------------|---|--|------------------------|--------------------------------|
| Man-PLL ₁₀₀ (1 a) | 100 | 44 | 44 % | 37.8 |
| Man-PLL ₂₅₀ (1 b) | 250 | 115 | 46 % | 95.0 |
| Man-PLL ₄₀₀ (1 c) | 400 | 156 | 39 % | 146.6 |
| Man-PLL ₃₀₀ (1 d) | 400 | 248 | 62 % | 167.9 |

Synthesis of Man-PLL 1 a–d

Mannose building block **4** was obtained in an overall yield of 25 % in a short synthetic sequence starting from D-mannose pentaacetate (**5**). α -Selective glycosylation with 3-chloropropan-1-ol yielded mannoside **6**. Azide substitution of chloride (\rightarrow 7), Zemlén deacetylation (\rightarrow 8) and catalytic hydrogenation gave the unprotected amine **9**. Finally, by reaction with γ -thiobutyrilactone building block **4** was obtained in good yield. According to this strategy, a series of Man-PLL of different lengths and loadings were prepared (Table 1).

Biophysical characterization of Man-PLL polymers

The size distribution and the shape of Man-PLL **1 a–d** in solution were elucidated by dynamic light scattering (DLS) experiments and analytical ultracentrifugation (AUC). As shown in Table 2 and Figure 1A, the measured hydrodynamic diameters (D_h) of **1 a–d** reflect the degree of polymerization. A D_h of 9.2 nm was found for Man-PLL₁₀₀ (**1 a**), which is roughly doubled for the 250-mer **1 b** (19.8 nm) and tripled for the larger 400-mers **1 c** and **1 d** (30 nm).

The polydispersity indices (\mathcal{D}) fall in a range of 0.3 to 0.4, indicating the presence of multiple species in the polymer samples, as expected for the polydisperse PLL scaffolds. Next, diffusion-deconvoluted differential sedimentation coefficient distributions [$c(s)$ distributions] were determined by analytical ultracentrifugation (AUC) and signal-weight average sedimentation coefficients (S) were calculated for each polymer (Table 2, Figure 1B). Values of frictional ratio (f/f_0) fitted from AUC data

| Compound | DLS D_h [nm] ^[a,b] | \mathcal{D} | AUC Sedimentation coefficient [S] ^[c] | f/f_0 | D_h [nm] |
|------------|---------------------------------|---------------|--|---------|------------|
| 1 a | 9.2 ± 0.4 | 0.4 ± 0.01 | 2.21 | 1.41 | 6.6 |
| 1 b | 19.8 ± 0.3 | 0.4 ± 0.05 | 4.04 | 2.50 | 20.9 |
| 1 c | 32.0 ± 0.4 | 0.3 ± 0.02 | 5.08 | 2.37 | 21.5 |
| 1 d | 27.2 ± 0.7 | 0.4 ± 0.02 | 5.24 | 2.52 | 24.3 |

[a] Z-Average values are reported as hydrodynamic diameters. [b] The standard deviation from three independent experiments is given as an estimation of experimental error. [c] Signal weighted average over the range 1–20 S. D_h , hydrodynamic diameter; \mathcal{D} , polydispersity index; f/f_0 , frictional ratio.

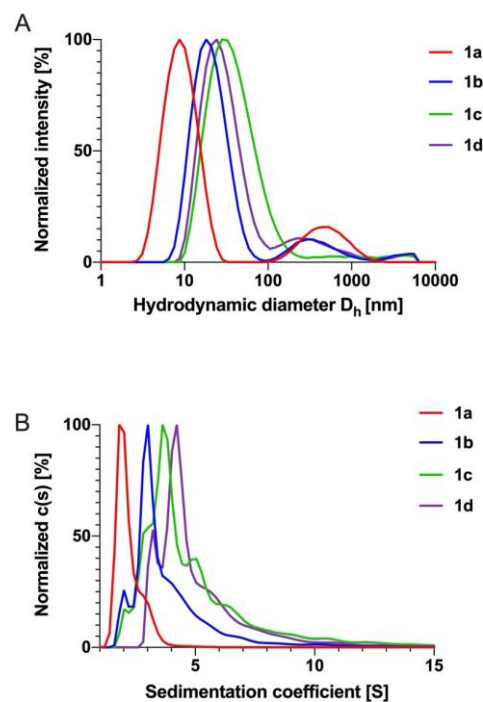


Figure 1. A) Normalized scattering intensity distribution for Man-PLL **1 a–d** as determined by DLS. B) Normalized diffusion-deconvoluted differential sedimentation coefficient distributions ($c(s)$ distributions) for **1 a–d** determined by sedimentation velocity AUC experiments. The magnitude of $c(s)$ at a given S value gives the proportion of the total material in that sample having that S value.

provide information about the shape of macromolecules in solution. Whereas a value for f/f_0 of 1 corresponds to a spherical shape, values >2.0 indicate a highly extended conformation. Based on sedimentation velocity data, a narrow distribution with an average sedimentation coefficient of 2.21 S was obtained for Man-PLL₁₀₀ (**1 a**). These parameters were used to calculate a molecular mass estimate of 39.6 kDa, which correlates well with the theoretical value of 37.8 kDa. For Man-PLL₁₀₀ (**1 a**), the recorded frictional ratio of 1.4 suggests a

globular shape, comparable to a folded protein. The hydrodynamic diameter (D_h) calculated from the average sedimentation coefficient is 6.6 nm. Experimental data for the larger glycopolymers **1b–d** showed more complex distributions, revealing the presence of multiple species with sedimentation coefficients between 2 and 15 S. Molecular mass estimations for these species correlate not only to monomers, but also dimers of the polymer and higher order aggregates (Figure S10). The calculated D_h from the average sedimentation coefficients are between 20.9 nm and 24.3 nm, a sign for larger particle sizes for the longer polymers compared with **1a**, which corroborates DLS data. Finally, based on the average frictional ratios with values between 2.37 and 2.52, a highly extended, rod-shaped conformation of the polymers can be assumed.

Competitive inhibition of viral glycoprotein binding to DC-SIGN⁺ cells

The potential of Man-PLL **1a–d** to inhibit the attachment of viral glycoproteins from SARS-CoV-2 (spike glycoprotein S1 subunit), ebola (EBOV glycoprotein), or HIV (gp120 envelope glycoprotein) to DC-SIGN⁺ B-THP-1 cells was investigated using a flow-cytometric assay (Figure 2). DC-SIGN⁺ cells or isotype controls were incubated with the viral glycoproteins labeled with the cyanine dye Cy5 in the presence of either logarithmic dilutions of glycopolymers **1a–d** or buffer, as described in the experimental section. The amount of fluorescently labeled glycoprotein bound to the cell surface was determined by mean fluorescence intensity and the resulting competition curves were fitted to a four parameter Hill model to determine IC_{50} values. The shortest Man-PLL₁₀₀ (**1a**) showed an IC_{50} value of 43 nM for SARS-CoV-2 spike S1 and 36 nM for EBOV glycoprotein. In contrast, the affinities for the intermediate length Man-PLL₂₅₀ (**1b**) are in the subnanomolar range (789 pM and 637 pM), which corresponds to an affinity gain of approximately a factor of 50. However, further elongation of the polymer backbone (**1b**→**1c**) and increased mannose loading (**1c**→**1d**) resulted only in a moderate enhancement of the binding affinities by a factor of two. With IC_{50} values around 200 pM, the polyvalent **1d** is a highly potent inhibitor of the interaction between SARS-CoV-2 spike S1, as well as EBOV glycoprotein with DC-SIGN. Compared with the monovalent epitope methyl α -D-mannoside (MeMan, IC_{50} =6.5 mM), the multivalent affinity enhancement is in the order of 10^7 . For HIV gp120, an identical trend in affinity was observed, however with absolute IC_{50} values being worse by a factor of five. For the most potent Man-PLL₄₀₀ (**1d**), this resulted in an IC_{50} value of 1.0 nM. Importantly, no binding was observed for DC-SIGN deficient control B-THP-1 cells. Given the well documented carbohydrate specificity of DC-SIGN,^[47] it can be assumed that the observed polymer interactions are specific for mannose presenting polymers and presumably other carbohydrate epitopes that are recognized by DC-SIGN.

The less potent inhibition of the gp120/DC-SIGN interaction is probably linked to a higher binding affinity of the heavily glycosylated gp120 compared with the other glycoproteins.^[16,48]

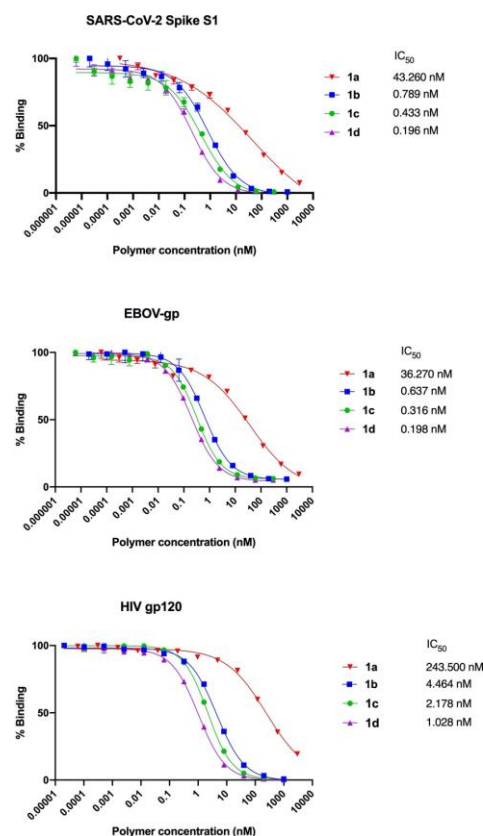


Figure 2. Inhibition of viral glycoprotein attachment to DC-SIGN⁺ B-THP-1 cells. Cells were incubated with Man-PLL **1a–d** in the presence of Cy5 labeled SARS-CoV-2 spike glycoprotein S1 subunit (10 nM), ebola glycoprotein (50 nM), or HIV gp120 (10 nM). Mean fluorescence intensity determined by flow cytometry was normalized before global fitting to a four parameter Hill model. Error bars represent the standard deviation from three independent experiments.

Intriguingly, the observed trend in affinity in the cellular assay correlates well with the solution properties of the Man-PLL glycopolymers determined by DLS and AUC (Table 2, Figure 1). The differences in size and shape are reflected in a significantly higher binding affinity (approximately a factor of 50) of rod-shaped polymers **1b–d** in cellular assays compared with the globular **1a**. By comparison, between **1b–d**, the variations in the degree of polymerization (**1b**→**1c**) and carbohydrate loading (**1c**→**1d**) influences affinity only by a factor of two. The observation that the elongated glycopolymers **1b–d** show much higher affinity compared to the globular **1a** is probably related to the fact that DC-SIGN has evolved to capture large pathogens, such as viruses (ca. 20–500 nm) or bacteria (1–2 μ m), and not soluble glycoproteins. A

similar influence of particle size of antigen formulations on DC-SIGN affinity and antigen uptake has been reported by the van Kooyk group.^[49]

Prolonged incubation of DC-SIGN⁺ B-THP-1 cells with the most potent inhibitor **1d** effectively blocked the DC-SIGN receptors, making them unavailable for binding to SARS-CoV-2 spike S1 for up to 6 h (Figure 3A). Importantly, no toxic effects were observed throughout the duration of the experiment. An effect could still be observed after only a 30 min exposure of the cells (Figure 3B). Whereas inhibition was incomplete compared to a prolonged exposure to Man-PLL₄₀₀ (**1d**), the binding of SARS-CoV-2 spike S1 was still significantly decreased for up to 6 h post incubation.

Uptake of Man-PLL 1 a–d into target cells

To study endocytosis into acidic cell compartments by flow cytometry and fluorescence microscopy, Man-PLL₄₀₀ was labeled with the pH-sensitive fluorescent dye rhodamine 6G (Man loading: 47% by NMR, for synthesis of **10**, see Supporting Information). As negative control, the fluorescently labeled PLL₄₀₀ **11** containing no mannose modification was used (for synthesis of **11**, see Supporting Information). Both polymers were incubated with DC-SIGN⁺ B-THP-1 cells and control B-

THP-1 cells. Again, no noticeable uptake was observed for DC-SIGN deficient control cells. Fluorescently labeled Man-PLL₄₀₀ **10** was internalized highly specifically by DC-SIGN-expressing B-THP-1 cells (Figure 4A) and the fluorescent signal increased over 6 h and diminished after 24 h. In contrast, no uptake was observed in control B-THP-1 cells and only minor uptake of non-mannosylated control PLL₄₀₀ **11** into both cell types was observed (Figure 4A). The same experiment was repeated with a fluorescent Man-PLL probe (**12**) featuring an intramolecular FRET system to study compound degradation (Figure 4C, for synthesis of **12**, see Supporting Information). As observed before, uptake reached a maximum at 6 h post treatment, after which progressive loss of FRET-signal indicated complete compound degradation in the lysosomes over the course of 24 h. A similar observation was previously described by Hoppe and Lee.^[45]

These observations further elucidate the mode of action of the Man-PLL. Multivalent binding to DC-SIGN on the cell surface causes effective inhibition of the binding of viral glycoproteins. Additionally, the compound is readily endocytosed via DC-SIGN. As a result, the availability of DC-SIGN on the cell surface is substantially reduced, and the glycopolymers are efficiently metabolized (Figure 4B).

Analysis of binding thermodynamics

To this point, we discussed the potency of Man-PLL **1a–d** exclusively on a cellular level and thus did not receive detailed information about the specifics of the interaction on a molecular level. To gain this additional insight into molecular details of the Man-PLL/DC-SIGN interaction, affinity, stoichiometry (*n*), and thermodynamics of binding with the tetrameric recombinant extracellular domain of DC-SIGN (ECD, 375 amino acids) were determined by isothermal titration calorimetry (ITC). It is important to note that this biophysical assay operates under fundamentally different prerequisites compared to the cellular assay. The ITC experiment records the interaction of soluble tetrameric DC-SIGN with polyvalent ligands, whereas in the cellular assay, the interaction of two mutually compatible multivalent surfaces is studied. Although equivalent affinity trends were observed in ITC experiments and the cellular assay, the trends are much less pronounced in ITC with soluble protein (factor of 3 to 5, Figure 5) compared to the cellular assay (factor of 50 to 200, Figure 2). Thus, in the ITC experiments, the multivalent presentation enhances affinity of the monovalent ligand MeMan ($K_D = 3.2$ mM) only by a factor of 2.6×10^3 for **1a** and up to a factor of 1.35×10^4 for **1d**. In the cellular assay, however, multivalent affinity enhancement of up to 10^7 was obtained. Obviously, the multivalent presentation of receptor molecules on the cell surface effectively potentiates the affinity enhancement from statistical rebinding by providing a much higher effective local concentration of receptors. In summary, on a cellular level, the interaction with DC-SIGN is controlled by effects, which are not fully reproduced in a biophysical assay employing soluble recombinant protein.

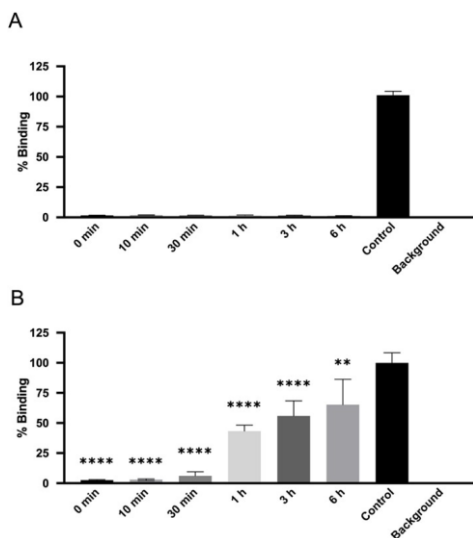


Figure 3. Inhibition of DC-SIGN on B-THP-1 cells by **1d**. A) Incubation of the cells with 100 nM **1d** lead to a sustained blocking of the receptor for at least 6 hours, thereby successfully preventing the binding of Cy5 labeled SARS-CoV-2 spike glycoprotein S1 subunit (10 nM). B) Pre-incubation of the cells with 100 nM **1d** for 30 min showed a time-dependent recovery of the receptor with a significantly decreased binding availability for at least 6 h. Results are shown as means with standard deviations from three independent experiments (one-way ANOVA, * $P \leq 0.05$, ** $P \leq 0.01$, *** $P \leq 0.001$, **** $P \leq 0.0001$).

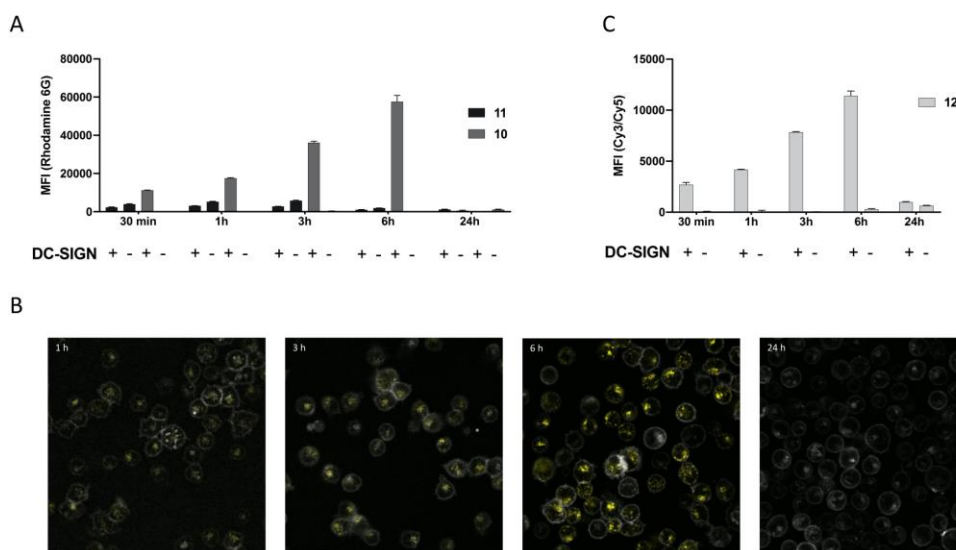


Figure 4. DC-SIGN mediated uptake and degradation of fluorescently labeled Man-PLL₄₀₀ **10** and **12** into B-THP-1 cells. A) DC-SIGN⁺ B-THP-1 cells and control B-THP-1 cells were incubated with 100 nM rhodamine 6G labeled Man-PLL₄₀₀ **10** or 100 nM rhodamine 6G labeled PLL₄₀₀ **11**. The internalization was quantified by measuring the pH-dependent mean fluorescence intensity with flow cytometry, showing the highly specific and time-dependent uptake of **10** and **12** by DC-SIGN⁺ B-THP-1 cells (+) in comparison to control B-THP-1 cells (–) and control **11**. Furthermore, after increasing fluorescence intensity over time, the signal disappeared after 24 h, indicating compound degradation. Error bars represent the standard deviation from three independent experiments. B) Representative images recorded with confocal microscopy reveal the time-dependent uptake of **10** in acidic cell compartments of DC-SIGN⁺ B-THP-1 cells and the effective degradation after 24 h. C) DC-SIGN⁺ B-THP-1 cells and control B-THP-1 cells were incubated with 100 nM sulfo-Cy3/sulfo-Cy5 labeled Man-PLL₄₀₀ **12**. The internalization was quantified by measuring Cy3/Cy5-FRET intensity with flow cytometry, showing uptake of **12** by DC-SIGN⁺ B-THP-1 cells (+) in comparison to control B-THP-1 cells (–). Furthermore, after increasing fluorescence intensity over time, the intramolecular FRET signal disappeared after 24 h, highlighting complete compound degradation. Error bars represent the standard deviation from two independent experiments.

The affinity trend in ITC measurements roughly follows the increase of the functional valency N , which is defined as the inverse of the experimentally determined fitting parameter n ($N = 1/n$) and corresponds to the number of interacting mannose epitopes on the glycopolymer. When N is related to the total number of mannose epitopes (N_{\max} , determined by ¹H-NMR, see Supporting Information), shorter polymers **1a** and **1b** appear to be fully saturated (N/N_{\max} 109% and 93%, respectively), whereas only a fraction of available mannose residues in the longer polymers **1c** and **1d** bind to the receptor (with N/N_{\max} 58% and 48%, respectively). Taking the broader distribution of the hydrodynamic diameters of the Man-PLL₄₀₀ **1c** and **1d** (Figure 1A) into account, it is likely that self-aggregation reduces the accessibility of their sugar residues. The reduction of the active mannose concentration is reflected by the ITC fitting parameter n and leads to reduced values for N/N_{\max} . A similar reduction of efficiency related to higher carbohydrate loading, not polymer length as in our case, has been observed for other glycopolymers.^[50–53] The availability of mannose epitopes on the polymer surface of **1a** and **1b** is not affected by aggregation. As observed for the binding affinity, the entropy-enthalpy compensation in the ITC experiments (Figure 5) scales with the functional valency N ($N = 1/n$).

The predominant model for the thermodynamics of binding in multivalent systems was developed in the Whitesides group.^[54,55] This model is an extension of Jencks considerations on the additivity of free energy of binding and assumes a simultaneous interactions of i epitopes with an i -valent receptor.^[56] The total free energy of binding is given by $\Delta G^\circ = \sum_{i=1}^{i_{\max}} \Delta G_i^\circ$ and the average contribution of each interacting epitope can be calculated as $\Delta G_{\text{norm}}^\circ = \Delta G^\circ / i$. In addition to the affinity between i epitopes and i receptor binding sites ($\Delta H_{\text{affinity}}^\circ$, $\Delta S_{\text{affinity}}^\circ$) the extended model accounts for contributions of $i-1$ scaffold/linker moieties, which can be dissected into rotational/translational entropy ($\Delta S_{\text{trans+rot}}^\circ$), enthalpy of potential linker interactions ($\Delta H_{\text{linker}}^\circ$), conformational entropy ($T\Delta S_{\text{conf}}^\circ$), cooperativity ($\Delta G_{\text{coop}}^\circ$), and a statistical factor ($RT \ln(\Omega_i/\Omega_0)$) that scales with the degeneracy (Ω) of the system [Equation (1)].^[55] The degeneracy prefactor Ω was originally introduced as avidity entropy ($\Delta S_{\text{avidity}}^\circ$) by Kitov and Bundle and accounts for disorder in the distribution of microscopic complexes.^[57]

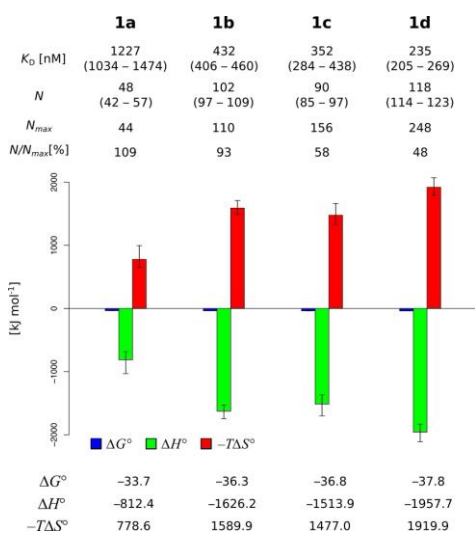


Figure 5. Thermodynamic fingerprints of the interaction of glycopolymers **1 a–d** with DC-SIGN ECD. The functional valency N is the inverse of the fitting parameter n determined in ITC experiments; N_{max} equals the total number of mannose epitopes on the polymer. A numeric estimation of experimental error is given in the Supporting Information.

$$\Delta G_N(i) = i\Delta H_{affinity}^\circ - iT\Delta S_{affinity}^\circ + (i-1)T\Delta S_{trans+rot}^\circ + (i-1)\Delta H_{linker}^\circ - (i-1)T\Delta S_{conf}^\circ + (i-1)\Delta G_{coop}^\circ - RT\ln(\Omega_i/\Omega_0) \quad (1)$$

Figure 6 shows the normalized thermodynamic fingerprints for an interacting mannose epitope of **1 a–d** according to this model. For comparison, the thermodynamic profile of the monovalent ligand MeMan was included. The thermodynamic profile of MeMan reveals an enthalpy-driven interaction ($\Delta H^\circ = -17.4 \text{ kJ mol}^{-1}$) that is partly compensated by an entropic penalty of $-T\Delta S^\circ = 3.1 \text{ kJ mol}^{-1}$. Intriguingly, the normalized thermodynamic profiles for Man-PLL **1 a–d** are identical to each other within the error of the experiment.

Thus, each carbohydrate epitope makes an average contribution to ΔH° of -17 kJ mol^{-1} . This is comparable to the monovalent ligand MeMan, and no additional enthalpy terms from linker interactions or cooperativity are present. However, compared to the monovalent interaction, a significant entropy penalty of $-T\Delta S^\circ \approx 13 \text{ kJ mol}^{-1}$ is observed. This effect results from a superposition of various counteracting entropy contributions. Whereas $T\Delta S_{trans+rot}^\circ$ and the degeneracy factor $-RT\ln(\Omega_i/\Omega_0)$ are considered to be favorable for multivalent interactions, the restriction in backbone and linker conformations ($T\Delta S_{conf}^\circ$) oppose these effects in an overwhelming fashion. Despite this, the additive nature of ΔG° gives rise to a sizeable enhancement of the macroscopic binding affinity. The design of model systems for an experimental approximation of

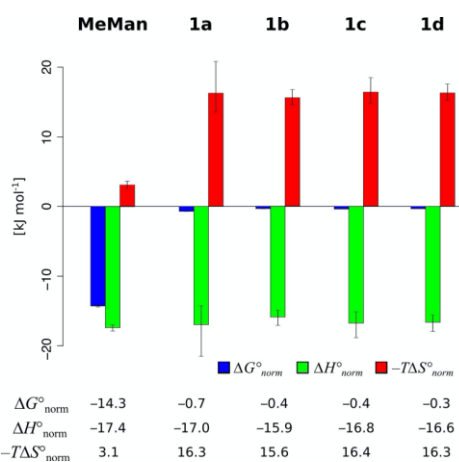


Figure 6. Thermodynamic fingerprint of MeMan and Man-PLL **1 a–d** calculated according to the model of Krishnamurthy, Estroff, and Whitesides⁵⁵ ($\Delta G_{norm}^\circ = \Delta G^\circ \times N^{-1}$; $\Delta H_{norm}^\circ = \Delta H^\circ \times N^{-1}$; $-T\Delta S_{norm}^\circ = -T\Delta S^\circ \times N^{-1}$). A numeric estimation of experimental error is given in the Supporting Information.

the individual entropy terms is currently under consideration in our lab.

A considerable limitation of the above model for the analysis of the interaction between Man-PLL and DC-SIGN is the fact that only the fully assembled, N -valent complex is considered to contribute to the interaction. An alternative model was proposed by Kitov and Bundle.⁵⁷ In addition to the fully assembled interaction of N epitopes with N receptor binding sites, their model also considers the contribution of all other bound species on the macroscopic binding affinity. In this case, the avidity association constant K_A can be expressed as the sum of all microscopic association constants (see Equation (2) for an expression in terms of dissociation constants K_D). A respective analysis of the data recorded for **1 a–d** affords microscopic dissociation constants in the range of 59–28 μM ($K_{D,norm_KB}$, Table 3). Evidently, the multivalent presentation enhances the affinity of each mannose epitope on the polymers by a factor of 54 to 113 compared to the monovalent analog MeMan. Unfortunately, a lack of knowledge about the distribution of species in the macroscopic complex prevents an in-depth analysis of these values in terms of thermodynamics.

| | MeMan | 1a | 1b | 1c | 1d |
|--|---------------------|---------------|---------------|---------------|---------------|
| $K_{D,norm_KB}^\circ$ [μM] | 3173 (3028–3325) | 59 (49–71) | 44 (41–47) | 35 (28–44) | 28 (24–32) |

$$K_D = \left(\sum_{i=1}^N \frac{1}{K_{D_i}} \right)^{-1} \quad (2)$$

The available thermodynamic models of multivalent interactions were developed for interactions of lower valency, such as pentameric toxins,^[54,55,57] and do not offer a complete description of the polyvalent systems under study here. Binding of Man-PLL **1a–d** to tetrameric DC-SIGN ECD represents the interaction of $N/4$ receptor tetramers with an N_{\max} -valent polyvalent ligand. True multivalency effects are likely superimposed by statistical rebinding effects that are best described as a shift of the ligand concentration in the unbound state from the standard concentration for the monovalent interaction to a higher effective concentration in multivalent systems or a reduction of the standard volume to a lower effective volume.^[56,58] Importantly, our analysis of the binding thermodynamics indicates that the binding enthalpy $\Delta H^{\circ}_{\text{norm}}$ of each individual interaction in **1a–d** resembles the ΔH° for the monovalent interaction. This strongly suggests that the introduction of glycomimetic ligands with an improved enthalpic signature holds the potential to significantly increase binding affinity of glycopolymers. Hypothetically, even small gains in monovalent binding enthalpy will be significantly enhanced by the multivalency effect.

Conclusion

In this study, we demonstrate that Man-PLL glycopolymers **1a–d** potentially inhibit the attachment of viral envelope glycoproteins to DC-SIGN⁺ cells. The presentation of mannose epitopes on the PLL scaffold resulted in a multivalent affinity enhancement of up to 10^7 (Figure 2). Intriguingly, the affinity of the glycopolymers is strongly correlated with their size and shape in solution. Large, elongated molecules (**1b–d**) were found to be more potent inhibitors of viral glycoprotein binding compared with the smaller, globular polymer **1a**, most likely because in elongated molecules the availability of epitopes for binding to a cell surface is spatially favored. Importantly, treatment of DC-SIGN⁺ cells with Man-PLL **1d** lead to a prolonged inhibition of SARS-CoV-2 spike S1 binding, highlighting the therapeutic potential of this approach.

The thermodynamic analysis of the Man-PLL/DC-SIGN interaction reveals a multivalent affinity enhancement, which is characterized by an enthalpic contribution of each interacting mannose on the polymer corresponding to the value obtained for the monovalent interaction (Figure 6). This finding has important implications for the future design of multivalent systems, as the presentation of glycomimetics with increased monovalent binding enthalpy on a multivalent support holds the potential to improve potency and selectivity for lectin binding.^[59] Further studies are needed to untangle the influence of various opposing entropy terms that contribute to the observed macroscopic entropy of binding.

Efficient clearance of nanometer-sized polymeric therapeutics is a prerequisite for a prolonged pulmonary application without compound accumulation and associated toxicity. We demonstrate that fully bio-compatible Man-PLL polymers^[64] are efficiently internalized and degraded by their target cells and, thus, are unlikely to accumulate in lung tissue after inhalation.

With respect to the ongoing SARS-CoV-2 pandemic, DC-SIGN targeted Man-PLL polymers represent a novel treatment option for severe COVID-19, which is characterized by an exuberant immune response with the release of pro-inflammatory cytokines. Inhibition of the DC-SIGN-mediated infection of myeloid cells by pulmonary application of Man-PLL may prevent progression of mild infections to severe forms of the disease.

Supporting Information

A previous version of this manuscript has been deposited on a preprint server (<https://doi.org/10.26434/chemrxiv.13072025.v1>).

Acknowledgements

The authors thank the NIH Aids Reagent Program for providing cell lines and recombinant proteins used in this study. The table of contents graphic was created with BioRender.com.

Conflict of Interest

A patent application (EP20200905: Antiviral compounds and polymers) was filed by the University of Basel, Inventors: Beat Ernst, Butrint Aliu, Jonathan Cramer, on October 8, 2020.

Keywords: C-type lectin receptors · glycoconjugate · multivalency · thermodynamics · viral infection

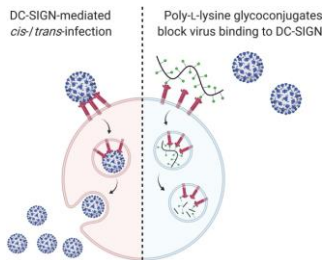
- [1] J. Monteiro, B. Lepenies, *Viruses* **2017**, *9*, 59.
- [2] M. Bermejo-Jambrina, J. Eder, L. C. Helgers, et al., *Front. Immunol.* **2018**, *9*, 590.
- [3] J. J. Garcia-Vallejo, Y. van Kooyk, *Immunity* **2015**, *42*, 983–985.
- [4] Y. van Kooyk, T. B. H. Geijtenbeek, *Nat. Rev. Immunol.* **2003**, *3*, 697–709.
- [5] A. Martin-Moreno, M. A. Muñoz-Fernández, *Front. Immunol.* **2019**, *10*, 2485.
- [6] A. Marzi, P. Möller, S. L. Hanna, et al., *J. Infect. Dis.* **2007**, *196*, S237–S246.
- [7] G. Simmons, J. D. Reeves, C. C. Grogan, et al., *Virology* **2003**, *305*, 115–123.
- [8] M. L. B. Hillaire, N. J. Nieuwkoop, A. C. M. Boon, et al., *PLoS One* **2013**, *8*, e56164.
- [9] S. Pöhlmann, J. Zhang, F. Baribaud, et al., *J. Virol.* **2003**, *77*, 4070–4080.
- [10] A. Marzi, T. Gramberg, G. Simmons, et al., *J. Virol.* **2004**, *78*, 12090–12095.
- [11] N. K. Routhu, S. D. Lehoux, E. A. Rouse, et al., *Int. J. Mol. Sci.* **2019**, *20*, 5206.
- [12] B. Tassaneeritthep, T. H. Burgess, A. Granelli-Piperno, et al., *J. Exp. Med.* **2003**, *197*, 823–829.
- [13] Z.-Y. Yang, Y. Huang, L. Ganesh, et al., *J. Virol.* **2004**, *78*, 5642–5650.
- [14] M. Colmenares, A. Puig-Kröger, O. M. Pello, et al., *J. Biol. Chem.* **2002**, *277*, 36766–9.

- [15] A. Brufsky, M. T. Lotze, *J. Med. Virol.* **2020**, *92*, 1396–1398.
- [16] Y. Watanabe, J. D. Allen, D. Wrapp, et al., *Science* **2020**, *369*, 330–333.
- [17] C. Gao, J. Zeng, N. Jia, et al., *Biorxiv* **2020**, 2020.07.29.227462.
- [18] R. Amraie, M. A. Napoleon, W. Yin, et al., *Biorxiv* **2020**, 2020.06.22.165803.
- [19] R. Amraei, N. Rahimi, *Cell* **2020**, *9*, 1652.
- [20] F. Chiodo, S. Bruijns, E. Rodriguez, et al., *Biorxiv* **2020**, DOI 10.1101/2020.05.13.092478.
- [21] M. Thepaut, J. Luczkowiak, C. Vives, et al., *Biorxiv* **2020**, 2020.08.09.242917.
- [22] D. H. Katz, U. A. Tahir, D. Ngo, et al., *Medrxiv* **2020**, 2020.06.09.20125690.
- [23] M. Mazzon, M. Marsh, *F1000Research* **2019**, *8*, 1628.
- [24] M. K. Zakaria, T. Carletti, A. Marcello, *Front. Cell. Infect. Microbiol.* **2018**, *8*, DOI 10.3389/fcimb.2018.00398.
- [25] M. Krishnan, M. Garcia-Blanco, *Viruses* **2014**, *6*, 683–708.
- [26] S. Ordanini, N. Varga, V. Porkolab, et al., *Chem. Commun.* **2015**, *51*, 3816–3819.
- [27] L. Rodríguez-Pérez, J. Ramos-Soriano, A. Pérez-Sánchez, et al., *J. Am. Chem. Soc.* **2018**, *140*, 9891–9898.
- [28] J. Ramos-Soriano, J. J. Reina, B. M. Illescas, et al., *J. Am. Chem. Soc.* **2019**, *141*, 15403–15412.
- [29] A. Schwegmann, F. Brombacher, *Sci. Signaling* **2008**, *1*, re8–re8.
- [30] T. K. Dam, C. F. Brewer, *Adv. Carbohydr. Chem. Biochem.* **2010**, *63*, 139–164.
- [31] T. K. Dam, T. A. Gerken, B. S. Cavada, et al., *J. Biol. Chem.* **2007**, *282*, 28256–28263.
- [32] T. K. Dam, C. F. Brewer, *Biochemistry* **2008**, *47*, 8470–8476.
- [33] R. T. Lee, Y. C. Lee, *Glycoconjugate J.* **2000**, *17*, 543–551.
- [34] C. R. Becer, M. I. Gibson, J. Geng, et al., *J. Am. Chem. Soc.* **2010**, *132*, 15130–15132.
- [35] S. Ng, N. J. Bennett, J. Schulze, et al., *Bioorg. Med. Chem.* **2018**, *26*, 5368–5377.
- [36] S.-K. Wang, P.-H. Liang, R. D. Astronomo, et al., *Proc. Natl. Acad. Sci. USA* **2008**, *105*, 3690–5.
- [37] O. Martínez-Ávila, L. M. Bedoya, M. Marradi, et al., *ChemBioChem* **2009**, *10*, 1806–9.
- [38] M. Taouai, V. Porkolab, K. Chakroun, et al., *Bioconjugate Chem.* **2019**, *30*, 1114–1126.
- [39] K. Owen, *Drug Chem. Toxicol.* **2013**, *36*, 109–118.
- [40] Y. H. Lim, K. M. Tiemann, D. A. Hunstad, et al., *Wiley Interdiscip. Rev. Nanomed. Nanobiotechnol.* **2016**, *8*, 842–871.
- [41] S. Bhatia, L. C. Camacho, R. Haag, *J. Am. Chem. Soc.* **2016**, *138*, 8654–8666.
- [42] R. Rai, S. Alwani, I. Badea, *Polymers (Basel)*. **2019**, *11*, 745.
- [43] R. Herrendorff, P. Hänggi, H. Pfister, et al., *Proc. Nat. Acad. Sci.* **2017**, *114*, E3689–E3698.
- [44] B. Aliu, D. Demeestere, E. Seydoux, et al., *J. Neurochem.* **2020**, *154*, 486–501.
- [45] C. A. Hoppe, Y. C. Lee, *Biochemistry* **1984**, *23*, 1723–1730.
- [46] G. Thoma, J. T. Patton, J. L. Magnani, et al., *J. Am. Chem. Soc.* **1999**, *121*, 5919–5929.
- [47] Y. Guo, H. Feinberg, E. Conroy, et al., *Nat. Struct. Mol. Biol.* **2004**, *11*, 591–598.
- [48] Y. Watanabe, T. A. Bowden, I. A. Wilson, et al., *Biochim. Biophys. Acta Gen. Subj.* **2019**, *1863*, 1480–1497.
- [49] C. M. Fehres, H. Kalay, S. C. M. Bruijns, et al., *J. Controlled Release* **2015**, *203*, 67–76.
- [50] C. W. Cairo, J. E. Gestwicki, M. Kanai, et al., *J. Am. Chem. Soc.* **2002**, *124*, 1615–1619.
- [51] J. E. Gestwicki, C. W. Cairo, L. E. Strong, et al., *J. Am. Chem. Soc.* **2002**, *124*, 14922–14933.
- [52] S. R. S. Ting, G. Chen, M. H. Stenzel, *Polym. Chem.* **2010**, *1*, 1392.
- [53] S. Igde, S. Röblitz, A. Müller, et al., *Macromol. Biosci.* **2017**, *17*, 1700198.
- [54] M. Mammen, S.-K. Choi, G. M. Whitesides, *Angew. Chem. Int. Ed.* **1998**, *37*, 2754–2794.
- [55] V. M. Krishnamurthy, L. A. Estroff, G. M. Whitesides, in *Fragm. Approaches Drug Discov.* (Eds.: W. Jahnke, D. Erlanson), **2006**, pp. 11–53.
- [56] W. P. Jencks, *Proc. Natl. Acad. Sci. USA* **1981**, *78*, 4046–4050.
- [57] P. I. Kitov, D. R. Bundle, *J. Am. Chem. Soc.* **2003**, *125*, 16271–16284.
- [58] H. X. Zhou, M. K. Gilson, *Chem. Rev.* **2009**, *109*, 4092–4107.
- [59] E. C. Wamhoff, J. Schulze, L. Bellmann, et al., *ACS Cent. Sci.* **2019**, *5*, 808–820.

Manuscript received: May 20, 2021
Accepted manuscript online: June 1, 2021
Version of record online: ■■■, ■■■■

FULL PAPERS

Mannose-functionalized poly-L-lysine glycoconjugates efficiently inhibit the DC-SIGN-mediated attachment of glycoproteins from pandemic viruses, including SARS-CoV-2, to susceptible cells in picomolar concentrations. The compounds are fully biocompatible and represent a promising therapeutic option to combat viral infections. A thermodynamic analysis of the multivalent interactions guides the path towards more potent compounds based on glycomimetic ligands.



Dr. J. Cramer, B. Aliu, Dr. X. Jiang, Dr. T. Sharpe, Dr. L. Pang, A. Hadorn, Dr. S. Rabbani, Prof. B. Ernst**

1 – 10

Poly-L-lysine Glycoconjugates Inhibit DC-SIGN-mediated Attachment of Pandemic Viruses



ChemMedChem

Supporting Information

Poly-L-lysine Glycoconjugates Inhibit DC-SIGN-mediated Attachment of Pandemic Viruses

Jonathan Cramer^{†,*}, Butrint Aliu[†], Xiaohua Jiang, Timothy Sharpe, Lijuan Pang, Adrian Hadorn, Said Rabbani, and Beat Ernst^{*}

Table of Contents

| | |
|---|------------|
| 1. Synthesis | S2 |
| 2. Protein Expression and Purification | S11 |
| 3. Isothermal Titration Calorimetry | S12 |
| 4. Dynamic Light Scattering | S19 |
| 5. Analytical Ultracentrifugation | S19 |
| 6. Mammalian cell culture, flow cytometry, and fluorescence microscopy | S20 |
| 7. References | S21 |

☐

☐

□

1 Synthesis

1.1 General methods

NMR spectra were recorded on a Bruker Avance III 500 MHz spectrometer. Assignment of ^1H and ^{13}C NMR spectra was achieved using 2D methods (COSY, HSQC, HMBC). Chemical shifts are expressed in ppm using residual CHCl_3 , CHD_2OD or HDO as references. Electron spray ionization mass spectra (ESI-MS) were obtained on a Waters micromass ZQ Mass Spectrometer. Reactions were monitored by TLC using glass plates coated with silica gel 60 F₂₅₄ (Merck, Darmstadt, Germany) and visualized by using UV light and/or by charring with a molybdate solution (a 0.02 M solution of ammonium cerium sulfate dihydrate and ammonium molybdate tetrahydrate in aqueous 10% H_2SO_4). MPLC separations were carried out on a CombiFlash Companion or R_f from Teledyne Isco (Lincoln, NE, USA) equipped with RediSep flash columns. For purification of glycopolymers, Vivaspin ultrafiltration devices with a molecular weight cutoff of 6 kDa or 50 kDa (Sartorius, Göttingen, Germany) were used. Commercially available reagents and dry solvents were purchased from Sigma-Aldrich, Alfa Aesar and Acros Organics. Poly-L-lysine HBr polymers were acquired from PtS (Valencia, Spain).

□

1.2 Synthesis of mannose building block 4^[1,2]

3-Chloropropyl-2,3,4,6-tetracetate- α -D-mannopyranoside (6)

To a mixture of D-mannose pentacetate (**5**, 532 mg, 1.36 mmol) and 3-chloro-1-propanol (98%) (114 μL , 1.36 mmol) in dry DCM (5.0 mL), $\text{BF}_3 \cdot \text{Et}_2\text{O}$ (671 μL , 4.0 mmol) was added at rt. The reaction mixture was stirred at rt overnight, then diluted with DCM, washed carefully with sat. aqueous NaHCO_3 and brine. The combined organic layers were dried over Na_2SO_4 . The solvent was removed under reduced pressure and the residue was purified by chromatography on silica gel (PE/EE, 7:3-6:4) to provide **6** (378 mg, 65%) as colorless oil.

^1H NMR (500 MHz, CDCl_3) δ 5.34 – 5.25 (m, 2H, H-5, H-4), 5.24 (dd, $J = 3.2, 1.8$ Hz, 1H, H-2), 4.83 (d, $J = 1.8$ Hz, 1H, H-1), 4.28 (dd, $J = 12.2, 5.5$ Hz, 1H, H-6b), 4.13 (dd, $J = 12.2, 2.5$ Hz, 1H, H-6a), 3.99 (ddd, $J = 9.4, 5.4, 2.4$ Hz, 1H, H-5), 3.92 (ddd, $J = 9.8, 7.3, 4.9$ Hz, 1H, $\text{ClCH}_2\text{CH}_2\text{CH}_2\text{O}$), 3.73 – 3.62 (m, 2H, $\text{ClCH}_2\text{CH}_2\text{CH}_2\text{O}$), 3.59 (ddd, $J = 9.8, 6.1, 5.1$ Hz, 1H, $\text{ClCH}_2\text{CH}_2\text{CH}_2\text{O}$), 2.16 (s, 3H, OAc), 2.10 (s, 3H, OAc), 2.08 (m, 2H, $\text{ClCH}_2\text{CH}_2\text{CH}_2\text{O}$), 2.05 (s, 3H, OAc), 2.00 (s, 3H, OAc),

□

S21

□

3-Azidopropyl-2,3,4,6-tetra-O-acetyl- α -D-mannopyranoside (7)

To a solution of chloride **6** (373 mg, 0.87 mmol) in DMF (4.0 mL), NaN₃ (342 mg, 5.26 mmol) was added at rt. The reaction mixture was stirred at 60°C for 2h and then the solvent was removed under reduced pressure. The residue was dissolved in EtOAc, washed with H₂O and brine. The organic layer was dried over Na₂SO₄, the solvent removed under reduced pressure and the residue purified by chromatography on silica gel (PE/EE, 7:3-6:4) to provide azide **7** (258 mg, 95%) as colorless oil.

¹H NMR (500 MHz, CDCl₃) δ 5.40 – 5.18 (m, 3H, H-4, H-3, H-2), 4.82 (d, J = 1.8 Hz, 1H, H-1), 4.28 (dd, J = 12.3, 5.4 Hz, 1H, H-6b), 4.13 (m, 1H, H-6a), 3.97 (ddd, J = 9.6, 5.4, 2.4 Hz, 1H, H-5), 3.82 (ddd, J = 9.9, 6.8, 5.5 Hz, 1H, N₃CH₂CH₂CH₂O), 3.53 (ddd, J = 9.9, 6.4, 5.4 Hz, 1H, N₃CH₂CH₂CH₂O), 3.43 (t, J = 6.5 Hz, 2H, N₃CH₂CH₂CH₂O), 2.16 (s, 3H, OAc), 2.11 (s, 3H, OAc), 2.05 (s, 3H, OAc), 2.00 (s, 3H, OAc), 1.90 (dtd, J = 12.1, 6.7, 5.4 Hz, 2H, N₃CH₂CH₂CH₂O).

3-Azidopropyl- α -D-mannopyranoside (8)

To a solution of azide **7** (587 mg, 1.96 mmol) in MeOH (10.0 mL), 0.155 mL of CH₃ONa/MeOH (0.437 N) was added at rt. The reaction mixture was stirred at rt overnight, then neutralized with Amberlyst-15 and filtered. The filtrate was concentrated *in vacuo* and the residue was purified by chromatography on silica gel (DCM/MeOH, 9:1-6:1) to provide **8** (298 mg, 83%) as colorless oil.

¹H NMR (500 MHz, MeOD) δ 4.75 (d, J = 1.8 Hz, 1H, H-1), 3.86 – 3.81 (m, 3H, H-6a, N₃CH₂CH₂CH₂O, H-2), 3.74 – 3.66 (m, 2H, H-6b, H-3), 3.61 (t, J = 9.5 Hz, 1H, H-4), 3.54 – 3.47 (m, 2H, H-5, N₃CH₂CH₂CH₂O), 3.41 (td, J = 6.7, 4.5 Hz, 2H, N₃CH₂CH₂CH₂O), 1.95 – 1.65 (m, 2H, N₃CH₂CH₂CH₂O).

3-Aminopropyl- α -D-mannopyranoside (9)

A suspension of azide **8** (298 mg, 1.132 mmol) and Pd(OH)₂/C (38.0 mg, 10% Pd) in MeOH (10.0 mL) was hydrogenated with a H₂ balloon at rt overnight. The reaction mixture was filtered through celite and the solvent was removed under reduced pressure. The residue was purified by reverse-phase C18 chromatography (H₂O/MeOH, 1:0-9:1) to provide amine **9** (226 mg, 84%) as a white solid (highly hygroscopic).

¹H NMR (500 MHz, D₂O) δ 4.88 (d, J = 1.7 Hz, 1H, H-1), 3.96 (dd, J = 3.4, 1.7 Hz, 1H, H-2), 3.91 (dd, J = 12.2, 1.8 Hz, 1H, H-6b), 3.86 – 3.72 (m, 3H), 3.69 – 3.54 (m, 3H), 2.86 – 2.74 (m, 2H NH₂CH₂CH₂CH₂O), 1.82 (tt, J = 14.1, 7.3 Hz, 2H, m, 2H, NH₂CH₂CH₂CH₂O).

□

S31

2

Synthesis of mannose building block 4

Aminopropyl α -D-mannopyranoside (**9**, 20 mg, 84 μ mol, 1 eq) was dissolved in 190 μ L water. 1 M NaOH (8.4 μ L, 84 μ mol, 0.1 eq), γ -thiobutyrolactone (72.8 μ L, 86 mg, 840 μ mol, 10 eq), and methanol (300 μ L) were added and the resulting mixture was stirred overnight. After removal of methanol under reduced pressure the aqueous phase was washed three times with EtOAc. After removal of insoluble material by centrifugation and lyophilization, the building block **4** was obtained as a colorless solid (24 mg, 71 μ mol, 84%). ^1H NMR (500 MHz, D_2O) δ 4.87 (d, $J = 1.8$ Hz, 1H, Man-*H1*), 3.97 (dd, $J = 3.4, 1.8$ Hz, 1H, Man-*H2*), 3.91 (dd, $J = 12.1, 2.1$ Hz, 1H, Man-*H6'*), 3.87 – 3.73 (m, 3H, Man-*H3*, Man-*H6''*, O-*CH2'*), 3.73 – 3.60 (m, 2H, Man-*H4*, Man-*H5*), 3.57 (m, 1H, RO-*CH2''*), 3.31 (m, 2H, *CH2*-NH(CO)), 2.57 (t, $J = 7.1$ Hz, 2H, *CH2*-SH), 2.39 (t, $J = 7.4$ Hz, 2H, *CH2*-CONH), 1.92 (m, 2H, *CH2*-*CH2*-SH), 1.89 – 1.81 (m, 2H, *CH2*-*CH2*-O). ^{13}C NMR (126 MHz, D_2O) δ 176.0 (CONH), 99.9 (Man-*C1*), 72.8 (Man-*C5*), 70.6 (Man-*C4*), 70.1 (Man-*C2*), 66.8 (Man-*C3*), 65.2 (*CH2*-O), 60.9 (Man-*C6*), 36.4 (*CH2*-NH(CO)), 34.5 (*CH2*-CONH), 29.5 (*CH2*-*CH2*-SH), 28.1 (*CH2*-*CH2*-O), 23.1 (*CH2*-SH). ESI⁺-MS Calculated for $\text{C}_{13}\text{H}_{24}\text{NNaO}_7\text{S}$ [M+Na]⁺: 362.39, found: 362.16.

1.3 Syntheses of chloroacetylated poly-L-lysine (3a-c)

Poly-L-lysine⁴⁰⁰ HBr (**2**, 100 mg, 0.48 mmol) was suspended in a mixture of DMF (2 mL) and 2,6-lutidine (0.5 mL). Chloroacetic anhydride (244 mg, dissolved in 0.5 mL of DMF) was added over 10 min under cooling with ice. The reaction mixture was stirred at 4°C for 16 h. The product precipitated after addition to 40 mL of a vigorously stirred 1:1 mixture of ethanol and diethyl ether and subsequent centrifugation (1000 rpm, 2 min, 4°C). The supernatant was discarded and the precipitate was washed three times with ethanol/diethylether (1:1, 30 mL). The purified product was dried under vacuum to yield chloroacetylated poly-L-lysine⁴⁰⁰ **3c** as a colorless solid (92 mg, 96%). NMR spectra were identical to previously reported data.^[3]

Chloroacetylated poly-L-lysine¹⁰⁰ **3a** was obtained as a colorless solid (90 mg, 92%). ^1H NMR (400 MHz, $\text{DMSO}-d_6$) δ 8.18 (s, 2H, 2 -NH(CO)-), 4.02 (s, 2H, -*CH2*Cl), 3.82 (s, 1H, -(CO)*CH*-NH-), 3.05 (s, 2H, CH_2), 1.83 (s, 2H, CH_2), 1.42 (m, 4H, 2 CH_2).

2

S4

□

Chloroacetylated poly-L-lysine²⁵⁰ **3b** was obtained as a colorless solid (30 mg, 62%). ¹H NMR (400 MHz, DMSO-*d*₆) δ 8.18 (s, 2H, 2 -NH(CO)-), 4.03 (s, 3H, -(CO)CH-NH-, and -CH₂Cl), 3.06 (s, 2H, CH₂), 1.43 (br, 6H, 3 CH₂).

1.3. Syntheses of Man-PLL **1a-d**

Synthesis of Man-PLL¹⁰⁰ **1a**

To a solution of chloroacetylated L-polylysine¹⁰⁰ (**3a**, 4.7 mg, 22.96 μmol) in DMF (200 μL) a solution of **4** [35 μL (3.5 mg, 10 μmol) of an aqueous stock solution (8.0 mg in water 80 μL)] was added under Argon. Then 1,8-diazabicyclo(5.4.0)undec-7-ene (3.4 μL, 22.96 μmol) was added. The reaction mixture was shaken in an Eppendorf tube at 25°C for 1 h with an Eppendorf thermomixer at 300 rpm. Then, thioglycerol (6.0 μL, 68.8 μmol) and Et₃N (9.6 μL, 68.8 μmol) were added and the mixture was shaken overnight. Next, the reaction mixture was dropped into a stirred solution of ethyl acetate/ethanol (1:1; 3.0 mL), leading to precipitation of the product. The precipitate was collected by centrifugation, washed with ethanol (3.0 mL), and then dissolved in water (3.0 mL). The aqueous solution was purified by ultracentrifugation using a Vivaspin centrifugal concentrator (Sartorius, Germany; 6 mL, MWCO 6 kDa, 3 times from 6.0 mL to 0.5 mL). The product in 1 ml H₂O was lyophilized within 4 hours yielding 3.9 mg (45%) Man-PLL¹⁰⁰ **1a** as a white solid (loading percentage based on HNMR: 44 %).

Synthesis of Man-PLL²⁵⁰ **1b**

To a solution of chloroacetylated L-polylysine²⁵⁰ (**3b**, 3.6 mg, 17.59 μmol) in DMF (200 μL) a solution of **4** [26.8 μL (2.68 mg, 6.1 μmol) of an aqueous stock solution (8.0 mg in water 80 μL)] was added under Argon. Then 1,8-diazabicyclo(5.4.0)undec-7-ene (2.6 μL, 17.59 μmol) was added. The reaction mixture was shaken in Eppendorf tube at 25°C for 1 h with Eppendorf thermomixer at 300 rpm. Then, thioglycerol (4.6 μL, 52.77 μmol) and Et₃N (7.4 μL, 52.77 μmol) were added and the mixture was shaken overnight. The reaction mixture was dropped into a stirred solution of ethyl acetate/ethanol (1:1; 3.0 mL), leading to precipitation of the product. The precipitate was collected by centrifugation, washed with ethanol (3.0 mL), and then dissolved in water (3.0 mL). The aqueous solution was purified by ultracentrifugation using a Vivaspin centrifugal concentrator (Sartorius, Germany; 6 mL, MWCO 6 kDa, 3 times from 6.0 mL to 0.5 mL). The product in 1 ml of water was lyophilized within 4 hours yielding 4.3 mg (64%) Man-PLL²⁵⁰ **1b** as a white solid (loading percentage based on HNMR: 46 %).

□

S51

□

Synthesis of Man-PLL⁴⁰⁰ **1c**

To a solution of chloroacetylated L-polylysine⁴⁰⁰ (**3c**, 5.7 mg, 27.85 μmol) in DMF (200 μL) was added a solution of **4** (3.3 mg, 9.74 μmol) in water (45 μL) under Argon. Then 1,8-diazabicyclo(5.4.0)undec-7-ene (4.2 μL , 27.85 μmol) was added. The reaction mixture was shaken in an Eppendorf tube at 25°C for 1 h with Eppendorf thermomixer at 300 rpm. Then, thioglycerol (7.2 μL , 83.55 μmol) and Et₃N (11.7 μL , 83.55 μmol) were added and the mixture was shaken overnight. Next, the reaction mixture was dropped into a stirred solution of ethyl acetate/ethanol (1:1; 3.0 mL), leading to precipitation of the product. The precipitate was collected by centrifugation, washed with ethanol (3.0 mL), and then dissolved in water (3.0 mL). The aqueous solution was purified by ultracentrifugation using a Vivaspin centrifugal concentrator (Sartorius, Germany; 6 mL, MWCO 50 kDa, 3 times from 6.0 mL to 0.5 mL). The product was lyophilized from 1-2 mL aqueous solution within 5.5 hours yielding 7.0 mg (68%) Man-PLL⁴⁰⁰ **1c** as a white solid (loading percentage based on HNMR: 39 %).

Synthesis of Man-PLL⁴⁰⁰ **1d**

To a solution of chloroacetylated L-polylysine⁴⁰⁰ (**3c**, 4.2 mg, 20.0 μmol) in DMF (200 μL) a solution of **4** [45 μL (3.13 mg, 9.2 μmol) of an aqueous stock solution (14.6 mg in 200 μL of water)], were added under Argon. Then, 1,8-diazabicyclo(5.4.0)undec-7-ene (3.0 μL , 20.0 μmol) was added. The reaction mixture was shaken in Eppendorf tube at 25°C for 1 h with Eppendorf thermomixer at 300 rpm. Then, thioglycerol (5.2 μL , 60.0 μmol) and Et₃N (8.4 μL , 60.0 μmol) were added and the mixture was shaken overnight. Next, the reaction mixture was dropped into a stirred solution of ethyl acetate/ethanol (1:1; 3.0 mL), leading to precipitation of the product. The precipitate was collected by centrifugation, washed with ethanol (3.0 mL), and then dissolved in water (3.0 mL). The aqueous solution was purified by ultracentrifugation using a Vivaspin centrifugal concentrator (Sartorius, Germany; 6 mL, MWCO 50 kDa, 3 times from 6.0 mL to 0.5 mL). The product was lyophilized from 1 mL aqueous solution within 5.5 hours yielding 4.3 mg (51%) of Man-PLL⁴⁰⁰ **1d** as a white solid (loading percentage based on HNMR: 62%).

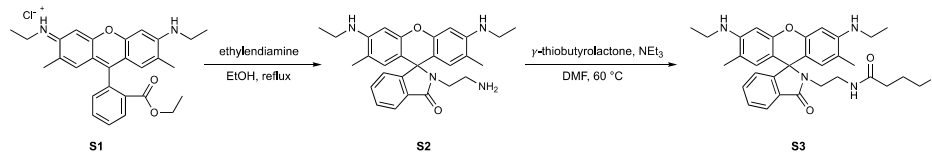
□

1.4. Synthesis of fluorescently labeled polymers 10–12

□

S6

Synthesis of Rhodamine 6G precursor S3



Scheme S1. Synthetic route toward Rhodamine 6G precursor S3

Rhodamin 6G derivative S2

Rhodamine 6G (**S1**, 500 mg, 1.04 mmol, 1 eq) and ethylenediamine (1.25 g, 20.8 mmol, 20 eq) were dissolved in EtOH and refluxed for 5 h. The solvent was removed under reduced pressure, and the crude product purified by silica gel chromatography (DCM/MeOH 10:1) to yield the product **S2** as a slightly pink solid (428 mg, 0.94 mmol, 90%). ^1H NMR (500 MHz, CDCl_3) δ 7.96 – 7.89 (m, 1H, H7_{isoindoline-1-one}), 7.49 – 7.40 (m, 2H, H5/6_{isoindoline-1-one}), 7.09 – 7.01 (m, 1H, H4_{isoindoline-1-one}), 6.34 (s, 2H, H4/5_{9H-xanthene}), 6.22 (d, $J = 0.9$ Hz, 2H, H1/8_{9H-xanthene}), 3.53 – 3.45 (m, 2H, Ar-NHCH₂CH₃), 3.25 – 3.17 (m, 4H, Ar-NHCH₂CH₃), 3.15 (t, $J = 6.7$ Hz, 2H, R₂NCH₂CH₂NH₂), 2.35 (t, $J = 6.7$ Hz, 2H, R₂NCH₂CH₂NH₂), 1.89 (s, 6H, Ar-CH₃), 1.32 (t, $J = 7.2$ Hz, 6H, Ar-NHCH₂CH₃). ^{13}C NMR (126 MHz, CDCl_3) δ 168.6 (CONH₂), 153.5 (C1a_{isoindoline-1-one}), 151.7 (C4a/5a_{9H-xanthene}), 147.5 (C3/6_{9H-xanthene}), 132.5 (C5_{isoindoline-1-one}), 131.2 (C3a_{isoindoline-1-one}), 128.3 (C1/8_{9H-xanthene}), 128.1 (C6_{isoindoline-1-one}), 123.8 (C4_{isoindoline-1-one}), 122.8 (C7_{isoindoline-1-one}), 118.0 (C2/7_{9H-xanthene}), 106.2 (C1a/8a_{9H-xanthene}), 96.5 (C4/5_{9H-xanthene}), 65.0 (C9_{9H-xanthene}), 44.0 (R₂NCH₂CH₂NH₂), 40.8 (R₂NCH₂CH₂NH₂), 38.4 (Ar-NHCH₂CH₃), 16.7 (Ar-CH₃), 14.7 (Ar-NHCH₂CH₃). ESI-MS m/z calculated for C₂₈H₃₃N₄O₂ [M+H]⁺: 457.60; found: 457.19.

Rhodamin 6G precursor S3

Rhodamin 6G derivative **S2** (100 mg, 0.22 mmol, 1 eq) and γ -thiobutyrolactone (224 mg, 2.19 mmol, 10 eq) were dissolved under Argon in dry DMF. The resulting mixture was heated to 60 °C for 5 h, then the solvent removed under reduced pressure, and the crude product purified by silica gel chromatography (DCM/MeOH 10:1) to yield the free thiol as a red oil (40 mg, 0.07 mmol, 33%) and the corresponding disulfide as a red oil (57 mg, 0.05 mmol, 46%). ^1H NMR (500 MHz, CDCl_3) δ 7.99 – 7.86 (m, 1H, H7_{isoindoline-1-one}), 7.51 – 7.43 (m, 2H, H5/6_{isoindoline-1-one}), 7.12 – 6.98 (m, 1H, H4_{isoindoline-1-one}), 6.92 – 6.72 (m, 1H, CONH), 6.34 (s, 2H, H4/5_{9H-xanthene}), 6.26 – 6.14 (m, 2H, H1/8_{9H-xanthene}), 3.55 (s, 2H, Ar-NHCH₂CH₃), 3.30 – 3.24 (m, 2H, Ar-NHCH₂CH₃), 3.21 (q, $J = 7.2$ Hz, 4H, Ar-NHCH₂CH₃), 3.02 – 2.89 (m, 2H, R₂NCH₂CH₂NH), 2.60 – 2.46 (m, 2H, HSC₂CH₂CH₂CONH), 2.19 (t, $J = 7.3$ Hz, 2H,

S7

□

HSCH₂CH₂CH₂CONH), 2.03 – 1.77 (m, 8H, HSCH₂CH₂CH₂CONH/Ar-CH₃), 1.33 (t, *J* = 7.2 Hz, 6H, Ar-NHCH₂CH₃). ¹³C NMR (126 MHz, CDCl₃) δ 172.7 (CONH), 170.1 (CONR₂), 153.9 (C1a_{isoindoline-1-one}), 151.9 (C4a/5a_{9H-xanthene}), 147.8 (C3/6_{9H-xanthene}), 133.0 (C5_{isoindoline-1-one}), 130.4 (C3a_{isoindoline-1-one}), 128.4 (C1/8_{9H-xanthene}), 128.1 (C6_{isoindoline-1-one}), 124.1 (C4_{isoindoline-1-one}), 123.0 (C7_{isoindoline-1-one}), 118.4 (C2/7_{9H-xanthene}), 105.4 (C1a/8a_{9H-xanthene}), 96.8 (C4/5_{9H-xanthene}), 65.7 (C9_{9H-xanthene}), 40.7 (R₂NCH₂CH₂NH), 40.1 (R₂NCH₂CH₂NH), 38.5 (Ar-NHCH₂CH₃), 35.0 (HSCH₂CH₂CH₂CONH), 29.9 (HSCH₂CH₂CH₂CONH), 24.3 (HSCH₂CH₂CH₂CONH), 16.9 (Ar-CH₃), 14.9 (Ar-NHCH₂CH₃). ESI-MS *m/z* calculated for C₃₂H₃₉N₄O₃S [M+H]⁺: 559.75; found: 559.38.

Synthesis of Rhodamine 6G labeled mannosylated polymer 10

The chloroacetylated PLL₄₀₀ (**3c**, 5 mg, 61 nmol, 1 eq), the rhodamine derivative **S2** (0.41mg, 732 nmol, 12 eq), and DBU (3.72 mg, 24.4 μmol, 400 eq) were dissolved in DMF under Argon and protected from light. The resulting mixture was stirred at rt for 15 min. Then, a solution of mannoside **4** (3.31 mg, 9.76 μmol, 160 eq) in water (30 μL) was added and stirring continued for additional 45 min. Thioglycerol (7.4 mg, 68.3 μmol, 1120 eq) and Et₃N (6.9 mg, 68.3 μmol, 1120 eq) were added and the solution was stirred for another 16 h at rt. The mixture was poured on 4 mL of a stirred 1:1 mixture of EtOH and Et₂O. After precipitation of the product was collected by centrifugation (5 min, 200 rpm, 25 °C) and washed three times with 3 ml EtOH. The resulting solid was dissolved in 5 mL water and purified by ultrafiltration (Vivaspin 6, 50 kDa MWCO, 4000 rpm, 25 °C, three times from 5 mL to 0.5 mL). The purified product **10** was lyophilized to obtain a colorless solid (4.8 mg, 31 nmol, 51%) with a mannose loading of 47% (by H-NMR).

Synthesis of Rhodamine 6G labeled non-mannosylated polymer 11

The chloroacetylated PLL₄₀₀ **3c** (5 mg, 61 nmol, 1 eq), the rhodamine derivative **S2** (0.41mg, 732 nmol, 12 eq), and DBU (3.72 mg, 24.4 μmol, 400 eq) were dissolved in DMF under Argon and protected from light. The resulting mixture was stirred at rt for 15 min. After the addition of 30 μL water stirring was continued for 45 min. Then, thioglycerol (7.4 mg, 68.3 μmol, 1120 eq) and Et₃N (6.9 mg, 68.3 μmol, 1120 eq) were added and the solution was stirred for 16 h at rt. The mixture was poured into 4 mL of a vigorously stirred 1:1 mixture of EtOH and Et₂O. The precipitated product was collected by centrifugation (5 min, 200 rpm, 25 °C) and washed three times with 3 ml EtOH. The resulting solid was suspended in 5 mL water and 1 M HCl was added until complete dissolution of the solid material. The product **11**

□

S8

was purified by ultrafiltration (Vivaspin 6, 50 kDa MWCO, 4000 rpm, 25 °C, three times from 5 mL to 0.5 mL) and lyophilized to obtain a pink solid (5.8 mg, 50 nmol, 82%).

Synthesis of sulfo-Cy3/sulfo-Cy5 labeled mannosylated polymer **12**

To a solution of sulfo-Cy3 NHS ester (0.12 mg, 153 nmol, 4.2 eq) and sulfo-Cy5 NHS ester (0.12 mg, 161 nmol, 4.4 eq) in 75 μ L dry DMF was added DIPEA (1.89 mg, 14.6 μ mol, 400 eq) and cysteamine (56 μ g, 730 nmol, 20 eq). The mixture was agitated at rt for 4 h. The crude reaction mixture was added to a stirred solution of chloroacetylated PLL₄₀₀ **3c** (2.99 mg, 37 nmol, 1 eq), and DBU (2.23 mg, 14.6 μ mol, 400 eq) in dry DMF under argon at rt. After 15 min, a solution of mannoside **4** (2.24 mg, 6.59 μ mol, 181 eq) in water (30 μ L) was added and stirring continued for additional 60 min. Thioglycerol (4.43 mg, 41 μ mol, 1120 eq) and Et₃N (4.19 mg, 41 μ mol, 1120 eq) were added and the solution was stirred for another 18 h at rt. The mixture was poured on 4 mL of a stirred 1:1 mixture of EtOH and Et₂O. After precipitation of the product was collected by centrifugation (5 min, 200 rpm, 25 °C) and washed three times with 3 ml EtOH. The resulting solid was dissolved in 5 mL water and purified by ultrafiltration (Vivaspin 6, 50 kDa MWCO, 4000 rpm, 25 °C, three times from 5 mL to 0.5 mL). The purified product **12** was lyophilized to obtain a green solid (3 mg, 20 nmol, 55%) with a mannose loading of 22% (by H-NMR).

1.4 NMR characterization of Man-PLL **1a-d**

Mannose loading was calculated from the ratio of integrals A and C' after equation S1, with *I* being the integral of signal A or C' and *N* the number of corresponding protons.

$$Man\% = \frac{\frac{I_A}{N_A}}{\frac{I_A}{N_A} + \frac{I_{C'}}{N_{C'}}} \times 100\% \quad \text{Equation S1}$$

?

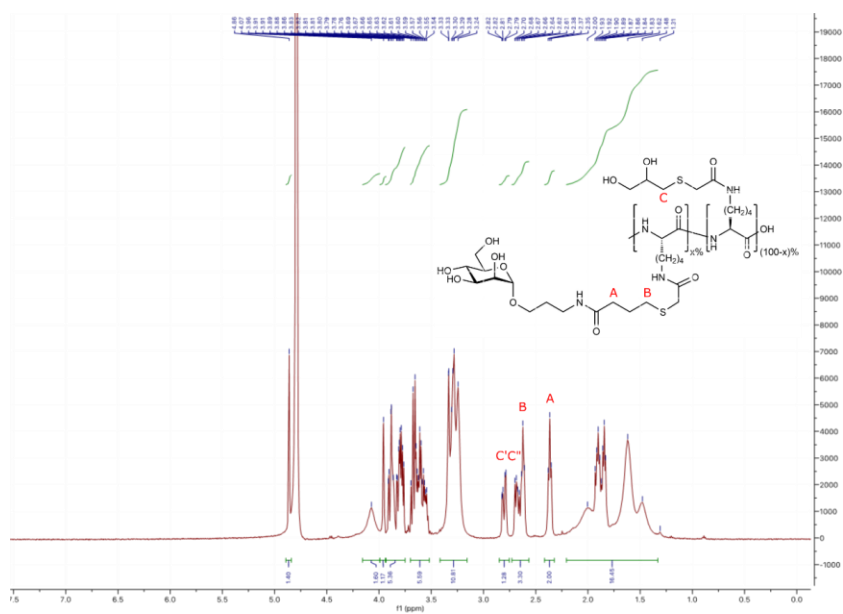


Figure S1. ¹H-NMR spectrum of **1a**.

?

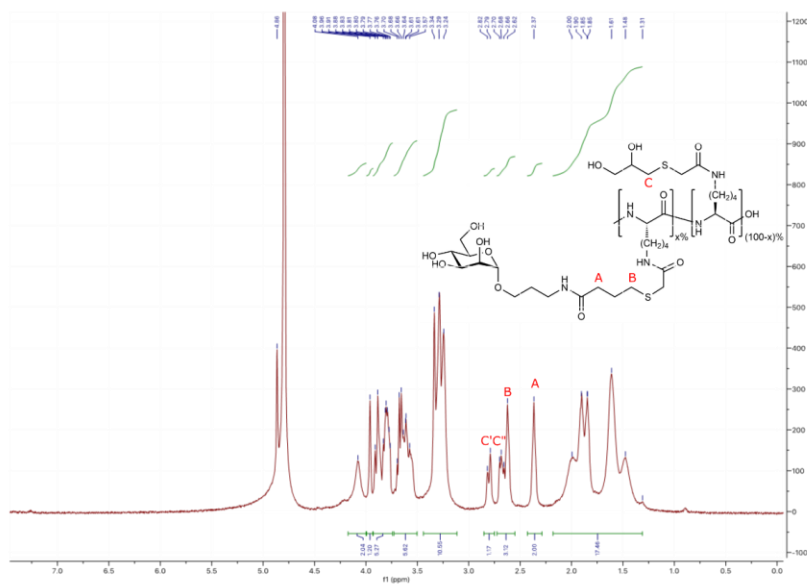


Figure S2. ¹H-NMR spectrum of **1b**.

?

?

?

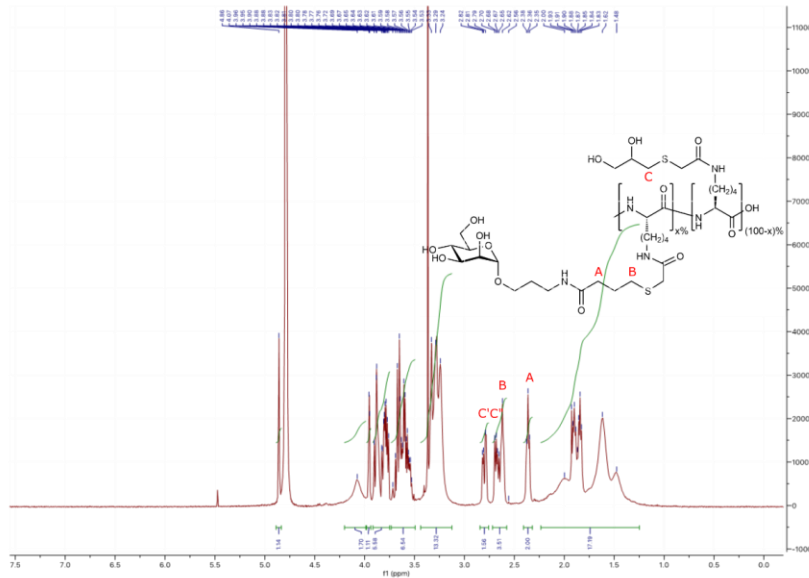


Figure S3. ¹H-NMR spectrum of 1c.

?

?

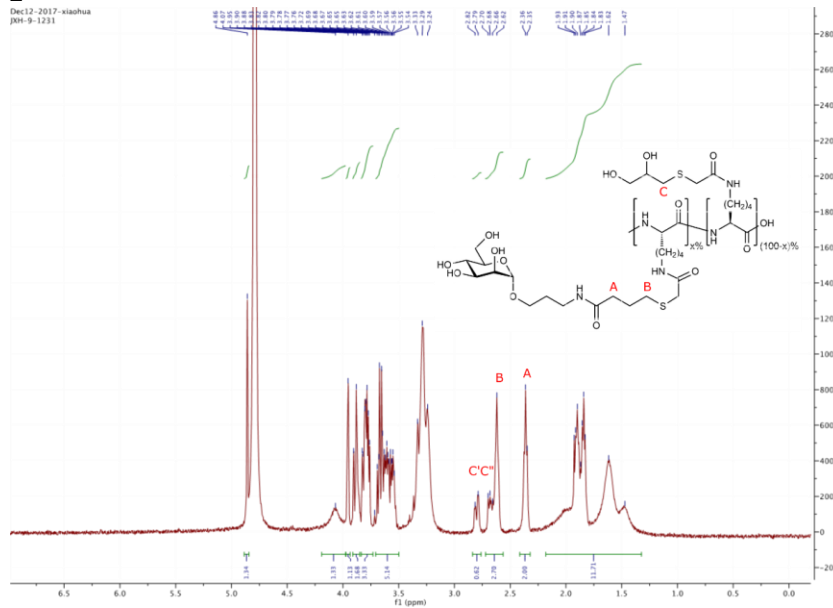


Figure S4. ¹H-NMR spectrum of 1d.

?

2 Protein expression and purification

E. coli BL21(DE3) cells were transfected with Novagen pET15b plasmids encoding for a recombinant DC-SIGN ECD linked to a thrombin cleavage site and an N-terminal His-Tag. Cells were initially cultivated overnight in 20 mL Luria Bertani medium substituted with 0.1

?

S11

□

mg/mL ampicillin at 37 °C and then transferred into 1 L Terrific Broth medium substituted with 0.1 mg/mL ampicillin. Cells were incubated for 8 h at 37 °C and DC-SIGN expression was induced by addition of 0.5 mM IPTG. After 16 h, cells were harvested by centrifugation (4,000 rpm, 20 min, 4 °C), resuspended in lysis buffer (50 mM Tris-HCl, 10 mM MgCl₂, 0.1% Triton X100), and lysed by sonication or addition of lysozyme and DNase I. The cell lysate was centrifuged (11000 rpm, 20 min, 4 °C), the supernatant discarded, and the precipitated material was washed three times with washing buffer (50 mM Tris-HCl, pH 8.0, 4 M urea, 500 mM NaCl, 1 mM EDTA). The purified inclusion bodies were dissolved in 20 mL of denaturation buffer (6 M guanidine hydrochloride, 100 mM Tris-HCl, pH 8.0, 1 mM DTT) for 1 h at 37 °C. After ultracentrifugation (22000 rpm, 30 min, 4 °C), the denatured protein was refolded by slow dilution into 100 mL refolding buffer (100 mM Tris-HCl, pH 8.0, 1 M L-arginine, 150 mM NaCl, 120 mM sucrose). The mixture was stirred for 2 d at 4 °C and dialyzed against binding buffer (20 mM Tris-HCl, 500 mM NaCl, 25 mM CaCl₂, pH 7.8). Precipitated protein was removed by ultracentrifugation (22000 rpm, 30 min, 4 °C) and the refolded soluble protein was purified by affinity chromatography on a mannose-sepharose column (elution buffer: 20 mM TRIS, 500 mM NaCl, 2 mM EDTA, pH 7.8).

□

3 Isothermal Titration Calorimetry

3.1. General Information

A MicroCal ITC200 instrument (MicroCal, Northampton, USA) was used for all ITC experiments. All measurements were performed at 25 °C using a reference power of 6 $\mu\text{cal s}^{-1}$, a stirring speed of 750 rpm, feedback mode high, and a filter period of 2 s. Prior to the experiments, all protein samples were extensively dialyzed against ITC buffer (20 mM HEPES, 150 mM NaCl, 1 mM CaCl₂, pH 7.4) and all non-protein samples were prepared using the dialysate buffer to minimize dilution effects. Protein concentration was determined photometrically with absorbance at 280 nm employing a calculated extinction coefficient of 70400 $\text{mol}^{-1} \text{cm}^{-1}$. In a typical experiment, a glycoconjugate sample (20 – 50 μM) was titrated into 50 μM DC-SIGN ECD. The concentration of the glycoconjugate sample was chosen to ensure sufficient protein saturation (> 80%) at the end of the experiment. A control titration was performed for experiments with large observed dilution enthalpies and experimental data was corrected by subtraction of the blank values. In general, experimental data could be used directly without correction, in which case enthalpy of dilution was included as a separate fitting parameter. Baseline correction and integration was performed with NITPIC.^[4,5]

□

S121

Sedphat was used for nonlinear regression analysis of experimental data, determination of confidence intervals, and calculation of two-dimensional error surface projections.^[5,6]

The thermograms of the ITC experiments with **1a-d** show no inflection point (Figure S5-9), indicating that the curve shape parameter defined as $c = nK_A[M]_t$ (n is the binding stoichiometry, K_A the association constant, and $[M]_t$ the total protein concentration) adopts a value equal to or below 1.^[7-9] The initial best-fit parameters suggested that this results from a low n value (multiple binding sites on the polymer), rather than from low binding affinity. For low curve shape parameters c , the fitting parameters n and ΔH° become highly correlated, usually precluding a simultaneous determination of both in a single experiment.^[8-11] To circumvent this problem, the stoichiometry parameter n is generally fixed at a value reported from other experiments (e.g. 1.0 for a 1:1 interaction). However, because for Man-PLL **1a-d** no *a priori* information on stoichiometry was available, nonlinear fitting was performed with n as a free fitting parameter and the correlation between n and ΔH° was analyzed from the two-dimensional error surface projection (2D ESP) of the χ^2 function. In Figure S5B & C the 2D ESPs for a low c titration with the monovalent low affinity ligand methyl α -D-mannoside (MeMan, Figure S5B) is compared with a low c titration with polymer **1c** (Figure S5C). The fitting parameters n and ΔH° are highly correlated for the monovalent low affinity interaction between $n = 0$ and 0.75 (Figure S5B), whereas the χ^2 function has a clearly defined minimum with narrow confidence intervals in the case of the multivalent interaction (Figure S5C). Thus, we conclude that all three parameters of interest, K_A , n , and ΔH° , can be reliably estimated from the observed low c thermograms for the interaction of DC-SIGN ECD with Man-PLL **1a-d**.

□

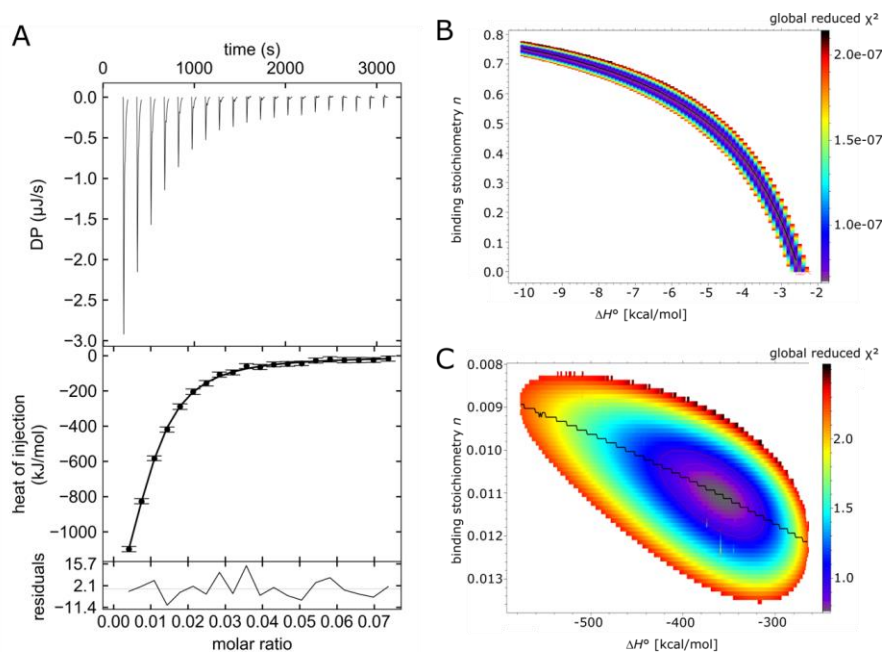


Figure S5. A) Representative thermogram from microcalorimetric experiments of Man-PLL **1a-d** and DC-SIGN ECD. B,C) Two-dimensional error surface projections exploring the correlation between n and ΔH° for methyl α -D-mannoside (B) and Man-PLL **1c** (C). Regions are colored according to the goodness of fit parameter (global reduced χ^2) and inner and outer confidence ellipses signify the correlated 68% and 95% confidence thresholds. □

It is important to note that the binding stoichiometries recorded under the applied experimental conditions represent ideal values that are not affected by positive or negative cooperativity effects resulting from high protein concentrations on the polymer under fully saturating conditions (molecular crowding). This can be shown when the equilibrium concentrations and the associated ratio of protein to polymer during a typical experiment are calculated (see below). For a titration of $50 \mu\text{M}$ **1a** into a solution of $50 \mu\text{M}$ DC-SIGN ECD in 20 injection of $1.7 \mu\text{L}$, the highest ratio of protein to polymer in the complex occurs after the first injection. In this state, 19.4 protein molecules bind to one polymer. This ratio converges to a final value of 4.6 when more polymer is added during the titration. The fitted functional valency at equilibrium is 48 and, thus, represents an extrapolation of experimental data that is not physically achieved during the experiment. Accurate values under saturating conditions could theoretically be determined in “reverse ITC” experiments, in which the cell is charged with a polymer sample and protein is titrated from the syringe. However, this

□

approach requires highly concentrated protein solutions, which are not feasible for the given system.

3.2. Calculation of Equilibrium Concentrations

Table S1 shows the equilibrium concentrations and protein to polymer ratios after each injection during a typical ITC experiment employing 20 injections of 1.7 μL of 50 μM polymer **1a** into 50 μM DC-SIGN ECD. The equilibrium concentration of bound protein was calculated from the quadratic binding model given in Equation S2, with $[NXM]$ being the equilibrium complex concentration, $[M]$ the protein concentration in the complex, $[X_i]$ the total polymer concentration after a given injection, $[M_t]$ the total protein concentration after a given injection, K_D the fitted equilibrium dissociation constant ($K_D = 1.22 \mu\text{M}$), and N the functional valency ($N = 48$). The total cell concentrations after each injection $[X_i]$ and $[M_t]$ were retrieved from the NITPIC data file. Normalization of $[XM]$, $[X_i]$, and K_D by the functional valency N gives the complex equilibrium concentration in terms of total interacting mannose residues.

$$[M] = [NXM] = \frac{([NX_t] + [M_t] + NK_D) - \sqrt{([NX_t] + [M_t] + NK_D)^2 - 4[NX_t][M_t]}}{2} \quad \text{Equation S2}$$

Table S1. Calculation of equilibrium concentrations during a typical ITC experiment

| Inj. volume [μL] | $[X_i]$ [μM] | $[NX_i]$ [μM] | $[M_i]$ [μM] | $[NXM]$ [μM] | $[M]/[X_i]$ |
|-------------------------------|---------------------------|----------------------------|---------------------------|---------------------------|-------------|
| | 0 | 0 | 50 | | |
| 0.4 | 0.10 | 4.71 | 49.90 | 2.13 | 21.7 |
| 1.7 | 0.51 | 24.62 | 49.49 | 9.97 | 19.4 |
| 1.7 | 0.92 | 44.36 | 49.08 | 16.08 | 17.4 |
| 1.7 | 1.33 | 63.94 | 48.67 | 20.77 | 15.6 |
| 1.7 | 1.74 | 83.36 | 48.26 | 24.34 | 14.0 |
| 1.7 | 2.14 | 102.62 | 47.86 | 27.07 | 12.7 |
| 1.7 | 2.54 | 121.72 | 47.46 | 29.18 | 11.5 |
| 1.7 | 2.93 | 140.67 | 47.07 | 30.81 | 10.5 |
| 1.7 | 3.32 | 159.47 | 46.68 | 32.07 | 9.7 |
| 1.7 | 3.71 | 178.11 | 46.29 | 33.07 | 8.9 |
| 1.7 | 4.10 | 196.61 | 45.90 | 33.84 | 8.3 |
| 1.7 | 4.48 | 214.96 | 45.52 | 34.45 | 7.7 |
| 1.7 | 4.86 | 233.16 | 45.14 | 34.92 | 7.2 |
| 1.7 | 5.23 | 251.22 | 44.77 | 35.29 | 6.7 |
| 1.7 | 5.61 | 269.14 | 44.39 | 35.56 | 6.3 |
| 1.7 | 5.98 | 286.91 | 44.02 | 35.76 | 6.0 |
| 1.7 | 6.34 | 304.55 | 43.66 | 35.90 | 5.7 |
| 1.7 | 6.71 | 322.05 | 43.29 | 35.99 | 5.4 |
| 1.7 | 7.07 | 339.42 | 42.93 | 36.04 | 5.1 |

2

| | | | | | |
|-----|------|--------|-------|-------|-----|
| 1.7 | 7.43 | 356.65 | 42.57 | 36.05 | 4.9 |
| 1.7 | 7.79 | 373.74 | 42.21 | 36.03 | 4.6 |

2

3.3. Thermodynamic Data

Table S2. Binding affinity and thermodynamic data for the interaction of **1a-d** with DC-SIGN ECD.

| Compound | K_D [nM] | ΔG° [kJ mol ⁻¹] | ΔH° [kJ mol ⁻¹] | $-T\Delta S^\circ$ [kJ mol ⁻¹] | n | $N = 1/n$ |
|-----------|-----------------------|---|---|---|-----------------------------|--------------------|
| MeMan | 3173 (3028 – 3325) | -14.3 (-14.1 – -14.4) | -17.4 (-17.8 – -17.0) | 3.1 (2.6 – 3.7) | 1 (fixed) | 1 |
| 1a | 1227 (1034 – 1474) | -33.7 (-33.3 – -34.2) | -812.4 (-1029.8 – -682.7) | 778.6 (648.5 – 996.6) | 0.0209 (0.0236 – 0.0175) | 48 (42 – 57) |
| 1b | 432 (406 – 460) | -36.3 (-36.2 – -36.5) | -1626.2 (-1745.5 – -1525.4) | 1589.9 (1488.9 – 1709.3) | 0.0098 (0.0103 – 0.0092) | 102 (97 – 109) |
| 1c | 352 (284 – 438) | -36.8 (-36.3 – -37.4) | -1513.9 (-1699.6 – -1366.6) | 1477.0 (1329.2 – 1663.3) | 0.0111 (0.0118 – 0.0103) | 90 (85 – 97) |
| 1d | 235 (205 – 269) | -37.8 (-37.5 – -38.2) | -1957.7 (-2108.6 – -1830.2) | 1919.9 (1792.1 – 2071.1) | 0.0085 (0.0088 – 0.0081) | 118 (114 – 123) |

Error estimates represent 68% confidence intervals from global nonlinear least squares fitting of two independent experiments.

2

Table S3. Normalized binding affinity and thermodynamic data for the interaction of **1a-d** with DC-SIGN ECD.

| Compound | $K_{D\text{ norm}}$ [nM] | $\Delta G^\circ_{\text{ norm}}$ [kJ mol ⁻¹] | $\Delta H^\circ_{\text{ norm}}$ [kJ mol ⁻¹] | $-T\Delta S^\circ_{\text{ norm}}$ [kJ mol ⁻¹] |
|-----------|-----------------------------|--|--|--|
| MeMan | 3173 (3028 – 3325) | -14.3 (-14.1 – -14.4) | -17.4 (-17.8 – -17.0) | 3.1 (2.6 – 3.7) |
| 1a | 59 (49 – 71) | -0.71 (-0.70 – -0.71) | -17.0 (-21.5 – -14.3) | 16.3 (13.6 – 20.8) |
| 1b | 44 (41 – 47) | -0.36 (-0.35 – -0.36) | -15.9 (-17.1 – -15.0) | 15.6 (14.6 – 16.8) |
| 1c | 32 (26 – 39) | -0.41 (-0.40 – -0.41) | -16.8 (-18.9 – -15.2) | 16.4 (14.8 – 18.5) |
| 1d | 28 (24 – 32) | -0.32 (-0.32 – -0.32) | -16.6 (-17.9 – -15.6) | 16.3 (15.2 – 17.6) |

Error estimates represent propagated 68% confidence intervals from global nonlinear least squares fitting of two independent experiments.

2

S16

2

3.4. Thermograms of the ITC Experiments with 1a-d and DC-SIGN ECD

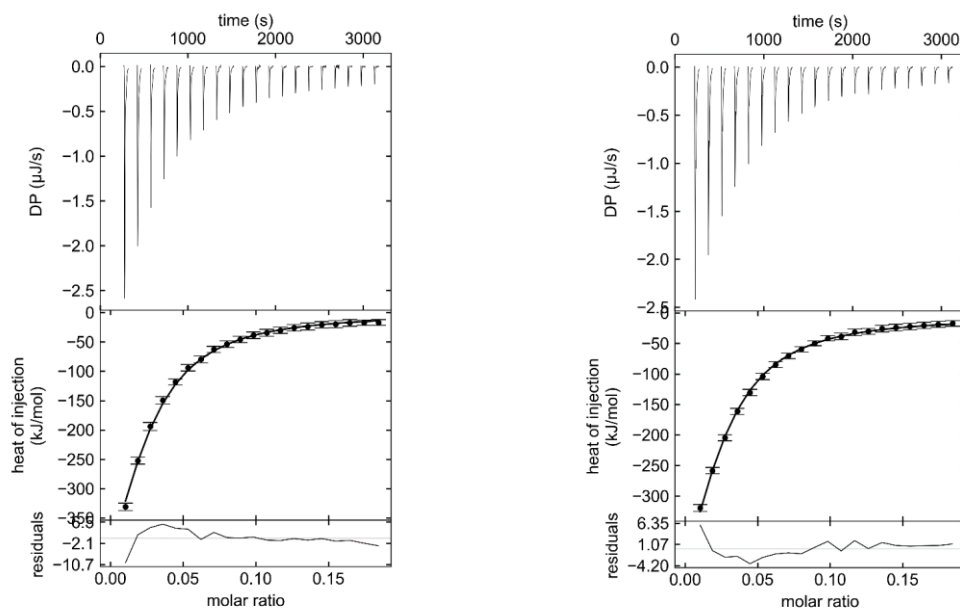


Figure S6. Thermograms and binding isotherms from two independent titrations of **1a** into DC-SIGN ECD. 2

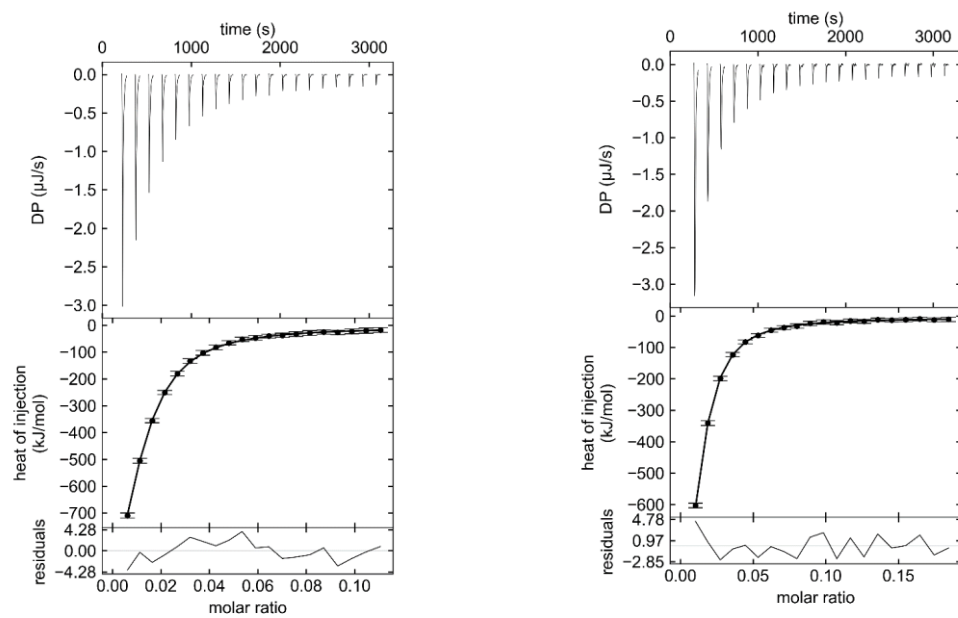


Figure S7. Thermograms and binding isotherms from two independent titrations of **1b** into DC-SIGN ECD. 2

2

S171

2

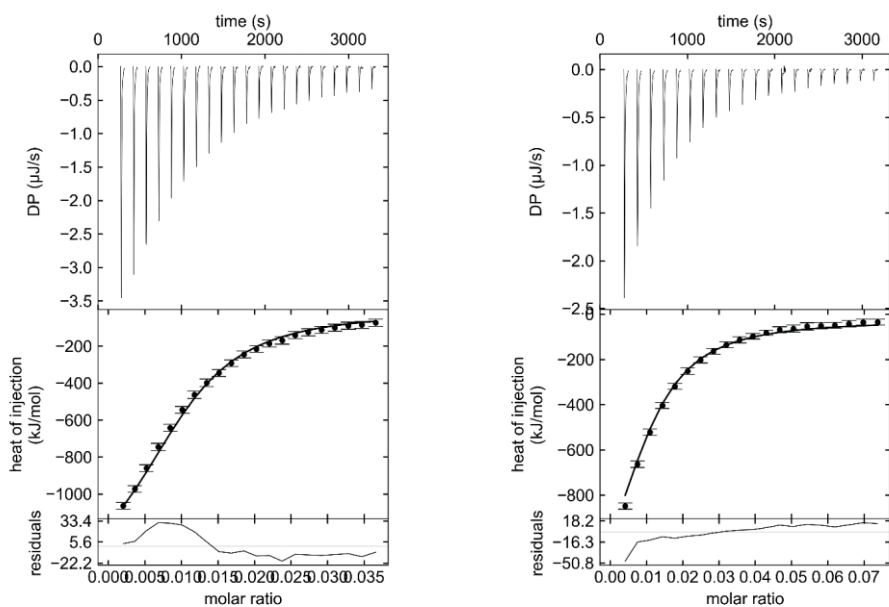


Figure S8. Thermograms and binding isotherms from two independent titrations of **1c** into DC-SIGN ECD.

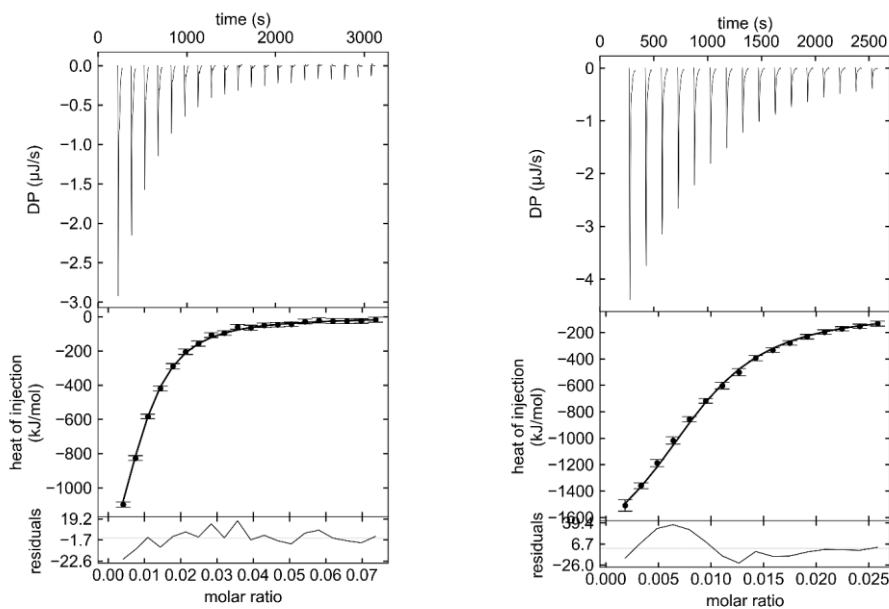


Figure S9. Thermograms and binding isotherms from two independent titrations of **1d** into DC-SIGN ECD.

2

S18

□

4 Dynamic light scattering

The size characteristics of Man-PLL **1a-d** were analyzed by DLS with a Malvern Zetasizer Nano instrument (Malvern Panalytical, Malvern, UK). Samples containing 10 μM **1a** (0.38 mg mL^{-1}) or 2 μM **1b-d** (0.02-0.34 mg mL^{-1}) were allowed to equilibrate at 20 °C for two minutes prior to the experiments. Experiments were performed in triplicate and experimental data were analyzed with the manufacturer supplied software to obtain hydrodynamic radii (Z-average), polydispersity indices, and size distribution data.

□

5 Analytical Ultracentrifugation

Sedimentation velocity experiments were performed for 410 μl samples at concentrations of 0.8 mg mL^{-1} (22 μM) for Man-PLL **1a**, 0.2 mg mL^{-1} (2 μM) for Man-PLL **1b**, 1.3 mg mL^{-1} (9 μM) for Man-PLL **1c**, and 0.2 mg mL^{-1} (1 μM) for Man-PLL **1d** at 20 °C in 20 mM HEPES, 150 mM NaCl, 1 mM CaCl_2 , pH 7.4. Centrifugation was performed at 42,000 rpm (128,000 \times g) using a Beckman XL-I Analytical Ultracentrifuge with an An-60 Ti rotor, and sedimentation was monitored using the interference optics with 12 mm double-sector charcoal-epon centerpieces. The data were analysed by fitting diffusion-deconvoluted differential sedimentation coefficient distributions (c(s) distributions) using the program SEDFIT,^[12] best-fit values of the frictional ratio (f/f_0), meniscus and bottom positions, and time- and radially-invariant noise profiles were determined for each data set. Values of buffer density and viscosity were obtained from Sednterp.^[13] Values of partial specific volume were calculated for individual components of Man-PLLs **1a-d**, namely lysine conjugated to mannose (0.797 ml g^{-1}) and for lysine conjugated to thioglycerol (0.772 ml g^{-1}) using the method of Durchschlag and Zipper.^[14] Partial specific volumes were then calculated for different polymers according to estimated mass fraction of mannose or thioglycerol conjugated lysine in the polymer (0.787 ml g^{-1} for Man-PLL **1a**, 0.787 ml g^{-1} for Man-PLL **1b**, 0.786 ml g^{-1} for Man-PLL **1c**, and 0.790 ml g^{-1} for Man-PLL **1d**). Signal-weighted average S values were calculated from c(s) distributions using the program GUSSE.^[15] Values of D_h were calculated from diffusion coefficients, which in turn were calculated from signal-weighted average S values and f/f_0 according to a standard scaling law.^[16]

□

S19

2

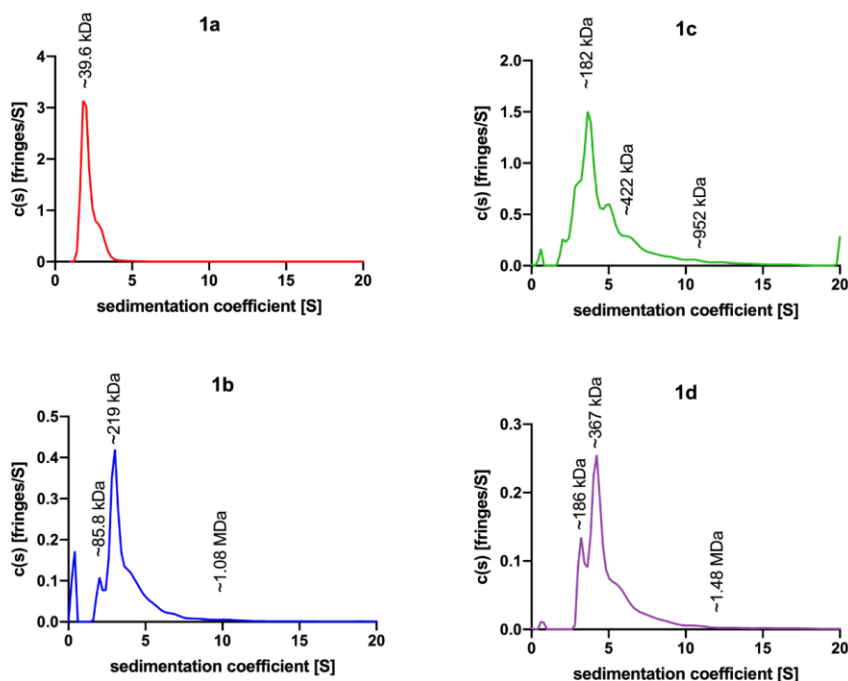


Figure S10. Plots of diffusion-deconvoluted differential sedimentation coefficient distributions ($c(s)$ distributions) with molecular mass estimates calculated using the fitted f/f_0 values for Man-PLL **1a-d**.

2

6 Mammalian cell culture, flow cytometry, and fluorescence microscopy

The following reagents were obtained through the NIH AIDS Reagent Program, Division of AIDS, NIAID, NIH: B-THP-1 DC-SIGN+ cells from Drs. Li Wu and Vineet N. KewalRamani (cat# 9941),^[17] HIV-1 JR-CSF Fc-gp120 Recombinant Protein (Cat#11556) from Aymeric de Parseval and Dr. John H. Elder.^[18] Recombinant ebola glycoprotein was obtained from R&D Systems (cat# 9016-EB-100), recombinant SARS-CoV-2 spike glycoprotein S1 subunit was purchased from Creative Biomart (cat# Spike-191V).

Cells were maintained in RPMI 1640 medium substituted with 10 % FCS at 37 °C. For IC50 measurements, 50000 cells were seeded in 50 μ L complete medium in a well of a 96-well plate. A serial dilution of the investigated ligand was prepared and mixed with an equal volume of Cy5-labeled glycoprotein. This mixture was added to the cell suspension to a final volume of 100 μ L and a final glycoprotein concentration of 10 nM (gp120), 10 nM (SARS-CoV-2 spike S1), or 50 nM (EBOV-gp). After incubation for 30 min (37°C, 5 % CO₂), the cells were centrifuged (5 min, 100g) and washed with warm PBS. Data were collected on a Cytotflex flow cytometer (Beckman Coulter, Indianapolis, USA) and analyzed with FlowJo

2

S20

2

(FlowJo LLC). Mean fluorescence intensities were plotted and a nonlinear regression analysis employing a four parameter Hill model was performed with Prism 8 (Graphpad, San Diego, USA). For receptor blocking analysis, 50000 B-THP-1 DC-SIGN⁺ cells were seeded and incubated with 100 nM **1d** for 0 min to 6h, before washing and incubation with Cy5-labeled recombinant SARS-CoV-2 spike glycoprotein S1 subunit according to the protocol of the IC₅₀ measurements. Additionally, B-THP-1 DC-SIGN⁺ cells were incubated with 100 nM **1d** for 30 min, washed, and incubated with Cy5-labeled recombinant SARS-CoV-2 spike glycoprotein S1 subunit after 0 min, 10 min, 30 min, 1h, 3h, and 6h. Internalization experiments were performed with B-THP-1 DC-SIGN⁺ cells and control B-THP-1 cells. 50000 cells were incubated with 100 nM **10** and 100 nM **11** for 30 min, 1h, 3h, 6h, and 24h, washed with PBS, and analyzed by flow cytometry. For microscopic analysis cells were additionally incubated with 5 µg/ml CellMask Deep Red Plasma membrane stain (C10046, Invitrogen, Thermo Fisher Scientific, Switzerland) for 10 min. Images were recorded with the Leica SP8 confocal point scanning microscope using a HC PL Apo CS 40x (NA 1.1) objective (Leica Microsystems, Germany). Comparisons between the conditions were performed using one-way ANOVA with Dunnett's multiple comparison posttest with a 0.05 confidence level accepted for statistical significance (*P ≤ 0.05, **P ≤ 0.01, ***P ≤ 0.001, ****P ≤ 0.0001).

7 References

- [1] C. Moylan, A. M. K. Sweed, Y. M. Shaker, E. M. Scanlan, M. O. Senge, *Tetrahedron* **2015**, *71*, 4145–4153.
- [2] W. Hayes, H. M. . Osborn, S. D. Osborne, R. A. Rastall, B. Romagnoli, *Tetrahedron* **2003**, *59*, 7983–7996.
- [3] G. Thoma, J. T. Patton, J. L. Magnani, B. Ernst, R. Öhrlein, R. O. Duthaler, *J. Am. Chem. Soc.* **1999**, *121*, 5919–5929.
- [4] T. H. Scheuermann, C. A. Brautigam, *Methods* **2015**, *76*, 87–98.
- [5] C. A. Brautigam, H. Zhao, C. Vargas, S. Keller, P. Schuck, *Nat. Protoc.* **2016**, *11*, 882–894.
- [6] G. Piszczek, *Methods* **2015**, *76*, 137–148.
- [7] T. Wiseman, S. Williston, J. F. Brandts, L.-N. Lin, *Anal. Biochem.* **1989**, *179*, 131–137.
- [8] W. B. Turnbull, A. H. Daranas, *J. Am. Chem. Soc.* **2003**, *125*, 14859–66.
- [9] J. Tellinghuisen, *Anal. Biochem.* **2008**, *373*, 395–7.
- [10] J. Tellinghuisen, *J. Phys. Chem. B* **2007**, *111*, 11531–7.

2

S211

2

- [11] J. Tellinghuisen, *Anal. Biochem.* **2012**, *424*, 211–220.
- [12] P. Schuck, *Biophys. J.* **2000**, *78*, 1606–1619.
- [13] T. M. Laue, B. D. Shah, T. M. Ridgeway, S. L. Pelletier, *Computer- Aided Interpretation of Analytical Sedimentation Data for Proteins*, The Royal Society Of Chemistry, Cambridge, United Kingdom, **1992**.
- [14] H. Durchschlag, P. Zipper, in *Prog. Colloid Polym. Sci.*, Springer-Verlag GmbH & Company KG, **1994**, pp. 20–39.
- [15] C. A. Brautigam, *Methods Enzymol.* **2015**, *562*, 109–133.
- [16] P. H. Brown, A. Balbo, P. Schuck, *Curr. Protoc. Immunol.* **2008**, *81*, Unit 18.15.
- [17] L. Wu, T. D. Martin, M. Carrington, V. N. KewalRamani, *Virology* **2004**, *318*, 17–23.
- [18] J. M. Binley, S. Ngo-Abdalla, P. Moore, M. Bobardt, U. Chatterji, P. Gallay, D. R. Burton, I. A. Wilson, J. H. Elder, A. de Parseval, *Retrovirology* **2006**, *3*, 39.

2

S221

Chapter 6

Sweet Drugs for Bad Bugs: A Glycomimetic Strategy Against the DC-SIGN-mediated Dissemination of SARS-CoV-2

Jonathan Cramer^{1,5}, Adem Lakkaichi¹, Butrint Aliu¹, Roman P. Jakob², Sebastian Klein², Ivan Cattaneo¹, Xiaohua Jiang¹, Said Rabbani¹, Oliver Schwardt¹, Gert Zimmer³, Matias Ciancaglini⁴,
Tiago Abreu-Mota⁴, Timm Maier², Beat Ernst¹

¹Institute of Molecular Pharmacy, Pharmacenter, University of Basel,
4056 Basel, Switzerland

²Focal Area Structural Biology, Biozentrum, University of Basel, 4056 Basel, Switzerland

³Institute of Virology and Immunology, 3147 Mittelhäusern, Switzerland

⁴Department Biomedicine, University of Basel, 4051 Basel, Switzerland

⁵Institute for Pharmaceutical and Medicinal Chemistry, Heinrich-Heine-University of Düsseldorf,
40225 Düsseldorf, Germany

Corresponding author:

Beat Ernst, +41 61 207 15 51, beat.ernst@unibas.ch

Contributions of Butrint Aliu

- Support in manuscript preparation and revision
- Cellular inhibition experiments
- Data analysis and interpretation

Sweet Drugs for Bad Bugs: A Glycomimetic Strategy Against the DC-SIGN-mediated Dissemination of SARS-CoV-2

Jonathan Cramer,^{1,5)} Adem Lakkaichi,¹⁾ Butrint Aliu,¹⁾ Roman P. Jakob,²⁾ Sebastian Klein,¹⁾ Ivan Cattaneo,¹⁾ Xiaohua Jiang,¹⁾ Said Rabbani,¹⁾ Oliver Schwardt,¹⁾ Gert Zimmer,³⁾ Matias Ciancaglini,⁴⁾ Tiago Abreu-Mota,⁴⁾ Timm Maier,²⁾ Beat Ernst^{1)*}

¹⁾ University of Basel, Institute of Molecular Pharmacy, Pharmacenter of the University of Basel, Klingelbergstrasse 50, 4056 Basel, Switzerland

²⁾ University of Basel, Department Biozentrum, Focal Area Structural Biology, Klingelbergstr. 70, 4056 Basel, Switzerland

³⁾ Institute of Virology and Immunology, Sensemattstr. 293, 3147 Mittelhäusern, Switzerland

⁴⁾ University of Basel, Department Biomedicine, Petersplatz 8, 40521 Basel, Switzerland

⁵⁾ Heinrich-Heine-University of Düsseldorf, Institute for Pharmaceutical and Medicinal Chemistry, Universitätsstraße 1, 40225 Düsseldorf, Germany

KEYWORDS *C-type lectin receptors, dendritic cells, SARS-CoV-2, glycomimetic, trans-infection.*

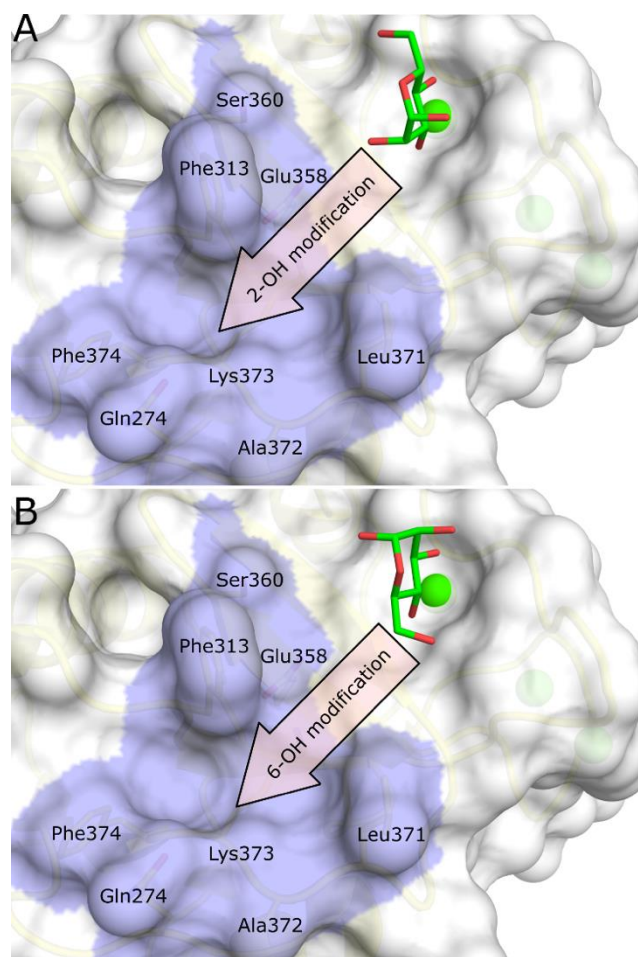
ABSTRACT: The C-type lectin receptor DC-SIGN is a pattern recognition receptor expressed on macrophages and dendritic cells. It has been identified as a promiscuous entry receptor for many pathogens, including epidemic and pandemic viruses such as SARS-CoV-2, Ebola virus, and HIV-1. In the context of the recent SARS-CoV-2 pandemic, DC-SIGN-mediated virus dissemination and stimulation of innate immune responses has been implicated as a potential factor in the development of severe COVID-19. Inhibition of virus binding to DC-SIGN, thus, represents an attractive host-directed strategy to attenuate the progression of the disease and prevent overshooting innate immune responses. In this study, we report on the discovery of a new class of potent glycomimetic DC-SIGN antagonists from a focused library of triazole-based mannose analogs. Structure-based optimization of an initial screening hit yielded a glycomimetic ligand with a more than 100-fold improved binding affinity compared to methyl α -D-mannopyranoside. Analysis of binding thermodynamics revealed an enthalpy-driven improvement of binding affinity that was enabled by hydrophobic interactions with a loop region adjacent to the binding site and displacement of a conserved water molecule. The identified ligand was employed for the synthesis of multivalent glycopolymers that were able to inhibit SARS-CoV-2 spike glycoprotein binding to DC-SIGN expressing cells, as well as DC-SIGN-mediated *trans*-infection of ACE2⁺ cells by SARS-CoV-2 spike protein-expressing viruses, in nanomolar concentrations. The identified glycomimetic ligands reported here open promising perspectives for the development of highly potent and fully selective DC-SIGN-targeted therapeutics for a broad spectrum of viral infections.

Introduction

Viral envelope glycoproteins are crucial to initiate the viral replication cycle by promoting the viral particle attachment to its cognate receptor in the target cell in a highly specific manner. Upon production, viral glycoproteins are decorated with host-derived carbohydrates, which can promote immune evasion, structural integrity, and even attachment to lectins on the surface of host cells.^{1,2} One of these lectins, the C-type lectin receptor (CLR) DC-SIGN (dendritic cell-specific intercellular adhesion molecule 3 grabbing non-integrin) can serve as an alternative unspecific entry receptor to the glycoprotein's

cognate receptor for the infection of innate immune cells by numerous, phylogenetically diverse viral pathogens.¹⁻⁴ DC-SIGN-mediated uptake of viral particles enables the infection of DC-SIGN⁺ dendritic cells (*cis* infection) or other cells after migration of infected myeloid cells to lymphatic tissue (*trans* infection). Besides its established role in the infection with HIV-1,⁵ Dengue virus,⁶ Zika virus,⁷ Ebola virus,^{8,9} SARS-CoV,¹⁰ and various other pathogens,¹ DC-SIGN-mediated infection and virus dissemination has received special attention in the context of the ongoing SARS-CoV-2 pandemic. The SARS-CoV-2 spike envelope glycoprotein is heavily glycosylated with high-mannose and

complex-type N-glycans that can serve as potential ligands for DC-SIGN.¹¹ The interaction of viral glycoproteins with DC-SIGN, its closely related analog DC-SIGNR, the macrophage mannose receptor (MR, CD206), and macrophage galactose-type lectin (MGL, CD301), represents an ACE2-independent route for a potential infection of innate immune cells.¹²⁻¹⁵ The correlation of the infection of innate immune cells with an excessive immune response observed in severe COVID-19 patients gave rise to speculation on the importance of DC-SIGN/R in the context of the disease.¹⁶ This hypothesis is supported by the increased DC-SIGN expression levels in patients with severe COVID-19.¹² Similarly, genetic variants in the *ABO* gene locus representing a risk factor for the development of a severe form of the disease were found to correlate with DC-SIGN expression levels.¹⁷ Just recently, Thépaut *et al.* demonstrated the ability of DC-SIGN⁺ cells for *trans*-infection of susceptible ACE2⁺ bystander cells, thereby clearly demonstrating the involvement of infected myeloid cells in virus dissemination.¹⁸ In their study, however, *cis* infection of monocyte-derived dendritic cells by SARS-CoV-2 pseudovirions could not be shown, indicating that DC-SIGN recognition by itself is insufficient to initiate viral



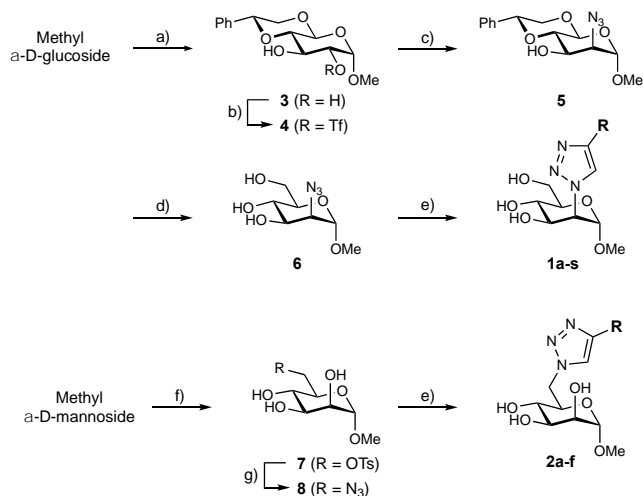
replication. These observations were recently confirmed in primary myeloid cells expressing DC-SIGN that were exposed to authentic SARS-CoV-2 viruses.¹⁹ Moreover, this study draws a strong connection between CLR engagement and hyperinflammation in

Figure 1. Mannose binding modes observed in X-ray structures of DC-SIGN CRD (PDB 2IT6). A) *Major binding mode* where 2-OH is oriented towards the shallow groove; B) *Minor binding mode* where 6-OH is oriented towards the shallow groove.

severe COVID-19. Considering the increasing evidence for an involvement of the innate immune system in COVID-19,²⁰ competitive inhibition of virus binding to DC-SIGN with glycomimetics represents a promising strategy for the development of broad-spectrum antiviral therapeutics. This host-directed approach might be highly resistant to viral mutations that can potentially bypass the immune response.

Glycomimetics are generally derived from natural carbohydrate ligands of lectins. The ligand design can either be based on a complex oligosaccharide, where all non-interacting moieties are removed (“top-down” approach), or on a minimal monosaccharide epitope, which is expanded to establish relevant secondary interactions with the binding site (“bottom-up” approach).²¹ Although the shallow and solvent-exposed binding site of DC-SIGN does not offer obvious possibilities for interaction outside the carbohydrate recognition domain (CRD), successful “bottom-up” approaches have been reported, yielding glycomimetic DC-SIGN ligands with affinity in the μM range.²²⁻²⁷ Furthermore, Aretz *et al.* recently identified a shallow groove near the carbohydrate binding site of DC-SIGN (Figure 1).²⁸ It is partly hydrophobic in nature and offers van der Waals interactions with Phe313, Leu371, Phe374 or the aliphatic side chain of Lys373, as well as polar interactions with Gln274, Ser360, or backbone amides. The authors hypothesized that linking small molecule fragments binding to this second site with the carbohydrate core could generate potent glycomimetic ligands.

Based on this information, we designed a novel family of DC-SIGN ligands. DC-SIGN binds mannose- and fucose-containing saccharides in a Ca^{2+} -dependent manner through complexation with its 3- and 4-hydroxyl groups.^{29,30} For mannose, two different orientations are possible. In the *major binding mode* (Figure 1A), the axial 2-OH points towards the adjacent shallow groove. Rotating the mannose core by 180° leads to the *minor binding mode* (Figure 1B). Now the 6-OH points towards shallow groove.³⁰ In addition, the rational design of **Scheme 1**:

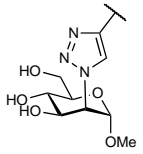
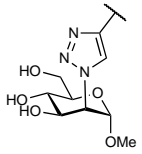
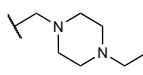
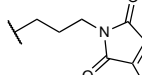
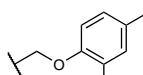
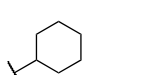
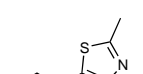
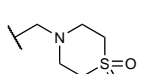
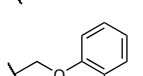
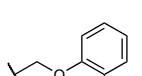
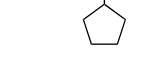
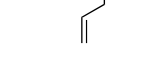
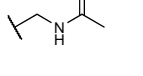
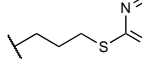
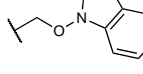
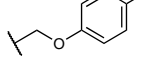
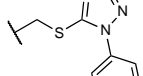
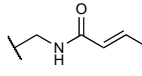
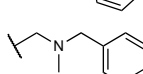
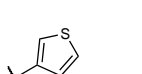
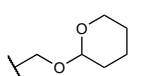


a) $\text{PhCH}(\text{OMe})_2$, CSA, DMF (81%); b) Tf_2O , pyr. DCM; c) NaN_3 ,

DMF (43% over 2 steps); d) Er(CF₃SO₃)₃, CH₃CN/H₂O (quant); e) R=, for details see Table 1 and 2, CuBr, tris[(1-benzyl-1H-

1,2,3-triazol-4-yl)methyl]amine, CH₃CN; f) TsCl, pyr. (85%); g) NaN₃, DMF (73%).

Table 1. 19 compounds from library 1 comprising of the triazoles 1a-s generated from methyl 2-azido-2-deoxy- α -D-mannopyranoside (6) and biophysical screening results.

| Compound |  | ΔT_m [°C] | ITC K_d [μ M] | Compound |  | ΔT_m [°C] | ITC K_d [μ M] |
|-----------|---|-------------------|----------------------|-----------|--|-------------------|----------------------|
| 1a |  | N/A ^a | > 1000 | 1k |  | 0.94 | |
| 1b |  | -0.40 | | 1l |  | 1.00 | 777 |
| 1c |  | 0.20 | | 1m |  | 1.07 | > 1000 |
| 1d |  | 0.47 | | 1n |  | 1.21 | 465 |
| 1e |  | 0.58 | | 1o |  | 1.24 | 250 |
| 1f |  | 0.59 | | 1p |  | 1.32 | 306 |
| 1g |  | 0.69 | | 1q |  | 1.41 | 348 |
| 1h |  | 0.73 | | 1r |  | 1.61 | 254 |
| 1i |  | 0.78 | | 1s |  | 2.51 | 160 |
| 1j |  | 0.86 | | | | | |

^a no nanoDSF data available for **1a** because of compound self-fluorescence at relevant wavelengths. Its affinity was directly determined in ITC experiments.

glycomimetic DC-SIGN ligands is further complicated because Ca²⁺-complexation via 2-OH and 3-OH has been observed in NMR experiments and MD simulations.³¹

To distinguish the two binding modes, hydrophobic extensions in the 2- and the 6-position of mannose were explored. When the aglycone was simultaneously modified, DC-SIGN antagonists with low micromolar affinity were obtained. Finally, when multivalently presented on a poly-l-lysine core, the interaction of SARS-CoV-2 spike glycoprotein with DC-SIGN expressing cells, as well as DC-

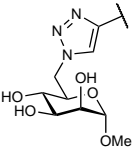
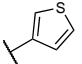
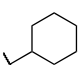
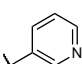
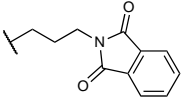
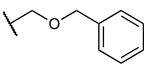
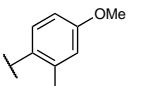
SIGN-mediated *trans*-infection of susceptible Vero E6 cells by vesicular stomatitis viruses (VSV) expressing the SARS-CoV-2 spike protein, could be inhibited at nanomolar concentrations.

Results and Discussion

Initial docking studies and library syntheses. The two virtual triazole libraries comprising of 100 methyl 2-triazoyl-2-deoxy- α -D-mannopyranosides of the general structure **1** (library 1) and 100 methyl 6-triazoyl-6-deoxy-

α -D-mannopyranosides of the general structure **2** (library 2) were generated *in silico* from the azide building blocks **6** and **8**, respectively and 100 in-house or commercially terminal acetylenes. Libraries 1 and 2 were subsequently docked into the primary carbohydrate binding site of DC-

Table 2. Six compounds from library 2 comprising of triazoles generated from methyl 6-azido-6-deoxy- α -D-mannopyranoside (8**) and biophysical screening results.**

| Compound |  | ΔT_m [°C] | ITC K_d [μ M] |
|-----------|---|-------------------|----------------------|
| 2a |  | 0.18 | |
| 2b |  | 0.19 | |
| 2c |  | 0.30 | |
| 2d |  | 0.34 | |
| 2e |  | 0.34 | |
| 2f |  | 1.84 | > 1000 |

SIGN using Glide.³² Based on a visual inspection of the binding poses, 19 triazoles from library 1 and 6 from library 2 were selected for synthesis (Tables 1 and 2).

Starting from methyl α -D-glucopyranoside and methyl β -D-mannopyranoside, azide **6** and **8**, respectively, were synthesized following previously reported procedures (Scheme 1). By copper-catalyzed azide-alkyne cycloaddition (CuAAC)³³ the 1,4-triazoles **1a-s** and **2a-f** were obtained.

Primary screening and evaluation of hits. In its native state, DC-SIGN is a membrane bound surface receptor consisting of 404 amino acids that tends to form tetramers. Oligomerization is controlled by a hydrophobic neck domain consisting of seven tandem repeats. The extracellular C-terminal CRD contains a carbohydrate binding site with the typical C-type lectin-like fold. As a minimal recombinant construct, the truncated monomeric CRD (residues 250–404) of DC-SIGN was recombinantly expressed in *E.coli* and employed to determine binding affinity for DC-SIGN by nanoDSF. In this assay, the melting temperature (T_m) of DC-SIGN CRD in the presence of the ligand (1 mM) was determined by monitoring intrinsic tryptophan fluorescence upon heating of the sample. Differences of the melting temperature (ΔT_m) in the presence and absence of a ligand of ≥ 1.0 °C was defined as cut-off for hits. By this definition, screening of the 25

selected triazoles **1a-s** and **2a-f** with the nanoDSF assay yielded 9 hits (Table 1 & 2, $\Delta T_m \geq 1.0$ °C in bold).

In isothermal titration calorimetry (ITC) measurements applied to further validate the nine hits, triazoles **1m**, and **2f** turned out to be inactive ($K_D > 1$ mM). For the remaining compounds, K_D s in the range between 777 to 160 μ M were obtained, representing a 4- to 21-fold improvement of affinity compared to methyl α -D-mannopyranoside ($K_D = 3.3$ mM, see Table S1). Interestingly, only ligands with triazole extensions in the 2-position of the mannose core and none modified in the 6-position were active.

Docking pose and crystal structure of initial hit 1s. In the docking pose of the most potent triazole **1s** (Figure 2A), the aromatic substituent points into the adjacent subsite (*major binding mode*, see Figure 1A) and establishes a hydrophobic interaction with Phe313, whereas the hydroxyls in the 3- and 4-position complex the calcium ion. Surprisingly, the X-ray structure of **1s** co-crystallized with the CRD of DC-SIGN (Figure 2B and 2C) revealed an inverse binding mode, in which the anomeric position is now pointing towards Phe313 and the axial pyridyl triazolyl substituent is oriented towards the so-called long loop (Trp343–Cys356), establishing a hydrophobic contact with Val351. This interaction has been previously shown to play an important role for the binding of blood group antigens³⁴ and dimannoside glycomimetics to DC-SIGN.^{24,25,35}

Lead optimization. To further enhance potency of **1s**, we first modified the pyridyl moiety, which could be easily realized by CuAAC chemistry (Figure 3).³³ A shift of the nitrogen to the *ortho* position (\rightarrow **10**) or conversion to a phenyl ring (\rightarrow **11**) had only minor effects, probably resulting from similar interactions and only slightly different solvation properties of the aromatic moieties.

Starting from **11**, substitution patterns of the aromatic ring were explored. Whereas *ortho*-substituents resulted in moderate to severe loss of affinity (\rightarrow **12-14**), an additional annelated phenyl ring gave minimally increased binding affinity via interaction with Val351 (\rightarrow **15**). Since all modifications only negligibly affected binding affinity, the *para*-position of the phenyl group was selected as linking position for multivalent DC-SIGN ligands (see below). Next, we focused on optimizing the aglycone. Glu358 was identified as a potential partner for a charge assisted hydrogen bond interaction. In the co-crystal structure with **1s**, the targeted position is occupied by a water molecule (Figure 2C), which offers the possibility for its replacement by an accordingly substituted aglycone. A similar approach was first described by Medve *et al.* and successfully yielded potent DC-SIGN glycomimetics based on a dimannoside analog.²⁴

Docking studies suggested that aglycones consisting of a three-carbon linker with a terminal hydrogen bond donor could reach Glu358, whereas heterocyclic moieties could potentially engage in additional hydrophobic interactions with Phe313. With this pharmacophore model the compounds displayed in Scheme 2 were identified. After initial glycosylation attempts using various glycosyl donors and promoters gave only insufficient yields, glycosylation was finally successful with the iodine promoted glycosylation reported by Ravindranathan *et al.*³⁶ Thus,

from methyl 2-azido-4,6-*O*-benzylidene-2-deoxy- α -d-mannopyranoside (**5**), the corresponding glycosyl bromide

16 was prepared by acid-promoted cleavage of the methyl glycoside and

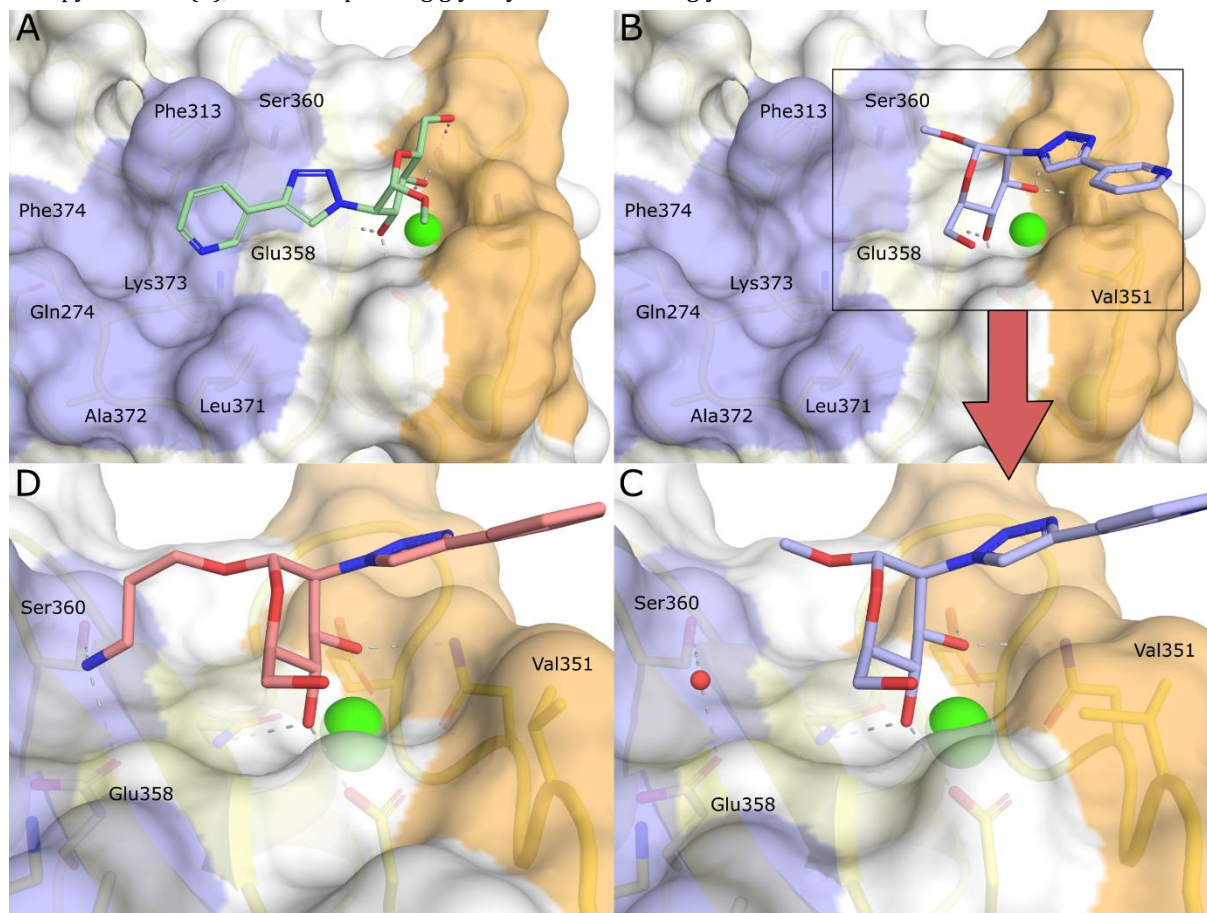


Figure 2. Binding modes of glycomimetic ligands. Amino acids in the initially targeted secondary binding site are colored in blue, the long loop is colored in orange. **A)** In the docked pose of **1s**, the pyridyl substituent is aligned with the shallow groove in blue and interacts with Phe313. **B)** In the X-ray crystal structure (PDB 7NL6), **1s** adopts an orientation rotated by 180°, which allows the pyridyl substituent to interact with Val351 in the long loop. **C)** Close-up view of the carbohydrate binding site. A water molecule engages in a charge-assisted hydrogen bond with Glu358 and Ser360 of the shallow groove in the vicinity of the aglycone of **1s**. **D)** X-ray crystal structure of **9** in complex with DC-SIGN CRD (PDB 7NL7). The aminopropyl aglycone of **9** assumes the position previously occupied by a water molecule.

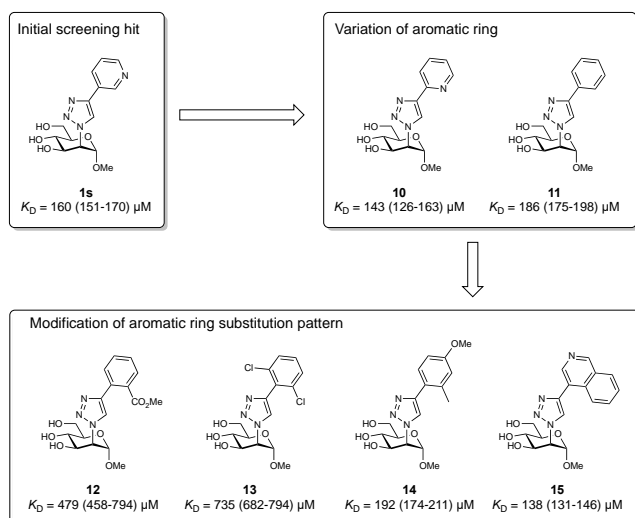


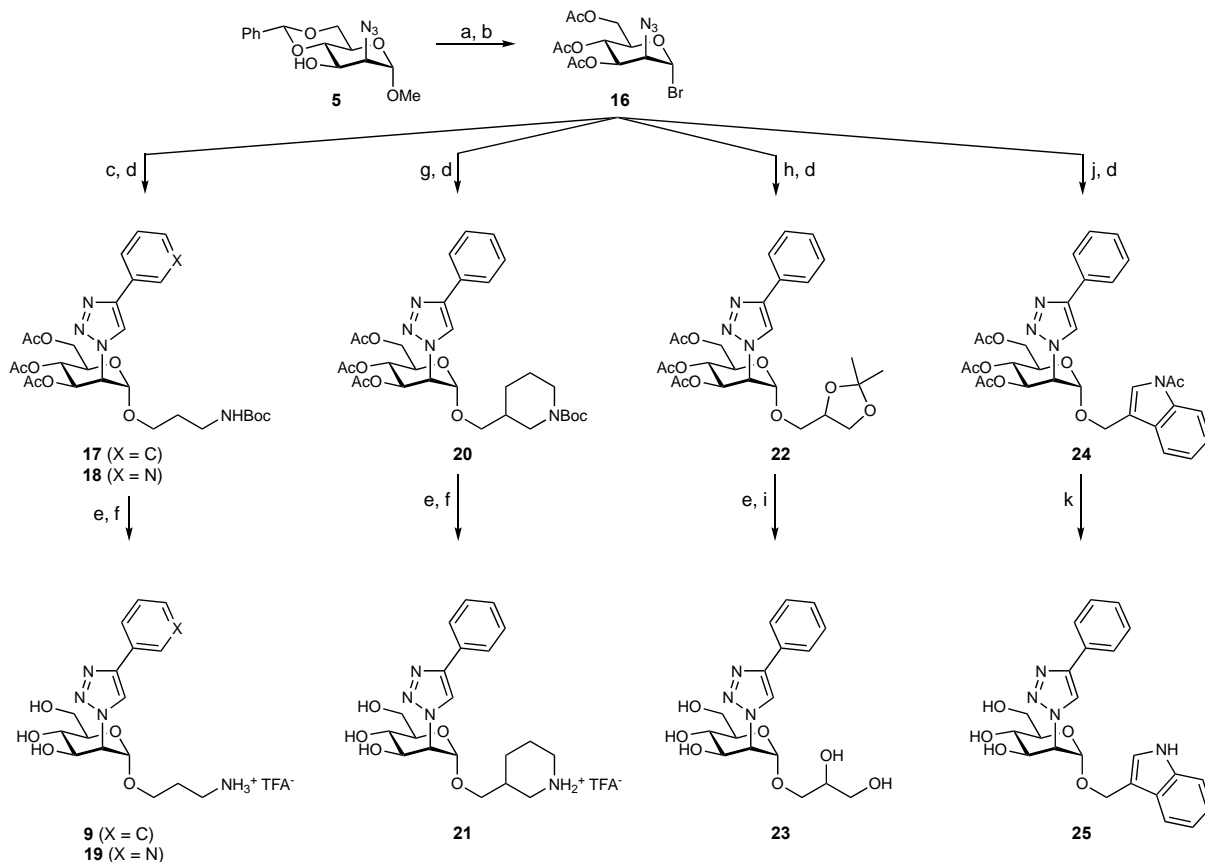
Figure 3. Exploration of modifications of the pyridyl ring on **1s**

peracetylation, followed by glycosyl bromide formation with trimethylsilyl bromide and BiBr_3 .³⁷ Iodine-promoted glycosylation in the presence of K_2CO_3 finally gave the mannosides **17**, **18**, **20**, **22**, and **24**, which after deprotection yielded the mannosides **9**, **19**, **21**, **23**, and **25**.

Thermodynamic evaluation of leads. Earlier thermodynamic analyses of glycopolymer-lectin binding revealed a close connection between the binding enthalpy of a monovalent carbohydrate epitope and the binding enthalpy of a respective multivalent form of the epitope.^{38,39} Accordingly, multivalent enthalpy is given as the product of the monovalent enthalpy and the number of interacting epitopes (functional valency). Whereas a decomposition of entropic components is hardly achievable in multivalent systems, the optimization of monovalent binding enthalpies represents a more manageable task and opens avenues for the rational optimization of multivalent glycopolymers. Thus, ligand optimization was closely followed by an evaluation of binding thermodynamics. Table 3 summarizes affinities and the thermodynamic profiles for the parent

compound **11** and mannosides **9**, **19**, **21**, **23**, and **25** interacting with DC-SIGN CRD. For the positively charged

compounds **9**, **19** and **21**, we observed the expected increase in binding



Scheme 2. a) Sulfuric acid, Ac₂O; b) BiBr₃, TMSBr, DCM; c) 3-(Boc-amino)-1-propanol, I₂, K₂CO₃, CH₃CN; d) for X = C: phenylacetylene, TBTA, CuBr, CH₃CN; for X = N: 3-ethynylpyridine, TBTA, CuBr, CH₃CN; e) NaOMe, MeOH; f) TFA, DCM; g) rac-1-Boc-3-(hydroxymethyl)piperidine, I₂, K₂CO₃, CH₃CN; h) rac-isopropylidenglycerol, Ag₂CO₃, I₂, DCM; i) 60% AcOH, H₂O; j) 1-(3-(hydroxymethyl)indol-1-yl)ethanone, TBTA, CuBr, CH₃CN; k) KOH, MeOH.

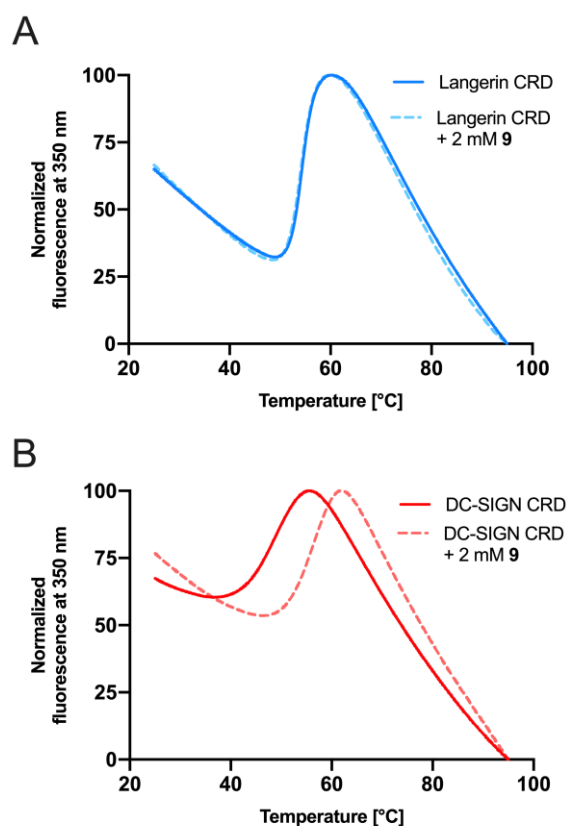
Table 3. Binding affinity and thermodynamic data for glycomimetic compounds.

| Compound | Structure | K_D [μ M] | ΔG° [kJ mol ⁻¹] | ΔH° [kJ mol ⁻¹] | $-T\Delta S^\circ$ [kJ mol ⁻¹] |
|--------------|-----------|-----------------------|--|--|--|
| MeMan | | 3314 (3107 – 3541) | -14.2 (-14.3 – -14.0) | -22.9 (-24.4 – -21.6) | 8.8 (7.3 – 10.4) |
| 11 | | 186 (175 – 198) | -21.3 (-21.4 – -21.1) | -28.3 (-28.9 – -27.3) | 7.0 (5.9 – 7.7) |
| 9 | | 32 (30 – 34) | -25.7 (-25.8 – -25.5) | -31.6 (-32.4 – -30.9) | 6.0 (5.1 – 6.9) |

| | | | | | |
|----|--|--------------------|--------------------------|--------------------------|-----------------------|
| 19 | | 29 (27 – 32) | -25.9 (-26.1 – -25.6) | -26.9 (-28.1 – -25.8) | 1.1 (-0.3 – 2.5) |
| 21 | | 42 (40 – 45) | -25.0 (-25.1 – -24.8) | -20.2 (-20.7 – -19.7) | -4.8 (-5.5 – -4.1) |
| 23 | | 134 (123 – 144) | -22.1 (-22.3 – -21.9) | -27.0 (-28.4 – -25.8) | 4.9 (3.5 – 6.4) |
| 25 | | 331 (294 – 375) | -19.9 (-20.2 – -19.6) | -27.0 (-30.8 – -19.6) | 7.2 (-0.6 – 11.3) |

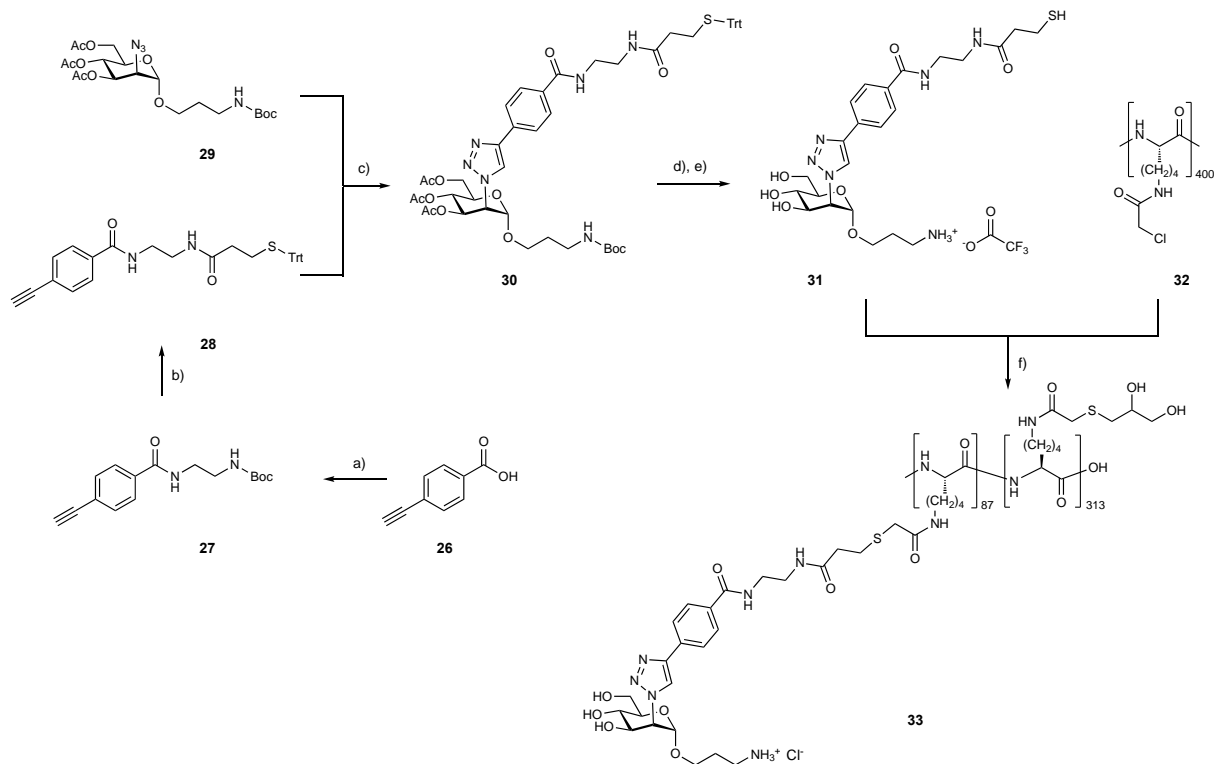
affinity with K_D values in the range of 30 to 40 μM . In contrast, the uncharged hydrogen bond donors in **23** and **25** do not increase the potency compared to parent compound **11**. From the similar enthalpy contributions of **11** and **23** ($\Delta\Delta H^\circ_{11 \rightarrow 23} = 1.3 \text{ kJ mol}^{-1}$), it can be assumed that the desolvation penalty for the polar glycerol chain of **23** cancels out the beneficial hydrogen bond interaction with Glu358. Finally, with the bulky indole moiety (\rightarrow **25**), the binding affinity was significantly reduced, probably due to steric conflict with Phe313.

The X-ray crystal structure of the complex of **9** with DC-SIGN (Figure 2D) confirmed the replacement of the structurally conserved water molecule by the positively charged ammonium group of **9**, thereby enabling a salt bridge with Glu358 and an additional hydrogen bond with Ser360. Compared to methyl β -D-mannopyranoside (MeMan) and antagonist **11**, the binding affinity of **9** is improved by a factor of 106 and 6, respectively. These gains in binding affinity are mainly related to an improved binding enthalpy. This is especially surprising for triazole **11** ($\Delta\Delta H^\circ_{\text{MeMan} \rightarrow 11} = -5.4 \text{ kJ mol}^{-1}$), since hydrophobic interactions are commonly not associated with an increase in binding enthalpy. It is conceivable that the interaction of the extended aromatic substituent alters the conformational landscape of the long loop region. Thus, the observed effect on binding enthalpy may be due to changes in protein conformational dynamics and not a direct



consequence of protein–ligand interactions (entropy–enthalpy transduction).⁴⁰ The aminopropyl aglycone further increases binding enthalpy, but only by $\Delta\Delta H^\circ_{11 \rightarrow 9} = -3.3 \text{ kJ mol}^{-1}$. The favorable ionic interaction between the terminal amino group and Glu358/Ser360 is seemingly superimposed by enthalpic costs for the displacement of the structural water molecule (Figure 2C), as well as

desolvation penalty related to the polar head group. In total, ligand optimization (MeMan to **9**) improved the enthalpy term by -8.7 kJ mol^{-1} , coinciding with an improvement in the entropy term by -2.8 kJ mol^{-1} . The replacement of the phenyl triazolyl (\rightarrow **9**) by the 3-pyridyl triazolyl substituent (\rightarrow **19**) was accompanied by an almost complete enthalpy-entropy compensation of $\pm 4.7 \text{ kJ mol}^{-1}$ with little resulting effect on the overall free energy of binding. This is likely related to the increased enthalpy penalty for the desolvation ($\Delta\Delta H_{\text{desolv}}^{\circ}$) of the polar pyridyl substituent in **19**, which is entirely compensated by the entropic benefit of



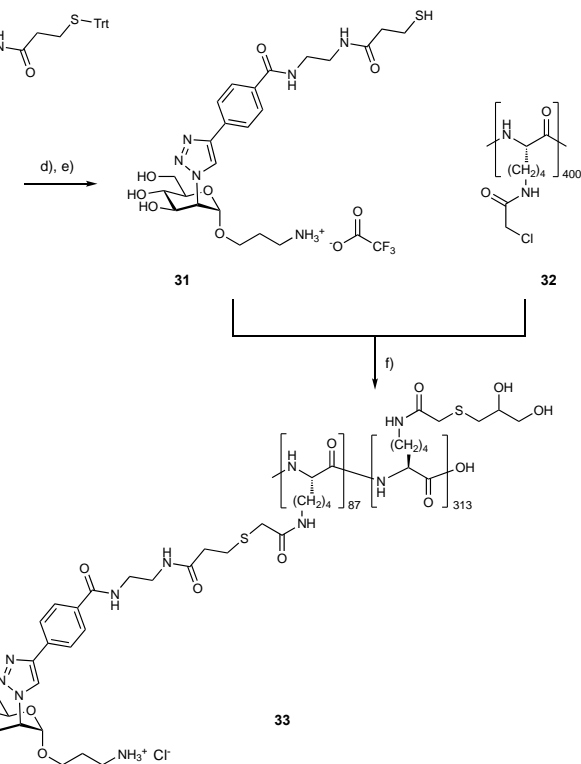
Scheme 3. Synthesis of glycopolymer **33**. a) EDC, HOBt, DIPEA, *tert*-butyl (2-aminoethyl)carbamate, DCM, rt, 16 h (70%); b) TFA, DCM, rt, 3h, then EDC, HOBt, DIPEA, 3-(tritylthio)propanoic acid, DMF, rt, 16 h (55%); c) CuBr, TBTA, THF, rt, 16 h (quant); d) NaOMe, MeOH, rt, 2h (89%); e) TFA, TIPS, DCM, rt, 4 h (55%); f) DBU, DMF, rt, 0.5 h, then thioglycerol, Et₃N, DMF, rt, 16 h (55%).

piperidyl moiety, the conformational flexibility of the aglycone is substantially reduced, inducing an entropic benefit. This is, however, compensated by a steric penalty overall leading to an enthalpic loss.

Selectivity against langerin. Whereas natural oligosaccharides and glycans usually bind to a plethora of related lectins, glycomimetics can be rationally optimized to selectively bind to a single target. An example is the long-standing concern that DC-SIGN ligands also bind to the off-target langerin.^{35,41} In the context of HIV infections, DC-SIGN-mediated *trans*-infection by mucosal dendritic cells is detrimental for the host, while HIV recognition by langerin on Langerhans cells, in contrast, elicits a protective immune response.¹ To avoid similar off-target effects in SARS-CoV-2 therapy using glycomimetics, carbohydrate-based therapeutics should bind selectively to DC-SIGN and avoid binding to langerin. We therefore compared the selectivity of **9** for DC-SIGN and langerin by nanoDSF and ITC. As evident from the melting curves (Figure 4A), the presence of 2 mM **9** did not influence the thermal melting profile of

langerin ($\Delta T_m = -0.2 \text{ }^{\circ}\text{C}$), whereas a ΔT_m value of $7.2 \text{ }^{\circ}\text{C}$ indicates a strong stabilization of the folded state of DC-SIGN (Figure 4B). Similarly, no heat signal was detected in a microcalorimetric titration of 10 mM **9** against 40 μM langerin (Figure S52), clearly indicating full selectivity of **9** for DC-SIGN over langerin.

Figure 4. Interaction of **9** with langerin and DC-SIGN. A) Thermal denaturation curve of langerin CRD in the absence and presence of 2 mM **9**. B) Thermal denaturation curve of DC-SIGN CRD in the absence and presence of 2 mM **9**.



langerin ($\Delta T_m = -0.2 \text{ }^{\circ}\text{C}$), whereas a ΔT_m value of $7.2 \text{ }^{\circ}\text{C}$ indicates a strong stabilization of the folded state of DC-SIGN (Figure 4B). Similarly, no heat signal was detected in a microcalorimetric titration of 10 mM **9** against 40 μM langerin (Figure S52), clearly indicating full selectivity of **9** for DC-SIGN over langerin.

Multivalent triazole glycomimetics. As we recently demonstrated, the normalized binding enthalpy of each carbohydrate epitope multivalently presented on poly-l-lysine scaffolds, matches with the monovalent interaction.³⁸ Thus, when polymers display carbohydrate ligands with improved enthalpy of binding, a strongly improved inhibition of viral attachment to DC-SIGN should be expected. To validate this hypothesis, we modified the aryl triazolyl substituent in **9** for linking with polymeric support (Scheme 3). Starting from 4-ethynyl benzoic acid (**26**), amide **27** was formed with *tert*-butyl (2-aminoethyl)carbamate. Boc-deprotection followed by amide formation with 3-(tritylthio)propanoic acid yielded the protected alkyne building block **28**, which was reacted

with azide **29** using standard CuAAC conditions with azide **29** to yield the protected intermediate **30**. After deprotection, thiol **31** was grafted onto the activated poly-L-lysine 400 scaffold **32** according to a previously published procedure.³⁸

From initial experiments, it was evident that polymers with increased epitope loading were entirely insoluble in aqueous solvents. Thus, the epitope loading was reduced to a value of 22% (**33**). The solubility of **33** was found to be sufficient for biological experiments. Dynamic light scattering experiments revealed a hydrodynamic size of 19 nm for **33** (Figure S42), with a polydispersity index of 0.22 (see Supporting Information). These properties are in line with other previously reported PLL₄₀₀ glycopolymers.³⁸

Next, binding affinity, thermodynamic fingerprints and the stoichiometry (n) of the interaction were determined with ITC using the glycopolymer **33** and the recombinant tetrameric DC-SIGN extracellular domain (ECD, residues 62–404). From this data, also the functional valency (N) of the polymer ($N = n^{-1}$) (Figure 5) was calculated. The macroscopic binding affinity of **33** is $K_D = 33$ nM, representing a multivalent affinity enhancement (β) of 10^3 compared

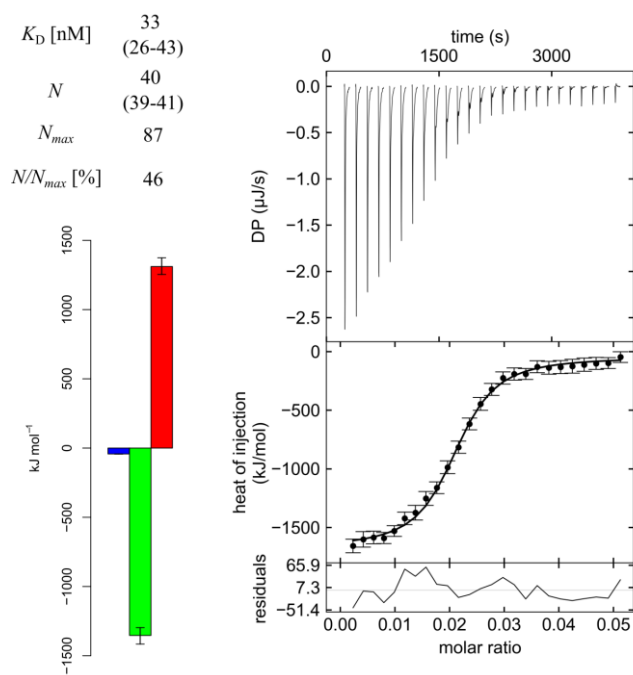


Figure 5. Isothermal titration calorimetry analysis of **33**. Thermodynamic data and representative enthalpogram of the interaction between **33** and DC-SIGN ECD.

with monovalent analog **9**. The recorded stoichiometry parameter revealed that 40 of the 87 glycomimetic epitopes on the polymer are involved in the interaction under equilibrium conditions. Related to the total loading of **33** determined by NMR spectroscopy (see Supporting Information), this represents 46% of the total number of available epitopes. In an earlier study, we attributed the reduced availability of epitopes to self-interaction and the formation of soluble aggregates.³⁸ Interestingly, the multivalent presentation of glycomimetic **9** on polymer **33**

results in a comparatively small multivalent affinity enhancement ($\beta_{33} = K_{D,9}/K_{D,33} \approx 10^3$) in ITC experiments compared to mannose-modified polymers described earlier ($\beta_{Man-PLL} = 10^5$).³⁸ Since relevant multivalency effects, such as statistical rebinding and avidity entropy, are a function of the valency of a multivalent ligand, the low loading of **33** likely contributes to this effect (loading **33**: 22% cf., loading Man-PLL: 40–60%). Since the normalized binding enthalpy $\Delta H^{\circ}_{33, norm} = \Delta H^{\circ}_{33}/N = -33.8$ kJ mol⁻¹ is very similar to the enthalpy determined for the monovalent ligand ($\Delta H^{\circ}_9 = -31.6$ kJ mol⁻¹), the comparatively low multivalent enhancement of **33** is almost entirely related to entropic phenomena, such as avidity entropy.

Since solubility has been identified as the main limitation for polymers displaying glycomimetic epitopes, future efforts will focus on the optimization of this parameter by varying the solubilizing thioglycerol groups on the multivalent construct. The interaction of glycomimetic **9** with DC-SIGN is likely dominated by the binding mode observed in the X-ray structure (Figure 2D), whereas simple monosaccharide epitopes, such as β -d-mannose, can benefit from a multitude of different low affinity binding modes employing different carbohydrate hydroxyl groups.³¹ It is yet unclear, how binding mode promiscuity on a monovalent level translates to multivalent interactions.

Inhibition of SARS-CoV-2 spike protein binding to DC-SIGN-expressing cells. To assess the potential of mono- and multivalent glycomimetics to inhibit viral glycoprotein binding on a cellular level, B-THP-1 cells, which have been engineered to display DC-SIGN on their surface, were incubated with fluorescently labeled SARS-CoV-2 spike glycoprotein in the presence of glycomimetic **9** or glycopolymer **33**. The inhibition of spike protein binding to DC-SIGN⁺ cells was quantified by flow cytometry (Figure 6A). Identical control B-THP-1 cells without DC-SIGN expression showed no binding of SARS-CoV-2 spike glycoprotein. Thus, interaction of the SARS-CoV-2 spike glycoprotein with engineered B-THP-1 cells is DC-SIGN mediated. For the monovalent glycomimetic **9**, an IC₅₀ of 89 μM was determined, which is in good agreement with the K_D of 31 μM observed in ITC experiments. Glycopolymer **33** inhibited SARS-CoV-2 spike glycoprotein binding to DC-SIGN⁺ cells with an IC₅₀ of 4.4 nM. Compared to the monovalent control MeMan, the monovalent glycomimetic **9** enhanced affinity 72-fold, whereas glycopolymer **33** improves affinity 1.5×10^6 -fold (Figure 6A). These results underscore that multivalent presentations on the poly-L-lysine scaffold can be leveraged for generating highly potent glyconanomaterials from fully selective monovalent

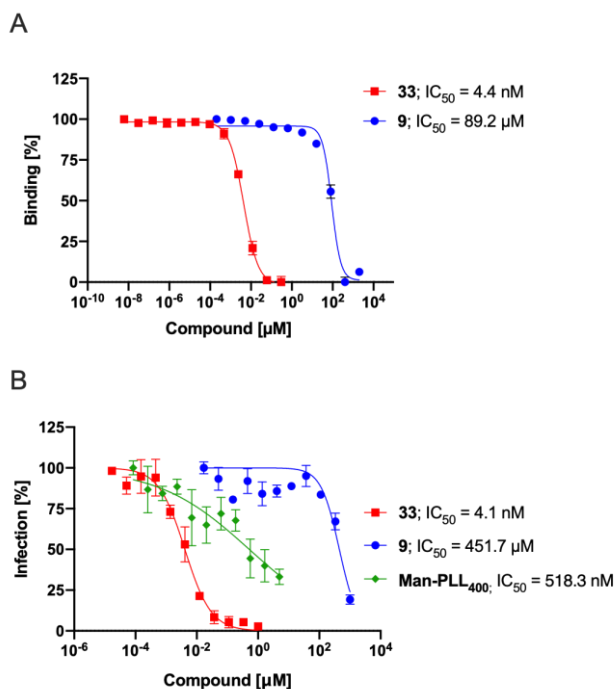


Figure 6. Cellular inhibition of DC-SIGN presenting cells. A) Glycoprotein binding assay: DC-SIGN⁺ B-THP-1 cells were incubated with 10 nM Cy5-labeled SARS-CoV-2 spike glycoprotein S1 subunit in the presence of **9** or **33**. B) *Trans*-infection assay: DC-SIGN⁺ B-THP-1 cells were inoculated in the presence of **9**, **33** or reference polymer **Man-PLL₄₀₀**³⁸ (50% loading) with 1000 PFU of VSV*ΔG-SARS-CoV-2-S_{Δ21} encoding the SARS-CoV-2 spike glycoprotein and GFP. After 1 h, the cells were thoroughly washed and then co-cultured with Vero E6 cells for 6 h and immediately analyzed. In both assays, mean fluorescence intensity was measured by flow cytometry.

glycomimetics. Notably, the more pronounced multivalent affinity enhancement ($\beta_{33} = K_{D,9}/K_{D,33} \approx 10^5$) is related to the interaction with the soluble receptor tetramer vs. receptor molecules on the cell surface of DC-SIGN expressing B-THP-1 cells.

In previous experiments with mannose-based glycopolymers, higher affinities in the picomolar range have been observed,³⁸ despite a lower monovalent affinity of the mannose epitope. This implies that polymer loading plays a crucial role in the interaction of glycopolymers with cell surfaces and underlines the importance of the solubility issue for polymers.

Inhibition of DC-SIGN-mediated *trans*-infection of ACE2⁺ cells by VSV expressing SARS-CoV-2 spike protein-pseudotyped viruses. To mimic the envisioned therapeutic application of DC-SIGN-targeted compounds, a *trans*-infection assay employing a chimeric VSV bearing the SARS-CoV-2 spike glycoprotein on the viral envelope and encoding the green fluorescent protein (GFP) reporter protein was developed (for detailed experimental setup see Supporting Information). In brief, the recombinant virus VSV*ΔG-SARS-CoV-2-S_{Δ21} was first incubated with DC-SIGN expressing B-THP-1 cells for 1 h in the presence or absence of monovalent inhibitor **9**, polymer **33** or reference polymer **Man-PLL₄₀₀**³⁸ (50% loading) and subsequently co-incubated with SARS-CoV-2 susceptible Vero E6 cells for 6

h. The efficiency of the DC-SIGN-mediated *trans*-infection process was immediately evaluated by flow cytometry (Figure 6B). In the *trans*-infection assay, the IC₅₀ value of 451 µM determined for the monovalent glycomimetic **9** is much lower compared with the assay systems detailed above. Evidently, the monovalent competitor is not able to interfere efficiently with the interaction between the extended virus spike protein surface and the cell surface, because even a low number of free valencies are sufficient to enable cell adhesion. In contrast, the multivalent glycopolymer **33** and **Man-PLL₄₀₀** potentially inhibited *trans*-infection of Vero E6 cells with IC₅₀ of 4.1 nM and 518.3 nM, respectively, emphasizing the potential of poly-l-lysine glycopolymers to restrict DC-SIGN-mediated virus dissemination via the lymphatic system and showing a more than 100-fold improved binding affinity of **33** compared to the mannose poly-l-lysine glycopolymer.

Conclusions

Starting from a virtual library of triazole-based glycomimetics, we identified a new class of mannose-based DC-SIGN ligands. Unexpectedly, aryl triazolyl substituents in the 2-position of mannose establish hydrophobic contacts with Val351 on the long loop (Figure 2B) and thus paved the way for anomeric extensions to the shallow, partly hydrophobic groove formed by Phe313, Glu358, Ser360 and Lys373. With K_D s around 30 µM, this new class of ligands are approx. 100-fold more potent compared to methyl α -D-mannopyranoside. As the thermodynamic analysis reveals, this gain in binding affinity is mainly driven by an improved enthalpic contribution, which is partly attributed to a modulation of the conformational dynamics of the long loop region.

When glycomimetic **31** was multivalently presented, solubility issues affecting the loading density became a serious problem. Finally, glycopolymer **33** with a loading of only 22% was found to be sufficiently soluble for biological experiments. Although lower loading reduces the benefit of multivalent affinity enhancement by statistical rebinding, glycopolymer **33** was found to inhibit the interaction of SARS-CoV-2 spike glycoprotein with DC-SIGN expressing cells with a IC₅₀ of 4.4 nM, representing a 1.5×10^6 improved binding affinity compared to the monovalent control MeMan (Figure 6A). Most importantly, the polymer also effectively inhibited the DC-SIGN-mediated *trans*-infection of ACE2⁺ Vero E6 cells with VSV expressing SARS-CoV-2 spike glycoprotein at nanomolar concentrations with 100-fold enhanced affinity compared to a mannose glycopolymer reference (Figure 6B).

In summary, DC-SIGN targeted glycopolymers are a potential treatment option for the prevention of severe COVID-19 and also represent an attractive strategy for the treatment of other viral infections, especially as an early response to pandemic outbreaks. Poly-l-lysine based glycopolymers carrying specific DC-SIGN-targeted glycomimetic epitopes are predestined for pulmonary application, because of their inherent biocompatibility and low toxicity.^{38,42,43} More importantly, the efficiency of a DC-SIGN-targeted therapeutic intervention is unlikely to be influenced by viral mutations since the target protein is encoded by the host genome.

Experimental Part

In silico library enumeration and molecular docking. DataWarrior v5.2⁴⁴ was used to enumerate a virtual chemical library of 200 glycomimetics from methyl 6-azido-6-deoxy- β -D-mannopyranoside or methyl 2-azido-2-deoxy- β -D-mannopyranoside and 100 in-house and commercially available terminal alkynes. Calculation of low-energy conformations and assignment of tautomers and protonation states was performed with LigPrep, as part of the Maestro 2016-4 software package, resulting in 230 molecules for docking.⁴⁵ An X-ray crystal structure of DC-SIGN CRD in complex with α -1,2-dimannose was retrieved from the PDB (PDB 2IT6) and prepared for docking by protonation, bond order and hydrogen bond assignment, and subsequent restrained minimization using the OPLS3 force field.⁴⁶ Glide was used for receptor grid generation and flexible ligand docking.³² To recreate experimentally observed mannose binding modes, hydrogen bonding constraints were imposed during docking, enforcing hydrogen bond interactions to Glu347 and Glu354.

Synthesis. General methods: NMR spectra were recorded on a Bruker Avance III (500 MHz) spectrometer. Assignment of ¹H and ¹³C NMR spectra was achieved using 2D methods (COSY, HSQC, HMBC). Chemical shifts are expressed in ppm using residual CHCl₃, CHD₂OD or HDO as references. Optical rotations were measured using Perkin-Elmer Polarimeter 341. Measurements were carried out in MeOH with *c* = 0.1. Electron spray ionization mass spectra (ESI-MS) were obtained on a Waters micromass ZQ Mass Spectrometer. HR-MS analyses were carried out using an Agilent 1100 LC equipped with a photodiode array detector and a Micromass QTOF I equipped with a 4 GHz digital-time converter. Compound purity was determined by HPLC using an Agilent 1200 instrument equipped with a Waters Atlantis T3 C18 3 μ m 2.1 \times 100 mm column and an Agilent 380 ELSD detector. Microwave-assisted reactions were carried out with CEM Discover and Explorer (CEM Corporation, Matthews, USA). Reactions were monitored by TLC using glass plates coated with silica gel 60 F₂₅₄ (Merck, Darmstadt, Germany) and were visualized by using UV light and/or by charring with a molybdate solution (a 0.02 M solution of ammonium cerium sulfate dihydrate and ammonium molybdate tetrahydrate in aqueous 10% H₂SO₄). MPLC separations were carried out on a CombiFlash Companion or R_f (Teledyne Isco, Lincoln, USA) equipped with RediSep normal-phase flash columns. For preparative reversed-phase HPLC purification, an Agilent 1260 Infinity II instrument equipped with a Waters XSelect C18 5 μ m 19 \times 250 mm column was used. All samples used for the determination of binding affinities are of >95% purity based on HPLC analysis. Commercially available reagents were purchased from Sigma-Aldrich, Alfa Aesar, TCI, and Acros Organics. Dry solvents were purchased from Acros Organics and Sigma-Aldrich.

The synthesis and analytical characterization of all previously unreported compounds is described in the Supporting Information.

Protein expression and purification. DC-SIGN ECD was produced as described previously.³⁸ For the production of recombinant DC-SIGN CRD, *E. coli* BL21(DE3) cells were transfected with pET15b plasmid encoding DC-SIGN CRD

(AA: 250-404) linked to a thrombin cleavage site and an N-terminal 6 His-tag. Bacteria were grown overnight in 20 mL Luria Bertani medium containing 0.1 mg/mL ampicillin at 37 °C, 300 rpm, and then transferred into 1 L Terrific Broth medium substituted with 0.1 mg/mL ampicillin and further incubated at 37 °C and 300 rpm. When an OD₆₀₀ of 1-1.2 was reached DC-SIGN expression was induced by addition of 0.5 mM IPTG. Cells were further cultivated at 37 °C and 300 rpm for 16h, harvested by centrifugation (5,000 rpm, 20 min, 4 °C), resuspended in lysis buffer (50 mM Tris-HCl, 10 mM MgCl₂, 0.1% Triton X100), and lysed by sonication. The cell lysate was centrifuged (11,000 rpm, 20 min, 4 °C), the supernatant discarded, and the pellet, containing the inclusion bodies, was washed three times with washing buffer (50 mM Tris-HCl, pH 8.0, 4 M urea, 500 mM NaCl, 1 mM EDTA). The inclusion bodies were dissolved in 20 mL of denaturation buffer (6 M guanidine hydrochloride, 100 mM Tris-HCl, pH 8.0, 1 mM DTT) for 1 h at 30 °C. After ultracentrifugation at 22,000 rpm, 30 min and 4 °C the denatured protein was refolded by rapid dilution into 100 mL refolding buffer (100 mM Tris-HCl, pH 8.0, 1 M L-arginine, 150 mM NaCl, 120 mM sucrose). The mixture was stirred for 2 d at 4 °C and dialyzed against binding buffer (20 mM Tris-HCl, 500 mM NaCl, 25 mM CaCl₂, pH 7.8). Precipitated protein was removed by ultracentrifugation (22,000 rpm, 30 min, 4 °C) and the refolded soluble protein was loaded on a mannose-sepharose column, followed by a washing step with binding buffer and eluted with elution buffer (20 mM TRIS, 500 mM NaCl, 2 mM EDTA, pH 7.8). The purity of the protein was verified by non-reducing SDS-PAGE.

Differential scanning fluorimetry (nanoDSF). Thermal shift data was generated using a Prometheus nanoDSF instrument (Nanotemper, München, Germany). A sample containing 20 μ M DC-SIGN CRD and a 1 mM concentration of a glycomimetic ligand was loaded into a nanoDSF capillary. The sample was heated from 25-95 °C at a rate of 1 °C/min and the melting curve was recorded as the ratio of fluorescence at 350 nm and 330 nm. A two-State model was fitted to the melting curves and inflection points were determined with the analysis software provided by the instrument supplier. T_m values were calculated by subtraction of the melting temperature of blank samples that were recorded in parallel to the samples. Each T_m value represents the mean of three independent experiments. Compounds with $T_m > 1.0$ °C were defined as hits.

Isothermal titration calorimetry. ITC experiments were performed using a MicroCal ITC200 instrument (MicroCal, Northampton, USA) at 25 °C using a reference power of 6 μ cal s⁻¹, a stirring speed of 750 rpm, feedback mode high, and a filter period of 2 s. All protein samples were extensively dialyzed against assay buffer (20 mM Hepes, 150 mM NaCl, 1 mM CaCl₂, pH 7.4) before use and all non-protein samples were prepared using the dialysate buffer to minimize dilution effects. Protein concentration was determined by absorbance at 280 nm employing a calculated extinction coefficient of 53,770 mol⁻¹ cm⁻¹ for DC-SIGN CRD or 70400 mol⁻¹ cm⁻¹ for DC-SIGN ECD. In a typical experiment with monovalent ligands, the ligand solution (2-

25 mM) was titrated into 30 μ M DC-SIGN CRD. The concentration of the ligand was chosen to ensure sufficient protein saturation (> 80%) at the end of the experiment for optimal accuracy of fitting parameters in a low c setup. For multivalent compound **33**, a 12 μ M ligand solution containing 5% DMSO was titrated into 40 μ M DC-SIGN ECD containing 5% DMSO. Baseline correction and integration was performed with NITPIC.^{47,48} Sedphat was used for global nonlinear regression analysis of experimental data and determination of confidence intervals.^{48,49} The stoichiometry was fixed at a value of 1 for all low c datasets with monovalent compounds.

Crystallization, data collection, and structure determination of DC-SIGN ligand complexes.

Crystallization experiments with **1s** were performed with the 6-His tagged DC-SIGN CRD construct. For experiments with **9**, the His-tag was cleaved to accelerate crystal formation. This was achieved by treatment of a protein sample with bovine thrombin (Sigma Aldrich, 5 units per mg protein) for 6 h at rt. After complete digestion, DC-SIGN CRD was repurified by affinity chromatography on a mannose-sepharose column. DC-SIGN CRD (~10 mg/ml in 20 mM Hepes, 150 mM NaCl, 1 mM CaCl₂, pH 7.4) with a threefold ligand excess was crystallized at room temperature in sitting-drop vapor diffusion experiments. Plate-like crystals of DC-SIGN/**1s** were grown in 20.5% PEG 3350 and 0.05 M NH₄NO₃. DC-SIGN/**9** crystals were obtained after one week in 0.1 M MgCl₂, 0.1 M Hepes pH 7.5, 10% PEG4000. Crystals were cryopreserved by a quick soak in reservoir solution with 25% ethylene glycol and flash frozen in liquid nitrogen. Data was collected at the SLS beamline X06SA (Swiss Light Source, Paul Scherrer Institute, Switzerland) at 100 K and integrated, indexed and scaled using the XDS software package^{50,51} and DIALS/AIMLESS.^{52,53} Both structures were solved by molecular replacement with the program PHASER,⁵⁴ using PDB ID: 1SL4²⁹ as a search model. Model building was performed with Coot⁵⁵ and the structures were refined with PHENIX.⁵⁶ MolProbity⁵⁷ was used to evaluate the final models and PyMOL⁵⁸ for protein model visualization. Data and refinement statistics are summarized in supplementary Table S2. The atomic coordinates have been deposited in the RCSB Protein Data Bank and are available under the accession code 7NL6 and 7NL7.

ASSOCIATED CONTENT

The Supporting Information is available free of charge at <https://pubs.acs.org>

AUTHOR INFORMATION

Corresponding Author

* Beat Ernst Tel.: +41 61 207 15 51; Fax: +41 61 207 15 52; Email: beat.ernst@unibas.ch

ACKNOWLEDGMENT

Langerin CRD for selectivity studies was kindly provided by Christoph Rademacher, University of Vienna, Austria.

ABBREVIATIONS

DC-SIGN, dendritic cell-specific intercellular adhesion molecule 3 grabbing non-integrin; HIV, human immunodeficiency virus; ACE2, angiotensin converting enzyme 2; CRD, carbohydrate recognition domain; ECD, extracellular domain; DSF, differential scanning fluorimetry; ITC, isothermal titration calorimetry; K_D , dissociation constant; DLS, dynamic light scattering; VSV, vesicular stomatitis virus; GFP, green fluorescent protein.

REFERENCES

- (1) Monteiro, J.; Lepenies, B. Myeloid C-Type Lectin Receptors in Viral Recognition and Antiviral Immunity. *Viruses* **2017**, *9* (3), 59.
- (2) Bermejo-Jambrina, M.; Eder, J.; Helgers, L. C.; Hertoghs, N.; Nijmeijer, B. M.; Stunnenberg, M.; Geijtenbeek, T. B. H. C-Type Lectin Receptors in Antiviral Immunity and Viral Escape. *Front. Immunol.* **2018**, *9*, 590.
- (3) van Kooyk, Y.; Geijtenbeek, T. B. H. DC-SIGN: Escape Mechanism for Pathogens. *Nat. Rev. Immunol.* **2003**, *3* (9), 697–709.
- (4) Garcia-Vallejo, J. J.; van Kooyk, Y. DC-SIGN: The Strange Case of Dr. Jekyll and Mr. Hyde. *Immunity* **2015**, *42* (6), 983–985.
- (5) Martín-Moreno, A.; Muñoz-Fernández, M. A. Dendritic Cells, the Double Agent in the War Against HIV-1. *Front. Immunol.* **2019**, *10*, 2485.
- (6) Tassaneetrithep, B.; Burgess, T. H.; Granelli-Piperno, A.; Trumpfheller, C.; Finke, J.; Sun, W.; Eller, M. A.; Pattanapanyasat, K.; Saravombath, S.; Birx, D. L.; Steinman, R. M.; Schlesinger, S.; Marovich, M. A. DC-SIGN (CD209) Mediates Dengue Virus Infection of Human Dendritic Cells. *J. Exp. Med.* **2003**, *197* (7), 823–829.
- (7) Routhu, N. K.; Lehoux, S. D.; Rouse, E. A.; Bidokhti, M. R. M.; Giron, L. B.; Anzurez, A.; Reid, S. P.; Abdel-Mohsen, M.; Cummings, R. D.; Byrareddy, S. N. Glycosylation of Zika Virus Is Important in Host–Virus Interaction and Pathogenic Potential. *Int. J. Mol. Sci.* **2019**, *20* (20), 5206.
- (8) Marzi, A.; Möller, P.; Hanna, S. L.; Harrer, T.; Eisemann, J.; Steinkasserer, A.; Becker, S.; Baribaud, F.; Pöhlmann, S. Analysis of the Interaction of Ebola Virus Glycoprotein with DC-SIGN (Dendritic Cell-Specific Intercellular Adhesion Molecule 3–Grabbing Nonintegrin) and Its Homologue DC-SIGNR. *J. Infect. Dis.* **2007**, *196* (s2), S237–S246.
- (9) Simmons, G.; Reeves, J. D.; Grogan, C. C.; Vandenberghe, L. H.; Baribaud, F.; Whitbeck, J. C.; Burke, E.; Buchmeier, M. J.; Soilleux, E. J.; Riley, J. L.; Doms, R. W.; Bates, P.; Pöhlmann, S. DC-SIGN and DC-SIGNR Bind Ebola Glycoproteins and Enhance Infection of Macrophages and Endothelial Cells. *Virology* **2003**, *305* (1), 115–123.
- (10) Marzi, A.; Gramberg, T.; Simmons, G.; Moller, P.; Rennekamp, A. J.; Krumbiegel, M.; Geier, M.; Eisemann, J.; Turza, N.; Saunier, B.; Steinkasserer, A.; Becker, S.; Bates, P.; Hofmann, H.; Pöhlmann, S. DC-SIGN and DC-SIGNR Interact with the Glycoprotein of Marburg Virus and the S Protein of Severe Acute Respiratory Syndrome Coronavirus. *J. Virol.* **2004**, *78* (21), 12090–12095.
- (11) Watanabe, Y.; Allen, J. D.; Wrapp, D.; McLellan, J. S.; Crispin, M. Site-Specific Glycan Analysis of the SARS-CoV-2 Spike. *Science* **2020**, *369* (6501), 330–333.
- (12) Gao, C.; Zeng, J.; Jia, N.; Stavenhagen, K.; Matsumoto, Y.; Zhang, H.; Li, J.; Hume, A. J.; Muehlberger, E.; van Die, I.; Kwan, J.; Tantisira, K.; Emili, A.; Cummings, R. D. SARS-CoV-2 Spike Protein Interacts with Multiple Innate Immune Receptors. *bioRxiv* **2020**, DOI: 10.1101/2020.07.29.227462.
- (13) Amraie, R.; Napoleon, M. A.; Yin, W.; Berrigan, J.; Suder, E.; Zhao, G.; Olejnik, J.; Gummuluru, S.; Muehlberger, E.; Chitalia, V.; Rahimi, N. CD209L/L-SIGN and CD209/DC-SIGN Act as Receptors for SARS-CoV-2 and Are Differentially Expressed in Lung and

Kidney Epithelial and Endothelial Cells. *Biorxiv* **2020**, DOI: 10.1101/2020.06.22.165803.

(14) Amraei, R.; Rahimi, N. COVID-19, Renin-Angiotensin System and Endothelial Dysfunction. *Cells* **2020**, *9* (7), 1652.

(15) Chiodo, F.; Bruijns, S. C. M.; Rodriguez, E.; Li, R. J. E.; Molinaro, A.; Silipo, A.; Di Lorenzo, F.; Garcia-Rivera, D.; Valdes-Balbin, Y.; Verez-Bencomo, V.; van Kooyk, Y. Novel ACE2-Independent Carbohydrate-Binding of SARS-CoV-2 Spike Protein to Host Lectins and Lung Microbiota. *Biorxiv* **2020**, DOI: 10.1101/2020.05.13.092478.

(16) Brufsky, A.; Lotze, M. T. DC/L-SIGNS of Hope in the COVID-19 Pandemic. *J. Med. Virol.* **2020**, *92* (9), 1396–1398.

(17) Katz, D. H.; Tahir, U. A.; Ngo, D.; Benson, M. D.; Bick, A. G.; Pampana, A.; Gao, Y.; Keyes, M. J.; Correa, A.; Sinha, S.; Shen, D.; Yang, Q.; Robbins, J. M.; Chen, Z.-Z.; Cruz, D. E.; Peterson, B.; Natarajan, P.; Vasani, R. S.; Smith, G.; Wang, T. J.; Gerszten, R. E. Proteomic Profiling in Biracial Cohorts Implicates DC-SIGN as a Mediator of Genetic Risk in COVID-19. *Medrxiv* **2020**, DOI: 10.1101/2020.06.09.20125690.

(18) Thépaut, M.; Luczkowiak, J.; Vivès, C.; Labiod, N.; Bally, I.; Lasala, F.; Grimoire, Y.; Fenel, D.; Sattin, S.; Thielens, N.; Schoehn, G.; Bernardi, A.; Delgado, R.; Fieschi, F. DC/L-SIGN Recognition of Spike Glycoprotein Promotes SARS-CoV-2 Trans-Infection and Can Be Inhibited by a Glycomimetic Antagonist. *PLoS Pathog.* **2021**, *17* (5), e1009576.

(19) Lu, Q.; Liu, J.; Zhao, S.; Gomez Castro, M. F.; Laurent-Rolle, M.; Dong, J.; Ran, X.; Damani-Yokota, P.; Tang, H.; Karakousi, T.; Son, J.; Kaczmarek, M. E.; Zhang, Z.; Yeung, S. T.; McCune, B. T.; Chen, R. E.; Tang, F.; Ren, X.; Chen, X.; Hsu, J. C. C.; Teplova, M.; Huang, B.; Deng, H.; Long, Z.; Mudianto, T.; Jin, S.; Lin, P.; Du, J.; Zang, R.; Su, T. T.; Herrera, A.; Zhou, M.; Yan, R.; Cui, J.; Zhu, J.; Zhou, Q.; Wang, T.; Ma, J.; Koralov, S. B.; Zhang, Z.; Aifantis, I.; Segal, L. N.; Diamond, M. S.; Khanna, K. M.; Stapleford, K. A.; Cresswell, P.; Liu, Y.; Ding, S.; Xie, Q.; Wang, J. SARS-CoV-2 Exacerbates Proinflammatory Responses in Myeloid Cells through C-Type Lectin Receptors and Tweety Family Member 2. *Immunity* **2021**, *54* (6), 1304–1319.

(20) Merad, M.; Martin, J. C. Pathological Inflammation in Patients with COVID-19: A Key Role for Monocytes and Macrophages. *Nat. Rev. Immunol.* **2020**, *20* (6), 355–362.

(21) Hevey, R. Strategies for the Development of Glycomimetic Drug Candidates. *Pharmaceuticals* **2019**, *12* (2), 55.

(22) Tomašić, T.; Hajšek, D.; Švajger, U.; Luzar, J.; Obermajer, N.; Petit-Haertlein, I.; Fieschi, F.; Anderluh, M. Monovalent Mannose-Based DC-SIGN Antagonists: Targeting the Hydrophobic Groove of the Receptor. *Eur. J. Med. Chem.* **2014**, *75*, 308–326.

(23) Anderluh, M.; Jug, G.; Svajger, U.; Obermajer, N. DC-SIGN Antagonists, a Potential New Class of Anti-Infectives. *Curr. Med. Chem.* **2012**, *19* (7), 992–1007.

(24) Medve, L.; Achilli, S.; Guzman-Caldentey, J.; Thépaut, M.; Senaldi, L.; Le Roy, A.; Sattin, S.; Ebel, C.; Vivès, C.; Martin-Santamaria, S.; Bernardi, A.; Fieschi, F. Enhancing Potency and Selectivity of a DC-SIGN Glycomimetic Ligand by Fragment-Based Design: Structural Basis. *Chem. - A Eur. J.* **2019**, *25* (64), 14659–14668.

(25) Reina, J. J.; Sattin, S.; Invernizzi, D.; Mari, S.; Martínez-Prats, L.; Tabarani, G.; Fieschi, F.; Delgado, R.; Nieto, P. M.; Rojo, J.; Bernardi, A. 1,2-Mannobioside Mimic: Synthesis, DC-SIGN Interaction by NMR and Docking, and Antiviral Activity. *ChemMedChem* **2007**, *2* (7), 1030–1036.

(26) Varga, N.; Sutkeviciute, I.; Guzzi, C.; McGeagh, J.; Petit-Haertlein, I.; Gugliotta, S.; Weiser, J.; Angulo, J.; Fieschi, F.; Bernardi, A. Selective Targeting of Dendritic Cell-Specific Intercellular Adhesion Molecule-3-Grabbing Nonintegrin (DC-SIGN) with Mannose-Based Glycomimetics: Synthesis and Interaction Studies of Bis(Benzylamide) Derivatives of a Pseudomannobioside. *Chem. - A Eur. J.* **2013**, *19* (15), 4786–4797.

(27) Sutkeviciute, I.; Thépaut, M.; Sattin, S.; Berzi, A.; McGeagh, J.; Grudinin, S.; Weiser, J.; Le Roy, A.; Reina, J. J.; Rojo, J.; Clerici, M.; Bernardi, A.; Ebel, C.; Fieschi, F. Unique DC-SIGN Clustering Activity

of a Small Glycomimetic: A Lesson for Ligand Design. *ACS Chem. Biol.* **2014**, *9* (6), 1377–1385.

(28) Aretz, J.; Baukmann, H.; Shanina, E.; Hanske, J.; Wawrzinek, R.; Zapol'skii, V. A.; Seeberger, P. H.; Kaufmann, D. E.; Rademacher, C. Identification of Multiple Druggable Secondary Sites by Fragment Screening against DC-SIGN. *Angew. Chemie Int. Ed.* **2017**, *56* (25), 7292–7296.

(29) Guo, Y.; Feinberg, H.; Conroy, E.; Mitchell, D. A.; Alvarez, R.; Blixt, O.; Taylor, M. E.; Weis, W. I.; Drickamer, K. Structural Basis for Distinct Ligand-Binding and Targeting Properties of the Receptors DC-SIGN and DC-SIGNR. *Nat. Struct. Mol. Biol.* **2004**, *11* (7), 591–598.

(30) Feinberg, H.; Castelli, R.; Drickamer, K.; Seeberger, P. H.; Weis, W. I. Multiple Modes of Binding Enhance the Affinity of DC-SIGN for High Mannose N-Linked Glycans Found on Viral Glycoproteins. *J. Biol. Chem.* **2007**, *282* (6), 4202–4209.

(31) Martínez, J. D.; Valverde, P.; Delgado, S.; Romanò, C.; Linclau, B.; Reichardt, N. C.; Oscarson, S.; Ardá, A.; Jiménez-Barbero, J.; Cañada, F. J. Unraveling Sugar Binding Modes to DC-SIGN by Employing Fluorinated Carbohydrates. *Molecules* **2019**, *24* (12), 2337.

(32) Friesner, R. A.; Banks, J. L.; Murphy, R. B.; Halgren, T. A.; Klicic, J. J.; Mainz, D. T.; Repasky, M. P.; Knoll, E. H.; Shelley, M.; Perry, J. K.; Shaw, D. E.; Francis, P.; Shenkin, P. S. Glide: A New Approach for Rapid, Accurate Docking and Scoring. 1. Method and Assessment of Docking Accuracy. *J. Med. Chem.* **2004**, *47* (7), 1739–1749.

(33) Himo, F.; Lovell, T.; Hilgraf, R.; Rostovtsev, V. V.; Noodleman, L.; Sharpless, K. B.; Fokin, V. V. Copper(I)-Catalyzed Synthesis of Azoles. DFT Study Predicts Unprecedented Reactivity and Intermediates. *J. Am. Chem. Soc.* **2005**, *127* (1), 210–216.

(34) Valverde, P.; Delgado, S.; Martínez, J. D.; Vendeville, J. B.; Malassis, J.; Linclau, B.; Reichardt, N. C.; Cañada, F. J.; Jiménez-Barbero, J.; Ardá, A. Molecular Insights into DC-SIGN Binding to Self-Antigens: The Interaction with the Blood Group A/B Antigens. *ACS Chem. Biol.* **2019**, *14* (7), 1660–1671.

(35) Porkolab, V.; Chabrol, E.; Varga, N.; Ordanini, S.; Sutkeviciute, I.; Thépaut, M.; García-Jiménez, M. J.; Girard, E.; Nieto, P. M.; Bernardi, A.; Fieschi, F. Rational-Differential Design of Highly Specific Glycomimetic Ligands: Targeting DC-SIGN and Excluding Langerin Recognition. *ACS Chem. Biol.* **2018**, *13* (3), 600–608.

(36) Ravindranathan Kartha, K. P.; Ballell, L.; Bilke, J.; McNeil, M.; Field, R. A. Iodine and Its Interhalogen Compounds: Versatile Reagents in Carbohydrate Chemistry. XIV. Glycosylated Amino Acid Synthesis. *J. Chem. Soc. Perkin 1* **2001**, No. 7, 770–772.

(37) Montero, J. L.; Winum, J. Y.; Leydet, A.; Kamal, M.; Pavia, A. A.; Roque, J. P. A Convenient Synthesis of Peracetylated Glycosyl Halides Using Bismuth(III) Halides as Catalysts. *Carbohydr. Res.* **1997**, *297* (2), 175–180.

(38) Cramer, J.; Aliu, B.; Jiang, X.; Sharpe, T.; Pang, L.; Hadorn, A.; Rabbani, S.; Ernst, B. Poly-L-lysine Glycoconjugates Inhibit DC-SIGN-mediated Attachment of Pandemic Viruses. *ChemMedChem* **2021**, cmdc.202100348.

(39) Dam, T. K.; Brewer, C. F. Thermodynamic Studies of Lectin-Carbohydrate Interactions by Isothermal Titration Calorimetry. *Chem. Rev.* **2002**, *102* (2), 387–429.

(40) Fenley, A. T.; Muddana, H. S.; Gilson, M. K. Entropy-Enthalpy Transduction Caused by Conformational Shifts Can Obscure the Forces Driving Protein-Ligand Binding. *Proc. Natl. Acad. Sci.* **2012**, *109* (49), 20006–20011.

(41) Andreini, M.; Doknic, D.; Sutkeviciute, I.; Reina, J. J.; Duan, J.; Chabrol, E.; Thépaut, M.; Moroni, E.; Doro, F.; Belvisi, L.; Weiser, J.; Rojo, J.; Fieschi, F.; Bernardi, A. Second Generation of Fucose-Based DC-SIGN Ligands: Affinity Improvement and Specificity versus Langerin. *Org. Biomol. Chem.* **2011**, *9* (16), 5778.

(42) Aliu, B.; Demeestere, D.; Seydoux, E.; Boucraut, J.; Delmont, E.; Brodovitch, A.; Oberholzer, T.; Attarian, S.; Théaudin, M.; Tsouni, P.; Kuntzer, T.; Derfuss, T.; Steck, A. J.; Ernst, B.; Herrendorff, R.; Hänggi, P. Selective Inhibition of Anti-MAG IgM

Autoantibody Binding to Myelin by an Antigen-specific Glycopolymers. *J. Neurochem.* **2020**, *154* (5), 486–501.

(43) Herrendorff, R.; Hänggi, P.; Pfister, H.; Yang, F.; Demeestere, D.; Hunziker, F.; Frey, S.; Schaeren-Wiemers, N.; Steck, A. J.; Ernst, B. Selective in Vivo Removal of Pathogenic Anti-MAG Autoantibodies, an Antigen-Specific Treatment Option for Anti-MAG Neuropathy. *Proc. Natl. Acad. Sci.* **2017**, *114* (18), E3689–E3698.

(44) Sander, T.; Freyss, J.; Von Korff, M.; Rufener, C. DataWarrior: An Open-Source Program for Chemistry Aware Data Visualization and Analysis. *J. Chem. Inf. Model.* **2015**, *55* (2), 460–473.

(45) Schrödinger Release 2016-4: Maestro Schrödinger LLC. New York, NY (USA) 2016.

(46) Harder, E.; Damm, W.; Maple, J.; Wu, C.; Reboul, M.; Xiang, J. Y.; Wang, L.; Lupyan, D.; Dahlgren, M. K.; Knight, J. L.; Kaus, J. W.; Cerutti, D. S.; Krilov, G.; Jorgensen, W. L.; Abel, R.; Friesner, R. A. OPLS3: A Force Field Providing Broad Coverage of Drug-like Small Molecules and Proteins. *J. Chem. Theory Comput.* **2016**, *12* (1), 281–296.

(47) Scheuermann, T. H.; Brautigam, C. A. High-Precision, Automated Integration of Multiple Isothermal Titration Calorimetric Thermograms: New Features of NITPIC. *Methods* **2015**, *76*, 87–98.

(48) Brautigam, C. A.; Zhao, H.; Vargas, C.; Keller, S.; Schuck, P. Integration and Global Analysis of Isothermal Titration Calorimetry Data for Studying Macromolecular Interactions. *Nat. Protoc.* **2016**, *11* (5), 882–894.

(49) Piszczek, G. SEDPHAT – A Platform for Global ITC Analysis and Global Multi-Method Analysis of Molecular Interactions. *Methods* **2015**, *76*, 137–148.

(50) Kabsch, W. Integration, Scaling, Space-Group Assignment and Post-Refinement. *Acta Crystallogr. Sect. D Biol. Crystallogr.* **2010**, *66* (2), 133–144.

(51) Kabsch, W. Xds. *Acta Crystallogr. D Biol. Crystallogr.* **2010**, *66* (Pt 2), 125–132.

(52) Evans, P. R.; Murshudov, G. N. How Good Are My Data and What Is the Resolution? *Acta Crystallogr. Sect. D Biol. Crystallogr.* **2013**, *69* (7), 1204–1214.

(53) Winter, G.; Waterman, D. G.; Parkhurst, J. M.; Brewster, A. S.; Gildea, R. J.; Gerstel, M.; Fuentes-Montero, L.; Vollmar, M.; Michels-Clark, T.; Young, I. D.; Sauter, N. K.; Evans, G. DIALS: Implementation and Evaluation of a New Integration Package. *Acta Crystallogr. Sect. D Struct. Biol.* **2018**, *74* (Pt 2), 85–97.

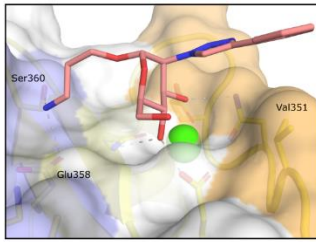
(54) McCoy, A. J.; Grosse-Kunstleve, R. W.; Adams, P. D.; Winn, M. D.; Storoni, L. C.; Read, R. J. Phaser Crystallographic Software. *J. Appl. Crystallogr.* **2007**, *40* (Pt 4), 658–674.

(55) Emsley, P.; Cowtan, K. Coot: Model-Building Tools for Molecular Graphics. *Acta Crystallogr. Sect. D Biol. Crystallogr.* **2004**, *60* (12), 2126–2132.

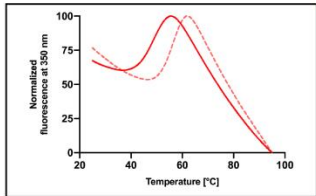
(56) Adams, P. D.; Afonine, P. V.; Bunkóczi, G.; Chen, V. B.; Davis, I. W.; Echols, N.; Headd, J. J.; Hung, L.-W.; Kapral, G. J.; Grosse-Kunstleve, R. W.; McCoy, A. J.; Moriarty, N. W.; Oeffner, R.; Read, R. J.; Richardson, D. C.; Richardson, J. S.; Terwilliger, T. C.; Zwart, P. H. PHENIX: A Comprehensive Python-Based System for Macromolecular Structure Solution. *Acta Crystallogr. Sect. D Biol. Crystallogr.* **2010**, *66* (2), 213–221.

(57) Chen, V. B.; Arendall, W. B.; Headd, J. J.; Keedy, D. A.; Immormino, R. M.; Kapral, G. J.; Murray, L. W.; Richardson, J. S.; Richardson, D. C. MolProbity: All-Atom Structure Validation for Macromolecular Crystallography. *Acta Crystallogr. Sect. D Biol. Crystallogr.* **2010**, *66* (1), 12–21.

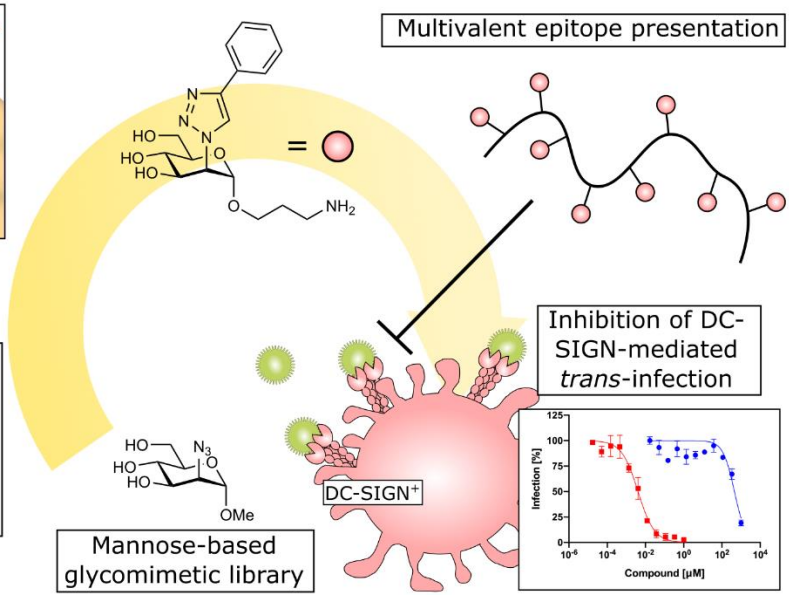
(58) Schrödinger LLC. The PyMOL Molecular Graphics System, Schrödinger LLC, New York, NY (USA). Schrödinger: New York, NY (USA).



Structure-guided hit optimization



Biophysical Screening



Supporting Information

Sweet Drugs for Bad Bugs: A Glycomimetic Strategy Against the DC-SIGN-mediated Dissemination of SARS-CoV-2

Jonathan Cramer^{1,5}, Adem Lakkaichi¹, Butrint Aliu¹, Roman P. Jakob², Sebastian Klein², Ivan Cattaneo¹, Xiaohua Jiang¹, Said Rabbani¹, Oliver Schwardt¹, Gert Zimmer³, Matias Ciancaglini⁴, Tiago Abreu-Mota⁴, Timm Maier², Beat Ernst¹

¹Institute of Molecular Pharmacy, Pharmacenter, University of Basel, 4056 Basel, Switzerland

²Focal Area Structural Biology, Biozentrum, University of Basel, 4056 Basel, Switzerland

³Institute of Virology and Immunology, 3147 Mittelhäusern, Switzerland

⁴Department Biomedicine, University of Basel, 4051 Basel, Switzerland

⁵Institute for Pharmaceutical and Medicinal Chemistry, Heinrich-Heine-University of Düsseldorf, 40225 Düsseldorf, Germany

Synthesis

Methyl 4,6-*O*-benzylidene- α -D-glucopyranoside (3). To a solution of methyl α -D-glucopyranoside (**6**, 20.1 g, 103.6 mmol, 1.00 eq) in DMF (100 mL) camphor sulfonic acid (2.41 g, 10.4 mmol, 0.10 eq), and benzaldehyde dimethyl acetal (31.1 mL, 207.1 mmol, 2.00 eq) were added. The solution was stirred at 60 °C at a pressure of 230 mbar on a rotary evaporator. After 5 h, the solvent was completely evaporated. The residue was dissolved in DCM and precipitated as white solid by slow addition of heptane. After filtration the solid was dried under reduced pressure overnight to obtain the product (23.5 g, 81%) as a colorless solid. ^1H NMR (500 MHz, CDCl_3): δ = 7.52–7.47 (m, 2H, Ar-H), 7.40–7.34 (m, 3H, Ar-H), 5.53 (s, 1H, PhCH), 4.80 (d, J = 3.9 Hz, 1H, H-1), 4.30 (dd, J = 9.9, 4.5 Hz, 1H, H-6), 3.93 (t, J = 9.2 Hz, 1H, H-3), 3.85–3.78 (m, 1H, H-2), 3.81–3.71 (m, 1H, H-6'), 3.63 (ddd, J = 9.2, 9.1, 3.9 Hz, 1H, H-5), 3.50 (t, J = 9.3 Hz, 1H, H-4), 3.46 (s, 3H, OCH_3); ^{13}C NMR (126 MHz, CDCl_3): δ = 137.1, 129.3, 128.4, 126.3 (6C, Ar-C), 102.0 (PhCH), 99.8 (C-1), 80.9 (C-4), 72.9 (C-5), 71.8 (C-3), 69.0 (C-6), 62.4 (C-2), 55.6 (OCH_3); ESI-MS: m/z : Calcd for $\text{C}_{14}\text{H}_{18}\text{NaO}_6$ $[\text{M}+\text{Na}]^+$: 305.3, found: 305.1.

Methyl 2-azido-4,6-*O*-benzylidene-2-deoxy- α -D-mannopyranoside (5). In a three-necked-flask, a solution of **3** (23.1 g, 81.9 mmol, 1.00 eq) in dry DCM (100 mL) was cooled to -30 °C under argon. After the addition of dry pyridine (20.6 mL, 163.7 mmol, 2.00 eq), a solution of trifluoromethanesulfonic anhydride (15.1 mL, 90.0 mmol, 1.10 eq) in 100 mL DCM was added slowly, maintaining the temperature at -30 °C. After 30 min, TLC analysis (DCM/MeOH, 10:1) indicated full consumption of the starting material. The reaction was quenched with water (50 mL), the resulting mixture was diluted with DCM (200 mL) and washed with 1 M HCl (100 mL), 1 M NaOH (100 mL), and brine (2 x 100 mL). The organic phase was dried over sodium sulfate and concentrated under reduced pressure to yield intermediate **4**. The intermediate then was dissolved in DMF (100 mL) and NaN_3 (16.0 g, 0.25 mol, 3.00 eq) was added. The suspension was stirred for 8 h at 60 °C, when the complete conversion of the starting material could be monitored by TLC (petroleum ether/EtOAc, 4:1). Then, the suspension was filtered and concentrated under reduced pressure. The residue was dissolved in EtOAc (200 mL), filtered, and concentrated under reduced pressure. The crude product was purified by flash chromatography (petroleum ether/EtOAc, 5:1) to afford **5** (10.6 g, 42%) as a colorless oil. ^1H NMR (500 MHz, CDCl_3): δ = 7.52–7.46 (m, 2H, Ar-H), 7.41–7.36 (m, 3H, Ar-H), 5.57 (s, 1H, PhCH), 4.69 (d, J = 1.4, 1H, H-1), 4.28–4.22 (m, 2H, H-3, H-6), 3.95 (dd, J = 3.9, 1.1 Hz, 1H,

H-2), 3.89 (dd, $J = 9.3$ Hz, 1H, H-4), 3.79 (t, $J = 9.7$ Hz, 1H, H-6'), 3.75 (m, 1H, H-5), 3.38 (s, 3H, OCH₃), 2.70 (d, $J = 3.2$ Hz, 1H, OH); ¹³C NMR (126 MHz, CDCl₃): $\delta = 137.1, 129.3, 128.4, 126.3$ (6C, Ar-C), 102.3 (PhCH), 100.1 (C-1), 79.0 (C-4), 68.9 (C-3), 68.7 (C-6), 63.6 (C-2), 63.3 (C-5), 55.2 (OCH₃); ESI-MS: m/z : Calcd for C₁₄H₁₇N₃NaO₅ [M+Na]⁺: 330.3, found: 330.1.

Methyl 2-azido-2-deoxy- α -D-mannopyranoside (6). Compound **5** (5.14 g, 16.7 mmol, 1.00 eq) was dissolved in MeCN/H₂O (9:1, 50 mL) and Er(CF₃SO₃)₃ (1.03 g, 1.67 mmol, 0.1 eq) was added. After stirring for 3 h at 50 °C, TLC control (petroleum ether/EtOAc, 4:1) showed full consumption of the starting material. The solvents were evaporated under reduced pressure and the residue was purified over silica gel (DCM/MeOH, 10:1) to afford **6** (3.67 g, quant.) as a colorless solid. ¹H NMR (500 MHz, CD₃OD): $\delta = 4.69$ (d, $J = 1.4$ Hz, 1H, H-1), 3.94 (dd, $J = 9.2, 4.0$ Hz, 1H, H-3), 3.88–3.81 (m, 2H, H-2, H-6), 3.68 (dd, $J = 11.9, 6.1$ Hz, 1H, H-6'), 3.58 (t, $J = 9.5$ Hz, 1H, H-4), 3.49 (ddd, $J = 8.7, 6.1, 2.2$ Hz, 1H, H-5), 3.40 (s, 3H, OCH₃); ¹³C NMR (126 MHz, CD₃OD): $\delta = 99.2$ (C-1), 73.2 (C-5), 71.1 (C-3), 67.3 (C-4), 64.3 (C-2), 61.4 (C-6), 53.9 (OCH₃); ESI-MS: m/z : Calcd for C₇H₁₃N₃NaO₅ [M+Na]⁺: 242.2, found: 241.9.

Methyl 6-O-tosyl- α -D-mannopyranoside (7). A solution of *p*-toluenesulfonyl chloride (6.38 g, 33.5 mmol, 1.30 eq) in pyridine (20 mL) was added dropwise to a cooled solution of methyl α -D-mannopyranoside (5.00 g, 25.8 mmol, 1.00 eq) in pyridine (50 mL). After stirring for 5 h at 0 °C, TLC (DCM/MeOH, 10:1) showed full consumption of the starting material. The reaction was quenched by the addition of MeOH (20 mL). The reaction mixture was concentrated under reduced pressure and the obtained residue was purified by flash chromatography (DCM/MeOH, 10:1) to yield **7** (7.62 g, 28.5 mmol, 85%) as a colorless oil. ¹H NMR (500 MHz, D₂O): $\delta = 7.88$ (d, $J = 8.2$ Hz, 2H, Ar-H), 7.53 (d, $J = 8.2$ Hz, 2H, Ar-H), 4.69 (s, 1H, H-1), 4.43 (dd, $J = 11.1, 1.9$ Hz, 1H, H-6), 4.34 (dd, $J = 11.3, 5.9$ Hz, 1H, H-6'), 3.91 (m, 1H, H-2), 3.74–3.68 (m, 2H, H-3, H-5), 3.62 (m, 1H, H-4), 3.32 (s, 3H, OCH₃), 2.47 (s, 3H, ArCH₃); ¹³C NMR (126 MHz, D₂O): $\delta = 146.8, 130.6, 130.2, 127.9$ (6C, Ar-C), 101.0 (C-1), 70.3 (C-5), 70.0 (C-3), 69.9 (C-6), 69.7 (C-2), 66.2 (C-4), 54.8 (OCH₃), 20.8 (ArCH₃); ESI-MS: m/z : Calcd for C₁₄H₂₀NaO₈S [M+Na]⁺: 371.1, found: 371.1.

Methyl 6-azido-6-deoxy- α -D-mannopyranoside (8). NaN₃ (4.19 g, 65.5 mmol, 3.00 eq) was added to a solution of **7** (7.60 g, 21.8 mmol, 1.00 eq) in DMF (80 mL). The suspension was

stirred for 12 h at 60 °C until TLC (DCM/MeOH, 10:1) showed full consumption of the starting material. Then, the suspension was filtered and the solvent evaporated under reduced pressure. The residue was dissolved in EtOAc and filtered to remove the excess of NaN₃. Afterwards, the solution was concentrated and the crude product was purified by chromatography on silica gel (DCM/MeOH, 10:1) to afford **8** (3.49 g, 73%) as a colorless oil. ¹H NMR (500 MHz, CDCl₃): δ = 4.72 (d, *J* = 0.9 Hz, 1H, H-1), 3.93 (dd, *J* = 3.1, 1.3 Hz, 1H, H-2), 3.76 (dd, *J* = 9.0, 3.3 Hz, 1H, H-3), 3.70–3.63 (m, 2H, H-4, H-5), 3.54 (d, *J* = 2.9 Hz, 2H, H-6), 3.41 (s, 3H, OCH₃); ¹³C NMR (126 MHz, CDCl₃): δ = 101.0 (C-1), 71.4 (C-5), 71.4 (C-3), 70.6 (C-2), 68.1 (C-4), 55.2 (OCH₃), 51.4 (C-6); ESI-MS: *m/z*: Calcd for C₇H₁₃N₃NaO₅ [M+Na]⁺: 242.1, found: 241.9.

General procedure A for CuAAC. Tris(1-benzyl-1*H*-1,2,3-triazol-4-yl)methylamine (TBTA, 0.20 eq) and CuBr (0.20 eq) were suspended in 10 mL MeCN/H₂O (2:1). A terminal alkyne (1.00 eq) and mannose building block **6** or **8** (1.00 eq) were added subsequently. The reaction mixture was stirred at 60 °C or under microwave irradiation until TLC (DCM/MeOH, 10:1) showed full consumption of the starting materials. The solvents were evaporated under reduced pressure and the residue was dissolved in DCM (2 mL). Then, QuadraSil MP was added and the mixture was stirred for 5 min. After filtration, the obtained residue was purified by chromatography on silica gel (DCM/MeOH, 0-10% or DCM/*i*-PrOH, 0-20%).

Methyl 2-(4-(4-(benzo[*d*][1,3]dioxol-5-yl-methyl)piperazin-1-yl)methyl)-1,2,3-triazol-1-yl)-2-deoxy- α -D-mannopyranoside (1a**).** According to general procedure A, CuBr (3 mg, 0.02 mmol, 0.20 eq), TBTA (10 mg, 0.02 mmol, 0.20 eq), 1-(benzo[*d*][1,3]dioxol-5-ylmethyl)-4-(prop-2-yn-1-yl)piperazine (24 mg, 0.09 mmol, 1.0 eq) and **6** (16 mg, 0.07 mmol, 0.8 eq) were reacted in MeCN/H₂O (2:1, 10 mL) to give **1a** (21 mg, 0.04 mmol, 60%) as a colorless solid. [α]_D²⁰ +36.9 (*c* 1.0, MeOH). ¹H NMR (500 MHz, CD₃OD): δ = 7.98 (s, 1H, triazole-H), 6.86 (d, *J* = 1.5 Hz, 1H, Ar-H), 6.83–6.74 (m, 2H, Ar-H), 5.93 (s, 2H, CH₂(OR)₂), 4.82 (m, 1H, H-6), 4.58 (d, *J* = 1.7 Hz, 1H, H-1), 4.54 (dd, *J* = 14.2, 8.2 Hz, 1H, H-6'), 3.82–3.75 (m, 2H, H-3, H-5), 3.74 (s, 2H, triazole-CH₂-NR₂), 3.66 (dd, *J* = 9.4, 3.4 Hz, 1H, H-3), 3.58 (s, 2H, Ar-CH₂-NR₂), 3.47 (t, *J* = 9.6 Hz, 1H, H-4), 3.09 (s, 3H, OCH₃), 2.62 (s, 8H, (CH₂)₂N(CH₂)₂); ¹³C NMR (126 MHz, CD₃OD): δ = 149.3, 148.8 (Ar-C), 143.7 (triazole-C_q), 130.0 (Ar-C), 127.0 (triazole-CH), 124.5, 110.9, 109.0 (Ar-C), 102.9 (C-1), 102.5 (CH₂(OR)₂), 72.8 (C-5), 72.3 (C-3), 71.8 (C-4), 69.6 (C-2), 63.0 (Ar-CH₂-NR₂), 55.2 (OCH₃), 53.2 (triazole-CH₂-NR₂), 53.1,

52.7 (4C, (CH₂)₂N(CH₂)₂), 52.6 (C-6); HRMS: *m/z*: Calcd for C₂₂H₃₁N₅NaO₇ [M+Na]⁺: 500.2116, found: 500.2117.

Methyl 2-(4-(2-bromo-4-methylphenoxy)methyl)-1,2,3-triazol-1-yl)-2-deoxy- α -D-mannopyranoside (1b). According to general procedure A, CuBr (7 mg, 0.05 mmol, 0.2 eq), TBTA (26 mg, 0.05 mmol, 0.2 eq), 2-bromo-4-methyl-1-(prop-2-yn-1-yloxy)benzene (56 mg, 0.25 mmol, 1.0 eq), and **6** (54 mg, 0.25 mmol, 1.0 eq) were reacted in MeCN/H₂O (2:1, 10 mL) to give **1b** (86 mg, 0.19 mmol, 77%) as a colorless solid. [α]_D²⁰ -2.0 (*c* 1.0, MeOH); ¹H NMR (500 MHz, CD₃OD): δ = 8.35 (s, 1H, triazole-H), 7.38 (d, *J* = 1.5 Hz, 1H, Ar-H), 7.16–7.07 (m, 2H, Ar-H), 5.21 (s, 2H, CH₂OAr), 5.10 (dd, *J* = 5.3, 1.3 Hz, 1H, H-2), 4.98 (d, *J* = 1.1 Hz, 1H, H-1), 4.18 (dd, *J* = 9.0, 5.3 Hz, 1H, H-3), 3.95–3.85 (m, 2H, H-6), 3.77–3.67 (m, 2H, H-4, H-5), 3.47 (s, 3H, OCH₃), 2.29 (s, 3H, ArCH₃); ¹³C NMR (126 MHz, CD₃OD): δ = 133.3, 132.3, 128.8 (Ar-C), 124.5 (triazole-CH), 114.2 (Ar-C), 99.0 (C-1), 73.4 (C-5), 68.9 (C-3), 66.4 (C-4), 64.2 (C-2), 62.5 (CH₂OAr), 60.7 (C-6), 54.1 (OCH₃), 18.8 (ArCH₃); ESI-MS: *m/z*: Calcd for C₁₇H₂₂BrN₃NaO₆ [M+Na]⁺: 466.0584, found: 466.0585.

Methyl 2-deoxy-2-(4-((5-methyl-1,3,4-thiadiazol-2-yl)thio)methyl)-1,2,3-triazol-1-yl)- α -D-mannopyranoside (1c). According to general procedure A, CuBr (6 mg, 0.04 mmol, 0.2 eq), TBTA (22 mg, 0.04 mmol, 0.2 eq), 2-methyl-5-(prop-2-yn-1-ylthio)-1,3,4-thiadiazole (36 mg, 0.21 mmol, 1.0 eq), and **6** (46 mg, 0.21 mmol, 1.0 eq) were reacted in MeCN/H₂O (2:1, 10 mL) to give **1c** (64 mg, 0.16 mmol, 76%) as a colorless solid. [α]_D²⁰ -9.3 (*c* 1.0, MeOH); ¹H NMR (500 MHz, CD₃OD): δ = 8.23 (s, 1H, Ar-H), 5.04 (dd, *J* = 5.2, 1.3 Hz, 1H, H-2), 4.91 (d, *J* = 1.2 Hz, 1H, H-1), 4.59 (d, *J* = 1.8 Hz, 2H, CH₂SAr), 4.15 (m, 1H, H-3), 3.91–3.86 (m, 2H, H-6), 3.69–3.63 (m, 2H, H-4, H-5), 3.45 (s, 3H, OCH₃), 2.74 (s, 3H, ArCH₃); ¹³C NMR (126 MHz, CD₃OD): δ = 167.6, 165.3 (Ar-C), 142.5 (triazole-C_q), 124.3 (triazole-CH), 99.0 (C-1), 73.3 (C-5), 68.8 (C-3), 66.4 (C-4), 64.1 (C-2), 60.7 (C-6), 54.1 (OCH₃), 28.9 (CH₂SAr), 13.9 (ArCH₃); HRMS: *m/z*: Calcd for C₁₃H₁₉N₅NaO₅S₂ [M+Na]⁺: 412.0720, found: 412.0720.

Methyl 2-(4-(2-cyclopentylphenoxy)methyl)-1,2,3-triazol-1-yl)-2-deoxy- α -D-mannopyranoside (1d). According to general procedure A, CuBr (3 mg, 0.02 mmol, 0.20 eq), TBTA (10 mg, 0.02 mmol, 0.20 eq), 1-cyclopentyl-2-(prop-2-yn-1-yloxy)benzene (17 mg, 0.09 mmol, 1.0 eq), and **6** (20 mg, 0.09 mmol, 1.0 eq) were reacted in MeCN/H₂O (2:1, 10 mL) to give **1d** (7 mg, 0.02 mmol, 24%) as a colorless solid. [α]_D²⁰ +10.0 (*c* 1.0, MeOH); ¹H NMR (500 MHz,

CD₃OD): δ = 8.30 (s, 1H, triazole-H), 7.20 (dd, J = 7.5, 1.7 Hz, 1H, Ar-H), 7.14 (ddd, J = 8.9, 7.4, 1.7 Hz, 1H, Ar-H), 7.06 (dd, J = 8.2, 1.2 Hz, 1H, Ar-H), 6.90 (m, 1H, Ar-H), 5.16 (s, 2H, CH₂OAr), 5.08 (dd, J = 5.2, 1.4 Hz, 1H, H-2), 4.95 (d, J = 1.3 Hz, 1H, H-1), 4.17 (dd, J = 8.7, 5.3 Hz, 1H, H-3), 3.94–3.79 (m, 2H, H-6), 3.76–3.64 (m, 2H, H-4, H-5), 3.45 (s, 3H, OCH₃), 3.33 (m, 1H, CH₂-CH-CH₂), 2.01–1.91 (m, 2H, CH₂), 1.83–1.70 (m, 2H, CH₂), 1.69–1.56 (m, 2H, CH₂), 1.59–1.50 (m, 2H, CH₂); ¹³C NMR (126 MHz, CD₃OD): δ = 157.7 (Ar-C), 145.2 (triazole-C_q), 136.3, 128.0, 127.9 (Ar-C), 125.9 (triazole-CH), 122.4, 113.4 (Ar-C), 100.6 (C-1), 74.9 (C-5), 70.5 (C-3), 68.0 (C-4), 65.7 (C-2), 63.0 (CH₂OAr), 62.3 (C-6), 55.7 (OCH₃), 40.5 (CH₂-CH-CH₂), 34.3 (CH₂), 34.3 (CH₂), 26.7 (CH₂); HRMS: m/z : Calcd for C₂₁H₂₉N₃NaO₆ [M+Na]⁺: 442.1949, found: 442.1950.

Methyl 2-(4-(acetamidomethyl)-1,2,3-triazol-1-yl)-2-deoxy- α -D-mannopyranoside (1e).

According to general procedure A, CuBr (9 mg, 0.06 mmol, 0.2 eq), TBTA (32 mg, 0.06 mmol, 0.2 eq), *N*-(prop-2-yn-1-yl)acetamide (30 mg, 0.30 mmol, 1.0 eq), and **6** (67 mg, 0.30 mmol, 1.0 eq) were reacted in MeCN/H₂O (2:1, 10 mL) to give **1e** (80 mg, 0.25 mmol, 82%) as a colorless solid. $[\alpha]_D^{20}$ +4.5 (*c* 1.0, MeOH); ¹H NMR (500 MHz, CD₃OD): δ = 8.14 (s, 1H, triazole-H), 5.05 (dd, J = 5.3, 1.3 Hz, 1H, H-2), 4.93 (d, J = 1.0 Hz, 1H, H-1), 4.45 (s, 2H, CH₂NHAc), 4.16 (dd, J = 9.3, 5.3 Hz, 1H, H-3), 3.93–3.87 (m, 2H, H-6), 3.74 (t, J = 9.6 Hz, 1H, H-4), 3.69 (m, 1H, H-5), 3.46 (s, 3H, OCH₃), 1.99 (s, 3H, CH₃CO); ¹³C NMR (126 MHz, CD₃OD): δ = 171.8 (CO), 144.4 (triazole-C_q), 123.2 (triazole-CH), 99.1 (C-1), 73.3 (C-5), 68.9 (C-3), 66.3 (C-4), 64.1 (C-2), 60.6 (C-6), 54.1 (OCH₃), 34.4 (CH₂NHAc), 21.0 (CH₃CO); ESI-MS: m/z : Calcd for C₁₂H₂₀N₄NaO₆ [M+Na]⁺: 339.1275, found: 339.1276.

Methyl 2-(4-(((1*H*-benzo[*d*][1,2,3]triazol-1-yl)oxy)methyl)-1,2,3-triazol-1-yl)-2-deoxy- α -D-mannopyranoside (1f).

According to general procedure A, CuBr (5 mg, 0.04 mmol, 0.2 eq), TBTA (19 mg, 0.04 mmol, 0.2 eq), 1-(prop-2-yn-1-yloxy)-1*H*-benzo[*d*][1,2,3]triazole (31 mg, 0.18 mmol, 1.0 eq), and **6** (35 mg, 0.18 mmol, 1.0 eq) were reacted in MeCN/H₂O (2:1, 10 mL) to give **1f** (51 mg, 0.13 mmol, 73%) as a colorless solid. $[\alpha]_D^{20}$ -8.0 (*c* 1.0, MeOH); ¹H NMR (500 MHz, CD₃OD): δ = 8.16 (s, 1H, triazole-H), 7.82 (d, J = 8.4 Hz, 1H, Ar-H), 7.39 (ddd, J = 8.1, 6.9, 0.8 Hz, 1H, Ar-H), 7.30 (ddd, J = 8.1, 6.9, 0.9 Hz, 1H, Ar-H), 7.24 (d, J = 8.3 Hz, 1H, Ar-H), 5.59 (s, 2H, CH₂Ar), 4.89 (dd, J = 5.3, 1.2 Hz, 1H, H-2), 4.56 (d, J = 1.2 Hz, 1H, H-1), 4.01 (dd, J = 9.1, 5.3 Hz, 1H, H-3), 3.78–3.69 (m, 2H, H-6), 3.58–3.43 (m, 2H, H-4, H-5), 3.30 (s, 3H, OCH₃); ¹³C NMR (126 MHz, CD₃OD): δ = 142.9 (Ar-C), 140.0 (triazole-C_q),

128.3, 127.9 (Ar-C), 126.5 (triazole-CH), 124.9, 119.0, 108.9 (Ar-C), 98.9 (C-1), 73.2 (C-5), 72.4 (CH₂Ar), 68.7 (C-3), 66.3 (C-4), 64.1 (C-2), 60.6 (C-6), 54.1 (OCH₃); ESI-MS: *m/z*: Calcd for C₁₆H₂₀N₆NaO₆ [M+Na]⁺: 415.1337, found: 415.1337.

Methyl 2-deoxy-2-(4-(((1-phenyl-1*H*-tetrazol-5-yl)thio)methyl)-1,2,3-triazol-1-yl)- α -D-mannopyranoside (1g). According to general procedure A, CuBr (5 mg, 0.04 mmol, 0.2 eq), TBTA (19 mg, 0.04 mmol, 0.2 eq), 1-phenyl-5-(prop-2-yn-1-ylthio)-1*H*-tetrazole (38 mg, 0.18 mmol, 1.0 eq), and **6** (39 mg, 0.18 mmol, 1.0 eq) were reacted in MeCN/H₂O (2:1, 10 mL) to give **1g** (71 mg, 0.16 mmol, 90%) as a colorless solid. [α]_D²⁰ -0.0 (*c* 1.0, MeOH); ¹H NMR (500 MHz, CD₃OD): δ = 8.29 (s, 1H, triazole-H), 7.69–7.57 (m, 5H, Ar-H), 5.04 (dd, *J* = 5.3, 1.3 Hz, 1H, H-2), 4.92 (d, *J* = 1.1 Hz, 1H, H-1), 4.71 (d, *J* = 2.3 Hz, 2H, CH₂SAr), 4.15 (dd, *J* = 8.8, 5.3 Hz, 1H, H-3), 3.94–3.85 (m, 2H, H-6), 3.71–3.63 (m, 2H, H-4, H-5), 3.45 (s, 3H, OCH₃); ¹³C NMR (126 MHz, CD₃OD): δ = 130.3, 129.7, 124.4 (Ar-C), 124.1 (triazole-CH), 98.9 (C-1), 73.4 (C-5), 68.8 (C-3), 66.4 (C-4), 64.1 (C-2), 60.8 (C-6), 54.1 (OCH₃), 27.1. (CH₂SAr); HRMS: *m/z*: Calcd for C₁₇H₂₁N₇NaO₅S [M+Na]⁺: 458.1217, found: 458.1217.

Methyl 2-(4-((benzyl(methyl)amino)methyl)-1,2,3-triazol-1-yl)-2-deoxy- α -D-mannopyranoside (1h). According to general procedure A, CuBr (3 mg, 0.02 mmol, 0.2 eq), TBTA (10 mg, 0.02 mmol, 0.2 eq), *N*-benzyl-*N*-methylethyamine (15 μ L, 0.091 mmol, 1.0 eq), and **6** (16 mg, 0.07 mmol, 0.80 eq) were reacted in MeCN/H₂O (2:1, 10 mL) to give **1h** (16 mg, 0.04 mmol, 58%) as a colorless solid. [α]_D²⁰ +8.7 (*c* 1.0, MeOH); ¹H NMR (500 MHz, CD₃OD): δ = 8.19 (s, 1H, triazole-H), 7.38–7.29 (m, 4H, Ar-H), 7.26 (m, 1H, Ar-H), 5.06 (dd, *J* = 5.2, 1.4 Hz, 1H, H-2), 4.95 (d, *J* = 1.3 Hz, 1H, H-1), 4.17 (dd, *J* = 9.4, 5.2 Hz, 1H, H-3), 3.94–3.84 (m, 2H, H-6), 3.75 (t, *J* = 9.6 Hz, 1H, H-4), 3.72 (s, 2H, triazole-CH₂), 3.68 (m, 1H, H-5), 3.57 (s, 2H, ArCH₂), 3.45 (s, 3H, OCH₃), 2.22 (s, 3H, NCH₃); ¹³C NMR (126 MHz, CD₃OD): δ = 144.7 (triazole-C_q), 139.0, 130.6, 129.4, 128.4 (Ar-C), 125.8 (triazole-CH), 100.5 (C-1), 74.7 (C-5), 70.3 (C-3), 67.8 (C-4), 65.5 (C-2), 62.1 (ArCH₂), 62.0 (C-6), 55.5 (OCH₃), 52.4 (triazole-CH₂), 42.0 (NCH₃); HRMS: *m/z*: Calcd for C₁₈H₂₆N₄NaO₅ [M+Na]⁺: 401.1795, found: 401.1797.

Methyl 2-deoxy-2-(4-(((tetrahydro-2*H*-pyran-2-yl)oxy)methyl)-1,2,3-triazol-1-yl)- α -D-mannopyranoside (1i). According to general procedure A, CuBr (3 mg, 0.02 mmol, 0.20 eq), TBTA (10 mg, 0.02 mmol, 0.20 eq), 2-(prop-2-yn-1-yloxy)tetrahydro-2*H*-pyran (15 μ L, 0.11

mmol, 1.2 eq), and **6** (20 mg, 0.09 mmol, 1.0 eq) were reacted in MeCN/H₂O (2:1, 10 mL) to give **1i** (17 mg, 0.05 mmol, 52%) as a colorless solid as a mixture of diastereomers. ¹H NMR (500 MHz, CD₃OD): δ = 8.23 (s, 1H, triazole-H), 5.07 (dd, *J* = 5.2, 1.4 Hz, 1H, H-2), 4.94 (d, *J* = 1.4 Hz, 1H, H-1), 4.80 (d, *J* = 12.3 Hz, 1H, CH₂OTHP), 4.75 (m, 1H, CH₂THP), 4.61 (d, *J* = 12.3 Hz, 1H, CH₂OTHP), 4.16 (dd, *J* = 9.4, 5.2 Hz, 1H, H-3), 3.94–3.86 (m, 3H, H-6, CH₂THP), 3.76 (t, *J* = 9.6 Hz, 1H, H-4), 3.68 (m, 1H, H-5), 3.55 (m, 1H, CH₂THP), 3.45 (s, 3H, OCH₃), 1.82 (s, 1H, CH₂THP), 1.71 (m, 1H, CH₂THP), 1.66–1.48 (m, 4H, CH₂THP); ¹³C NMR (126 MHz, CD₃OD): δ = 144.31, 144.25 (triazole-C_q), 124.1 (triazole-CH), 99.1, 98.03 (C-1), 98.00 (C-1), 73.3 (CH₂THP), 68.9 (C-5), 66.28 (C-3), 66.26 (C-4), 64.1 (C-2), 61.9 (CH₂CH₂O_{THP}), 61.8 (CH₂O_{THP}), 60.50, 60.49 (C-6), 59.7, 59.6 (CH₂OTHP), 54.1 (OCH₃), 30.1 (CH₂THP), 25.1 (CH₂THP), 18.91, 18.89 (CH₂THP); HRMS *m/z*: Calcd for C₁₅H₂₅N₃NaO₇ [M+Na]⁺: 382.1585, found: 382.1585.

Methyl 2-(4-(benzyloxy)methyl)-1,2,3-triazol-1-yl)-2-deoxy-α-D-mannopyranoside (1j).

According to general procedure A, CuBr (3 mg, 0.02 mmol, 0.20 eq), TBTA (10 mg, 0.02 mmol, 0.20 eq), ((prop-2-yn-1-yloxy)methyl)benzene (16 μL, 0.11 mmol, 1.2 eq) and **6** (20 mg, 0.09 mmol, 1.0 eq) were reacted in MeCN/H₂O (2:1, 10 mL) to give **1j** (22 mg, 0.06 mmol, 66%) as a colorless solid. [α]_D²⁰ +10.0 (*c* 1.0, MeOH); ¹H NMR (500 MHz, CD₃OD): δ = 8.32 (s, 1H, triazole-H), 7.39–7.31 (m, 4H, Ar-H), 7.28 (m, 1H, Ar-H), 5.08 (d, *J* = 5.2 Hz, 1H, H-2), 4.93 (s, 1H, H-1), 4.63 (s, 2H, CH₂), 4.58 (s, 2H, CH₂), 4.17 (dd, *J* = 9.4, 5.1 Hz, 1H, H-3), 3.88 (d, *J* = 3.3 Hz, 2H, H-6), 3.75 (t, *J* = 9.6 Hz, 1H, H-4), 3.68 (m, 1H, H-5), 3.44 (s, 3H, OCH₃); ¹³C NMR (126 MHz, CD₃OD): δ = 145.4 (triazole-C_q), 139.3, 129.4, 129.1, 128.8 (Ar-C), 124.6 (triazole-CH), 100.4 (C-1), 74.7 (C-5), 73.4 (CH₂), 70.3 (C-3), 67.7 (C-4), 65.6 (C-2), 64.1 (CH₂), 61.9 (C-6), 55.5 (OCH₃); HRMS: *m/z*: Calcd for C₁₇H₂₃N₃NaO₆ [M+Na]⁺: 388.1479, found: 388.1480.

Methyl 2-deoxy-2-(4-((1,3-dioxoisindolin-2-yl)propyl)-1,2,3-triazol-1-yl)-α-D-mannopyranoside (1k).

According to general procedure A, CuBr (5 mg, 0.03 mmol, 0.2 eq), TBTA (18 mg, 0.03 mmol, 0.2 eq), 2-(pent-4-yn-1-yl)isoindoline-1,3-dione (37 mg, 0.17 mmol, 1.0 eq), and **6** (38 mg, 0.17 mmol, 1.0 eq) were reacted in MeCN/H₂O (2:1, 10 mL) to give **1k** (60 mg, 0.14 mmol, 81%) as a colorless solid. [α]_D²⁰ +0.0 (*c* 1.0, MeOH); ¹H NMR (500 MHz, CD₃OD): δ = 8.08 (s, 1H, triazole-H), 7.90–7.86 (m, 2H, Ar-H), 7.85–7.79 (m, 2H, Ar-H), 5.01 (dd, *J* = 5.3, 1.3 Hz, 1H, H-2), 4.89 (d, *J* = 1.3 Hz, 1H, H-1), 4.15 (dd, *J* = 9.4, 5.3 Hz, 1H, H-

3), 3.94–3.89 (m, 2H, CH₂N), 3.79–3.73 (m, 3H, H-4, H-6), 3.67 (m, 1H, H-5), 3.46 (s, 3H, OCH₃), 2.77 (t, *J* = 7.6 Hz, 2H, CH₂), 2.15–2.01 (m, 2H, CH₂); ¹³C NMR (126 MHz, CD₃OD): δ = 168.6 (CO), 146.3 (triazole-C_q), 134.0, 132.0, 122.7 (Ar-C), 122.5 (triazole-CH), 99.1 (C-1), 73.3 (C-5), 69.0 (C-3), 66.4 (C-4), 64.0 (C-2), 60.6 (CH₂N), 54.1 (OCH₃), 36.9 (C-6), 27.7 (CH₂), 22.4 (CH₂); ESI-MS: *m/z*: Calcd for C₂₀H₂₄N₄NaO₇ [M+Na]⁺: 455.1537, found: 455.1537.

Methyl 2-(4-(cyclohexyl)-1,2,3-triazol-1-yl)-2-deoxy-α-D-mannopyranoside (1l).

According to general procedure A, CuBr (3 mg, 0.02 mmol, 0.20 eq), TBTA (10 mg, 0.02 mmol, 0.20 eq), cyclohexylacetylene (14 μL, 0.11 mmol, 1.2 eq), and **6** (20 mg, 0.09 mmol, 1.0 eq) were reacted in MeCN/H₂O (2:1, 10 mL) to give **1l** (17 mg, 0.05 mmol, 47%) as a colorless solid. [α]_D²⁰ +9.7 (*c* 1.0, MeOH); ¹H NMR (500 MHz, CD₃OD): δ = 7.99 (s, 1H, triazole-H), 5.01 (dd, *J* = 5.2, 1.4 Hz, 1H, H-2), 4.90 (d, *J* = 1.4 Hz, 1H, H-1), 4.14 (dd, *J* = 9.5, 5.2 Hz, 1H, H-3), 3.94–3.83 (m, 2H, H-6), 3.78 (t, *J* = 9.7 Hz, 1H, H-4), 3.65 (ddd, *J* = 9.8, 3.6, 2.5 Hz, 1H, H-5), 3.44 (s, 3H, OCH₃), 2.72 (m, 1H, CH), 2.07–1.97 (m, 2H, CH₂), 1.88–1.78 (m, 2H, CH₂), 1.74 (m, 1H, CH₂), 1.52–1.39 (m, 4H, 2 CH₂), 1.31 (m, 1H, CH₂); ¹³C NMR (126 MHz, CD₃OD): δ = 154.2 (triazole-C_q), 122.3 (triazole-CH), 100.5 (C-1), 74.6 (C-5), 70.3 (C-3), 67.5 (C-4), 65.4 (C-2), 61.7 (C-6), 55.5 (OCH₃), 36.5 (CH), 34.0 (CH₂), 34.0 (CH₂), 27.2 (2C, 2 CH₂), 27.1 (CH₂); HRMS: *m/z*: Calcd for C₁₅H₂₅N₃NaO₅ [M+Na]⁺: 350.1686, found: 350.1686.

Methyl 2-deoxy-2-(4-((1,1-dioxidothiomorpholino)methyl)-1,2,3-triazol-1-yl)-α-D-mannopyranoside (1m).

According to general procedure A, CuBr (3 mg, 0.02 mmol, 0.20 eq), TBTA (10 mg, 0.02 mmol, 0.20 eq), 4-propargylthiomorpholine 1,1-dioxide (16 mg, 0.09 mmol, 1 eq), and **6** (20 mg, 0.09 mmol, 1 eq) were reacted in MeCN/H₂O (2:1, 10 mL) to give **1m** (33 mg, 0.08 mmol, 93%) as a colorless solid. [α]_D²⁰ -9.7 (*c* 1.0, MeOH); ¹H NMR (500 MHz, CD₃OD): δ = 8.24 (s, 1H, triazole-H), 5.06 (d, *J* = 5.2 Hz, 1H, H-2), 4.94 (s, 1H, H-1), 4.17 (dd, *J* = 9.4, 5.2 Hz, 1H, H-3), 3.94–3.84 (m, 2H, H-6), 3.84 (s, 2H, CH₂NR₂), 3.74 (t, *J* = 9.6 Hz, 1H, H-4), 3.67 (m, 1H, H-5), 3.45 (s, 3H, OCH₃), 3.12 (s, 4H, CH₂-SO₂-CH₂), 3.03 (s, 4H, CH₂-NR-CH₂); ¹³C NMR (126 MHz, CD₃OD): δ = 146.5 (triazole-C_q), 125.7 (triazole-CH), 100.5 (C-1), 74.7 (C-5), 70.2 (C-3), 67.6 (C-4), 65.6 (C-2), 61.8 (C-6), 55.5 (OCH₃), 52.4 (CH₂NR₂), 52.2 (CH₂-SO₂-CH₂), 51.5 (CH₂-NR-CH₂); HRMS: *m/z*: Calcd for C₁₄H₂₄N₄NaO₇S [M+Na]⁺: 415.1258, found: 415.1259.

Methyl 2-(4-(2-allylphenoxy)methyl)-1,2,3-triazol-1-yl)-2-deoxy- α -D-mannopyranoside (1n). According to general procedure A, CuBr (3 mg, 0.02 mmol, 0.20 eq), TBTA (10 mg, 0.02 mmol, 0.20 eq), 1-allyl-2-(ethynyloxy)benzene (19 mg, 0.11 mmol, 1.2 eq), and **6** (20 mg, 0.09 mmol, 1.0 eq) were reacted in MeCN/H₂O (2:1, 10 mL) to give **1n** (22 mg, 0.08 mmol, 70%) as a colorless solid. $[\alpha]_{\text{D}}^{20} +7.0$ (*c* 1.0, MeOH); ¹H NMR (500 MHz, CD₃OD): δ = 8.30 (s, 1H, triazole-H), 7.19 (m, 1H, Ar-H), 7.12 (dd, *J* = 7.5, 1.7 Hz, 1H, Ar-H), 7.08 (dd, *J* = 8.2, 1.1 Hz, 1H, Ar-H), 6.90 (m, 1H, Ar-H), 5.94 (m, 1H, Allyl-CH), 5.17 (s, 2H, CH₂OAr), 5.08 (dd, *J* = 5.2, 1.4 Hz, 1H, H-2), 4.99 (m, 1H, Allyl-CH₂), 4.99–4.93 (m, 2H, H-1, Allyl-CH₂), 4.17 (dd, *J* = 9.0, 5.3 Hz, 1H, H-3), 3.93–3.82 (m, 2H, H-6), 3.76–3.65 (m, 2H, H-4, H-5), 3.45 (s, 3H, OCH₃), 3.37–3.31 (m, 2H, CH₂); ¹³C NMR (126 MHz, CD₃OD): δ = 157.4 (Ar-C), 144.9 (triazole-C_q), 138.3 (Allyl-CH), 131.0, 130.3, 128.5 (Ar-C), 125.7 (triazole-CH), 122.3 (Ar-C), 115.7 (Allyl-CH₂), 113.2 (Ar-C), 100.4 (C-1), 74.8 (C-5), 70.3 (C-3), 67.8 (C-4), 65.5 (C-2), 62.8 (CH₂OAr), 62.1 (C-6), 55.5 (OCH₃), 35.3 (CH₂); HRMS: *m/z*: Calcd for C₁₉H₂₅N₃NaO₆ [M+Na]⁺: 414.1636, found: 414.1637.

Methyl 2-deoxy-2-(4-(3-((4,6-dimethylpyrimidin-2-yl)thio)propyl)-1,2,3-triazol-1-yl)- α -D-mannopyranoside (1o). According to general procedure A, CuBr (3 mg, 0.02 mmol, 0.2 eq), TBTA (12 mg, 0.02 mmol, 0.2 eq), 4,6-dimethyl-2-(pent-4-yn-1-ylthio)pyrimidine (24 mg, 0.12 mmol, 1.0 eq), and **6** (26 mg, 0.12 mmol, 1.0 eq) were reacted in MeCN/H₂O (2:1, 10 mL) to give **1o** (31 mg, 0.07 mmol, 60%) as a colorless solid. $[\alpha]_{\text{D}}^{20} -0.0$ (*c* 1.0, MeOH); ¹H NMR (500 MHz, CD₃OD): δ = 8.04 (s, 1H, triazole-H), 6.88 (s, 1H, Ar-H), 5.02 (dd, *J* = 5.3, 1.3 Hz, 1H, H-2), 4.91 (d, *J* = 1.5 Hz, 1H, H-1), 4.14 (dd, *J* = 9.5, 5.3 Hz, 1H, H-3), 3.89–3.85 (m, 2H, H-6), 3.75 (dd, *J* = 9.7 Hz, 1H, H-4), 3.65 (dt, *J* = 9.9, 3.2 Hz, 1H, H-5), 3.43 (s, 3H, OCH₃), 3.25–3.18 (m, 2H, CH₂SR), 2.86 (t, *J* = 7.6 Hz, 2H, CH₂), 2.38 (s, 6H, 2 ArCH₃), 2.15–2.06 (m, 2H, CH₂); ¹³C NMR (126 MHz, CD₃OD): δ = 122.8 (triazole-CH), 115.4 (Ar-C), 99.1 (C-1), 73.3 (C-5), 68.9 (C-3), 66.2 (C-4), 64.0 (C-2), 60.5 (C-6), 54.1 (OCH₃), 29.4 (CH₂SR), 28.9 (CH₂), 24.1 (CH₂), 22.2 (2C, ArCH₃); HRMS: *m/z*: Calcd for C₁₈H₂₇N₅NaO₅S [M+Na]⁺: 448.1625, found: 448.1626.

Methyl 2-deoxy-2-(4-((4-nitrophenyloxy)methyl)-1,2,3-triazol-1-yl)- α -D-mannopyranoside (1p). According to general procedure A, CuBr (3 mg, 0.02 mmol, 0.20 eq), TBTA (10 mg, 0.02 mmol, 0.20 eq), 1-nitro-4-(prop-2-yn-1-yloxy)benzene (19 mg, 0.11 mmol, 1.2

eq), and **6** (20 mg, 0.09 mmol, 1.0 eq) were reacted in MeCN/H₂O (2:1, 10 mL) to give **1p** (30 mg, 0.08 mmol, 88%) as a colorless solid. $[\alpha]_D^{20}$ -0.8 (*c* 1.0, MeOH); ¹H NMR (500 MHz, CD₃OD): δ = 8.40 (s, 1H, triazole-H), 8.25–8.18 (m, 2H, Ar-H), 7.22–7.15 (m, 2H, Ar-H), 5.31 (s, 2H, CH₂OAr), 5.10 (dd, *J* = 5.3, 1.4 Hz, 1H, H-2), 4.94 (d, *J* = 1.3 Hz, 1H, H-1), 4.17 (dd, *J* = 9.3, 5.3 Hz, 1H, H-3), 3.89 (d, *J* = 3.2 Hz, 2H, H-6), 3.74 (t, *J* = 9.6 Hz, 1H, H-4), 3.68 (dt, *J* = 9.8, 3.2 Hz, 1H, H-5), 3.44 (s, 3H, OCH₃); ¹³C NMR (126 MHz, CD₃OD): δ = 164.8 (Ar-C), 143.7 (triazole-C_q), 143.1, 126.8 (Ar-C), 126.2 (triazole-CH), 116.1 (Ar-C), 100.4 (C-1), 74.7 (C-5), 70.2 (C-3), 67.6 (C-4), 65.6 (C-2), 63.0 (CH₂OAr), 61.9 (C-6), 55.5 (OCH₃); HRMS: *m/z*: Calcd for C₁₆H₂₀N₄NaO₈ [M+Na]⁺: 419.1173, found: 419.1173.

Methyl 2-(4-cinnamidomethyl)-1,2,3-triazol-1-yl)-2-deoxy- α -D-mannopyranoside (1q).

According to general procedure A, CuBr (4 mg, 0.03 mmol, 0.2 eq), TBTA (15 mg, 0.03 mmol, 0.2 eq), *N*-(prop-2-yn-1-yl)cinnamide (25 mg, 0.14 mmol, 1.0 eq), and **6** (30 mg, 0.14 mmol, 1.0 eq) were reacted in MeCN/H₂O (2:1, 10 mL) to give **1q** (52 mg, 0.13 mmol, 95%) as a colorless solid. $[\alpha]_D^{20}$ -0.9 (*c* 1.0, MeOH); ¹H NMR (500 MHz, CD₃OD): δ = 8.17 (s, 1H, triazole-H), 7.62–7.52 (m, 3H, Ar-H), 7.42–7.34 (m, 3H, Ar-H), 6.62 (d, *J* = 15.8 Hz, 1H, CH-CONH), 5.05 (dd, *J* = 5.3, 1.5 Hz, 1H, H-2), 4.93 (d, *J* = 1.2 Hz, 2H, H-1), 4.57 (s, 2H, CH₂NH), 4.15 (dd, *J* = 9.2, 5.3 Hz, 1H, H-3), 3.92–3.84 (m, 2H, H-6), 3.73 (t, *J* = 9.6 Hz, 1H, H-4), 3.67 (m, 1H, H-5), 3.44 (s, 3H, OCH₃); ¹³C NMR (126 MHz, CD₃OD): δ = 140.8, 128.6, 127.5 (Ar-C), 123.4 (triazole-CH), 120.1 (Ar-C), 99.1 (C-1), 73.3 (C-5), 68.9 (C-3), 66.4 (C-4), 64.1 (C-2), 60.7 (C-6), 54.1 (OCH₃), 34.5 (CH₂NH); HRMS: *m/z*: Calcd for C₁₉H₂₄N₄NaO₆ [M+Na]⁺: 427.1588, found: 427.1588.

Methyl 2-deoxy-2-(4-(thiophen-3-yl)-1,2,3-triazol-1-yl)- α -D-mannopyranoside (1r).

According to general procedure A, CuBr (5 mg, 0.03 mmol, 0.2 eq), TBTA (17 mg, 0.03 mmol, 0.2 eq), 3-ethynylthiophene (18 mg, 0.16 mmol, 1.0 eq), and **6** (36 mg, 0.16 mmol, 1.0 eq) were reacted in MeCN/H₂O (2:1, 10 mL) to give **1r** (40 mg, 0.12 mmol, 74%) as a colorless solid. $[\alpha]_D^{20}$ -9.7 (*c* 1.0, MeOH); ¹H NMR (500 MHz, CD₃OD): δ = 8.47 (s, 1H, triazole-H), 7.76 (m, 1H, Ar-H), 7.50 (d, *J* = 2.1 Hz, 2H, Ar-H), 5.10 (dd, *J* = 5.2, 1.5 Hz, 1H, H-2), 4.99 (d, *J* = 1.3 Hz, 1H, H-1), 4.19 (dd, *J* = 9.5, 5.2 Hz, 1H, H-3), 3.95 (dd, *J* = 12.0, 3.7 Hz, 1H, H-6), 3.90 (dd, *J* = 12.0, 2.4 Hz, H-6'), 3.84 (t, *J* = 9.7 Hz, 1H, H-4), 3.69 (ddd, *J* = 9.9, 3.7, 2.3 Hz, 1H, H-5), 3.46 (s, 3H, OCH₃); ¹³C NMR (126 MHz, CD₃OD): δ = 145.1 (triazole-C_q), 133.0, 127.6, 126.8 (Ar-C), 122.4 (triazole-CH), 122.2 (Ar-C), 100.5 (C-1), 74.7 (C-5), 70.3

(C-3), 67.5 (C-4), 65.6 (C-2), 61.8 (C-6), 55.6 (OCH₃); HRMS: *m/z*: Calcd for C₁₃H₁₈N₃O₅S [M+H]⁺: 328.0962, found: 328.0963.

Methyl 2-deoxy-2-(4-(pyridine-3-yl)-1,2,3-triazol-1-yl)- α -D-mannopyranoside (1s).

According to general procedure A, CuBr (6 mg, 0.04 mmol, 0.2 eq), TBTA (21 mg, 0.04 mmol, 0.2 eq), 3-ethynynlpyridine (21 mg, 0.20 mmol, 1.0 eq), and **6** (44 mg, 0.20 mmol, 1.0 eq) were reacted in MeCN/H₂O (2:1, 10 mL) to give **1s** (46 mg, 0.14 mmol, 70%) as a colorless solid. [α]_D²⁰ -25.0 (*c* 1.0, MeOH); ¹H NMR (500 MHz, CD₃OD): δ = 9.04 (d, *J* = 1.6 Hz, 1H, Ar-H), 8.73 (s, 1H, triazole-H), 8.51 (dd, *J* = 4.8, 1.4 Hz, 1H, Ar-H), 8.31 (ddd, *J* = 8.0, 2.2, 1.7 Hz, 1H, Ar-H), 7.52 (ddd, *J* = 8.0, 4.9, 0.8 Hz, 1H, Ar-H), 5.16 (dd, *J* = 5.2, 1.4 Hz, 1H, H-2), 5.03 (d, *J* = 1.2 Hz, 1H, H-1), 4.23 (dd, *J* = 9.5, 5.3 Hz, 1H, H-3), 3.96 (dd, *J* = 12.0, 3.7 Hz, 1H, H-6), 3.91 (dd, *J* = 12.0, 2.3 Hz, 1H, H-6'), 3.85 (t, *J* = 9.7 Hz, 1H, H-4), 3.72 (ddd, *J* = 9.8, 3.3, 2.6 Hz, 1H, H-5), 3.49 (s, 3H, OCH₃); ¹³C NMR (126 MHz, CD₃OD): δ = 148.1, 145.9 (Ar-C), 143.8 (triazole-C_q), 133.5, 124.2 (Ar-C), 122.0 (triazole-CH), 99.0 (C-1), 73.3 (C-5), 68.9 (C-3), 66.1 (C-4), 64.3 (C-2), 60.3 (C-6), 54.2 (OCH₃); HRMS: *m/z*: Calcd for C₁₄H₁₈N₄NaO₅ [M+Na]⁺: 345.1169, found: 345.1169.

Methyl 6-deoxy-6-(4-(thiophen-3-yl)-1,2,3-triazol-1-yl)- α -D-mannopyranoside (2a).

According to general procedure A, CuBr (3 mg, 0.02 mmol, 0.2 eq), TBTA (10 mg, 0.02 mmol, 0.2 eq), 3-ethynynlthiophene (10 mg, 0.09 mmol, 1.0 eq), and **8** (20 mg, 0.09 mmol, 1.0 eq) were reacted in MeCN/H₂O (2:1, 10 mL) to give **2a** (24 mg, 0.07 mmol, 81%) as a colorless solid. [α]_D²⁰ -22.4 (*c* 1.0, MeOH); ¹H NMR (500 MHz, CD₃OD): δ = 8.27 (s, 1H, triazole-H), 7.75 (m, 1H, Ar-H), 7.52–7.46 (m, 2H, Ar-H), 4.89 (dd, *J* = 14.1, 2.3 Hz, 1H, H-6), 4.61 (d, *J* = 1.6 Hz, 1H, H-1), 4.56 (dd, *J* = 14.1, 8.5 Hz, 1H, H-6'), 3.85 (ddd, *J* = 10.5, 8.6, 2.3 Hz, 1H, H-5), 3.79 (dd, *J* = 3.4, 1.7 Hz, 1H, H-2), 3.68 (dd, *J* = 9.3, 3.4 Hz, 1H, H-3), 3.55 (t, *J* = 9.6 Hz, 1H, H-4), 3.09 (s, 3H, OCH₃); ¹³C NMR (126 MHz, CD₃OD): δ = 145.0 (triazole-C_q), 132.9, 127.6, 126.7 (Ar-C), 123.6 (triazole-CH), 122.1 (Ar-C), 102.8 (C-1), 72.8 (C-5), 72.4 (C-3), 71.9 (C-4), 69.7 (C-2), 55.1 (OCH₃), 52.7 (C-6); HRMS: *m/z*: Calcd for C₁₃H₁₇N₃NaO₅S [M+Na]⁺: 350.0781, found: 350.0780.

Methyl 6-(4-cyclohexyl-1,2,3-triazol-1-yl)-6-deoxy- α -D-mannopyranoside (2b). According to general procedure A, CuBr (3 mg, 0.02 mmol, 0.20 eq), TBTA (10 mg, 0.02 mmol, 0.20 eq), cyclohexylacetylene (14 μ L, 0.11 mmol, 1.2 eq), and **8** (20 mg, 0.09 mmol, 1.0 eq) were reacted

in MeCN/H₂O (2:1, 10 mL) to give **2b** (10 mg, 0.03 mmol, 33 %) as a colorless solid. $[\alpha]_{\text{D}}^{20} +60.9$ (*c* 1.0, MeOH); ¹H NMR (500 MHz, CD₃OD): δ = 7.77 (s, 1H, triazole-H), 4.83 (m, 1H, H-6), 4.58 (d, *J* = 1.7 Hz, 1H, H-1), 4.45 (dd, *J* = 14.1, 8.8 Hz, 1H, H-6'), 3.80–3.72 (m, 2H, H-2, H-5), 3.65 (dd, *J* = 9.3, 3.4 Hz, 1H, H-3), 3.52 (t, *J* = 9.6 Hz, 1H, H-4), 3.06 (s, 3H, OCH₃), 2.73 (m, 1H, CH), 2.03–1.95 (m, 2H, CH₂), 1.87–1.78 (m, 2H, CH₂), 1.74 (m, 1H, CH₂), 1.50–1.39 (m, 4H, (CH₂)₂), 1.31 (m, 1H, CH₂); ¹³C NMR (126 MHz, CD₃OD): δ = 154.4 (triazole-C_q), 123.2 (triazole-CH), 102.8 (C-1), 73.0 (C-5), 72.4 (C-3), 71.9 (C-2), 69.7 (C-4), 55.0 (OCH₃), 52.5 (C-6), 36.5 (CH), 34.2 ((CH₂)₂), 27.2 (CH₂), 27.1 (CH₂); HRMS: *m/z*: Calcd for C₁₅H₂₅N₃NaO₅ [M+Na]⁺: 350.1686, found: 350.1687.

Methyl 6-deoxy-6-(4-(3-pyridinyl)-1,2,3-triazol-1-yl)- α -D-mannopyranoside (2c).

According to general procedure A, CuBr (3 mg, 0.02 mmol, 0.20 eq), TBTA (10 mg, 0.02 mmol, 0.20 eq), 3-ethynylpyridine (9 mg, 0.09 mmol, 1.0 eq), and **8** (20 mg, 0.09 mmol, 1.0 eq) were reacted in MeCN/H₂O (2:1, 10 mL) to give **2c** (33 mg, 0.07 mmol, 75%) as a colorless solid. $[\alpha]_{\text{D}}^{20} +32.9$ (*c* 1.0, MeOH); ¹H NMR (500 MHz, D₂O): δ = 8.90 (s, 2H, Ar-H), 8.50 (s, 1H, triazole-H), 8.22 (d, *J* = 7.7 Hz, 1H, Ar-H), 7.60 (s, 1H, Ar-H), 4.95 (dd, *J* = 14.5, 2.4 Hz, 1H, H-6), 4.72 (d, *J* = 1.7 Hz, 1H, H-1), 4.69 (dd, *J* = 14.5, 8.7 Hz, 1H, H-6'), 3.96 (m, 1H, H-5), 3.94 (m, 1H, H-2), 3.80 (dd, *J* = 9.6, 3.5 Hz, 1H, H-3), 3.64 (t, *J* = 9.7 Hz, 1H, H-4), 3.08 (s, 3H, OCH₃); ¹³C NMR (126 MHz, D₂O): δ = 123.9 (triazole-CH), 100.9 (C-1), 70.9 (C-5), 70.5 (C-3), 69.8 (C-4), 68.0 (C-2), 54.4 (OCH₃), 51.2 (C-6); presumably due to long T₂ relaxation times of aromatic nuclei, some signals for **2c** could not be observed, even with prolonged measurement times; HRMS: *m/z*: Calcd for C₁₄H₁₉N₄O₅ [M+H]⁺: 323.1350, found: 323.1349.

Methyl 6-deoxy-6-(4-((1,3-dioxoisindolin-2-yl)propyl)-1,2,3-triazol-1-yl)- α -D-mannopyranoside (2d).

According to general procedure A, CuBr (3 mg, 0.02 mmol, 0.20 eq), TBTA (10 mg, 0.02 mmol, 0.20 eq), *N*-(4-pentynyl)-phthalimide (19 mg, 0.09 mmol, 1.0 eq), and **8** (20 mg, 0.09 mmol, 1.0 eq) were reacted in MeCN/H₂O (2:1, 10 mL) to give **2d** (19 mg, 0.04 mmol, 55%) as a colorless solid. $[\alpha]_{\text{D}}^{20} -52.1$ (*c* 1.0, MeOH); ¹H NMR (500 MHz, CD₃OD): δ = 7.88–7.81 (m, 3H, triazole-H, Ar-H), 7.83–7.76 (m, 2H, Ar-H), 4.79 (dd, *J* = 14.1, 2.3 Hz, 1H, H-6), 4.59 (d, *J* = 1.7 Hz, 1H, H-1), 4.45 (dd, *J* = 14.1, 8.6 Hz, 1H, H-6'), 3.81–3.74 (m, 2H, H-2, H-5), 3.71 (t, *J* = 7.0 Hz, 2H, CH₂NPhth), 3.65 (dd, *J* = 9.4, 3.4 Hz, 1H, H-3), 3.49 (t, *J* = 9.6 Hz, 1H, H-4), 3.09 (s, 3H, OCH₃), 2.75 (t, *J* = 7.4 Hz, 2H, CH₂), 2.08–1.99 (m, 2H,

CH₂); ¹³C NMR (126 MHz, CD₃OD): δ = 169.8 (CO), 147.8 (triazole-C_q), 135.4, 133.4 (Ar-C), 124.9 (triazole-CH), 124.1 (Ar-C), 102.8 (C-1), 72.9 (C-5), 72.4 (C-3), 71.9 (C-4), 69.7 (C-2), 55.2 (OCH₃), 52.5 (C-6), 38.2 (CH₂NPhth), 29.3 (CH₂), 23.7 (CH₂); HRMS: *m/z*: Calcd for C₂₀H₂₄N₄NaO₇ [M+Na]⁺: 455.1537, found: 455.1537.

Methyl 6-(4-(benzyloxy)methyl)-1,2,3-triazol-1-yl)-6-deoxy-α-D-mannopyranoside (2e).

According to general procedure A, CuBr (3 mg, 0.02 mmol, 0.20 eq), TBTA (10 mg, 0.02 mmol, 0.20 eq), ((prop-2-yn-1-yloxy)methyl)benzene (16 μL, 0.11 mmol, 1.2 eq), and **8** (20 mg, 0.09 mmol, 1.0 eq) were reacted in MeCN/H₂O (2:1, 10 mL) to give **2e** (20 mg, 0.05 mmol, 60%) as a colorless solid. [α]_D²⁰ +53.9 (*c* 1.0, MeOH); ¹H NMR (500 MHz, CD₃OD): δ = 8.03 (s, 1H, triazole-H), 7.37–7.30 (m, 4H, Ar-H), 7.28 (m, 1H, Ar-H), 4.88 (m, 1H, H-6), 4.64 (s, 2H, CH₂OBn), 4.58 (d, *J* = 1.7 Hz, 1H, H-1), 4.57–4.48 (m, 3H, H-6', CH₂Ar), 3.83–3.75 (m, 2H, H-2, H-5), 3.66 (dd, *J* = 9.3, 3.4 Hz, 1H, H-3), 3.52 (t, *J* = 9.6 Hz, 1H, H-4), 3.05 (s, 3H, OCH₃); ¹³C NMR (126 MHz, CD₃OD): δ = 145.7 (triazole-C_q), 139.3, 129.4, 129.0, 128.8 (Ar-C), 126.6 (triazole-CH), 102.8 (C-1), 73.2 (CH₂Ar), 72.8 (C-5), 72.4 (C-3), 71.9 (C-2), 69.7 (C-4), 64.0 (CH₂OBn), 55.1 (OCH₃), 52.6 (C-6); HRMS: *m/z*: Calcd for C₁₇H₂₃N₃NaO₆ [M+Na]⁺: 388.1479, found: 388.1479.

Methyl 6-deoxy-6-(4-(4-methoxy-2-methylphenyl)-1,2,3-triazol-1-yl)-α-D-mannopyranoside (2f).

According to general procedure A, CuBr (3 mg, 0.02 mmol, 0.20 eq), TBTA (10 mg, 0.02 mmol, 0.20 eq), 1-ethynyl-4-methoxy-2-methylbenzene (13 mg, 0.09 mmol, 1 eq), and **8** (20 mg, 0.09 mmol, 1eq) were reacted in MeCN/H₂O (2:1, 10 mL) to give **2f** (21 mg, 0.06 mmol, 62%) as a colorless solid. [α]_D²⁰ -53.4 (*c* 1.0, MeOH); ¹H NMR (500 MHz, CD₃OD): δ = 8.09 (s, 1H, triazole-H), 7.50 (d, *J* = 8.4 Hz, 1H, Ar-H), 6.85 (d, *J* = 2.7 Hz, 1H, Ar-H), 6.83 (dd, *J* = 8.5, 2.7 Hz, 1H, Ar-H), 4.91 (dd, *J* = 14.1, 2.3 Hz, 1H, H-6), 4.61 (d, *J* = 1.7 Hz, 1H, H-1), 4.58 (dd, *J* = 14.1, 8.5 Hz, 1H, H-6'), 3.85 (ddd, *J* = 10.5, 8.5, 2.4 Hz, 1H, H-5), 3.81 (s, 3H, OCH₃), 3.79 (dd, *J* = 3.4, 1.7 Hz, 1H, H-2), 3.68 (dd, *J* = 9.4, 3.4 Hz, 1H, H-3), 3.55 (m, 1H, H-4), 3.11 (s, 3H, OCH₃), 2.38 (s, 3H, ArCH₃); ¹³C NMR (126 MHz, CD₃OD): δ = 161.2 (Ar-C), 147.6 (triazole-C_q), 138.6, 131.3 (Ar-C), 125.3 (triazole-CH), 123.7, 117.1, 112.5 (Ar-C), 102.9 (C-1), 72.9 (C-5), 72.4 (C-3), 71.9 (C-4), 69.7 (C-2), 55.7 (OCH₃), 55.1 (OCH₃), 52.6 (C-6), 21.4 (ArCH₃); HRMS: *m/z*: Calcd for C₁₇H₂₃N₃NaO₆ [M+Na]⁺: 388.1479, found: 388.1481.

Methyl 2-deoxy-2-(4-(pyridine-2-yl)-1,2,3-triazol-1-yl)- α -D-mannopyranoside (10).

According to general procedure A, CuBr (3 mg, 0.02 mmol, 0.2 eq), TBTA (11 mg, 0.02 mmol, 0.2 eq), 2-ethynylpyridine (12 mg, 0.12 mmol, 1.2 eq), and **6** (22 mg, 0.10 mmol, 1.0 eq) were reacted in MeCN/H₂O (2:1, 10 mL) to give **10** (30 mg, 0.09 mmol, 93%) as a colorless solid. $[\alpha]_{\text{D}}^{20}$ -26.4 (*c* 1.0, MeOH); ¹H NMR (500 MHz, CD₃OD): δ = 8.73 (s, 1H, triazole-H), 8.57 (br, 1H, Ar-H), 8.08 (d, *J* = 8.1 Hz, 1H, Ar-H), 7.91 (td, *J* = 7.8, 1.5 Hz, 1H, Ar-H), 7.36 (m, 1H, Ar-H), 5.14 (dd, *J* = 5.3, 1.4 Hz, 1H, H-2), 5.02 (d, *J* = 1.4 Hz, 1H, H-1), 4.21 (dd, *J* = 9.3, 5.3 Hz, 1H, H-3), 3.99–3.87 (m, 2H, H-6), 3.78 (t, *J* = 9.5 Hz, 1H, H-4), 3.72 (ddd, *J* = 9.8, 4.5, 2.6 Hz, 1H, H-5), 3.47 (s, 3H, OCH₃); ¹³C NMR (126 MHz, CD₃OD): δ = 150.4, 139.0 (Ar-C), 124.6 (2C, Ar-C, triazole-CH), 121.7 (Ar-C), 100.4 (C-1), 74.9 (C-5), 70.3 (C-3), 67.9 (C-4), 65.6 (C-2), 62.3 (C-6), 55.6 (OCH₃); ESI-MS: *m/z*: Calcd for C₁₄H₁₈N₄NaO₅ [M+Na]⁺: 345.1169, found: 345.1170.

Methyl 2-deoxy-2-(4-phenyl-1,2,3-triazol-1-yl)- α -D-mannopyranoside (11).

According to general procedure A, CuBr (3 mg, 0.02 mmol, 0.2 eq), TBTA (11 mg, 0.02 mmol, 0.2 eq), phenyl acetylene (15 mg, 0.15 mmol, 1.5 eq), and **6** (22 mg, 0.10 mmol, 1.0 eq) were reacted in MeCN/H₂O (2:1, 10 mL) to give **11** (26 mg, 0.08 mmol, 81%) as a colorless solid. $[\alpha]_{\text{D}}^{20}$ -23.6 (*c* 1.0, MeOH); ¹H NMR (500 MHz, CD₃OD): δ = 8.57 (s, 1H, triazole-H), 7.87–7.78 (m, 2H, Ar-H), 7.47–7.39 (m, 2H, Ar-H), 7.34 (m, 1H, Ar-H), 5.11 (dd, *J* = 5.2, 1.3 Hz, 1H, H-2), 5.00 (d, *J* = 1.5 Hz, 1H, H-1), 4.20 (dd, *J* = 9.5, 5.2 Hz, 1H, H-3), 4.00–3.80 (m, 3H, H-4, H-6), 3.69 (ddd, *J* = 9.8, 3.7, 2.1 Hz, 1H, H-5), 3.46 (s, 3H, OCH₃); ¹³C NMR (126 MHz, CD₃OD): δ = 148.6 (triazole-C_q), 131.8, 129.9, 129.3, 126.7 (Ar-C), 122.6 (triazole-CH), 100.5 (C-1), 74.7 (C-5), 70.3 (C-3), 67.5 (C-4), 65.6 (C-2), 61.7 (C-6), 55.5 (OCH₃); ESI-MS: *m/z*: Calcd for C₁₅H₁₉N₃NaO₅ [M+Na]⁺: 344.1217, found: 344.1218.

Methyl 2-deoxy-2-(4-(2-methoxycarbonyl)phenyl)-1,2,3-triazol-1-yl)- α -D-mannopyranoside (12).

According to general procedure A, CuBr (3 mg, 0.02 mmol, 0.2 eq), TBTA (11 mg, 0.02 mmol, 0.2 eq), methyl 2-ethynylbenzoate (20 mg, 0.12 mmol, 1.2 eq), and **6** (22 mg, 0.10 mmol, 1.0 eq) were reacted (μ w, 120 °C, 200 W, 2 h) in MeCN/H₂O (2:1, 10 mL) to give **12** (36 mg, 0.10 mmol, 95%) as a colorless solid. $[\alpha]_{\text{D}}^{20}$ -1.8 (*c* 1.0, MeOH); ¹H NMR (500 MHz, CD₃OD): δ = 8.41 (s, 1H, triazole-H), 7.81 (dd, *J* = 7.8, 1.1 Hz, 1H, Ar-H), 7.71 (dd, *J* = 7.7, 0.9 Hz, 1H, Ar-H), 7.63 (td, *J* = 7.6, 1.3 Hz, 1H, Ar-H), 7.51 (td, *J* = 7.6, 1.2 Hz, 1H, Ar-H), 5.13 (dd, *J* = 5.2, 1.2 Hz, 1H, H-2), 5.03 (d, *J* = 1.5 Hz, 1H, H-1), 4.22 (dd, *J* = 9.5,

5.2 Hz, 1H, H-3), 3.92 (d, $J = 3.3$ Hz, 2H, H-6), 3.87–3.79 (m, 4H, H-4, CO₂CH₃), 3.72 (dt, $J = 9.8, 3.3$ Hz, 1H, H-5), 3.49 (s, 3H, OCH₃); ¹³C NMR (126 MHz, CD₃OD): $\delta = 170.4$ (CO), 146.8 (triazole-C_q), 132.6, 132.2, 131.4, 131.2, 130.8, 129.5 (Ar-C), 124.8 (triazole-CH), 100.5 (C-1), 74.8 (C-5), 70.3 (C-3), 67.7 (C-4), 65.6 (C-2), 62.0 (C-6), 55.5 (OCH₃), 52.9 (CO₂CH₃); ESI-MS: m/z : Calcd for C₁₇H₂₁N₃NaO₇ [M+Na]⁺: 402.1272, found: 402.1272.

Methyl 2-deoxy-2-(4-(2,6-dichlorophenyl)-1,2,3-triazol-1-yl)- α -D-mannopyranoside (13).

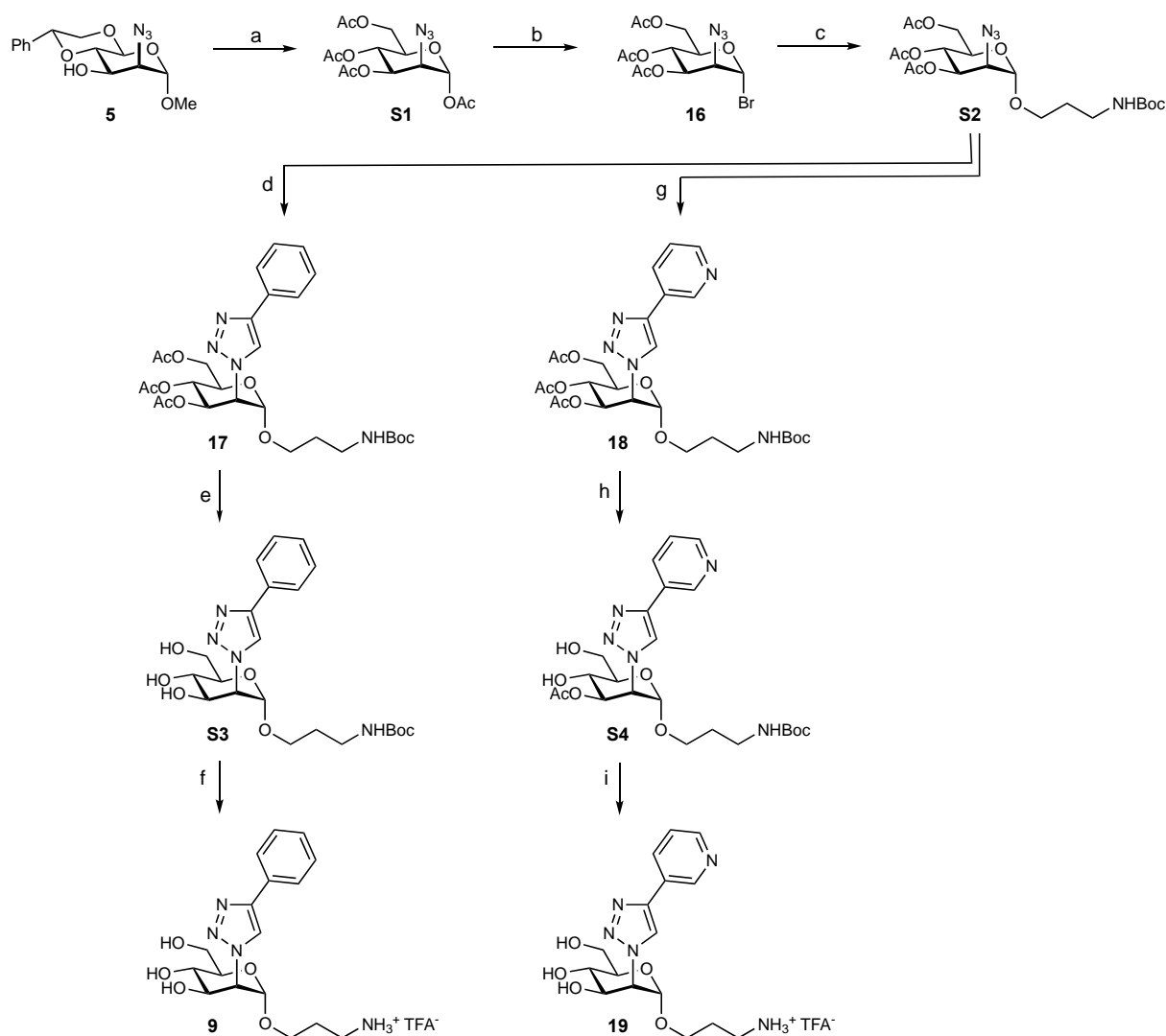
According to general procedure A, CuBr (3 mg, 0.02 mmol, 0.2 eq), TBTA (11 mg, 0.02 mmol, 0.2 eq), 1,3-dichloro-2-ethynylbenzene (20 mg, 0.12 mmol, 1.2 eq), and **6** (22 mg, 0.10 mmol, 1.0 eq) were reacted (μ w, 120 °C, 200 W, 5 h) in MeCN/H₂O (2:1, 10 mL) to give **13** (36 mg, 0.09 mmol, 92%) as a colorless solid. $[\alpha]_{\text{D}}^{20} +8.0$ (c 1.0, MeOH); ¹H NMR (500 MHz, CD₃OD): $\delta = 8.43$ (s, 1H, triazole-H), 7.53–7.49 (m, 2H, Ar-H), 7.41 (dd, $J = 8.7, 7.5$ Hz, 1H, Ar-H), 5.16 (dd, $J = 5.1, 1.1$ Hz, 1H, H-2), 5.05 (d, $J = 1.7$ Hz, 1H, H-1), 4.23 (dd, $J = 9.5, 5.1$ Hz, 1H, H-3), 3.87 (d, $J = 3.2$ Hz, 2H, H-6), 3.80 (t, $J = 9.7$ Hz, 1H, H-4), 3.69 (dt, $J = 9.8, 3.2$ Hz, 1H, H-5), 3.47 (s, 3H, OCH₃); ¹³C NMR (126 MHz, CD₃OD): $\delta = 142.5$ (triazole-C_q), 137.3, 132.1, 130.3, 129.5 (Ar-C), 126.9 (triazole-CH), 100.5 (C-1), 74.8 (C-5), 70.2 (C-3), 67.6 (C-4), 65.6 (C-2), 61.8 (C-6), 55.6 (OCH₃); HRMS: m/z : Calcd for C₁₅H₁₇Cl₂N₃NaO₅ [M+Na]⁺: 412.0438, found: 412.0437.

Methyl 2-deoxy-2-(4-(4-methoxy-2-methylphenyl)-1,2,3-triazol-1-yl)- α -D-mannopyranoside (14). According to general procedure A, CuBr (3 mg, 0.02 mmol, 0.2 eq), TBTA (11 mg, 0.02 mmol, 0.2 eq), 1-ethynyl-4-methoxy-2-methylbenzene (15 mg, 0.12 mmol, 1.2 eq), and **6** (22 mg, 0.10 mmol, 1.0 eq) were reacted (μ w, 120 °C, 200 W, 5 h) in MeCN/H₂O (2:1, 10 mL) to give **14** (35 mg, 0.10 mmol, 96%) as a colorless solid. $[\alpha]_{\text{D}}^{20} -9.5$ (c 1.0, MeOH); ¹H NMR (500 MHz, CD₃OD): $\delta = 8.34$ (s, 1H, triazole-H), 7.56 (d, $J = 8.4$ Hz, 1H, Ar-H), 6.87–6.80 (m, 2H, Ar-H), 5.11 (dd, $J = 5.2, 1.3$ Hz, 1H, H-2), 5.00 (d, $J = 1.5$ Hz, 1H, H-1), 4.21 (dd, $J = 9.6, 5.2$ Hz, 1H, H-3), 3.96–3.84 (m, 3H, H-4, H-6), 3.81 (s, 3H, ArOCH₃), 3.68 (ddd, $J = 9.6, 3.5, 2.1$ Hz, 1H, H-5), 3.46 (s, 3H, OCH₃), 2.41 (s, 3H, ArCH₃). ¹³C NMR (126 MHz, CD₃OD): $\delta = 161.1$ (Ar-C), 147.7 (triazole-C_q), 138.6, 131.2 (Ar-C), 124.2 (triazole-CH), 123.6, 117.1, 112.5 (Ar-C), 100.5 (C-1), 74.6 (C-5), 70.3 (C-3), 67.5 (C-4), 65.5 (C-2), 61.6 (C-6), 55.7 (ArOCH₃), 55.5 (OCH₃), 21.5 (ArCH₃); HRMS: m/z : Calcd for C₁₇H₂₃N₃NaO₆ [M+Na]⁺: 388.1479, found: 388.1479.

Methyl 2-deoxy-2-(4-(quinoline-3-yl)-1,2,3-triazol-1-yl)- α -D-mannopyranoside (15).

According to general procedure A, CuBr (4 mg, 0.03 mmol, 0.2 eq), TBTA (16 mg, 0.03 mmol, 0.2 eq), 4-ethynylisoquinoline (26 mg, 0.17 mmol, 1.1 eq), and **6** (33 mg, 0.15 mmol, 1.0 eq) were reacted in MeCN/H₂O (2:1, 10 mL) to give **15** (48 mg, 0.13 mmol, 86%) as a light yellow solid. $[\alpha]_D^{20} -32.7$ (*c* 1.0, MeOH); ¹H NMR (500 MHz, CD₃OD): δ = 9.33 (br, 1H, Ar-H), 8.81 (s, 1H, triazole-H), 8.70 (s, 1H, Ar-H), 8.15–7.86 (m, 2H, Ar-H), 7.76 (m, 1H, Ar-H), 7.61 (dd, *J* = 8.0, 7.0 Hz, 1H, Ar-H), 5.18 (dd, *J* = 5.2, 1.2 Hz, 1H, H-2), 5.05 (d, *J* = 1.5 Hz, 1H, H-1), 4.25 (dd, *J* = 9.5, 5.2 Hz, 1H, H-3), 4.03–3.93 (m, 2H, H-6), 3.91 (t, *J* = 9.8 Hz, 1H, H-4), 3.73 (ddd, *J* = 9.8, 3.5, 2.4 Hz, 1H, H-5), 3.48 (s, 3H, OCH₃); ¹³C NMR (126 MHz, CD₃OD): δ = 149.0 (Ar-C), 145.6 (triazole-C_q), 133.5, 131.2, 129.6, 129.3, 128.7 (Ar-C), 123.6 (triazole-CH), 100.4 (C-1), 74.7 (C-5), 70.3 (C-3), 67.5 (C-4), 65.7 (C-2), 61.8 (C-6), 55.6 (OCH₃); HRMS: *m/z*: Calcd for C₁₈H₂₀N₄NaO₅ [M+Na]⁺: 395.1326, found: 395.1327.

Synthesis of DC-SIGN antagonists **9** and **19**.



Scheme S1. a) Sulfuric acid, Ac₂O (85%); b) BiBr₃, Me₃SiBr, DCM (92%); c) 3-(Boc-amino)-1-propanol, I₂, K₂CO₃, MeCN (34%); d) phenylacetylene, TBTA, CuBr, MeCN (86%); e) MeONa, MeOH (67%); f) TFA, DCM (98%); g) 3-ethynylpyridine, TBTA, CuBr, MeCN (74%); h) MeONa, MeOH (70%); i) TFA, DCM (90%).

General procedure B for glycosylation. To a solution of glycosyl bromide (1.00 eq) in dry MeCN (0.10 mmol/ml) in a heat-dried two-neck flask, 4 Å molecular sieves, the glycosyl acceptor (1.10 eq), K₂CO₃ (1.50 eq) and I₂ (1.50 eq) were successively added under argon. The reaction mixture was stirred at rt for 6 h to 18h under argon. After filtration over celite, the filtrate was concentrated under reduced pressure and purified by flash chromatography to yield the desired product.

General procedure C for Zemplén deacetylation. To a solution of the acetylated mannopyranoside (1.00 eq) in MeOH (0.07 mmol/ml), a 25 wt. % solution of sodium

methoxide in MeOH (0.30 eq.) was added. The reaction mixture was stirred at rt until TLC analysis indicated the complete consumption of starting material. The crude product was concentrated under reduced pressure and purified by flash chromatography to yield the desired product.

1,3,4,6-Tetra-*O*-acetyl-2-azido-2-deoxy- α -D-mannopyranoside (S1). To a solution of **5** (2.60 g, 8.46 mmol, 1.00 eq) in Ac₂O (47 ml) sulfuric acid (1.50 ml, 27.9 mmol, 3.30 eq) was added. The reaction mixture was stirred at rt under argon for 2 h. The reaction was followed by TLC and MS. After complete consumption of the starting material, the reaction mixture was diluted with EtOAc followed by dropwise addition of cold satd. aq. NaHCO₃ at 0 °C. The water layer was separated and extracted three time with EtOAc. The combined organic layers were washed twice with water, dried over Na₂SO₄, filtered and concentrated under reduced pressure. The crude product was purified by flash chromatography (petroleum ether/EtOAc, 7:3) to yield **S1** (2.70 g, 7.23 mmol, 85%) as a colorless solid. ¹H NMR (500 MHz, CDCl₃): δ = 6.12 (d, *J* = 1.9 Hz, 1H, H-1), 5.44–5.34 (m, 2H, H-3, H-4), 4.25 (dd, *J* = 12.4, 4.5 Hz, 1H, H-6), 4.10 (dd, *J* = 12.5, 2.4 Hz, 1H, H-6'), 4.06–3.99 (m, 2H, H-2, H-5), 2.17, 2.12, 2.10, 2.06 (4 s, 12H, 4 COCH₃); ¹³C NMR (126 MHz, CDCl₃): δ = 170.9, 170.2, 169.5, 168.3 (4 CO), 91.6 (C-1), 70.9 (C-2), 70.7 (C-3), 65.5 (C-4), 61.9 (C-6), 60.7 (C-5), 21.0, 20.9, 20.8, 20.7 (4 CH₃CO); ESI-MS: *m/z*: Calcd for C₁₄H₁₉N₃NaO₉ [M+Na]⁺: 396.3, found: 396.0.

3,4,6-Tri-*O*-acetyl-2-azido-2-deoxy- α -D-mannopyranosyl bromide (16). To a solution of **S1** (1.80 g, 4.82 mmol, 1.00 eq) and BiBr₃ (108 mg, 0.24 mmol, 0.05 eq) in DCM (35 ml) trimethylsilyl bromide (2.50 ml, 19.3 mmol, 4.00 eq) was added under argon. The reaction mixture was stirred at rt under argon until complete consumption of starting material (1 h). Then, water (30 ml) was added to the reaction mixture. The water layer was separated and extracted three times with DCM. The combined organic layers were washed twice with water, dried over Na₂SO₄, filtered and concentrated under reduced pressure to yield **16** (1.75 g, 4.44 mmol, 92%). ¹H NMR (500 MHz, CDCl₃): δ = 6.36 (d, *J* = 1.6, 1H, H-1), 5.69 (dd, *J* = 10.0, 3.8 Hz, 1H, H-3), 5.40 (t, *J* = 10.1 Hz, 1H, H-4), 4.33 (dd, *J* = 3.8, 1.6 Hz, 1H, H-2), 4.30 (dd, *J* = 12.6, 4.3 Hz, 1H, H-6), 4.17 (m, 1H, H-5), 4.11 (dd, *J* = 12.6, 2.1 Hz, 1H, H-6'), 2.12, 2.11, 2.08 (3 s, 9H, 3 COCH₃); ¹³C NMR (126 MHz, CDCl₃): δ = 170.8, 170.1, 169.6 (3 CO), 83.8 (C-1), 73.0 (C-5), 70.0 (C-3), 64.9 (C-2, C-4), 61.2 (C-6), 20.9, 20.8, 20.7 (3 CH₃CO). ESI-MS: *m/z*: Calcd for C₁₂H₁₇BrO₇ [M+H]⁺: 394.0 (100%) and 396.0 (99.7%), found: 396.2.

***N*-(*tert*-Butyloxycarbonyl)-3-aminopropyl 3,4,6-tri-*O*-acetyl-2-azido-2-deoxy- α -D-mannopyranoside (**S2**).** According to general procedure B, **16** (500 mg, 1.27 mmol, 1.00 eq), MeCN (15 ml), *tert*-butyl (3-hydroxypropyl)carbamate (233 mg, 1.33 mmol, 1.05 eq), K₂CO₃ (263 mg, 1.80 mmol, 1.50 eq), I₂ (482 mg, 1.90 mmol, 1.50 eq) were reacted for 18 h. Purification by flash chromatography (petroleum ether/EtOAc, 13:7) gave **S2** (210 mg, 0.43 mmol, 34%; α/β ratio: 8/2) as a colorless oil. ¹H NMR (500 MHz, CDCl₃): δ = 5.36 (dd, *J* = 9.8, 3.7 Hz, 1H, H-3), 5.31 (t, *J* = 9.8 Hz, 1H, H-4), 4.82 (d, *J* = 1.7 Hz, 1H, H-1), 4.63 (s, 1H, NH), 4.25 (dd, *J* = 12.3, 4.9 Hz, 1H, H-6), 4.08 (dd, *J* = 12.3, 2.4 Hz, 1H, H-6'), 4.03 (m, 1H, H-2), 3.93 (m, 1H, H-5), 3.75 (dt, *J* = 9.9, 6.0 Hz, 1H, CH₂O), 3.49 (dt, *J* = 9.9, 6.1 Hz, 1H, CH₂O), 3.29–3.16 (m, 2H, CH₂N), 2.10, 2.09, 2.04 (3 s, 9H, 3 COCH₃), 1.79 (m, 2H, CH₂), 1.44 (s, 9H, C(CH₃)₃); ¹³C NMR (126 MHz, CDCl₃): δ = 170.8, 170.0, 169.6 (3 CO), 156.0 (NC=O), 98.3 (C-1), 79.4 (C(CH₃)₃), 71.1 (C-3), 68.6 (C-5), 66.0 (2C, C-4, CH₂O), 62.3 (C-6), 61.6 (C-2), 37.7 (CH₂N), 29.8 (CH₂), 28.4 (C(CH₃)₃), 20.8, 20.7, 20.6 (3 COCH₃); ESI-MS: *m/z*: Calcd for C₂₀H₃₂N₄NaO₁₀ [M+Na]⁺: 511.5, found : 511.2.

***N*-(*tert*-Butyloxycarbonyl)-3-aminopropyl 3,4,6-tri-*O*-acetyl-2-deoxy-2-(4-phenyl-1,2,3-triazol-1-yl)- α -D-mannopyranoside (**17**).** According to general procedure A, **S2** (210 mg, 0.43 mmol, 1.00 eq), MeCN (20 ml), phenylacetylene (57 μ l, 0.52 mmol, 1.20 eq), CuBr (12 mg, 86 μ mol, 0.20 eq.), and TBTA (45 mg, 86 μ mol, 0.20 eq) were stirred for 18 h. Purification by flash chromatography (petroleum ether/EtOAc, 6:4) yielded **17** (220 mg, 0.37 mmol, 86%; α/β ratio: 8/2) as a colorless oil. ¹H NMR (500 MHz, CDCl₃): δ = 8.28 (s, 1H, Ar-H), 7.88–7.83 (m, 2H, Ar-H), 7.48–7.40 (m, 2H, Ar-H), 7.36 (m, 1H, Ar-H), 5.52 (dd, *J* = 10.1, 5.2 Hz, 1H, H-3), 5.47 (dd, *J* = 5.2, 1.4 Hz, 1H, H-2), 5.32 (t, *J* = 10.0 Hz, 1H, H-4), 5.11 (d, *J* = 1.3 Hz, 1H, H-1), 4.67 (s, 1H, NH), 4.38 (m, 1H, H-6), 4.22–4.15 (m, 2H, H-5, H-6'), 3.85 (m, 1H, CH₂O), 3.58 (m, 1H, CH₂O), 3.31–3.23 (m, 2H, CH₂N), 2.16, 2.04, 1.96 (3 s, 9H, 3 COCH₃), 1.94–1.78 (m, 2H, CH₂), 1.43 (s, 9H, C(CH₃)₃); ¹³C NMR (126 MHz, CDCl₃): δ = 170.6, 170.2, 169.5 (3 CO), 148.3, 130.5, 129.0, 128.6, 125.9, 119.4 (Ar-C), 98.1 (C-1), 79.2 (C(CH₃)₃) 68.7 (2C, C-3, C-5), 66.6 (CH₂O), 64.9 (C-4), 62.2 (C-6), 60.5 (C-2), 37.7 (CH₂N), 30.0 (CH₂), 28.5 (C(CH₃)₃), 20.9, 20.8, 20.7 (3 COCH₃); ESI-MS: *m/z*: Calcd for C₂₈H₃₈N₄NaO₁₀ [M+Na]⁺: 613.6, found: 613.2.

***N*-(*tert*-Butyloxycarbonyl)-3-aminopropyl 2-deoxy-2-(4-phenyl-1,2,3-triazol-1-yl)- α -D-mannopyranoside (**S3**).** According to general procedure C, **17** (210 mg, 0.36 mmol, 1.00 eq), and a 25 wt.% solution of NaOMe in MeOH (30 μ l, 0.11 mmol, 0.30 eq) were stirred for 1 h

in MeOH (6 ml). Purification by flash chromatography (DCM/MeOH, 95:5) yielded **S3** (110 mg, 0.24 mmol, 67%; 100 % α) as a colorless oil. ^1H NMR (500 MHz, CD_3OD): δ = 8.57 (s, 1H, Ar-H), 7.85–7.80 (m, 2H, Ar-H), 7.46–7.40 (m, 2H, Ar-H), 7.34 (m, 1H, Ar-H), 5.14 (dd, J = 5.2, 1.4 Hz, 1H, H-2), 5.10 (d, J = 1.4 Hz, 1H, H-1), 4.23 (dd, J = 9.5, 5.2 Hz, 1H, H-3), 3.95 (dd, J = 12.0, 3.7 Hz, 1H, H-6), 3.89 (dd, J = 12.3, 2.7 Hz, 1H, H-6'), 3.87–3.79 (m, 2H, H-4, CH_2O), 3.73 (dt, J = 10.3, 2.9 Hz, 1H, H-5), 3.54 (dt, J = 9.9, 6.0 Hz, 1H, CH_2O), 3.26–3.12 (m, 2H, CH_2N), 1.81 (m, 2H, CH_2), 1.43 (s, 9H, $\text{C}(\text{CH}_3)_3$); ^{13}C NMR (126 MHz, CD_3OD): δ = 158.6 (NC=O), 148.6, 131.8, 130.0, 129.3, 126.7, 122.6 (Ar-C), 99.6 (C-1), 80.00 ($\text{C}(\text{CH}_3)_3$), 74.9 (C-5), 70.4 (C-3), 67.6 (C-4), 66.5 (CH_2O), 65.7 (C-2), 61.7 (C-6), 38.4 (CH_2N), 30.8 (CH_2), 28.8 ($\text{C}(\text{CH}_3)_3$); ESI-MS: m/z : Calcd for $\text{C}_{22}\text{H}_{32}\text{N}_4\text{NaO}_7$ [$\text{M}+\text{Na}$] $^+$: 487.5, found:487.3.

3-Aminopropyl 2-deoxy-2-(4-phenyl-1,2,3-triazol-1-yl)- α -D-mannopyranoside trifluoroacetate salt (9). A mixture of **S3** (20 mg, 43 μmol , 1.00 eq) in DCM (0.5 ml) and TFA (0.5 ml) was stirred at rt under argon for 30 min. The solution was concentrated under reduced pressure, diluted with water and lyophilized to yield **9** (20 mg, 42 μmol , 98%) as a white solid. $[\alpha]_{\text{D}}^{20}$ +6.6 (c 1.0, MeOH); ^1H NMR (500 MHz, CD_3OD): δ = 8.56 (s, 1H, Ar-H), 7.93–7.77 (m, 2H, Ar-H), 7.51–7.40 (m, 2H, Ar-H), 7.35 (m, 1H, Ar-H), 5.15 (m, 2H, H-1, H-2), 4.23–4.16 (m, 1H, H-3), 3.98–3.89 (m, 3H, H-6, CH_2O), 3.86 (t, J = 9.4 Hz, 1H, H-4), 3.71 (m, 1H, H-5), 3.62 (m, 1H, CH_2O), 3.18–3.01 (m, 2H, CH_2N), 2.08–1.93 (m, 2H, CH_2); ^{13}C NMR (126 MHz, CD_3OD): δ = 147.3, 130.3, 128.6, 128.0, 125.3, 121.2 (Ar-C), 98.0 (C-1), 73.9 (C-5), 69.0 (C-3), 66.3 (C-4), 64.5 (CH_2O), 64.0 (C-2), 60.4 (C-6), 37.2 (CH_2N), 27.0 (CH_2); ESI-MS: m/z : Calcd for $\text{C}_{17}\text{H}_{24}\text{N}_4\text{NaO}_5$ [$\text{M}+\text{Na}$] $^+$: 387.1639, found: 387.1639.

***N*-(tert-Butyloxycarbonyl)-3-aminopropyl 3,4,6-tri-*O*-acetyl-2-deoxy-2-(4-pyridin-3-yl-1,2,3-triazol-1-yl)- α -D-mannopyranoside (18)**. According to general procedure A, **S2** (50 mg, 0.10 mmol, 1.00 eq), MeCN (5 ml), 3-ethynylpyridine (11.5 mg, 0.11 mmol, 1.10 eq), CuBr (3 mg, 20 μmol , 0.20 eq), and TBTA (11 mg, 20 μmol , 0.20 eq) were stirred for 18 h. Purification by flash chromatography (DCM/*i*PrOH, 19:1) yielded **18** (44 mg, 74 μmol , 74 %; 100 % α) as a colorless oil. ^1H NMR (500 MHz, CD_3OD): δ = 9.14 (s, 1H, Ar-H), 8.66 (s, 2H, Ar-H), 8.35 (d, J = 7.9 Hz, 1H, Ar-H), 7.60 (s, 1H, Ar-H), 5.55 (dd, J = 10.0, 5.1 Hz, 1H, H-3), 5.49 (m, 1H, H-2), 5.40 (t, J = 10.0 Hz, 1H, H-4), 5.27 (s, 1H, H-1), 4.42 (dd, J = 12.1, 4.1 Hz, 1H, H-6), 4.30–4.20 (m, 2H, H-5, H-6), 3.89 (dt, J = 9.8, 6.0 Hz, 1H, CH_2O), 3.61 (dt, J =

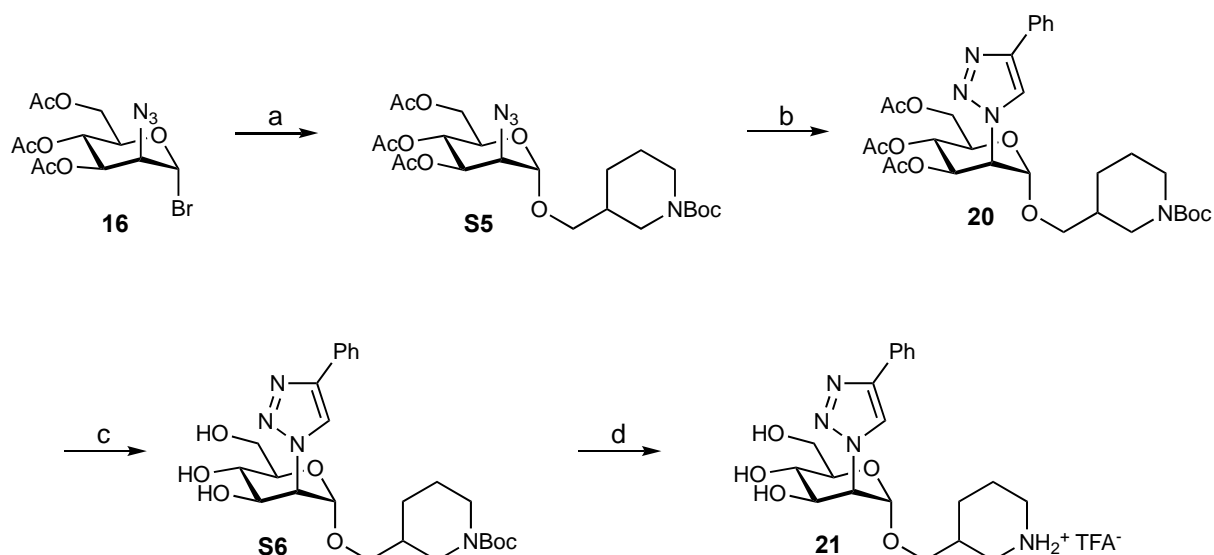
9.9, 6.1 Hz, 1H, CH₂O), 3.23 (q, $J = 6.3$ Hz, 2H, CH₂N), 2.11, 2.05, 1.93 (3 s, 9H, 3 COCH₃), 1.85 (t, $J = 6.5$ Hz, 2H, CH₂), 1.43 (s, 9H, C(CH₃)₃); ¹³C NMR (126 MHz, CD₃OD): $\delta = 172.3$, 171.4, 171.4 (3 CO), 144.1, 134.9, 123.0 (Ar-C), 99.1 (C-1), 80.0 (C(CH₃)₃), 70.3 (C-3), 70.0 (C-5), 67.1 (CH₂O), 66.5 (C-4), 63.4 (C-6), 62.2 (C-2), 38.2 (CH₂N), 30.7 (CH₂), 28.8 (C(CH₃)₃), 20.8, 20.6, 20.5 (3 COCH₃); ESI-MS: m/z : Calcd for C₂₇H₃₈N₅O₁₀ [M+H]⁺: 592.6, found: 592.3.

***N*-(*tert*-Butyloxycarbonyl)-3-aminopropyl 2-deoxy-2-(4-pyridin-3-yl-1,2,3-triazol-1-yl)- α -D-mannopyranoside (S4).** According to general procedure C, **18** (40 mg, 67 μ mol, 1.00 eq), and a 25 wt.% solution of NaOMe in MeOH (6 μ l, 20 μ mol, 0.30 eq) were stirred for 1 h in MeOH (1 ml). Purification by flash chromatography (DCM/ *i*PrOH, 85:15) yielded **S4** (22 mg, 47 μ mol, 70 %) as a colorless oil. ¹H NMR (500 MHz, CD₃OD): $\delta = 9.02$ (dd, $J = 2.3, 0.8$ Hz, 1H, Ar-H), 8.71 (s, 1H, Ar-H), 8.51 (dd, $J = 4.9, 1.6$ Hz, 1H, Ar-H), 8.29 (dt, $J = 8.0, 1.9$ Hz, 1H, Ar-H), 7.53 (ddd, $J = 7.9, 4.9, 0.9$ Hz, 1H, Ar-H), 5.17 (dd, $J = 5.2, 1.4$ Hz, 1H, H-2), 5.11 (d, $J = 1.4$ Hz, 1H, H-1), 4.24 (dd, $J = 9.5, 5.2$ Hz, 1H, H-3), 3.95 (dd, $J = 12.0, 3.7$ Hz, 1H, H-6), 3.90 (dd, $J = 12.0, 2.3$ Hz, 1H, H-6'), 3.87–3.80 (m, 2H, CH₂O, H-4), 3.73 (dt, $J = 10.4, 3.0$ Hz, 1H, H-5), 3.54 (dt, $J = 9.8, 6.2$ Hz, 1H, CH₂O), 3.26–3.11 (m, 2H, CH₂N), 1.81 (p, $J = 6.5$ Hz, 2H, CH₂), 1.43 (s, 9H, C(CH₃)₃); ¹³C NMR (126 MHz, CD₃OD): $\delta = 149.5, 147.3, 145.1, 135.0, 128.8, 125.6, 123.4$ (Ar-C), 99.5 (C-1), 80.0 (C(CH₃)₃), 74.9 (C-5), 70.3 (C-3), 67.5 (C-4), 66.5 (CH₂O), 65.8 (C-2), 61.7 (C-6), 38.3 (CH₂N), 30.8 (CH₂), 28.8 (C(CH₃)₃); ESI-MS: m/z : Calcd for C₂₁H₃₂N₅O₇ [M+H]⁺: 466.5, found: 466.2.

3-Aminopropyl 2-deoxy-2-(4-pyridin-3-yl-1,2,3-triazol-1-yl)- α -D-mannopyranoside trifluoroacetate salt (19). A mixture of **S4** (14 mg, 30 μ mol, 1.00 eq) in DCM (0.5 ml) and TFA (0.5 ml) was stirred at rt under argon for 30 min. The product was concentrated under reduced pressure, diluted with water and lyophilized to yield **19** (13 mg, 27 μ mol, 90 %) as a white solid. $[\alpha]_D^{20} +5.8$ (c 1.0, MeOH); ¹H NMR (500 MHz, CD₃OD): $\delta = 9.21$ (s, 1H, Ar-H), 8.75 (s, 1H, Ar-H), 8.53 (d, $J = 8.0$ Hz, 1H, Ar-H), 7.77 (s, 1H, Ar-H), 5.20 (dd, $J = 5.2, 1.6$ Hz, 1H, H-2), 5.17 (d, $J = 1.5$ Hz, 1H, H-1), 4.21 (dd, $J = 9.3, 5.2$ Hz, 1H, H-3), 4.01–3.87 (m, 3H, H-6, CH₂O), 3.83 (t, $J = 9.5$ Hz, 1H, H-4), 3.72 (m, 1H, H-5), 3.63 (m, 1H, CH₂O), 3.15–3.06 (m, 2H, CH₂N), 2.07–1.97 (m, 2H, CH₂); ¹³C NMR (126 MHz, CD₃OD): $\delta = 137.3, 124.0$ (Ar-C), 99.4 (C-1), 75.2 (C-5), 70.4 (C-3), 67.7 (C-4), 66.0 (CH₂O), 65.5 (C-2), 61.8 (C-6),

38.6 (CH₂N), 28.5 (CH₂). ESI-MS: *m/z*: Calcd for C₁₆H₂₃N₅NaO₅ [M+Na]⁺: 388.1591, found: 388.1591.

Synthesis of DC-SIGN antagonist **21**.



Scheme S2. a) *rac*-1-Boc-3-(hydroxymethyl)piperidine, I₂, K₂CO₃, CH₃CN (50%); b) phenylacetylene, TBTA, CuBr, CH₃CN (84%); c) NaOMe, MeOH (86%); d) TFA, DCM (81%).

((3*RS*)-1-(*tert*-Butyloxycarbonyl)-piperidin-3-yl)methyl 3,4,6-tri-*O*-acetyl-2-azido-2-deoxy- α -D-mannopyranoside (S5**). According to general procedure B, **16** (100 mg, 0.25 mmol, 1.00 eq), MeCN (5 ml), *rac*-1-Boc-3-(hydroxymethyl)piperidine (20 mg, 0.28 mmol, 1.10 eq), K₂CO₃ (53 mg, 0.38 mmol, 1.50 eq), I₂ (97 mg, 0.38 mmol, 1.50 eq) were reacted for 18 h. Filtration by flash chromatography (petroleum ether/EtOAc, 7:3) gave a mixture of **S5** and *rac*-1-Boc-3-(hydroxymethyl)piperidine as a colorless oil. This crude product was dissolved in DCM (3 ml) and treated with pyridine (45 μ L) and acetic anhydride (44 μ L). The reaction mixture was stirred overnight. The product was concentrated in vacuo and purified by flash chromatography (petroleum ether/EtOAc, 7:3) to yield **S5** (30 mg, 57 μ mol, 25%) as a colorless oil. ¹H NMR (500 MHz, CDCl₃): δ = 5.39–5.26 (m, 4H, H-3_{a,b}, H-4_{a,b}), 4.80 (m, 2H, H-1_{a,b}), 4.23 (dd, *J* = 12.3, 4.9 Hz, 2H, H-6_{a,b}), 4.12–4.06 (m, 2H, H-6'_{a,b}), 4.06–3.99 (m, 2H, H-2_{a,b}), 3.99–3.71 (m, 6H, H-5_{a,b}, CH₂), 3.56 (dd, *J* = 9.8, 5.6 Hz, 2H, OCH₂_{a,b}), 3.32 (dd, *J* = 9.8, 6.9 Hz, 2H, OCH₂_{a,b}), 2.99–2.78 (m, 2H, CH₂), 2.75 (dd, *J* = 13.1, 9.3 Hz, 1H, CH₂), 2.65 (dd, *J* = 13.1, 9.7 Hz, 1H, CH₂), 2.11–2.01 (m, 18H, COCH₃), 1.89–1.73 (m, 4H, CH, CH₂), 1.63 (d, *J* = 12.0 Hz, 3H, CH₂), 1.52–1.38 (m, 18H, C(CH₃)₃), 1.31–1.16 (m, 3H, CH₂); ¹³C NMR (126 MHz, CDCl₃): δ = 170.8, 170.0, 169.7 (3 CO), 155.0 (NC=O), 98.7 (C-1_a), 98.2**

(C-1_b), 79.7 (C(CH₃)₃), 71.3 (C-3_a), 71.2 (C-3_b), 70.9 (OCH₂ a), 70.6 (OCH₂ b), 68.7 (C-5_{a,b}), 66.1 (C-4_a), 66.0 (C-4_b), 62.4 (C-6_a), 62.3 (C-6_b), 61.7 (C-2_a), 61.6 (C-2_b), 46.8 (CH₂), 44.5 (CH₂), 35.8 (CH), 28.6 (C(CH₃)₃), 27.5 (CH₂), 24.4 (CH₂), 20.9, 20.8, 20.7 (COCH₃); ESI-MS: *m/z*: Calcd for C₂₃H₃₆N₄NaO₁₀ [M+Na]⁺: 551.6, found: 551.2.

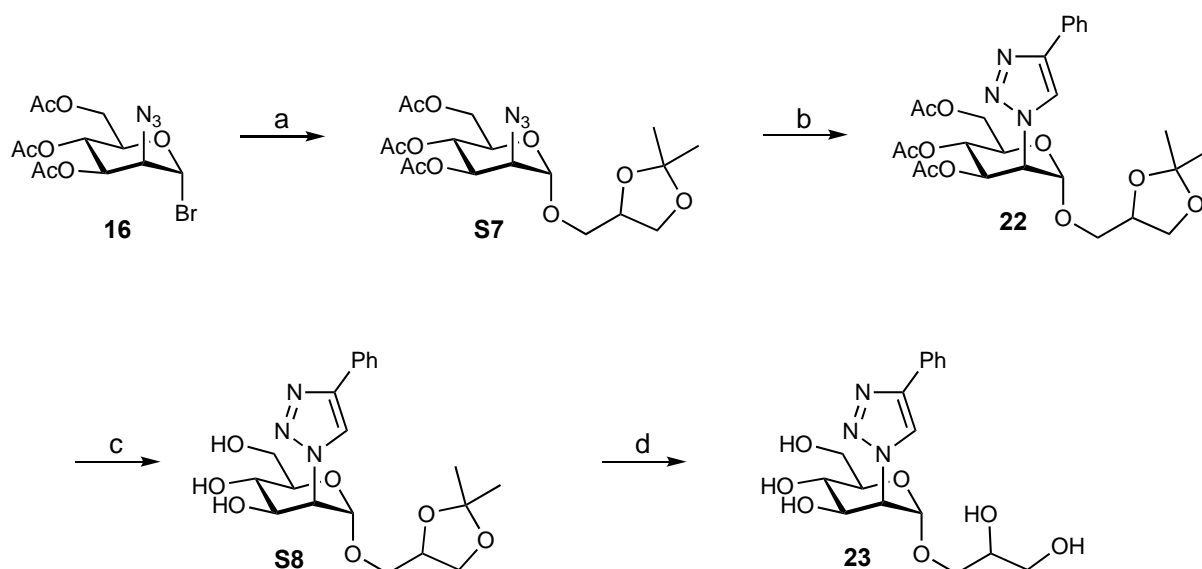
((3*RS*)-1-(*tert*-Butyloxycarbonyl)-piperidin-3-yl)methyl 3,4,6-tri-*O*-acetyl-2-deoxy-2-(4-phenyl-1,2,3-triazol-1-yl)- α -D-mannopyranoside (20**).** According to general procedure A, **S5** (13 mg, 25 μ mol, 1.00 eq), MeCN (0.5 ml), phenylacetylene (3 μ l, 30 μ mol, 1.10 eq), CuBr (1 mg, 5 μ mol, 0.20 eq), and TBTA (3 mg, 5 μ mol, 0.20 eq) were stirred for 18 h. Purification by flash chromatography (petroleum ether/EtOAc, 13:7) yielded **20** (13 mg, 21 μ mol, 84%) as a colorless oil. ¹H NMR (500 MHz, CDCl₃): δ = 8.28 (d, *J* = 3.7 Hz, 2H, Ar-H), 7.89–7.83 (m, 4H, Ar-H), 7.44 (dd, *J* = 8.4, 7.0 Hz, 4H, Ar-H), 7.39–7.32 (m, 2H, Ar-H), 5.55–5.50 (m, 2H, H-3_{a,b}), 5.49–5.44 (m, 2H, H-2_{a,b}), 5.36–5.30 (m, 2H, H-4_{a,b}), 5.14–5.04 (m, 2H, H-1_{a,b}), 4.37 (dd, *J* = 12.4, 3.7 Hz, 2H, H-6_{a,b}), 4.25–4.09 (m, 4H, H-5_{a,b}, H-6'_{a,b}), 4.06–3.56 (m, 6H, OCH₂ a,b, CH₂), 3.49–3.25 (m, 2H, OCH₂ a,b), 3.09–2.58 (m, 4H, CH₂), 2.16, 2.04, 1.96 (3 s, 18H, 3 COCH₃ a,b), 1.94–1.80 (m, 4H, CH, CH₂), 1.73–1.62 (m, 2H, CH₂), 1.49–1.43 (m, 18H, C(CH₃)₃ a,b), 1.25 (s, 4H, CH₂); ¹³C NMR (126 MHz, CDCl₃): δ = 170.5, 170.1, 169.4 (3 CO), 155.1 (NC=O), 148.3, 130.5, 129.0, 128.6, 125.9, 119.4 (Ar-C), 98.4 (C-1_{a,b}), 79.8 (C(CH₃)₃ a,b), 71.3 (OCH₂ a), 71.1 (OCH₂ b), 68.8 (C-5_{a,b}), 68.7 (C-3_{a,b}), 64.9 (C-4_{a,b}), 64.8 (C-6_{a,b}), 62.2 (C-2_{a,b}), 60.5 (CH₂), 45.7 (CH₂), 44.62 (CH₂), 35.9 (CH), 28.6 (C(CH₃)₃), 27.5 (CH₂), 24.3 (CH₂), 20.9, 20.8, 20.7 (3 COCH₃); ESI-MS: *m/z*: Calcd for C₃₁H₄₂N₄NaO₁₀ [M+Na]⁺: 653.7, found: 653.2.

((3*RS*)-1-(*tert*-Butyloxycarbonyl)-piperidin-3-yl)methyl 2-deoxy-2-(4-phenyl-1,2,3-triazol-1-yl)- α -D-mannopyranoside (S6**).** According to general procedure C, **20** (13 mg, 21 μ mol, 1.00 eq), and a 25 wt.% solution of NaOMe in MeOH (2 μ l, 7 μ mol, 0.30 eq) were stirred for 1 h in MeOH (0.5 ml). Purification by flash chromatography (DCM/MeOH, 18.5:1.5) yielded **S6** (9 mg, 18 μ mol, 86%) as a colorless oil. ¹H NMR (500 MHz, CD₃OD): δ = 8.57 (s, 2H, Ar-H), 7.87–7.77 (m, 4H, Ar-H), 7.38 (m, 6H, Ar-H), 5.19–5.12 (m, 2H, H-2_{a,b}), 5.11–5.06 (m, 2H, H-1_{a,b}), 4.31–4.19 (m, 2H, H-3_{a,b}), 4.10 (m, 1H, CH₂), 4.04–3.77 (m, 9H, H-4_{a,b}, H-6_{a,b}, H-6'_{a,b}, CH₂), 3.76–3.67 (m, 3H, H-5_{a,b}, OCH₂ a), 3.63 (dd, *J* = 9.8, 7.7 Hz, 1H, OCH₂ b), 3.43 (dd, *J* = 9.8, 4.8 Hz, 1H, OCH₂ a), 3.37 (dd, *J* = 9.7, 7.3 Hz, 1H, OCH₂ b), 3.01–2.55 (m, 4H, CH₂), 1.91–1.75 (m, 4H, CH₂), 1.72–1.64 (m, 2H, CH), 1.46 (s, 9H, C(CH₃)₃ a), 1.45 (s, 9H, C(CH₃)₃ b), 1.44–1.39 (m, 2H, CH₂), 1.39–1.20 (m, 2H, CH₂); ¹³C NMR (126 MHz,

CD₃OD): δ = 156.6, 148.6, 131.8, 130.0, 129.3, 126.7, 122.6 (Ar-C), 99.8 (C-1_a), 99.3 (C-1_b), 81.1 (C(CH₃)₃ a,b), 75.0 (C-5_{a,b}), 71.1 (OCH₂ a,b), 70.4 (C-3_{a,b}), 67.5 (C-4_{a,b}), 65.7 (C-2_{a,b}), 61.8 (C-6_{a,b}), 47.9 (CH₂), 45.7 (CH₂), 37.4 (CH), 28.7 (C(CH₃)₃ a,b), 28.3 (CH₂), 25.7 (CH₂); ESI-MS: m/z : Calcd for C₂₅H₃₇N₄O₇ [M+H]⁺: 505.6, found: 505.3.

((3*RS*)-Piperidin-3-yl)methyl 2-deoxy-2-(4-phenyl-1,2,3-triazol-1-yl)- α -D-mannopyranoside trifluoroacetate salt (21). A mixture of **S6** (55 mg, 109 μ mol, 1.00 eq) in DCM (1 ml) and TFA (1 ml) was stirred at rt under argon for 30 min. The product was concentrated in vacuo, diluted with water and lyophilized to yield **21** (46 mg, 89 μ mol, 81%) as a colorless solid. $[\alpha]_D^{20}$ +7.4 (*c* 1.0, MeOH); ¹H NMR (500 MHz, CD₃OD): δ = 8.55 (s, 2H, Ar-H), 7.87–7.79 (m, 4H, Ar-H), 7.43 (dd, *J* = 8.4, 7.0 Hz, 4H, Ar-H), 7.39–7.30 (m, 2H, Ar-H), 5.17–5.10 (m, 4H, H-1_{a,b}, H-2_{a,b}), 4.20 (dd, *J* = 9.3, 5.1 Hz, 2H, H-3_{a,b}), 4.01–3.89 (m, 4H, H-6_{a,b}, H-6'_{a,b}), 3.89–3.83 (m, 2H, H-4_{a,b}), 3.80 (dd, *J* = 9.9, 5.2 Hz, 1H, OCH₂ a), 3.75–3.62 (m, 3H, H-5_{a,b}, OCH₂ b), 3.58–3.44 (m, 3H, OCH₂ a, CH₂), 3.44–3.33 (m, 3H, OCH₂ b, CH₂), 2.92 (td, *J* = 12.8, 3.2 Hz, 2H, CH₂), 2.83 (q, *J* = 12.1 Hz, 2H, CH₂), 2.21–2.07 (m, 2H, CH), 2.02–1.83 (m, 4H, CH₂), 1.84–1.67 (m, 2H, CH₂), 1.49–1.34 (m, 2H, CH₂); ¹³C NMR (126 MHz, CD₃OD): δ = 148.7, 131.7, 130.0, 129.4, 126.7, 122.6 (Ar-C), 99.7 (C-1_a), 99.4 (C-1_b), 75.3 (C-5_a), 75.2 (C-5_b), 70.6 (OCH₂ a), 70.5 (C-3_{a,b}), 70.4 (OCH₂ b), 67.7 (C-4_a), 67.6 (C-4_b), 65.3 (C-2_{a,b}), 61.8 (C-6_{a,b}), 47.8 (CH₂), 47.7 (CH₂), 45.4 (CH₂), 35.5 (CH), 35.4 (CH), 26.3 (CH₂), 26.2 (CH₂), 23.1 (CH₂), 23.0 (CH₂); ESI-MS: m/z : Calcd for C₂₀H₂₈N₄NaO₅ [M+Na]⁺: 402.1952, found: 402.1952.

Synthesis of DC-SIGN antagonist 23.



Scheme S3. a) *rac*-Isopropylidenglycerol, Ag₂CO₃, I₂, DCM (19%); b) phenylacetylene, TBTA, CuBr, MeCN (82%); c) NaOMe, MeOH (84%); d) 60% AcOH, H₂O (90%).

((4*RS*)-2,2-Dimethyl-1,3-dioxolan-4-yl)methyl 3,4,6-tri-*O*-acetyl-2-azido-2-deoxy- α -*D*-mannopyranoside (S7). A mixture of *rac*-isopropylidenglycerol (50 mg, 0.38 mmol, 1.00 eq), Ag₂CO₃ (105 mg, 0.38 mmol, 1.00 eq) and powdered molecular sieves 4Å in DCM (6 ml) was stirred at rt under argon for 15 min. Then I₂ (10 mg, 38 μ mol, 0.10 eq) and a solution of **16** (150 mg, 0.38 mmol, 1.00 eq) in DCM (2 ml) was added to the reaction mixture, which then was stirred overnight at rt under argon. Then, the reaction mixture was filtered over celite and the filtrate was concentrated under reduced pressure. The crude product was purified by flash chromatography (petroleum ether/EtOAc, 7:3) to yield **S7** (32 mg, 0.47 mmol, 19%; α/β ratio: 9/1) as a colorless oil. ¹H NMR (500 MHz, CDCl₃): δ = 5.42–5.28 (m, 4H, H-3_a, H-3_b, H-4_a, H-4_b), 4.93 (d, *J* = 1.7 Hz, 1H, H-1_a), 4.90 (d, *J* = 1.7 Hz, 1H, H-1_b), 4.35–4.21 (m, 4H, H-6_a, H-6_b, Glyc-H2_{a,b}), 4.14–4.01 (m, 6H, H-2_a, H-2_b, H-6'_a, H-6'_b, Glyc-H3_{a,b}), 4.00–3.92 (m, 2H, H-5_a, H-5_b), 3.77 (dd, *J* = 8.5, 5.9 Hz, 1H, Glyc-H3_a), 3.74–3.67 (m, 3H, Glyc-H3_b, Glyc-H1_{a,b}), 3.57–3.50 (m, 2H, Glyc-H1_{a,b}), 2.11–2.03 (m, 18H, 3 COCH₃_{a,b}), 1.44–1.34 (m, 12H, C(CH₃)₂_{a,b}); ¹³C NMR (126 MHz, CDCl₃): δ = 171.0, 170.9, 170.2, 170.1, 169.8 (CO), 110.0 (C(CH₃)₂_a), 109.9 (C(CH₃)₂_b), 98.3 (C-1_a), 98.2 (C-1_b), 74.4 (Glyc-C2_a), 74.1 (Glyc-C2_b), 71.0 (C-3_a), 70.9 (C-3_b), 68.7 (Glyc-C1_{a,b}), 68.6 (C-5_{a,b}), 66.4 (Glyc-C3_a), 66.0 (Glyc-C3_b), 65.9 (C-4_a), 65.8 (C-4_b), 62.1 (C-6_a), 62.1 (C-6_b), 61.4 (C-2_{a,b}), 26.9, 26.8, 25.5, 25.4 (C(CH₃)₂_{a,b}), 21.0, 20.9, 20.8, 20.7 (CH₃CO); ESI-MS: *m/z*: Calcd for C₁₈H₂₇N₃NaO₁₀ [M+Na]⁺: 468.4, found: 468.2.

((4*RS*)-2,2-Dimethyl-1,3-dioxolan-4-yl)methyl 3,4,6-tri-*O*-acetyl-2-deoxy-2-(4-phenyl-1,2,3-triazol-1-yl)- α -*D*-mannopyranoside (22). According to general procedure A, **S7** (30 mg, 67 μ mol, 1.00 eq), MeCN (3 ml), phenylacetylene (9 μ l, 80 μ mol, 1.20 eq), CuBr (2 mg, 14 μ mol, 0.20 eq), and TBTA (8 mg, 14 μ mol, 0.20 eq) were stirred for 18 h. Purification by flash chromatography (petroleum ether/EtOAc, 13:7) yielded **22** (30 mg, 55 μ mol, 82%; α/β ratio: 9/1) as a colorless oil. ¹H NMR (500 MHz, CDCl₃): δ = 8.27 (s, 2H, Ar-H), 7.89–7.83 (m, 4H, Ar-H), 7.43 (t, *J* = 7.7 Hz, 4H, Ar-H), 7.39–7.32 (m, 2H, Ar-H), 5.58–5.43 (m, 4H, H-3_a, H-3_b, H-2_a, H-2_b), 5.33 (td, *J* = 10.1, 3.2 Hz, 2H, H-4_a, H-4_b), 5.22 (d, *J* = 1.3 Hz, 1H, H-1_a), 5.18 (d, *J* = 1.3 Hz, 1H, H-1_b), 4.42–4.31 (m, 4H, H-6_a, H-6_b, Glyc-H2_{a,b}), 4.28–4.15 (m, 4H, H-5_a, H-5_b, H-6'_a, H-6'_b), 4.15–4.07 (m, 2H, Glyc-H3_{a,b}), 3.84–3.76 (m, 4H, Glyc-H1_{a,b}, Glyc-H3_{a,b}), 3.68–3.61 (m, 2H, Glyc-H1_{a,b}), 2.16, 2.04, 1.96 (3 s, 18H, 3 COCH₃_{a,b}), 1.44–1.38 (m, 12H, C(CH₃)₂_{a,b}); ¹³C NMR (126 MHz, CDCl₃): δ = 170.5, 170.2, 169.4 (3 CO), 148.3,

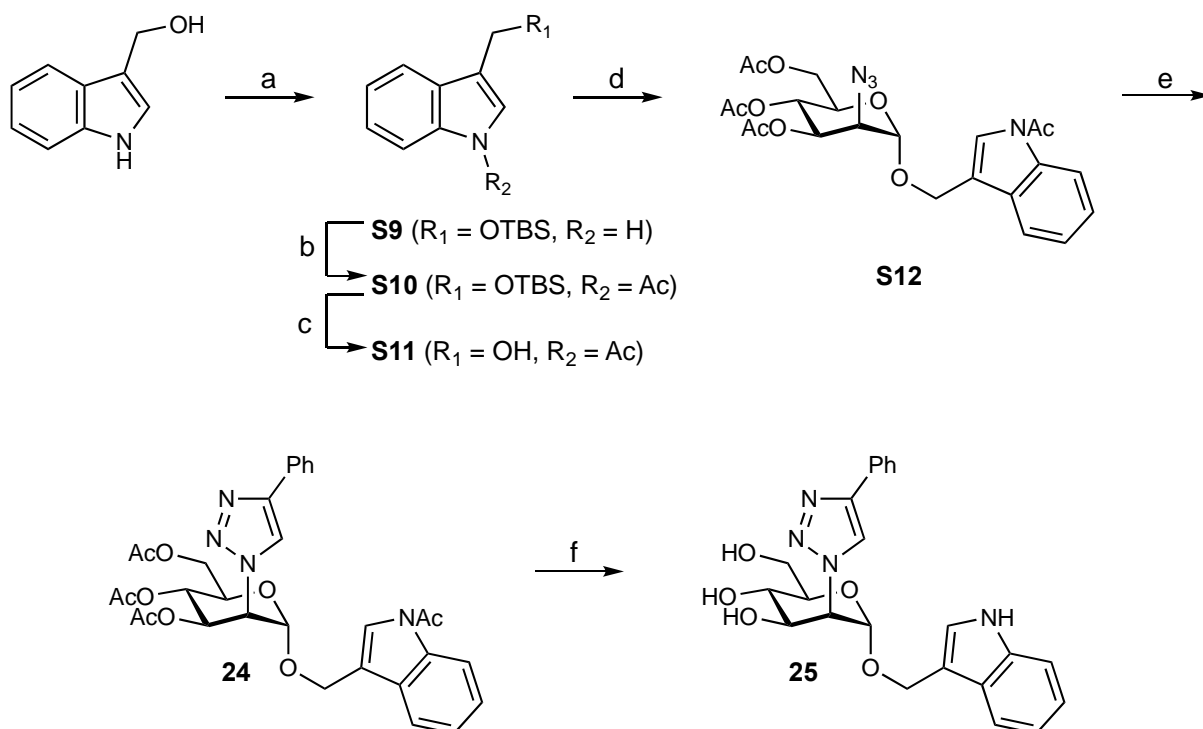
130.5, 129.0, 128.6, 125.9, 119.4, 119.3 (Ar-C), 110.0 (C(CH₃)_{2 a,b}), 98.2 (C-1_a), 98.0 (C-1_b), 74.4 (Glyc-C2_a), 74.2 (Glyc-C2_b), 69.3 (Glyc-C1_{a,b}), 68.7 (C-5_{a,b}), 68.6 (C-3_{a,b}), 66.4 (Glyc-C3_a), 66.2 (Glyc-C3_b), 64.8 (C-4_{a,b}), 62.1 (C-6_a), 62.0 (C-6_b), 60.4 (C-2_{a,b}), 26.9, 26.8, 25.5, 25.4 (C(CH₃)_{2 a,b}), 20.9, 20.7 (CH₃CO); ESI-MS: *m/z*: Calcd for C₂₆H₃₄N₃O₁₀ [M+H]⁺: 548.6, found: 548.2.

((4*RS*)-2,2-Dimethyl-1,3-dioxolan-4-yl)methyl 2-deoxy-2-(4-phenyl-1,2,3-triazol-1-yl)- α -D-mannopyranoside (S8). According to general procedure C, **22** (34 mg, 62 μ mol, 1.00 eq), and a 25 wt.% solution of NaOMe in MeOH (5 μ l, 19 μ mol, 0.30 eq) were stirred for 1 h in MeOH (1 ml). Purification by flash chromatography (DCM/MeOH, 19:1) yielded **S8** (22 mg, 52 μ mol, 84%; 100 % α) as a colorless solid. ¹H NMR (500 MHz, CD₃OD): δ = 8.57 (s, 2H, Ar-H), 7.86–7.80 (m, 4H, Ar-H), 7.46–7.40 (m, 4H, Ar-H), 7.38–7.30 (m, 2H, Ar-H), 5.18 (d, *J* = 1.5 Hz, 2H, H-1_{a,b}), 5.16 (m, 2H, H-2_{a,b}), 4.41–4.31 (m, 2H, Glyc-H2_{a,b}), 4.27–4.20 (m, 2H, H-3_{a,b}), 4.14–4.06 (m, 2H, Glyc-H3_{a,b}), 3.98–3.92 (m, 2H, H-6_{a,b}), 3.92–3.72 (m, 10H, H-4_{a,b}, H-5_{a,b}, H-6'_{a,b}, Glyc-H3_{a,b}, Glyc-H1_{a,b}), 3.62 (ddd, *J* = 23.3, 10.7, 5.2 Hz, 2H, Glyc-H1_{a,b}), 1.41, 1.40, 1.35, 1.35 (4 s, 12H, C(CH₃)_{2 a,b}); ¹³C NMR (126 MHz, CD₃OD): δ = 148.7, 131.8, 130.0, 129.3, 126.7, 122.6 (Ar-C), 110.8, 110.7 (C(CH₃)_{2 a,b}), 99.7 (C-1_{a,b}), 76.0 (Glyc-C2_a), 75.9 (Glyc-C2_b), 75.0 (C-5_{a,b}), 70.3 (C-3_a), 70.2 (C-3_b), 69.7 (Glyc-C1_a), 69.3 (Glyc-C1_b), 67.5 (C-4_{a,b}), 67.3 (Glyc-C3_a), 67.2 (Glyc-C3_b), 65.5 (C-2_{a,b}), 61.7 (C-6_{a,b}), 27.1, 27.0, 25.6 (C(CH₃)_{2 a,b}); ESI-MS: *m/z*: Calcd for C₂₀H₂₇N₃NaO₇ [M+Na]⁺: 444.2, found: 444.3.

(2*RS*)-2,3-Dihydroxypropyl 2-deoxy-2-(4-phenyl-1,2,3-triazol-1-yl)- α -D-mannopyranoside (23). A solution of **S8** (22 mg, 52 μ mol, 1.00 eq) in 60% aq. acetic acid (1 ml) was stirred at 60 °C under argon for 2 h. The mixture was concentrated under reduced pressure and purified by flash chromatography (DCM/MeOH, 17:3). Then, the product was diluted with water and lyophilized to yield **23** (17 mg, 45 μ mol, 86%) as a colorless solid. [α]_D²⁰ +0.0 (*c* 1.0, MeOH); ¹H NMR (500 MHz, CD₃OD): δ = 8.58 (d, *J* = 0.7 Hz, 2H, Ar-H), 7.83 (dd, *J* = 8.4, 1.3 Hz, 4H, Ar-H), 7.47–7.40 (m, 4H, Ar-H), 7.38–7.31 (m, 2H, Ar-H), 5.22–5.16 (m, 2H, H-2_{a,b}), 5.15 (dd, *J* = 3.6, 1.4 Hz, 2H, H-1_{a,b}), 4.29–4.23 (m, 2H, H-3_{a,b}), 3.95 (dd, *J* = 12.0, 3.5 Hz, 2H, H-6_{a,b}), 3.93–3.73 (m, 10H, H-4_{a,b}, H-5_{a,b}, H-6'_{a,b}, Glyc-H1_{a,b}, Glyc-H2_{a,b}), 3.67–3.49 (m, 6H, Glyc-H3_{a,b}, Glyc-H1_{a,b}); ¹³C NMR (126 MHz, CD₃OD): δ = 148.6, 131.8, 130.0, 129.3, 126.7, 122.6 (Ar-C), 100.0 (C-1_a), 99.6 (C-1_b), 74.9 (C-5_a), 74.8 (C-5_b), 72.2 (Glyc-C2_a), 71.9 (Glyc-C2_b), 70.4 (Glyc-C1_a), 70.3 (C-3_{a,b}), 70.0 (Glyc-C1_b), 67.5 (C-4_{a,b}), 65.5 (C-2_{a,b}), 64.2

(Glyc-C3_a), 64.1 (Glyc-C3_b), 61.7 (C-6_{a,b}); ESI-MS: *m/z*: Calcd for C₁₇H₂₃N₃NaO₇ [M+Na]⁺: 404.1428, found: 404.1428.

Synthesis of DC-SIGN antagonist **25**.



Scheme S4. a) TBSCl, imidazole, DMF (65%); b) Ac₂O, TEA, DCM (52%); c) HCl, MeOH/H₂O (72%); d) **16**, Ag₂CO₃, I₂, DCM (40%); e) phenylacetylene, TBTA, CuBr, MeCN (83%); f) KOH, MeOH (96%).

3-(((*tert*-Butyldimethylsilyl)oxy)methyl)-1*H*-indole (S9**).** To a solution of indole-3-carbinol (770 mg, 5.22 mmol, 1.00 eq) and imidazole (885 mg, 13.1 mmol, 2.50 eq) in DMF (5 ml) was added TBSCl (1.58 g, 10.4 mmol, 2.00 eq). The reaction mixture was stirred at rt under argon until complete consumption of starting material (according to TLC). Then water was added to the reaction mixture and the organic layer was extracted with EtOAc. The organic layer was washed twice with water and the combined aqueous layers were extracted twice with EtOAc. The combined organic layers were dried over Na₂SO₄, filtered and concentrated under reduced pressure. The crude product was purified by flash chromatography (petroleum ether/EtOAc, 19:1) to give **S9** (880 mg, 3.37mmol, 65%) as a yellowish solid. ¹H NMR (500 MHz, CDCl₃): δ = 7.99 (s, 1H, NH), 7.67 (dq, *J* = 7.8, 0.9 Hz, 1H, Ar-H), 7.35 (dt, *J* = 8.1, 0.9 Hz, 1H, Ar-H), 7.20 (ddd, *J* = 8.2, 7.0, 1.2 Hz, 1H, Ar-H), 7.16–7.10 (m, 2H, Ar-H), 4.95 (d, *J* = 0.9 Hz, 2H, CH₂O), 0.95 (s, 9H, C(CH₃)₃), 0.12 (s, 6H, Si(CH₃)₂); ¹³C NMR (126 MHz, CDCl₃): δ =

136.6, 126.7, 122.3, 122.2, 119.7, 119.5, 117.0, 111.2 (Ar-C), 58.4 (CH₂O), 26.2 (C(CH₃)₃), 18.6 (C(CH₃)₃), -5.0 (Si(CH₃)₂).

1-(3-(((*tert*-Butyldimethylsilyl)oxy)methyl)-1*H*-indol-1-yl)ethan-1-one (S10). To a solution of **S9** (0.500 mg, 1.91 mmol, 1.00 eq) and TEA (0.50 ml, 3.56 mmol, 1.87 eq) in DCM (2 ml), was added Ac₂O (0.33 ml, 3.56 mmol, 1.87 eq). The reaction mixture was refluxed under argon until TLC analysis indicated the complete consumption of starting material. Then the crude product was concentrated under reduced pressure and purified by flash chromatography (petroleum ether/EtOAc, 19:1) to give **S10** (300 mg, 0.99 mmol, 52%) as a colorless solid. ¹H NMR (500 MHz, CDCl₃): δ = 8.43 (d, *J* = 8.2 Hz, 1H, Ar-H), 7.55 (m, 1H, Ar-H), 7.36 (ddd, *J* = 8.4, 7.2, 1.3 Hz, 2H, Ar-H), 7.28 (m, 1H, Ar-H), 4.89 (d, *J* = 1.3 Hz, 2H, CH₂O), 2.62 (s, 3H, COCH₃), 0.96 (s, 9H, C(CH₃)₃), 0.14 (s, 6H, Si(CH₃)₂); ¹³C NMR (126 MHz, CDCl₃): δ = 168.6 (CO), 136.4, 129.2, 125.5, 123.6, 123.2, 122.2, 119.3, 116.8 (Ar-C), 58.2 (CH₂O), 26.1 (C(CH₃)₃), 24.1 (CH₃CO), 18.6 (C(CH₃)₃), -5.1 (Si(CH₃)₂); ESI-MS: *m/z*: Calcd for C₁₅H₂₃NNaOSi [M+Na]⁺: 326.5, found: 326.3.

1-(3-(Hydroxymethyl)-1*H*-indol-1-yl)ethan-1-one (S11). To a solution of **S10** (200 mg, 0.66 mmol, 1.00 eq) in MeOH (8 ml) was added 37% aq. HCl (0.2 ml, excess). The reaction mixture was stirred at rt for 30 min. Then the reaction was quenched with satd aq. NaHCO₃ and the organic layer was extracted with EtOAc and washed twice with water. The aqueous layers were extracted twice with EtOAc and the combined organic layers were dried over Na₂SO₄, filtered, and concentrated under reduced pressure. The crude product was purified by flash chromatography (petroleum ether/EtOAc, 11:9) to give **S11** (90 mg, 0.47 mmol, 72%) as a yellowish solid. ¹H NMR (500 MHz, CDCl₃): δ = 8.43 (d, *J* = 8.3 Hz, 1H, Ar-H), 7.62 (tt, *J* = 8.7, 1.1 Hz, 1H, Ar-H), 7.43–7.35 (m, 2H, Ar-H), 7.30 (m, 1H, Ar-H), 4.88 (s, 2H, CH₂OH), 2.61 (s, 3H, COCH₃); ¹³C NMR (126 MHz, CDCl₃): δ = 168.7 (CO), 136.3, 129.2, 125.8, 123.9, 123.0, 122.5, 119.3, 116.9 (Ar-C), 57.4 (CH₂OH), 24.1 (CH₃CO).

(1-Acetyl-1*H*-indol-3-yl)methyl 3,4,6-tri-*O*-acetyl-2-azido-2-deoxy- α -D-mannopyranoside (S12). According to general procedure B, **16** (100 mg, 254 μ mol, 1.00 eq), MeCN (3 ml), **S11** (50 mg, 265 μ mol, 1.05 eq), K₂CO₃ (53 mg, 384 μ mol, 1.50 eq), and I₂ (97 mg, 384 μ mol, 1.50 eq) were reacted for 18 h. Purification by flash chromatography (petroleum ether/EtOAc, 13:7) gave **S12** (50 mg, 100 μ mol, 40%) as a colorless oil. ¹H NMR (500 MHz, CDCl₃): δ = 8.45 (d, *J* = 8.3 Hz, 1H, Ar-H), 7.62 (dt, *J* = 7.8, 1.1 Hz, 1H, Ar-H), 7.45 (s, 1H, Ar-H), 7.41 (m, 1H,

Ar-H), 7.34 (m, 1H, Ar-H), 5.43 (dd, $J = 9.8, 3.8$ Hz, 1H, H-3), 5.35 (t, $J = 9.9$ Hz, 1H, H-4), 4.92 (d, $J = 1.7$ Hz, 1H, H-1), 4.89 (dd, $J = 12.5, 1.0$ Hz, 1H, CH₂O), 4.71 (dd, $J = 12.5, 0.7$ Hz, 1H, CH₂O), 4.27 (dd, $J = 12.3, 4.6$ Hz, 1H, H-6), 4.09 (dd, $J = 12.3, 2.5$ Hz, 1H, H-6'), 4.01 (ddd, $J = 10.0, 4.7, 2.5$ Hz, 1H, H-5), 3.97 (dd, $J = 3.8, 1.8$ Hz, 1H, H-2), 2.66 (s, 3H, NCOCH₃), 2.12, 2.09, 2.05 (3 s, 9H, 3 COCH₃); ¹³C NMR (126 MHz, CDCl₃): $\delta = 170.7, 170.0, 169.6, 168.5$ (4 CO), 136.1, 129.3, 125.9, 125.0, 124.0, 119.1, 117.2, 116.9 (Ar-C), 96.3 (C-1), 71.1 (C-3), 68.8 (C-5), 66.0 (C-4), 62.2 (C-6), 61.6 (C-2), 60.8 (CH₂O), 24.0 (CH₃CON), 20.8, 20.7, 20.6 (3 CH₃CO); ESI-MS: m/z : Calcd for C₂₃H₂₆N₄NaO₉ [M+Na]⁺: 525.5, found: 525.1.

(1-Acetyl-1*H*-indol-3-yl)methyl 3,4,6-tri-*O*-acetyl-2-deoxy-2-(4-phenyl-1,2,3-triazol-1-yl)- α -D-mannopyranoside (24). According to general procedure A, **S12** (50 mg, 100 μ mol, 1.00 eq), MeCN (5 ml), phenylacetylene (13 μ l, 110 μ mol, 1.10 eq), CuBr (3 mg, 20 μ mol, 0.20 eq), and TBTA (11 mg, 20 μ mol, 0.20 eq) were stirred for 18 h. Purification by flash chromatography (petroleum ether/EtOAc, 13:7) yielded **24** (50 mg, 83 μ mol, 83%) as a colorless oil. ¹H NMR (500 MHz, CDCl₃): $\delta = 8.42$ (d, $J = 8.2$ Hz, 1H, Ar-H), 8.23 (s, 1H, Ar-H), 7.85–7.81 (m, 2H, Ar-H), 7.65 (dt, $J = 7.7, 1.1$ Hz, 1H, Ar-H), 7.50 (s, 1H, Ar-H), 7.46–7.38 (m, 3H, Ar-H), 7.38–7.31 (m, 2H, Ar-H), 5.59 (dd, $J = 10.1, 5.2$ Hz, 1H, H-3), 5.42 (dd, $J = 5.2, 1.4$ Hz, 1H, H-2), 5.34 (t, $J = 10.1$ Hz, 1H, H-4), 5.21 (d, $J = 1.3$ Hz, 1H, H-1), 4.98 (dd, $J = 12.6, 1.0$ Hz, 1H, CH₂O), 4.82 (dd, $J = 12.5, 0.7$ Hz, 1H, CH₂O), 4.37 (dd, $J = 12.3, 3.5$ Hz, 1H, H-6), 4.23 (ddd, $J = 10.1, 3.5, 2.3$ Hz, 1H, H-5), 4.17 (dd, $J = 12.3, 2.4$ Hz, 1H, H-6'), 2.66 (s, 3H, NCOCH₃), 2.18, 2.03, 1.96 (3 s, 9H, 3 COCH₃); ¹³C NMR (126 MHz, CDCl₃): $\delta = 170.6, 170.2, 169.5, 168.6$ (4 CO), 148.3, 136.2, 130.4, 129.3, 129.0, 128.6, 126.1, 125.9, 125.2, 124.3, 119.4, 119.2, 116.9 (Ar-C), 96.3 (C-1), 69.0 (C-5), 68.7 (C-3), 65.0 (C-4), 62.1 (C-6), 61.5 (CH₂O), 60.5 (C-2), 24.2 (CH₃CON), 20.9, 20.8, 20.7 (3 CH₃CO); ESI-MS: m/z : Calcd for C₃₁H₃₃N₄O₉ [M+H]⁺: 605.6, found: 605.3.

(1*H*-Indol-3-yl)methyl 2-deoxy-2-(4-phenyl-1,2,3-triazol-1-yl)- α -D-mannopyranoside (25). To a solution of **24** (50 mg, 83 μ mol, 1.00 eq) in MeOH (2 ml), a 1 M solution of KOH in MeOH (13 μ l, 13 μ mol, 0.15 eq) was added. The reaction mixture was stirred at rt for 1h under argon. Then the crude product was concentrated under reduced pressure, purified by flash chromatography (DCM/MeOH, 9:1) and lyophilized from water to give **25** (35 mg, 80 μ mol, 96%) as a colorless solid. ¹H NMR (500 MHz, CD₃OD): $\delta = 8.51$ (s, 1H, Ar-H), 7.82–7.76 (m, 2H, Ar-H), 7.67 (dt, $J = 7.9, 1.0$ Hz, 1H, Ar-H), 7.45–7.38 (m, 2H, Ar-H), 7.37 (m,

1H, Ar-H), 7.35–7.29 (m, 2H, Ar-H), 7.12 (m, 1H, Ar-H), 7.06 (m, 1H, Ar-H), 5.20 (d, $J = 1.5$ Hz, 1H, H-1), 5.06–4.99 (m, 2H, H-2, CH₂O), 4.83 (m, 1H, CH₂O), 4.24 (m, 1H, H-3), 3.95 (dd, $J = 12.0, 3.1$ Hz, 1H, H-6), 3.92–3.81 (m, 3H, H-4, H-5, H-6'); ¹³C NMR (126 MHz, CD₃OD): $\delta = 129.9, 129.3, 126.7, 126.4, 122.8, 122.6, 120.4, 119.6, 112.5$ (Ar-C), 97.8 (C-1), 75.0 (C-5), 70.4 (C-3), 67.7 (C-4), 65.9 (C-2), 62.7 (CH₂O), 61.8 (C-6); ESI-MS: m/z : Calcd for C₂₃H₂₄N₄NaO₅ [M+Na]⁺: 459.1639, found: 459.1640.

tert-Butyl (2-(4-ethynylbenzamido)ethyl)carbamate (27). 4-Ethynylbenzoic acid (**26**, 438 g, 3.0 mmol, 1.0 eq), *tert*-butyl (2-aminoethyl)carbamate (523 mg, 3.3 mmol, 1.1 eq), EDC (559 mg, 3.6 mmol, 1.2 eq), and HOBt (486 mg, 3.6 mmol, 1.2 eq) were dissolved in DCM. DIPEA (776 mg, 6.0 mmol, 2.0 eq) was added and the reaction mixture was stirred at rt for 16 h. The solvent was evaporated and the residue taken up in EtOAc. The solution was washed with 1 M HCl, satd aq. NaHCO₃ solution, and brine. The organic phase was dried over Na₂SO₄, the solvent was evaporated, and the crude product was purified by silica gel chromatography (petroleum ether/EtOAc, 25-80% EtOAc over 15 min). The product **27** (605 mg, 2.10 mmol, 70%) was obtained as a light yellow solid. ¹H NMR (500 MHz, CDCl₃): $\delta = 7.78$ (d, $J = 8.0$ Hz, 2H, Ar-H), 7.53 (dd, $J = 8.3, 1.8$ Hz, 2H, Ar-H), 7.34 (s, 1H, CONH), 5.04 (s, 1H, Boc-NH), 3.65–3.49 (m, 2H, CH₂), 3.48–3.34 (m, 2H, CH₂), 3.18 (s, 1H, C≡CH), 1.42 (s, 9H, (CCH₃)₃). ¹³C NMR (126 MHz, CDCl₃): $\delta = 167.1$ (CO), 134.3, 132.3, 127.1, 125.4 (Ar-C), 83.0 (C(CH₃)₃), 80.3 (C≡CH), 79.5 (C≡CH), 42.6 (CH₂), 40.0 (CH₂), 28.5 (C(CH₃)₃); ESI-MS: m/z : Calcd for C₁₆H₂₀N₂NaO₃ [M+Na]⁺: 331.3, found: 331.16.

4-Ethynyl-N-(2-(3-(tritylthio)propanamido)ethyl)benzamide (28). Compound **27** (100 mg, 0.35 mmol, 1.0 eq) was dissolved in TFA/DCM (1:1, 2 mL). After stirring for 3 h, the solution was evaporated to dryness and the residue was taken up in dry DMF. 3-(Tritylthio)propanoic acid (145 mg, 0.42 mg, 1.2 eq), EDC (65 mg, 0.42 mmol, 1.2 eq), HOBt (57 mg, 0.42 mmol, 1.2 eq), and DIPEA (194 mg, 1.50 mmol, 4.0 eq) were added and the reaction mixture was stirred at rt for 16 h. The solvent was evaporated and the residue taken up in EtOAc. The solution was washed with 1 M aq. HCl, satd aq. NaHCO₃ solution, and brine. The organic phase was dried over Na₂SO₄, the solvent was evaporated, and the crude product was purified by silica gel chromatography (petroleum ether/EtOAc, 30-90% EtOAc over 15 min) to give **28** (99 mg, 0.19 mmol, 55%) as a colorless solid. ¹H NMR (500 MHz, CDCl₃): $\delta = 7.78$ –7.68 (m, 2H, Ar-H), 7.49–7.44 (m, 2H, Ar-H), 7.39–7.34 (m, 6H, Ar-H), 7.29–7.24 (m, 6H, Ar-H),

7.22–7.17 (m, 3H, Ar-H), 6.01 (s, 1H, NH), 3.59–3.47 (m, 2H, NCH₂), 3.47–3.38 (m, 2H, NCH₂), 3.19 (s, 1H, C≡CH), 2.54–2.42 (m, 2H, SCH₂), 2.07–1.98 (m, 2H, CH₂); ¹³C NMR (126 MHz, CDCl₃): δ = 173.2, 167.3 (2 CO), 144.7, 134.0, 132.4, 129.7, 128.1, 127.1, 126.9, 125.4 (Ar-C), 83.0 (C≡CH), 79.5 (C≡CH), 67.2 (CPh₃), 41.8 (NCH₂), 39.6 (NCH₂), 35.6 (CH₂), 27.8 (SCH₂); ESI-MS: *m/z*: Calcd for C₃₃H₃₀N₂NaO₅S [M+Na]⁺: 541.7, found: 541.3.

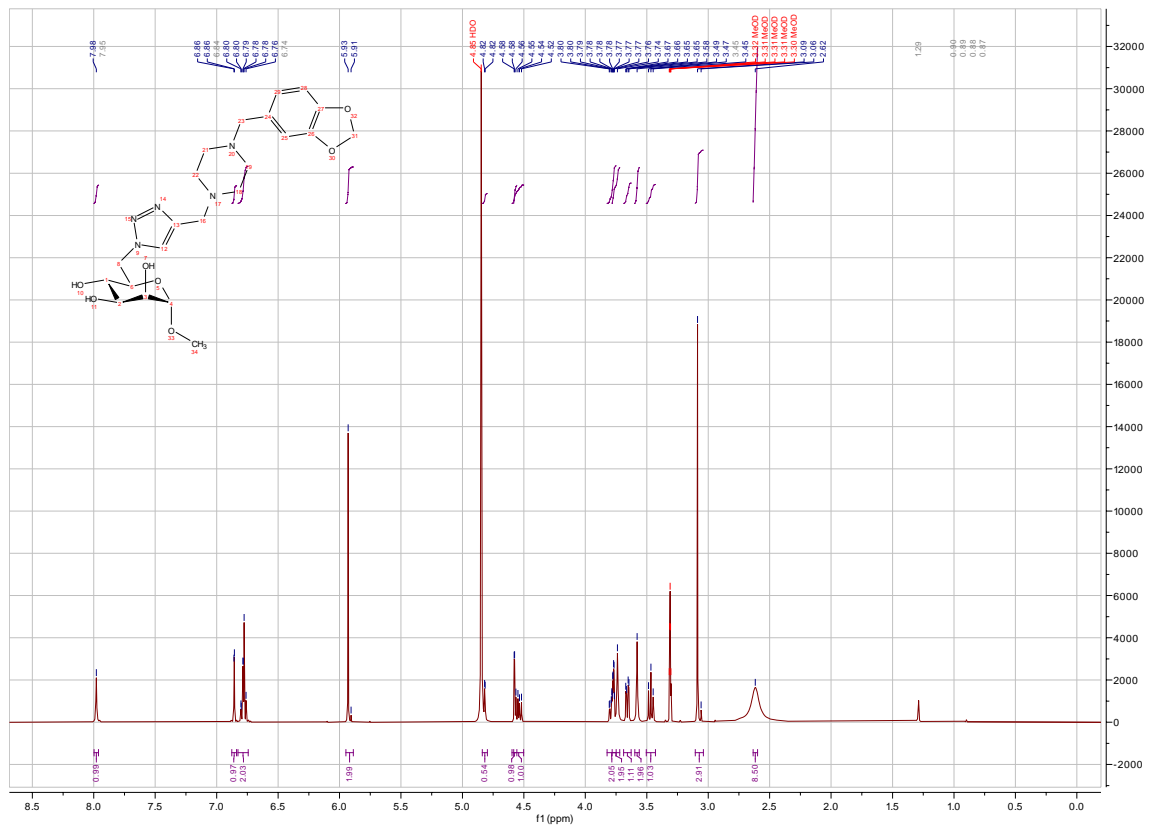
***N*-(*tert*-Butyloxycarbonyl)-3-aminopropyl 3,4,6-tri-*O*-acetyl-2-deoxy-2-(4-(4-((2-(3-(tritylthio)propanamido)ethyl)carbamoyl)phenyl)-1,2,3-triazol-1-yl)- α -D-mannopyranoside (**30**).** A solution of **S2** (55 mg, 0.11 mmol, 1.0 eq), **28** (64 mg, 0.12 mmol, 1.1 eq), TBTA (12 mg, 0.02 mmol, 0.2 eq), and CuBr (3 mg, 0.02 mmol, 0.2 eq) in THF (5 mL) was stirred at rt for 16 h. After evaporation of all volatile components, the crude product was purified by silica gel chromatography (petroleum ether/EtOAc, 50–100% EtOAc over 15 min) to yield **30** (114 mg, 0.11 mmol, quant.) as a colorless solid. ¹H NMR (500 MHz, CDCl₃): δ = 8.32 (s, 1H, triazole-H), 7.85–7.82 (m, 4H, Ar-H), 7.40–7.34 (m, 6H, Ar-H), 7.26–7.21 (m, 6H, Ar-H), 7.20–7.14 (m, 3H, Ar-H), 6.20 (s, 1H, NH), 5.54 (m, 1H, H-3), 5.46 (m, 1H, H-2), 5.33 (m, 1H, H-4), 5.12 (s, 1H, H-1), 4.75 (s, 1H, NH), 4.35 (m, 1H, H-6), 4.22–4.15 (m, 2H, H-5, H-6'), 3.88 (m, 1H, OCH₂), 3.59 (m, 1H, OCH₂), 3.55–3.50 (m, 2H, NCH₂), 3.47–3.34 (m, 2H, NCH₂), 3.34–3.18 (m, 2H, NCH₂), 2.56–2.45 (m, 2H, SCH₂), 2.12 (s, 3H, COCH₃), 2.08–2.01 (m, 5H, COCH₃, CH₂), 1.96 (s, 3H, COCH₃), 1.93–1.78 (m, 2H, CH₂), 1.43 (s, 9H, C(CH₃)₃); ¹³C NMR (126 MHz, CDCl₃): δ = 173.0, 170.5, 170.2, 169.5, 167.7 (5 CO), 147.3 (triazole-C_q), 144.7, 133.6, 133.5, 129.7, 128.1, 127.9, 126.9, 125.9 (Ar-C), 120.2 (triazole-CH), 98.0 (C-1), 78.9 (C(CH₃)₃), 68.73 (C-5), 68.69 (C-3), 67.0 (OCH₂), 66.6 (CPh₃), 64.9 (C-4), 62.2 (C-6), 60.6 (C-2), 41.4 (NCH₂), 39.7 (NCH₂), 37.6 (NCH₂), 35.6 (CH₂), 30.0 (CH₂), 28.5 (C(CH₃)₃), 27.8 (SCH₂), 20.9, 20.8, 20.7 (3 COCH₃); ESI-MS: *m/z*: Calcd for C₅₃H₆₂N₆NaO₁₂S [M+Na]⁺: 1030.2, found: 1030.0.

***N*-(*tert*-Butyloxycarbonyl)-3-aminopropyl 2-deoxy-2-(4-(4-((2-(3-(tritylthio)propanamido)ethyl)carbamoyl)phenyl)-1,2,3-triazol-1-yl)- α -D-mannopyranoside (**S13**).** To a solution of **30** (50 mg, 50 μ mol, 1.0 eq) in dry MeOH (5 mL) was added NaOMe (0.8 mg, 15 μ mol, 0.3 eq) under argon and the mixture was stirred at rt for 2 h. After evaporation of all volatile components, the crude product was dissolved in DCM/MeOH (10:1) and passed over a short pad of silica gel to yield **S13** (39 mg, 39 μ mol, 89%) as a colorless solid. ¹H NMR (500 MHz, CD₃OD): δ = 8.65 (s, 1H, triazole-H), 7.97–7.76 (m, 4H, Ar-H), 7.36–7.28 (m, 6H, Ar-

H), 7.28–7.16 (m, 6H, Ar-H), 7.19–7.09 (m, 3H, Ar-H), 6.44 (m, 1H, NH), 5.16 (dd, $J = 5.2$, 1.4 Hz, 1H, H-2), 5.10 (d, $J = 1.5$ Hz, 1H, H-1), 4.25 (dd, $J = 9.5$, 5.2 Hz, 1H, H-3), 4.06–3.89 (m, 2H, H-6), 3.89–3.80 (m, 2H, H-4, OCH₂), 3.73 (m, 1H, H-5), 3.57 (m, 1H, OCH₂), 3.53–3.43 (m, 2H, NCH₂), 3.43–3.35 (m, 2H, NCH₂), 3.30–3.01 (m, 2H, NCH₂), 2.40 (t, $J = 7.3$ Hz, 2H, SCH₂), 2.19 (t, $J = 7.3$ Hz, 2H, CH₂), 1.94–1.74 (m, 2H, CH₂), 1.42 (s, 9H, C(CH₃)₃); ¹³C NMR (126 MHz, CD₃OD): $\delta = 174.5$, 169.8 (2 CO), 158.6 (O(CO)NH), 147.5 (triazole-C_q), 146.1, 135.0, 134.9, 130.7, 129.0, 128.9, 127.8, 126.6 (Ar-C), 123.4 (triazole-CH), 99.5 (C-1), 79.9 (C(CH₃)₃), 74.9 (C-5), 70.3 (C-3), 67.7 (CPh₃), 67.6 (C-4), 66.5 (OCH₂), 65.7 (C-2), 61.8 (C-6), 41.0 (NCH₂), 40.0 (NCH₂), 38.3 (NCH₂), 36.0 (CH₂), 30.8 (CH₂), 28.9 (SCH₂), 28.8 (C(CH₃)₃); ESI-MS: m/z : Calcd for C₄₇H₅₆N₆NaO₉S [M+Na]⁺: 904.1, found: 904.0.

3-Aminopropyl 2-deoxy-2-(4-(4-((2-(3-mercaptopropanamido)ethyl)carbamoyl)phenyl)-1,2,3-triazol-1-yl)- α -D-mannopyranoside trifluoroacetate salt (31). To a solution of **S13** (32 mg, 36 μ mol, 1.0 eq) in DCM (1 mL) were added TFA (1 mL) and TIPS (57 mg, 363 μ mol, 10.0 eq) and the mixture was stirred at rt for 4 h. After evaporation of all volatile components, the residue was dissolved in MeOH and water was added until the side product triphenylmethane precipitated as a colorless solid. The mixture was filtered over a short pad of RP-8 silica gel and the filtrate was purified by preparative reversed-phase HPLC (RP-18, H₂O + 0.1% TFA/MeCN + 0.1% TFA, 0–50% over 15 min) to give **31** (13 mg, 20 μ mol, 55%) as a colorless solid. ¹H NMR (500 MHz, D₂O): $\delta = 8.53$ (s, 1H, triazole-H), 7.93–7.82 (m, 2H, Ar-H), 7.82–7.71 (m, 2H, Ar-H), 5.34–5.17 (m, 2H, H-1, H-2), 4.35 (dd, $J = 9.2$, 5.1 Hz, 1H, H-3), 4.09–3.92 (m, 3H, H-6, OCH₂), 3.92–3.77 (m, 2H, H-4, H-5), 3.71 (m, 1H, OCH₂), 3.64–3.52 (m, 2H, NCH₂), 3.52–3.37 (m, 2H, NCH₂), 3.36–3.06 (m, 2H, NCH₂), 2.74 (t, $J = 6.7$ Hz, 2H, CH₂SH), 2.55 (t, $J = 6.7$ Hz, 2H, CH₂), 2.19–1.97 (m, 2H, CH₂); ¹³C NMR (126 MHz, D₂O): $\delta = 174.7$, 170.1 (2 CO), 146.5 (triazole-C_q), 133.3, 132.8, 127.9, 125.8 (Ar-C), 122.9 (triazole-CH), 97.4 (C-1), 73.1 (C-5), 68.6 (C-3), 66.2 (C-4), 65.2 (OCH₂), 63.6 (C-2), 60.4 (C-6), 39.41 (CH₂), 39.35 (NCH₂), 38.5 (NCH₂), 37.4 (NCH₂), 26.6 (CH₂), 19.9 (CH₂SH); ESI-MS: m/z : Calcd for C₂₃H₃₅N₆O₇S [M+H]⁺: 539.6, found: 539.2.

NMR spectra of Glycomimetic DC-SIGN Ligands



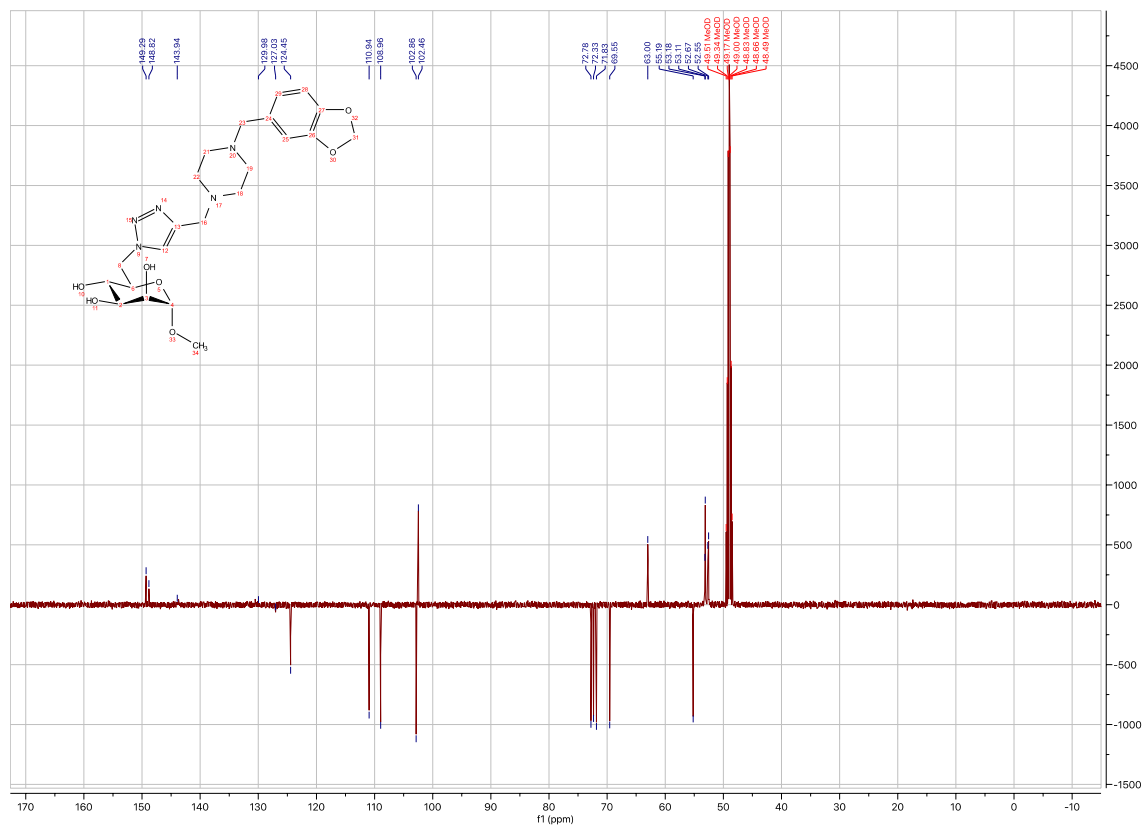


Figure S1. ¹H and ¹³C APT NMR spectra of 1a.

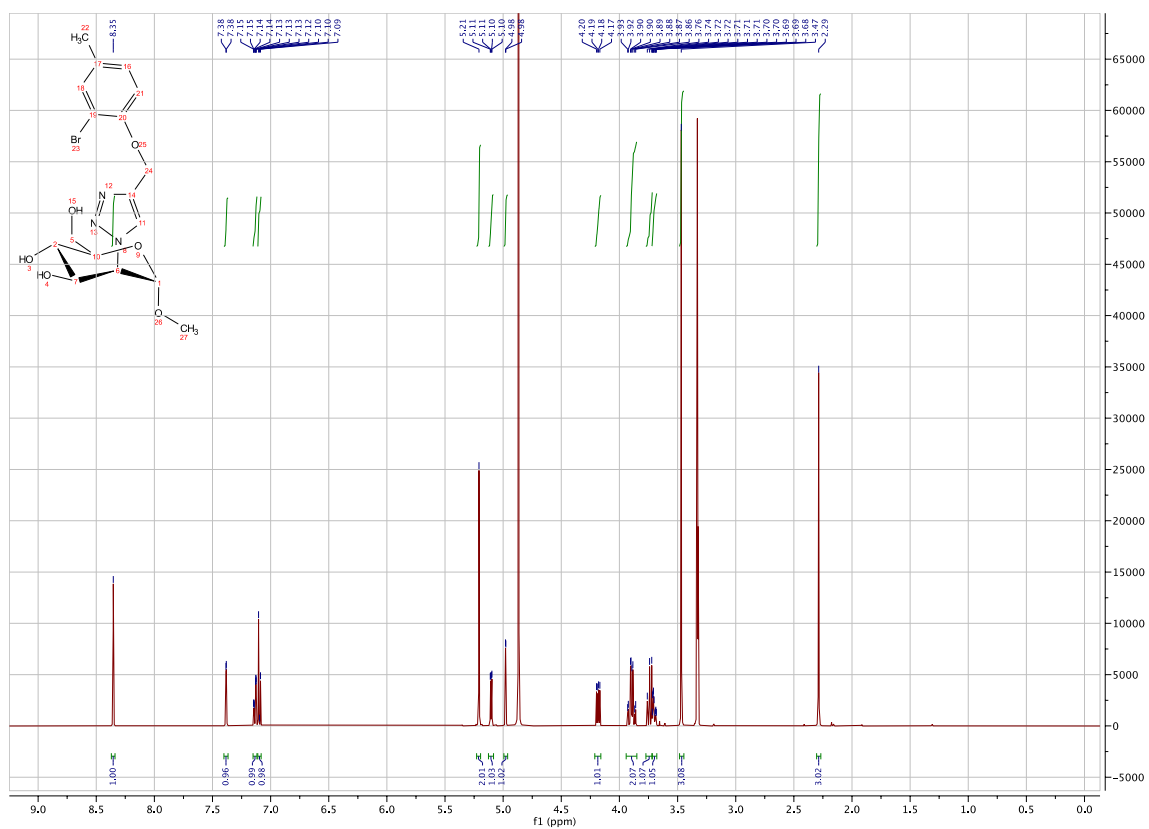
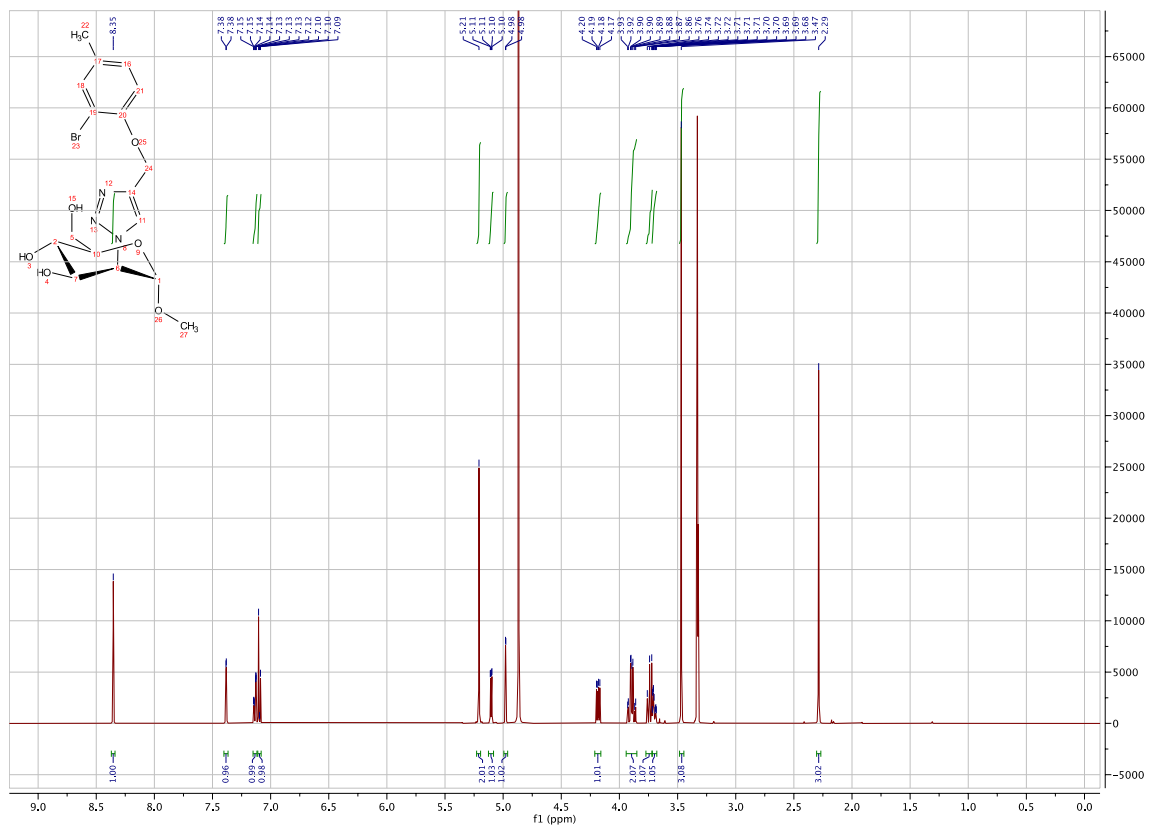


Figure S2. ^1H and ^{13}C APT NMR spectra of **1b**.

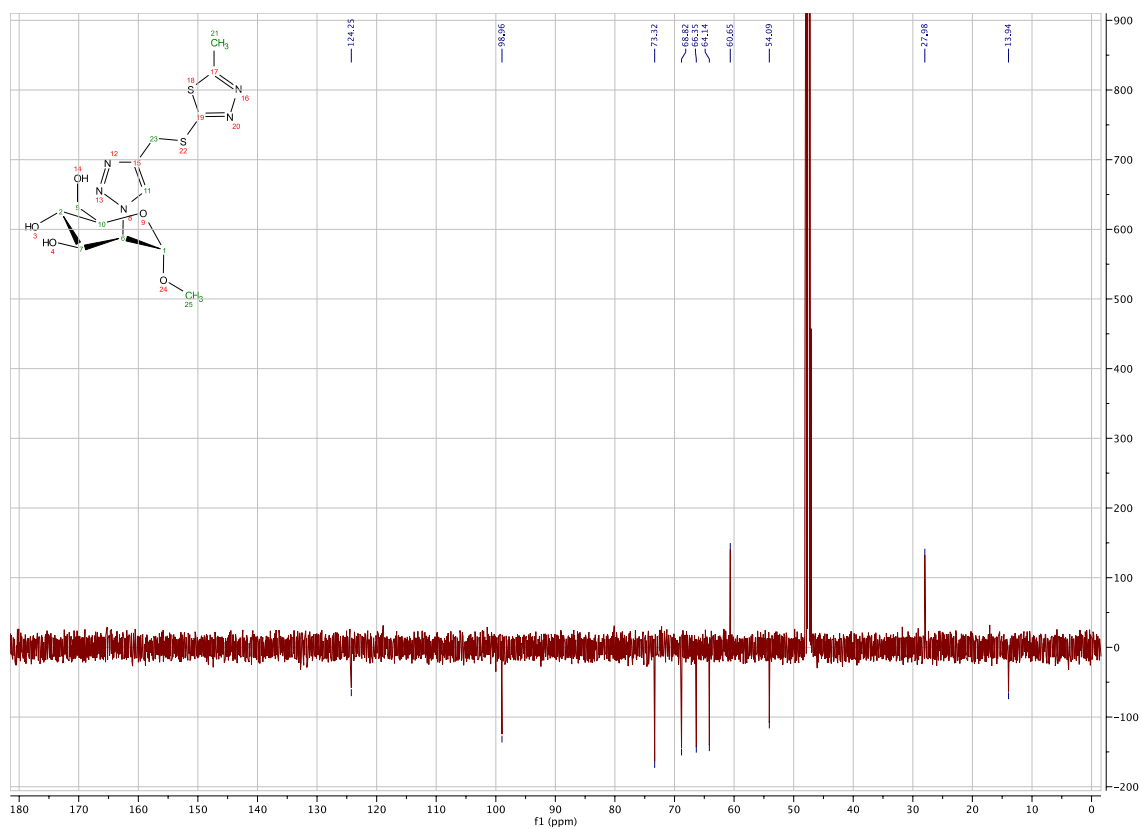
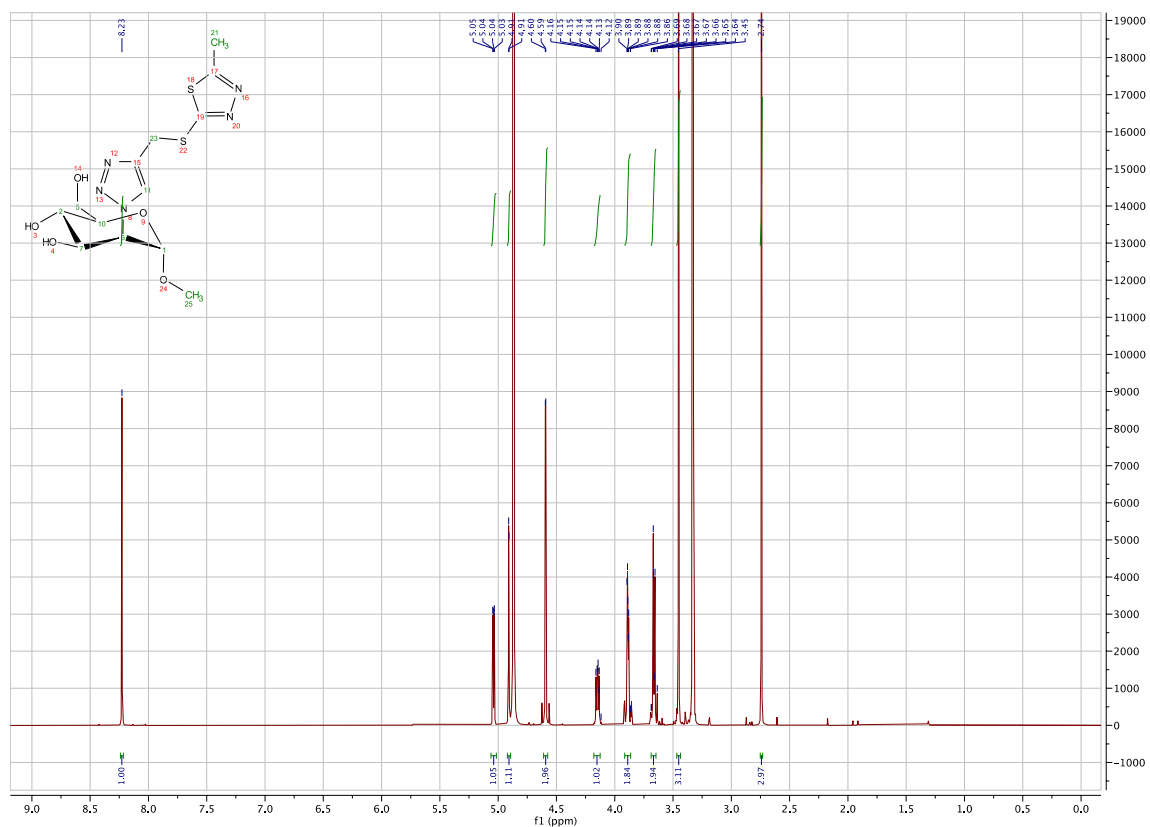


Figure S3. ¹H and ¹³C APT NMR spectra of 1c.

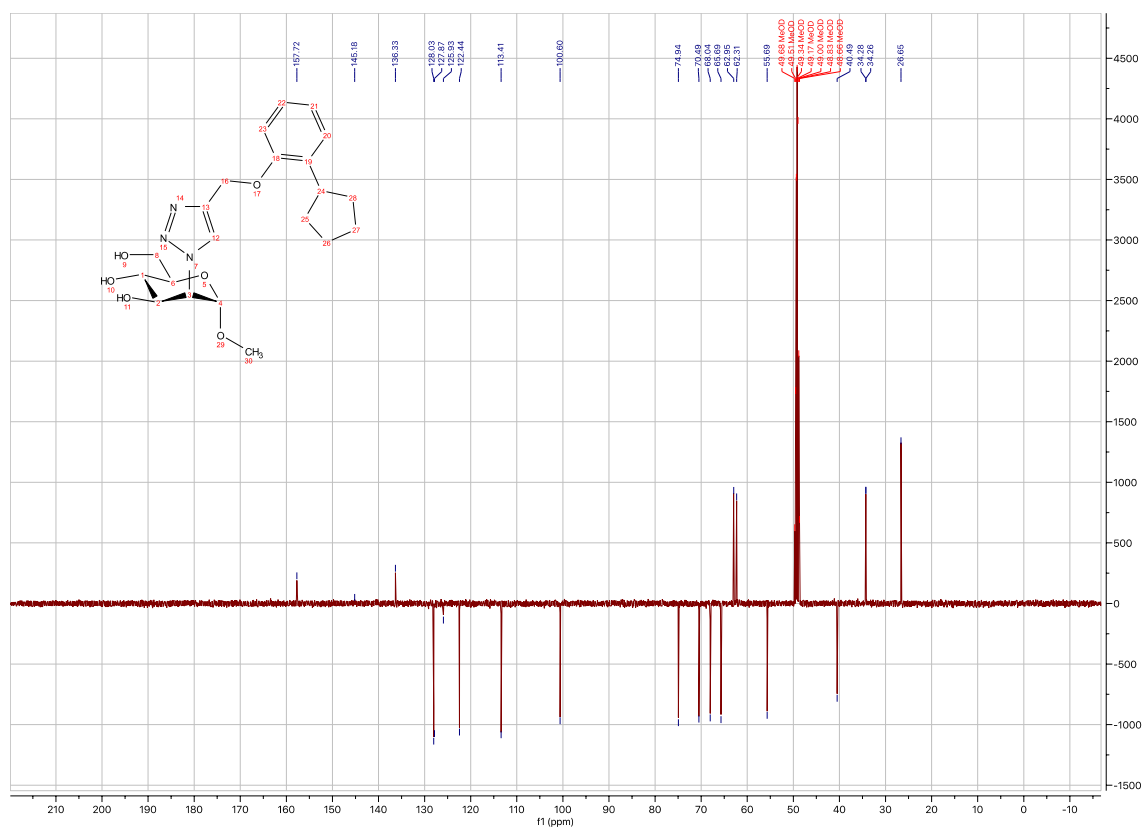
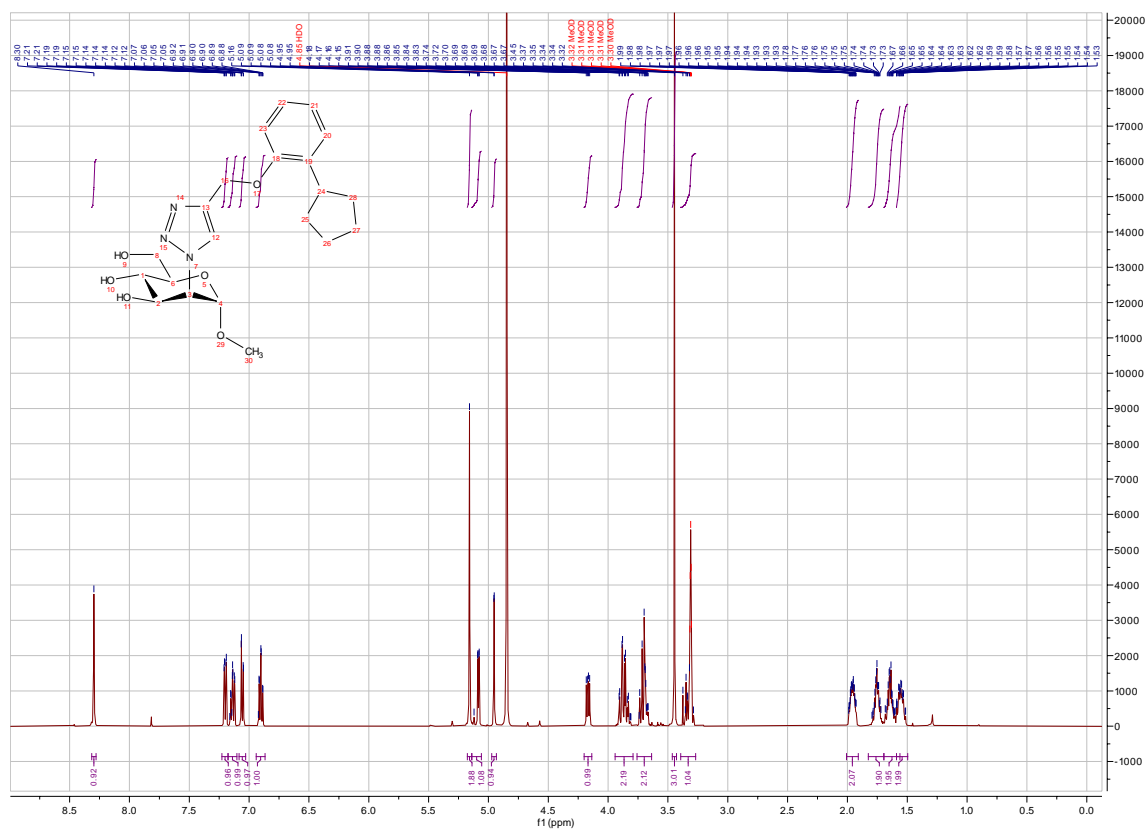


Figure S4. ¹H and ¹³C APT NMR spectra of **1d**.

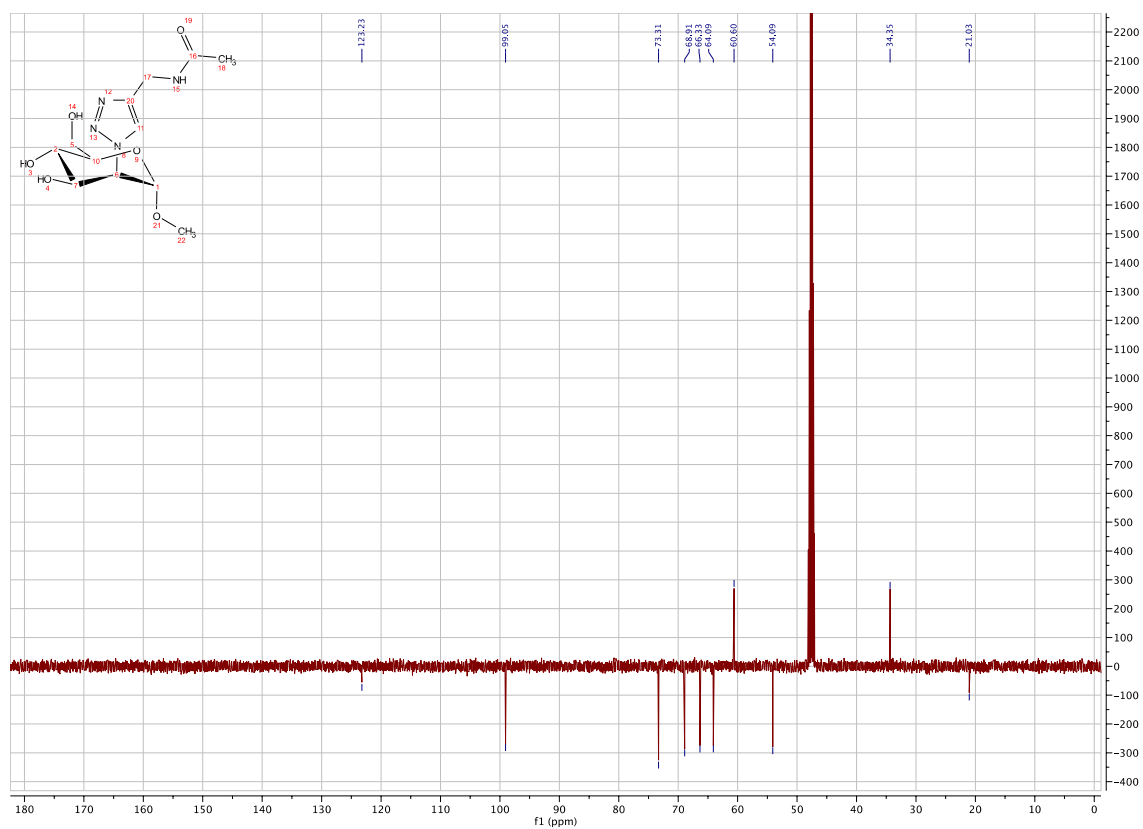
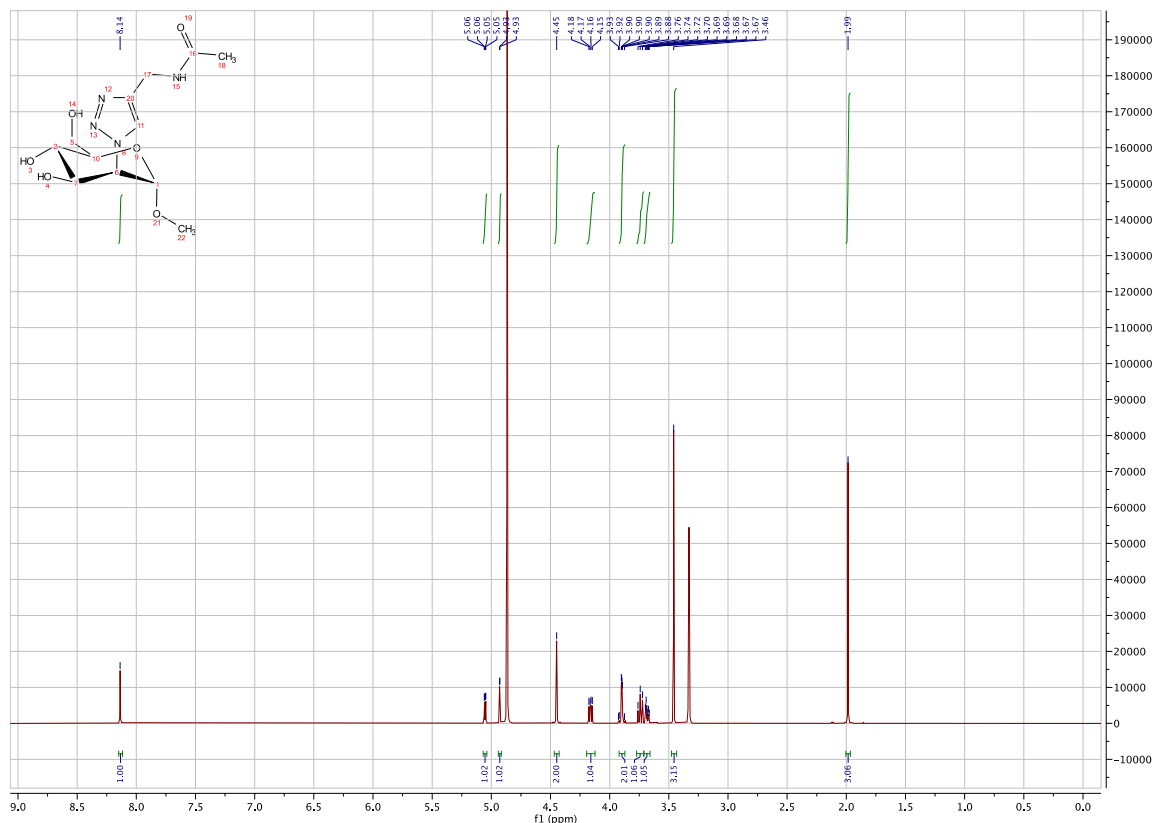


Figure S5. ¹H and ¹³C APT NMR spectra of 1e.

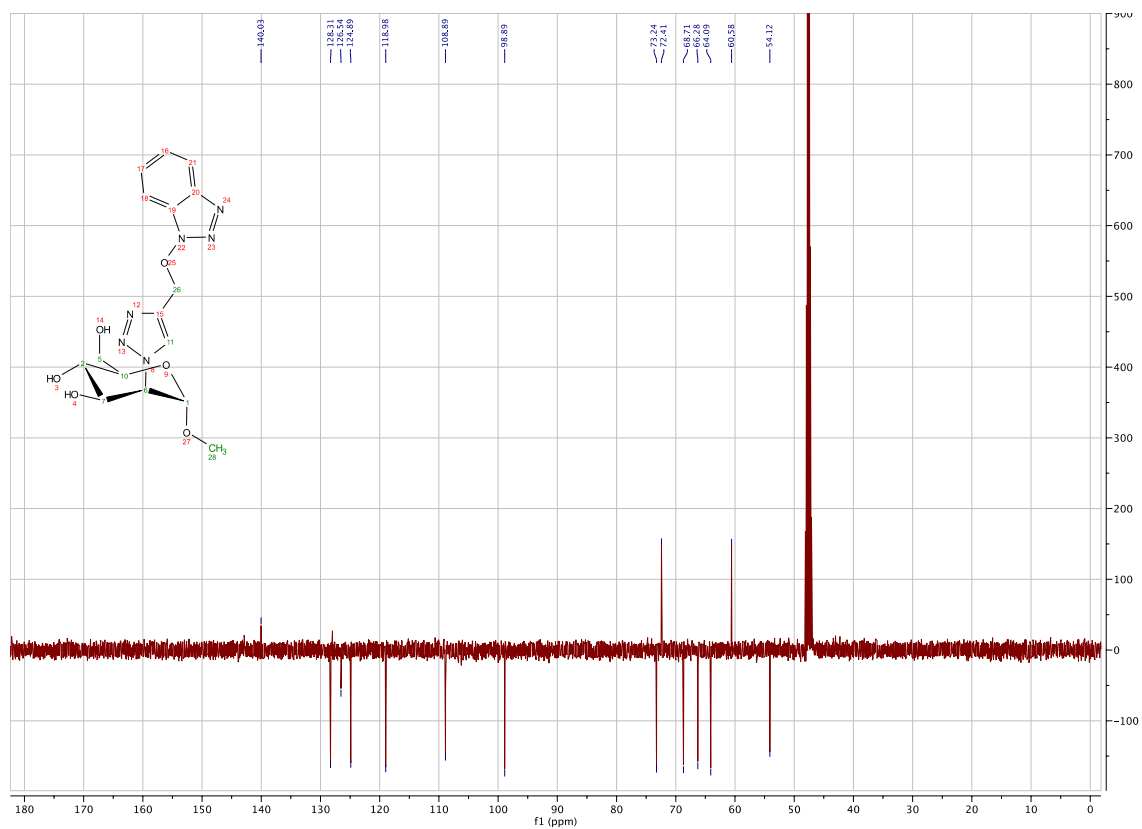
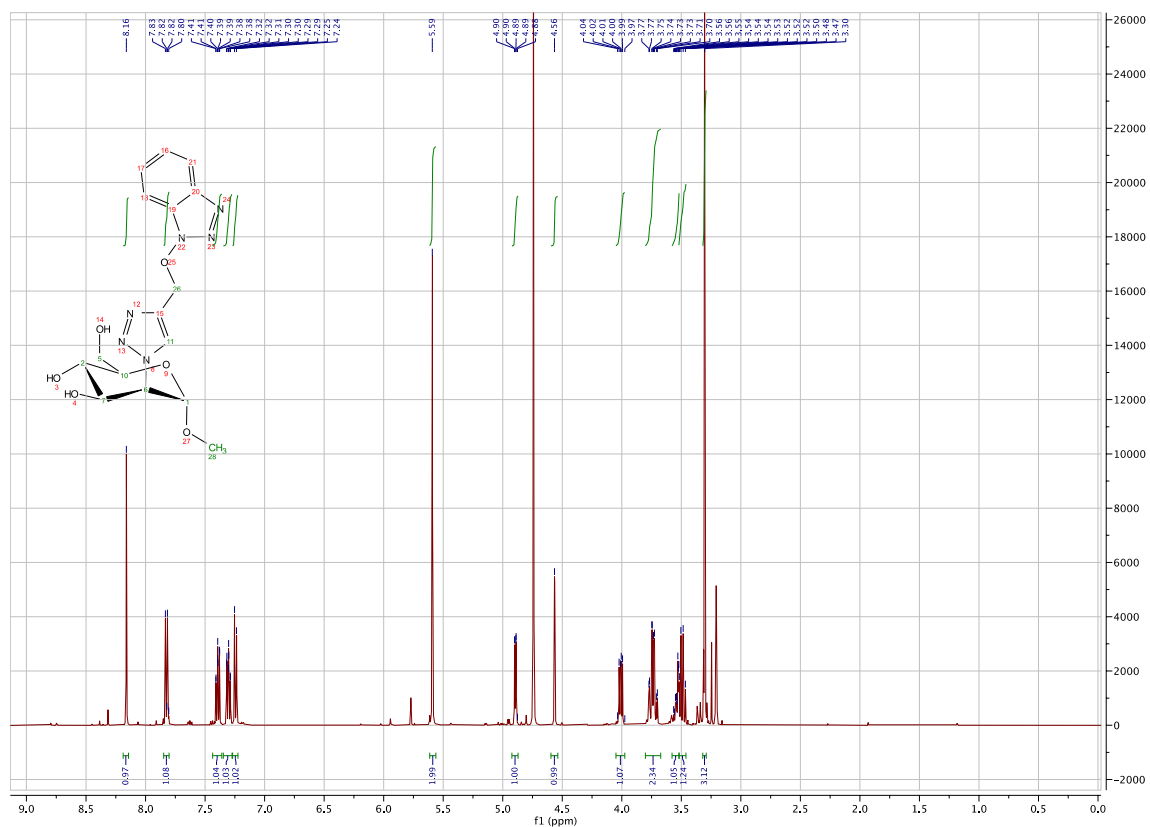


Figure S6. ¹H and ¹³C APT NMR spectra of 1f.

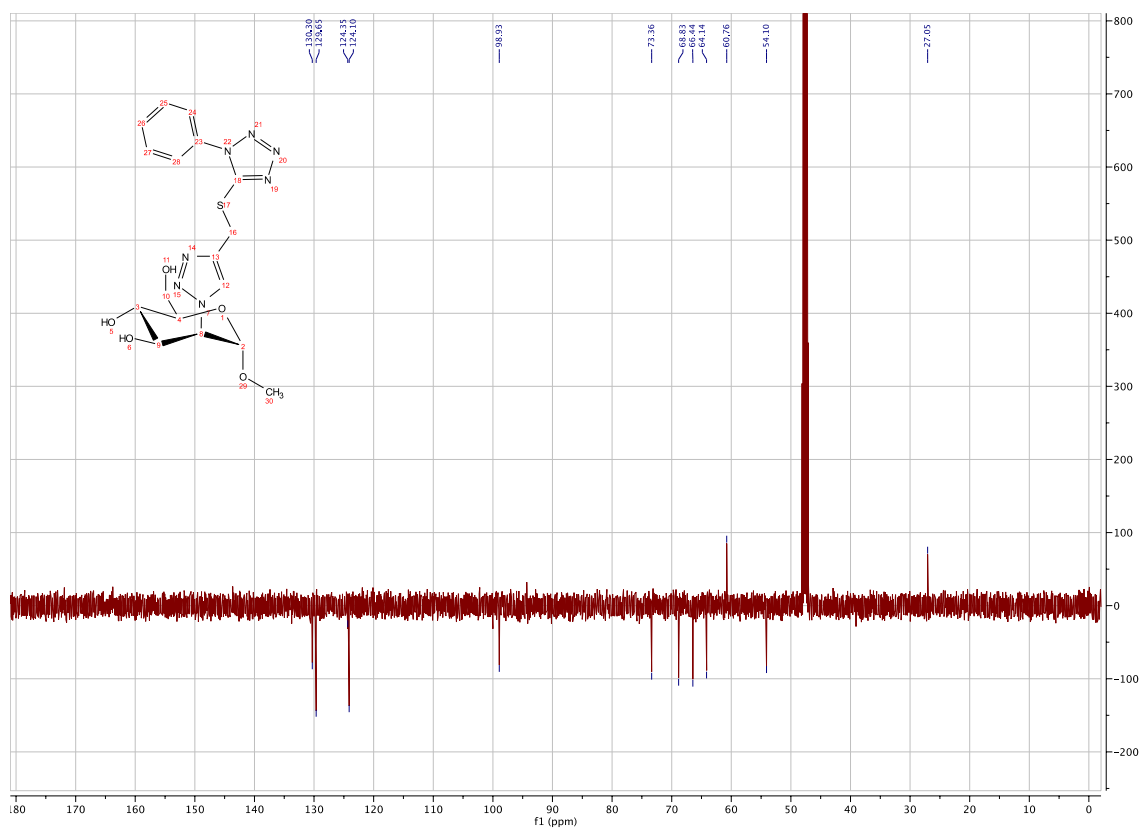
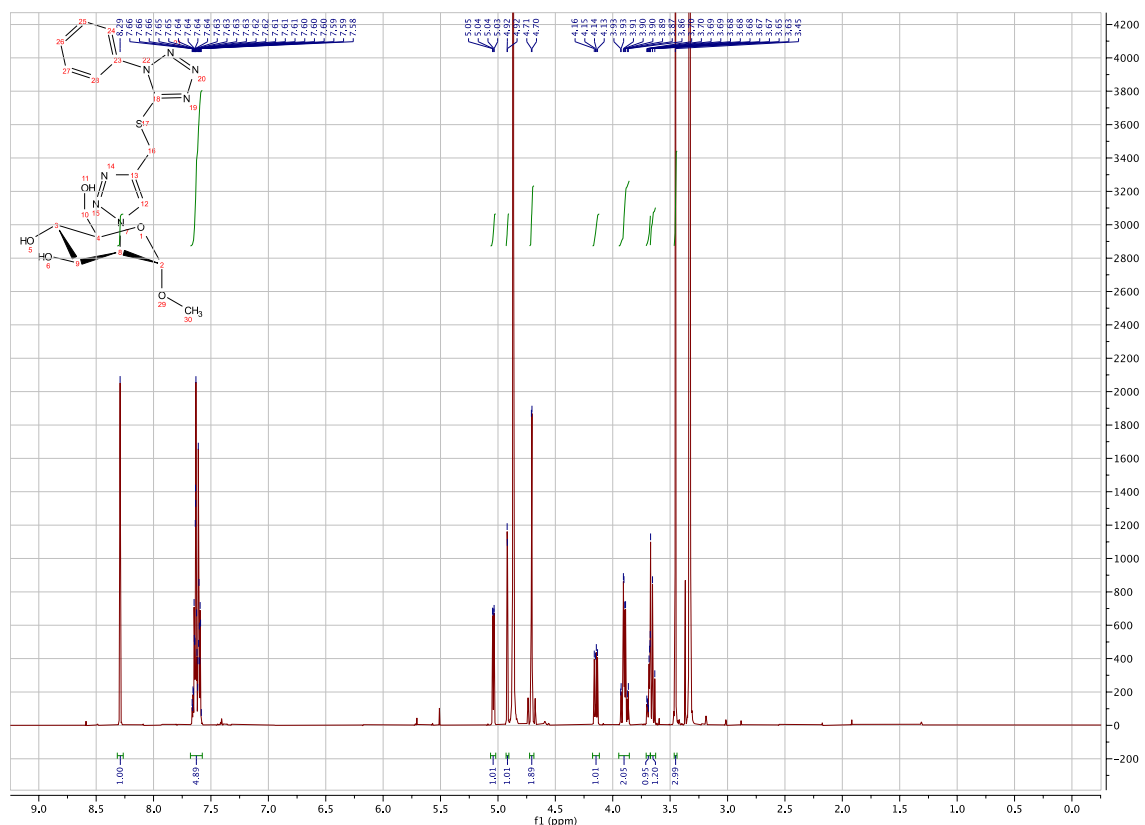


Figure S7. ¹H and ¹³C APT NMR spectra of 1g.

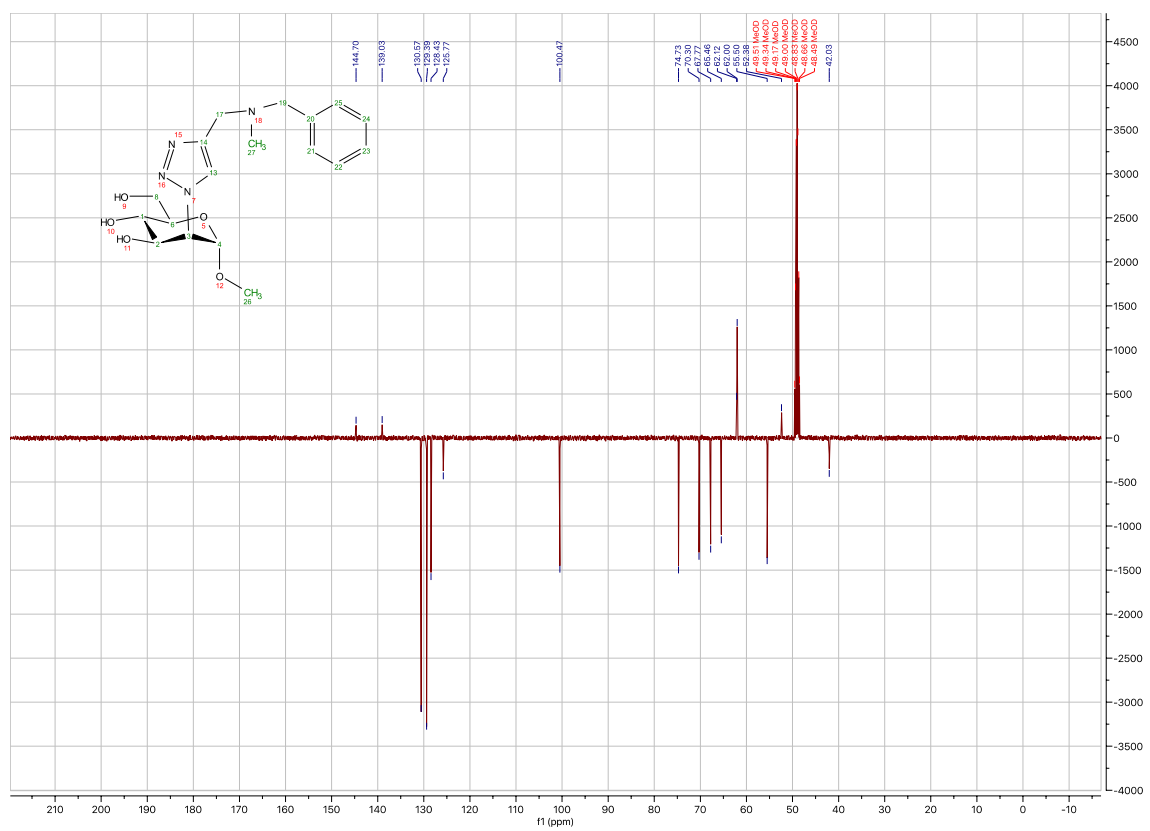
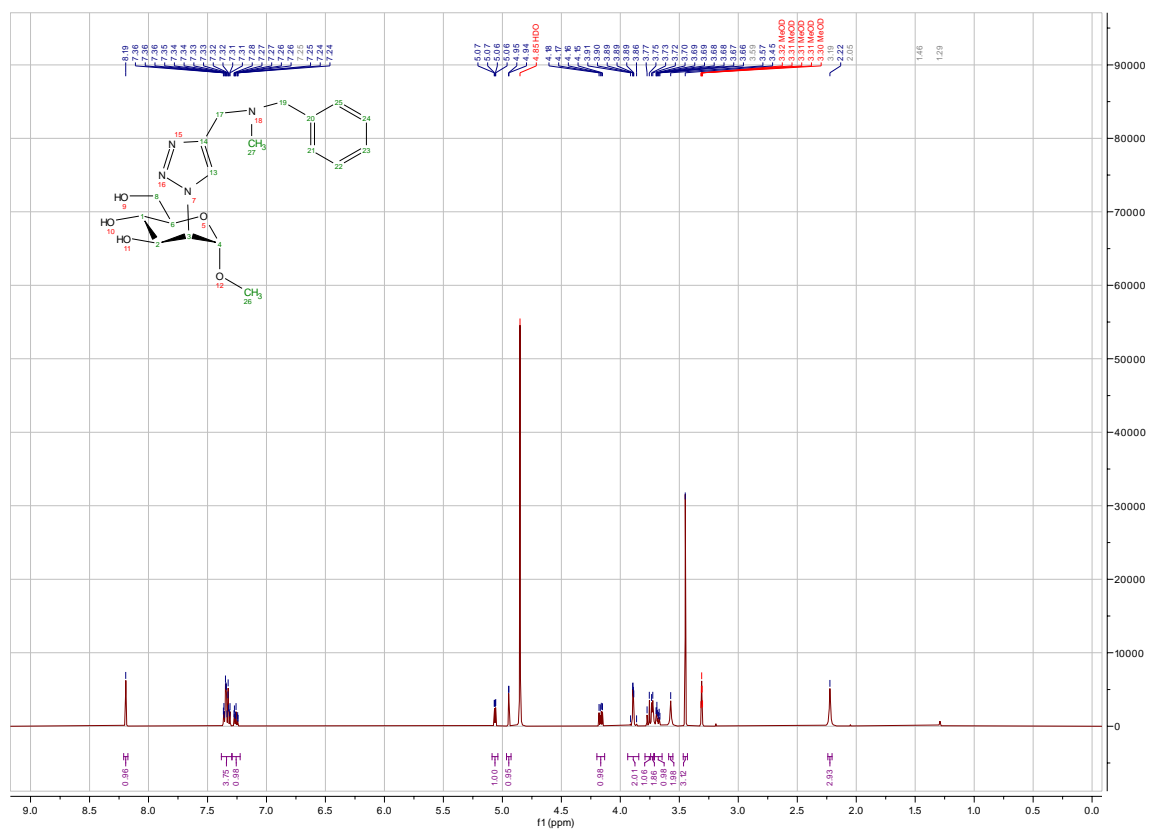


Figure S8. ¹H and ¹³C APT NMR spectra of 1h.

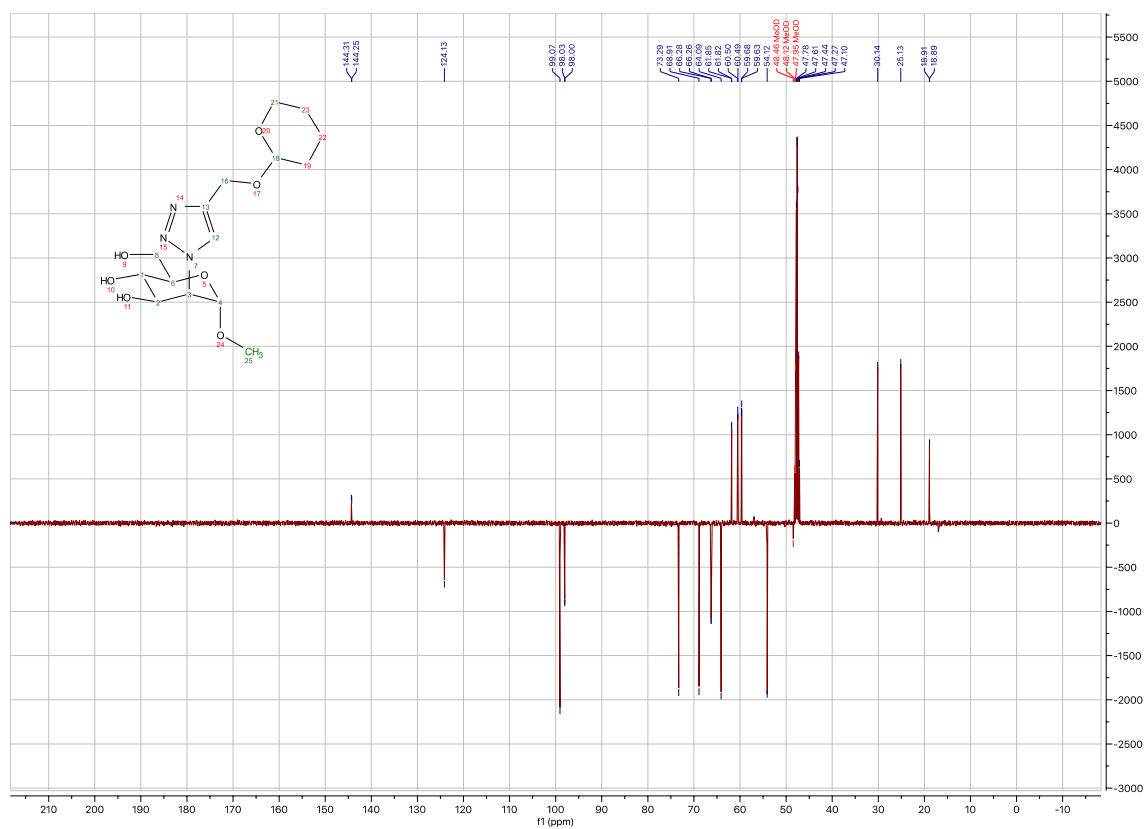
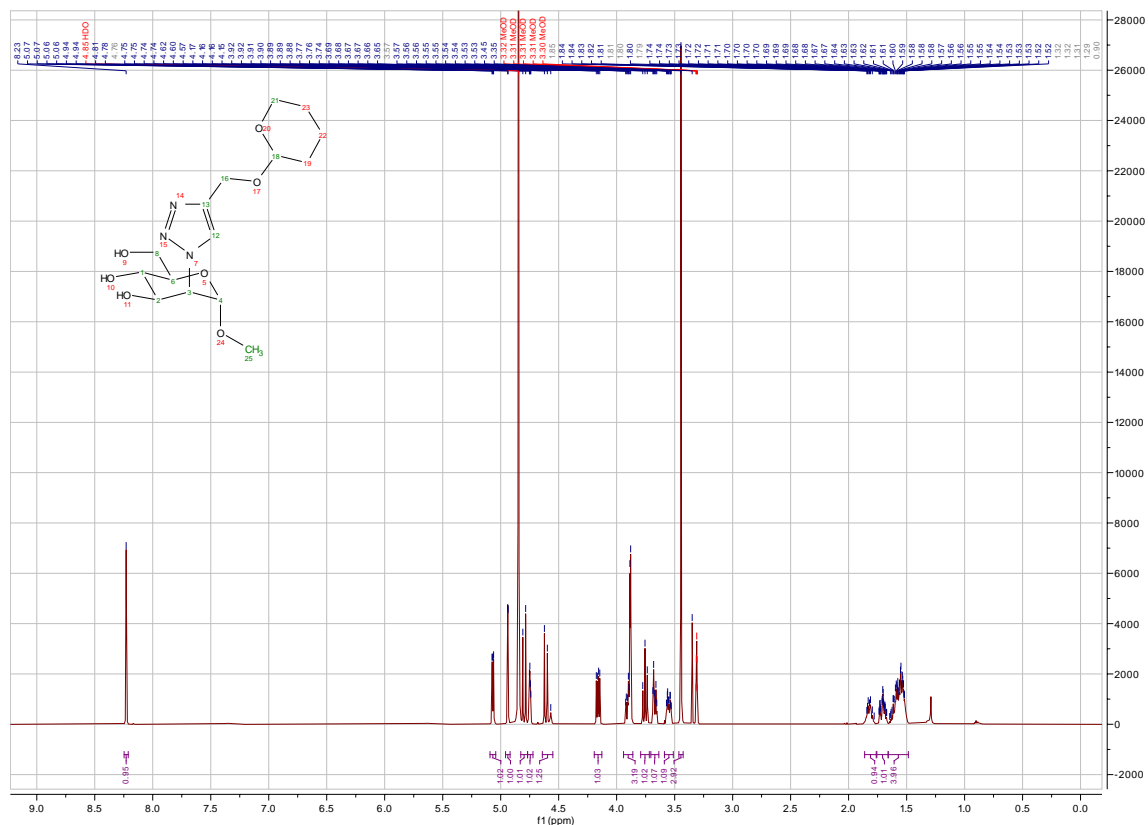


Figure S9. ¹H and ¹³C APT NMR spectra of 1i.

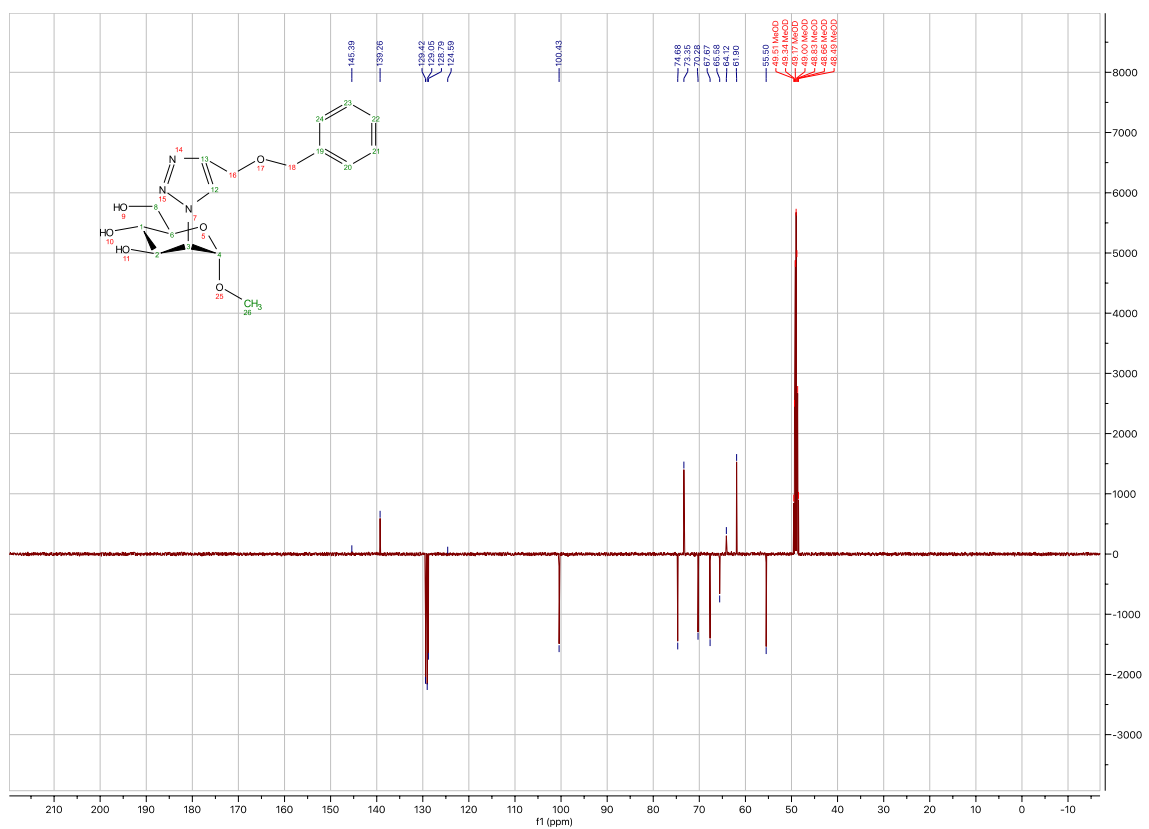
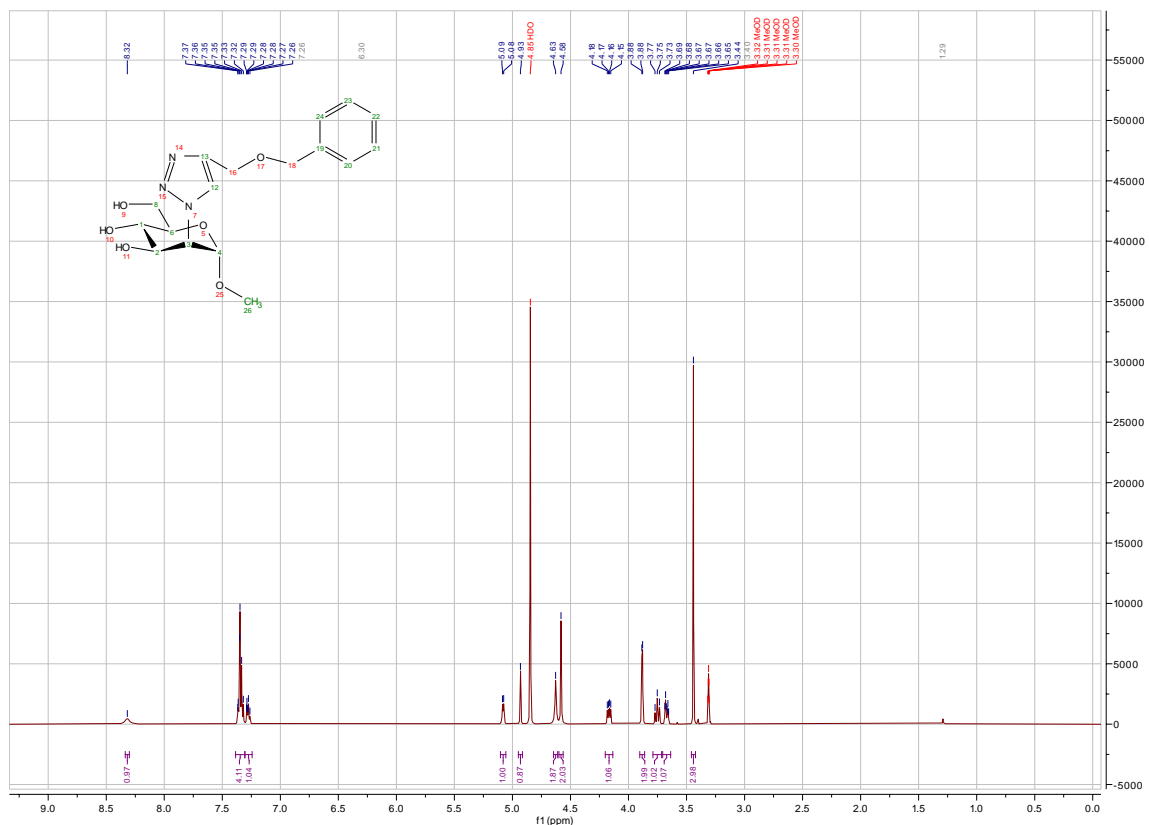


Figure S10. ¹H and ¹³C APT NMR spectra of 1j.

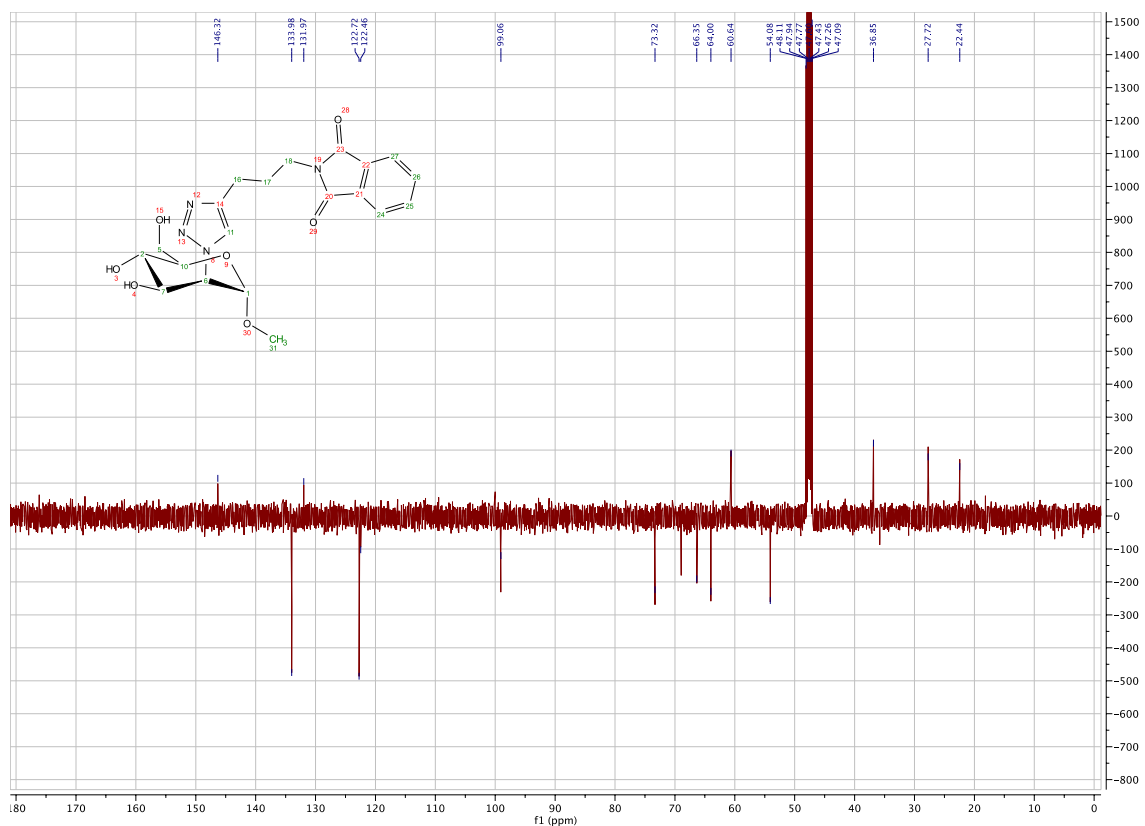
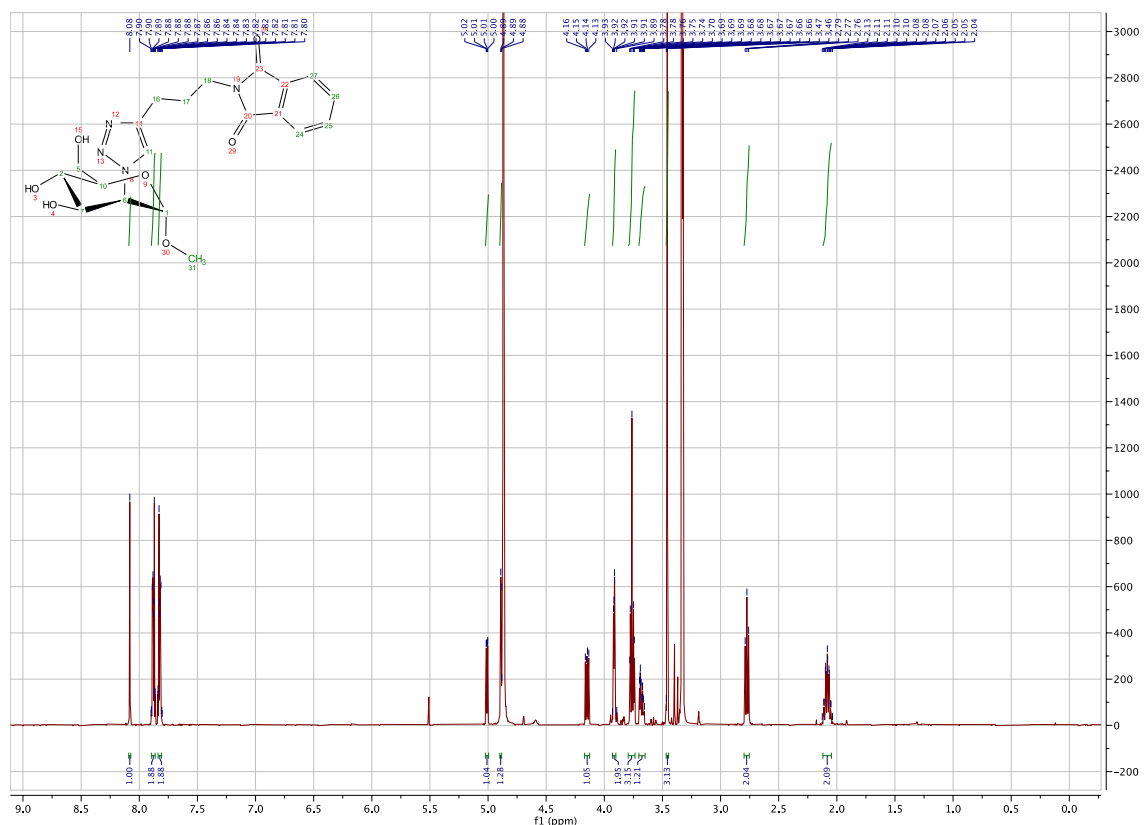


Figure S11. ¹H and ¹³C APT NMR spectra of 1k.

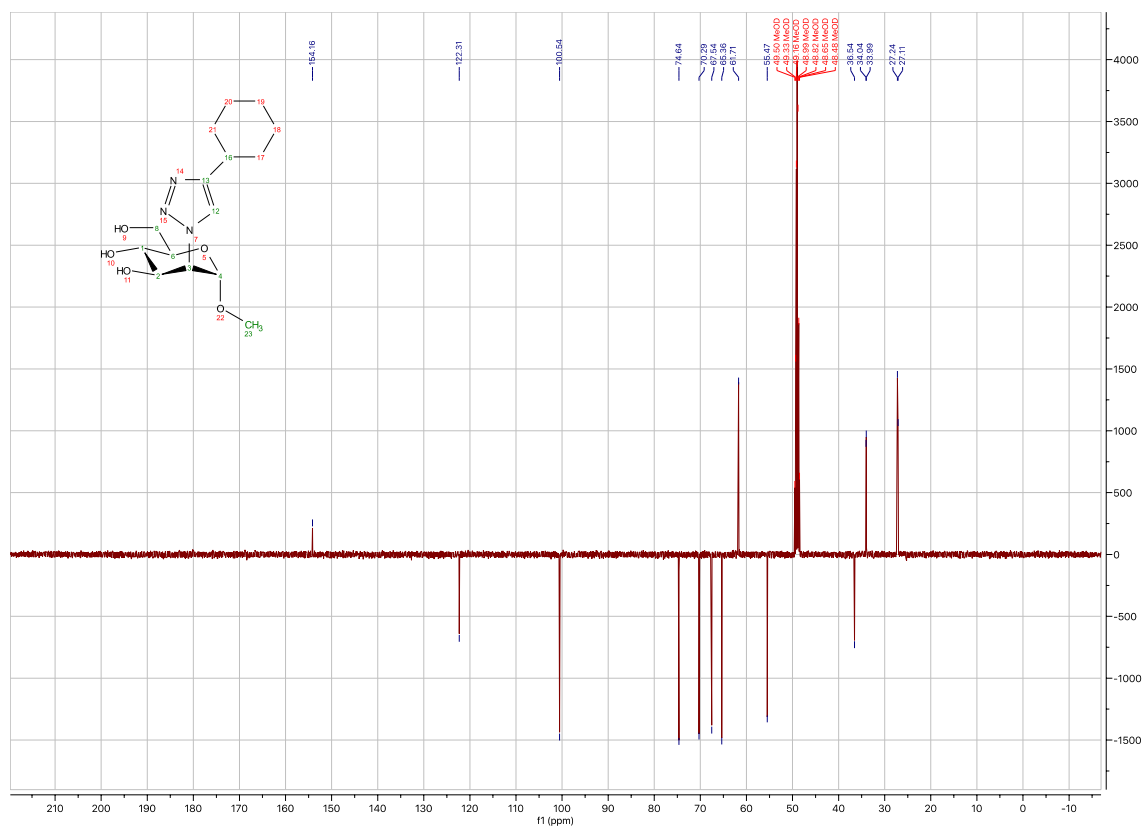
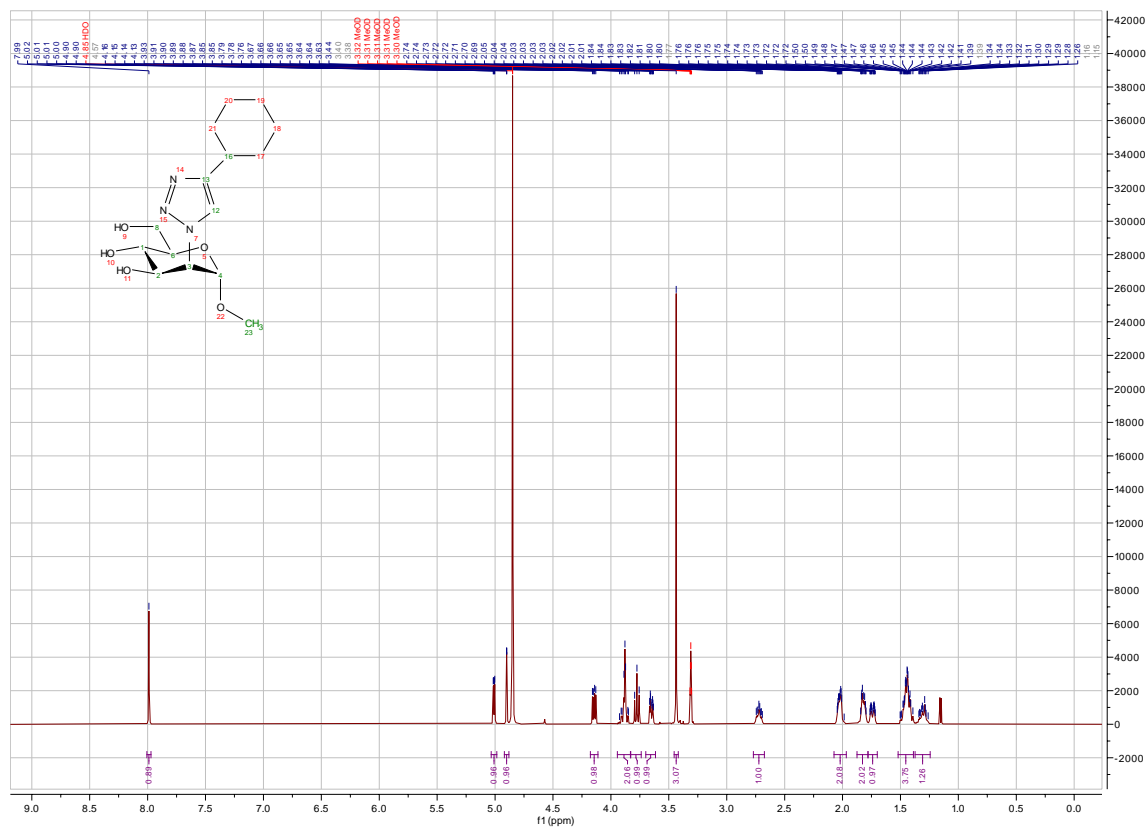


Figure S12. ¹H and ¹³C APT NMR spectra of 11.

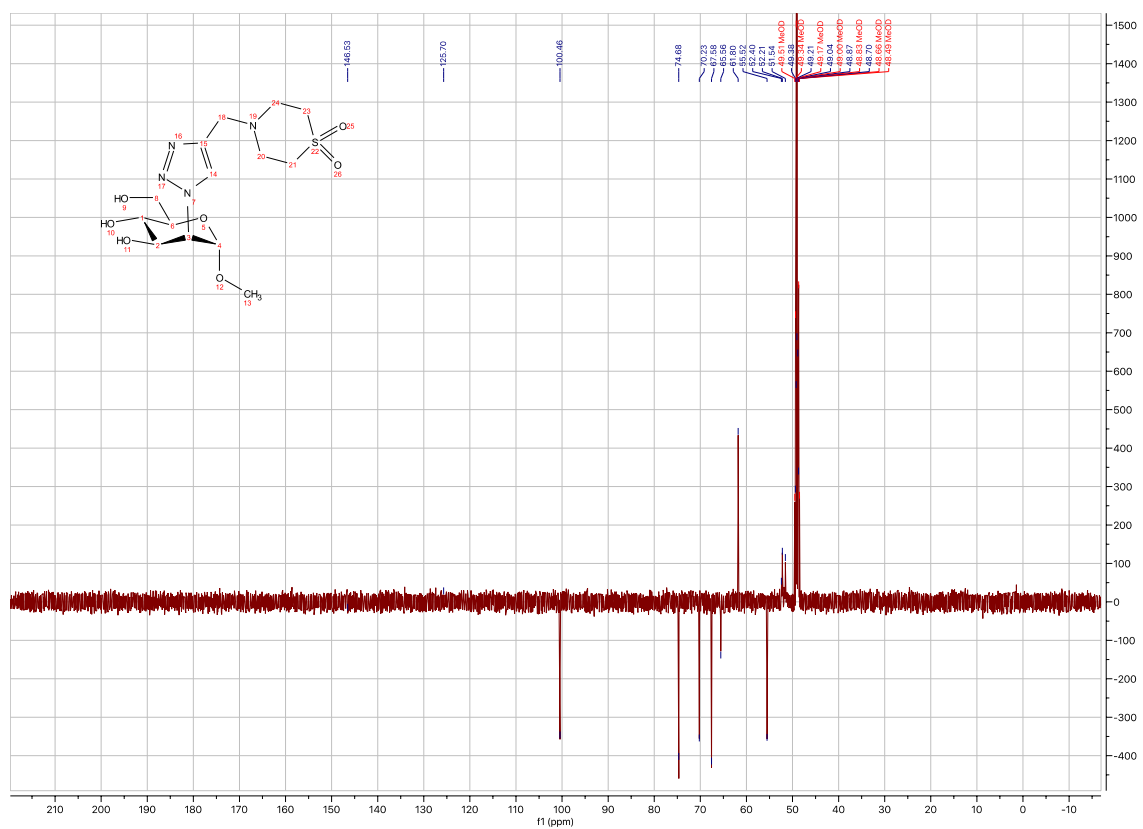
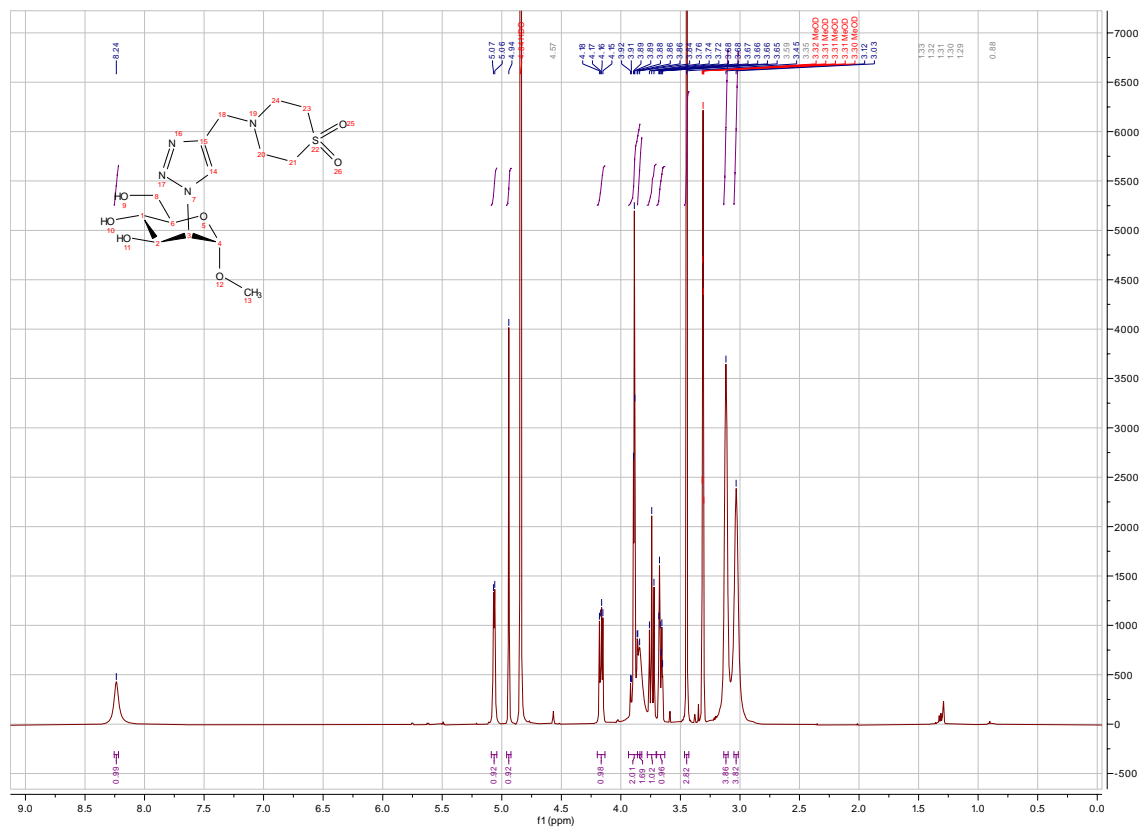


Figure S13. ¹H and ¹³C APT NMR spectra of 1m.

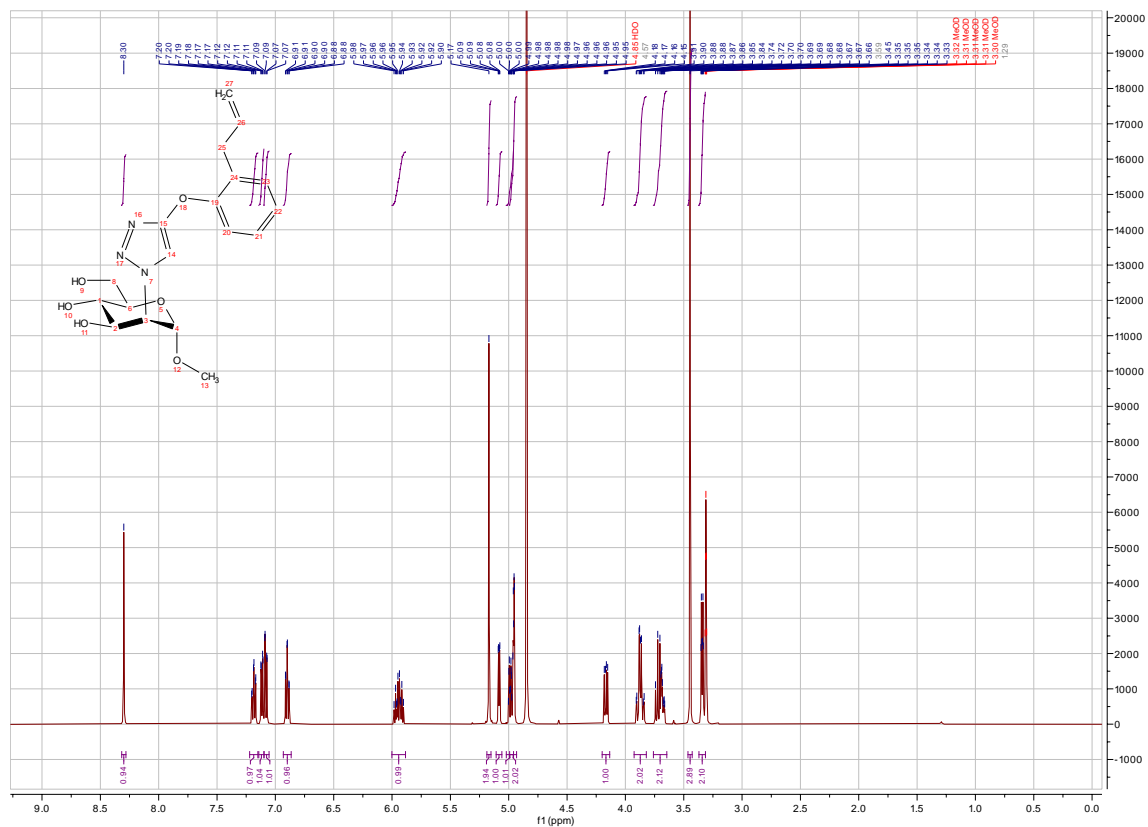


Figure S14. ^1H and ^{13}C APT NMR spectra of **1n**.

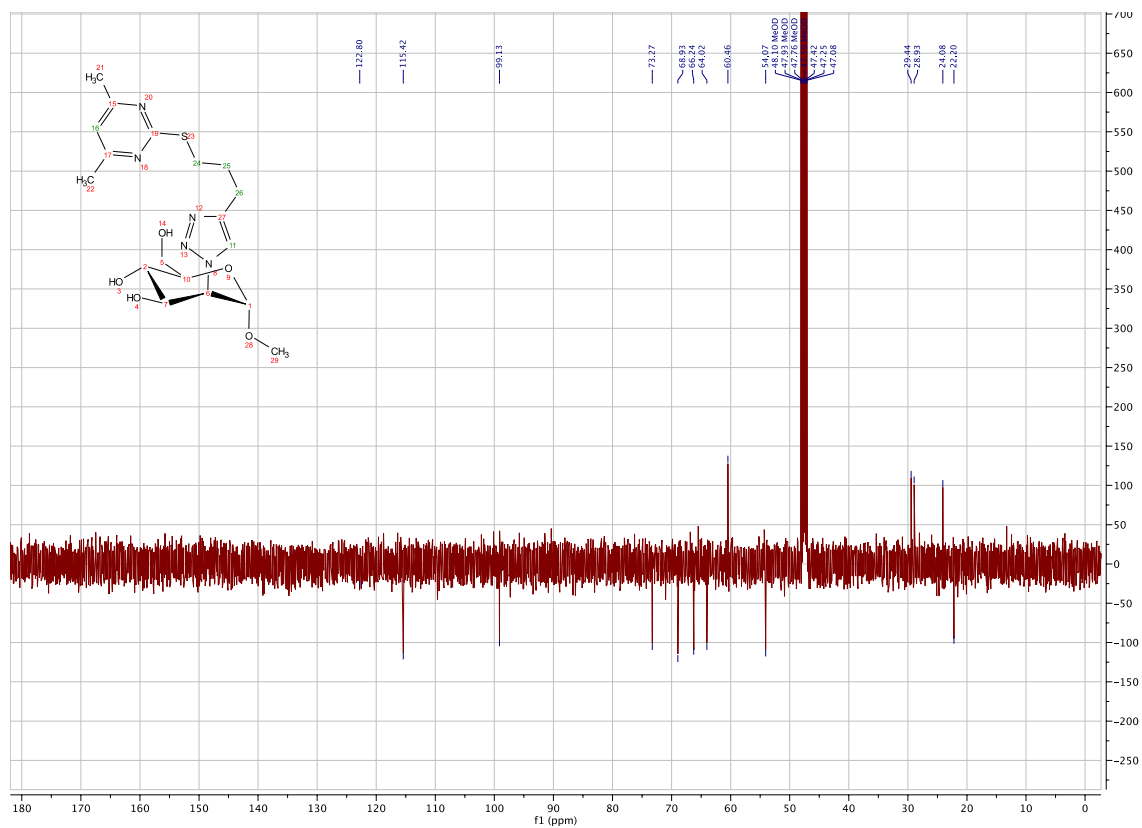
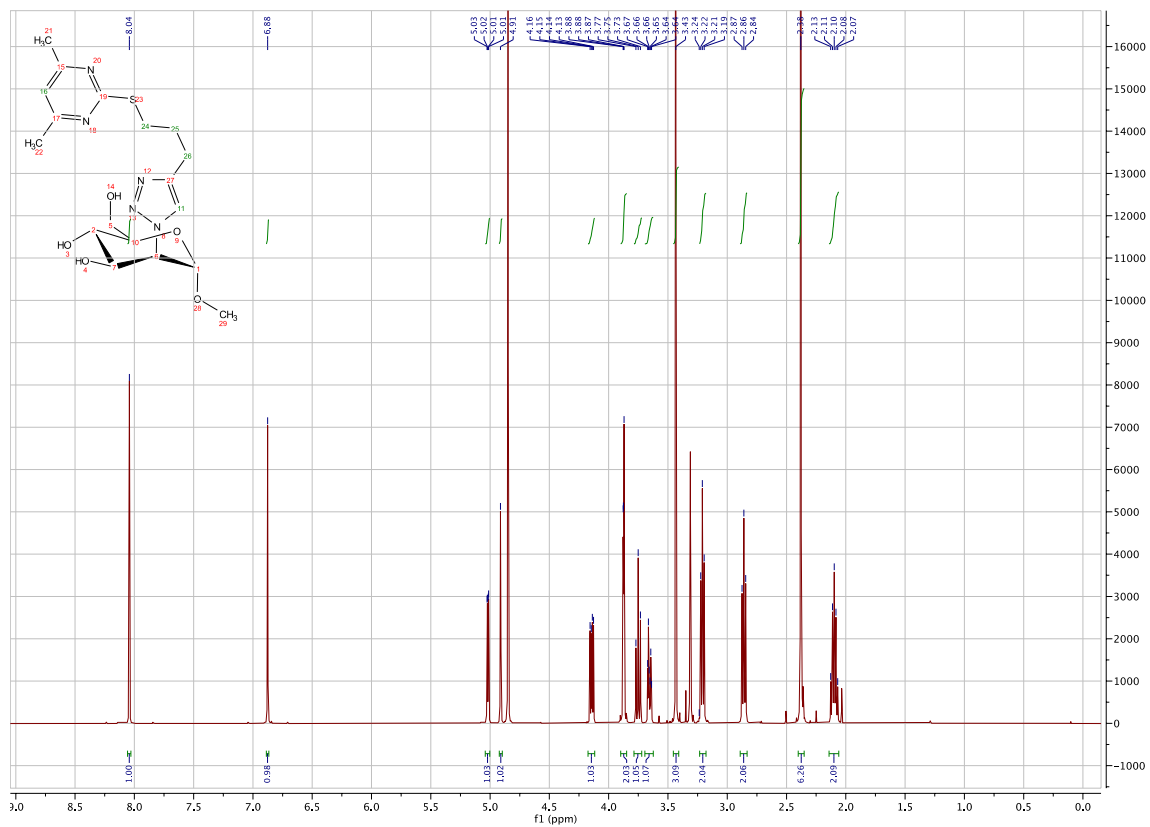


Figure S15. ¹H and ¹³C APT NMR spectra of 10.

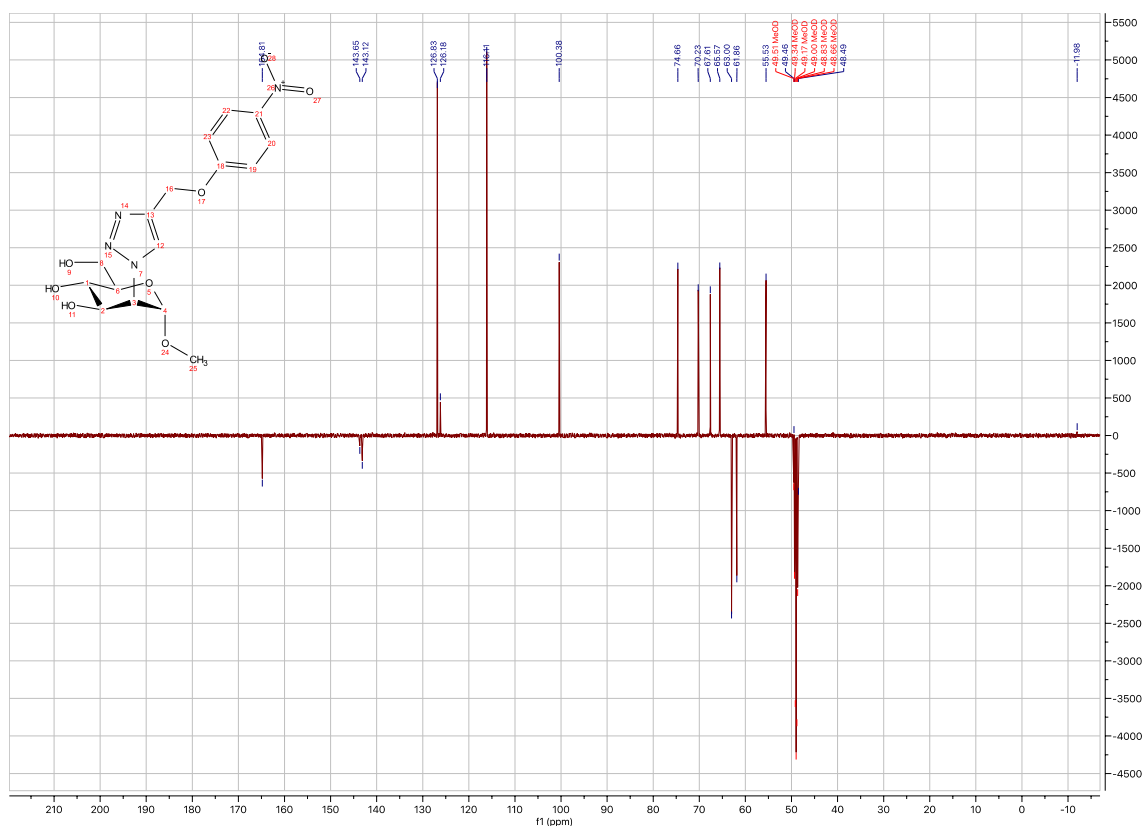
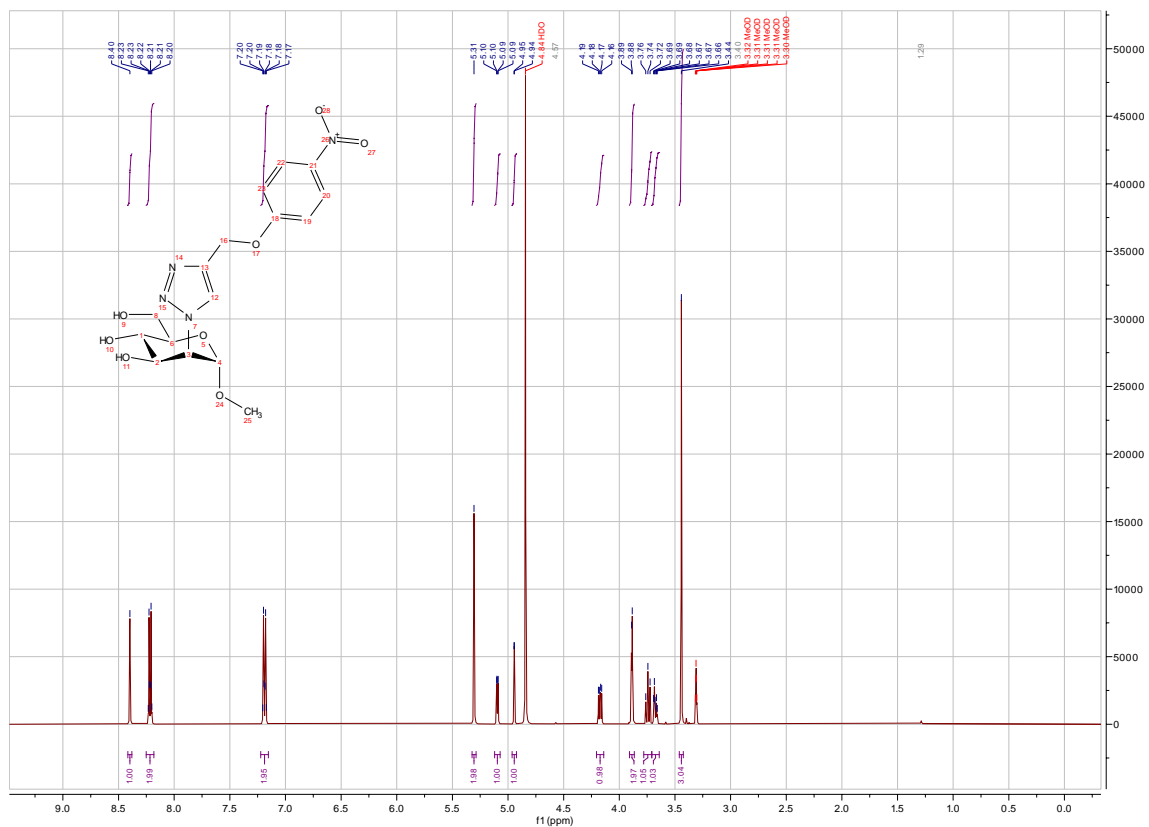


Figure S16. ¹H and ¹³C APT NMR spectra of 1p.

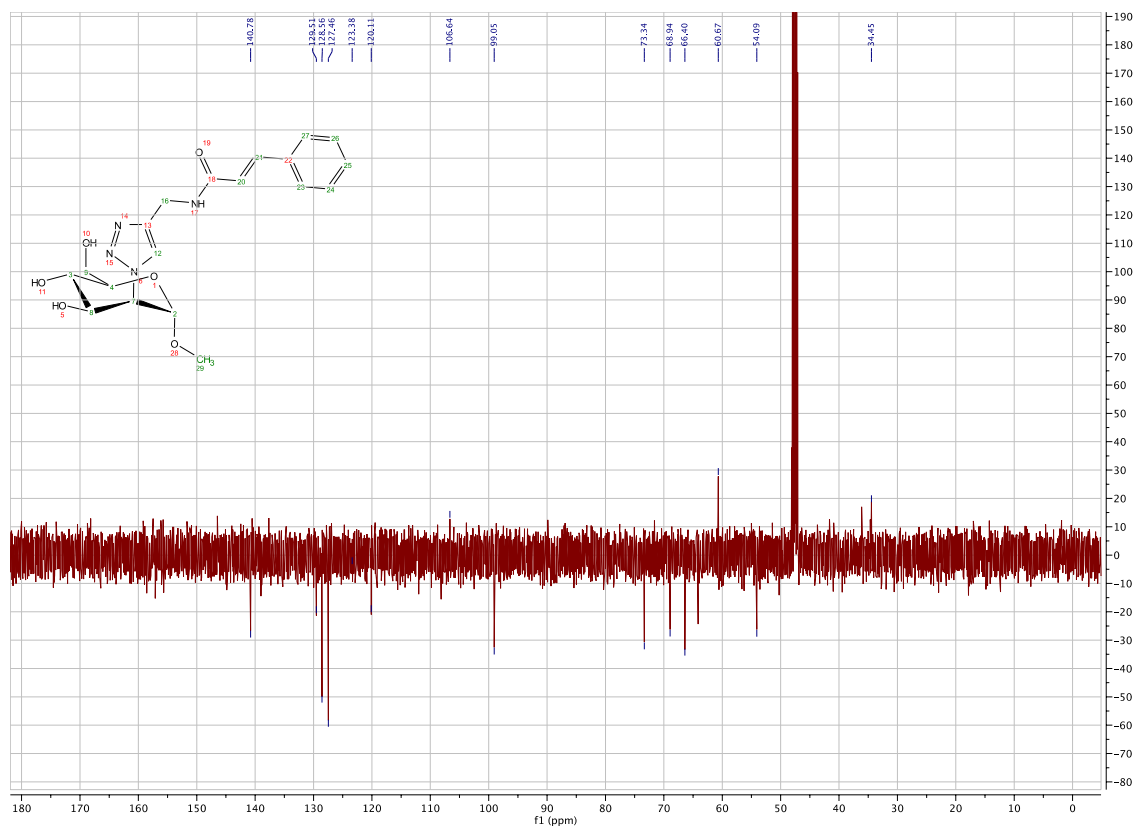
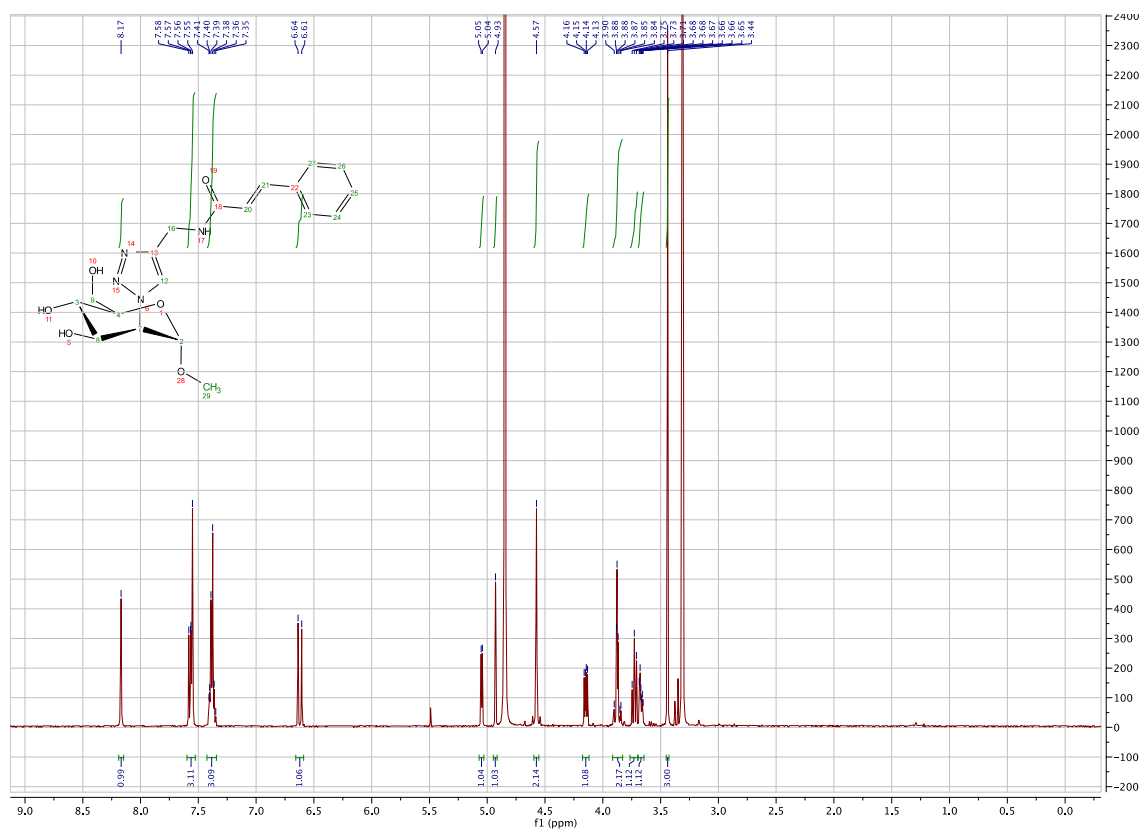


Figure S17. ¹H and ¹³C APT NMR spectra of 1q.

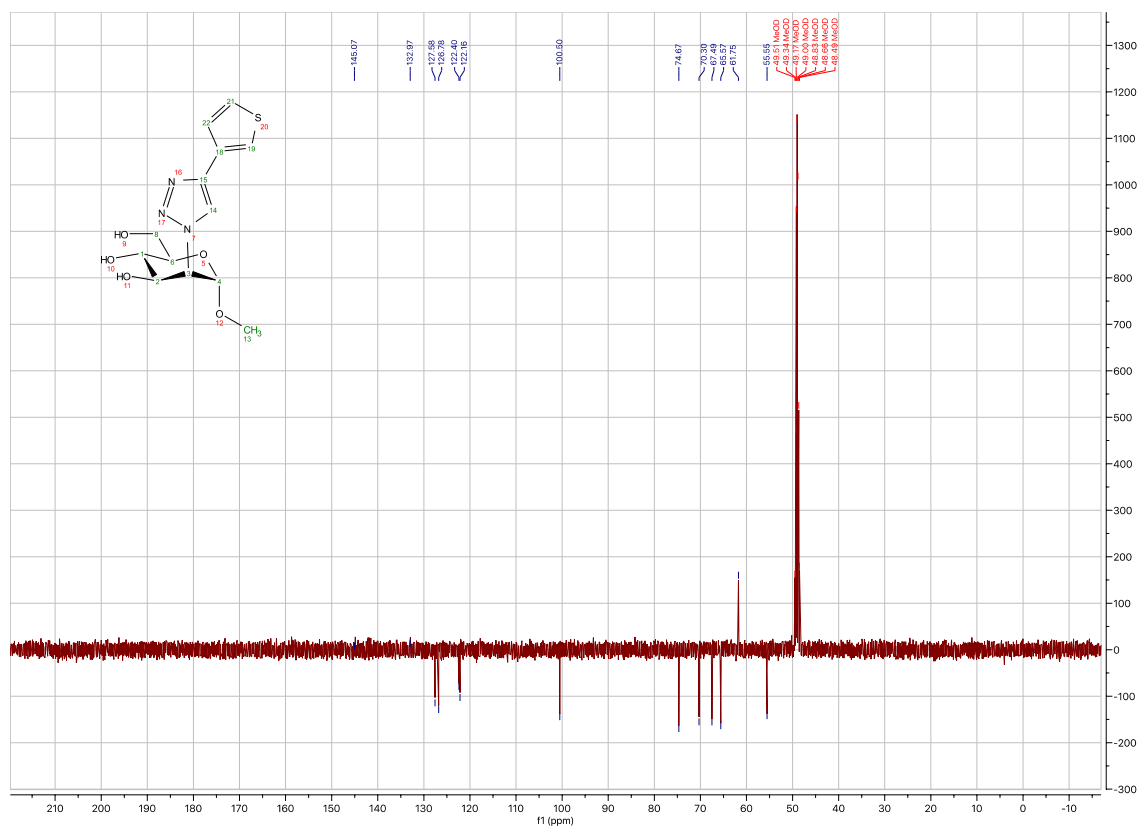
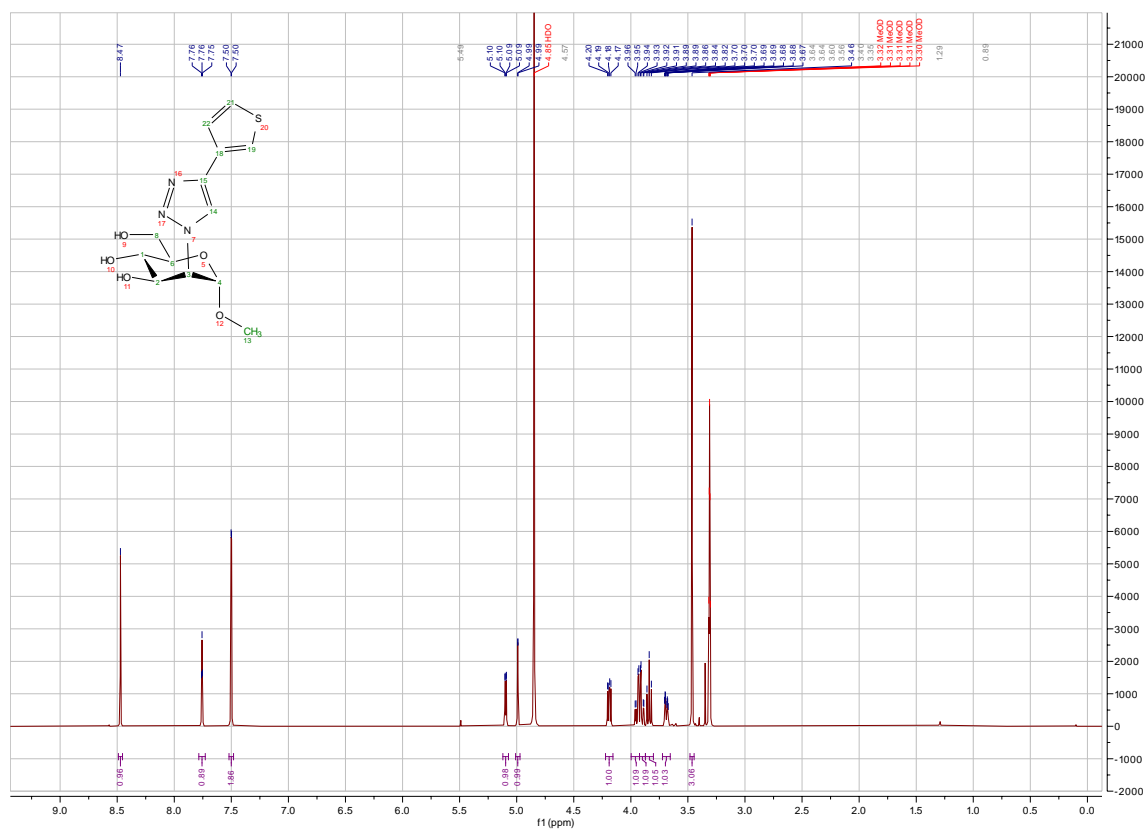


Figure S18. ^1H and ^{13}C APT NMR spectra of **1r**.

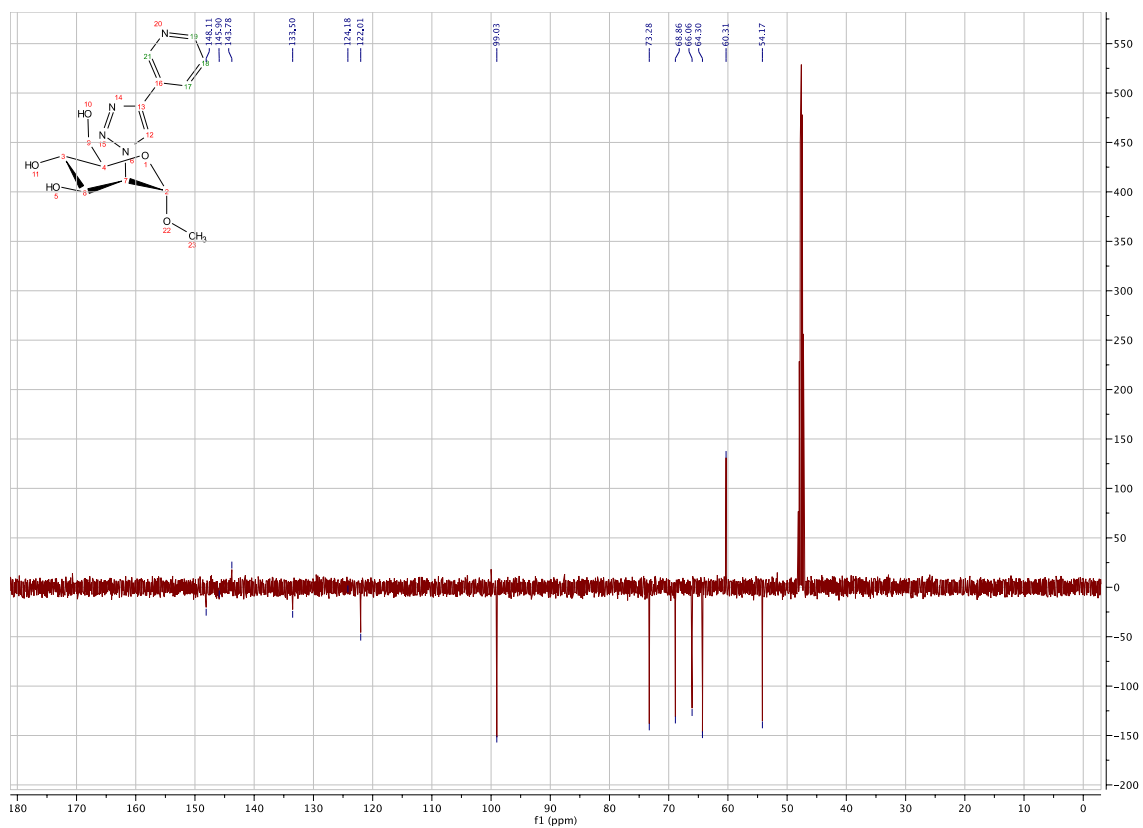
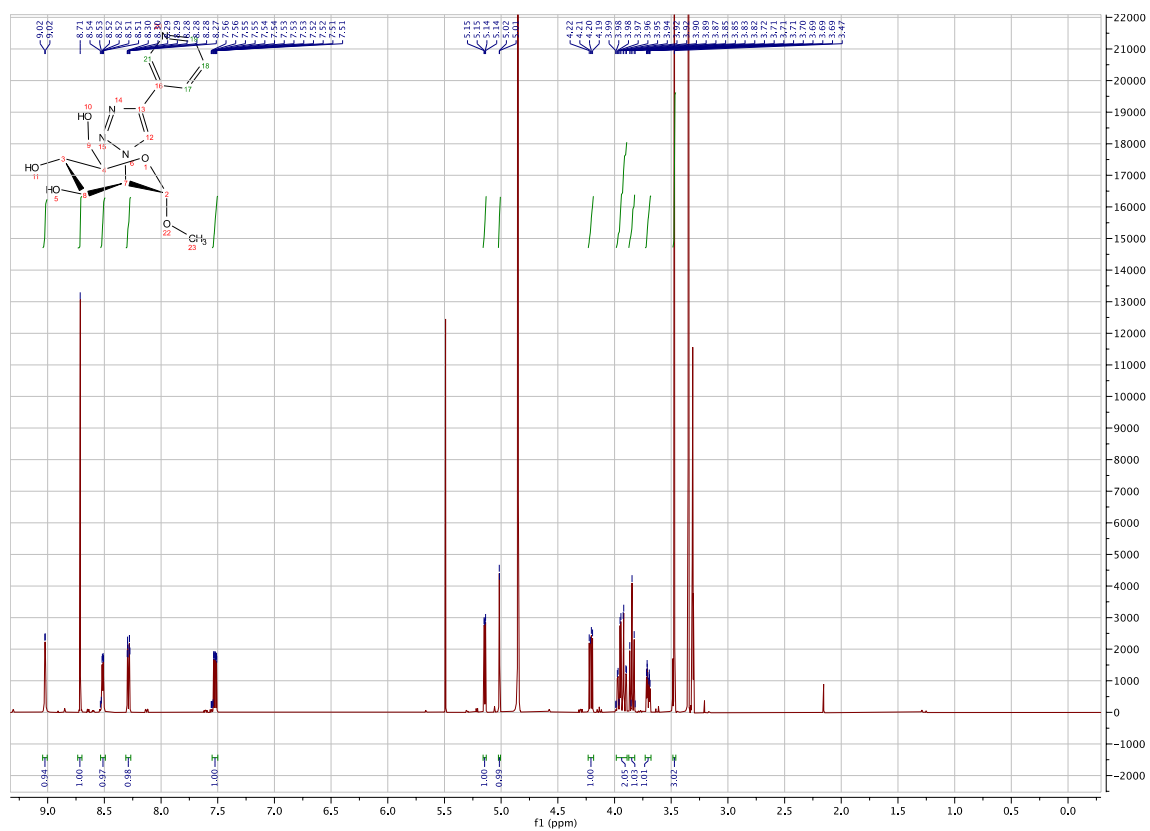


Figure S19. ¹H and ¹³C APT NMR spectra of 1s.

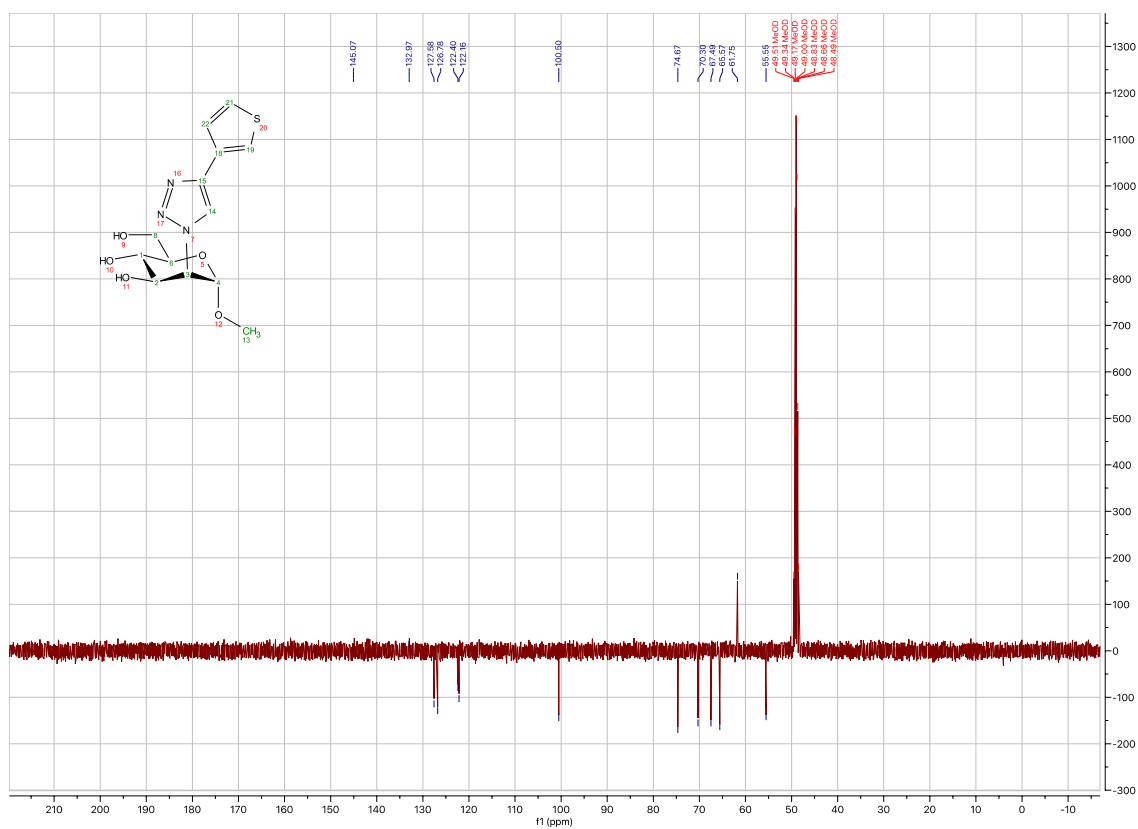
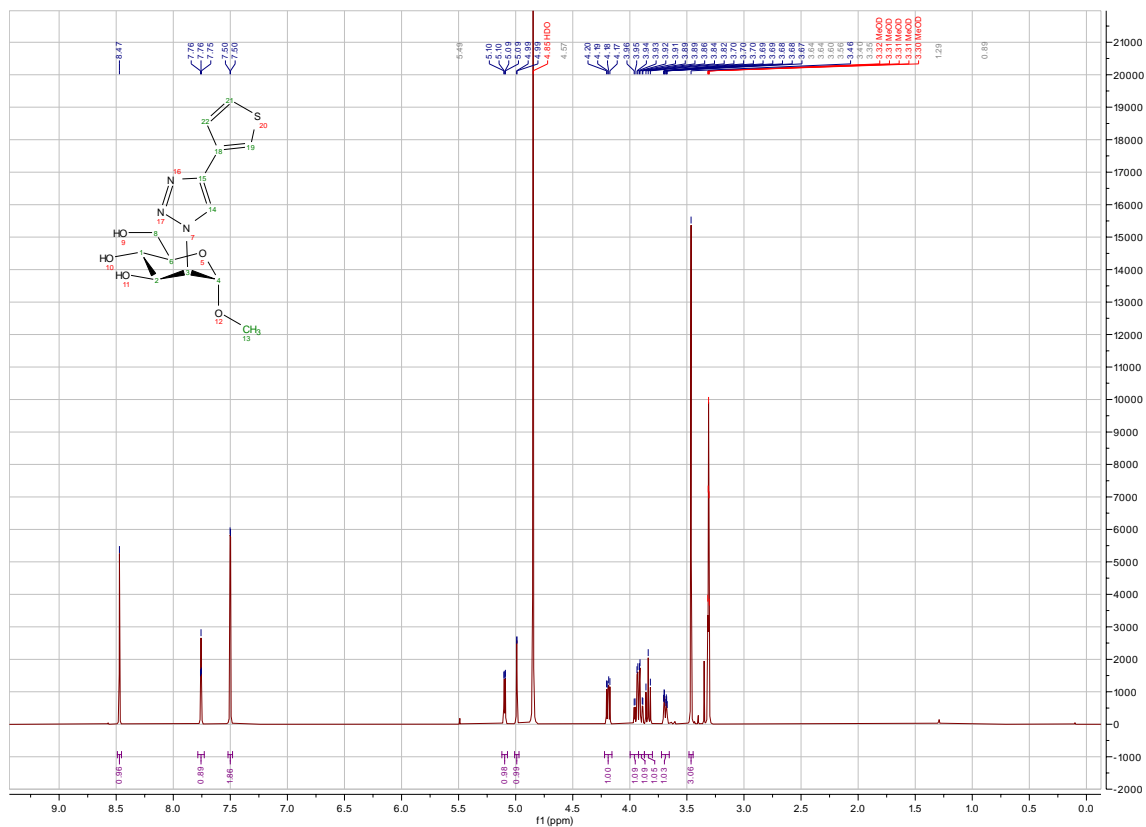


Figure S20. ¹H and ¹³C APT NMR spectra of 2a.

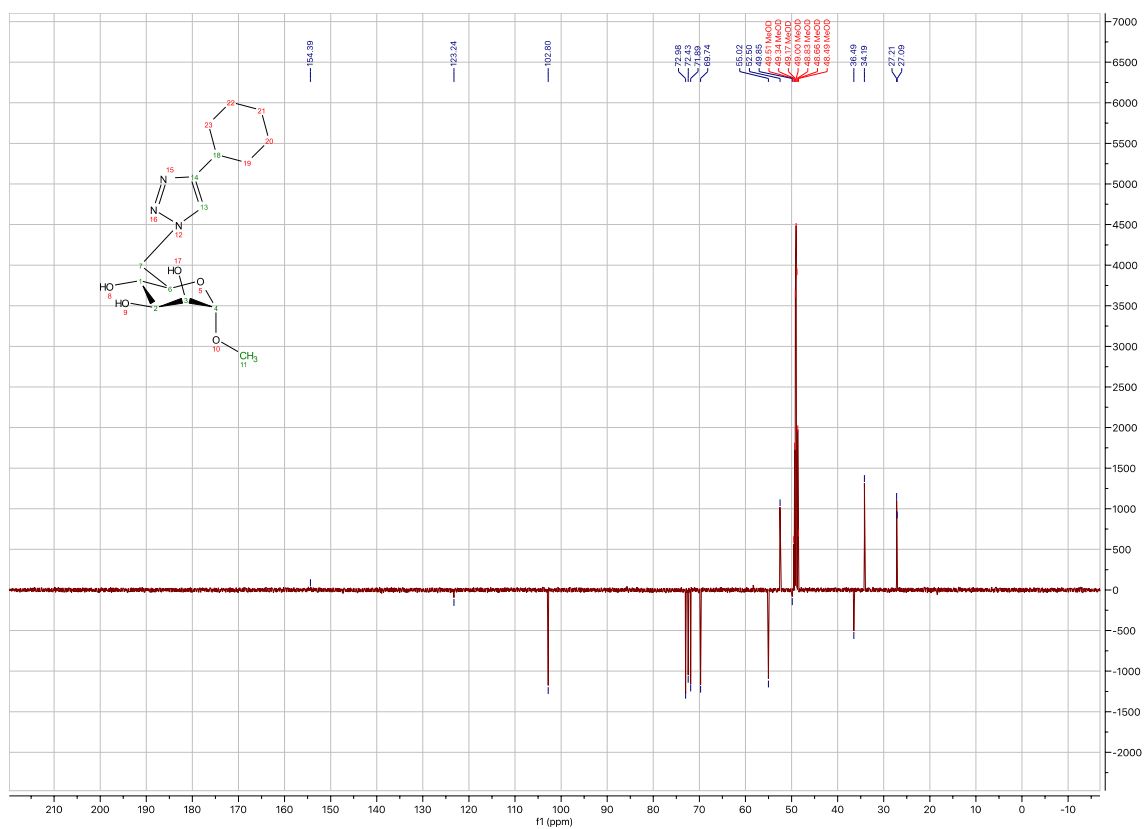
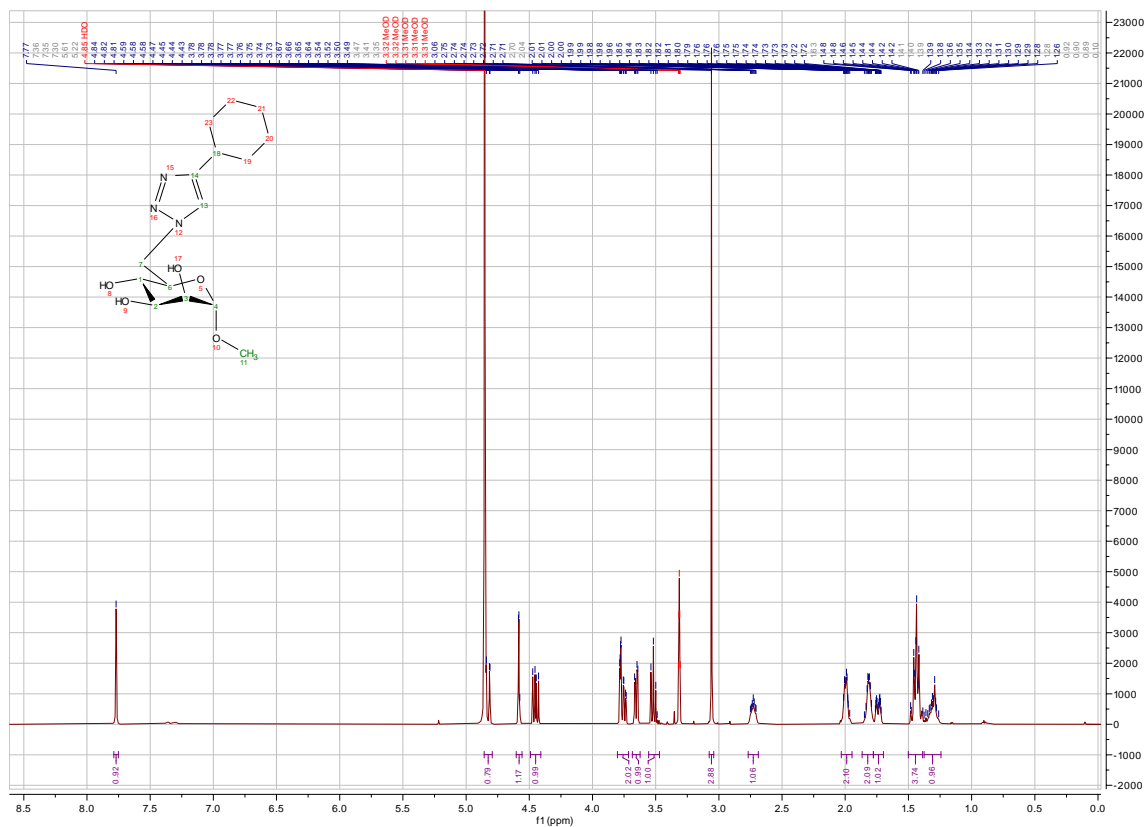


Figure S21. ¹H and ¹³C APT NMR spectra of 2b.

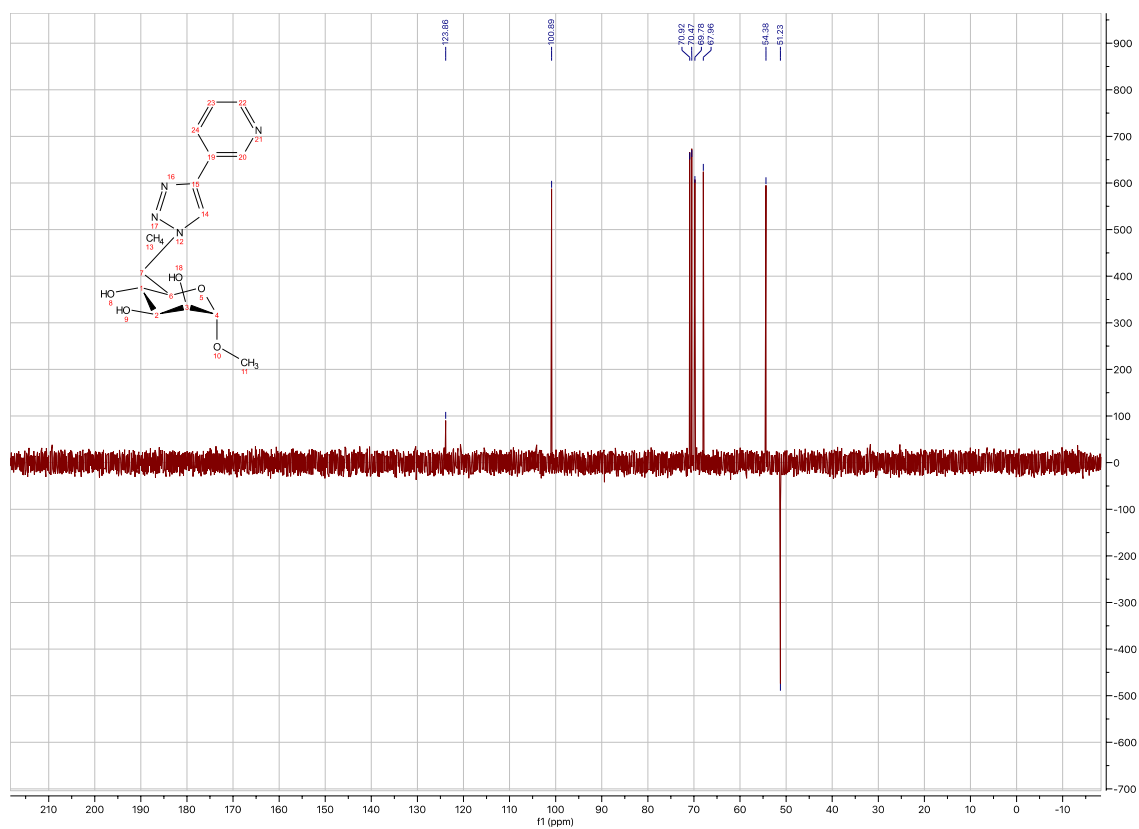
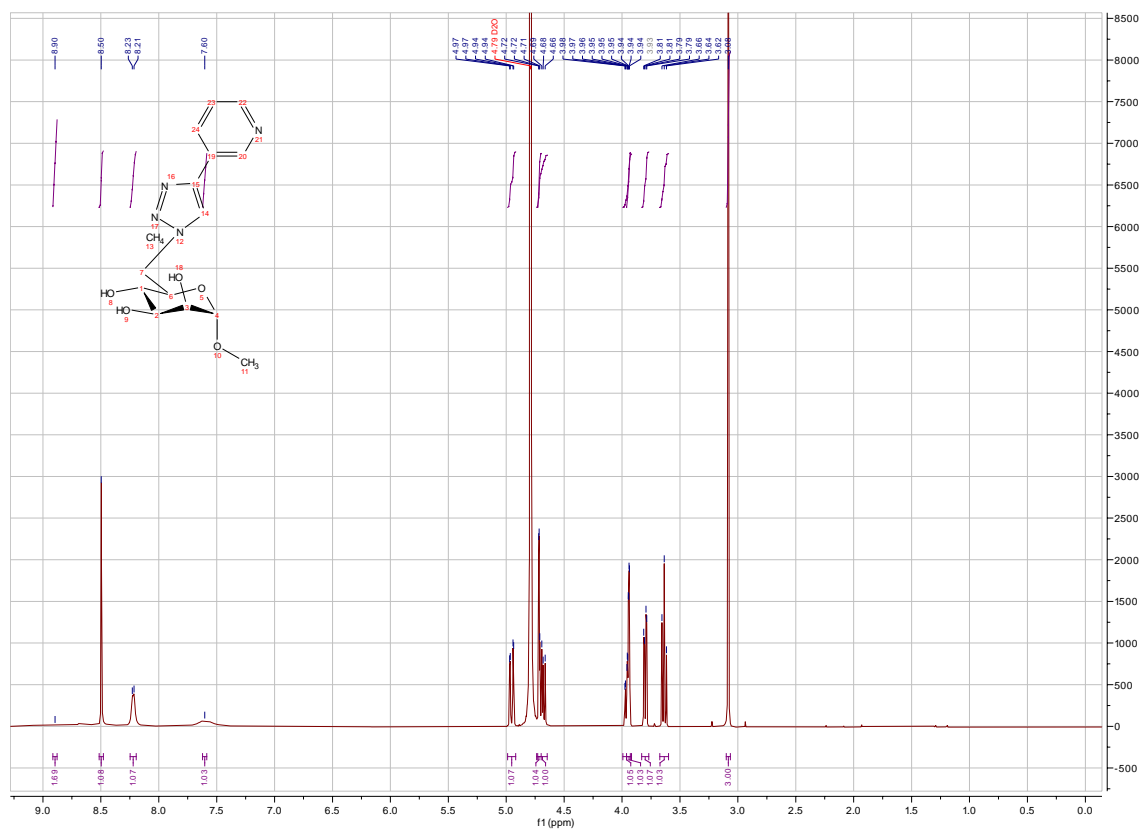


Figure S22. ¹H and ¹³C APT NMR spectra of 2c.

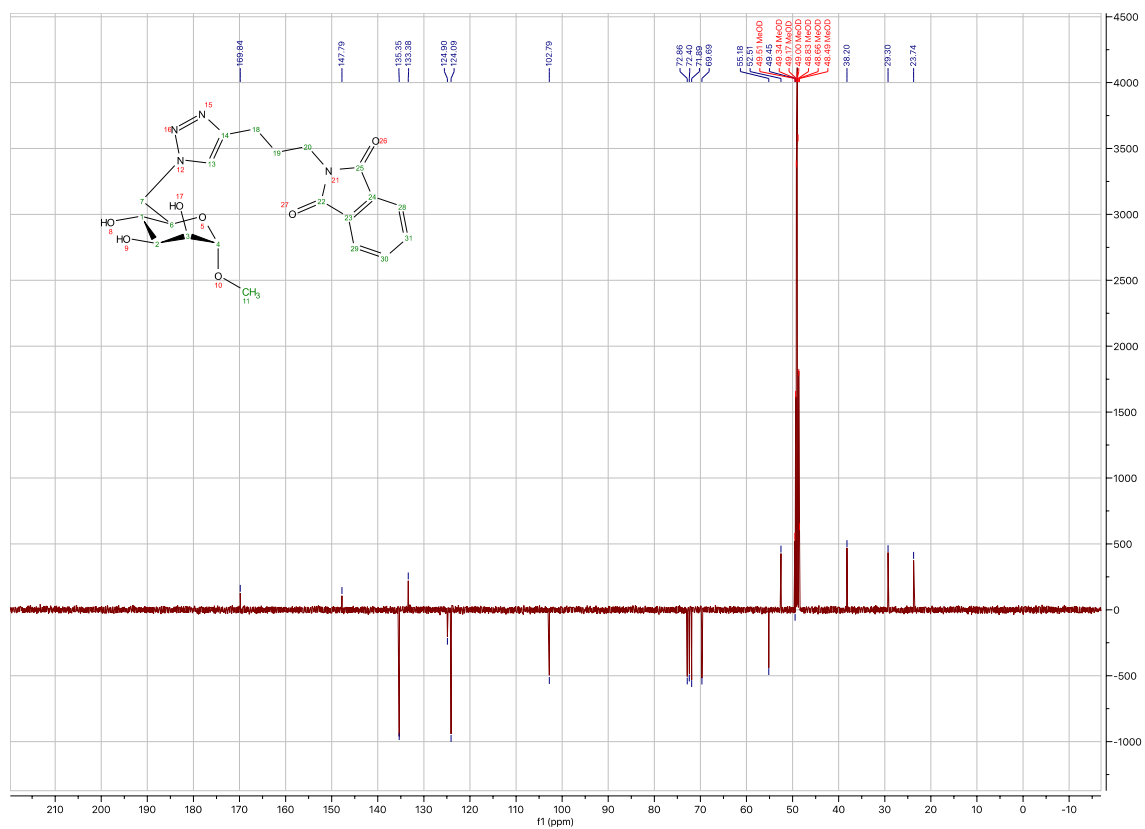
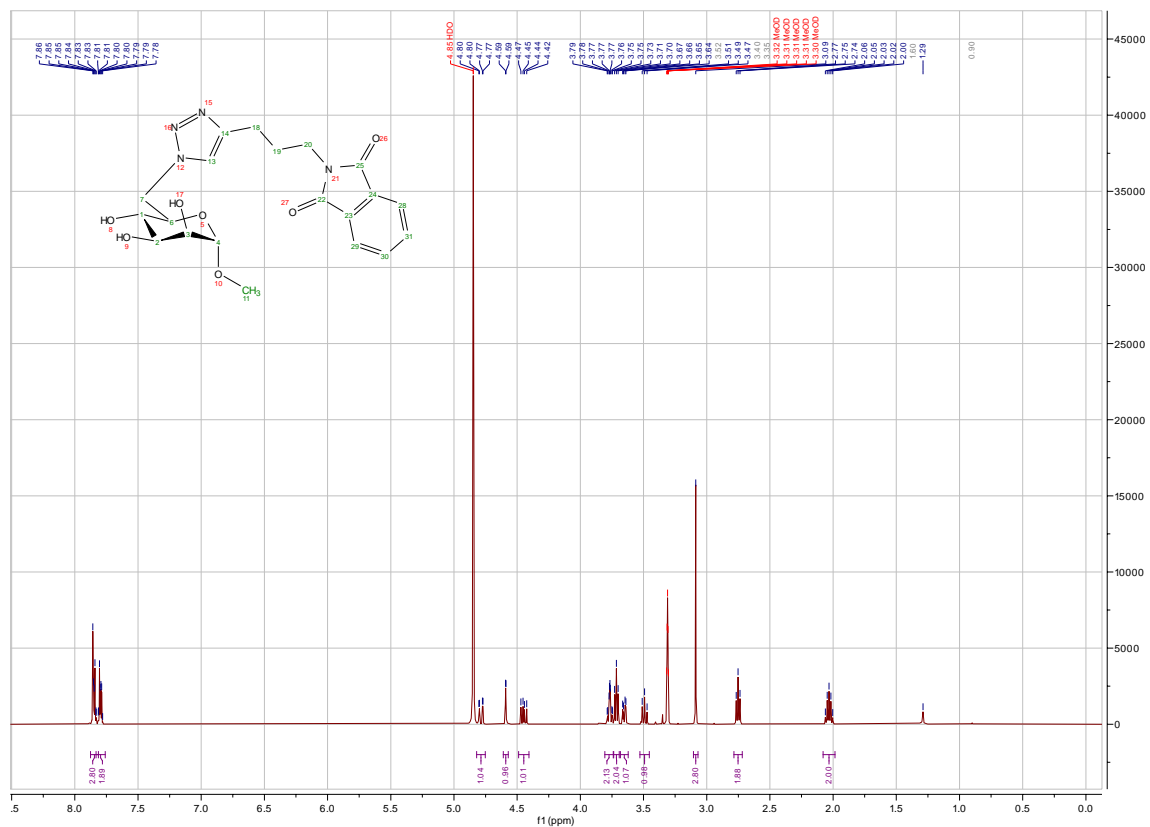


Figure S23. ¹H and ¹³C APT NMR spectra of 2d.

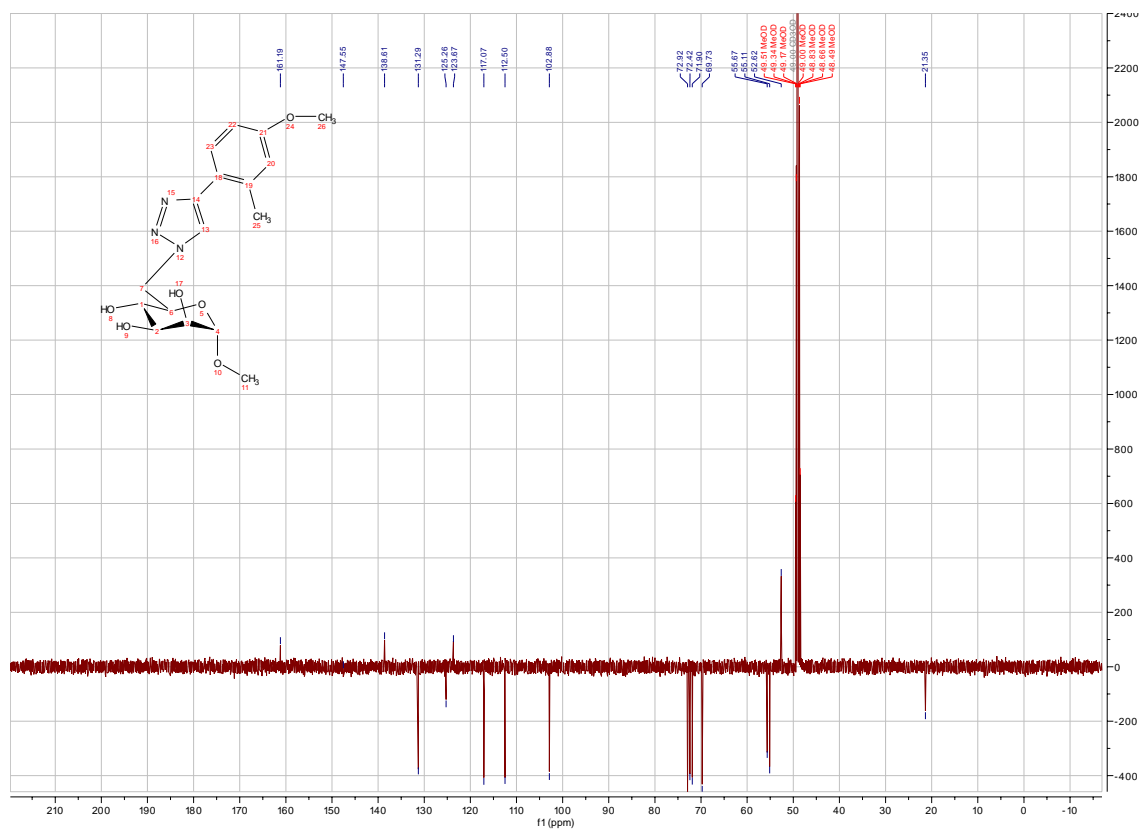
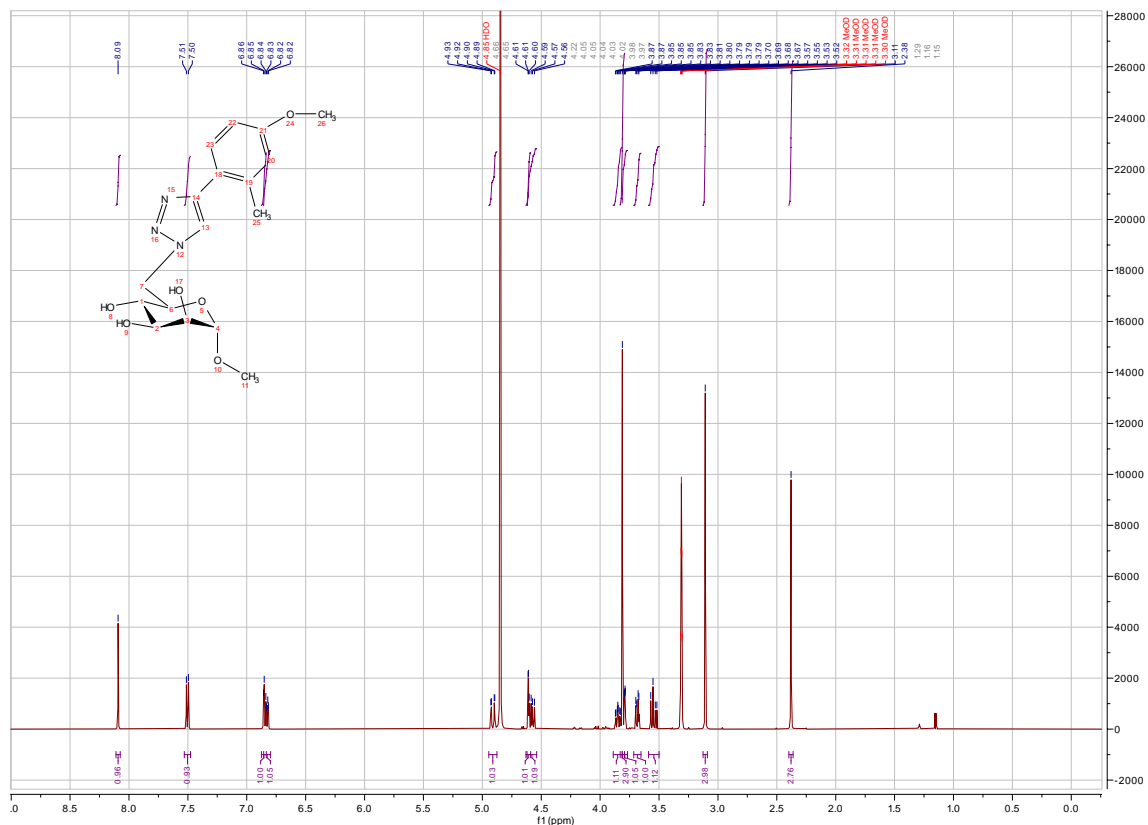


Figure S25. ¹H and ¹³C APT NMR spectra of 2f.

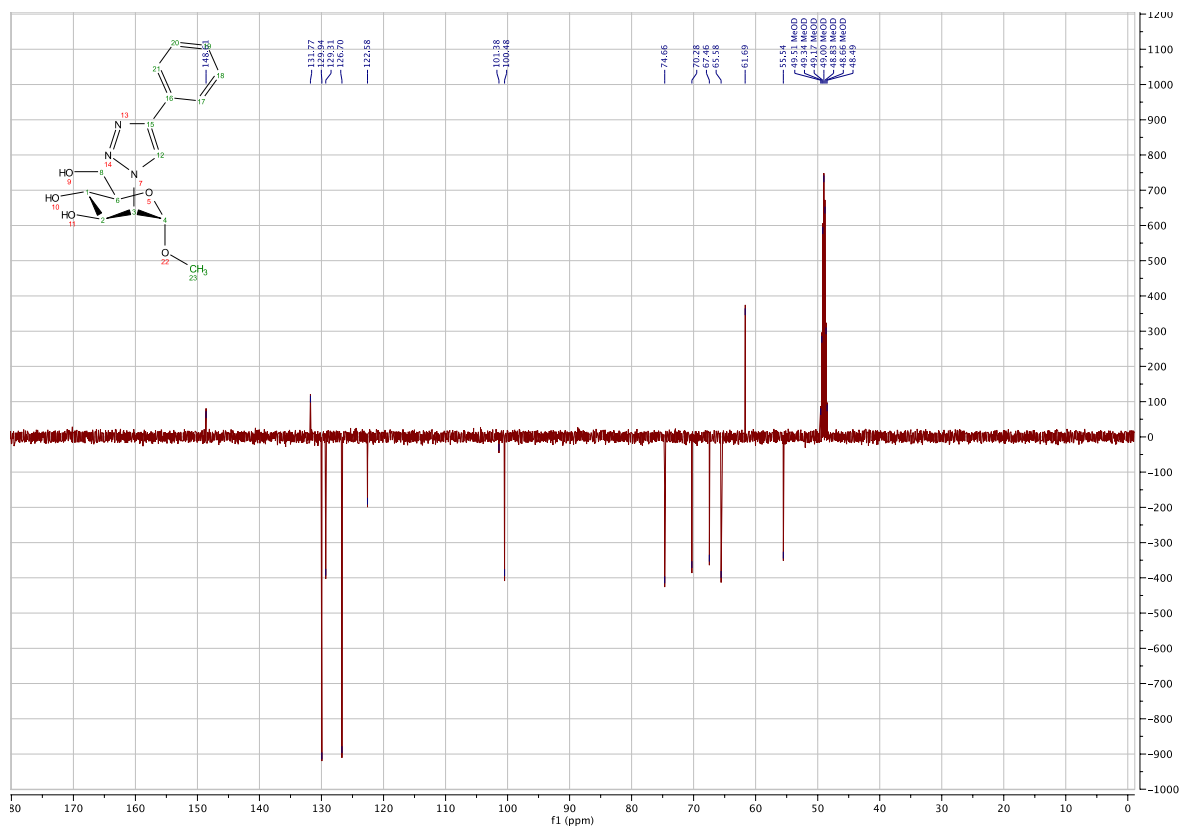
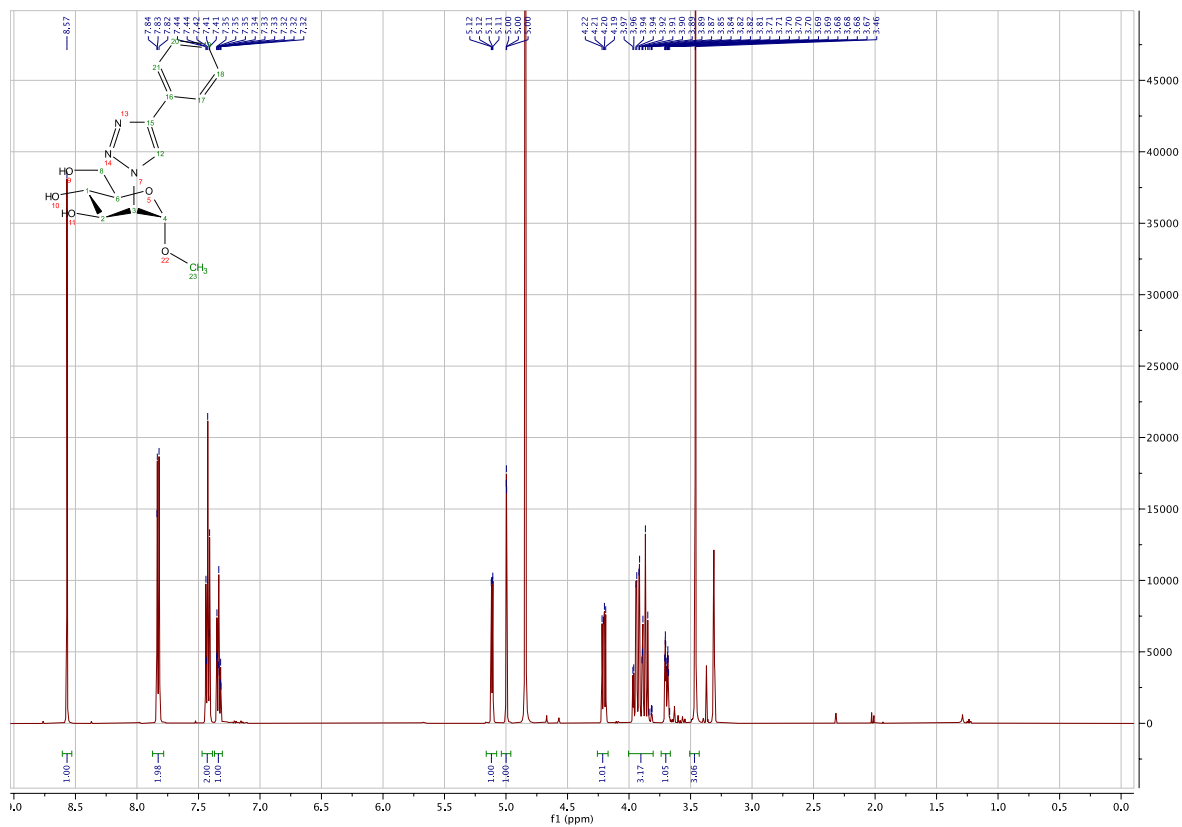


Figure S27. ¹H and ¹³C APT NMR spectra of 11.

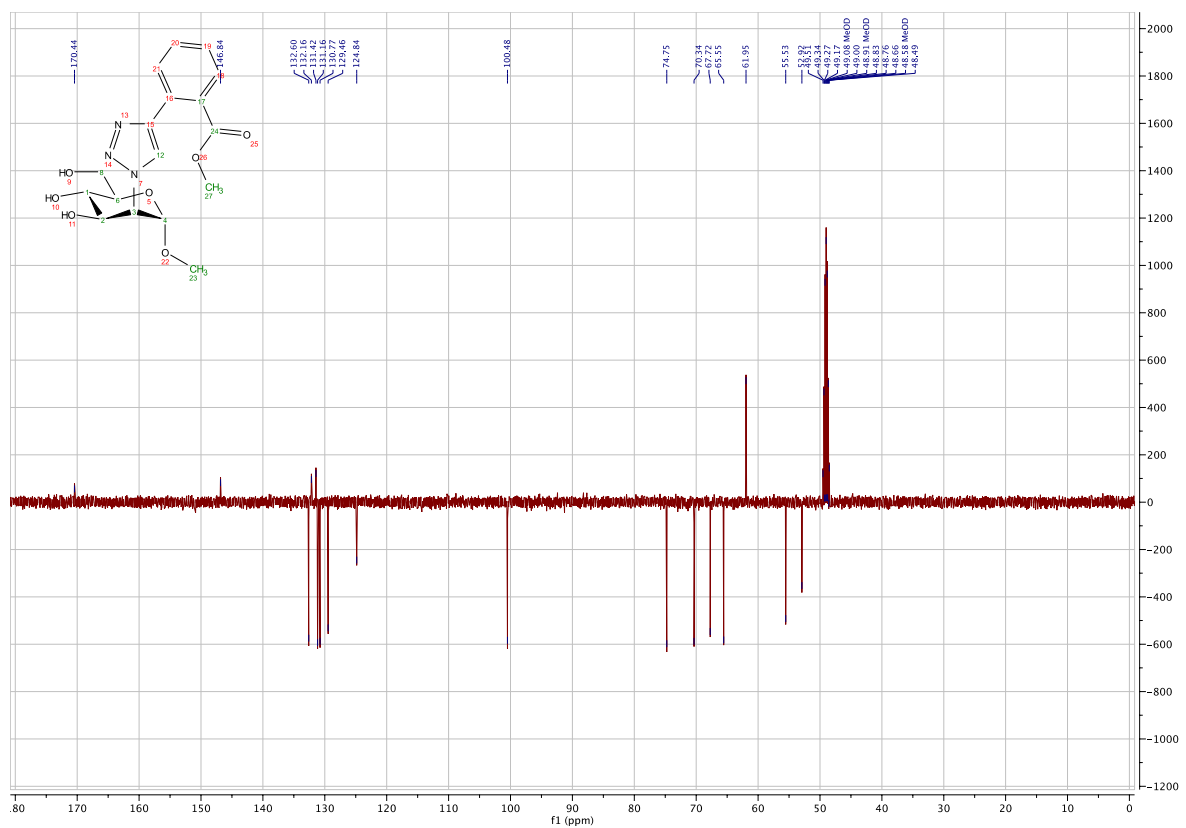
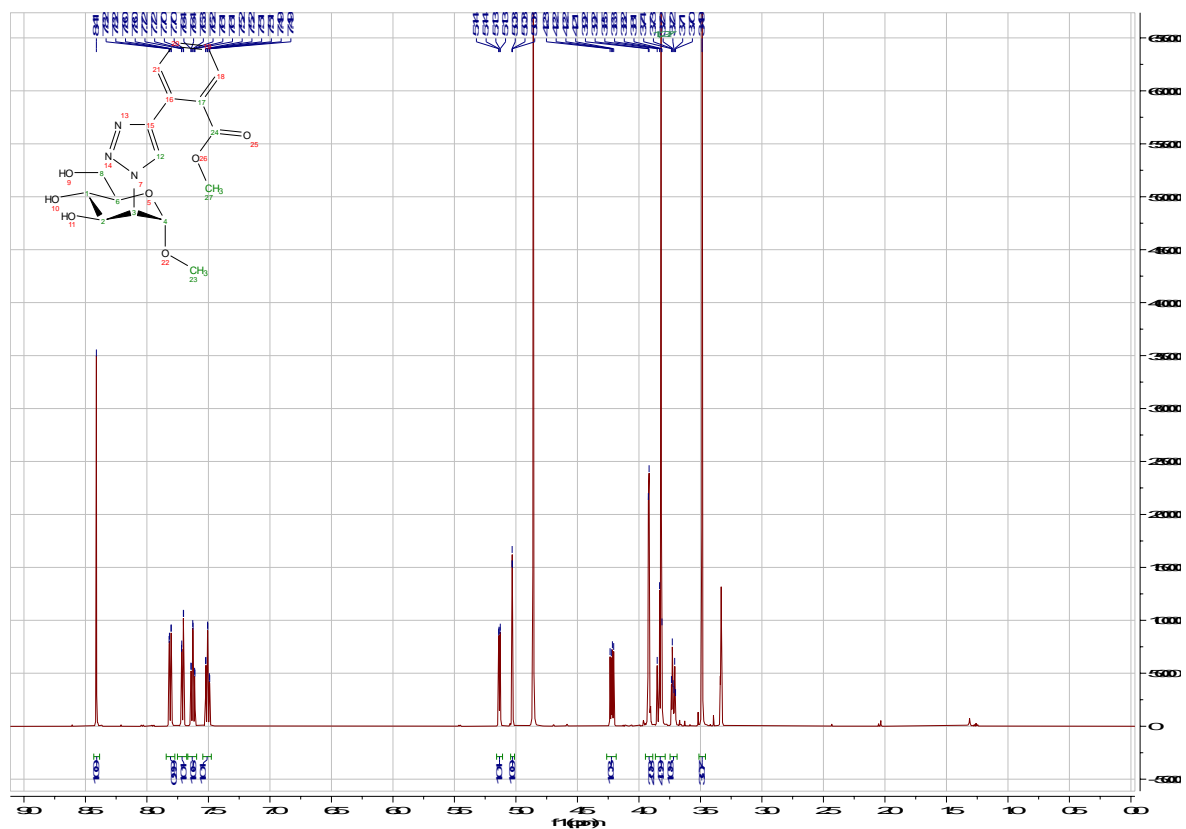


Figure S28. ¹H and ¹³C APT NMR spectra of 12.

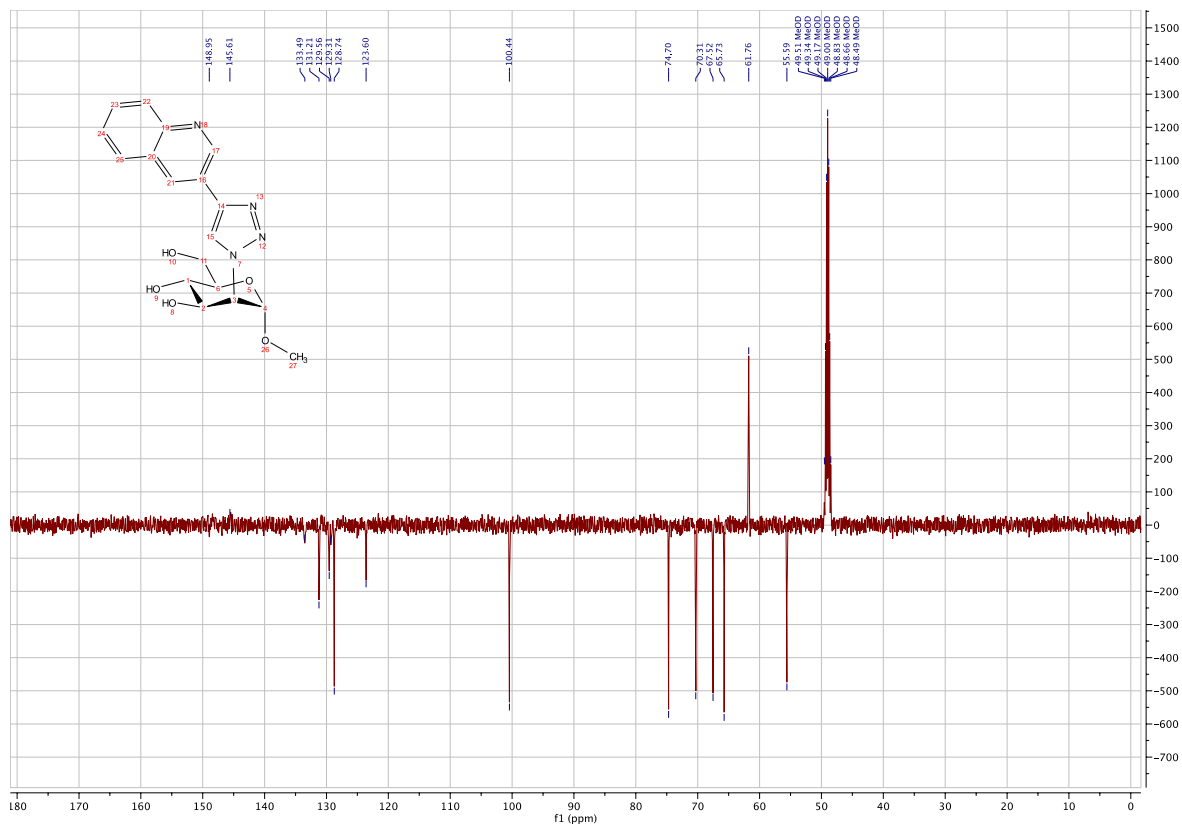
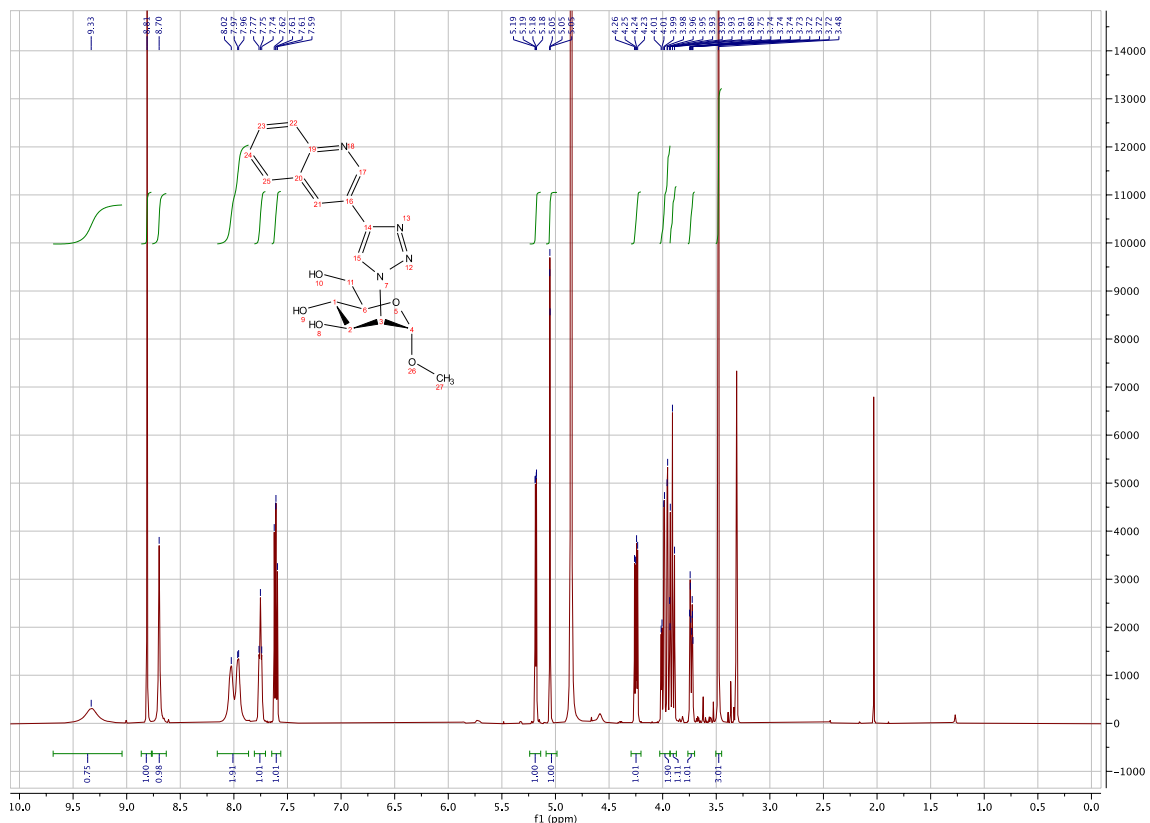


Figure S31. ¹H and ¹³C APT NMR spectra of 15.

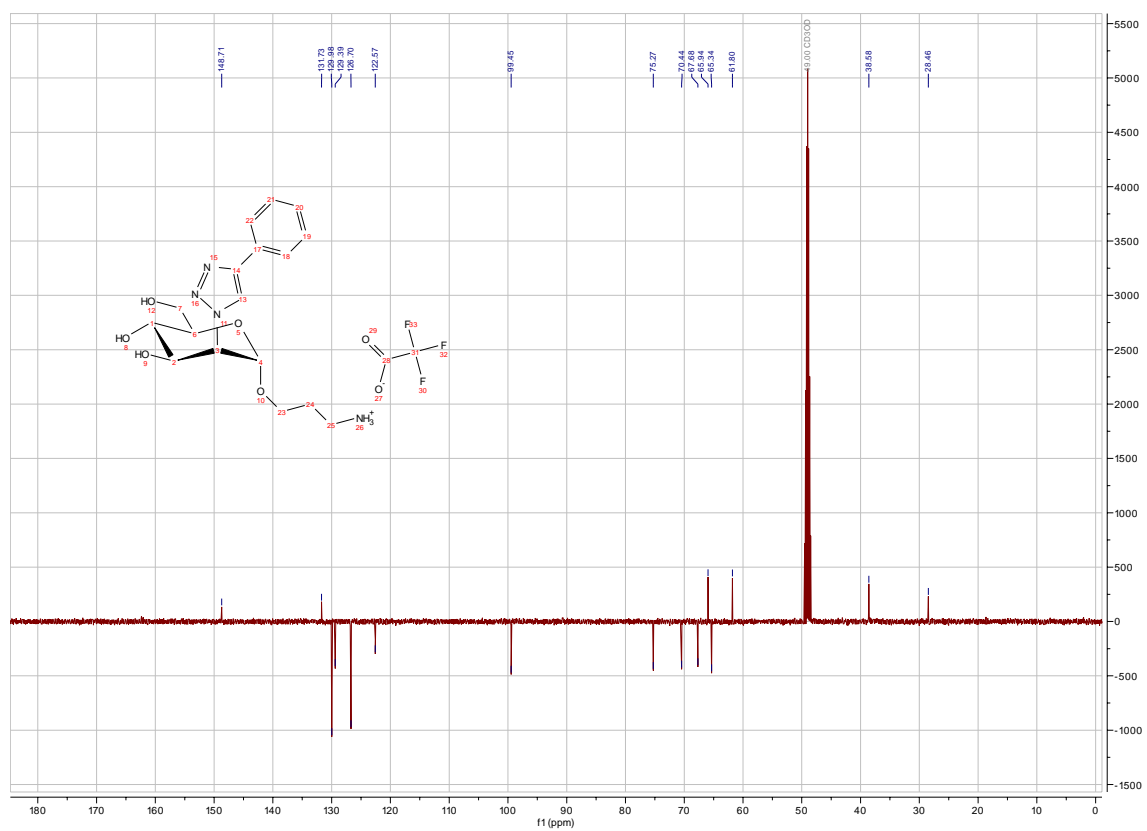
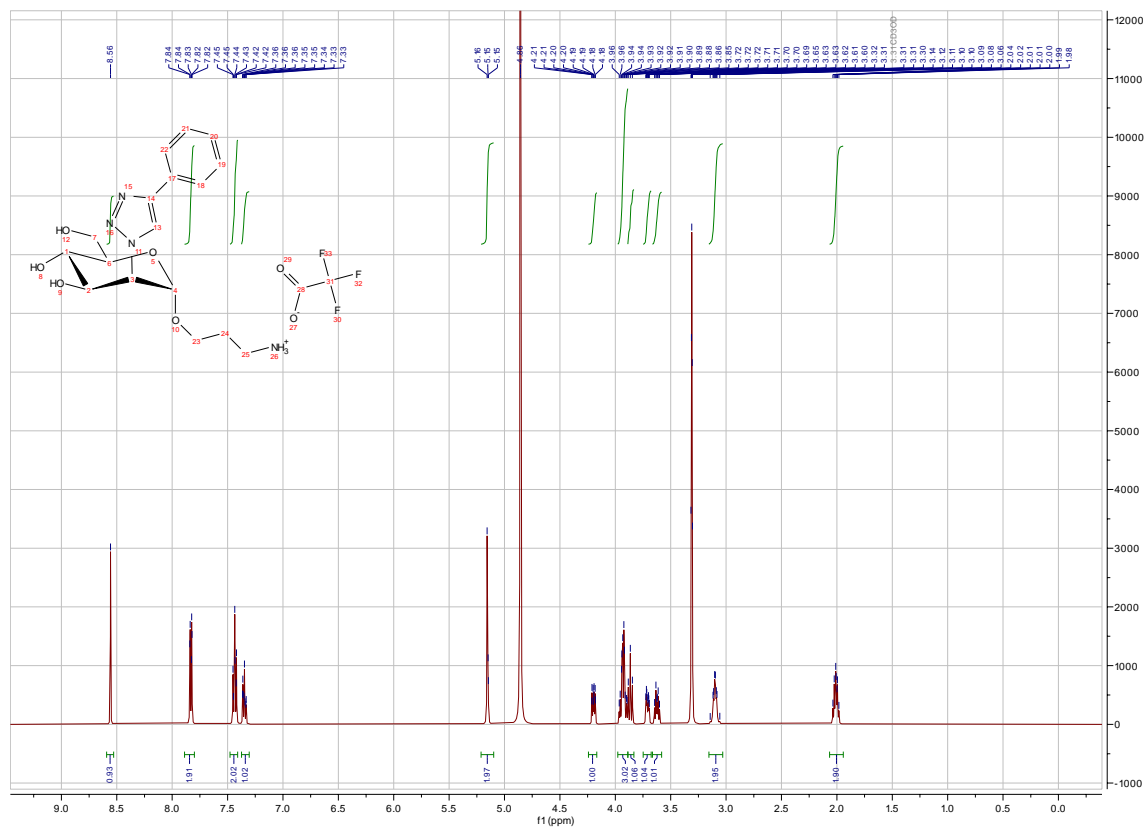


Figure S32. ¹H and ¹³C APT NMR spectra of 9.

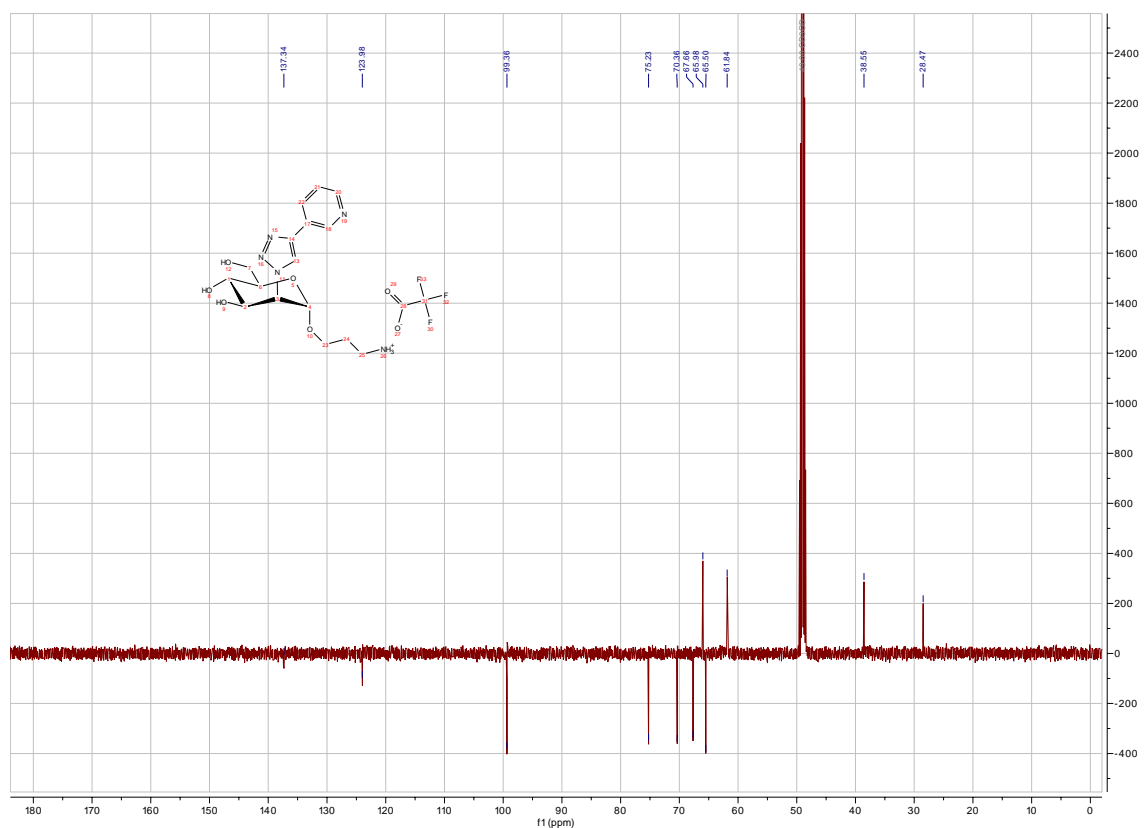
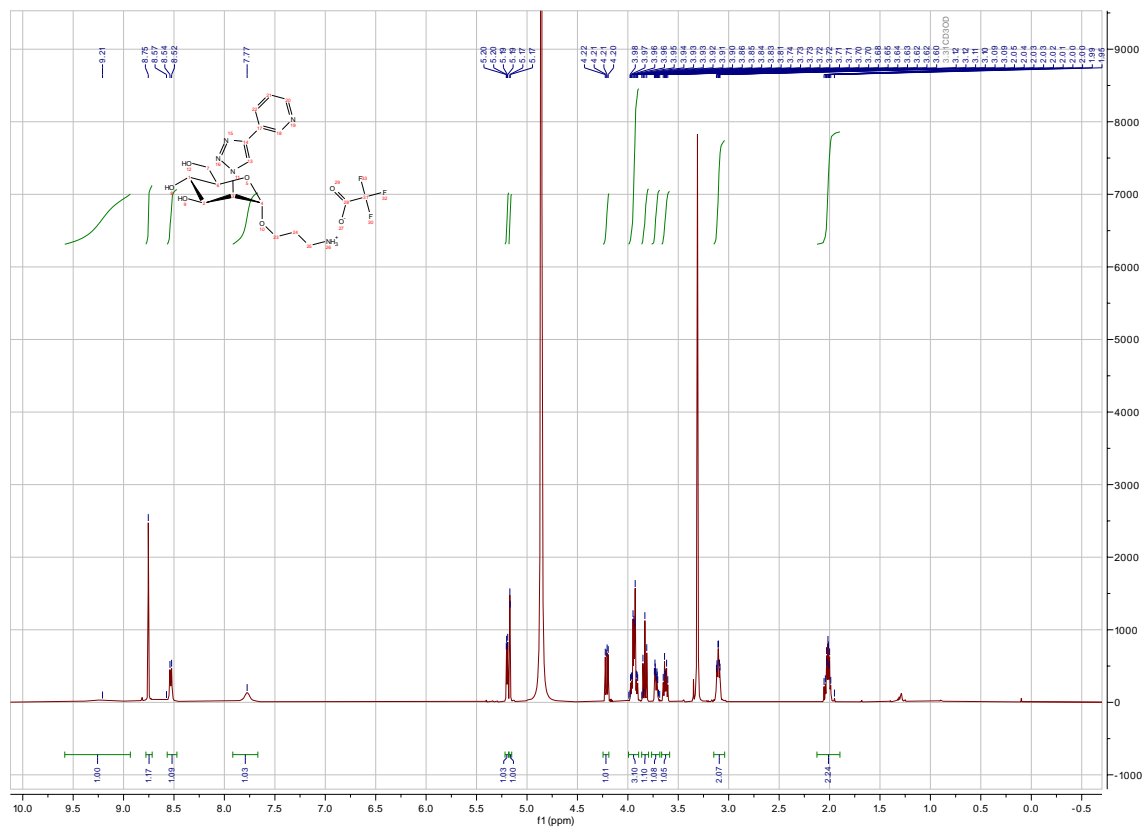


Figure S33. ¹H and ¹³C APT NMR spectra of 19.

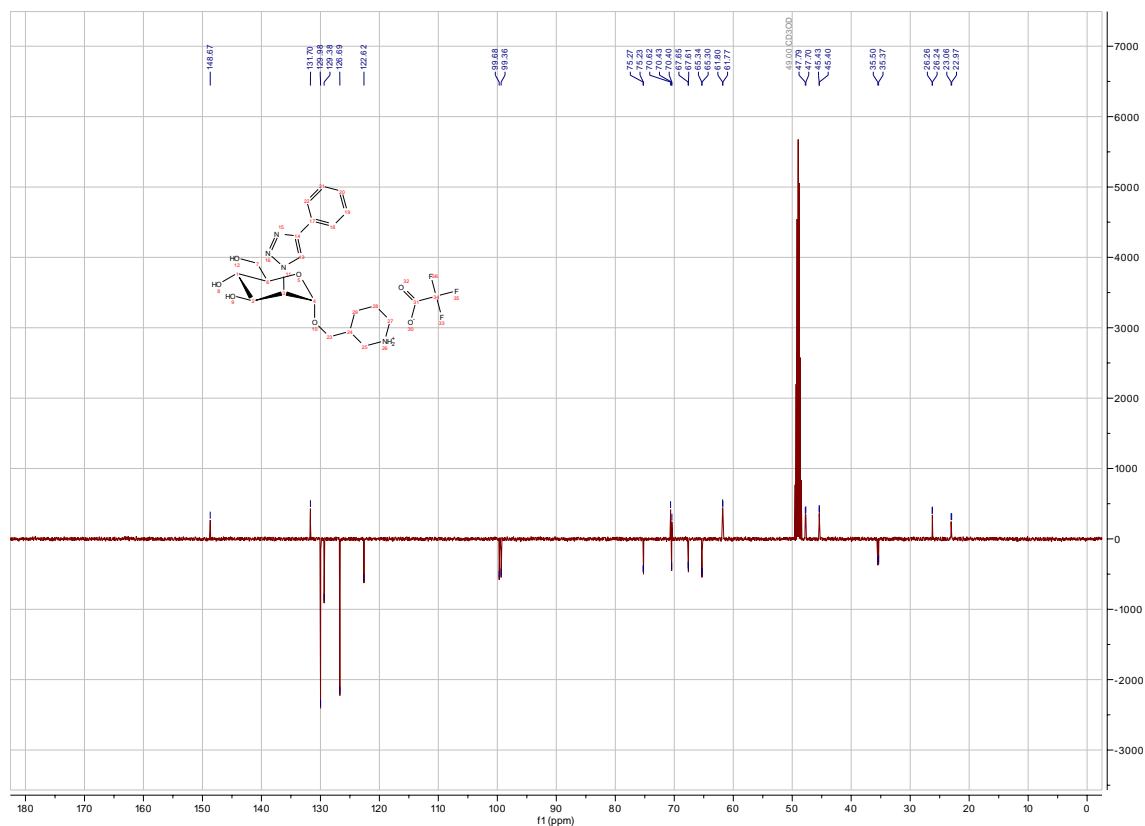


Figure S34. ¹H and ¹³C APT NMR spectra of **21**.

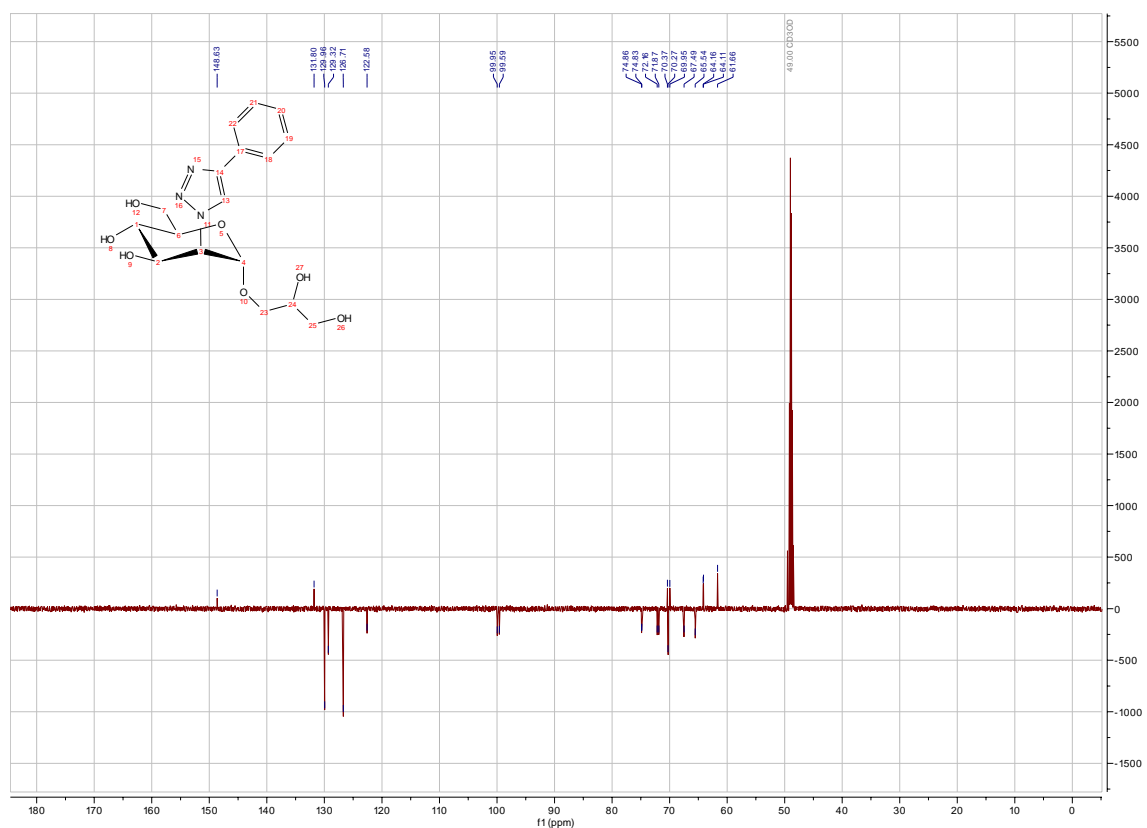
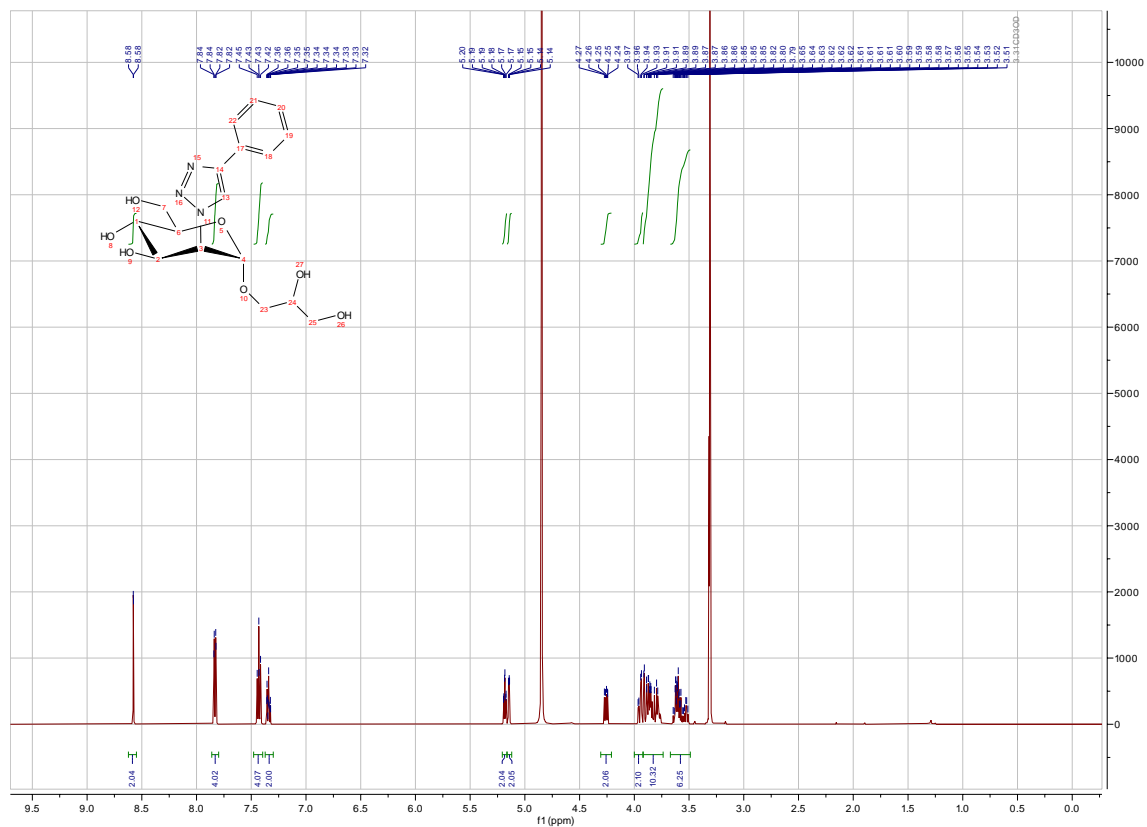


Figure S35. ¹H and ¹³C APT NMR spectra of 23.

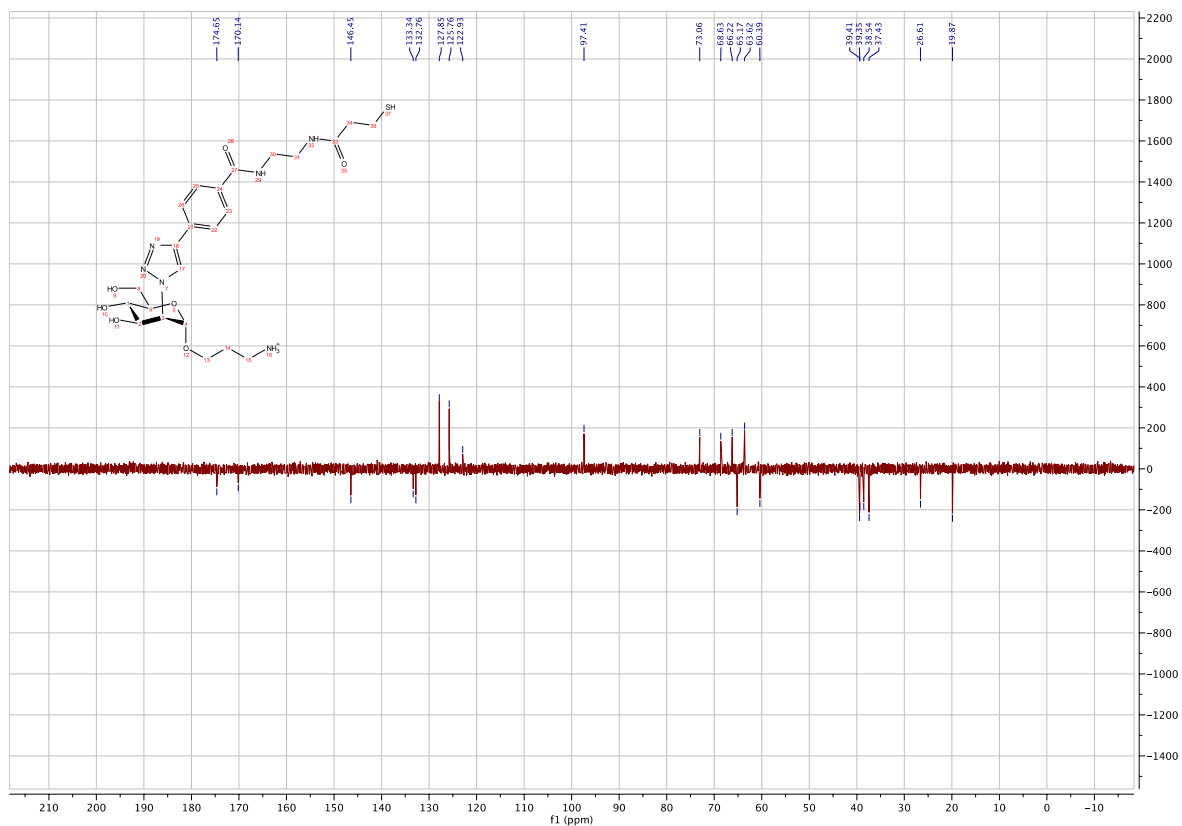
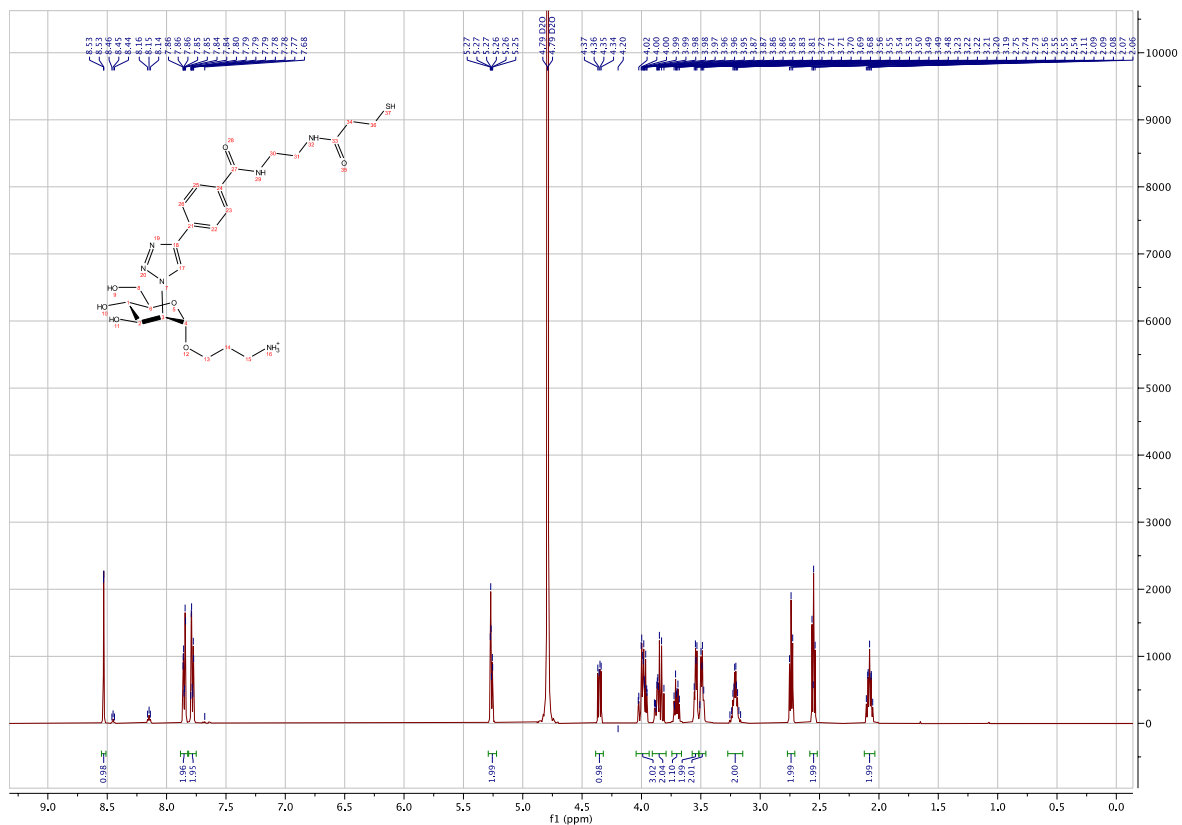


Figure S37. ¹H and ¹³C APT NMR spectra of 31.

HPLC Chromatograms of Glycomimetic DC-SIGN Ligands

Compound purity of >95% was determined by HPLC using an Agilent 1200 instrument equipped with a Waters Atlantis T3 C18 3 μ M 2.1 \times 100 mm column and an Agilent 380 ELSD detector. A gradient elution protocol (5–95% B over 20 min) employing water (+0.1% TFA) and MeCN (+0.1% TFA) as mobile phase was used.

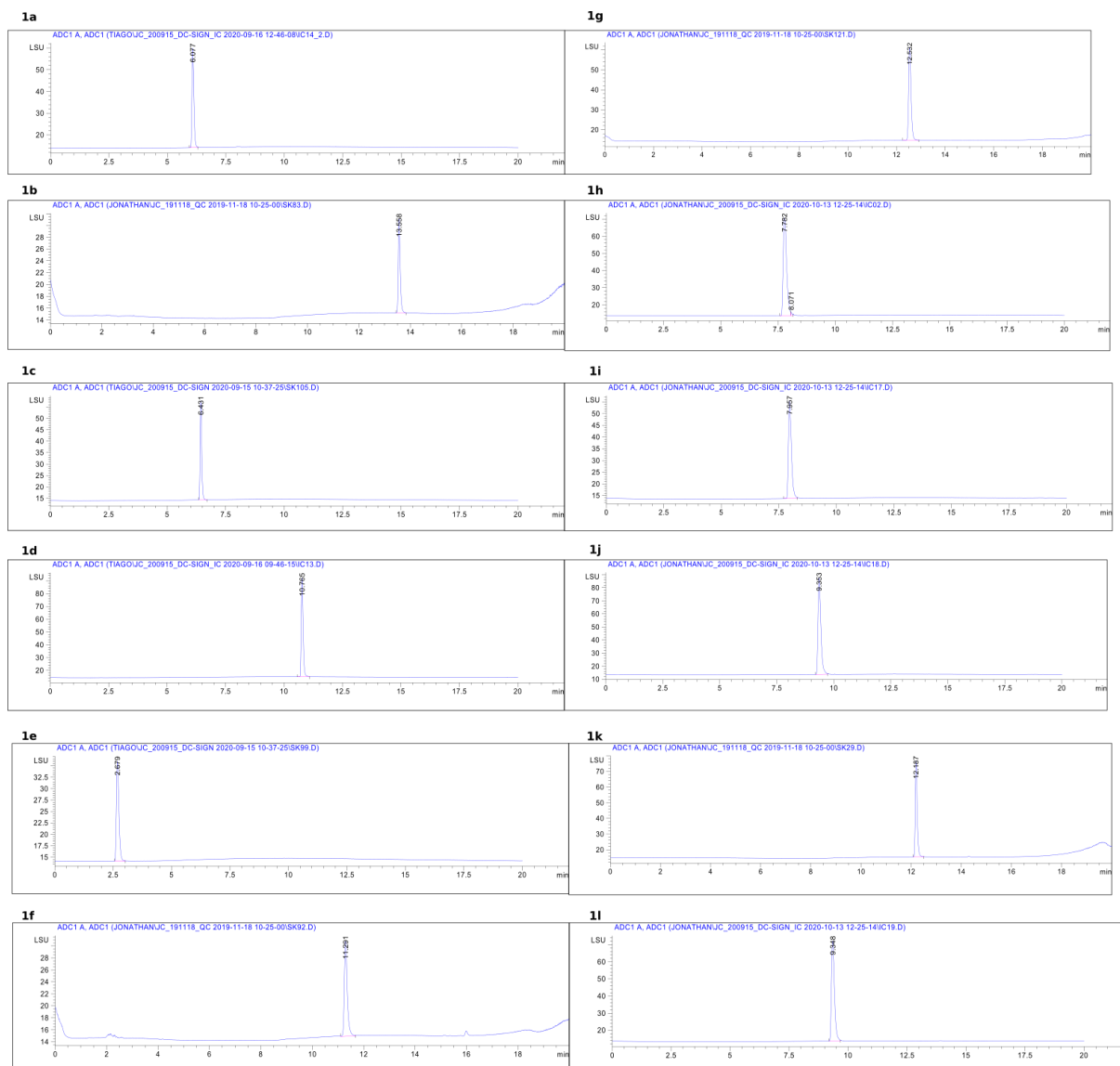


Figure S38. ELSD traces of HPLC chromatograms with compounds 1a–1l.

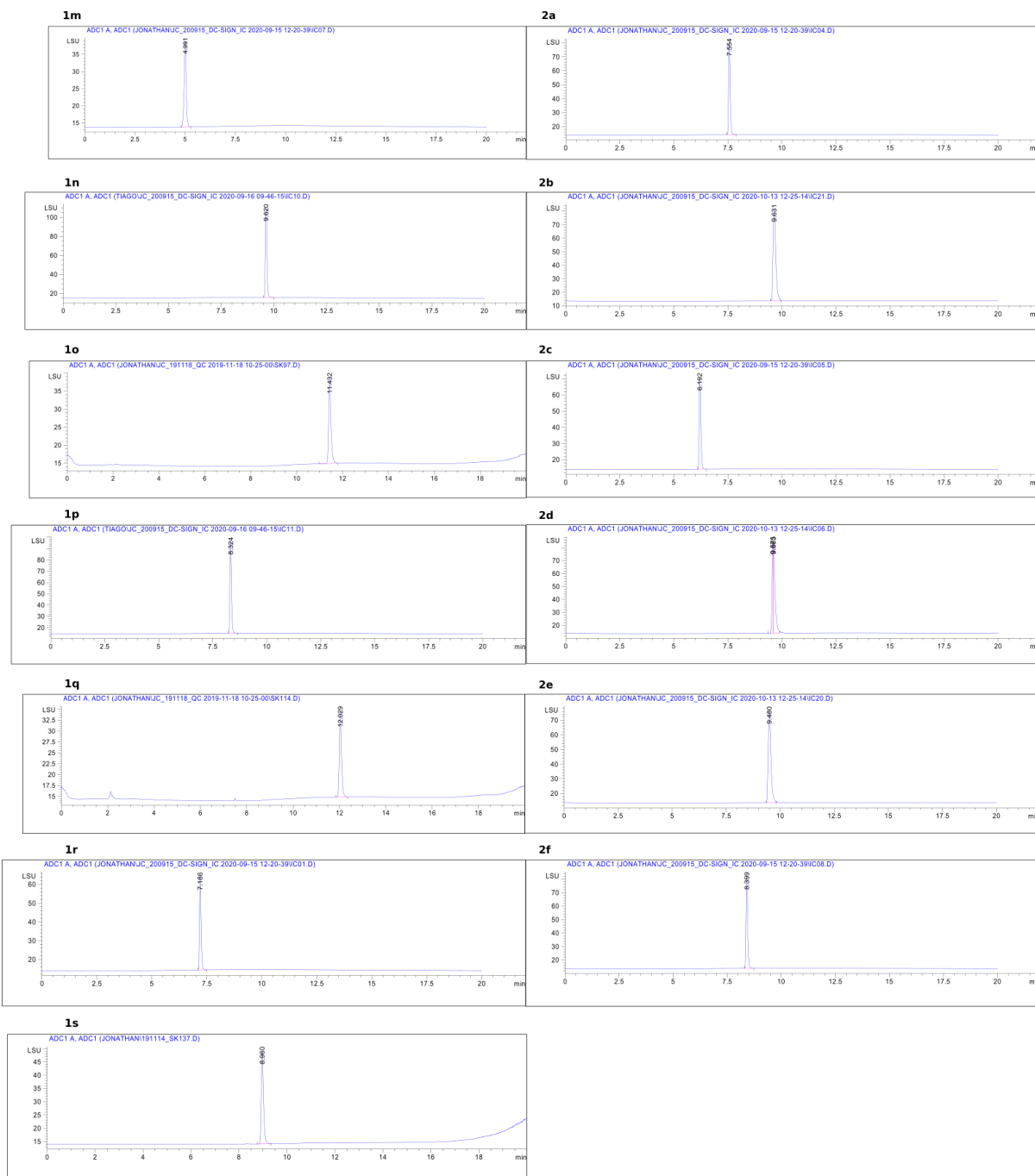


Figure S39. ELSD traces of HPLC chromatograms with compounds **1m**–**2f**.

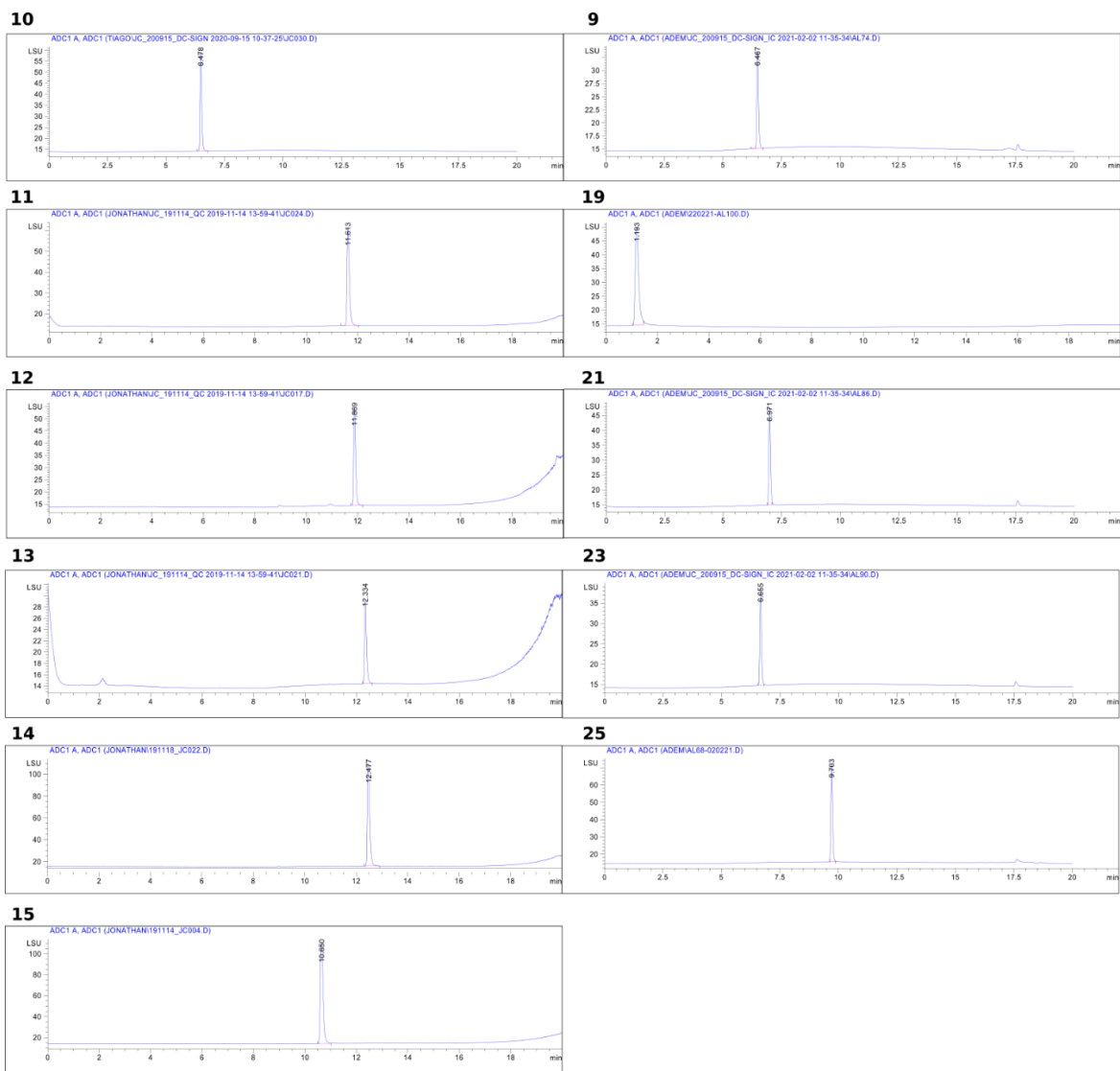


Figure S40. ELSD traces of HPLC chromatograms with compounds 9–15, 19, 21, 23, and 25.

Synthesis of Man-PLL⁴⁰⁰ Polymer **33** and Calculation of Polymer Loading

To a solution of chloroacetylated l-polylysine⁴⁰⁰ (**32**, 3.0 mg, 36.6 nmol)^[1] in DMF (200 μ L), a solution of **31** (3.8 mg, 5.9 μ mol, 160 eq) in DMF was added under argon. Then 1,8-diazabicyclo(5.4.0)undec-7-ene (2.2 mg, 2.0 μ L, 14.6 μ mol, 400 eq) was added. The reaction mixture was stirred at 25 °C for 15 min. Then, a mixture of thioglycerol (4.4 mg, 3.5 μ L, 41.0 μ mol, 1120 eq) and 1,8-diazabicyclo(5.4.0)undec-7-ene (2.2 mg, 2.0 μ L, 14.6 μ mol, 400 eq) in DMF were added. Subsequently, Et₃N (4.2 mg, 5.7 μ L, 41.0 μ mol, 1120 eq) was added and the mixture was stirred overnight. Next, the reaction mixture was dropped into a stirred solution of ethyl acetate/ethanol (1:1; 3.0 mL), leading to the precipitation of the product. The precipitate was collected by centrifugation, washed with ethanol (3.0 mL), and then was dissolved in 0.1 M aq. HCl (3.0 mL). The aqueous solution was purified by ultracentrifugation using a Vivaspin centrifugal concentrator (Sartorius, Germany; 6 mL, MWCO 6 kDa, 3 times from 6.0 mL to 0.5 mL). The solution of the product in H₂O (1 ml) was lyophilized within 6 h to yield Man-PLL⁴⁰⁰ polymer **33** (3.0 mg, 16.6 nmol, 45%) as a white solid.

Carbohydrate loading of polymer **33** was calculated from the relative proportion of normalized integrals attributable to the glycomimetic epitope (GM) and thioglycerol (TG), as reported earlier (Figure S41).^[1] Due to signal overlap in the critical region between 2.5-2.8 ppm, the thioglycerol content was estimated by subtraction of glycomimetic signals A+B from the total integral A+B+C.

$$H_{GM} = \frac{Int_D + Int_E + Int_{F+G}}{n_D + n_E + n_{F+G}} = \frac{4.51 + 1.15 + 2.00}{4 + 1 + 2} = 1.09$$

$$H_{TG} = \frac{Int_{A+B+C} - 4 \times H_{GM}}{n_C} = \frac{12.29 - 4 \times 1.09}{2} = 3.96$$

$$Loading (\%) = \frac{H_{GM}}{H_{GM} + H_{TG}} \times 100\% = \frac{1.09}{1.09 + 3.96} \times 100\% = 21.6\%$$

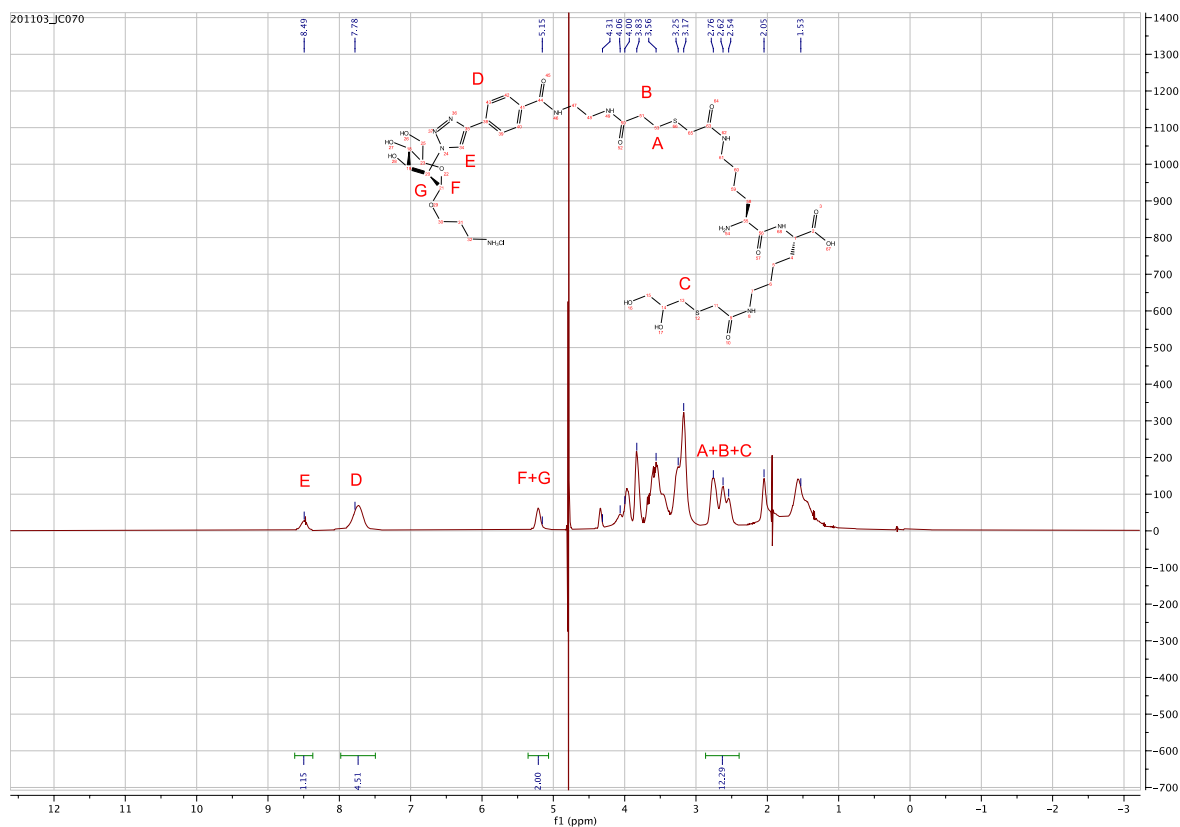


Figure S41. ¹H spectrum with water suppression (NOESYGPPR1D) of **33**.

Dynamic Light Scattering (DLS)

The size characteristics of **33** were analyzed by DLS with a Malvern Zetasizer Nano instrument (Malvern Panalytical, Malvern, UK). Samples containing 12 μ M **33** (0.38 mg mL⁻¹) were allowed to equilibrate at 20 °C for 2 min prior to the experiments. Experiments were performed in triplicate and experimental data were analyzed with the software supplied by the manufacturer to obtain hydrodynamic radii (Z-average), polydispersity indices, and size distribution data.

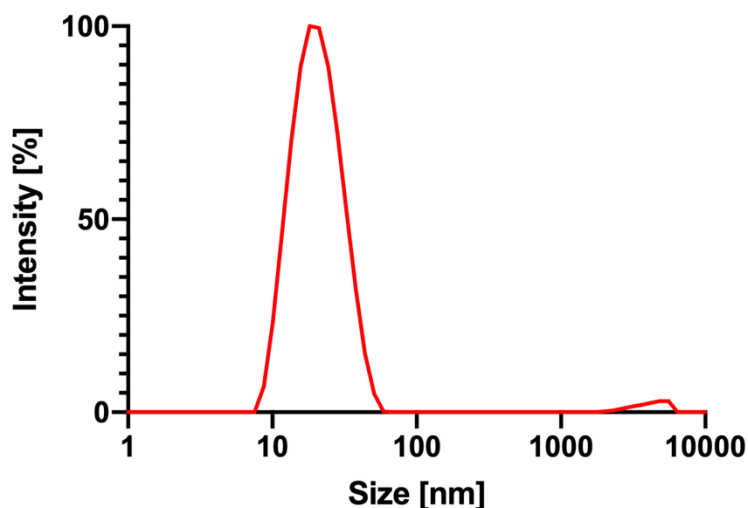


Figure S42. Intensity distribution profile of **33** from DLS measurements.

Isothermal Titration Calorimetry

General Information

The interpretation of thermodynamic data in the given system is complicated by the comparatively low affinity and resulting necessity for low c ITC setups that demand an artificial fixing of the fitting parameter n to 1.0. Since the parameter accurately determined by the nonlinear fitting algorithm in this setup is the product $n \times \Delta H^\circ$, inaccuracies in the active protein fraction directly translate into errors in ΔH° .^[2-4] This potential source of error is mitigated by the fact that all ITC experiments reported here were performed with a single protein batch, which mostly cancels out systematic errors in the relative comparison of binding enthalpies between compounds and allows the extraction of general trends in structure–thermodynamics relationships. Careful experimental design, especially by ensuring a high signal to noise ratio and a titration to >80% protein saturation can further reduce experimental errors.^[3-5] In this regime, the errors of the fitting parameters K_D and ΔH° are lowest. This goal was generally achieved for higher affinity compounds ($K_D < 300 \mu\text{M}$).

5. Table S1. Binding affinity and thermodynamic data of primary screening hits from ITC experiments.

| 6. Compound | 7. K_D [μM] | 8. ΔG° [kJ mol ⁻¹] | 9. ΔH° [kJ mol ⁻¹] | 10. $-T\Delta S^\circ$ [kJ mol ⁻¹] |
|-------------|----------------------------|---|---|--|
| | 12. 3315 | 14. -14.2 | 16. -22.9 | 18. 8.80 |
| 11. MeMan | 13. (3107 – 3541) | 15. (-14.3 – 14.0) | 17. (-24.4 – 21.6) | 19. (7.3 – 10.4) |
| | 21. 777 | 23. -17.7 | 25. -25.8 | 27. 8.1 |
| 20. 1l | 22. (648 – 945) | 24. (-18.2 – 17.3) | 26. (-31.7 – 21.5) | 28. (3.3 – 14.5) |
| | 30. 465 | 32. -19 | 34. -30.2 | 36. 11.2 |
| 29. 1n | 31. (480 – 451) | 33. (-18.9 – 19.1) | 35. (-31.1 – 29.4) | 37. (10.3 – 12.1) |
| | 39. 252 | 41. -20.5 | 43. -24 | 45. 3.5 |
| 38. 1o | 40. (240 – 265) | 42. (-20.7 – 20.4) | 44. (-24.8 – 23.3) | 46. (2.7 – 4.4) |
| | 48. 285 | 50. -20.2 | 52. -24.8 | 54. 4.6 |
| 47. 1p | 49. (259 – 314) | 51. (-20.5 – 20) | 53. (-26.9 – 23) | 55. (2.5 – 6.9) |
| | 57. 231 | 59. -20.8 | 61. -19.6 | 63. -1.2 |
| 56. 1q | 58. (192 – 275) | 60. (-21.2 – 20.3) | 62. (-21.1 – 18.2) | 64. (-3 – 0.8) |
| | 66. 260 | 68. -20.5 | 70. -27.2 | 72. 6.8 |
| 65. 1r | 67. (230 – 293) | 69. (-20.8 – 20.2) | 71. (-30.4 – 24.5) | 73. (3.8 – 10.2) |
| | 75. 141 | 77. -22 | 79. -23.1 | 81. 1.1 |
| 74. 1s | 76. (128 – 156) | 78. (-22.2 – 21.7) | 80. (-24.5 – 21.8) | 82. (-0.4 – 2.8) |
| | 84. 166 | 86. -21.6 | 88. -30.4 | 90. 8.8 |
| 83. 10 | 85. (161 – 171) | 87. (-21.6 – 21.5) | 89. (-30.8 – 30) | 91. (8.4 – 9.3) |
| | 93. 192 | 95. -21.2 | 97. -28.9 | 99. 7.7 |
| 92. 11 | 94. (188 – 195) | 96. (-21.3 – 21.2) | 98. (-29.2 – 28.7) | 100. (7.4 – 8) |
| | 102. 463 | 104. -19 | 106. -30.2 | 108. 11.2 |
| 101. 12 | 103. (429 – 502) | 105. (-19.2 – 18.8) | 107. (-32.6 – 28.1) | 109. (8.9 – 13.7) |
| | 111. 713 | 113. -18 | 115. -31.5 | 117. 13.5 |
| 110. 13 | 112. (682 – 745) | 114. (-18.1 – 17.9) | 116. (-32.7 – 30.4) | 118. (12.3 – 14.9) |

| | | | | |
|---------------------------|------------------------|---------------------------|---------------------------|--------------------------|
| | 120.207 | 122.-21 | 124.-27.9 | 126.6.9 |
| 119.14 | 121.(199 – 214) | 123.(-21.1 – 20.9) | 125.(-28.5 – 27.3) | 127.(6.2 – 7.5) |
| | 129.138 | 131.-22 | 133.-27.5 | 135.5.4 |
| 128.15^a | 130.(131 – 146) | 132.(-22.2 – 21.9) | 134.(-28.3 – 26.7) | 136.(4.5 – 6.4) |
| | 138.32 | 140.-25.7 | 142.-31.6 | 144.6.0 |
| 137.9 | 139.(30 – 34) | 141.(-25.8 – 25.5) | 143.(-32.4 – 30.9) | 145.(5.1 – 6.9) |
| | 147.29 | 149.-25.9 | 151.-26.9 | 153.1.1 |
| 146.19 | 148.(27 – 32) | 150.(-26.1 – 25.6) | 152.(-28.1 – 25.8) | 154.(-0.3 – 2.5) |
| | 156.42 | 158.-25 | 160.-20.2 | 162.-4.8 |
| 155.21 | 157.(40 – 45) | 159.(-25.1 – 24.8) | 161.(-20.7 – 19.7) | 163.(-5.5 – 4.1) |
| | 165.134 | 167.-22.1 | 169.-27.0 | 171.4.9 |
| 164.23 | 166.(123 – 144) | 168.(-22.3 – 21.9) | 170.(-28.4 – 25.8) | 172.(3.5 – 6.4) |
| | 174.331 | 176.-19.9 | 178.-27 | 180.7.2 |
| 173.25 | 175.(294 – 375) | 177.(-20.2 – 19.6) | 179.(-30.8 – 19.6) | 181.(-0.6 – 11.3) |
| 182. | 183. | 184. | 185. | 186. |

187. Error estimates represent 68% confidence intervals from nonlinear least squares fitting of two independent experiments.

^a Due to the high enthalpy of dilution observed for **15**, a buffer correction was performed prior to data fitting.

Representative ITC thermograms and fitted binding isotherms

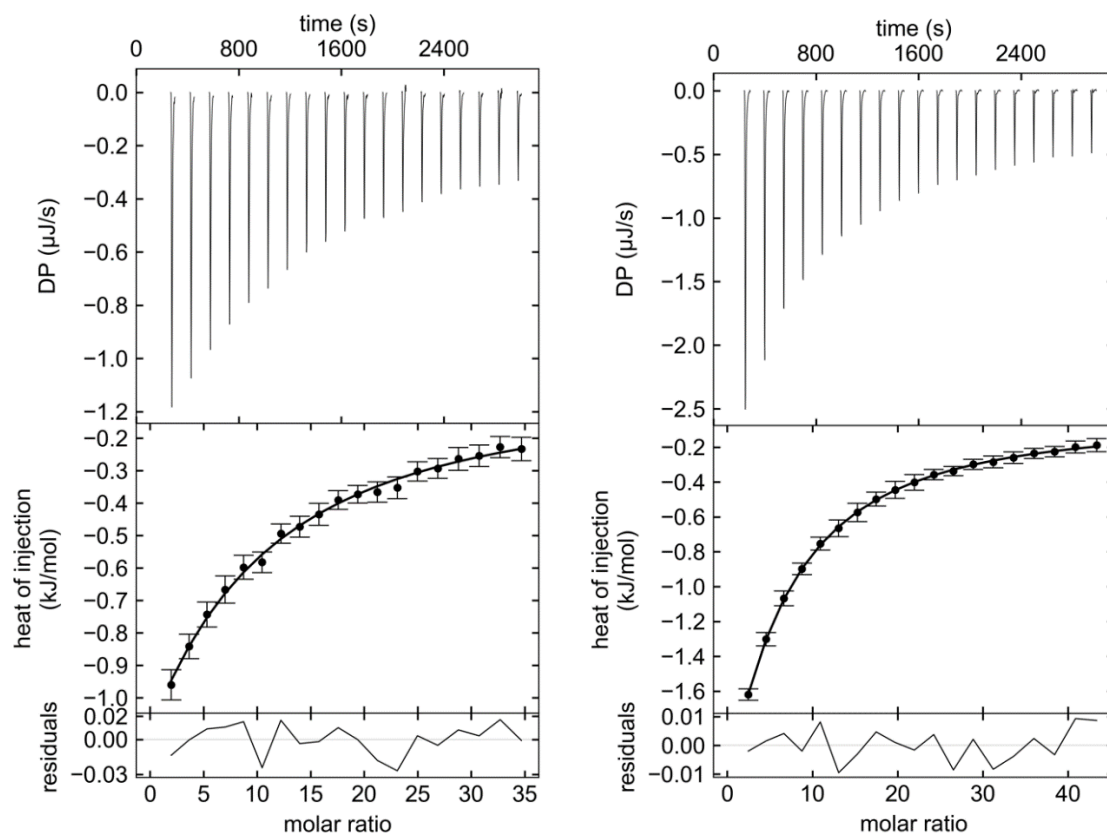


Figure S43. Thermograms and binding isotherms from ITC experiments with **1l** (left) and **1n** (right).

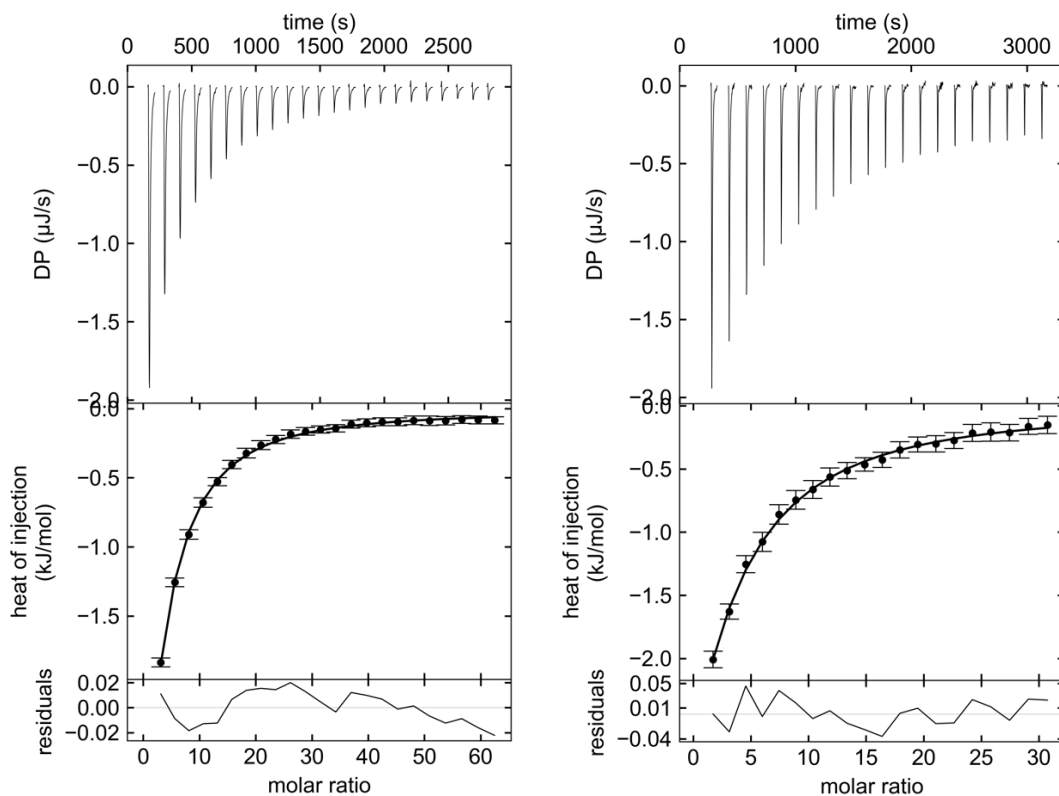


Figure S44. Thermograms and binding isotherms from ITC experiments with **1o** (left) and **1p** (right).

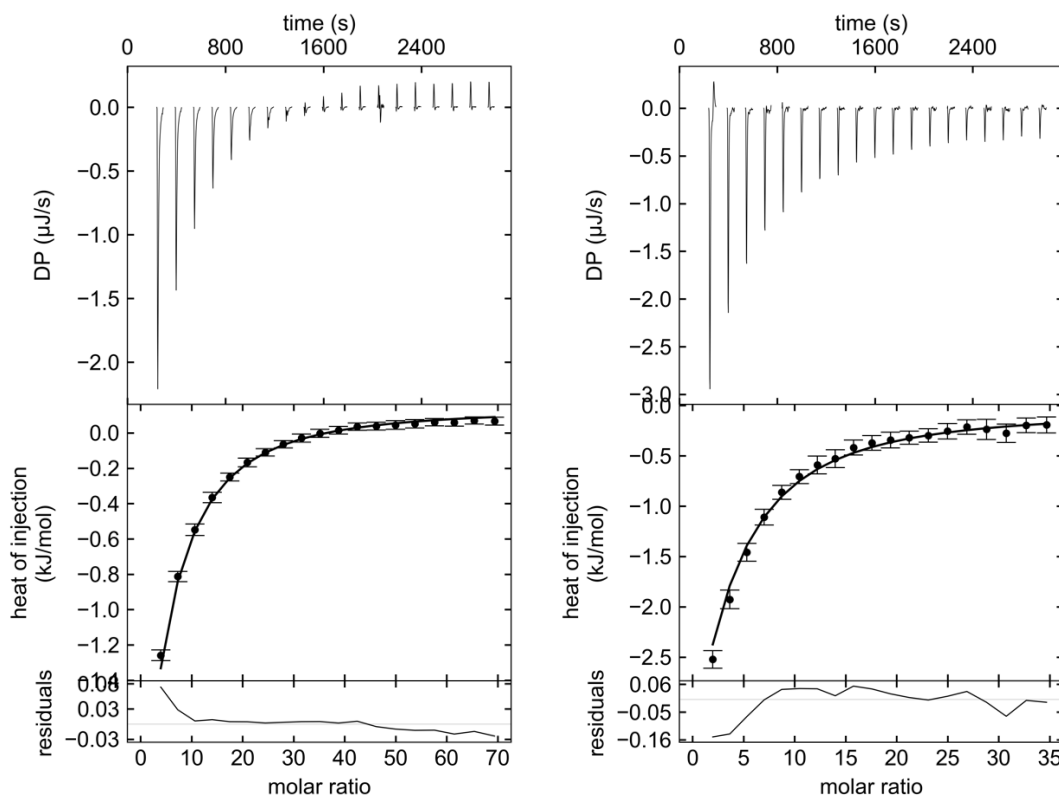


Figure S45. Thermograms and binding isotherms from ITC experiments with **1q** (left) and **1r** (right).

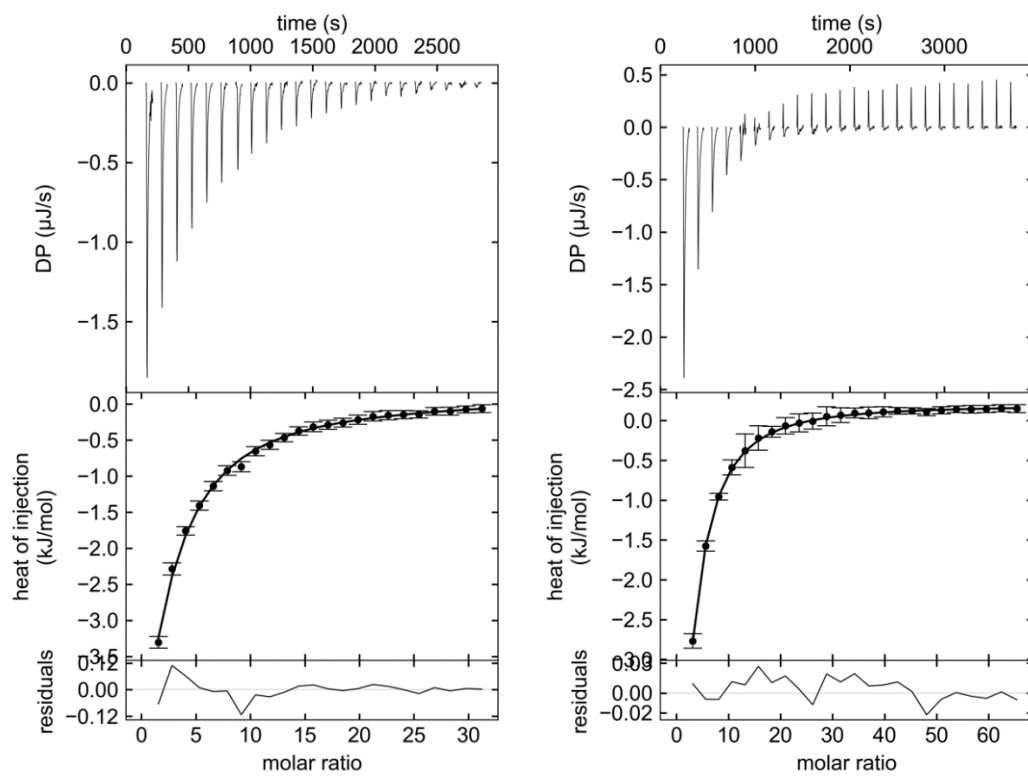


Figure S46. Thermograms and binding isotherms from ITC experiments with **1s** left and **10** (right).

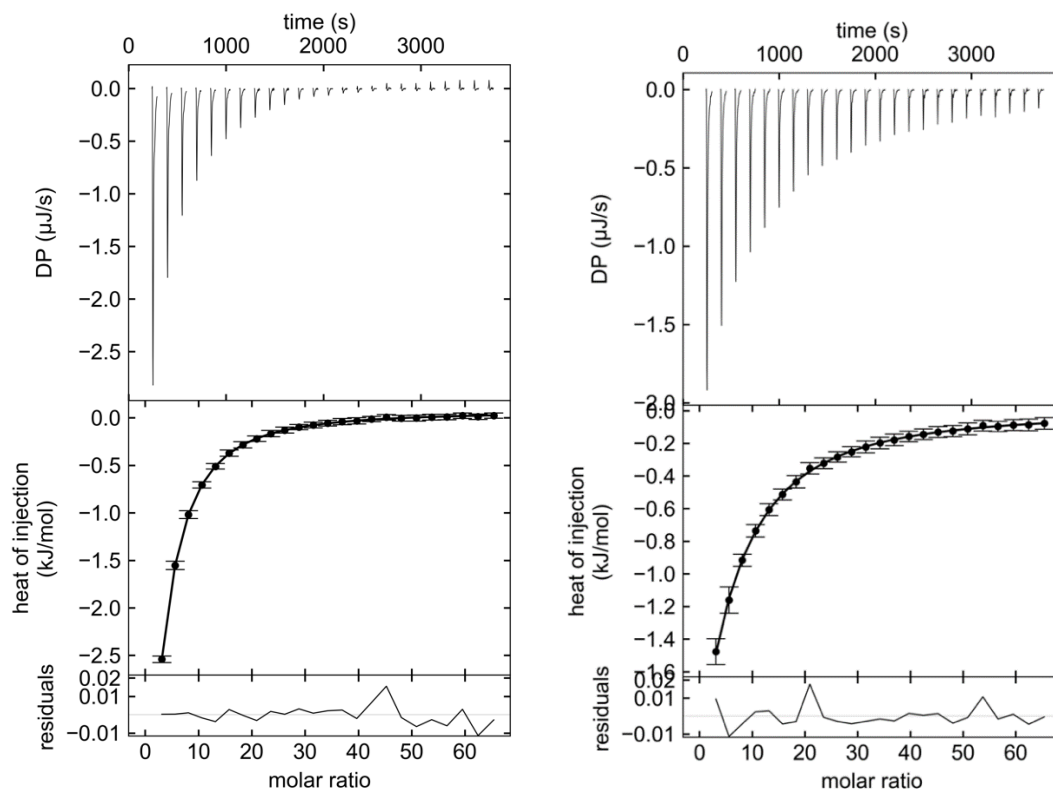


Figure S47. Thermograms and binding isotherms from ITC experiments with **11** (left) and **12** (right).

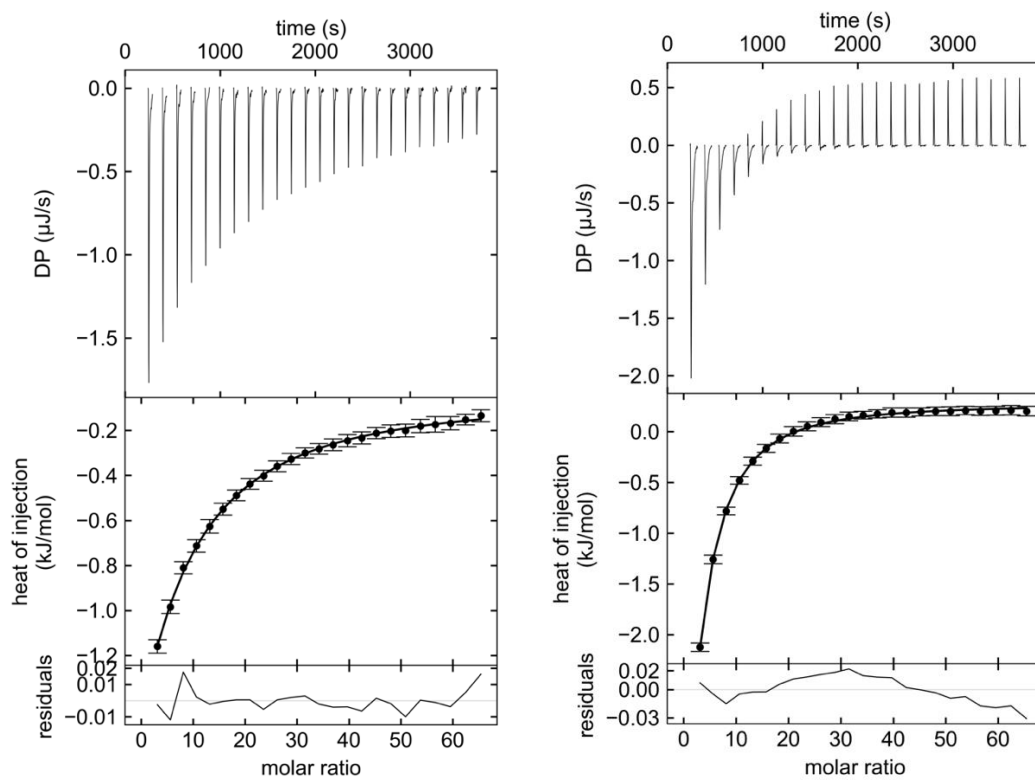


Figure S48. Thermograms and binding isotherms from ITC experiments with **13** (left) and **14** (right).

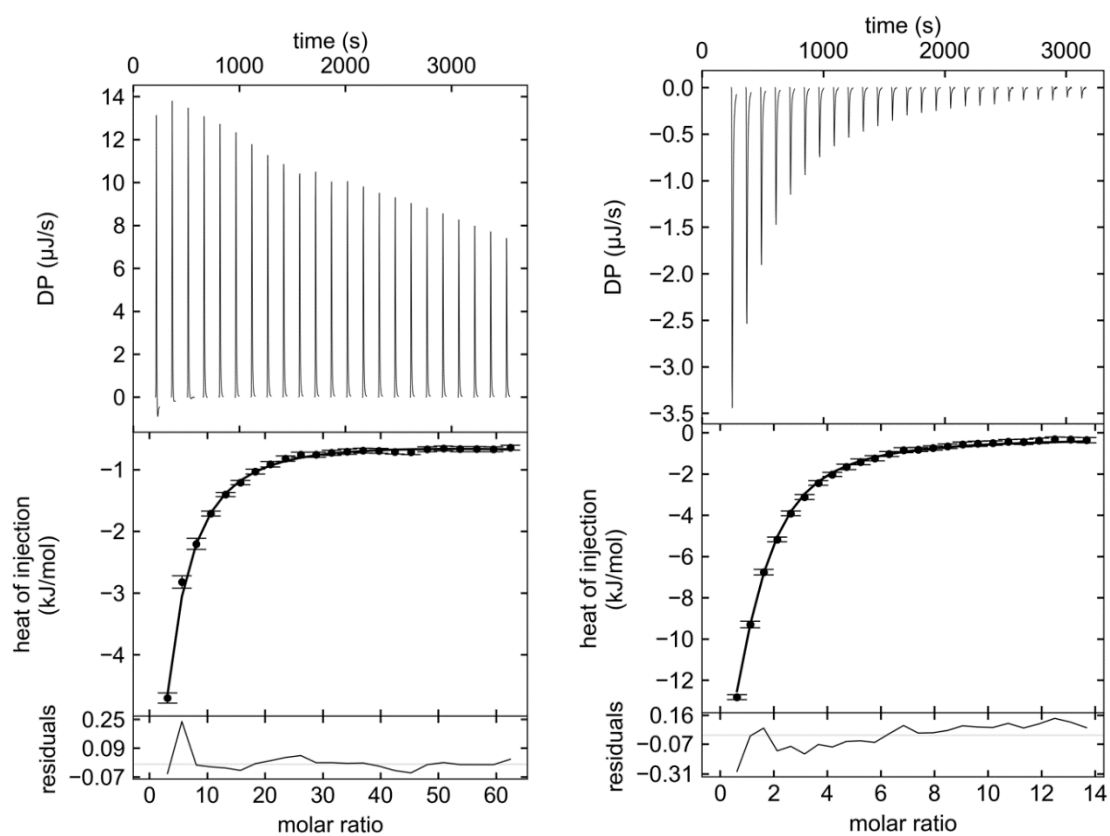


Figure S49. Thermograms and binding isotherms from ITC experiments with **15** (left) and **9** (right).

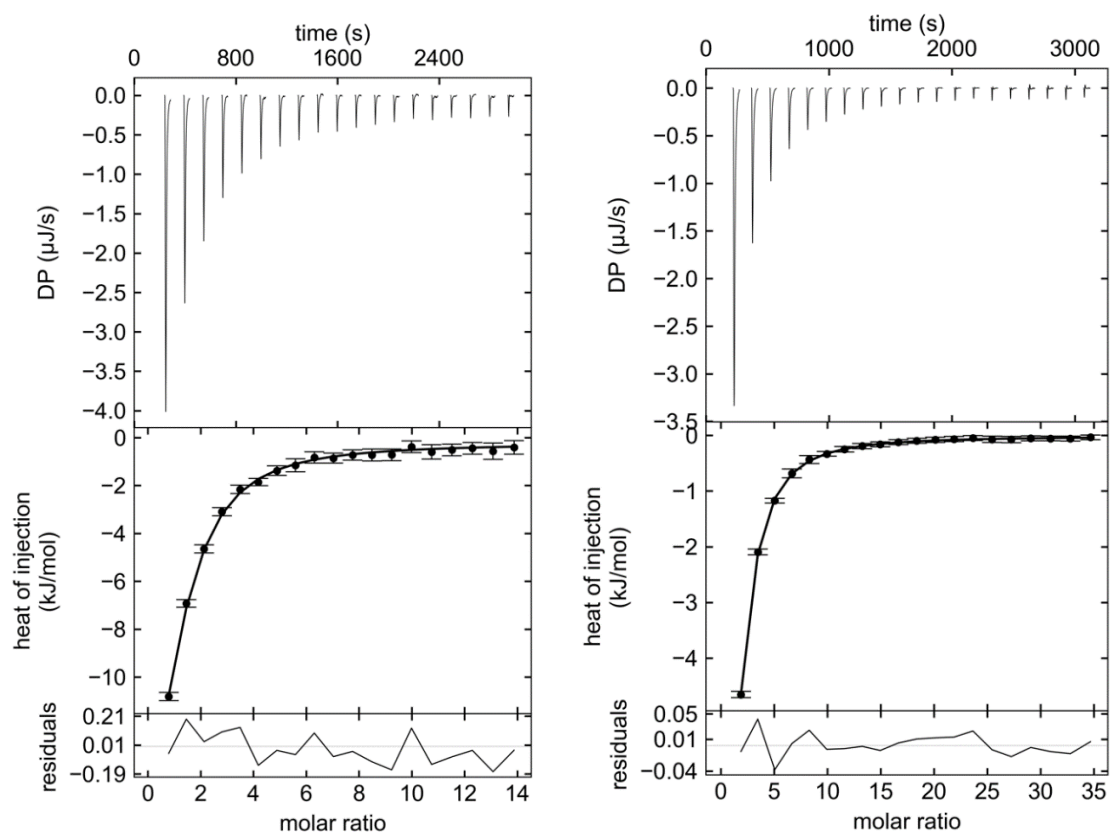


Figure S50. Thermograms and binding isotherms from ITC experiments with **19** (left) and **21** (right).

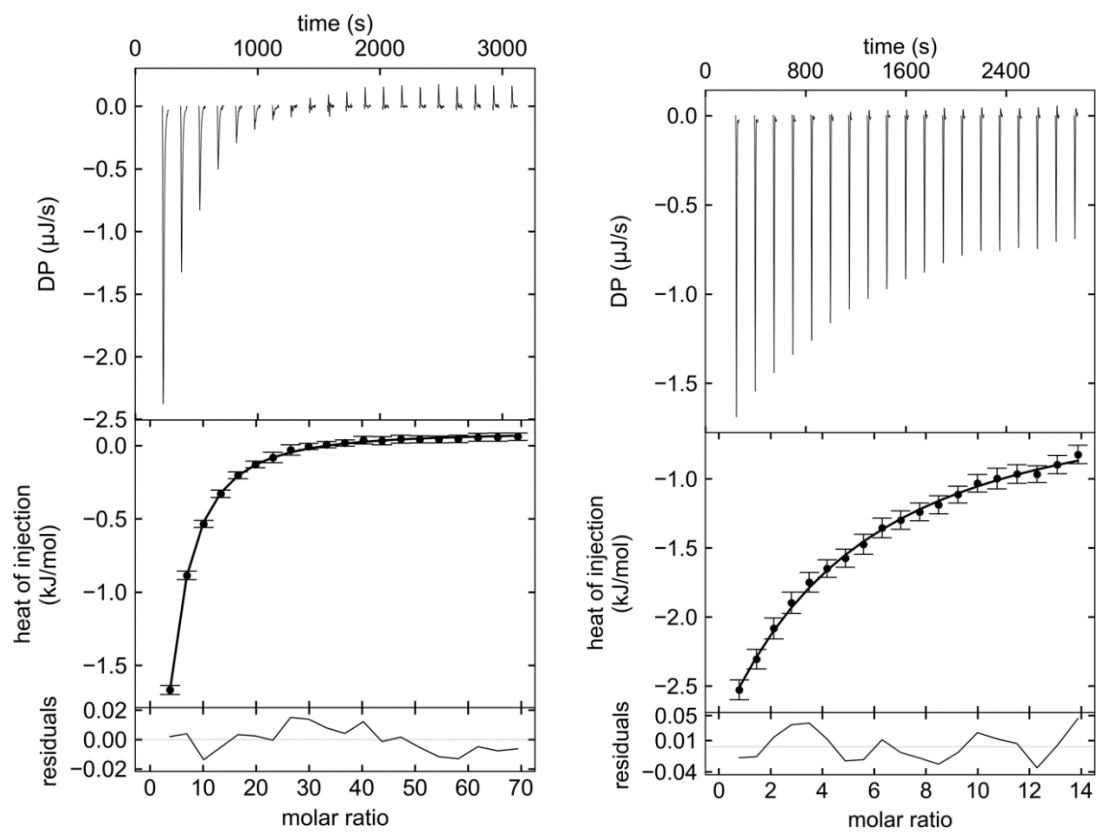


Figure S51. Thermograms and binding isotherms from ITC experiments with **23** (left) and **25** (right).

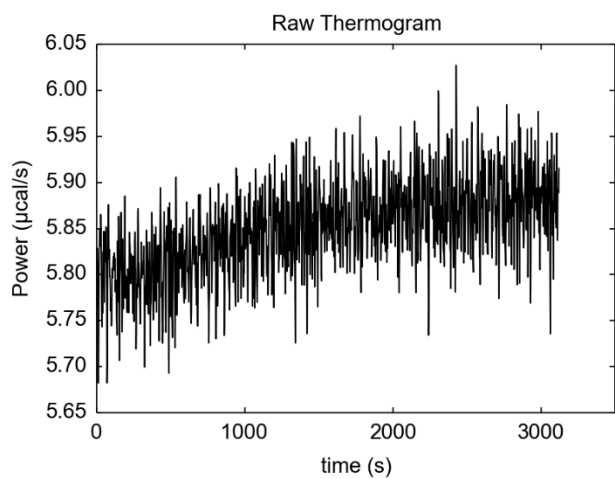


Figure S52. Raw thermogram from the titration of 10 mM **9** into 40 µM Langerin CRD.

X-ray Crystallography

Table S2. Statistics on diffraction data and refinement of DC-SIGN

ligand complexes

| | 1s | 9 |
|-----------------------------|----------------|----------------|
| PDB Identifier | 7NL6 | 7NL7 |
| Wavelength (Å) | 1.00004 | 1.00001 |
| Resolution range | 42.26 - 2.2 | 51.40 - 2.1 |
| (Å) | (2.28 - 2.2)* | (2.18 - 2.1)* |
| Space group | P 3 2 1 | P 3 2 1 |
| Unit cell | 59.5 59.5 73.9 | 59.3 59.3 75.2 |
| α, β, γ (°) | 90 90 120 | 90 90 120 |
| Total reflections | 105589 (10598) | 182378 (18326) |
| Unique reflections | 8051 (795) | 9333 (906) |
| Multiplicity | 13.1 (13.3) | 19.5 (20.2) |
| Completeness (%) | 99.8 (100.0) | 99.9 (100.0) |
| Mean I/sigma(I) | 6.5 (1.1) | 5.1 (1.9) |
| Wilson B-factor | 28.1 | 29.1 |
| R-merge (%) | 0.295 (1.75) | 0.408 (2.35) |
| Rpim (%) | 0.084 (0.49) | 0.094 (0.53) |
| CC1/2 | 0.991 (0.468) | 0.987 (0.745) |
| Reflections used in | | |
| Refinement | 8047 (795) | 9331 (906) |
| R-work | 0.194 (0.324) | 0.193 (0.279) |
| R-free | 0.229 (0.386) | 0.218 (0.321) |
| Number of atoms | 1202 | 1179 |
| water | 102 | 80 |
| Protein residues | 135 | 135 |
| RMS(bonds) | 0.005 | 0.007 |
| RMS(angles) | 0.95 | 0.93 |
| Ramachandran | 99.2 | 98.4 |

| | | |
|------------------|------|------|
| favored (%) | | |
| Ramachandran | | |
| outliers (%) | 0.0 | 0 |
| Rotamer | | |
| outliers (%) | | |
| Clashscore | 0.97 | 4.84 |
| Average B-factor | 32.0 | 36.0 |

*The values in parentheses correspond to the highest resolution shell

Cellular Glycoprotein Binding and *trans*-Infection Assays

B-THP-1 DC-SIGN⁺ cells (cat# 9941, lot# 170243) and B-THP-1 cells (cat# 9940, lot# 170242) were obtained through the NIH AIDS Reagent Program, Division of AIDS, NIAID, NIH: from Drs. Li Wu and Vineet N. KewalRamani^[6] and maintained in RPMI 1640 medium (Sigma Aldrich, R8758, Lot RNBJ7502) supplemented with 10 % FBS (Gibco, 10270-106, Lot 2275-124), 1 % penicillin-streptomycin (Sigma Aldrich, P4333, Lot 109324) at 37 °C. Vero E6 cells were cultured in Dulbecco's modified Eagle medium (DMEM, Sigma Aldrich, D6546, Lot RNBJ7247) supplemented with 10% FBS (Gibco, 10270-106, Lot 2275-124), 2 mM L-glutamine (BioConcept, 5-10K00-H, Lot MC07939P), and 1 % penicillin-streptomycin (Sigma Aldrich, P4333, Lot 109324). Recombinant SARS-CoV-2 spike S1-His glycoprotein was obtained from Sino Biological (cat# 40591-V08H) and labeled with Cy5-NHS ester (Lumiprobe, cat# 13020). Viral stocks of VSVΔG-SARS-CoV-2-SΔ21-GFP were propagated on Vero E6 cells at a MOI=0.01 in DMEM supplemented with 10% FBS and 2 mM L-glutamine at 37 °C. After 72 h of incubation, when extensive cytopathic effect was observed, viral supernatants were harvested and centrifuged at 1000 g for 5 min, to remove cell debris. The supernatant was aliquoted and stored at -80 °C until use, without additional freeze-thaw cycles.

For generation of a chimeric vesicular stomatitis virus (VSV) lacking the homotypic glycoprotein G but rather expressing the spike protein of SARS-CoV-2 (Wuhan-Hu-1 strain) along with the green fluorescent protein (GFP), a cDNA encoding the spike protein with the mutations R685G, H655Y, D253N, W64R, G261R, A372T and C1253*^[7] was synthesized by Genscript (Piscataway, NJ, USA) and inserted into the plasmid pVSV*ΔG(MERS-S),^[8]

thereby replacing the MERS-CoV spike gene. The recombinant virus was generated according to a published procedure.^[9] Viral stocks of VSV Δ G-SARS-CoV-2-S Δ 21-GFP were propagated on Vero E6 cells at a MOI=0.01 in DMEM supplemented with 10% FBS and 2 mM L-glutamine at 37 °C. After 72 h of incubation, when extensive cytopathic effect was observed, viral supernatants were harvested and centrifuged at 1000 g for 5 min, to remove cell debris. The supernatant was aliquoted and stored at -80 °C until use, without additional freeze-thaw cycles.

For SARS-CoV-2 spike glycoprotein binding assays, 50000 cells were seeded in 50 μ L complete medium in a well of a 96-well plate. A serial dilution of the investigated ligand was prepared and mixed with an equal volume of Cy5-labeled glycoprotein. This mixture was added to the cell suspension to a final volume of 100 μ L and a final glycoprotein concentration of 10 nM. After incubation for 30 min (37 °C, 5 % CO₂), the cells were centrifuged (5 min, 100 g) and washed with warm PBS. Data were collected on a Cytoflex flow cytometer (Beckman Coulter, Indianapolis, USA) and analyzed with FlowJo (FlowJo LLC). Mean fluorescence intensities were plotted and a nonlinear regression analysis employing a four parameter Hill model was performed with Prism 8 (Graphpad, San Diego, USA).

For trans-infection inhibition studies, B-THP-1 cells (2×10^4) and B-THP-1 DC-SIGN cells (2×10^4) were incubated with **9** and **33** for 30 min before addition of SARS-CoV-2 pseudotyped viruses (VSV Δ G-SARS-CoV2-S Δ 21-GFP, 1000 PFU) and further incubation for 1 h at rt with gentle rotation. The cells were then washed twice with PBS (Sigma Aldrich, D8662, Lot RNBH0978) and co-cultivated with adherent Vero E6 cells (2×10^4) for 6 h at 37 °C, 5% CO₂ on a 96-well plate. The wells were washed with medium to remove suspension cells (B-THP-1/B-THP-1 DC-SIGN) and the remaining Vero E6 cells were trypsinized with 0.25% trypsin-EDTA (Gibco, 25200-056, Lot 2246812) until they detached. The reaction was stopped by addition of DMEM and the cells were immediately analyzed using a Cytoflex flow cytometer (Beckman Coulter, Indianapolis, USA) by recording the GFP signal. To assess the inhibitory activity of the compounds, the infection efficiency (GFP positive cells) was plotted and a nonlinear regression analysis employing a four parameter Hill model was performed with Prism 8 (Graphpad, San Diego, USA). In absence of inhibitors, *trans*-infection resulted in infection rates around 20%, while direct *cis*-infection of Vero E6 cells with 1000 PFU, resulted in infection rates of around 90% (after 6h incubation). Incubation with control B-THP-1 cells did not lead to *trans*-infection.

References

- [1] J. Cramer, B. Aliu, X. Jiang, T. Sharpe, L. Pang, A. Hadorn, Rabbani, B. Ernst, *ChemMedChem* **2021**, Temporary Reference.
- [2] J. Tellinghuisen, *Biochim. Biophys. Acta - Gen. Subj.* **2016**, *1860*, 861–867.
- [3] J. Tellinghuisen, *Anal. Biochem.* **2012**, *424*, 211–220.
- [4] W. B. Turnbull, A. H. Daranas, *J. Am. Chem. Soc.* **2003**, *125*, 14859–66.
- [5] J. Tellinghuisen, *Anal. Biochem.* **2016**, *513*, 43–46.
- [6] L. Wu, T. D. Martin, M. Carrington, V. N. KewalRamani, *Virology* **2004**, *318*, 17–23.
- [7] M. E. Dieterle, D. Haslwanter, R. H. Bortz, A. S. Wirchnianski, G. Lasso, O. Vergnolle, S. A. Abbasi, J. M. Fels, E. Lauder Milch, C. Florez, A. Mengotto, D. Kimmel, R. J. Malonis, G. Georgiev, J. Quiroz, J. Barnhill, L. anne Pirofski, J. P. Daily, J. M. Dye, J. R. Lai, A. S. Herbert, K. Chandran, R. K. Jangra, *Cell Host Microbe* **2020**, *28*, 486-496.e6.
- [8] S. Pfaender, K. B. Mar, E. Michailidis, A. Kratzel, I. N. Boys, P. V'kovski, W. Fan, J. N. Kelly, D. Hirt, N. Ebert, H. Stalder, H. Kleine-Weber, M. Hoffmann, H. H. Hoffmann, M. Saeed, R. Dijkman, E. Steinmann, M. Wight-Carter, M. B. McDougal, N. W. Hanners, S. Pöhlmann, T. Gallagher, D. Todt, G. Zimmer, C. M. Rice, J. W. Schoggins, V. Thiel, *Nat. Microbiol.* **2020**, *5*, 1330–1339.
- [9] S. Locher, M. Schwenecker, J. Hausmann, G. Zimmer, *J. Gen. Virol.* **2018**, *99*, 866–879.

Acknowledgements

An exciting journey is coming to an end and I would like to take this opportunity to thank all the amazing people who I had the pleasure to work with and meet during my PhD. I am grateful for the great time we could spend together.

First and foremost, I would like to thank **Prof. Dr. Beat Ernst** for the great support over the last few years. Thank you Beat for your guidance, encouragement, and motivation. Thank you for giving me the opportunity to explore exiting scientific areas, I learned a lot from you.

Many thanks to **Prof. Dr. Daniel Ricklin** for co-supervising my PhD thesis. I appreciated your kind support, always making time if I needed your help and making sure to remove any obstacles along the way.

Special thanks go to **Pascal** and **Ruben** for welcoming me into your big adventure. I really appreciate all the support I received from you guys and that you took me along on this journey. I learned a lot from you two during these years. Thank you Pascal for believing in me, for all your help and for making sure we never had a boring day at work.

I want to thank **Prof. Dr. Henriette Meyer zu Schwabendissen** for accepting the role as my second supervisor and **Dr. John Gatfield** for offering to co-referee my thesis.

Big thanks go to my lab mate **Jonathan** for being kind, supportive and a great companion. Thank you for always taking the time when I bothered you with weird questions and for somehow always giving the right advice. Thank you **Gabriele** and **Adem** for creating a nice atmosphere in our lab. It made working in a chemistry lab much more bearable.

I would like to thank all you people on 4th floor. I really appreciated all the fun we had. Thank you **Rachel** for being kind and keeping the group together. And for hosting all our movie and fondue nights, I'm sure we will eventually manage to actually watch a movie.

Thanks to **Christina**, and **Clement** for hosting me when I needed a break. Thank you **Richard** for being helpful all the times I bothered you with scientific questions. Special thanks to **Kevin** for all the time we spent together either hunting coffee spots or coffee machines or just enjoying a break.

Thank you to the Italian fraction **Benedetta, Taigo, and Ivan** for bringing some southern energy to our floor.

Big thanks to all current and former Polyneuron people. Thank you **Li, Delphine, Horst, Pragya, Emilie, Thomas, Marjorie, Kea, Ramona Jeremy, and Ouliana** for all your help and support. I was always looking forward to coming to the lab in Allschwil or at Stücki because I knew we would be having a great talks and a great time.

I started with my thesis while many of you former IMP members were finishing up and being in the same position now, I think I can finally relate. I greatly enjoyed the time we had together **Philip, Christoph, Priska and Marleen**. Lunch and coffee breaks were always stimulating and lots of fun.

Special thanks to **Claudia, Xiaohua, and Bea** for all the support. You always had a solution to every problem.

Dear **Martin, Olly, and Said** lunch breaks with you guys were always enjoyable. No matter if we were talking politics or stock market.

Special thanks to **Tim and Wolf** for all your help with technical and scientific assistance. I knew you would always have the right answer to my questions.

Last but not least, I want to thank my family for the unconditional love and support and for all sacrifices you made for us to live a better life.